UNIVERSITY OF SOUTHAMPTON

FACULTY OF NATURAL AND ENVIRONMENTAL SCIENCES

Chemistry

Volume 1 of 1

Beyond standard resolution experimental structural studies of anion-receptor complexes.

by

Isabelle Louise Kirby

Thesis for the degree of Doctor of Philosophy

October 2014

Dedication:

To my Mum, Stephanie Kirby (1953-2011), the first Dr. Kirby.

Thank you for all the love you gave me, the faith you had in me, and the amazing example you were for me.

UNIVERSITY OF SOUTHAMPTON

ABSTRACT

FACULTY OF NATURAL AND ENVIRONMENTAL SCIENCES

Chemistry

Thesis for the degree of Doctor of Philosophy

BEYOND STANDARD RESOLUTION EXPERIMENTAL STRUCTURAL STUDIES OF ANION-RECEPTOR COMPLEXES.

Isabelle Louise Kirby

This thesis reports the anion recognition properties of a family of (thio)urea-based receptors and their anion-receptor complexes. A comprehensive, systematic structural analysis has been undertaken in the solid-state by single crystal X-ray and neutron diffraction experiments, complemented by proton NMR titration studies in solution. The experimental electron density distribution in a series of these complexes has then been modelled and analysed using the 'Quantum Theory of Atoms in Molecules' (QTAIM).

Three modifications have been made to the complexes, with changes in anion type, receptor substituent pattern, and hydrogen bond donor group. The strength of hydrogen bonding has been quantified and for the first time the correlation in anion-receptor complexes between hydrogen bond strength and anion basicity observed in the solid-state. The necessity of these studies to categorically determine the existence of non-covalent interactions is demonstrated. The effect of substituent and crystal structure environment on the electron density distribution across the individual units of the complexes is illustrated through mapping of the experimental electrostatic potential distributions and comparison of the QTAIM atomic charges.

Table of Contents

List of tables

List of figures

List of accompanying materials

Electronic Appendix with the Crystallographic Information Files for the crystal structures reported in this thesis. These are organised according to the chapter in which the main discussion of the crystal structure occurs and are accompanied by full crystallographic tables for the standard resolution datasets and by the xd_geom output files for the high resolution multipole refinements of the crystal structures, which gives tables of atomic coordinates, bond distances and angles and multipole populations.

Receptor and crystal structure numbering guide.

Guide to anion-receptor molecules.

DECLARATION OF AUTHORSHIP

I, Isabelle Louise Kirby

declare that this thesis and the work presented in it are my own and has been generated by me as the result of my own original research.

Beyond standard resolution structural determination of anion–receptor complexes.

I confirm that:

1. This work was done wholly or mainly while in candidature for a research degree at this University;
2. Where any part of this thesis has previously been submitted for a degree or any other qualification at this University or any other institution, this has been clearly stated;
3. Where I have consulted the published work of others, this is always clearly attributed;
4. Where I have quoted from the work of others, the source is always given. With the exception of such quotations, this thesis is entirely my own work;
5. I have acknowledged all main sources of help;
6. Where the thesis is based on work done by myself jointly with others, I have made clear exactly what was done by others and what I have contributed myself;
7. Parts of this work have been published as:

- Systematic structural analysis of a series of anion receptor complexes. Kirby, I. L; Pitak, M. B; Wenzel, M; Wilson, C; Sparkes, H. A; Coles, S. J; Gale, P. A., *CrystEngComm*, 2013, **15**, 9003 – 9010.
- Systematic experimental charge density analysis of anion receptor complexes. Kirby, I. L; Brightwell, M; Pitak, M. B; Wilson, C; Coles, S. J; Gale, P. A., *Phys. Chem. Chem. Phys.*, 2014, **16**, 10943 – 10958.
- Systematic experimental charge density: linking structural modifications to electron density distributions. Kirby, I. L; Pitak, M. B; Coles, S. J; Gale, P. A., *Chem. Letts.*, 2015, **44**, 2 – 9.

Signed: .....

Date: .....

Acknowledgements

I have received an incredible amount of support over the past four years and am very grateful. Thanks in particular go to:

My supervisors, Phil Gale and Simon Coles, for the opportunity to undertake this doctorate and the supportive research environment they've provided.

Mateusz ‘Pole Dancer’ Pitak and Claire ‘Diamond Gal’ Wilson for late night data collections, an incredible amount of advice and for generally being awesome.

Gale group: Louise ‘Karagenius’ Karagiannidis, Franci Piana, Nathalie Busschaert, Jenny Hiscock, Wim van Rossom, Harriet Clarke, Cally Haynes, Steve Moore, Sam Keltie, Marco Wenzel, Stuart Berry, Mike Spooner, Xin Wu and my project student Mark Brightwell.

NCS team: Pete ‘Ninja Pete’ Horton, Graham ‘King Brilliant’ Tizzard, Sarah Milsted, and fellow PhD students Phil Adler, Lisa ‘Scottish’ Blair and Lucy Mapp.

Mark Light (X-ray), Neil Wells (NMR), John Langley and Julie Herniman (Mass spectrometry), and Hazel Sparkes (ISIS Neutron source). Thanks also to Karl, Clive, Keith and Mark in stores.

Great friends: Alice Beech, Rachael Millar, Rose Chappell, Martyn Hiscock, Matthew Potter, Adam Fisher, Andy Naylor, Lloyd Sayer, Tim Kamps, Arinze Ekwosimba, Rebecca Driesener, James Justin Roges, Dominique Barretto, Davide 'The Italian' Zilli, Virginia Adnan, Catherine Cruz and Valentina Stilo.

Special thanks to my family, for everything. Love you lots. My amazing Dad, my super big sis, Ellie and much loved and missed Mum.

Finally, thanks be to God, who working in us can do more than we can possibly imagine.

Definitions and Abbreviations

A: Acceptor

ADPs: Anisotropic displacement parameters

Å: Angstrom

BCP: Bond critical point

BP: Bond path

CAHB: Charge assisted hydrogen bond

CCD: Charge coupled detectors

CCP: Cage critical point

CFTR: Cystic fibrosis transmembrane conductance regulator

CIF: Crystallographic Information File

cm: centimetres

CP: Critical point

CSD: Cambridge Structural Database

D: Donor

DCM: Dichloromethane

DFT: Density functional theory

DMSDAs: Difference of mean-square displacement amplitudes

DMSO: Dimethylsulfoxide

DNA: Deoxyribonucleic acid

e: electrons

ESP: Electrostatic potential

Eq.: Equation

eq.: equivalents

g: grams

GoF: Goodness of Fit

H: Hydrogen atom

HF: Hartree-Fock

IAM: Independent atom model

IHB: Isolated hydrogen bond

ITC: Isothermal titration calorimetry

K: Kelvin

K_{ass}: Association constant

kJ: kilo Joule

LCAO: Linear combination of atomic orbitals

M: Molarity

MH: Mega Hertz

mL: millilitres

MM: Multipole model

mm: millimetres

mol: moles

MP: Melting point

NA: Nuclear attractor

nd: not determined

N_{ref}/ N_{var}: Ratio of number of reflections to number of variables

NMR: Nuclear magnetic resonance

PAHB: Polarization assisted hydrogen bond

pK_a: Acid dissociation constant

ppm: parts per million

QSAR: Quantitative Structure Activity Relationship

QTAIM: Quantum Theory of Atoms in Molecules

RAHB: Resonance assisted hydrogen bond

RDA: Residual density analysis

RCP: Ring critical point

R_{ij}: Bond path length

SHADE: Simple Hydrogen Anisotropic Displacement Estimator

TBA: Tetrabutylammonium

TEA: Tetraethylammonium

TMA: Tetramethylammonium

Tren: Tris(2-aminoethyl)amine

UV-Vis: Ultraviolet-visible (spectroscopy)

µm: microlitres

V: Volume

VSCCs: Valence shell charge concentrations

VSCDs: Valence shell charge depletions

Chapter 1: Supramolecular chemistry

1.1 Supramolecular chemistry

Supramolecular chemistry, 'Chemistry beyond the molecule'[1] is the study of how individual chemical entities come together and form molecular assemblies. The association between molecules in these assemblies is governed by intermolecular non-covalent interactions. These supramolecular systems can be viewed as consisting of '*host*' molecules and '*guest*' molecules. *Hosts* were defined by Cram as molecular substances possessing convergent binding sites and *guests* as entities containing a divergent binding site.[2] During the development of supramolecular chemistry, chemists have become more experienced in the design of supramolecular systems to tailor specific interactions between desired *hosts* and *guests*. With a wide range of biological, physiological and environmental processes involving supramolecular systems and governed by non-covalent interactions this has become an increasingly vital field of research. Selective and specific interactions between *hosts* and *guests* can be engineered through complementary matching of the stereoelectronic arrangements of their recognition (*binding*) sites. *Guest* molecules range from monoatomic cations and inorganic anions, to amino acids and larger complex molecules such as peptides, hormones and deoxyribonucleic acid (DNA). This thesis focuses on the interactions between anionic guest species and simple synthetic hosts for these anions, termed anion-receptors, and specifically the resulting complexes, referred to as anion-receptor complexes.

1.2 Anions

1.2.1 Occurrence and prevalence

Anions exist in a wide range of forms and are found in a variety of settings.[3] They play a crucial role in physiological mechanisms, with 70–75% of the substrates and cofactors engaged in biological processes being negatively charged.[4] Hydrogensulfate (HSO_4^-) and dihydrogenphosphate ($H_2PO_4^-$) play a structural role in proteins, while chloride, phosphate and sulfate have been shown to regulate the flux of metabolites in and out of cells.[3] Misregulation of these mechanisms are associated with a variety of disease states, for instance the presence of a faulty malfunctioning cystic fibrosis transmembrane conductance regulator (CFTR) chloride transport channel causes cystic fibrosis.[5] Anions are also environmental pollutants; nitrates and phosphates found in agricultural fertilisers are a major cause of the eutrophication of lakes, and the pertechnetate anion (TcO_4^-) is a radioactive waste product of nuclear fuel reprocessing.[6]

1.2.2 Nature and character

Anions cover a broad range of sizes from the small fluoride anion (1.33 Å)[7] to the large complex structure of DNA (up to 85 nm long). They also tend to be larger and more diffuse in nature than their isoelectronic cations.[8]

A variety of different shaped anions are found:

- Spherical – halogen atom based anions e.g. F^-, Cl^-, Br^-, I^-
- Linear – examples include cyanide (^-CN) and hydroxide (^-OH)
- Trigonal planar (Y-shaped) – carbonate (CO_3^{2-}), nitrate (NO_3^-) and carboxylates (RCO_2^-)

- Tetrahedral – sulfate (SO_4^{2-})
- Octahedral – $Fe(CN)_6^{4-}$
- Complex structures – many biologically important anions have complex shapes for example nucleotides, proteins and the double stranded helix of DNA

The hydrophobicity of anions also alters following the trend described by the Hofmeister series[9], with the hydrophilicity increasing from left to right.

$ClO_4^- < SCN^- < I^- < NO_3^- < Br^- < Cl^- < HCO_3^- < H_2PO_4^- < F^- < SO_4^{2-} < HPO_4^{2-}$

Sulfate and hydrogenphosphate are far more strongly solvated than the anions such as perchlorate (ClO_4^-) on the left hand side of the series.

The differences in the basicity of anions can also be examined by comparison of the pK_a values of the anions' conjugate acids.

1.3 Anion-receptor chemistry

The prevalence of anions in our environment (discussed in Section 1.2.1) and their pivotal roles in key biological processes means that much interest is directed in designing and tailoring receptor molecules that are capable of interacting with them. Such receptors have applications as sensors, catalysts and therapeutic agents. The variety in the nature and character of anions means that the design of receptors is a challenge, but there is also the opportunity to confer selectivity for a particular anion by specifically tailoring the receptor shape and electronics to suit the character of the anion. There is a large 'arsenal' of non-covalent interactions for supramolecular chemists to utilise when designing anion-receptors and these will be described in further detail.

1.3.1 Anion binding interactions

A wide variety of non-covalent interactions are used in anion recognition. These may be a direct interaction between the anion and receptor or a serendipitous interaction that serves to stabilise the resulting anion-receptor complex.

i. Electrostatic interactions: Charge-charge interactions for example ion-ion, ion-dipole and dipole-dipole interactions. These tend to be the strongest non-covalent interactions with high bond energies of 100 - 350 kJ mol^{-1}, 50 - 200 kJ mol^{-1} and 5 - 50 kJ mol^{-1} respectively.

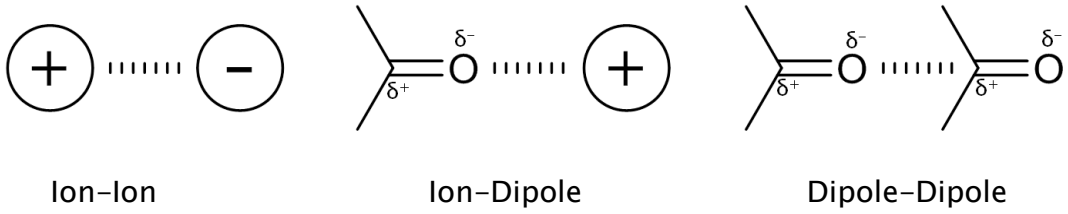

Figure 1.1: Schematic representation of the types of electrostatic interactions.

ii. Halogen bonding: The attractive interaction between an electrophilic region of a halogen atom and a nucleophilic electron rich molecular fragment, e.g. R—Halogen···Y.[10,11] Their bond energies cover a range of 5 - 180 kJ mol^{-1}.

iii. Anion···π interactions: Interaction of an electron deficient π-system with an anion. The bond energy is low. The analogous cation···π interactions between a positively charged species and electron-rich π-system are also exploited in supramolecular chemistry.

iv. Hydrophobic and solvophobic effects: The attractive interaction between two or more components, which share a common solvophobicity or hydrophobicity.

v. van der Waals interactions: Weak interactions caused by a temporary dipole in one atom or molecule inducing a dipole in an adjacent atom or molecule. The bond energies are usually $\leq$ 5 kJ mol^{-1} but can cumulatively become important for anion binding.

vi. Lewis acid···Lewis base interactions: The Lewis acid-based receptor accepts an electron pair from the anion.

vii. Hydrogen bonding: The attraction of a dipole to a hydrogen atom attached to an electronegative atom or electron-withdrawing group. Bond energies are between 1 - 160 kJ mol^{-1}. Hydrogen bonds can coordinate neutral and anionic guests. Due to the prominence of hydrogen bonding in anion recognition this interaction will be described in further detail below.

1.3.2 Hydrogen bonding

Described by Desiraju[12] as the most reliable and directional interaction in supramolecular chemistry, it is no surprise these interactions are the workhorse of supramolecular systems.

The interaction is of the type X—H···Y, where the hydrogen bond donor atom (X) is an electronegative atom and removes electron density from the hydrogen atom (H). This forms a partial positive charge on the hydrogen atom leading to a coulombic attractive interaction between the hydrogen atom and the

hydrogen bond acceptor atom (Y). Traditionally, hydrogen bond donor atoms are oxygen, fluorine, sulfur and nitrogen and the hydrogen bond acceptor atoms are oxygen, nitrogen, fluorine, sulfur, carbon or an anionic species. These are often termed 'strong' or 'conventional' hydrogen bonds, with O—H···O and N—H···O classic examples. The energies of these 'strong' hydrogen bonds range from 20 – 40 kJ mol^{-1}. Many geometric evaluations of hydrogen bonding have been performed and it has been shown that for the above interactions the H···A distance (distance between the hydrogen atom and acceptor atom) are 1.80 – 2.00 Å (N—H···O) and 1.60 – 1.80 Å (O—H···O). Ranges for the DHA angle (the angle between the donor atom, hydrogen atom and acceptor atom) are 150 –160° and 120 – 130° respectively. As well as the linear arrangement outlined bifurcated and trifurcated configurations are also observed in solid-state structures. Weaker hydrogen bonding interactions have been the subject of some controversy, but have been studied and are becoming more widely accepted as an additional tool in supramolecular chemistry and crystal engineering. Weaker hydrogen bonds reported include C—H···O, O—H···π, C—H···N and N—H···π interactions. Alkenes and alkynes are also capable of behaving as acceptor atoms. The strengths of these interactions are much lower (2 – 20 kJ mol^{-1}). Numerous studies based on the crystal structures deposited in the Cambridge structural database (CSD)[13] have set out geometric criteria for C—H···O bonds, with DHA angles $< 120°$ ruled out as genuine interactions.[14–16]

By combining multiple hydrogen bonding interactions in unison to bind an anion, selectivity and improved binding strength can be achieved. Intramolecular hydrogen bonds can also be used to pre-organise anion-receptor systems and can stabilise and promote particular conformations of molecules in the solid-state.

Despite there being no definitive hydrogen bonding model, one useful theory, which will be applied in the later chapters in this thesis, is that of Gilli and Gilli.[17] In their study they describe five classes into which O—H···O bonds can be divided, which are also applicable to N—H···O and O—H···N hydrogen bonds (see Table 1.1).

Table 1.1: Table of hydrogen bond classifications according to Gilli and Gilli[17].

Class	Strength	Formula	Name	Acronym
A	Strong	[–O···H···O–]$^-$	Negative charge assisted hydrogen bonds (also known as salt bridges)	(–)CAHB
B	Strong	[=O···H···O=]$^+$	Positive charge assisted hydrogen bonds	(+)CAHB
C	Strong	–O···H···O= The two oxygen atoms are connected by a π–conjugated system	Resonance assisted hydrogen bonds	RAHB
D	Moderate	···(R)O–H···O(R)–H···	Polarization assisted hydrogen bonds	PAHB
E	Weak	–O–H···O(R)$_2$	Isolated hydrogen bonds	IHB

1.3.3 Characterising anion-receptor interactions

It is important to be able to fully characterise the relationship between a receptor and an anionic species, in order to determine the strength of association and the selectivity of a receptor for certain anions. The stoichiometry (the ratio and absolute value of the receptor to the anion) is also required to explain the function of anion-receptors. Often the ability of a series of related receptors to complex anions is compared. See for instance the QSAR analysis of the binding and transport abilities of a series of thiourea-based receptors.[18] This information allows chemists to design better structures for particular functions by assessing which functional groups best promote the desired behaviour. The interactions can be, and are, typically studied in both solution and the solid-state, with each environment having different challenges and conditions that require consideration. In addition to the methods outlined below, theoretical calculations, whether gas phase or periodic can supplement knowledge of the anion-receptor complexes, and mass spectrometry can also give information about the binding stoichiometry in the gas phase.

1.3.3.1 Solution state interactions

The strength of a host: guest interaction in solution (in this thesis the receptor: anion association) is measured by the affinity of a system. The association constant (also known as the binding constant), K_{ass} for a 1:1 (host: guest) system is defined as:[19]

(Eq. 1.1) $$K_{ass} = \frac{[HG]}{[H][G]}$$

with [*G*] the concentration of guest in mol dm^{-3} (M), [*H*] the concentration of host (again in M) and [*HG*] is the concentration of the host: guest complex (M).

The units of K_{ass} is thus M^{-1}, and in solution is dependent on numerous factors, including ion-pairing and critically the solvent in which the interaction is studied. Strongly coordinating solvents, especially more polar solvents with the ability to hydrogen bond to the receptor and anion, will compete with the host and guest. With weaker, less polar solvents this competition is reduced and hence the binding constant is higher. This means that the K_{ass} for different receptors and anions can only be compared if they were measured under identical solvent conditions. Common methods for determining the association constants are UV-Vis and NMR titration experiments. The method used depends on the magnitude of the binding constant. Further to this, isothermal titration calorimetry (ITC) is used to determine the thermodynamic parameters of the interactions between the anion and receptor, including not only K_{ass} but also the binding stoichiometry, the change in enthalpy (ΔH), the change in entropy (ΔS) and the change in Gibbs free energy (ΔG).

1.3.3.2 Solid-state interactions

In the solid-state the effect of solvent is largely irrelevant, and the direct interaction between the anion and receptor can be more easily studied. Loss of information about the effect of solvent can be detrimental for systems where the anion-receptor is expected to function in such conditions (e.g. molecules that transport anions across biological membranes or sense environmental pollutants in water sources). However, it can mirror the environment of molecular based machines and simplify the study of the association between an anion and a receptor molecule. Single crystal X-ray diffraction, as already commented on by Braga[20], has become one of the main tools of investigating supramolecular structures and their interactions in the solid-state. It is able to determine the anion: receptor ratio and the actual number of anions and receptors interacting with each other. The shape, orientation and geometry of

both the anion and receptor can be determined as well as the orientation and geometries of the anion and receptor in relation to each other. The strength of hydrogen bonding between anions and receptors is typically estimated from the geometry observed in crystal structures, with shorter distances between the D—H donor unit and the acceptor atom (the D—H···A distance) indicating stronger hydrogen bonding. These distances are often (and will be in this thesis) compared to the van der Waals radii of the atoms and the ionic radii of the ions involved in the interaction, to illustrate how close the contact is between the atoms and therefore give an idea of the relative strength of the hydrogen bonding interaction. These radii are shown in Table 1.2 for the appropriate atoms and ions (those that form hydrogen bonds in the crystal structures reported in this thesis) and are calculated from X-ray diffraction data.

Table 1.2: Table of van der Waals radii (from Bondi *et al.*,[21] except those of hydrogen which come from Rowland and Taylor[22]) and ionic radii (taken from Shannon[8]) for atoms and ions involved in hydrogen bonding interactions in the crystal structures discussed in this thesis.

Atom	Van der Waals radius (Å)	Ionic radius (Å)
Chlorine	1.75	1.81 (Cl^-)
Fluorine	1.47	1.33 (F^-)
Hydrogen	1.09	-
Nitrogen	1.55	-
Oxygen	1.52	-

The weak X-ray scattering power of hydrogen atoms means the accurate positions of hydrogen atoms is not possible using X-ray diffraction studies.

However, the use of neutron diffraction data does determine accurate hydrogen atom positions and can thus aid in the characterisation of supramolecular systems, indicating if hydrogen bonds are associated with a proton transfer event.[23]

1.3.4 Theoretical studies

Quantum mechanical studies are a valued technique in supramolecular chemistry and play an integral role in both predicting and explaining the behaviour of supramolecular systems (see the examples presented in the review of Gale and co-workers[24]), complementing the experimental studies carried out on these systems. It will be shown in Section 2.3 that the electron density distribution in a crystal system can also be obtained from experimental X-ray diffraction studies, and that this is the main focus of this thesis. However, the electron density of any gas phase or solid molecule can be calculated, and computational studies are often used in combination with experimental studies in charge density research. In this thesis computational studies are used to supplement, verify and critically evaluate the experimental studies performed in Chapters 4 and 5.

1.3.4.1 Theory of computational studies

In order to obtain the electron density, computational chemistry approaches must 'solve' the non-relativisitic, time-independent Schrödinger equation (Eq. 1.1):

(Eq. 1.1) $$\hat{H}\Psi = E\Psi$$

here $\hat{H}$ is the Hamilton operator, Ψ is the wavefunction (eigenfunction) and E is the energy of the system (eigenvalue). $\hat{H}$ is a differential operator, which represents the total energy, with M and N representing the nuclei and electrons

in the system (Eq 1.2). The first two terms describe the kinetic energy of the electrons and nuclei respectively, M_A is the mass of the nucleus A.[25]

(Eq. 1.2)

$$\hat{H} = -\frac{1}{2}\sum_{i=1}^{N}\nabla_i^2 - \frac{1}{2}\sum_{A=1}^{M}\frac{1}{M_A}\nabla_A^2 - \sum_{i=1}^{N}\sum_{A=1}^{M}\frac{Z_A}{r_{iA}} + \sum_{i=1}^{N}\sum_{j>i}^{N}\frac{1}{r_{ij}} + \sum_{A=1}^{M}\sum_{B>A}^{M}\frac{Z_A Z_B}{R_{AB}}$$

where $\nabla^2 = \frac{\partial^2}{\partial x_q^2} + \frac{\partial^2}{\partial y_q^2} + \frac{\partial^2}{\partial z_q^2}$

The energy of a system can be calculated using a rearranged form of the Schrödinger equation (Eq. 1.3)

(Eq. 1.3) $$E = \frac{\int \Psi \hat{H} \Psi^* d\tau}{\int \Psi \Psi^* d\tau}$$

The Schrödinger equation can only be solved exactly for the hydrogen atom and therefore for any larger system a series of approximations must be used. These include the Born-Oppenheimer approximation, where it is assumed that the electronic and nuclear motion can be separated. As nuclei move much slower than electrons, it is assumed that the nuclei positions are fixed and only the electronic motion need be taken into account. Therefore, the nuclei kinetic energy is zero and the potential energy due to nucleus-nucleus repulsion merely a constant. This reduces Equation 1.2 to the so-called electronic Hamiltonian $\hat{H}_{elec}$ (Eq 1.4)[25]:

(Eq. 1.4) $$\hat{H}_{elec} = -\frac{1}{2}\sum_{i=1}^{N}\nabla_i^2 - \sum_{i=1}^{N}\sum_{A=1}^{M}\frac{Z_A}{r_{iA}} + \sum_{i=1}^{N}\sum_{j>i}^{N}\frac{1}{r_{ij}}$$

$$= T_e + V_{ne} + V_{ee}$$

The energy now is the sum of the E_{elec} and the constant nuclear repulsion term (Eq 1.5)

(Eq. 1.5) $$E_{tot} = E_{elec} + E_{nuc}$$

where $E_{nuc} = \sum_{A=1}^{M} \sum_{B>A}^{M} \frac{z_A z_B}{R_{AB}}$

The Schrödinger equation is in this case referred to as the electronic Schrödinger equation (Eq. 1.6).

(Eq. 1.6) $\hat{H}_{elec} \Psi_{elec} = E_{elec} \Psi_{elec}$

The second assumption used is that of the linear combination of atomic orbitals (LCAOs). This assumes that the wavefunction of a polyelectronic system is the linear sum of all the one electron molecular wavefunctions and that each molecular wavefunction is a linear combination of the atomic wavefunctions.

Computational methods that use the above outlined principles are known as *ab-initio* methods and the most commonly used is the Hartree-Fock (HF) method.[26]

1.3.4.2 Density functional theory (DFT)

A popular alternative to the *ab-initio* methods discussed above is density functional theory (DFT). The estimation of a wavefunction is a computationally demanding process. In DFT the energy of the ground-state system is described by only the electron density and hence is less computationally demanding. Hohenberg and Kohn[27] provided proof for the correlation of the ground state of the electronic system and its electron density. The energy functional is calculated as the sum of two terms (see Eq. 1.7), the interaction of the electron with an external potential, $V_{ext}(\mathbf{r})$, and the contributions from the kinetic energy of the electrons and interelectronic interactions, $F[\rho(\mathbf{r})]$.

(Eq. 1.7) $E[\rho(\mathbf{r})] = \int V_{ext}(\mathbf{r}) \rho(\mathbf{r}) d\mathbf{r} + F[\rho(\mathbf{r})]$

Kohn and Sham developed a formalism for $F[\rho(\mathbf{r})]$[28] (see Eq. 1.8)

(Eq. 1.8) $$F[\rho(\mathbf{r})] = E_{KE}[\rho(\mathbf{r})] + E_H[\rho(\mathbf{r})] + E_{XC}[\rho(\mathbf{r})]$$

with $E_{KE}[\rho(\mathbf{r})]$ the kinetic energy of a system of non-interacting electrons with the same density ($\rho(\mathbf{r})$) as the real system. $E_H[\rho(\mathbf{r})]$ is the Hartree electrostatic energy calculated from the classical interaction between two charge densities. $E_{XC}[\rho(\mathbf{r})]$ is the contribution from exchange and correlation. Different functional forms can be used for $E_{XC}[\rho(\mathbf{r})]$. They include the local density approximation and the generalised gradient approximation. In this thesis the B3LYP hybrid functional[29,30] is used, which utilises a combination of Hartree-Fock exchange energy and exchange-correlation energy.

The discussion above has focused on gas phase calculations, where an isolated molecule is considered, and so external perturbations such as the electric field or other molecules (as in a crystal structure) are ignored. It is therefore of increasing interest to look at periodic electron densities, which can mimic crystal structures. This is possible using the CRYSTAL software package developed by Dovesi *et al.*, which incorporates Hartree-Fock and DFT-based methods and can model crystalline solids in 230 different space groups.[31]

In this thesis all the quantum mechanical studies are based on gas phase DFT methods.

1.4 Conclusions

A thorough understanding of the interactions that are inherent in anion-receptor complexes is needed to enable the development of new and improved receptors for a wide range of functions and to fully explain the roles anion-receptor interactions play in natural processes.

Within anion-receptor chemistry and supramolecular chemistry as a whole crystallography is a highly important tool for investigating structures.

In the next chapter the advantages of X-ray crystallography, the information it can give, and how it provides the opportunity to increase our knowledge of anion-receptor complexes will be presented. Some of the background theory of crystallography will also be described.

Chapter 2: Single crystal X-ray diffraction and charge density analysis

2.1 Crystallography and the basis of X-ray diffraction

Crystallography is the study of condensed matter and aims to decipher the atomic and molecular structure of a particular material and relate this to both the physical and chemical properties of the investigated substance.

A crystal is a highly ordered structure, where a vast number of identical chemical units are arranged in a precise, regular and repeated pattern in all three directions. The repeat geometry of the crystal structure is defined as the *unit cell*, and consists of three lengths; *a*, *b* and *c*, and three angles, α, β and γ. The unit cell is chosen as the smallest sized shape that represents the full symmetry of the repeat unit, and will belong to one of the seven crystal systems- triclinic, monoclinic, orthorhombic, tetragonal, rhombohedral, hexagonal and cubic.

The molecules that build up a crystal interact with a beam of some type and diffraction of the beam occurs. Diffraction is the spreading or bending of waves when they meet an obstacle or slit comparable in size to their wavelength. Individually, the diffraction caused by a single molecule is too weak to be detected but magnification of this effect due to the repeat nature of the crystal means the diffraction of a crystal can be measured. The beam that is diffracted can be comprised of electrons (which interact with both the nucleus and the surrounding electrons), neutrons (which are scattered by the nucleus of the atoms) and X-rays (which interact with the valence electrons). Hard X-rays have a wavelength of 1-2 Å, comparable to the size of atoms

(0.3–3 Å). This thesis will mainly comprise crystal structure elucidation via single crystal X-ray diffraction, with some additional, complementary single crystal neutron diffraction studies.

2.2 Single crystal X-ray diffraction

Since the collection of the first diffraction pattern by Max von Laue (1912)[32] and the related discovery (published in 1913) by father and son duo William and Lawrence Bragg[33], that X-ray diffraction could be used as the basis for structural determination, single crystal diffraction has become a benchmark technique applied across the physical and biological sciences. Its wide applicability to a broad variety of molecular structures, from small organic molecules and simple salts to larger natural and synthetic materials and even to large biological molecules (proteins and membranes) highlights the potency of the technique. Notable successes include the work of Rosalind Franklin, whose X-ray diffraction images captured the helix shape of DNA[34,35], and the structural determination of other important biological molecules including Vitamin B_{12} and insulin by Dorothy Hodgkin[36]. In small molecule crystallography (where the unit cell dimensions are generally $\leq$ 50 Å) discoveries such as the structure of hexamethylbenzene by Kathleen Lonsdale[37], which led to increased understanding of aromatic compounds and the resonance between chemical bonds, have and continue not only to provide important structural information to chemists such as bond lengths and bond angles but additionally, deepen understanding of and shed new light on fundamental chemical principles. The sheer volume of structures in the CSD[13] (658,007 structures as of February 2014) illustrates the success and prominence of crystallography today.

2.2.1 Bragg's Law and structure solution

William and Lawrence Bragg determined the geometrical conditions under which diffraction results in constructive interference and the diffraction from a crystal is observed (shown below in Figure 2.1), known as Bragg's Law[38]:

(Eq. 2.1) $$2d_{hkl}sin\theta = n\lambda$$

with θ the Bragg angle, λ the wavelength of the X-rays and d the plane spacing. $n\lambda$ is the additional path length the wave must travel as it passes through the crystal and must be a whole wavelength to result in constructive interference. The value of n is conventionally taken as 1, as multiples of the wavelength can be taken into account by the diffraction indices h,k and l (known as the Miller indices) of any particular reflection.

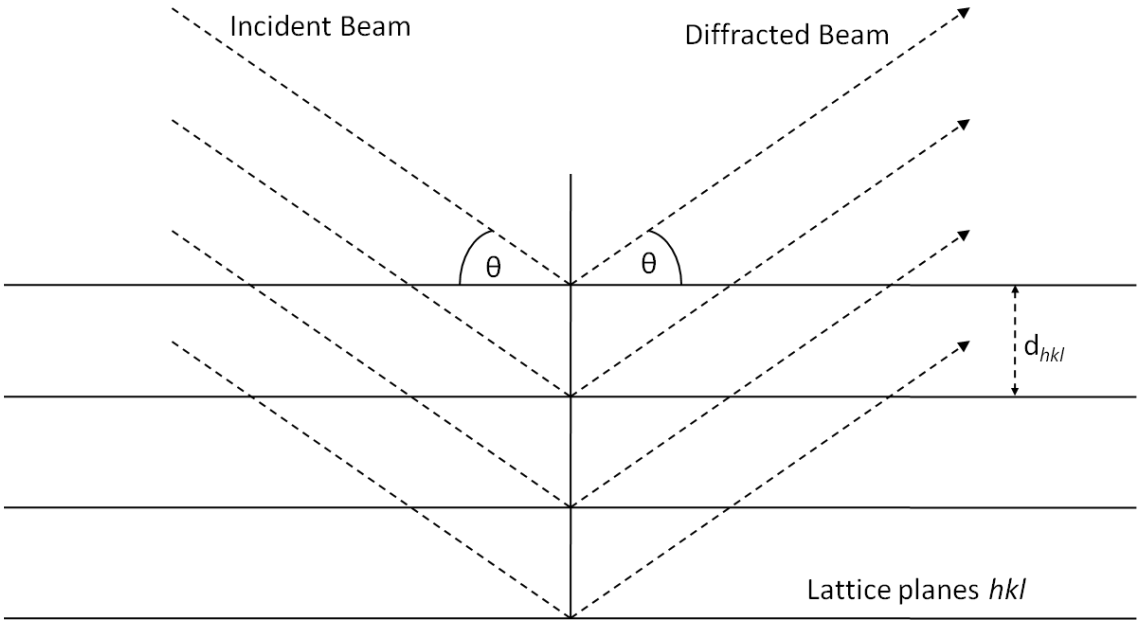

Figure 2.1: Bragg's Law: The geometric criteria for the observation of diffraction.

The resulting diffraction pattern is (see example in Figure 2.2) a lattice formed of spots with defined positions and differing intensities. This lattice has a reciprocal relationship to the crystal structure. The spacing of the diffraction lattice (*reciprocal space*) provides information about the distances in the crystal (*real space*). Small spacing between the lattice points of the diffraction pattern indicate a large spacing in the crystal. While the geometry of the diffraction pattern provides information about the regular arrangements of the molecules in the crystal structure (the *unit cell*), the intensities of the spots of the X-ray diffraction experiment provide information about the atom type and their location within the unit cell.[39] An important concept is that of the resolution of the diffraction data. This is the position of the highest resolvable peak in the diffraction pattern and relates to the accuracy of the atomic positions. Where there are resolvable peaks further to the edge of the diffraction pattern the accuracy of the atomic positions is higher and therefore during a diffraction experiment the aim is to collect data of the highest possible resolution (usually the crystal should diffract to 0.84 Å).

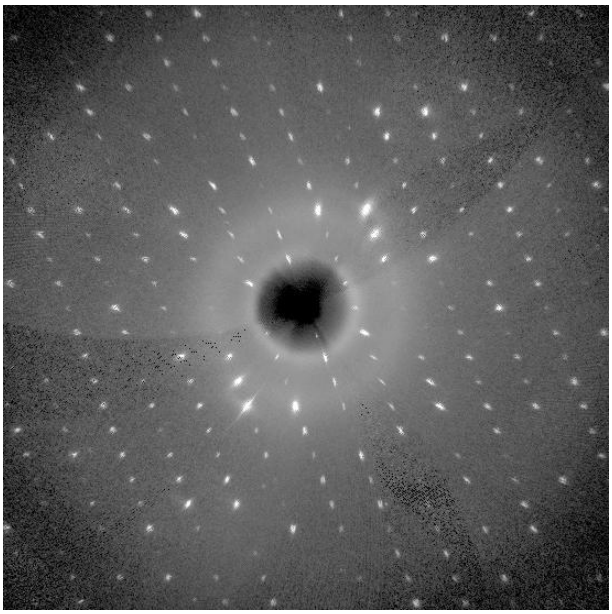

Figure 2.2: Typical X-ray diffraction pattern of an organic crystal.

Two numerical values are associated with each reflection in a crystal diffraction pattern: the amplitude ($|F|$), which is proportional to the square root of the intensity and the phase (ϕ). These are needed in order to determine the electron density at a given point in the unit cell and hence solve the crystal structure. The intensities can be obtained directly from the X-ray diffraction experiment, however the information on the phase of the diffracted beam is lost and must be obtained indirectly, this is known as the phase problem. The phase can be approximated by a variety of different techniques. Together the phase and amplitude combine to give the structure factor $F_{(hkl)}$ (Eq. 2.2) for the reflection with indices *h*, *k* and *l*.

(Eq. 2.2) $$F_{(hkl)} = |F_{(hkl)}| \text{ x } \exp\left[i\phi_{(hkl)}\right]$$

The structure factor is related to the electron density distribution (the contents of the unit cell) via Fourier transformation (Eq. 2.3). Reverse Fourier transformation relates the electron density to the structure factor (Eq. 2.4).

(Eq 2.3) $$F_{(hkl)} = \int_{cell} \rho_{(xyz)} \text{ x } exp[2\pi i(hx + ky + lz)]\mathrm{d}V$$

(Eq 2.4) $$\rho_{(xyz)} = \frac{1}{V} \sum_{h,k,l} F_{(hkl)} \text{ x } exp[-2\pi i(hx + ky + lz)]$$

This shows that the structure factor for reflection *hkl* is given by taking the value of the electron density at each point in the unit cell $\rho_{(xyz)}$, multiplying by the complex number in the exponential term and integrating over the whole of the unit cell volume. Here the electron density distribution ρ at every point in a single unit cell is calculated, with V the volume of the unit cell.[40]

As information on the phase is lost during the diffraction experiment in order to solve the structure starting estimates of the phase are used. From this first solution these initial estimates are refined to improve the resulting crystal structure. This leads to a fitting procedure where calculated structure factors ($F_{(calc)}$) are compared to the observed structure factors ($F_{(obs)}$) by means of a least squares fitting. The quality of the fit is indicated by the value of the residual factors or R-indices.[39]

2.2.2 The independent atom model (IAM model)

Today, crystal structure elucidation has been incorporated into many software packages. The majority of these use the independent atom model (IAM) to derive the calculated structure factors.[41]

The model assumes that maxima in the electron density are the positions of the atomic nuclei. This follows from the chemical principle that electron density is accumulated around the nuclei of atoms. This density is assumed to be spherical in nature and reverse Fourier transform of this density results in the generation of spherical scattering factors.

Generally nine parameters for each atom can be optimised during the least squares refinement process of crystal structure determination. These are the three positional parameters (*x*, *y* and *z*) and six anisotropic displacement parameters (ADPs). Hydrogen atoms are typically described by the three positional parameters and a single isotropic displacement parameter.[42] An occupancy parameter can also be varied. Using this information distances and angles between atomic centres can be calculated and used to describe the relationship between the individual atoms in a crystal structure.

IAM is a suitable approximation for the bulk of crystallographic studies, because it provides the precise atomic coordinates and molecular connectivity, which is the ultimate aim of these studies. As such IAM constitutes the standard of crystal structure determination.

2.2.2.1 The failings of the independent atom model

Despite the clear success of IAM demonstrated above, considerable limitations exist. A notable failing of the IAM is that bonds involving hydrogen atoms X—H (where X = O, N, F etc) are anomalously short. This is due to the hydrogen atom containing only one electron, which is polarised significantly away from the nuclear region towards another atom when forming a covalent bond. This illustrates how structure determination using IAM fails to accurately describe the electron density distribution in chemical bonds.[43] This is unfortunate as a chemist's understanding of the reactivity and properties of both natural and synthetic molecules derives from the accurate knowledge of the bonding (both covalent and non-covalent) between the atoms in a chemical compound and limits the ability of chemists to specifically tailor molecules to desired applications. Other problems with the IAM have been described, Pauling warned in 1932 that it is not always possible to deduce the bond type from

geometric knowledge of the atomic arrangements[44]. This has been illustrated more recently in the observation that short bonds do not automatically imply a strong bond, and that bond length and reactivity do not necessarily correlate[45].

Methods to overcome these limitations and extract more direct information about chemical bonding within chemical structures using X-ray diffraction data will now be described.

2.3 Charge density analysis

Modern chemistry recognises the inherent relationship between a chemical compound's structure and its properties. Covalent bonding links atoms chemically by sharing electrons and this influences the property of individual molecules. The non-covalent interactions described in Section 1.3.1, control how molecules relate to each other and hence how compounds behave and function in various environments. Again, these non-covalent interactions rely to a high degree on the electron density distribution. Knowledge of this electron density distribution and its perturbation upon bonding between atoms is therefore vitally important to modern chemists. As described in Section 2.1 it is the electrons in atoms that scatter X-rays and so it should be possible to use diffraction experiments to observe the arrangement of electrons in a crystal structure. This is possible although, as will be shown, requires both more advanced and complicated data collection and structural refinements. This field, known as electron density or charge density analysis, started developing in the 1960s and has since matured into an established field of solid-state structural analysis[41,46].

2.3.1 The aspherical atom model

The independent atom model described in Section 2.2.2 assumes that atoms are spherical and therefore employs spherical atomic scattering factors. However, electron density distribution is distorted by bonding causing atoms to be non-spherical, therefore an aspherical description is needed. A number of approaches have been developed (including those by Dawson[47], Stewart[48] and Hirshfeld[49]) however the multipole model (MM) of Hansen and Coppens[50] is the most successful and commonly used model that describes atomic asphericity to date. Although other methods are now being developed, such as the Hirshfeld atom refinement[51,52] or X-ray constrained wavefunction refinement of Jayatilaka and co-workers[53,54], the Hansen-Coppens multipole model forms the basis of the work described in this thesis and as such will now be discussed in further detail.

2.3.1.1 The Hansen-Coppens formalism

Multipole models build heavily upon the IAM. The total molecular density is expanded from atom-centred functions. In the Hansen-Coppens formalism (Eq. 2.5) the electron density ($\rho(\boldsymbol{r})$) is split into three terms:

(Eq. 2.5)

$$\rho(\boldsymbol{r}) = \rho_c(r) + P_v\kappa^3\rho_v(\kappa r) + \sum_{l=0}^{lmax}\kappa'^3 R_l(\kappa' r)\sum_{m=0}^{+l} P_{lm}\mathrm{d}_{lm\pm}(\vartheta,\varphi)$$

The $\rho_c(r)$ term accounts for the spherical core electron density (that centred on the atomic nucleus), the $\rho_v(r)$ term describes the spherical valence electron density and finally the summation term represents the deformation valence density (the electron density perturbed by chemical bonding).[50] The core and spherical valence densities are calculated from Hartree-Fock (HF)[55] or relativistic HF[56] atomic wavefunctions, with values tabulated in the literature.

Radial functions of the deformation valence density are taken as Slater functions[57] and described by spherical harmonics (multipole parameters). κ and κ' are radial scaling parameters that describe the expansion or contraction of the spherical and aspherical valence density respectively.

Therefore, in the multipole model, in addition to the three positional and six anisotropic displacement parameters described in IAM the charge density parameters of P_v, P_{lm}, κ and κ' can be also be optimised (more than 20 extra parameters per atom) in the least-squares refinement based on the measured structure factors. This large number of additional parameters can cause computational difficulties in larger chemical systems.

2.3.2 Requirements for charge density datasets

The increased number of parameters for optimisation in the multipole model can create problems for a least-squares refinement. It is normally assumed that a reflection to parameter ratio of 10 is necessary to avoid correlation between the individual parameters and to prevent too large an uncertainty on each parameter.[46] This means that highly redundant datasets, with 100% completeness to high resolution, are desired when collecting data for charge density refinement. Lower temperature (at least $\leq$ 100K) data collection is standard, as the scattering power of the sample increases meaning higher resolution data are obtained and thermal diffuse scattering is reduced.[41] At lower temperatures the atomic positions are also more accurate as the atoms oscillate less. Using a shorter wavelength (λ) as the radiation source in the X-ray diffraction experiment (for example molybdenum K_α radiation with λ = 0.7107 Å or lower) also aids in increasing the resolution of the data. Another benefit of shorter wavelength radiation is the reduction of systematic effects, which include extinction. In this regard synchrotron radiation is desirable, with

the added flux of the source also decreasing the time needed to collect the necessary high resolution, high redundancy data. Iversen and co-authors have recently outlined the benefits of using synchrotron radiation in charge density analysis.[58] However, one drawback of synchrotron radiation is beam instability, as the intensity of the source can vary over the course of the experiment and effect the intensities of the observed reflections. This must be corrected for. In comparison, laboratory based sources have particularly stable beam intensities. High resolution, typically diffraction data measured to 0.5 Å, is essential, as it enables the deconvolution of thermal effects and nuclear positions.[59] It has been shown that the scattering power of valence electrons decreases with resolution rapidly (Farrugia has recently discussed this[60]), while the decay in the scattering power of core electrons does not decrease at the same speed, meaning the higher resolution data gives vital information about the positions of the nuclei of the atoms in a structure. The low order reflections give the information about the valence electrons and are therefore equally important. The combination of these two pieces of information allows the electron density in chemical bonds to be determined in charge density analysis, which makes it such an attractive and desirable tool for chemists.

Advances in data collection, particularly the use of area detectors, such as CCDs (charge coupled detectors), which reduce significantly the time required to collect highly redundant datasets, and advances in computing power and software have widened the ability for the charge density analysis of crystal structures. Hence, charge density analysis is becoming attractive outside the crystallographic community, to chemists working in a wide variety of research areas. This thesis, which seeks to apply charge density analysis to anion binding chemistry, demonstrates this. However, a caveat must be added that data collection, reduction and refinement in charge density is still highly

involved and requires much time and expertise. An inherent limit for any crystallographer is the crystal quality, and this is particularly so in charge density studies, where almost perfect crystals, which display little extinction or absorption effects, have high scattering ability and ideally no disorder in the structure are necessary. As heavy atoms have a higher proportion of core to valence electrons the deformation in the electron density distribution upon bonding is harder to observe for transition metal complexes and intermetallic systems and alloys.[46,61] Thus atoms in the lowest periods of the periodic table are not generally appropriate for charge density refinement but they are not normally used in anion-receptors and their complexes.

2.3.3 Critical evaluation of the modelled electron density distribution

The qualitative evaluation of how well the diffraction data are fitted in the aspherical model will be discussed and the level of confidence that can be placed in the analysis of the electron density distribution outlined.

As in the IAM approach the multipole model uses a least-squares refinement to minimise the difference between observed and calculated structure factors. Thus, one method for measuring how well these match is the R-value (Eq. 2.6). The lower the R-value the better the fit.[42]

(Eq. 2.6) $$R_1 = \frac{\sum_H ||F_{obs}| - |F_{calc}||}{\sum_H |F_{obs}|}$$

The residual electron density, the difference between the modelled and observed electron density is another key indicator of the quality of the refinement and is calculated through a Fourier summation (Eq. 2.7).[46]

(Eq. 2.7)

$$\Delta\rho(\boldsymbol{r})_{residual} = \frac{1}{V}\sum_{h,k,l}(F^0 - F^1)\exp[-2\pi\varphi^1]\exp[-2\pi i(hx + ky + lz)]$$

F^1 and φ^1 are the structure factor modulus (amplitude) and phase calculated with a given model, and F^0 is the modulus of the observed structure factor.

The lower this residual density the better the model describes the molecular electron density. With IAM, due to the inability of spherical approximations to model the bonding electron density this will be larger in the regions between atoms. An aspherical refinement should reduce the residual density as the electron density not centred on atoms can be properly modelled (see Figure 2.3). Any large residuals indicate a problem with the data or model and a flat and featureless residual density has been described as a necessary condition to judge that a multipole refinement has adequately modelled the electron density.[42] This can also be judged by residual density analysis (RDA), which has been developed by Meindl and Henn[62]. A statistical analysis is performed across the entire unit cell to determine if the residual density is distributed in a Gaussian style, indicating if it is merely the result of noise in the data. Deviations from a Gaussian distribution suggest that there is a systematic error in the model, and RDA can indicate whether this is due to uncorrected extinction or absorption effects, or incorrectly refined scale factors or expansion/contraction (κ and κ') parameters.

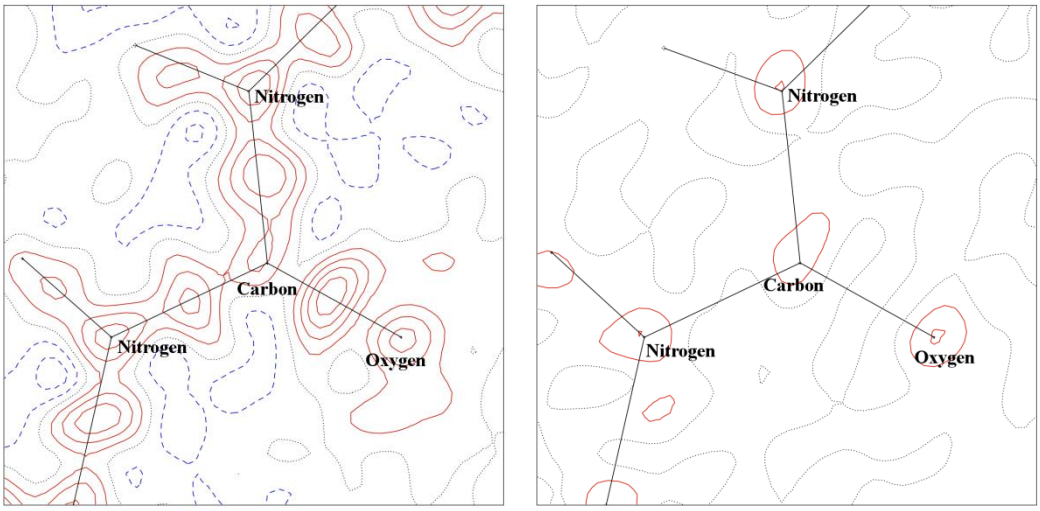

Figure 2.3: Residual density in a urea molecule after IAM refinement (*left*) and after multipole refinement using the Hansen-Coppens formalism (*right*). Positive electron density is shown in red and negative electron density in blue. Zero-level contours are dashed. Contours are at 0.1 e Å^{-3}. Solid black lines represent the bonds between atoms. The maps illustrate both that the residual density is lowered after multipole refinement and that it is no longer located in the bonding areas.

The modelled electron density tends to be dominated by the core electrons and the effects of bonding can be hard to distinguish. For this reason deformation densities are used to amplify the features of bonding. The static deformation density ($\Delta\rho_{static}(\mathbf{r})$) (see Eq. 2.8) is the difference between the thermally averaged density from the multipole model ($\rho_{MM}(\mathbf{r})$) and the spherically averaged density of the IAM ($\rho_{IAM}(\mathbf{r})$).[63]

(Eq. 2.8) $$\Delta\rho(\mathbf{r})_{static} = \rho_{MM}(\mathbf{r}) - \rho_{IAM}(\mathbf{r})$$

The static deformation density is a very useful diagnostic tool to test the quality of an aspherical electron density refinement. Density accumulations in bonds and lone pairs are readily distinguishable in static deformation density plots. The deformation density is derived from the functions and populations of the aspherical atom refinement and does not include the effect of thermal

smearing. However, any features beyond experimental resolution are highly dependent on the basis set functions used in the refinement. Comparison with deformation densities from theoretical calculations can serve as a method to evaluate and validate both methods.

The Goodness of Fit (S, GoF) (see Eq. 2.9) is another measure of the model quality. It determines how far the F_{calc} and F_{obs} vary, and is a measure of the over-determination of refined parameters.

(Eq. 2.9) $$S = \sqrt{\frac{\sum(w_H(F_{obs}^2 - F_{calc}^2)^2)}{(n-p)}}$$

where n is the number of reflections, w_H is the weighting scheme applied, and p is the number of parameters. S should be 1, however higher values of GoF are due to systematic underestimation of the uncertainties of the reflections at higher Bragg angles. Therefore the GoF for a multipole refinement is usually higher than 1 due to the weighting scheme applied.[42]

Finally, the Hirshfeld rigid bond test determines if the thermal motion has been effectively deconvoluted from the static electron density model.[59] It measures the difference of the mean-square displacement amplitudes (DMSDAs) of each chemical bond. The ADPs are tested against a rigid-body motion model. For each covalent bond between atoms A and B the following relationship (Eq. 2.10) should be fulfilled, where $z^2_{A,B}$ is the mean-square displacement amplitude of atom A in the direction of atom B and $z^2_{B,A}$ the corresponding displacement amplitude for atom B in the direction of atom A.

(Eq. 2.10) $$\Delta_{A,B} = z^2_{A,B} - z^2_{B,A}$$

DMSDAs ($\Delta_{A,B}$) values $<1 \times 10^{-3}$ Å^2 for bonds between atoms of equal masses indicate that the thermal motion has been correctly deconvoluted from the electron density. The value may be higher for heteronuclear bonds, but when

this is significantly higher it indicates there may be unresolved valence density asphericities or unrecognised disorder.[42]

The discussion above demonstrates that the electron density distribution modelled by the Hansen-Coppens formalism[50] can be critically evaluated by a variety of criteria, to ensure an accurate model of the charge density in a crystal structure. These tests will be used to assess the multipole refinements of the crystal structures discussed in this thesis in Chapters 4 and 5.

More interest has recently been taken in the reproducibility between the electron density distribution obtained from different datasets for the same crystal structure. Kamiński *et al.*[64] have statistically analysed the effect of data resolution, the type of X-ray diffractometer used etc., on the multipole parameters and the properties of the electron density, e.g. atomic charges and the electrostatic potential distribution. Sources of error were shown to relate mainly to the experimental setup and methodology inaccuracies. Variations in derived properties are larger when data collection is performed on a greater variety of instruments. The authors suggest integrated atomic charges deviate by 0.1 *e* and that the electrostatic potential distribution should be treated qualitatively. Again, this is important for allowing comparison of the electron density distribution across a series of structures with a known level of accuracy and to set interpretation limits.

2.3.4 QTAIM analysis

Once the multipole refinement has been performed and the spherical and aspherical electron density distribution accurately described, the modelled electron density will contain information about the interactions between atoms. To interpret this electron density distribution one key method is the 'Quantum Theory of Atoms in Molecules' (QTAIM) developed by Richard Bader.[65,66]

In QTAIM chemical bonding and the structure of a chemical system are based on the topology of the electron density. The electron density and derivatives of the electron density are used to define the character of bonds. The electron density can also be partitioned in various ways to define atomic basins associated with individual atoms in the molecular structure and the properties of the atoms within the molecule described. QTAIM assumes the properties of a molecule can be accurately described by the sum of the properties of its atoms.[67]

2.3.4.1 QTAIM definition of atoms

The way the electron density varies across a region of space, in this case in the crystal structure, is described using a scalar field. The topology of the electron density distribution can be best examined by analysing the gradient vector field. This gradient is defined in Equation 2.11.[43]

$$\nabla\rho(\boldsymbol{r}) = \boldsymbol{i}\frac{\delta\rho}{\delta x} + \boldsymbol{j}\frac{\delta\rho}{\delta y} + \boldsymbol{k}\frac{\delta\rho}{\delta z} \qquad \text{(Eq. 2.11)}$$

Paths following the largest increase in electron density ($\rho(\mathbf{r})$) can be tracked and are known as gradient paths or trajectories. A gradient path is always perpendicular to the contours of $\rho(\mathbf{r})$ and does not meet another unless at a nucleus (this is illustrated in Figure 2.4). Each nucleus acts as an attractor for gradient paths, which make up the basin of the attractor (*atomic basin*). This basin is bordered by a surface, not crossed by any trajectories and is known as the zero flux surface (Eq. 2.12) and it represents the boundary of the atom. The basin inside the zero flux surface is the atom itself.[67] Integration of the electron density over the volume of this atomic basin allows the topological charge of the atom to be determined.[43]

(Eq. 2.12) $\nabla\rho(\boldsymbol{r}) \,.\, n(\boldsymbol{r}) = 0$

where $n(\boldsymbol{r})$ is a vector normal to the surface.

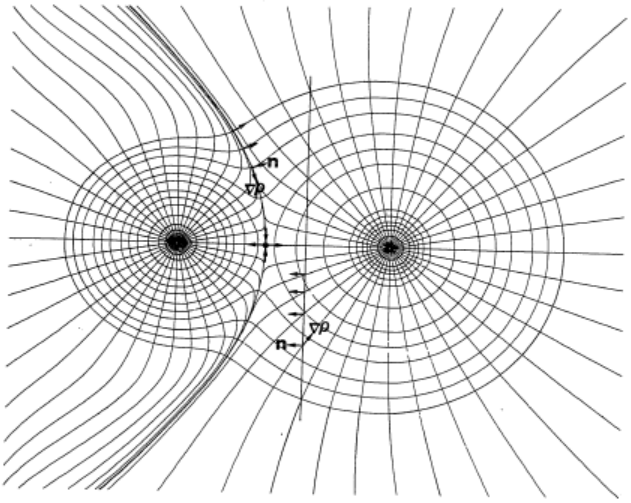

Figure 2.4: Contour map for NaCl overlaid with trajectories of $\nabla\rho$. With the exception of the four trajectories associated with the (3, -1) critical point (denoted by a dot), the trajectories originate at infinity and terminate at one of the two nuclei. Two trajectories originate at infinity and terminate at the (3, -1) critical point, while two others originate at this point and terminate, one each, at the nuclei. The property of the zero flux in the gradient vectors of ρ is illustrated for the interatomic surface whose intersection with this plane is given by the two trajectories which terminate at the critical point. An arbitrarily drawn surface is shown not to have this property of zero flux. This figure is reproduced with kind permission from Atoms in Molecules: A Quantum Theory by R. F. W. Bader © Oxford University Press.[66]

2.3.4.2 QTAIM definition of bonding

Gradient paths that do not terminate at a nucleus, can link two attractors (nuclei) to each other. A pair of gradient paths linking two atoms is known as an atomic interaction line and is found between each pair of nuclei that share a common interatomic surface. (See Figure 2.5 which displays the gradient

trajectories of a phenyl ring.) In a crystal structure this interaction line of locally maximum electron density is called a *bond path* (BP). The network generated by linking these bond paths in a molecule is a *molecular graph*.[46] A bond path is not however the same as the bond (usually referred to as an *interatomic vector*) defined by Lewis and taught to undergraduate chemists. (For an interesting description of the nature of a bond path see Bader's discussion paper.[68]) Bond paths are not straight: it will be demonstrated later that the ellipticity of the bond (see Section 2.3.4.4.2) reflects to some extent its nature.[67] From the bond path we cannot distinguish the number of electrons in the bond, whether it is two centre covalent bonding, or a double or triple bond.[46] To gain this kind of insight into the nature of a bond, the properties of the electron density at certain points (called *bond critical points*- BCPs) must be examined.

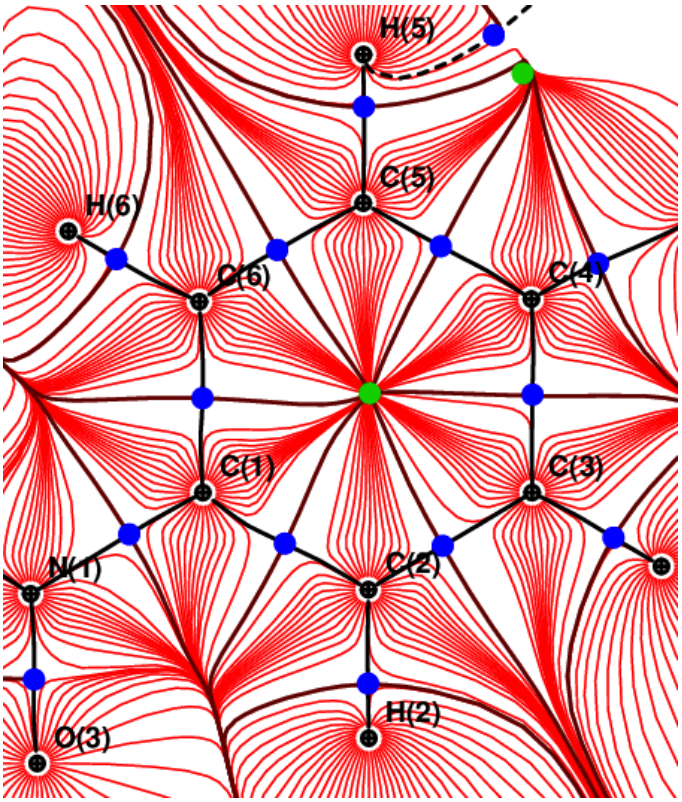

Figure 2.5: Gradient vector field map in the plane of a phenyl ring. Gradient trajectories are shown in red, atomic positions are black spheres, bond critical points (BCPs) are in blue and ring critical points (RCPs) are in green.

2.3.4.3 Critical points

The gradient paths described above start and end at extrema values of $\rho(\mathbf{r})$, known as *critical points* (CPs). These are maxima, saddle points or minima and each has a vanishing $\nabla\rho(\mathbf{r})$. Depending on the extrema the CPs can be categorised into core(nuclear attractor)-, bond-, ring-, and cage-critical points. These have been tabulated below in Table 2.1.

Table 2.1: Critical point classifications and signs of each of the eigenvalues (λ_1, λ_2 and λ_3) in each type of CP.

Critical point	Abbrevation	Extrema type	λ_1	λ_2	λ_3	Classification (ω, σ)
Nuclear attractor	NA	Maximum	−	−	−	(3, −3)
Bond critical point	BCP	Saddle point	−	−	+	(3, −1)
Ring critical point	RCP	Saddle point	−	+	+	(3, +1)
Cage critical point	CCP	Minimum	+	+	+	(3, +3)

The table shows each critical point is characterised by the rank (ω) and the signature (σ). These are linked to the second-order derivatives of the electron density at the critical point, which describe the local curvature. There are nine second derivatives that describe the curvatures of the electron density at a point in space. These form an ordered 3 x 3 array known as the Hessian matrix of the charge density (see Eq. 2.13).[63]

(Eq. 2.13) $$H(\boldsymbol{r}) = \begin{pmatrix} \frac{\delta^2\rho(\boldsymbol{r})}{\delta x^2} & \frac{\delta^2\rho(\boldsymbol{r})}{\delta x \delta y} & \frac{\delta^2\rho(\boldsymbol{r})}{\delta x \delta z} \\ \frac{\delta^2\rho(\boldsymbol{r})}{\delta y \delta x} & \frac{\delta^2\rho(\boldsymbol{r})}{\delta y^2} & \frac{\delta^2\rho(\boldsymbol{r})}{\delta y \delta z} \\ \frac{\delta^2\rho(\boldsymbol{r})}{\delta z \delta x} & \frac{\delta^2\rho(\boldsymbol{r})}{\delta z \delta y} & \frac{\delta^2\rho(\boldsymbol{r})}{\delta z^2} \end{pmatrix}$$

This Hessian matrix is diagonalised to provide three eigenvalues: λ_1, λ_2 and λ_3 (with $\lambda_1 \leq \lambda_2 \leq \lambda_3$). These eigenvalues each correspond to an eigenvector, which yields the direction in which the curvature is measured. The rank is the number of non-zero eigenvalues of a critical point and the signature the sum of the signs of the eigenvalues. The critical points can therefore be determined and distinguished by the eigenvalues.[67] In an isolated molecule the number of critical points should fulfil the Poincaré-Hopf equation (Eq. 2.14)[69]:

(Eq. 2.14) $$n_{NA} - n_{BCP} + n_{RCP} - n_{CCP} = 1$$

with n_{CCP}, n_{RCP}, n_{BCP}, the number of cage, ring, and bond critical points respectively and n_{NA} the number of nuclear attractors.

As previously described a CP where the curvatures are negative, a maxima, ($\omega = 3$, $\sigma = -3$) is a nuclear position (nuclear attractor, NA). The BCP is a saddle point, with $\omega = 3$, $\sigma = -1$. The saddle point ring critical point (RCP), is formed by the linking of BCPs, and can for example be found in the centre of a phenyl ring, and the minima extrema- the cage critical point (CCP) is found in the interior of a molecule enclosed by ring surfaces, such as in the centre of P_4.[67]

2.3.4.4 Properties of the electron density

It has been previously mentioned that to determine the nature of a bond the properties of the electron density at the BCP must be analysed. The different properties of the electron density will now be examined and their physical relevance discussed.

2.3.4.4.1 The Laplacian of the electron density

Small fluctuations in the electron density distribution (caused by different bonding interactions) can be difficult to detect, therefore by calculating second-order derivatives these effects can be amplified (see Figure 2.6 which graphically displays this). This is performed using the Hessian matrix described above. The Laplacian of the electron density ($\nabla^2\rho(\mathbf{r})$) is the trace of the Hessian matrix[43,63]:

(Eq. 2.15) $$\nabla^2\rho(\mathbf{r}) = \frac{\delta^2\rho(\mathbf{r})}{\delta x^2} + \frac{\delta^2\rho(\mathbf{r})}{\delta y^2} + \frac{\delta^2\rho(\mathbf{r})}{\delta z^2} = \lambda_1 + \lambda_2 + \lambda_3$$

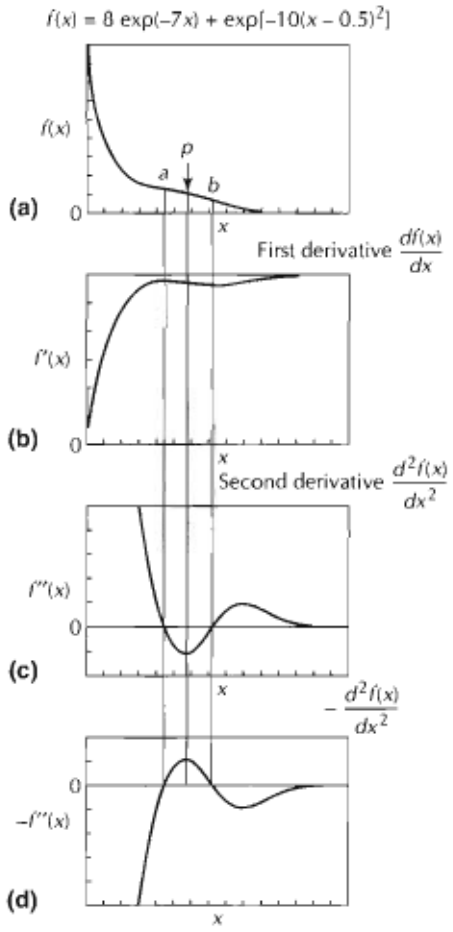

Figure 2.6: Plots of a monotonically decreasing function *f*(x) **(a)**, its first **(b)** and second **(c)** derivatives, and the negative of its second derivative **(d)**. The shoulder in *f*(x) is converted to a pronounced maximum in the negative of the second derivative − *f*″(x). Figure reproduced by kind permission from Chemical Bonding and Molecular Geometry by R.J. Gillespie and P. L. A. Popelier © Oxford University Press.[67]

The value of the Laplacian of the electron density indicates where there is charge concentration (($\nabla^2\rho(\mathbf{r}) < 0$)) or charge depletion (($\nabla^2\rho(\mathbf{r}) > 0$). Local charge concentrations, known as valence shell charge concentrations (VSCCs) can be associated with bonding electron pairs or lone pairs of electrons. At BCPs the value of $\nabla^2\rho(\mathbf{r})$ can be used to characterise the type of bonding.[43] Covalent bonds are associated by overlapping of the VSCCs and so there is an accumulation of charge density ($\nabla^2\rho(\mathbf{r}_{BCP}) < 0$) for a covalent bond. These are

known as 'open-shell' or 'shared' interactions. Conversely, where there is a 'closed-shell' interaction, such as ionic bonds or non-covalent interactions, there is no overlap of the VSCCs and so the BCP is shifted towards the charge depletion at the more electropositive atom of the bond and $\nabla^2\rho(\mathbf{r}_{BCP}) > 0$ characterises this type of bonding. However, defining the bonding by the value of the Laplacian of the electron density at the BCP is not always unambiguous, especially in the case of weak bonds.[63] Looking at the shape of the electron density along the bond (the bond ellipticity) and using the additional properties described below can also be helpful.

2.3.4.4.2 Ellipticity

The ellipticity (ϵ) is defined as[43]:

(Eq. 2.16) $$\epsilon = \frac{|\lambda_1|}{|\lambda_2|} - 1$$

λ_1 and λ_2 are negative eigenvalues of the Hessian matrix and as λ_1 is defined to be larger or equal to λ_2, the ellipticity cannot be negative. For single bonds there is perfect rotational cylindrical symmetry along the bond path and hence ϵ should be zero. Therefore values greater than zero indicate double bonding or deformation. The ellipticity values in ethane, benzene and ethene (0.00, 0.23 and 0.45 respectively)[70] are indicative of the bonding character. When examining triple bonds the rotational symmetry is again present along the bond path and ϵ should be close to zero. Looking at the ellipticity along the entire bond path is important for characterising polar bonds.

2.3.4.4.3 Source function

Gatti has proposed that the Green's function of the electron density[71]

(Eq. 2.17) $$\rho(\mathbf{r}) = \int LS(\mathbf{r}, \mathbf{r}').d\mathbf{r}'$$

where *LS* is the local source:

(Eq. 2.18) $$LS(\mathbf{r},\mathbf{r}') = -\left(4\pi.\left|\mathbf{r}-\mathbf{r}'\right|\right)^{-1}.\nabla^2\rho(\mathbf{r}')$$

can be applied to interpret the electron density distribution in molecules and describe the bonding in molecules. The density at point **r** is determined by contributions from a source function LS(**r**,**r**') where **r**' represents all other points. The electron density can be equated to a sum of S(**r**;Ω) (terms integrated over each atomic basin Ω)

(Eq. 2.19) $$\rho(\mathbf{r}) = S(\mathbf{r},\Omega) + \sum_{\Omega'\neq\Omega} S(\mathbf{r},\Omega')$$

This allows the electron density at any point in the molecule to be viewed as consisting of contributions from a local source operating at all other points of the space. The individual and relative importance of an atom or group's contribution to the electron density at a point can be calculated. Groups can be viewed as '*sources'* for the electron density at a point (positive contribution) or '*sinks'* (negative contribution).[72] This can be applied to describe the nature of the chemical bonding in a structure, for instance the contribution of the hydrogen atom to the electron density in the BCP of a hydrogen bond has been shown to characterise the type and strength of the hydrogen bond.[17]

2.3.4.4.4 Local energy densities

It is possible to derive the energetic properties of hydrogen bonds from the values of the electron density and Laplacian of the electron density at the BCPs associated with the hydrogen bonding interactions. Using the formulae of Abramov[73] the local kinetic energy density ($G(\mathbf{r}_{BCP})$), the local potential energy ($V(\mathbf{r}_{BCP})$), the total energy density ($H(\mathbf{r}_{BCP})$) and hydrogen bond energy (E_{HB}) (Eqs. 2.20 – 2.23) can be calculated as shown by Espinosa *et al.*[74] The values of these energy densities are part of the criteria used to describe and classify the

nature of the hydrogen bonding. In the examples given in Section 2.4.1 the relationship between these properties and the nature of a bond are shown.

(Eq. 2.20) $$G(\mathbf{r}_{\mathrm{BCP}}) = \left(\frac{3}{10}\right)(3\pi^2)^{\frac{2}{3}}\rho(\mathbf{r}_{\mathrm{BCP}})^{\frac{5}{3}} + \left(\frac{1}{6}\right)\nabla^2\rho(\mathbf{r}_{\mathrm{BCP}})$$

(Eq. 2.21) $$V(\mathbf{r}_{\mathrm{BCP}}) = \left(\frac{\hbar^2}{4m}\right)\nabla^2\rho(\mathbf{r}_{\mathrm{BCP}}) - 2G(\mathbf{r}_{\mathrm{BCP}})$$

(Eq. 2.22) $$H(\mathbf{r}_{\mathrm{BCP}}) = G(\mathbf{r}_{\mathrm{BCP}}) + V(\mathbf{r}_{\mathrm{BCP}})$$

(Eq. 2.23) $$E_{HB} = \left(\frac{1}{2}\right) \mathrm{x}\, V(\mathbf{r}_{\mathrm{BCP}})$$

2.3.4.4.5 Electrostatic potential

Using the formalism of Su and Coppens the electrostatic potential distribution can be calculated independently from the crystal environment.[56] This is useful information as it provides chemists with information about the spatial arrangement of nucelophilic and electrophilic regions in a molecule. The electrostatic potential (ESP) at a certain position in space is defined as the energy needed to bring a positive unit of charge from an infinite distance to this point. An advantage of experimentally derived electrostatic potentials compared to those from single-molecule calculations outlined by Koritsanszky and Coppens is that many-body effects in the crystal are accounted for.[41] Effects of intermolecular interactions and the environment are therefore included in the experimentally determined ESP.

2.3.4.5 Atomic properties

By defining the atom as being enclosed within the zero flux surface it is possible to calculate the individual properties of each atom in a molecule, which should be additive. Below some of the common atomic descriptors are defined.

2.3.4.5.1 Atomic volume

The atomic volume is the sum of the volume elements that occupy all the space defined by the interatomic surfaces and the $\rho = 0.001$ a.u. contour. It is calculated by integrating the volume elements $d\tau$ over the atomic basin (Eq. 2.24).[67]

(Eq. 2.24) $$v(\Omega) = \int_{\Omega} d\tau$$

2.3.4.5.2 Electron population and atomic charge

There are various methods to calculate the charge of an atom depending on the method used to partition the space. The electron density partitioning may be a discrete boundary scheme, where the density at each point is assigned to a specific basin, or a fuzzy boundary partitioning, where the density at a point may be assigned to overlapping functions centred at different locations. In this thesis stockholder charges (derived from discrete boundary partitioning) and QTAIM charges (also known as Bader charges, calculated using a fuzzy boundary partitioning) will be used and discussed.

In QTAIM the electron population of the atom can be calculated by integrating the density of a volume element over the atomic basin as in Equation 2.25.[67]

(Eq. 2.25) $$N(\Omega) = \int_{\Omega} \rho d\tau$$

The atomic charge can then be obtained by subtracting the electron population from the charge of the nucleus inside the atomic basin.[67] The electron density is integrated over the volume of the basin to yield the charge. The electron density at a specific point in the molecular structure must be assigned to a centre in the proximity of that point. QTAIM or Bader partitioning, which generates the QTAIM or Bader charges is a fuzzy boundary scheme, based on the QTAIM definition of an atom, described above, as being an atomic basin

enclosed in a zero flux surface. In contrast to the stockholder charges described below, QTAIM charges tend to be larger than those from other space partitioning methods.[43]

Hirshfeld developed stockholder partitioning from which stockholder charges are derived. It uses a continuous sampling function ($w_i(\mathbf{r})$) to assign the density among the consistent atoms. The sampling function is based on the spherical atom promolecule density, and is defined as the relative contribution of atom *i* to the promolecule density.[43]

(Eq. 2.26) $$w_i(\mathbf{r}) = \frac{\rho_i^{sphericalatom}(\mathbf{r})}{\sum_i \rho_i^{sphericalatom}(\mathbf{r})} = \frac{\rho_i^{sphericalatom}(\mathbf{r})}{\rho^{promolecule}(\mathbf{r})}$$

The density assigned to the atom *i* is given by:

(Eq. 2.27) $$\rho_i^{at}(\mathbf{r}) = w_i(\mathbf{r})\rho^{total}(\mathbf{r})$$

Each atom receives a fraction of the charge density at a point proportional to its '*investment*' in the promolecule density at that point. Due to the use of the promolecule term in the partitioning the stockholder charges tend to be smaller than those calculated from other methods.

2.3.4.5.3 Bonding radius

The bonding radius of an atom (r_b) is the distance from the bond critical point to the nucleus of the atom. Unlike the covalent radius, which is assumed to be constant for each atom independent of the chemical environment, the bonding radius changes as the chemical environment does.[67]

2.4 Charge density studies

Having looked at the background to charge density analysis and the theory of electron density distribution modelling, the criteria for evaluating the model

and the properties that can be derived from it, the application of charge density analysis in a range of systems is now discussed.

2.4.1 Non-covalent interactions in charge density

Modelling the electron density in a crystal structure allows the study and understanding of chemical systems to move beyond geometric criteria and values to an evaluation of the electron density distribution and its relationship to the non-covalent interactions that hold these structures together and account for the functions of these systems. Below are outlined some interesting examples of experimental charge density studies, which have provided information about a range of non-covalent interactions.

2.4.1.1 Hydrogen bonding

Many charge density studies have focused on hydrogen bonding. Full discussion of these studies would be beyond the scope of this thesis. The highly relevant examples described below, aim to provide the reader with a background to the development of the study of hydrogen bonding in charge density analysis and the sort of information available from such investigations.

Some of the earliest work in this area was carried out by Espinosa and co-workers. Starting from classical hydrogen bonding interactions (X—H···O where X = C, N, O) they were able to show the relationship between topological properties of the electron density at the bond critical points and the geometrical parameters of hydrogen bonding (see Figure 2.7 which illustrates the exponential relationship of both the values of the electron density and the Laplacian of the electron density at the BCP to the hydrogen atom and acceptor atom of the hydrogen bond).[75]

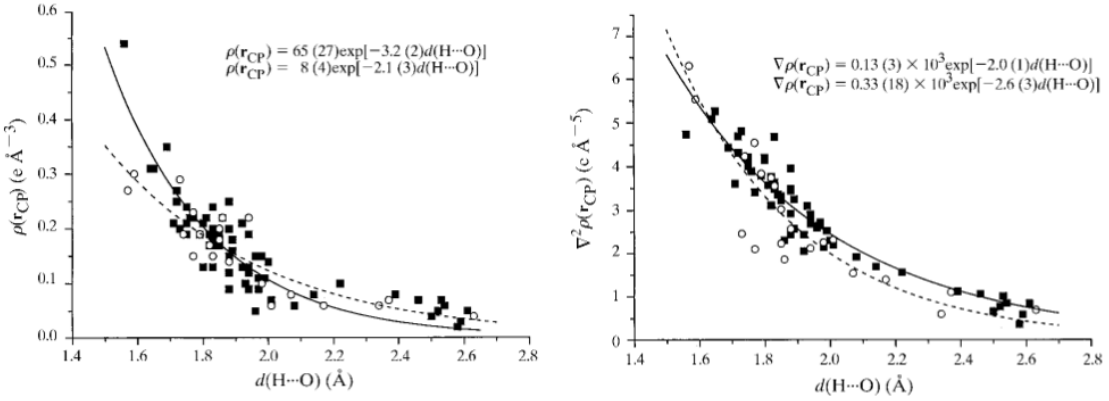

Figure 2.7: Espinosa *et al.* demonstrated the link between the hydrogen atom and oxygen acceptor atom distance d(H···O) of a hydrogen bond and the electron density and Laplacian of the electron density at the hydrogen bond BCP.[75] Figure reproduced from *Acta Crystallogr. Sect. B.*, 1999, **55**, 563-572 by kind permission of the IUCr (http://dx.doi.org/10.1107/S0108768199002128).

They established a link between the local energetic properties; the local kinetic energy density $G(\mathbf{r}_{BCP})$, the local potential energy density $V(\mathbf{r}_{BCP})$ and the total energy density $H(\mathbf{r}_{BCP})$, and the topological properties at the CPs in a structure.[74,76] The interaction potential for hydrogen bonding could also be extracted from the analysis of the topology of the electron density distribution in hydrogen bonds.[77] Expanding the range of hydrogen bonding studies to include X—H···F hydrogen bonding systems[78] and also H···X interactions[79] (with X = H, C, N, O, F, S, Cl, π), Espinosa and co-workers have provided criteria for determining the nature of the hydrogen bonding (whether it is a pure closed-shell type, a shared-shell interaction (covalent nature) or an intermediate/boundary case) based on the topological and energetic properties at the hydrogen bonding BCPs. In the discussion of the results of this thesis (Chapters 4 and 5) these will be invaluable and well-used criteria.

Building on this foundation, Rozas *et al.*, studied a series of ylides with N, O and C atoms as hydrogen bond acceptors and classified the bonding into three

types based on the values of the interaction energies and showed the properties of the electron density at the BCP were characteristic of the bonding for each type of interaction with weak hydrogen bonds having values of $\nabla^2\rho(\mathbf{r}_{BCP})$ and $H(\mathbf{r}_{BCP}) > 0$, medium hydrogen bonds $\nabla^2\rho(\mathbf{r}_{BCP}) > 0$ and $H_{BCP} < 0$ and strong hydrogen bonding $\nabla^2\rho(\mathbf{r}_{BCP})$ and $H(\mathbf{r}_{BCP}) < 0$.[80]

Woźniak and co-workers performed studies on the non-covalent interactions in a series of Schiff bases[81] and DMAN (1,8-bis(dimethylamino)naphthalene) complexes[82] (see Figure 2.8). Again, they were able to show an exponential relationship between the local kinetic and potential energy density values, the electron density and the Laplacian of the electron density at the BCP to the internuclear distance of the H···A interaction and that the values of the topological properties were characteristic of the type of hydrogen bonding. Based on the value of the total energy density and the ratio of the local kinetic energy density to the electron density at the BCP three regions of closed-shell, intermediate character and shared-shell interaction were found in the range of non-covalent interactions studied. (Also see Section 2.4.2.)

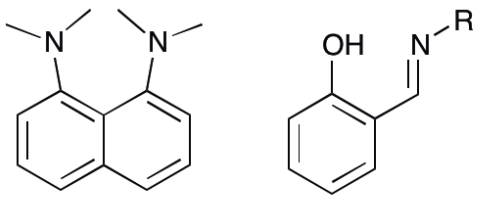

Figure 2.8: DMAN[81] and Schiff base[82] scaffolds

In work by Rao and co-authors, who have analysed a range of hydrogen bond types the exponential relationship between both the electron density at the BCP and the Laplacian of the electron density at the BCP to the H···A distance of

the hydrogen bond was again observed.[83] The authors note that there is an even better correlation between the positive curvature of the electron density (λ_3) and the hydrogen bond H···A distance. This relationship was given by the formula $0.47 \times 10^3 \exp(-2.5 \times d_{(H\cdots A)})$ for the 218 hydrogen bonds studied.

In related research Guru Row and co-workers have looked at a range of hydrogen bonding and used the criteria outlined above to characterise three types of hydrogen bonding: strong hydrogen bonding, weak hydrogen bonding and van der Waals interactions (see Figure 2.9).[84,85] This included examination of weak C—H···O and C—H···π interactions present in substituted coumarins.[86] As can be seen in Figure 2.9 the three groups have defined ranges for the bond path length (R_{ij}) and electron density value at the BCP. For the strong hydrogen bonding the $\rho(\mathbf{r}_{BCP}) > 0.1$ *e* Å^{-3} and $R_{ij} < 2.2$ Å, while the weak hydrogen bonding has values of 0.08 *e* Å^{-3} $> \rho(\mathbf{r}_{BCP}) > 0.02$ *e* Å^{-3} and 2.2 Å $< R_{ij} < 2.8$ Å, and van der Waals interactions $\rho(\mathbf{r}_{BCP}) < 0.05$ *e* Å^{-3} and $R_{ij} > 2.8$ Å.

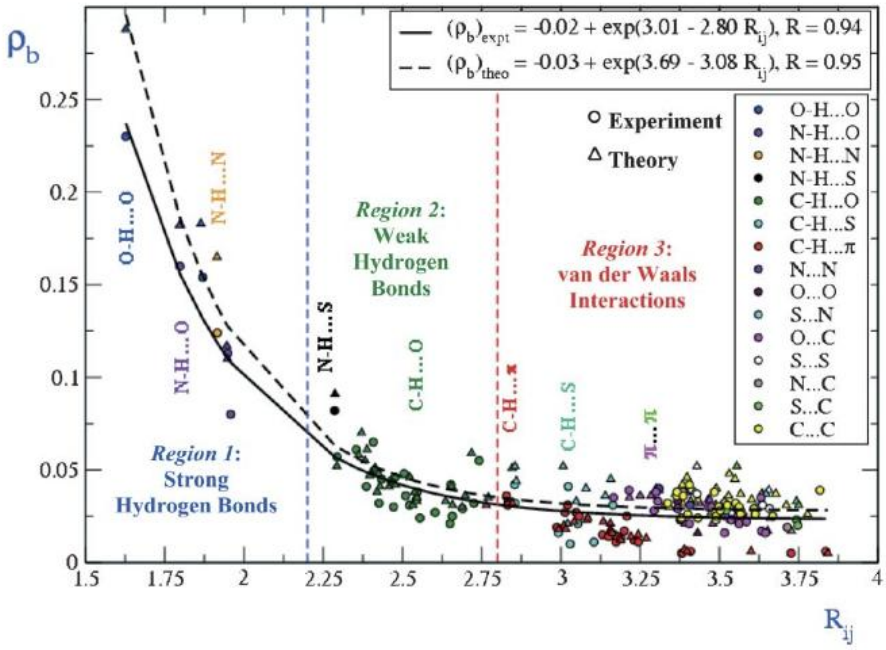

Figure 2.9: Munshi and Guru Row looked at the exponential dependence of the electron density (ρ_b) on R_{ij} and divided the hydrogen bonding into three categories based on this. Figure reproduced from *CrystEngComm*, 2005, **7**, 608–611 by permission of The Royal Society of Chemistry (RSC).[84]

A particularly interesting example that builds upon the work outlined above is that of Englert and co-authors, where the electron density distribution in N, N-dimethylbisguanidinium bis(hydrogensquarate) was analysed.[87] The authors note how the structure contains an impressive range of hydrogen bonds and by combining the criteria discussed above the nature of each interaction was found and the different interactions compared. The presence of a short O—H···O hydrogen bond, partially covalent in nature was determined by both the properties of the electron density and the energy densities at the BCP. This is just one study where charge density analysis draws out information on the nature and strength of hydrogen bonding.

2.4.1.2 Halogen bonding

Halogen bonding is growing in popularity in supramolecular chemistry and is increasingly being used as an alternative to or in concert with hydrogen bonding.[24] A number of charge density studies have added to the understanding of the nature and behaviour of halogen bonds. The strength and nature of halogen bonds have been determined in a number of crystal structures, with halogen bonds of both closed-shell nature and transit type interactions which span the closed-shell/ shared-shell boundary region observed. The location of valence shell charge concentrations (VSCCs) and valence shell charge depletion (VSCDs) zones around the halogen atoms, and the favourable interaction of charge depletion areas of the halogen atom with areas of charge concentration associated with the nucleophilic component of the halogen bond may partially explain the strong directionality and geometric preferences of halogen bonds (this is illustrated graphically in Figure 2.10).[88-93]

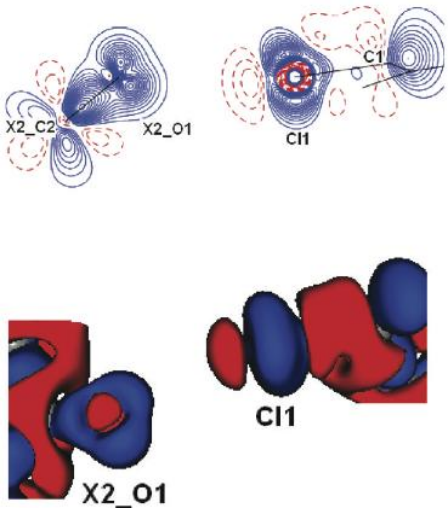

Figure 2.10: Static deformation density maps of a C—Cl···O=C halogen bond (*top* 2D and *bottom* 3D). Positive contours are solid blue lines and negative contours broken red lines. Contours drawn at intervals of 0.05 *e* Å^{-3}. X2 represents the symmetry code -x +1, y+ 1/2, -z +1/2. Figure reprinted (adapted) with permission from (*Cryst. Growth Des.*, 2011, **11**, 1855-1862). Copyright (2011) American Chemical Society.[91]

A related study, this time of chalcogen bonding, looking at the electron density of crystalline $C_8O_2H_4Se$ characterised the directionality and strength of the chalcogen (Se···O and Se···Se) and hydrogen (Se···H) bonding interactions in the structure.[94] In each interaction the values of $\rho(\mathbf{r}_{BCP})$, $\nabla^2\rho(\mathbf{r}_{BCP})$, $G(\mathbf{r}_{BCP})$ and $V(\mathbf{r}_{BCP})$ suggest they are weak interactions and the value of $|V|/G$ classifies them as closed-shell interactions.

2.4.2 Systematic charge density studies

The examples outlined above in Section 2.4.1 illustrate how charge density analysis can be used to explain the nature and strength of non-covalent interactions. In some of the examples the electron density distribution in a number of related structures has been modelled, which gives an idea of the generality of properties of interactions of a certain type or in a series of compounds. Looking at a series of related structures in a systematic way also allows the effect of changes to the chemical make-up on the electron density distribution in the structures to be determined and can be linked to differences in the behaviour and properties of related molecules. Previous studies, which have followed this approach, and provided both inspiration and a model for the systematic methodology undertaken in this thesis will now be described.

Pinkerton and co-authors have reported a series of studies on both steroidal and non-steroidal estrogens.[95-100] The aim of these studies was to explain the biological activity of these molecules on the estrogenic receptor by linking their activity to the electron density distribution in the structures and other observable properties. First, the authors introduced a standard local coordinate system to be maintained for the estrogen core in each structure when performing the aspherical refinement using the Hansen-Coppens model, to allow for fair comparison across the different structures.[95] The compounds

studied (shown in Figure 2.11) included estrone[100], both the 17β-estradiol: urea[99] and the 17α-estradiol: H_2O[96] complexes, genistein[98], and diethylstilbestrol and dienestrol[97]. After modelling the electron density distribution in each structure, the experimental electrostatic potential distributions were modelled. These showed areas of negative electrostatic potential above and below the aromatic rings of the estrogens and around the hydroxyl groups. Using both the electrostatic potential distributions and QTAIM derived atomic charges, an initial 'ligand-receptor' binding mode was suggested by the authors.[100] The electrostatic potential distribution was shown to be similar across the structures even in the case of significant structural differences.[98] The surface electrostatic potential is also linked to the observed relative binding affinities of the molecules for the estrogen receptor.[96]

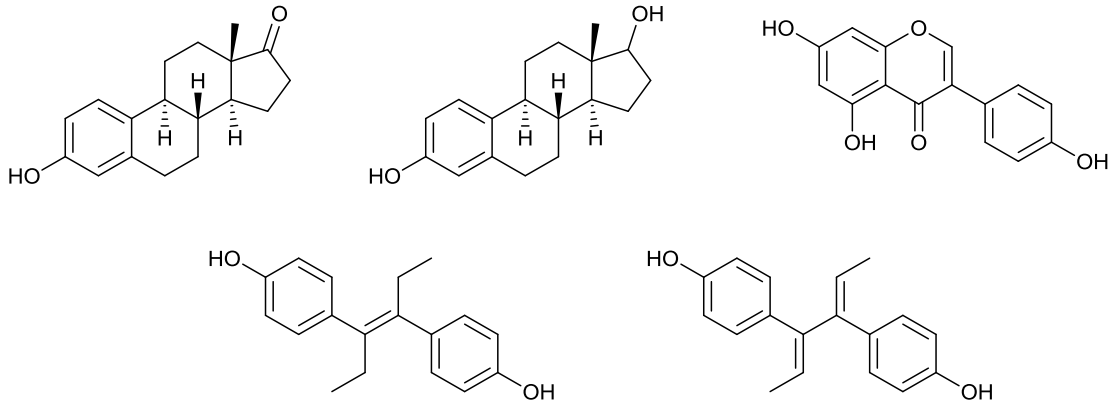

Figure 2.11: Steroidal and non-steroidal estrogens, top from *left* to *right*: estrone, estradiol and genistein and bottom diethylstilbestrol (*left*) and dienestrol (*right*).

Woźniak and co-workers have studied the neutral O—H···N and ionic N^+—H···O^- hydrogen bonding in a series of Schiff bases (see Figure 2.8).[81] They were able to show that the neutral O—H···N interaction was stronger than the ionic N^+—H···O^- hydrogen bond through the combination of geometric arguments and

analysis of the properties of the electron density at the BCPs associated with each hydrogen bonding interaction. Later, the study was extended to look at a range of different strength O—H···O and N—H···O hydrogen bonds in the Schiff base *N*-(5-methoxy-salicylidene)-*o*-hydroxybenzylamine (Figure 2.12), and the nature of these bonds classified by the properties of the electron density at the BCP, the values of the energy density at the BCP and the source function approach of Gatti[71] outlined in Section 2.3.4.4.3.

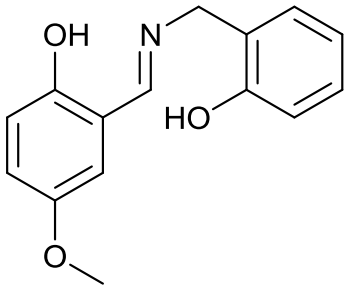

Figure 2.12: *N*-(5-methoxy-salicylidene)-*o*-hydroxybenzylamine.

In other work, Woźniak and co-authors have studied a series of ionic complexes of 1,8-bis(dimethylamino)naphthalene (DMAN) (see Figure 2.8), a proton sponge.[101-103] Proton sponges have interesting properties including high proton affinity, low nucleophilicity, slow protonation/deprotonation equilibria, and applications in modelling enzymatic catalytic processes. In their analysis, the authors focus on characterising the hydrogen bonding in the $DMANH^+$ cation in each complex. They propose a multicentre model of hydrogen bonding of the type $[Me_2N—H\cdots NMe_2]^{+}\cdots X^{\delta-}$ and fully characterise the range of hydrogen bonding seen, which transitions from weak hydrogen bonding to covalent type hydrogen bonding.[102] The role of C—H···O hydrogen bonding in the complexes is also elucidated.[103] The effect of protonation is

discussed by studying the electron density distribution in the uncomplexed DMAN compound, which differs to that observed in the $DMANH^+$ cation.[104]

Polymorphism is a particularly important field of research in crystallography. It is of particular relevance in the pharmaceutical industry, as different polymorphs can have different physical properties and behaviours. For this reason, several groups have looked at comparing the electron density distributions in polymorphic structures and linking this to any observed differences in the behaviour of polymorphic structures. The variation in the electron density distribution differs across sets of polymorphs. In their study of two polymorphs of hydrated 1,8-bis(dimethylamino)napthalene (DMAN) hydrochloride Hoser *et al.*[105] noted that the electron density distribution displayed minor differences, mainly seen in the properties of the intermolecular interactions. However, in another study differences in properties were observed for two polymorphs of benzidine dihydrochloride, particularly in the charges of the chloride anions in the structures and in the electrostatic potential distributions.[106]

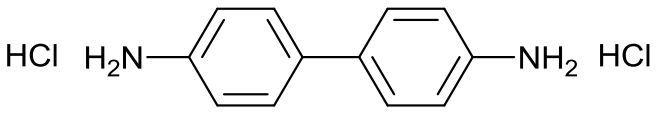

Figure 2.13: Benzidine dihydrochloride.

In the analysis of polymorphs of both coumarin and acetylcoumarin (see Figure 2.14) Guru Row and co-workers noted significant differences in the nature of the electron density distribution, observable through the disparity of the molecular dipole moments, calculated lattice energies, and variations in the

electrostatic potential distribution in the different forms of the two compounds.[107,108]

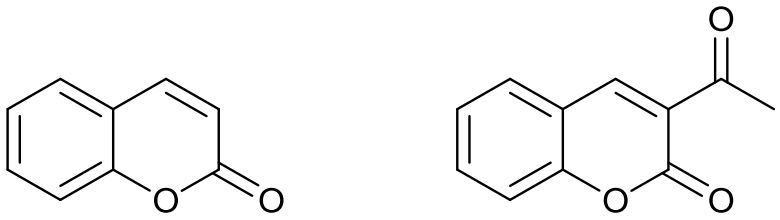

Figure 2.14: Coumarin (*left*) and acetylcoumarin (*right*).

The above examples illustrate how a systematic approach can allow the effect of subtle differences in molecular structure on the electron density distribution to be determined, and how this can be linked to changes in the properties and behaviour of these compounds.

2.5 Additional crystallographic tools

In this following section additional supplementary crystallographic methods and approaches used to assist and complement the charge density studies of the crystal structures reported in this thesis will be described.

2.5.1 Hirshfeld surface analysis

Hirshfeld surface analysis is a tool developed by Spackman and co-workers, which provides an increasingly popular, novel and detailed approach for the study of molecular packing and intermolecular interactions in crystal structures.[109–111] It is based on a similar theory to that of stockholder partitioning outlined in Section 2.3.4.5.2.

Underlying Hirshfeld surface analysis is the molecular Hirshfeld surface, which contains information about all the intermolecular interactions in a crystal structure.

The Hirshfeld surface is given by Equation 2.28 below,

(Eq. 2.28) $$w(\boldsymbol{r}) = \sum_{i\epsilon molecule} \rho_i(\mathbf{r}) / \sum_{i\epsilon crystal} \rho_i(\mathbf{r})$$

with w(**r**) a weight function equal to 0.5. $\rho_i(\mathbf{r})$ is the spherical atomic electron distribution located at the i^{th} nucleus. The weight function represents the ratio between the sum of the spherical atom electron densities for a molecule (known as the *promolecule*) and the same sum for the entire crystal (referred to as the *procrystal*).[112]

The Hirshfeld surface envelops the region of space surrounding a particular molecule in a crystal where the electron distribution exceeds that due to any other molecule. Two parameters can be used to uncover information about the contact distances from a point on the surface to atomic positions (d_i and d_e).

d_i is the distance from the surface to the nearest atom interior to the surface and d_e is the distance from the surface to the nearest atom exterior to the surface.[110]

As d_i and d_e do not take the size of the atom into account a further parameter d_{norm} is defined in terms of the van der Waals radii of the atoms to provide a normalised contact distance (Eq. 2.29).[113]

(Eq. 2.29) $$d_{norm} = \frac{d_i - r_i^{vdW}}{r_i^{vdW}} + \frac{d_e - r_e^{vdW}}{r_e^{vdW}}$$

Using d_i and d_e a fingerprint plot can be generated, which provides a concise 2D survey of the intermolecular interactions in the crystal.[112] This graphically displays the contacts in the crystal, with interactions associated with distances

of d_{norm} shorter than the van der Waals separation shown in red, those of similar length to the van der Waals separation white and those contacts with a longer separation than the van der Waals distances blue.[111]

A typical Hirshfeld surface and fingerprint plot (generated with CrystalExplorer 3.1[114]) are shown in Figure 2.15 and the Hirshfeld surface analyses performed in Chapters 3 and 5 of this thesis will highlight the information that this method provides on intermolecular contacts.

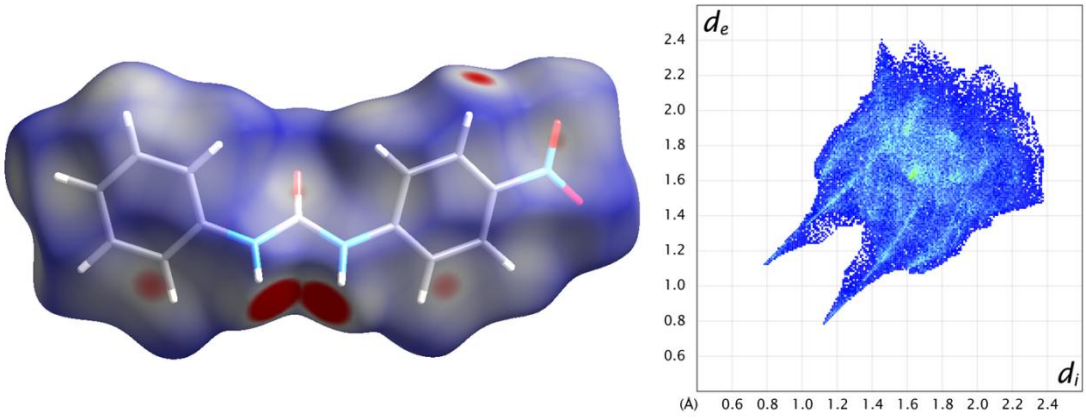

Figure 2.15: Hirshfeld surface (*left*) and 2D fingerprint plot (*right*) of the 1-(4-nitrophenyl)-3-phenylurea crystal structure.

2.5.2 Invariom refinement

The invariom approach has been developed to reproduce the electron density distribution from diffraction data of lower resolution than required for 'traditional' full Hansen-Coppens multipolar refinement. It was also designed to generate more accurate and precise geometries from IAM refinement.[115]

An invariom is defined as an invariant atom, which is assigned to each chemically unique atom in a structure. It is designated in terms of its nearest neighbours and dependant on the bond order. For example for methane the invariom for the hydrogen atoms is H1c and for the carbon atom C1h1h1h1h.

Each element has a finite number of invarioms, which differ depending on the atom's chemical environment.[115] A database (known as the generalised invariom database)[116] holds multipole parameters for each invariom (calculated using quantum chemical approximations), which can be transferred into the packages performing the Hansen-Coppens multipole refinement using the preprocessor tool InvariomTool.[117] Depending on the need of the chemist and the quality of the dataset the multipole parameters can be fixed or refined (in a particular manner outlined by Dittrich and co-workers[117]) and a model of the electron density distribution obtained. The application of the invariom approach to obtaining the electron density distribution from lower resolution datasets has been investigated and validated, with particular studies focusing on peptide-based crystal structures.[118–121]

However, as the constraints used in invariom refinement are stronger than a full multipole refinement they are used herein to provide a model for the electron density distribution in crystal structures where only lower resolution datasets are available and to deal with cases of disorder (crystal structures containing disorder significantly complicate full multipole refinement and the invariom approach has had some success in treating disorder[122,123]).

2.6 Aims:

Linking structure to function is a key goal in anion-receptor chemistry and has been described in Chapter 1. This is done systematically by evaluating the effects of designed modifications to anion-receptor molecules on the efficacy of their function. Single crystal X-ray diffraction studies are already a major tool in analysing anion-receptor complexes. Chapter 2 has shown that moving beyond normal resolution X-ray diffraction methods and using the multipole aspherical atom model can give a description of the electron density distribution in a crystal structure, which has been successfully exploited to study non-covalent interactions in a range of chemical systems.

The aim of this thesis is thus to apply experimental charge density analysis to anion-receptor chemistry in a systematic manner, to investigate the electron density distribution in anion-receptor complexes, and link this to the properties of the complexes. The modifications supramolecular chemists perform to tailor their anion-receptor molecules to give particular affinities and functions will be assessed.

This thesis seeks to answer three key research questions:

1. What effect different anion types have on the electron density distribution and hydrogen bonding strength in anion-receptor complexes.
2. How altering chemical substituents at the periphery of an anion-receptor molecule change the hydrogen bonding and electron density distribution in the crystal structure.
3. The differences in hydrogen bond behaviour and electron density distribution caused by varying the central hydrogen bond donor group

used for anion binding in receptor molecules that share structural similarities.

This thesis aims to demonstrate that performing experimental charge density analysis substantially supplements standard resolution structural studies and provides important information not available from any other techniques. Therefore, full standard resolution structural studies of the crystal structures will be given before the electron density distribution obtained from high resolution X-ray diffraction studies is discussed for each set of structures reported this thesis.

Chapter 3: Standard resolution studies of symmetrically nitro-substituted urea-based anion-receptor complexes

3.1 Introduction to ureas

This chapter focuses on the characterisation of the anion binding properties of a series of urea-based receptors in both solution and the solid-state. The majority of this work has been published as Systematic structural analysis of a series of anion receptor complexes, *CrystEngComm*, 2013, **15**, 9003 - 9010[124] and is reproduced by permission of the Royal Society of Chemistry (see A.8 for copyright permissions).

http://pubs.rsc.org/en/content/articlelanding/2013/ce/c3ce41503a#!divAbstract

Urea ($CO(NH_2)_2$) was first artificially synthesised by Friedrich Wöhler in 1828.[125] Urea derivatives are easy to synthesise, possess both hydrogen bond donor and acceptor groups and are easily fuctionalised. For this reason, urea has found applications across a diverse range of supramolecular systems, including gels[126], organocatalysts[127], anion binding[128] and anion transport[129]. Urea, with its efficient hydrogen bond forming ability is also a good choice as a co-crystal component in solid-state studies.

3.1.1 Ureas in the solid-state

Urea-based molecules are known to crystallise well. The α-tape motif, shown in Figure 3.1 is frequently observed in crystal structures containing urea molecules.[126]

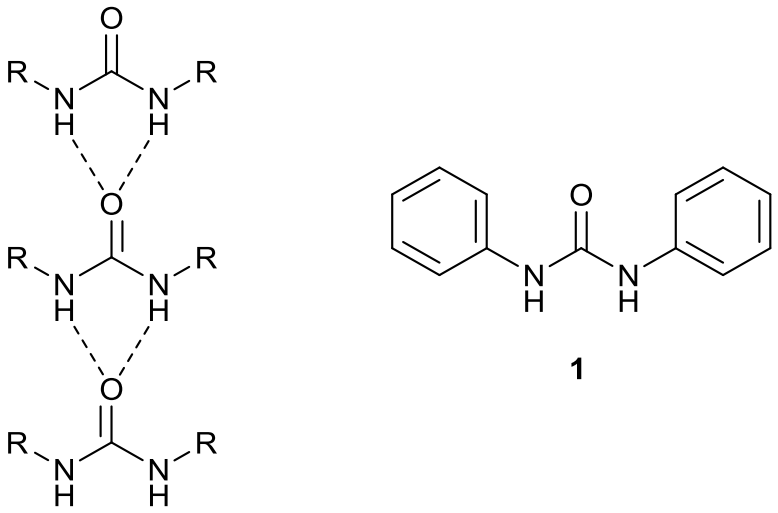

Figure 3.1: α-Tape motif of hydrogen bond donor: acceptor self association often seen in the crystal structures of urea-based molecules and the N,N'-diphenylurea scaffold (**1**).

This tape motif was noted by Nangia and co-workers in their study of the crystal structures of a series of substituted N,N'-diphenylureas, in which the authors discussed the ability of electron-withdrawing substituents on the phenyl rings to promote the formation of co-crystals and solvates with hydrogen bond acceptor rich molecules.[130] Other studies by Etter *et al.*, on the hydrogen bond properties of 1,3-bis(3-nitrophenyl)urea solvates and co-crystals made similar observations and noted other hydrogen bonding motifs in the crystal structures.[131] They also found that flat planar aromatic substituents attached to a central urea unit provide little or no steric hindrance

to hydrogen bonding by the urea functional group, suggesting this scaffold is particularly attractive for the purposes of this study.

3.1.2 Ureas as anion-receptors

As described above, ureas have been used extensively in anion binding. While an overview of some urea-based anion-receptors will now be given, this is by no means extensive and serves only to highlight the principles used in designing the molecules studied in this chapter. For a more extensive overview of urea-based systems in anion-receptor chemistry readers are directed to the review of Gale and co-workers and references therein.[24]

One major advantage of urea-based receptors is that they are able to coordinate both spherical anions, such as the halides (fluoride, chloride, bromide and iodide) and other shaped anions including Y-shaped oxoanions (for example carboxylates, phosphates and nitrates etc.).

One of the earliest examples came from the Wilcox group, who showed (using UV-Vis spectroscopy) that aryl urea **2** complexed oxoanions in a 1:1 ratio in chloroform at 298 K. The association constants (K_{ass}) suggest strong affinity and selectivity for benzoate (27,000 M^{-1}) over diphenylphosphate (9,000 M^{-1}), norbornyl sulfonate (6,900 M^{-1}) and tosylate (6,100 M^{-1}), with the anions added as their tetrabutylammonium (TBA) salts.[132]

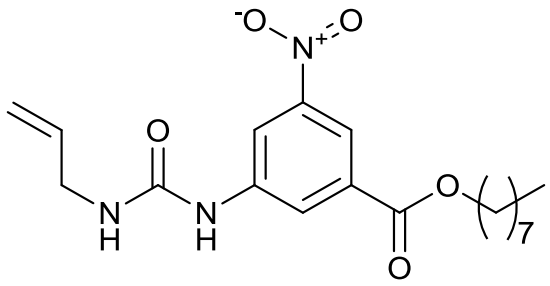

2

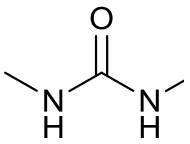

3

Figure 3.2: Wilcox's aryl urea (**2**)[132] and Hamilton's 1,3-dimethylurea (**3**)[133].

Hamilton demonstrated that even simple 1,3-dimethylurea (**3**) is able to bind acetate in the competitive solvent DMSO with a K_{ass} of 45 M^{-1}. The binding was studied by NMR titration experiments with the anion added as tetramethylammonium acetate.[133]

Rebek and co-authors introduced multiple urea groups to a receptor based on the xanthene scaffold. This convergent hydrogen bond array (**4**) had increased affinity for tetramethylammonium benzoate over mono-urea **5** (200,000 M^{-1} *vs.* 400 M^{-1} respectively) as measured in $CDCl_3$ using NMR titration studies. Job plots confirmed the 1:1 anion to receptor ratio and suggest that concerted hydrogen bonding between all the N—H donors in the cleft of the bis-urea is the reason for its increased anion affinity.[134]

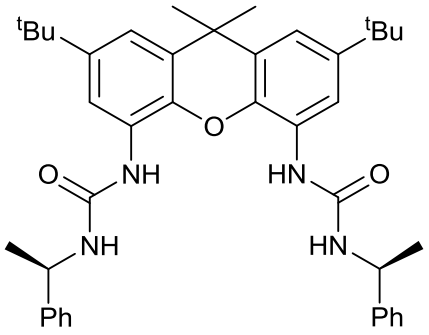

4

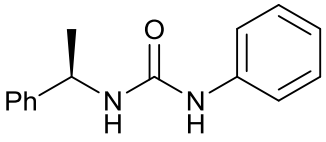

5

Figure 3.3: Rebek's xanthene-based urea anion-receptor (**4**) and mono-urea analogue (**5**)[134].

Convergent bis-ureas have also been used by Gale and co-authors, with receptor **6** (based on the *o*-phenylenediamine scaffold) binding acetate, benzoate and dihydrogen phosphate with K_{ass} of 3210, 1330, and 732 M^{-1} respectively in a 0.5% H_2O-d_6-DMSO solvent system determined from NMR titration studies.[135] The authors also showed modification of the central and pendant phenyl rings with electron-withdrawing substituents increased anion affinity by acidifying the N—H hydrogen bond donor groups and by pre-organising the cleft for anion binding.

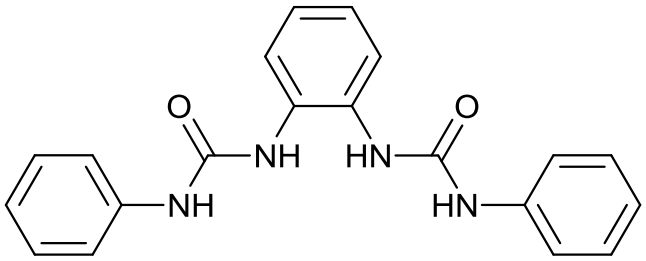

6

Figure 3.4: Phenylenediamine bis-urea anion-receptor **6**[135].

Building on this, urea has been incorporated into tris(2-aminoethyl)amine (tren) based systems[136,137], mixed-amide urea receptors and macrocyclic hosts.[138,139] They have also been combined with halogen bonding in a series of receptors reported by Chudzinksi *et al.*, which bind both oxoanions and halides through concerted halogen and hydrogen bonding.[140]

Recent advances have seen urea-based anion-receptors incorporated into a multitude of systems for a variety of purposes outlined below. Urea groups are used for hydrogen bonding in mechanically interlocked architectures, for example the catenane species of Chas and Ballester.[141] Custelcean *et al.* have used urea ligands to construct cages in the presence of tetrahedral anions EO_4^{n-} (E= S, Se, Cr, Mo, W where n=2 and P where n=3), with these anions acting as a template for the assembly of the cages.[142] Other supramolecular architectures containing the urea moiety include the foldamers reported by Jeong and co-authors, which form 1:1 complexes with chloride and sulfate, with the presence of either anion promoting helical formation.[143]

Numerous examples of sensors containing urea groups can be found. Recently Johnson, Haley and co-workers have reported ON-OFF and OFF-ON fluorescence selective chloride sensors (**7-9**) based on the bis(anilinoethynyl)pyridine scaffold.[144] The peripheral substituent tailors the response of each receptor to HCl.

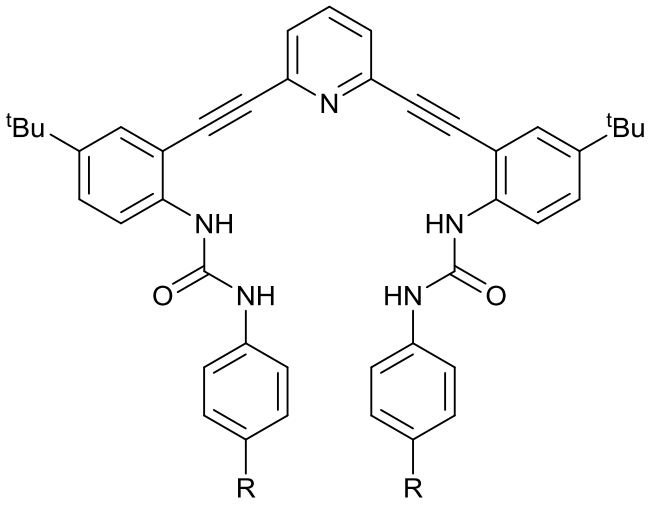

7 = R = H
8 = R = OMe
9 = R = NO_2

Figure 3.5: Chloride selective sensors **7–9** reported by Haley, Johnson and co-workers.[144]

A gold(I) acetylide complex with a urea group (**10a**) reported by Zhou *et al.*, allows the 'naked-eye' detection of fluoride in DMSO by a colour change from colourless to yellow/orange. UV-Vis titrations determined that this corresponded to the deprotonation of the urea N—H upon addition of fluoride to the receptor under these conditions.[145] The crystal structure of the related receptor (**10b**) is shown in Figure 3.7, with two independent receptor molecules present in the asymmetric unit of the unit cell.

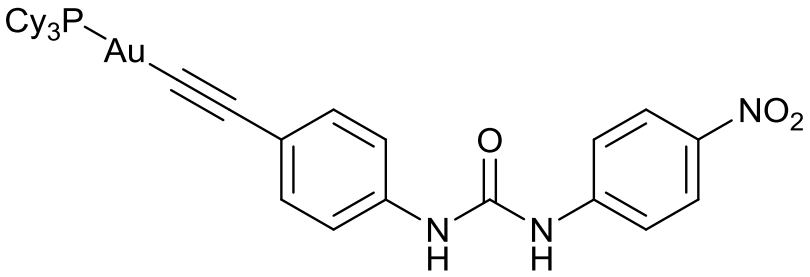

10a

Figure 3.6: Colorimetric fluoride sensor **10a**.[145]

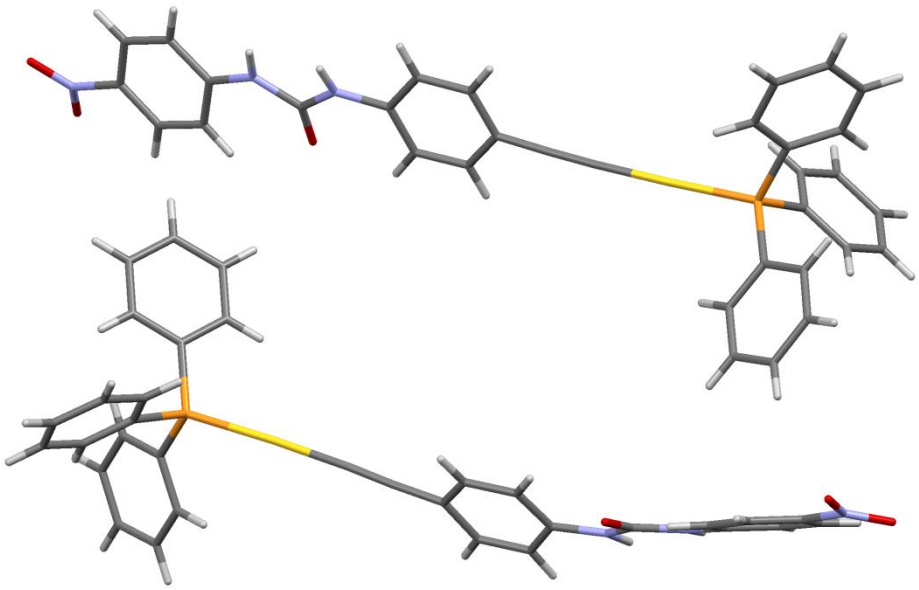

Figure 3.7: Crystal structure of the gold(I) acetylide receptor (**10b**)[145] with urea groups that functions as a 'naked-eye' fluoride sensor. Atoms are drawn as capped sticks with carbon atoms grey, oxygen atoms red, nitrogen atoms blue, phosphorus atoms orange and gold ion yellow. Hydrogen atoms light grey.

An elegant use of urea-based receptors for the extraction of sulfate from aqueous $NaNO_3$-Na_2SO_4 into $CDCl_3$ (anions added as TBA salts) is described by Yang and co-workers.[146] The tripodal hexa-urea **11** encapsulates sulfate with twelve hydrogen bonds, this represents the first example of a single organic

receptor that is able to fully saturate the sulfate anion. The K_{ass} was determined by NMR titration studies in a 25% H_2O-d_6-DMSO solvent mixture to be $>10^4$ M^{-1}. The crystal structure in Figure 3.8 illustrates how **11** wraps around the sulfate anion to form a pseudo-tetrahedral cage surrounding the sulfate in the cavity, with each N—H hydrogen bond donor group pointing directing towards the anion.

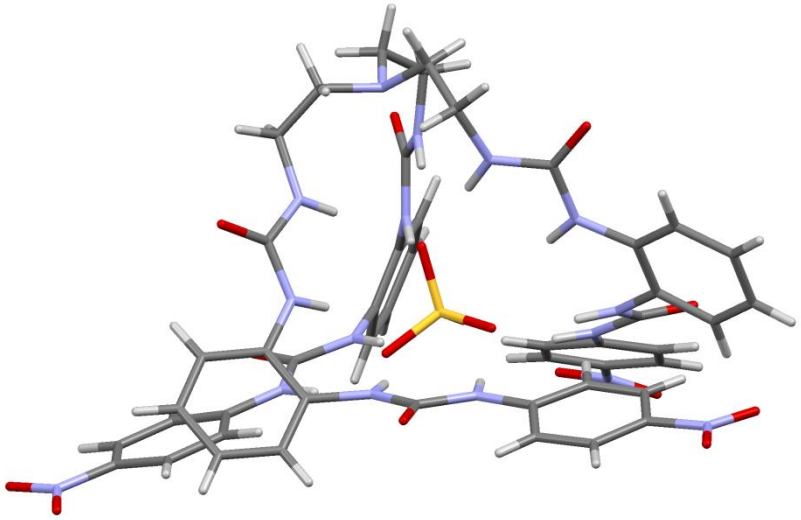

Figure 3.8: Sulfate encapsulated by hexameric urea-based receptor **11**[146]. The DMSO solvent molecule and TBA counter-cations are omitted for clarity. Atoms drawn as capped sticks. Nitrogen = blue, oxygen = red, sulfur = yellow, carbon = grey, hydrogen = light grey.

Finally, various research groups have incorporated urea N—H hydrogen bond donors into receptors to facilitate anion transport across synthetic lipid bilayers.[147,148]

3.2 Systematic family under investigation

As illustrated above, the urea moiety is an attractive and popular group for binding anions. The aim of this thesis is to better understand the relationship between receptors and anions, in terms of the electronic distribution of each individual component and the molecular ensemble as a whole. From this information the interactions between the receptor and anion and the strength and properties of these interactions can be obtained.

Building on the information gained from the literature examples outlined above, a series of receptors was designed to systematically investigate the electronic distribution in anion-receptor complexes. As the urea group is incorporated into receptor scaffolds of varying degrees of sophistication and complexity, in this study the basic scaffold of the receptor was stripped down to contain a single urea. This was to simplify the investigation of the key interaction in these systems, namely the urea N—H bonds with anions. As outlined above in Section 3.1.1, flat planar aromatic substituents ensure there is minimal steric hindrance to anion binding, hence these were incorporated into the scaffold design. This also allowed for diversity to be introduced to the receptor motif by altering the type and position of substituents on the phenyl rings. Thus modifications such as electron-withdrawing substituents, which increase the acidity of the N—H bonds and improve their hydrogen bond donor ability, can be studied to see their effect on the electronic distribution in the anion-receptor complex.

3.2.1 1,3-Diphenylurea scaffold

The starting point of the designed receptor series was 1,3-diphenylurea (**1**). This has been investigated by Gale and co-workers who found that despite its

simple structure it is an efficient binder of acetate with an association constant of 1260 M^{-1} in a 0.5% H_2O-d_6-DMSO solvent mix at 298 K calculated from NMR titration studies. The K_{ass} for chloride, benzoate and dihydrogen phosphate were 31, 674 and 523 M^{-1} respectively (anions in the form of their TBA salts).[149]

From this promising start a series of receptors was designed incorporating the electron-withdrawing nitro groups as a substituent on the phenyl ring (see Figure 3.9) to further acidify the N—H bonds and increase the potency of the anion-receptors. Maintaining the receptor's bis-substitution, the position of the nitro group was varied from *ortho* (**12**) to *meta* (**13**) to *para* (**14**). This allows the effect of substituent position, and hence different electron-withdrawing abilities, on the anion binding to be investigated. The diversity was further increased by including a di-bis substituted receptor 1,3-bis(3,5-dinitrophenyl)urea **15**. This was postulated to be the substitution pattern with the largest electron-withdrawing ability and hence the most acidic N-H bonds.

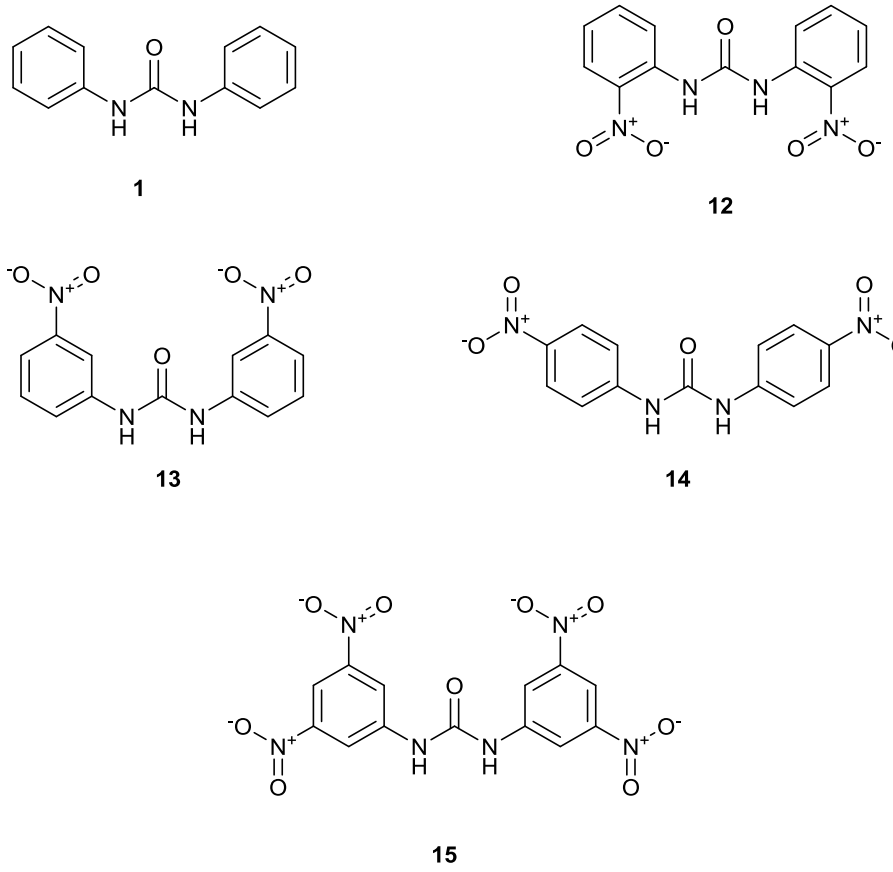

Figure 3.9: Family of urea-based receptor structures designed and investigated for anion binding properties in solution and the solid-state (**12**-**15**).

Compound **14** (1,3-bis(4-nitrophenyl)urea), the *para* substituted receptor, has previously been studied by Fabbrizzi and co-workers by X-ray crystallography, UV-Vis spectroscopy and ^{1}H NMR titration techniques.[150] They found it formed 1:1 complexes with a wide variety of anions with the association constants shown to decrease in the following trend: CH_3COO^- > $C_6H_5COO^-$ > $H_2PO_4^-$ > NO_2^- > HSO_4^- > NO_3^-. This suggested the nitro substituted receptors were an appealing series of receptors to target in this study. The crystal structures of a range of polymorphs of the free ligand **13** (*meta* substituted receptor) and its co-crystals with neutral molecules have been reported in the CSD.

3.3 Results and discussion

Receptors **12**–**15** were synthesised using adapted literature procedures by reacting the appropriate aniline with the corresponding isocyanate in DCM or toluene (see Section 7.1.3 for more details).

A series of crystallisations were undertaken of the four receptors, in a variety of solvents, both as single and mixed solvent systems. The aim was to crystallise both the free ligands, and the anion-receptor complexes. To limit the likelihood of disordered cations in the structures, which would present difficulties during subsequent multipole refinements (see Chapter 4 for details), the tetramethylammonium (TMA) cation was used as the counter ion in these crystallisations. The full details of the crystallisation procedures can be found in Chapter 7. The table below details the crystal structures that were obtained across the series of receptors and the numbering of these crystal structures in this thesis.

Table 3.1: Crystal structures of free ligands and complexes of **12**–**15**.

Receptor	Free ligand	Solvates	Chloride complex	Acetate complex	Fluoride complex	Sulfate complex
Ortho (**12**)	✓ (**c.s.1**)	×	×	×	×	×
Meta (**13**)	✓(**c.s.2**)	×	✓(**c.s.5**)	✓(**c.s.8**)	×	×
Para (**14**)	✓(**c.s.3**)	×	✓(**c.s.6**)	✓(**c.s.9**)	✓(**c.s.11**)	✓(**c.s.12**)#
3,5-Dinitro (**15**)	×	✓(DMSO) (**c.s.4**)	✓(**c.s.7**)#	✓(**c.s.10**)	×	×

#Crystal structures reported for completeness but not discussed in this thesis.

The Crystallographic Information Files for these structures can be found in the electronic Appendix included in this thesis. In the case of **c.s.2** the unit cell parameters obtained from the diffraction pattern of the crystals matched those reported in the CSD (discussed in Section 3.2.1[131]) and so a full data collection was not undertaken. For **c.s.11** a polymorphic structure was observed at lower temperature (60K) for which unit cell parameters were obtained but no definitive structure could be refined. **c.s.7** is a complex structure, in the *C*2/*m* space group, with TMA cations and MeCN solvent molecules situated on mirror planes. The entire system comprises two full TMA cations, two receptor molecules, two chloride anions and two solvent molecules. Due to the greater complexity of this structure with the presence of solvent molecules, this structure is reported in this thesis for completeness but will not be discussed in any further detail in this chapter. An additional crystal structure (**c.s.12**), a sulfate complex of 1,3-bis(4-nitrophenyl)urea, was obtained which also has a water solvent molecule coordinated to the urea that is involved in hydrogen bonding to the sulfate anion. The complexity of the structure means it is outside the main scope of this thesis and is included as a CIF in the Appendix for completeness. The crystallographic details of the crystal structures are found below in Table 3.2 (those for **c.s.3** are found in Table 4.8 in Section 4.4.6.1 and **c.s.5**, **6**, **9**, **10** and **11** in Table 4.1 in Section 4.4.1 as they contain the details of the fitting statistics of the multipole refinements performed on these crystal structures in Chapter 4.)

Table 3.2: Crystallographic details for crystal structures **c.s.1**, **c.s.4**, **c.s.7**, **c.s.8** and **c.s.12**.

Structure	**c.s.1**	**c.s.4**	**c.s.7**	**c.s.8**	**c.s.12**
Formula	$C_{13}H_{10}N_4O_5$	$C_{17}H_{20}N_6O_{11}S_2$	$C_{72}H_{86}Cl_4N_{30}O_{36}$	$C_{19}H_{25}N_5O_7$	$C_{34}H_{46}N_{10}O_{15}S$
Crystal system	Orthorhombic	Orthorhombic	Monoclinic	Monoclinic	Monoclinic
Space group	*Pca*2$_1$	*Pccn*	*C*2/*m*	*P*2$_1$/*n*	*P*2$_1$/*n*
a (Å)	21.8064(19)	5.2600(4)	26.6631(6)	12.5269(3)	6.5775(5)
b (Å)	4.6133(3)	19.2327(14)	24.0557(4)	6.6896(2)	27.1142(19)
c (Å)	12.5773(11)	22.6139(16)	17.3853(4)	25.2440(9)	21.9859(15)
α (°)	90.00	90.00	90.00	90.00	90.00
β (°)	90.00	90.00	120.995(1)	93.856(2)	93.063(7)
γ (°)	90.00	90.00	90.00	90.00	90.00
V (Å^3)	1265.3(2)	2287.7(3)	9558.7(3)	2110.7(1)	3915.4(5)
Final R indexes [I>=2σ (I)]	R_1 = 0.0541 wR_2 = 0.1238	R_1 = 0.0364 wR_2 = 0.0905	R_1 = 0.0614 wR_2 = 0.1580	R_1 = 0.0605 wR_2 = 0.1355	R_1 = 0.0501 wR_2 = 0.1126
Final R indexes [all data]	R_1 = 0.0621 wR_2 = 0.1303	R_1 = 0.0483 wR_2 = 0.0969	R_1 = 0.0839 wR_2 = 0.1708	R_1 = 0.1257 wR_2 = 0.1634	R_1 = 0.0830 wR_2 = 0.1258
GoF on F^2	1.098	1.054	1.091	1.047	1.017
$\Delta\rho$(**r**) (*e* Å^{-3})	0.29/-0.24	0.42/-0.40	0.88/-0.76	0.32/-0.28	0.24/-0.40

The free ligand and solvate structures (**c.s.1**–**4**) and the anion receptor complexes (**c.s.5**, **6**, **8**–**11**) were first studied by the standard resolution techniques and it is these results that are reported in this chapter.

3.3.1 Solution state studies

To assess the affinity of receptors **12**–**15** for the anions in our structural family in solution, ^{1}H NMR titration studies were performed in a mixed solvent system of 0.5% H_2O–d_6–DMSO. Full details of the methodology for these studies can be found in the experimental section of this thesis (Section 7.3). Although the counter ion in the crystal structures was the TMA cation, the TBA chloride and fluoride salts were used in these titration studies. This was due to the limited solubility of the TMA chloride and fluoride salt in the selected solvent system. The solvent system used in solution was not the same as that used in the

crystallisation studies of these receptors. It was chosen to compare to the majority of studies in this research area. In addition, due to the less competitive nature of acetonitrile (the solvent generally used during crystallisation), the affinity of each receptor might have been too high to critically compare and assess the differing selectivity and strength of interaction between each receptor and the three anions. It can be assumed that changing the tetraalkylammonium cation in this system is not significantly altering the environment experienced by the anion-receptor complex as tetraalkylammonium cations are non-coordinating and should thus not interfere with the binding event.

The results of the NMR titrations are shown below in Table 3.3. Generally the shift in the resonance of the N—H protons of the urea was followed during the course of the titration and fitted using the WinEQNMR program.[151] Stack plots of each titration and the fit plots from WinEQNMR can be found in Appendix A.1. For each receptor the binding was fitted to a 1:1 receptor: anion ratio. Representative Job plots of **14** with TMA acetate and TBA chloride (see Appendix A.1) supported a 1:1 binding mode. The behaviour of fluoride will be discussed further below.

Table 3.3: Association constants, K_{ass} (M^{-1}) from proton NMR titration studies: error in value given in brackets.

Receptor	TMA OAc	TBA Cl	TBA F
Ortho nitro (**12**)	514 (9%)	<10	61 (15%)†
Meta nitro (**13**)	>10^4	56 (1%)	182 (8%)†
Para nitro (**14**)	>10^4	118 (2%)	<10†
3,5-dinitro (**15**)	1239 (2%)†	*nd*	*nd*

† The NH resonance disappears at the beginning of the titration and cannot be followed so a CH resonance from the phenyl ring is selected and followed, and the shift in this resonance fitted to give the association constant reported.

For each receptor (**12**-**15**) the strongest binding is observed for acetate with higher affinity over chloride and fluoride. The selectivity for acetate over chloride may be due to the higher basicity of the acetate anion. In the case of fluoride, the disappearance of the N—H peak in each titration suggests that under these conditions fluoride deprotonates these receptors in solution. This was tested by titrating **14** with TBA OH and the resulting stack plot was similar to that for TBA fluoride. Additionally, a Job plot of **14** with TBA fluoride also did not reflect a 1:1 binding mode (See Appendix A.1). The binding affinity for each receptor with chloride increases as the position of the electron-withdrawing nitro group is altered from the *ortho* to *meta* to *para* position of the phenyl ring. This case is mirrored for acetate with K_{ass} increasing for *ortho* < *meta* ~ *para*. This can be attributed to the nitro groups at the *ortho* position blocking the binding site, as suggested by Brooks *et al.*[135]. The nitro groups at the *para* position have a better ability to withdraw electron density from the urea N—H bonds, acidifying them more strongly than *meta* substituted nitro groups, as the resonance electron-withdrawing effect of the *para* group is

stronger than the inductively electron-withdrawing *meta* nitro group. This means the *para* substituted receptor **14** is the strongest anion binder of **12**-**15**. Receptor **14** was hypothesised to be a weaker binder than receptor **15**, which is 3,5-dinitro substituted on each phenyl ring. However, the table shows the affinity for actetate of **15** is lower. The loss of the NH resonance upon titration of TMA OAc and the similarity between this titration and that with TBA OH (see Appendix A.1) suggests this is another case of the anion deprotonating the receptor in solution. This appears to have been caused by the increased number of electron-withdrawing units on the phenyl rings.

3.3.2 Solid-state analysis

In each of the crystal structures of the free ligands (**c.s.1**-**3**) the asymmetric part of the unit cell is comprised of a single receptor molecule. In the DMSO solvate (**c.s.4**) the asymmetric unit consists of half a receptor molecule and a DMSO solvent molecule with the total number of each component in the unit cell 4: 8 receptor: DMSO. (See Figure 3.10 for free ligand and solvate structures.)

For complexes **c.s.5**, **c.s.6**, and **c.s.8**-**10** the asymmetric unit is comprised of one anion, one TMA cation and one receptor molecule. However, in **c.s.11** the asymmetric unit consists of half a TMA cation, half a fluoride anion and one receptor molecule. Figure 3.11 displays the anion binding interactions in each of the crystal structures of the anion-receptor complexes discussed in this chapter.

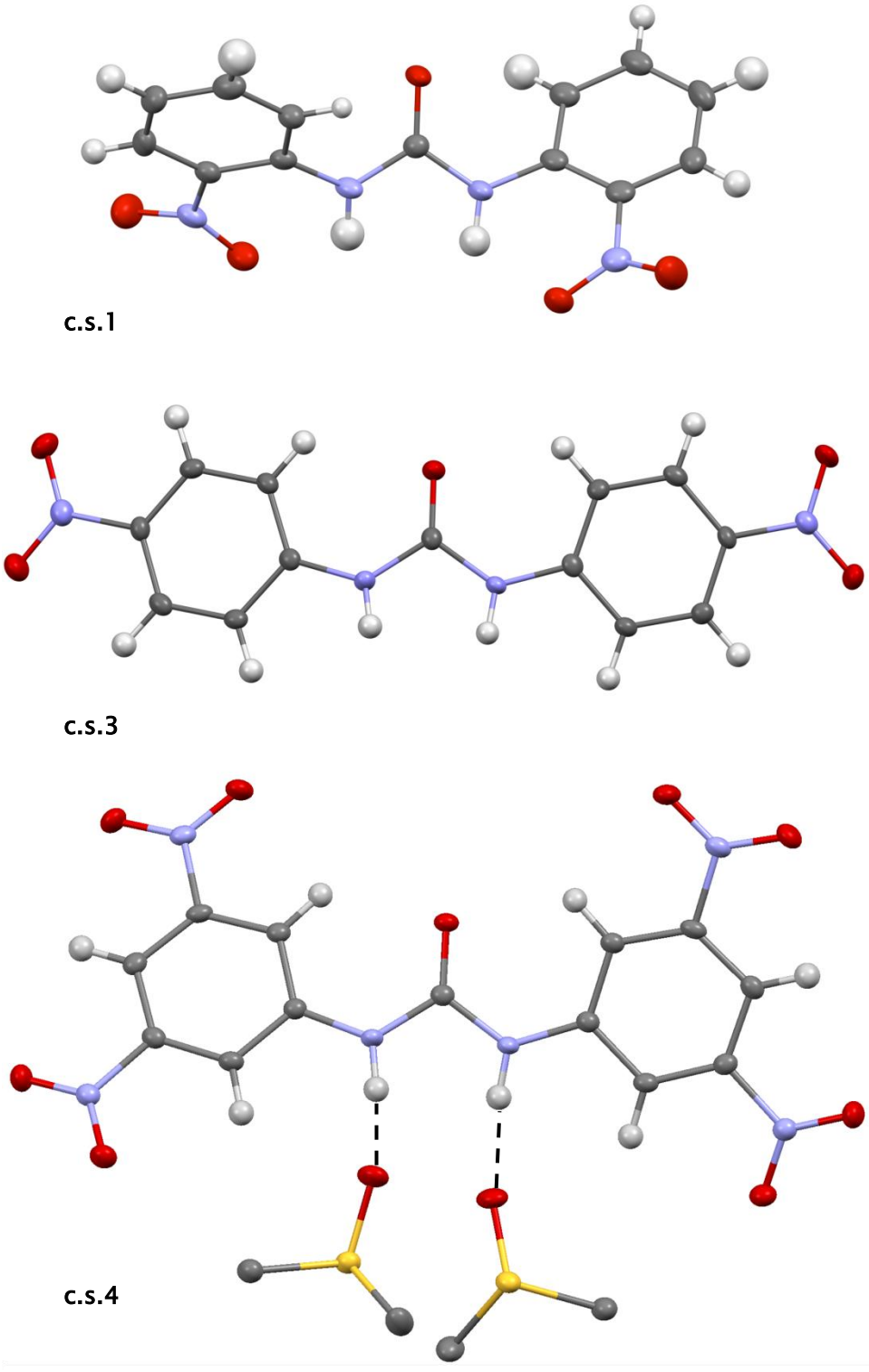

Figure 3.10: **c.s.1**, **c.s.3** and **c.s.4**. Diagrams are drawn with ellipsoid plots for non-hydrogen atoms at the 50% probability level. Hydrogen atoms of DMSO in **c.s.4** omitted for clarity. Hydrogen bonding represented by dashed lines. Oxygen = red, nitrogen = blue, carbon = grey and hydrogen = light grey.

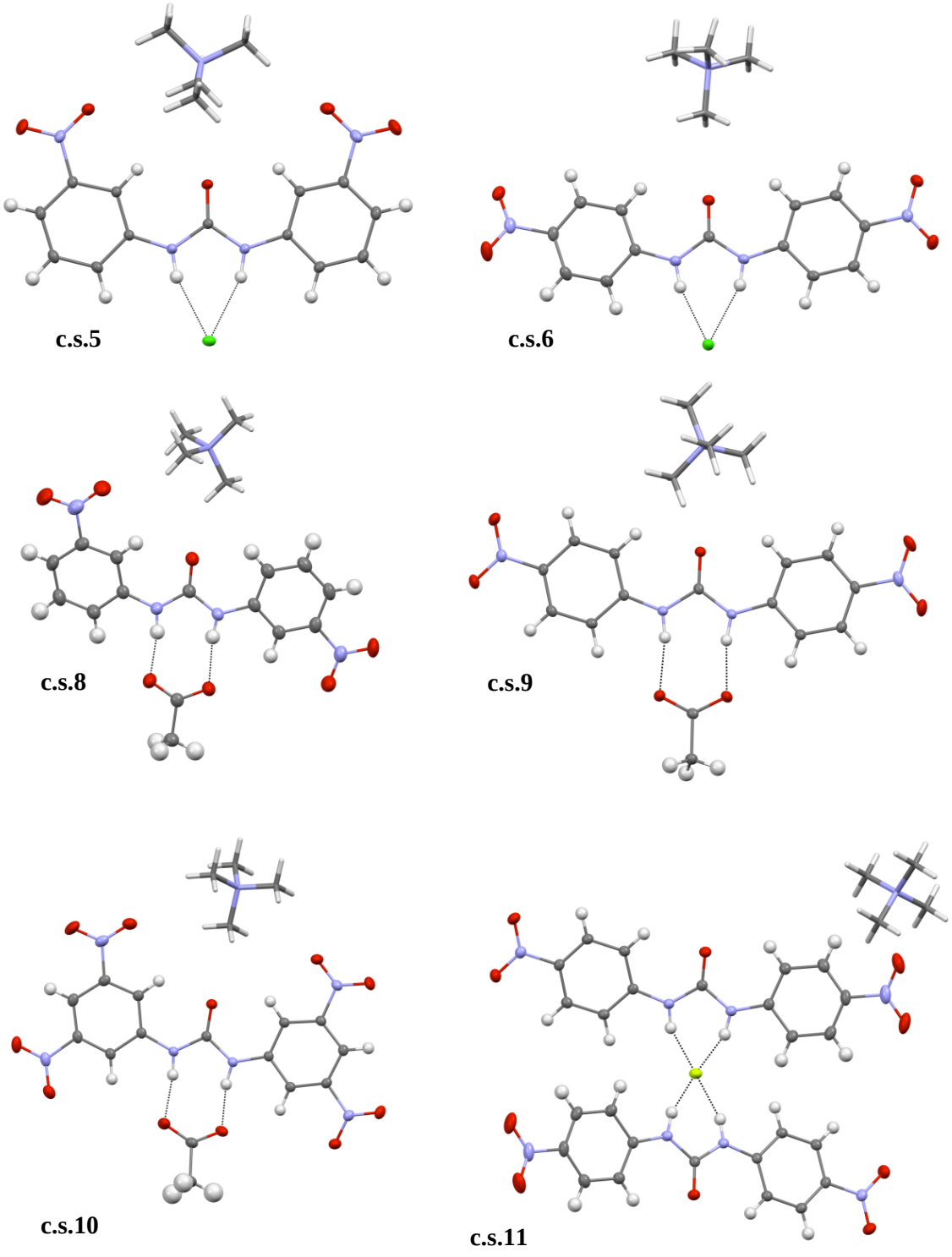

Figure 3.11: **c.s.5**, **6**, **8**, **9**, **10** and **11** displaying each receptor: anion complex. Diagrams are drawn with ellipsoid plots for non-hydrogen atoms at the 50% probability level. The TMA cation is depicted as capped sticks for clarity. Hydrogen bonding represented by dashed lines. Chloride anion is shown in green and fluoride anion in yellow.

Figure 3.12 displays the crystal packing observed in **c.s.11**, where the receptor and anion unit appear to adopt a criss-cross motif and the TMA cations form layers separating individual anion: receptor units across the *a* axis.

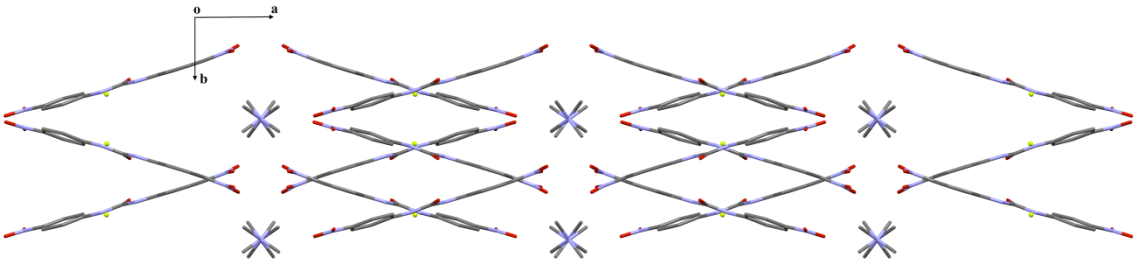

Figure 3.12: Molecular packing diagram of **c.s.11**, viewed down the *c* axis of the unit cell, displaying the twisted conformation of the urea groups and the positions of the TMA groups between the receptor: anion units, forming a channel down the *c* axis. Hydrogen atoms are omitted for clarity; fluoride ions are drawn as ball and stick while the other atoms are capped sticks. Red = oxygen, blue = nitrogen, grey = carbon.

3.3.2.1 Single crystal neutron diffraction

Following from the observation that deprotonation of the receptors by the more basic anions (acetate and fluoride) can occur in solution, it was desirable that the precise positions of the protons in the crystal structures were determined. It has already been proved that proton transfer reactions in these types of urea receptors can occur when binding basic anions. Before deprotonation it is possible that the proton of the donor atom can migrate partially along the vector between the donor and acceptor and become more closely associated with the anion.[152] This would influence the chemistry and hydrogen bonding in these complexes and so ascertaining to what extent, if at all, this proton migration occurs in the complexes was crucial. Neutron diffraction is the definitive method for determining hydrogen atom positions and thermal displacement parameters. Hence neutron diffraction studies were

performed at the ISIS Neutron Spallation Source (Chilton, U.K) aided by Dr. Hazel A. Sparkes, who directed the experiments on these compounds on the SXD instrument[153] (for full experimental procedure see Section 7.6.1). The experiments were run at 100K and ambient pressure in order to be consistent with the single crystal X-ray diffraction studies (see Section 3.3.2.2 below). Two neutron diffraction datasets were collected, one for **c.s.5** and **c.s.9**. The average N—H bond distance for the urea group in the studied structures (1.034 Å), was within the range quoted by the International Tables of Crystallograhy[154,155] (typically 1.009 Å). It can be confidently stated that no proton transfer occurs and the hydrogen atoms are associated with the urea nitrogen atoms.

3.3.2.2 Single crystal X-ray diffraction

The molecular conformations and overall crystal structures of the anion-receptor complexes and free ligands are directed, as expected by the N/O—H donor and O/N acceptor atoms in the individual molecules that make up the complexes. Differences between the free ligands and anion-receptor complexes were however observed.

3.3.2.3 Hydrogen bonding

3.3.2.3.1 Free ligand crystal structures

In the free ligands there is a variation in the types of hydrogen bonding observed (see Table 3.4). The more linear hydrogen bonds in **c.s.1** correspond to classic alpha tape urea N-H···O interactions. They are accompanied by intramolecular N—H···O urea: nitro hydrogen bonds, which may be the cause of the receptor's poor affinity for anions as the binding site is blocked. The hydrogen bonding in **c.s.3**, which is the most linear, is of the N—H···O urea:

nitro group type and is an apparent consequence of the *para* substitution having an effect on the crystal packing, as in the *meta* substituted analogue, alpha tape urea hydrogen bonding was reported. The shortest hydrogen bonds are those of the 3,5-dinitro receptor DMSO solvate (2.784 Å), where each urea NH hydrogen bonds to DMSO solvent molecule.

Table 3.4: Table of free ligand hydrogen bond properties.

Free ligand	D–H (Å)	H···A (Å)	D···A (Å)	∠DHA (°)
c.s.1	0.88	2.04#	2.844 (4)	151.8
	0.88	2.18	2.643 (5)	112.2
	0.88	2.16#	2.915 (4)	144.1
	0.88	2.18	2.665 (5)	114.2
c.s.3	0.88†	2.19	3.067 (2)	170.9
	0.88†	2.06	2.916 (2)	165.3
c.s.4	0.88	1.98	2.784 (2)	151.1

†Symmetry to generate interaction: x+1/2, -y+3/2, z-1 # symmetry to generate interaction: x, y+1, z

3.3.2.3.2 Anion-receptor complexes crystal structures

In the complexes the primary interactions are the N—H···anion hydrogen bonds between the receptor and anion, which give rise to 1:1 complexes in all structures except **c.s.11**, where the ratio of receptor to anion is 2:1. In the case of the halide anion complexes (**c.s.5**, **6** and **11**) chelation of the anion by bifurcation of the N—H bonds of the urea is observed, while in the case of the acetate complexes (**c.s.8**, **9** and **10**) the more linear arrangement of the hydrogen bonds better satisfies the geometry of the urea group. Moving from

the halide complexes (average ~158°) to those of acetate (average ~168°) the DHA angle moves closer to 180°. In **c.s.10** the acetate and urea are not coplanar, which may account for the less linear (~165°) hydrogen bonding angles observed. The D···A distance decreases across the *para* substituted receptor complexes, **c.s.6**, **9** and **11** with chloride > acetate > fluoride, however there is only a marginal difference in this distance between the two chloride structures (**c.s.5** and **6**). When comparing the three acetate complexes **c.s.8**, **9** and **10**, the average D···A distance for the N—H···O interactions decreases from **c.s.8** – **9** – **10** as we move from *meta* to *para* to 3,5-dinitro substitution of the phenyl rings.

Table 3.5: Hydrogen bonding properties in the anion-receptor complexes.

Complex	D—H (Å)	H···A (Å)	D···A (Å)	∠DHA (°)
c.s.6	1.034	2.230	3.206 (1)	156.7
	1.034	2.185	3.160 (1)	156.5
c.s.9	1.036 (9)	1.754 (9)	2.786 (5)	173.9 (8)
	1.040 (8)	1.692 (9)	2.725 (5)	171.4 (9)
c.s.11	1.034	1.726	2.686 (1)	152.5
	1.034	1.645	2.627 (1)	156.8
c.s.5	1.032 (6)	2.197 (7)	3.186 (4)	160.0 (5)
	1.027 (8)	2.137 (7)	3.155 (4)	163.4 (6)
c.s.8	1.034	1.763	2.778 (3)	166.0
	1.034	1.811	2.836 (2)	170.8
c.s.10	1.034	1.745	2.677 (2)	158.9
	1.034	1.655	2.735 (2)	167.6

3.3.2.4 Crystal packing analysis

3.3.2.4.1 Free ligand crystal structures

The free ligand structures adopt a twisted geometry, with the dihedral angle between the two phenyl rings in the range of 22 - 88° and a large torsion angle present between the urea group and the phenyl ring. In the crystal structures of 1,3-bis(2-nitrophenyl)urea (**c.s.1**), 1,3-diphenylurea (**1**) and 1,3-bis(3-nitrophenyl)urea (**c.s.2**) (obtained in a variety of polymorphs in the CSD), the maximum torsion angles are around 40°. In the crystal structure of 1,3-bis(4-nitrophenyl)urea (**c.s.3**) the torsion angles are less extreme, 11.50 and -18.19°. The angles between the phenyl rings vary greatly depending on the position of the nitro substituent. In the case of the free ligand with *para* substituted nitro groups (**c.s.3**) the angle between the rings is 23°. Due to a possible steric clash in the *ortho* structure if the nitro groups were closer, the angle between the rings in this structure is much larger (88°).

T-shaped edge to face interactions are observed in 1,3-diphenylurea while the introduction of nitro groups into the 1,3-bis(4-nitrophenyl)urea, 1,3-bis(3-nitrophenyl)urea and 1,3-bis(2-nitrophenyl)urea free ligand structures leads to offset $\pi\cdots\pi$ stacking in all these structures (**c.s.1-3**). Both these observations indicate that the nitro group drives offset stacking, but its position does not have an effect on this packing motif. The presence of additional nitro groups in the DMSO solvate of 1,3-bis(3,5-dinitrophenyl)urea (**c.s.4**) seems to drive the packing to be based on $NO_2\cdots\pi$ and $C{=}O\cdots\pi$ interactions.

3.3.2.4.2 Complexes

Upon anion binding the two phenyl rings become essentially coplanar (this is not the case in the DMSO solvate of 1,3-bis(3,5-dinitrophenyl)urea). In each of these complexes, except **c.s.10** (-15°), the torsion angle is below 6°.

In the two complexes of the *meta* substituted receptor **13** (**c.s.5** and **c.s.8**) some variation in the conformation of the receptor was observed, potentially mediated by altering the anion. In these complexes two of the possible configurations of the *meta* substituted nitro groups are seen. In the chloride structure (**c.s.5**) the nitro groups adopt the *syn-syn* orientation while in the acetate structure (**c.s.8**) these groups are in a *syn-anti* arrangement. The varied orientation of the nitro groups may result in the most efficient packing for the different structures.

Although the members of this series are not isostructural and have different packing motifs, they all (excluding **c.s.11**) display some degree of $\pi\cdots\pi$ stacking interaction which can be defined according to the categories described by Janiak[156] (Figure 3.13). In **c.s.5**, **6**, and **9** the centroid-centroid distances and angles are all in a similar range of 3.20 - 3.80 Å and 23 - 26°. This suggests off-centred parallel stacking which arises from the presence of electron-withdrawing nitro groups.[157] Both **c.s.8** and **c.s.10** exhibit a larger centroid-centroid distance of 4.20 - 4.80 Å with a larger angle of offset of around 45°. This is indicative of moving to a situation where C=O$\cdots\pi$ contacts in **c.s.8** and $NO_2\cdots\pi$ contacts in **c.s.10** dominate the packing.

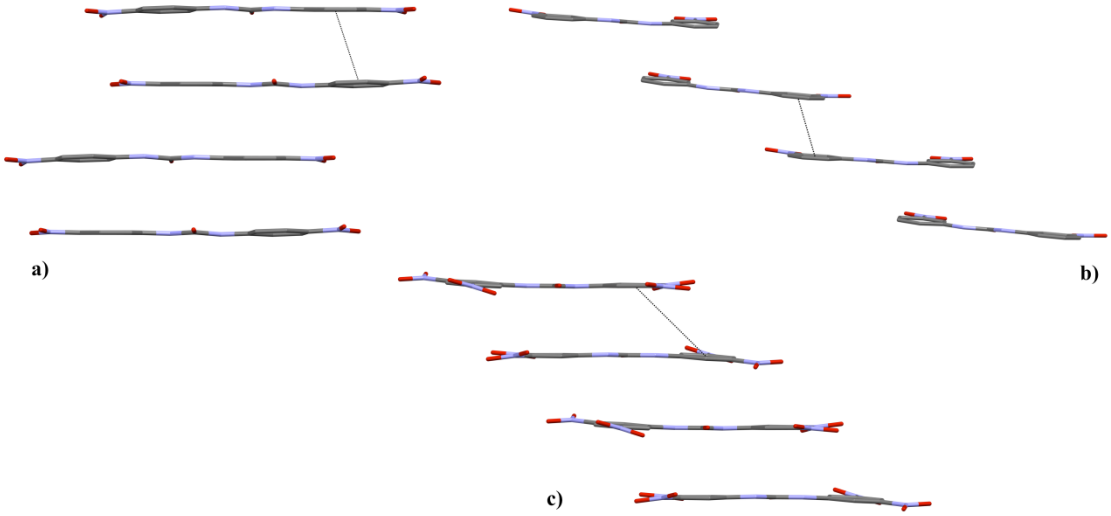

Figure 3.13: Diagram displaying the $\pi\cdots\pi$ interactions between the receptor molecules in each of the structures; off-centred parallel $\pi\cdots\pi$ stacking in a) **c.s.9**, and b) **c.s.5**, representative also of **c.s.6**, and $NO_2\cdots\pi$ contacts in c) **c.s.10**, representative also of **c.s.8**. The TMA, anion and hydrogen atoms are omitted for clarity. Atoms are drawn as capped sticks. The offset distance between the ring centroids in the $\pi\cdots\pi$ stacking interactions is represented as a dotted line.

In all structures excluding **c.s.11**, where the TMA group is situated in an entirely different part of the unit cell, the TMA group is located in close proximity to the urea C=O bond and a variety of non-covalent interactions between the oxygen and the TMA methyl groups are detected. In structures **c.s.8** and **c.s.10** a single $(CH_2)H\cdots O$ contact is present, while in structures **c.s.5** and **c.s.9** bifurcated C—H···O interactions between the urea and two C—H bonds from different methyls of the TMA groups are found. In **c.s.6** a trifurcated C—H···O interaction between a single methyl group of TMA and the urea C=O oxygen atom can be observed. In comparison in **c.s.11** the TMA group is involved in short contacts to a C—H bond of the phenyl ring of another receptor molecule.

3.3.2.5 Hirshfeld surface analysis

3.3.2.5.1 Free ligand and solvate crystal structures

The Hirshfeld surfaces[109–113] of the three novel crystal structures are shown in Figure 3.14. The packing in the DMSO solvate of 1,3-bis(3,5-dinitrophenyl)urea (**c.s.4**) is the least compact, while that of the free ligands of 1,3-bis(2-nitrophenyl)urea (**c.s.1**) and 1,3-bis(4-nitrophenyl)urea (**c.s.3**) are very efficient, more efficient than that of the anion-receptor complexes discussed below. This shows that the strength of the interactions between the anion and receptor must be strong enough to mitigate the less efficient packing that results. The fingerprint plots suggest that the Hirshfeld surface is dominated by O···H interactions in each structure (~45% in **c.s.3**, 41% in **c.s.1** and 42% in **c.s.4**). These correspond to the urea tape interactions in **c.s.1**, nitro···urea contacts in **c.s.3** and N—H···O interactions between the urea and DMSO solvent molecules in **c.s.4**. The next most prominent interactions in each structure's Hirshfeld surface are those for the π···π stacking, (C···H and H···H contacts) which for **c.s.1**, **3** and **4** are 35.6, 30.2 and 30.4% respectively.

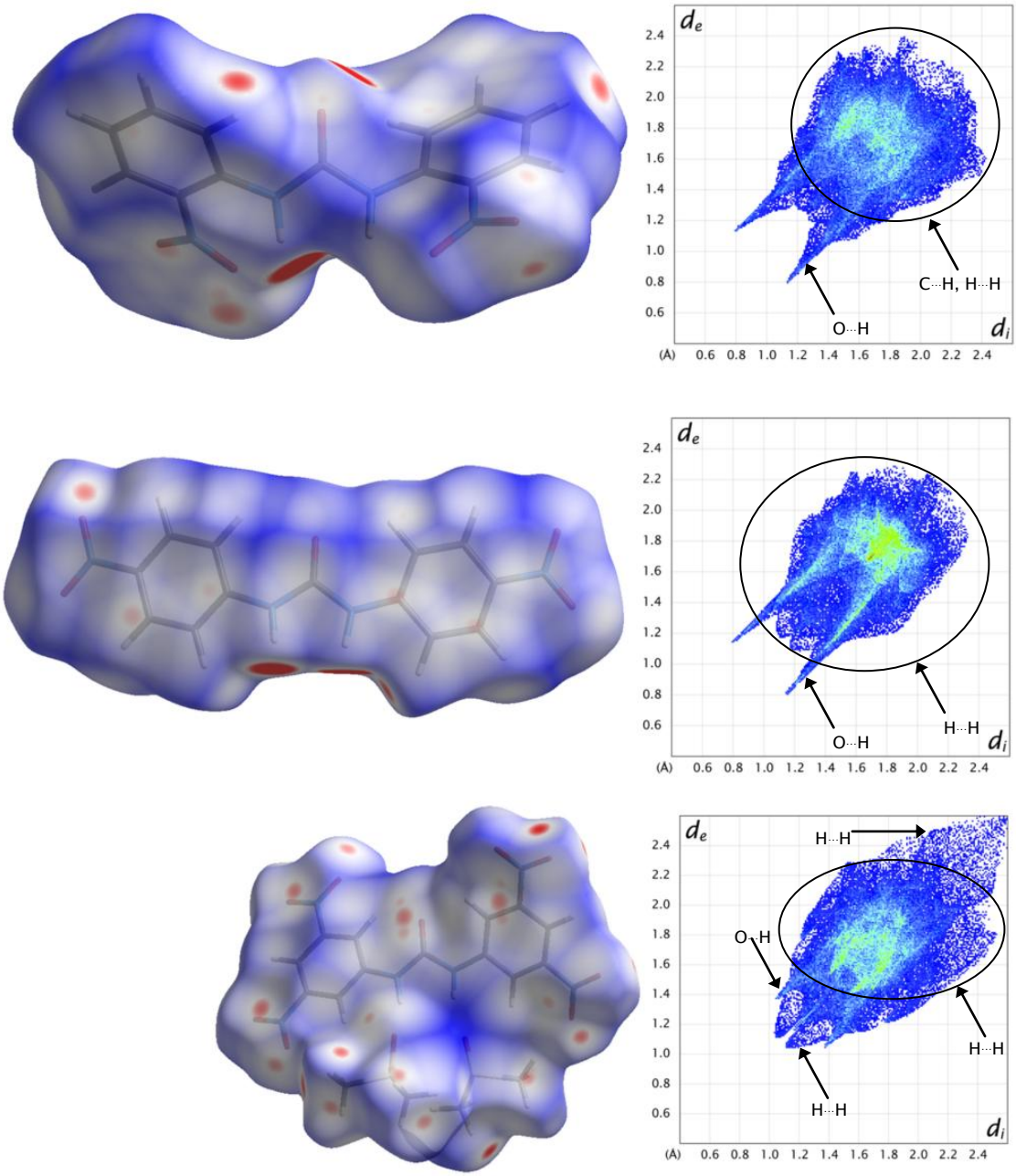

Figure 3.14: Hirshfeld surfaces (*left*) and fingerprint plots (*right*) of top **c.s.1**, middle **c.s.3** and bottom **c.s.4**. The areas of the fingerprint plots associated with the different intermolecular interactions in each crystal structure are highlighted on each plot. The spikes labelled at lower d_{norm} distances represented the shortest interaction distances of each type (e.g. O···H contacts) of interaction. In each crystal structure the majority of the surface is comprised of O···H, H···H and C···H contacts, with the O···H interactions tending to be in ascendancy at shorter d_{norm} distances and H···H and C···H more prominent at longer d_{norm} distances.

3.3.2.5.2 Complexes

Hirshfeld surfaces and fingerprint plots[109–113] shown in Figure 3.15 provide further insight into the packing and intermolecular contacts in the structures.

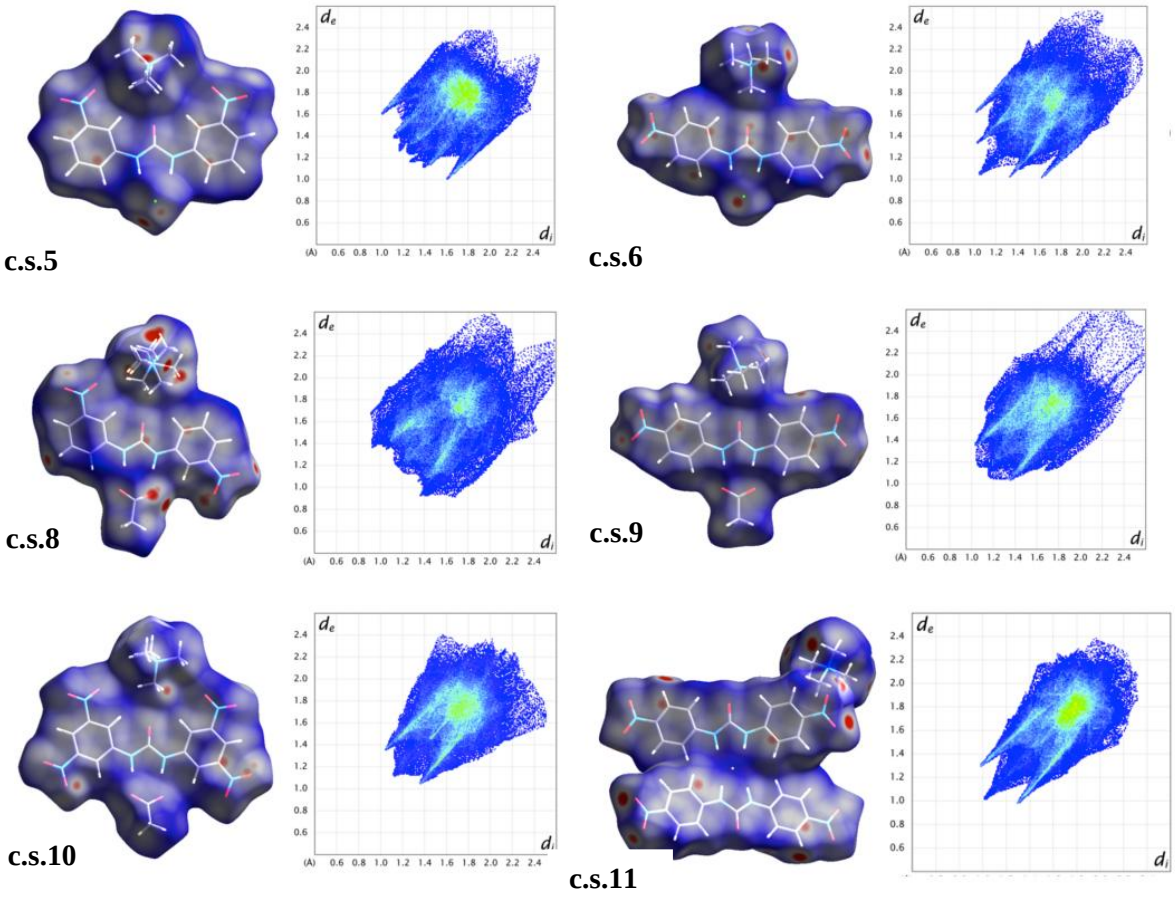

Figure 3.15: Hirshfeld surface plots of **c.s.5**, **6**, and **8–11**.

In each structure the Hirshfeld surface was modelled over the entire anion-receptor and counter ion unit. However, it is worth noting that the fingerprint plots of the receptor alone are strikingly similar to those of the entire anion unit. This suggests that the geometry and interactions of the central receptor molecule dominate the properties of the intermolecular contacts and packing in these structures (see Appendix A.2 for the Hirshfeld surface and fingerprint

plots of the receptor molecules for each anion complex). The fingerprint plot of **c.s.3**, the free ligand of 1,3-bis(4-nitrophenyl)urea is different however, suggesting a significant change in crystalline environment upon anion complexation. Comparison of the fingerprint plots of the chloride structures **c.s.5** and **c.s.6** suggest that the packing in **c.s.6**, whose fingerprint plot has a more diffuse 'tail' with larger distances, is less efficient. This is likely to be due to the larger cross sectional width of receptor **c.s.6** when compared to **c.s.5** (14.77 Å *vs.* 12.24 Å) indicating that the whole receptor-anion unit is more compact in **c.s.5**. This situation is mirrored in **c.s.8**, **9** and **c.s.10** with packing efficiency increasing across the series of *para* > *meta* > 3,5-dinitro substitution. This is probably due to a combination of factors including cross sectional width, which is largest in **c.s.9** and similar in **c.s.8** and **c.s.10**, 14.79 Å *vs.* 12.13 Å *vs.* 12.21 Å. The vertical cross sectional distance (from the methyl group of the acetate anion to the furthest methyl group of the TMA cation) decreases following the trend of increased packing efficiency (12.44 Å *vs.* 13.57 Å *vs.* 11.40 Å). Additionally a change in packing from offset $\pi\cdots\pi$ stacking to $\pi\cdots NO_2$ stacking contacts may be having an influence with the latter being increasingly present in **c.s.10** due to the larger number of NO_2 groups and leading to a different, more compact packing. Structure **c.s.11** exhibits one of the highest packing efficiencies in our series and this could result from the location of the TMA cation in this structure being rather different than in the other structures (TMA forms a variety of interactions with the urea C=O, none of which are observed in **c.s.11**). Alternatively, the 2:1 receptor: anion ratio observed in this structure may be a more efficient way of packing – in fact, given the small size of the F^- anion, this packing arrangement might be the most favoured for the receptors. However, it is not possible to get this degree

of proximity in the other structures due to the presence of larger bound anions.

In each structure the 'wings' at higher distances, which suggest the presence of C···H and H···H interactions, indicate the presence of $\pi \cdots \pi$ stacking. These wings are most prominent in **c.s.10**.

For all the anion-receptor complexes, the largest contributions to the Hirshfeld surfaces are from O···H and H···H interactions. The H···H interactions in **c.s.6** and **c.s.11** extend to particularly short distances. For the chloride structures, **c.s.6** and **c.s.5**, the contributions from each short contact are essentially the same (see Figure 3.16).

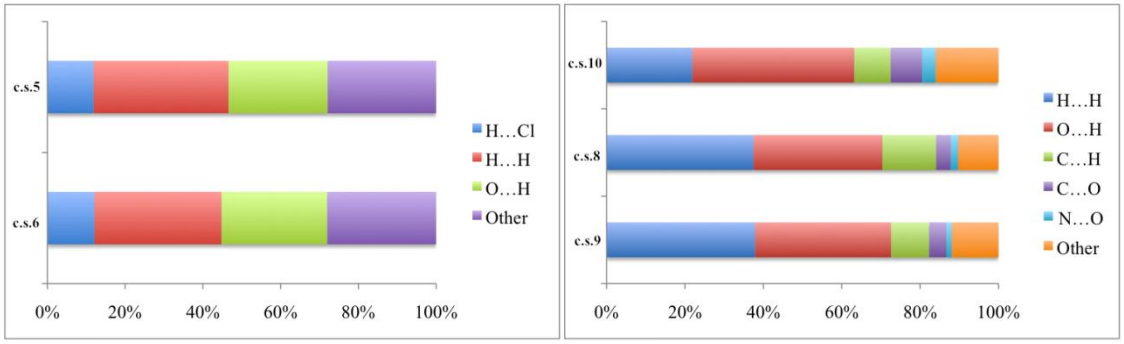

a) **b)**

Figure 3.16: Contribution of non-covalent interactions to the Hirshfeld surface in **a) c.s.5** and **c.s.6** and **b) c.s.8**, **c.s.9** and **c.s.10**.

Spikes at d_{norm} values of 1.7 Å, indicate H···Cl contacts which are shown to comprise ~12% of the Hirshfeld surface in each of these structures. The magnitude of the common interactions comprising the Hirshfeld surfaces in **c.s.9** and **c.s.8** are also strikingly similar to those in **c.s.6** and **c.s.5** (the H···Cl contacts are not present in **c.s.9** and **c.s.8**, however an increase in contribution of the O···H contacts arising from the acetate anion replaces these). In **c.s.5**, **6**, **8** and **c.s.9** H···H interactions comprise between 32 and 38% of the surface, with

O···H contributions of around 35% for the acetate structures and combined H···Cl and O···H contacts in the chloride structures accounting for around 38% of the Hirshfeld surface. In **c.s.10** there is an increase in the contribution of C···O, N···O and O···H contacts and a corresponding decrease in H···H interactions, implying a change in the packing due to the increased number of nitro groups. In **c.s.11** the H···F contacts are at a short distance and make a very small contribution to the Hirshfeld surface.

3.4 Conclusions

Systematically altering the position and number of electron-withdrawing substituents at the periphery of a common receptor scaffold was shown to influence the strength of the interaction between the receptor and anion. Geometric analysis of the hydrogen bonding interactions within the anion-receptor complexes suggests that moving from *meta* to *para* to 3,5-dinitro substitution increases the hydrogen bond strength. Proton NMR titration studies in solution support the trend of increasing hydrogen bond strength observed in the solid-state structures and that the more basic anion acetate associates with the receptors through stronger hydrogen bonds than chloride. Deprotonation by fluoride was suggested in solution by NMR titration studies.

Through neutron diffraction studies the positions and displacement parameters of the hydrogen atoms in two complexes could be accurately determined and indicated that no significant migration or transfer of the urea N—H protons occurs in the solid-state.

As expected, the geometry of the hydrogen bonds depends on the shape of the anion, with more linear hydrogen bonds observed for the Y-shaped acetate anion than for the spherical halides.

The planar geometry of the receptor molecule in each anion-receptor complex, in comparison to the twisted conformation of the phenyl rings observed in the free ligand crystal structures, is dictated by the recognition event between the anion and receptor. Changes in the Hirshfeld surface and fingerprint plots from the free ligand structures to the anion-receptor complexes also suggests that the recognition event substantially changes the packing motif in the structures and that the strength of the hydrogen bonding in the complexes must compensate for the less efficient packing in these structures compared to the free ligand crystal structures.

A variety of packing arrangements were observed across the complexes illustrating the diversity introduced in the solid-state arrangements by subtle structural modifications. The varying nature of the intermolecular contacts upon substitutional adaptation of the receptors is illustrated *via* the Hirshfeld surface. How systematic structural modifications to a common receptor scaffold can successfully tune the strength of interactions for a particular application has been demonstrated.

The in-depth structural analysis undertaken in this chapter, using a variety of techniques; single crystal X-ray and neutron diffraction experiments, Hirshfeld surface mapping, and complemented by ^{1}H NMR titration studies provided detailed information and understanding of the chemistry and solid-state arrangement, as well as the anion binding properties of the receptor molecules in solution. By studying the properties of the anion-receptors and their resulting anion-receptor complexes, insight into the effect of modifications to the systems was provided. Despite this, however detailed the analysis, the conclusions reached at standard resolution are limited to deductions based on geometric arguments and assumptions (in the case of hydrogen bonding

analysis) and/or qualitative discussion of the crystal structure assembly (Hirshfeld surface analysis).

The following two chapters of this thesis will move beyond standard resolution structural determination to look at the atomic level and electron density distribution in the crystal structures of the anion-receptor complexes reported. It is hoped that this will provide experimentally a fundamental quantitative description of the nature of these systems, unobtainable in any other manner.

Chapter 4: High resolution studies of symmetrically nitro-substituted urea-based anion-receptor complexes

4.1 Motivation for charge density analysis

The work in this chapter has been published by Kirby, I. L; Brightwell, M; Pitak, M. B; Wilson, C; Coles, S. J; Gale, P. A., in *Phys. Chem. Chem. Phys.*, 2014, **16**, 10943 - 10958[158] and is reproduced by permission of the PCCP Owner Societies (see A.8 for copyright permissions). http://pubs.rsc.org/en/content/articlelanding/2014/cp/c3cp54858a#!divAbstract

Having performed an in-depth standard resolution structural analysis of the anion-receptor complexes described in Chapter 3, which was complemented by solution phase binding studies, these systems were examined using charge density analysis. The aim was to ascertain the additional information about these systems that could be obtained, and to move from a geometric description of the complexes to one based on the observed electron density distribution. Whether this description could give greater insight into the properties and nature of these complexes was investigated. In this chapter the electron density distribution for **c.s.5**, **6**, **9**, **10** and **11** (see Figure 4.1), for which suitable quality crystals and high resolution X-ray diffraction data could be obtained, is the main focus. This allows the effect of both the nature of the anion, and the substituent position of the electron-withdrawing group on the urea-based receptor to be investigated. The electron density distribution in the

free ligand (**14**) is also discussed. This is done with the caveat that the dataset is of lower quality than would generally be expected and desired in a charge density study, due to smeared nature of the diffraction pattern and presence of split peaks in the collected images.

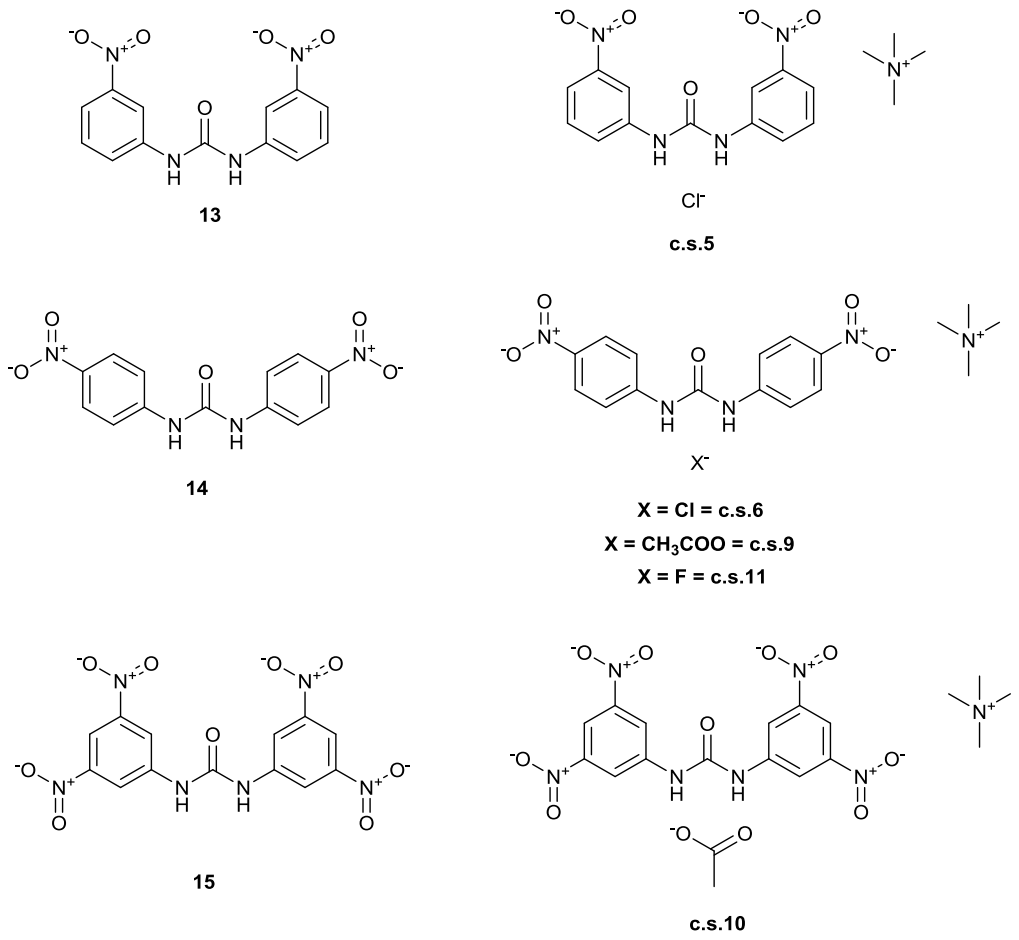

Figure 4.1: Receptors (**13**–**15**) and anion-receptor complexes (**c.s.5**, **6**, **9**, **10** and **11**).

4.2 Related studies

The focus on the effect of peripheral electron-withdrawing groups builds on earlier work by Grabowsky *et al.*, who have looked at the effect of electron-

withdrawing substituents on the electron density distribution in epoxide rings and related this to their relative reactivities.[159] Englert and co-workers have looked at the electron density distribution in both sulfadiazine and several of its salts. Their study rationalised the different protonation states observed in the structures and provided conclusive evidence about the position of the hydrogen atoms, which agreed with those that had been suggested by geometric arguments based on hydrogen bond requirements.[160] In related work Guru Row and co-authors describe how experimental charge density studies on a salt and a co-crystal of nicotinamide have been used to provide quantitative topological criteria that allow chemists to distinguish between co-crystals and salts.[161] The authors aim to further study a variety of weak and strong charge transfer compounds so as to provide characterising values for charge density derived properties across the co-crystal to salt range.

4.2.1 Urea in charge density studies

Urea has been a model structure throughout the development of both charge density analysis and the Hansen-Coppens multipole model. It has been used to test the effectiveness of extracting the electron density distribution from diffraction data in a series of studies[162-165], with the topological analysis of the experimentally obtained model compared to those from theoretical studies. This means there are a variety of literature sources, which can be compared to the models in this thesis, and used to test the validity of the multipole refinements that have been performed on the series of crystal structures reported within. Areas of similarity, such as the urea C=O should have similar electron density distributions, and hence properties of the electron density at the BCPs will therefore be alike. It also provides a measure of what can be classed as a variation in the electron density distribution upon alteration of the

receptor scaffold, to be described below. In addition, several co-crystal systems of urea, such as those reported by Gryl *et al.*,[166] again provide a comparison set of data to the electron density distribution models outlined below for these anion-receptor complexes, and an idea of both the type of and properties of the intermolecular interactions present in multiple component systems and how these may perturb the electron density distribution. Finally, the most closely related crystals studied using charge density analysis to the structures in this thesis are the structures of N'-methylurea, N'-phenylurea and N,N'-diphenylurea examined by Dittrich and co-workers[54]. These will provide another comparison for validating the modelling of the structures reported in this thesis and also help to look at the role of electron-withdrawing substituents on the electron density distribution in the anion-receptor complexes.

4.2.2 Host-guest interactions

One of the few examples where charge density analysis has been applied to host-guest interactions comes from Hibbs and co-authors.[167] The authors describe the electron density distribution in a synthetic terephthaloyl receptor complexed to adipic acid. Quantitative characterisation of the host-guest complex described the various intermolecular interactions holding the complex together in a more comprehensive nature than that allowed by structural methods alone. This rare study illustrates the scope available for studying host-guest interactions and the relevance and potential of the series of complexes described in this thesis. It also demonstrates the complexity of these systems, compared to literature examples, which tend to be at most two component and do not contain multiple charged entities, as is the case in the structures studied in this thesis.

4.2.3 Nitro groups

Nitro groups are a main feature of the anion-receptor complexes reported in this thesis. Their presence on the receptor scaffold is postulated to have a varying influence on the electronic distribution of the receptor depending on the nitro group's position, and hence affect the interaction strength between the anion and the receptor in the complexes. Due to its significance in the structures, it is useful that several charge density investigations have included structures containing nitro groups. Woźniak and co-workers in their study of N,N-dipicrylamine and its ionic complexes have thoroughly detailed the properties of the electron density distribution in nitro groups and the character of the N···O contacts found to be present in the structures.[168,169] These studies showed that the N···O interaction is attractive and that both the $\rho(\mathbf{r}_{BCP})$ and $\nabla^2\rho(\mathbf{r}_{BCP})$ values have a linear relationship to the N···O distance. The curved nature of the bond paths between the nitrogen and oxygen atoms was also noted. Fedyanin and Lyssenko in their high resolution study of 2,4,6-trinitroaniline observed and characterised an O···O interaction between nitro groups in its crystal structure.[170] The low value of $\rho(\mathbf{r}_{BCP})$ and the low positive value of $\nabla^2\rho(\mathbf{r}_{BCP})$ allowed the characterisation of this O···O contact as a closed-shell interaction. In unison with O=N···H—N hydrogen bonds this O···O interaction leads to the formation of a centrosymmetric dimer with a total interaction energy of 25 kJ mol^{-1}.

These literature studies again provide a way to validate that the electron density distribution of this group has been correctly modelled in the structures, and suggest whether intermolecular interactions found to be present are typical for the functional group.

4.3 Technical aspects of charge density analysis

Before discussing the results of the multipole refinement of structures **c.s.3**, **c.s.5**, **c.s.6**, **c.s.9**, **c.s.10** and **c.s.11**, some of the technical aspects of the modelling will be described. Data collection was performed with the aid of Mateusz Pitak (in the case of X-ray diffraction datasets collected at the University of Southampton) and Claire Wilson (in the case of X-ray diffraction datasets collected at the I19 beam line[171] at Diamond Light Source).

4.3.1 Hydrogen atom treatment

Much focus has been directed to the proper treatment of hydrogen atom parameters in charge density analysis.

The use of accurate positional and thermal motion parameters for all atoms is vitally important for reliable estimation of the properties derived from the electron density distribution. It is even more imperative in the case of hydrogen atoms.[172] The incorporation of incorrect hydrogen atom positions and the incorrect deconvolution of the thermal motion of hydrogen atoms in multipole modelling introduce a bias to static charge density models. The use of isotropic displacement parameters has been shown to be a severe approximation, because the isotropic displacements correlate with the monopole parameters of the multipole model.[173] The importance of having correct and accurate positions and ADPs of hydrogen atoms when characterising both strong and weak non-covalent interactions (as in this thesis) has been demonstrated.[172] However, as previously discussed, the fact that hydrogen atoms only possess a single valence electron means they have a weak scattering power in X-ray diffraction experiments and their positions and ADPs cannot be accurately determined by this technique.

Neutron diffraction (where scattering strength is independent of atomic number) can be used to accurately determine both hydrogen positions and ADPs. Using positional and anisotropic displacement parameters determined from neutron diffraction studies has therefore been shown to be the 'gold standard' in multipole modelling. However, the demands placed on the crystal size and quality by neutron diffraction studies and the limited access to neutron sources in comparison to the ease of access to X-ray diffraction means that alternative approaches are also required. Of these, estimating ADPs based on a combination of rigid body motion and internal motion, using the SHADE (Simple Hydrogen Anisotropic Displacement Estimator) server[174] has been shown to be the best alternative.[172] This should be combined with determining accurate positions by low order refinement, usually refining the positions against $\sin(\theta)/\lambda < 0.7$ and extending to average bond lengths from neutron diffraction.

In this study, atomic positions and ADPs for **c.s.5** and **c.s.9** were obtained from neutron diffraction studies and transferred without scaling to the multipole models of these structures, and in the remaining cases, **c.s.3**, **c.s.6**, **c.s.10** and **c.s.11**, hydrogen atom positions were refined against low resolution X-ray diffraction data, and extended along the bond vector to standard distances derived from neutron diffraction studies and taken from International Tables of Crystallography. ADPs for the hydrogen atoms were estimated using the SHADE server[174] and a rigid body model was included for the urea-based receptor molecule in each structure. Studies have also indicated that it is only meaningful to compare topological properties in different systems where the same level of multipole expansion has been used. Hydrogen atoms were refined as a bond directed dipole in all six structures.

In **c.s.11** the hydrogen atoms of the TMA were kept isotropic due to the large displacement parameters of the carbon atoms to which they are attached (caused by the disorder of this part of the crystal structure see Section 4.3.2 below) and because the positional and anisotropic displacement parameters of the atoms in the TMA cation (which was modelled using InvariomTool[117]) were kept fixed throughout the multipole refinement. The derived ADPs from the SHADE server were physically unreasonable and suggested that this group was not fully rigid due to the disorder of this unit.

4.3.2 Treatment of the TMA cation in c.s.11

The treatment of disorder in charge density studies is non-trivial. Typically the presence of disorder prevents the deconvolution of thermal effects from the static electron density. There are a small number of examples where the electron density in the disordered section of a crystal structure has been modelled using multipole parameters based on theoretical values, taken from one of the libraries of transferable multipole parameters.[123,175]

The TMA cation in **c.s.11**, the fluoride complex of the *para* nitro substituted receptor, was initially modelled as ordered with the central nitrogen atom lying on a 2-fold rotation axis and just two independent methyl groups. However, this model resulted in large, elongated thermal ellipsoids and an unsatisfactory modelling of the electron density distribution of this cation with unacceptably large peaks in the residual electron density (-0.854/ 0.981 *e*). To address this problem attempts were made to obtain a very low temperature (35K) high resolution X-ray diffraction dataset. However this approach was hampered by a phase transition, which occurred below 60K and the resulting unit cell has a much larger asymmetric unit and split diffraction peaks (see Chapter 3) making

it unsuitable for a charge density study. A 65K high resolution X-ray diffraction dataset was collected, and mirrored the behaviour observed in the 100K structure so the higher temperature, 100K, dataset was retained for consistency with the rest of the structures in the series.

In order to improve upon the initial model a disorder model for the TMA cation was introduced in which the central nitrogen atom no longer lies on the 2-fold axis but is slightly displaced from it and forms the centre of a half-occupied TMA cation with four independent methyl groups. A second orientation of TMA cation is generated by the application of the 2-fold rotation.

To correctly model the electron density distribution in this disordered cation a similar method to that employed by Kratzert *et al.*[122] was used. The IAM model was first imported into the XD program, the positions and ADPs for the non-hydrogen atoms in the TMA group were kept fixed and those of the hydrogen atoms extended along the bond vector to neutron diffraction derived distances and then fixed. The invariom database was then used to designate the multipole populations and κ and κ' values for each atom of TMA and transferred to the XD input using InvariomTool. These database multipole parameters for TMA were then kept fixed during the refinement of the electron density in the remaining parts of the structure. This final model using a combination of the disorder model and the invariom database values was considered to be more suitable due to the significant drop in R(F) factor, GoF and the substantial reduction in the residual density around the TMA cation. The residual density analysis and fractal dimension distribution plots (found in Appendix A.3) also graphically illustrate this improvement in the model.

4.3.3 Modelling procedure

Details of the data collection, including the set-up at the I19 beam line are included in the Experimental section, along with details of the data processing. Across each crystal structure a consistent approach was used when performing the multipole refinement and is described in Section 7.5.4.

4.4 Results and discussion

The electron density distribution in each of the crystal structures (**c.s.3**, **5**, **6**, **9**, **10** and **11**) and the quantitative analysis of the static electron density model (performed with the XDPROP module of XD2006) will now be discussed.

4.4.1 Evaluation of model

Table 4.1 shows the results of the multipole refinement of each of the anion-receptor complexes discussed in this chapter.

Table 4.1: Selected crystallographic information for the anion-receptor complexes.

Structure	**c.s.6**	**c.s.9**	**c.s.11**	**c.s.5**	**c.s.10**
Formula	$C_{17}H_{22}ClN_5O_5$	$C_{19}H_{25}N_5O_7$	$C_{30}H_{32}FN_9O_{10}$	$C_{17}H_{22}ClN_5O_5$	$C_{19}H_{23}N_7O_{11}$
Crystal system	Triclinic	Triclinic	Orthorhombic	Orthorhombic	Triclinic
Space group	$P\bar{1}$	$P\bar{1}$	*Pcca*	*Pna*2$_1$	$P\bar{1}$
a (Å)	7.6033(2)	7.797(2)	35.929(6)	6.8211(5)	9.602(3)
b (Å)	11.4827(3)	11.214(3)	7.0153(11)	14.4139(11)	10.807(3)
c (Å)	11.8705(4)	12.211(3)	12.624(2)	19.7918(16)	12.433(4)
α (°)	83.1860(10)	91.753(5)	90	90	109.859(5)
β (°)	71.662(2)	104.560(7)	90	90	96.598(3)
γ (°)	80.423(2)	95.232(13)	90	90	103.5372(5)
V (Å^3)	967.59(5)	1027.5(5)	3181.9 (9)	1945.9(3)	1152.7(6)
			Multipole Refinement		
R(F)	0.0377	0.0531	0.0293	0.0381	0.0396
R(F^2)	0.0279	0.0519	0.0362	0.0329	0.0520
GoF	1.3971	1.6452	2.0665	1.1727	1.6196
Nref/Nvar	23.25	25.99	21.29	48.90	18.95
$\Delta\rho$(**r**) (*e* Å^{-3})	-0.334/0.619	-0.304/0.354	-0.396/0.392	-0.329/0.540	-0.432/0.451

The high quality of the final model for each structure is indicated by the low R(F) value for the least squares refinement and the GoF value. The Gaussian distribution of the residual electron density (see fractal dimension distribution plots in Appendix A.3) suggests that the residual density is experimental noise and that the electron density has been successfully fitted in the models.[62] The high data to parameter ratio (~20 for each crystal structure and significantly higher for **c.s.5**) demonstrates that sufficient diffraction data has been collected and that overfitting of the model has been avoided.

For all the crystal structures the Hirshfeld rigid bond test[59] was applied in the final stages of the refinement and the values of the difference of mean square displacement amplitudes (DMSDAs) were $< 10^{-4}$ for all the non hydrogen atom bonds except some of those of the TMA groups in **c.s.10** and **c.s.11**. This vibrational lability may be due to the lower rigidity of the methyl groups and in the case of **c.s.11** could be a consequence of the disorder of the TMA cation.

4.4.2 Common structural features

Throughout the family of structures some common features are retained, for example the TMA cation is present in all five structures. The common structural elements such as the TMA cation and phenyl rings should not be greatly perturbed by changes in the substitution pattern or anion. These groups can act as internal standards and provide validation of the quality and consistency of the multipole modelling. Below the properties of these common structural elements are briefly described and are consistent with this hypothesis.

In each complex the TMA group has an overall positive charge (0.02 – 0.75 *e*) and the anion a negative charge (-0.29 – -0.68 *e*). The low positive charge of

the TMA in **c.s.11** (0.02 *e*) compared to the other structures may be due to modelling this group using the invariom approach, or its differing position in the crystal structure compared to the other structures.

The electronic properties at the bond critical points (BCPs) are used to characterise the bonds between atoms. In each of the structures these values are consistent with what would be expected for the differing types of covalent interactions predicted to be present in the systems from geometrical considerations. Generally, single bonds were shown to have electron density ($\rho(\mathbf{r}_{BCP})$) and Laplacian of the electron density ($\nabla^2\rho(\mathbf{r}_{BCP})$) values of ~ 1.8 *e* Å^{-3} and −15.0 *e* Å^{-5} respectively, while those of C=C aromatic bonds were generally > 2.0 *e* Å^{-3} and −17.0 *e* Å^{-5} respectively, and hetero C=O double bonds ~ 3.0 *e* Å^{-3} and −40.0 *e* Å^{-5} respectively. The conjugated, aromatic nature of the bonds in the phenyl rings is supported by the high bond ellipticity values, which were between 0.06 and 0.33 at the BCPs in the C−C bonds, and the profile of the bond ellipticity along the bond path (see Appendix A.5). These are similar across the five structures apart from in **c.s.10** where the additional nitro groups and their associated increased electron-withdrawing effect seems to perturb the electron density in the aromatic region sufficiently to alter the bond ellipticity profile along the aromatic bond paths.

Though the charges on the phenyl ring carbon atoms in all the structures vary, C(4) and C(8), the atoms connected to the urea group, are generally the most positive phenyl ring atoms in each structure and the carbons to which the nitro groups are attached, are also all positively charged (apart from one of these atoms in **c.s.10**) due to the inductive (-I) electron-withdrawing effect of these groups. The positions and interactions of the TMA cation relative to the receptor in **c.s.6**, **c.s.9** and **c.s.11** vary across the series (constant *para* receptor

with different anion), particularly that of the TMA cation in the fluoride structure **c.s.11**, however the range of the $\rho(\mathbf{r}_{BCP})$ and $\nabla^2\rho(\mathbf{r}_{BCP})$ values at the C—N BCPs are consistent with those reported by Munshi *et al.* in the related tetramethylalkyldiammonium salt.[176] In **c.s.11** the multipole populations for TMA were taken from the invariom database enabling the modelling of the electron density of this region, however the similarity of the properties of the $\rho(\mathbf{r}_{BCP})$ at the BCPs in **c.s.11** with those in the rest of the series of structures in this chapter and with those found in the literature suggest that the invariom model is an acceptable one for this group in **c.s.11**. As expected, with no alteration in the cation between structures **c.s.5** (*meta* chloride complex) and **c.s.6** (*para* chloride complex), and a similar position and interaction environment in both, the properties of the BCPs between the TMA nitrogen atom and methyl carbons, N(5)—C(14/15/16/17) do not vary significantly in **c.s.5** and **c.s.6**. Such agreement in the properties at the TMA group C—N BCPs was also noted between **c.s.9** (*para* acetate complex) and **c.s.10** (3,5-dinitro acetate complex). Properties of the urea group display more variation across the series of complexes and appear to be a result of both anion changes and modification of the receptor. This was envisaged when designing the comparison system and these differences will be discussed in greater detail.

4.4.3 Variation of the anion

Studying complexes of 1,3-bis(4-nitrophenyl)urea (**14**) and changing the anion from chloride to acetate to fluoride (**c.s.6** *vs.* **c.s.9** *vs.* **c.s.11**), enables the variations in the electron density distributions across the crystal structures to be related to the basicity of the anion, $Cl^- < {}^-OAc < F^-$. The charge density distribution in the crystal structure of **c.s.6** is displayed in Figure 4.2 and Figure 4.3 (static deformation charge density distribution plot and negative

Laplacian of the electron density charge density distribution map respectively, both plotted in the plane of the urea molecule).

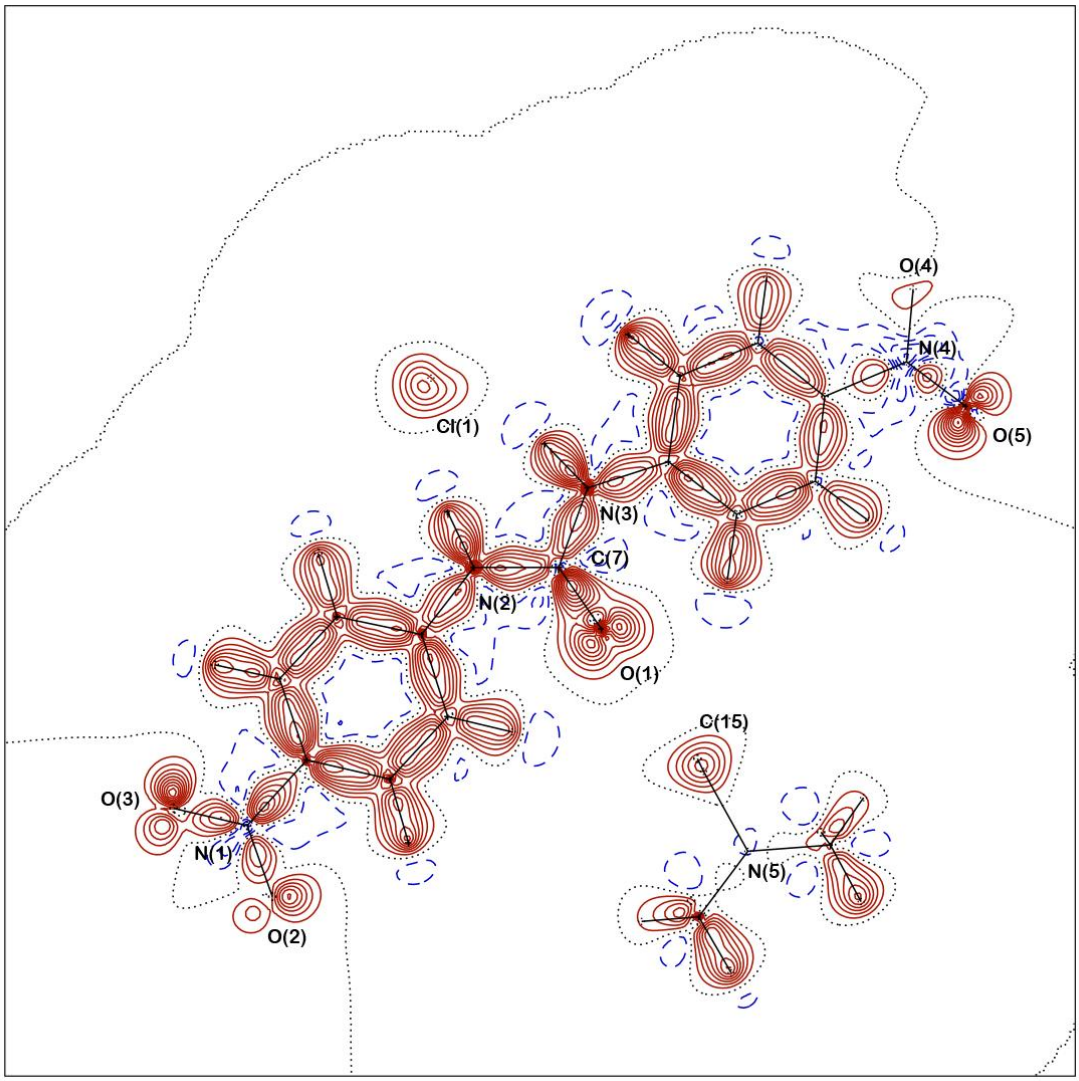

Figure 4.2: Static deformation charge density distribution plot of **c.s.6** in the plane of the urea group of the receptor molecule. The TMA and nitro groups are out of the plane in which the map is drawn. Positive electron density shown in red, negative electron density in blue. Zero contours are dashed. Contours are at 0.1 *e* $Å^{-3}$.

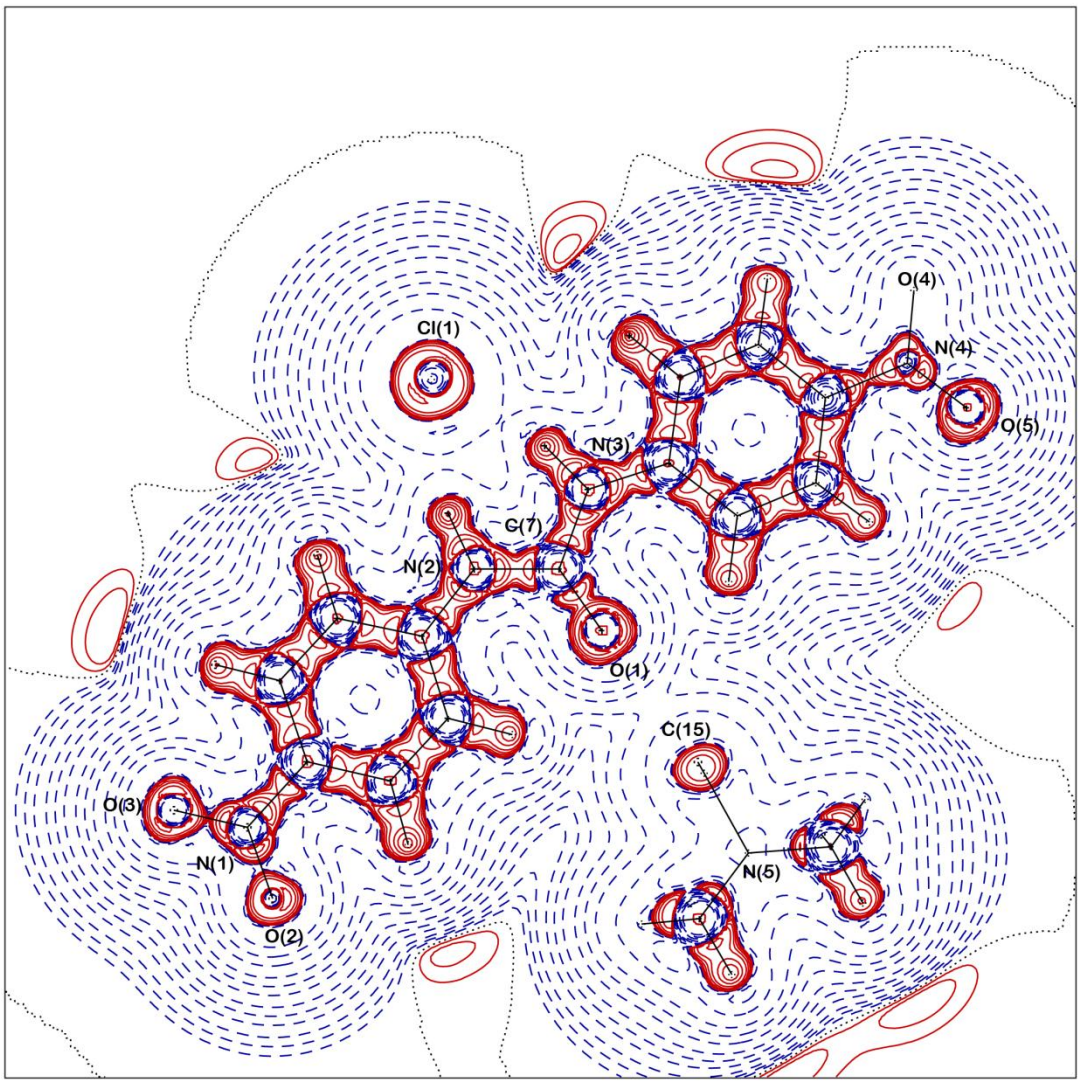

Figure 4.3 Negative Laplacian of the electron density charge density distribution map of **c.s.6** in the plane of the urea group of the receptor molecule. The TMA and nitro groups are out of the plane in which the map is drawn. Positive electron density shown in red, negative electron density in blue. Contours are in a logarithmic scale (e Å^{-5}).

Figure 4.2 displays some of the bonding features for **c.s.6**, bonding density between the carbon atoms of the phenyl rings, the areas of negative electron density corresponding to the shift in the electron density of the hydrogen atoms into the bonding region, and the lone pairs of the urea oxygen atoms. In

Figure 4.3 the lone pairs of the urea oxygen atom and chloride anion and bonding interactions in **c.s.6** are clearly visible. The similarity with plots of the remaining crystal structures (see Appendix A.5) show common regions of the structures (e.g. the phenyl rings) have comparable electron density distributions.

4.4.3.1 X—H···anion interactions and their strengths

The hydrogen bonding interactions between the N—H donor group and anions in the sets of complexes under investigation were assigned using the criteria outlined by Koch and Popelier.[177]

Their criteria for determining the presence of hydrogen bonds, developed by studying in particular C—H···O contacts, are:

1. The presence of a bond path linking the two interacting nuclei.
2. The value of the electron density at the bond critical point, which is usually an order of magnitude smaller than that of a covalent bond.
3. The value of the Laplacian of the electron density, which is usually positive for non-covalent interactions.
4. The mutual penetration of the hydrogen and the acceptor atom.
5. The loss of charge of the hydrogen atom.
6. The energetic destabilisation of the hydrogen atom.
7. The decrease in the volume of the hydrogen atom.

Figure 4.4 shows the position of the BCPs and the bond paths (that illustrate these interactions) linking the nuclei of the atoms in structure **c.s.9**. Full quantitative details of the hydrogen bonding interactions can be found in Table 4.2. The electron density and Laplacian of the electron density values at the BCP of the hydrogen bond give an indication of the comparative bond strength

in each complex. Typically, for hydrogen bonding interactions the $\rho(\mathbf{r}_{BCP})$ value is low and the value of $\nabla^2\rho(\mathbf{r}_{BCP})$ positive, and this is observed for all the X—H···anion interactions in the five complexes. Figure 4.5 illustrates that as the basicity of the anion increases (maintaining the *para* substitution of the receptor) from chloride to acetate to fluoride (**c.s.6** – **c.s.9** – **c.s.11**) (pK_as of the conjugate acids in DMSO are 1.8[178], 12.6[179] and 15[178] respectively), the electron density and the Laplacian of the electron density values also increase in magnitude.

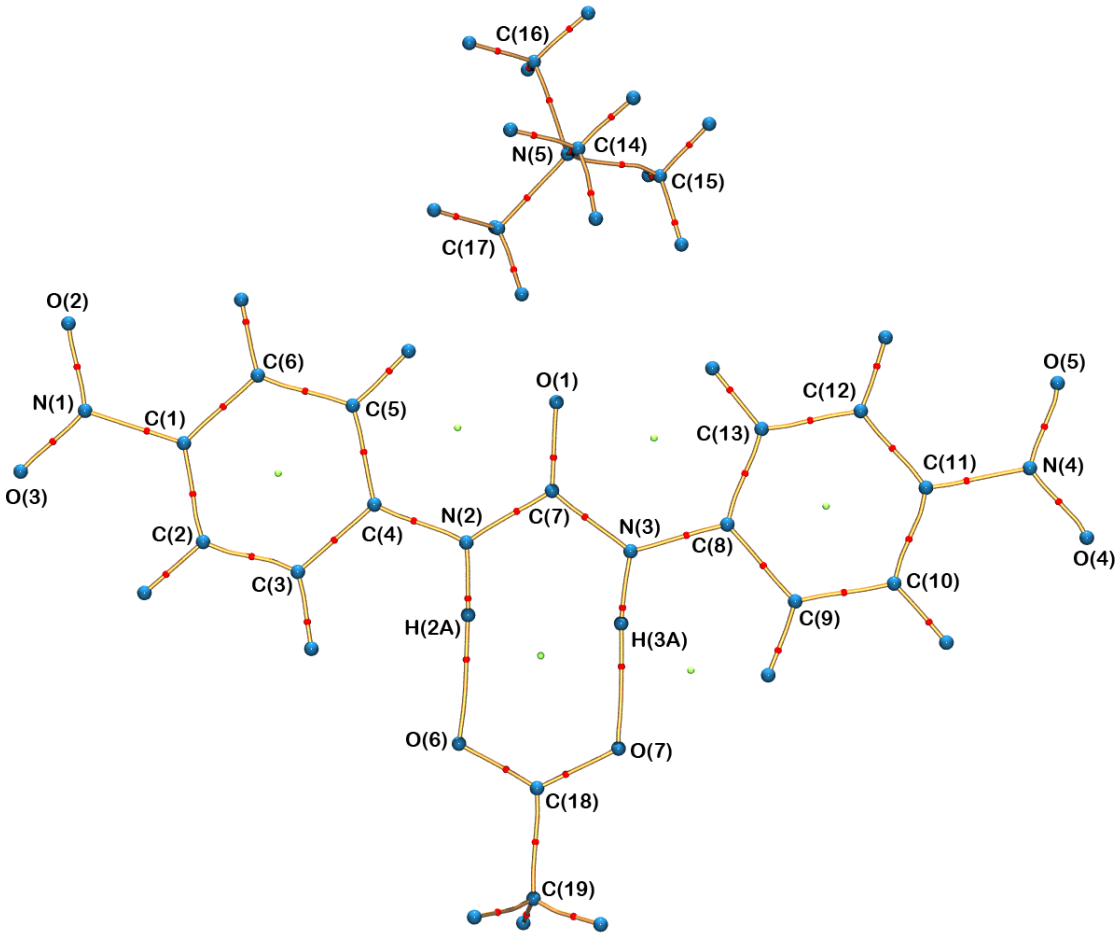

Figure 4.4: Molecular graph of **c.s.9** displaying the nuclear positions (blue), bond paths (yellow) and the BCPs (red).

Table 4.2: Topological analysis of the X—H···anion interactions in the anion receptor complexes.

D−H···A	$\rho(\mathbf{r}_{BCP})$ (e Å^{-3})	$\nabla^2\rho(\mathbf{r}_{BCP})$ (e Å^{-5})	R_{ij} H···A (Å)	A−BCP (Å)	H−BCP (Å)	D−BCP (Å)	$G(\mathbf{r}_{BCP})$ (a.u)	$V(\mathbf{r}_{BCP})$ (a.u)	$\lvert V(\mathbf{r}_{BCP})\rvert / G(\mathbf{r}_{BCP})$	E_{HB} (kJ mol^{-1})	$H(\mathbf{r}_{BCP})$ (kJ mol^{-1})
	c.s.6. *Para* receptor with chloride										
N(2)−H(2A)···Cl(1)	0.120(1)	1.949(4)	2.2423	1.4656	0.7767	1.744	0.017	−0.014	0.808	−17.980	8.561
N(3)−H(3A)···Cl(1)	0.125(2)	2.319(7)	2.1854	1.4562	0.7292	1.705	0.020	−0.016	0.783	−20.303	11.277
	c.s.9. *Para* receptor with acetate										
N(2)−H(2A)···O(6)	0.191(3)	4.19(3)	1.7647	1.1783	0.5863	1.628	0.037	−0.030	0.810	−38.855	18.258
N(3)−H(3A)···O(7)	0.313(3)	4.29(3)	1.6905	1.1022	0.5883	1.631	0.047	−0.049	1.051	−64.595	−6.230
C(3)−H(3)···O(6)	0.061(6)	1.055(2)	2.4065	1.4295	0.9971	–	0.008	−0.006	0.701	−7.746	6.621
C(9)−H(9)···O(7)	0.080(6)	1.225(2)	2.3356	1.3879	0.9476	–	0.010	−0.008	0.759	−10.207	6.475
	c.s.11. *Para* receptor with fluoride										
N(2)−H(2A)···F(1)	0.256(2)	4.27(2)	1.7244	1.0994	0.6250	1.598	0.042	−0.039	0.941	−51.681	6.494
N(3)−H(3A)···F(1)	0.279(2)	4.94(2)	1.6766	1.0701	0.6065	1.568	0.048	−0.046	0.940	−59.696	7.589
	c.s.5. *Meta* receptor with chloride										
N(2)−H(2A)···Cl(1)	0.129(2)	2.28(1)	2.2201	1.5093	0.7108	1.679	0.020	−0.016	0.800	−20.635	10.359
N(3)−H(3A)···Cl(1)	0.152(2)	2.43(1)	2.1518	1.4400	0.7117	1.689	0.022	−0.019	0.853	−24.565	8.499
	c.s.10. *3,5-dinitro* receptor with acetate										
N(3)−H(3A)···O(10)	0.318(4)	4.19(3)	1.7359	1.0932	0.6426	1.649	0.047	−0.050	1.068	−65.377	−8.291
N(4)−H(4A)···O(11)	0.353(4)	3.92 (4)	1.6774	1.0889	0.5884	1.593	0.048	−0.056	1.155	−72.957	−19.562

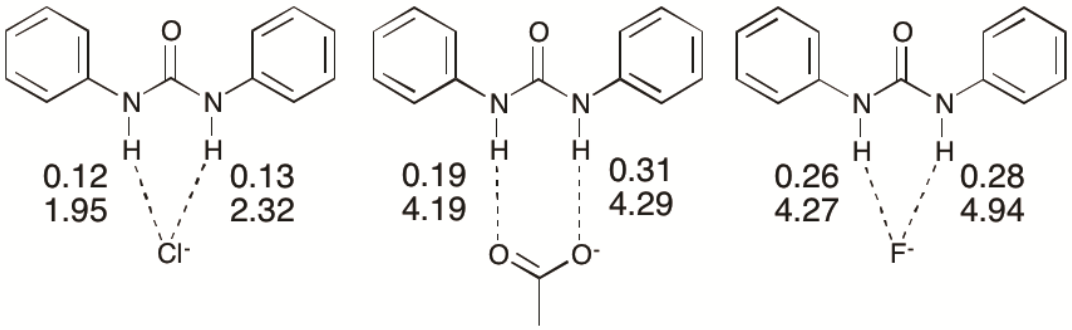

Figure 4.5 Trends in the electron density (top value in units of *e* Å^{-3}) and Laplacian of the electron density values (lower value units of *e* Å^{-5}) at the BCPs between each urea N−H and anion in the *para* series of structures **c.s.6**, **c.s.9** and **c.s.11**.

Plots of the average $\rho(\mathbf{r}_{BCP})$ and $\nabla^2\rho(\mathbf{r}_{BCP})$ for the N—H···anion hydrogen bonds for each complex of **14** against the pK_as of the anion are shown in Figure 4.6 and illustrate the increase in hydrogen bond strength as basicity increases. This increase in electron density at the BCPs as basicity increases indicates a stronger interaction and matches the observed binding affinities in solution where chloride was shown to have a markedly weaker association with receptor **14** than acetate (see Chapter 3.3.1).

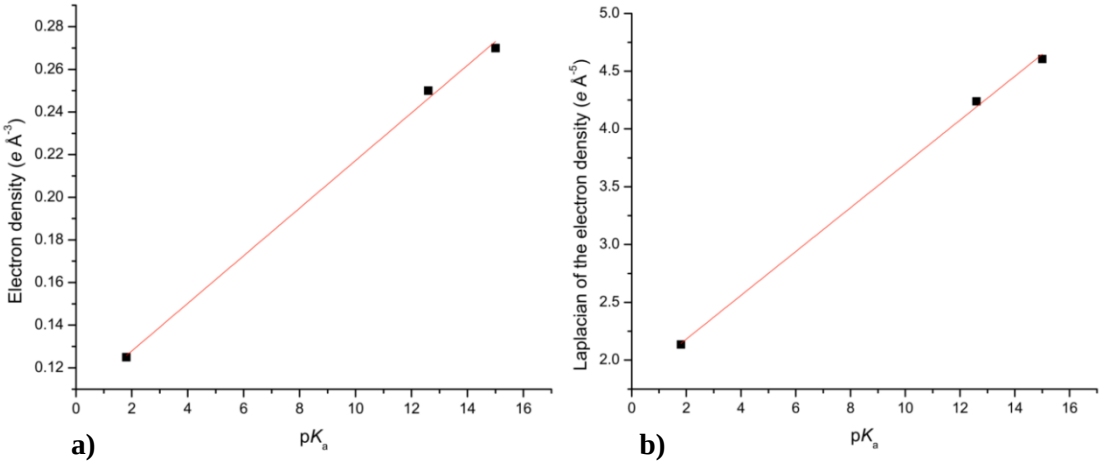

Figure 4.6: **a)** Linear relationship (R^2 of the linear fit is 0.996) between the average electron density (units of e Å^{-3}) at the hydrogen bonding BCPs and pK_a of the anion in **c.s.6**, **9** and **11**. **b)** Linear relationship (R^2 of the linear fit is 0.998) between the average Laplacian of the electron density (units of e Å^{-5}) at the hydrogen bonding BCPs and pK_a of the anion in **c.s.6**, **9** and **11**.

The nature of the hydrogen bonding interaction, i.e. whether it is electrostatic or covalent is a source of debate in many systems similar to this. In charge density analysis the nature of the hydrogen bonding can be determined by analysing the properties of the electron density at the BCPs.[80] The energetic properties; the local kinetic energy density, $G(\mathbf{r}_{BCP})$, the local potential energy density, $V(\mathbf{r}_{BCP})$, the total energy density, $H(\mathbf{r}_{BCP})$, and the hydrogen bond energy, E_{HB} are indicators of hydrogen bond nature and these have been calculated for the hydrogen bonds in this series using the equations given in Section 2.3.4.4.4.[73]

In the set of complexes under investigation the N—H···anion hydrogen bonds of the halide structures (**c.s.5**, **6**, and **11**) are purely electrostatic, while those in the acetate complexes (**c.s.9** and **10**) occupy the intermediate or boundary region between closed-shell and covalent character. This is illustrated by the

$|V(\mathbf{r}_{BCP})|/G(\mathbf{r}_{BCP})$ ($<$ 1.00 a.u. in **c.s.5**, **6**, and **11** and $>$ 1.00 in **c.s.9** and **10**) and the $H(\mathbf{r}_{BCP})$ ($>$ 0.00 a.u. in **c.s.5**, **6**, and **11**, and $<$ 0.00 **c.s.9** and **10**) values obtained from our experimental electron density distributions.[80]

The exponential relationship of both $\rho(\mathbf{r}_{BCP})$ and $\nabla^2\rho(\mathbf{r}_{BCP})$ with the H···A distance has previously been noted in charge density studies of hydrogen bonding.[75,82,84] Similar exponential relationships exist in this study, as illustrated in Figure 4.7, which plots the exponential relationship between H···A distance and the electron density at the BCP in this family of anion-receptor complexes. Espinosa and co-workers have shown in multiple studies on X—H···O interactions that the geometric parameters of hydrogen bonds can be correlated to the topology of $\rho(\mathbf{r}_{BCP})$ in the hydrogen bonding region, which itself is intrinsically linked to the energetic properties at the BCP.[75–77] The exponential relationship observed between the H···A distance and both $V(\mathbf{r}_{BCP})$ and $G(\mathbf{r}_{BCP})$ has also been rationalised.[74]

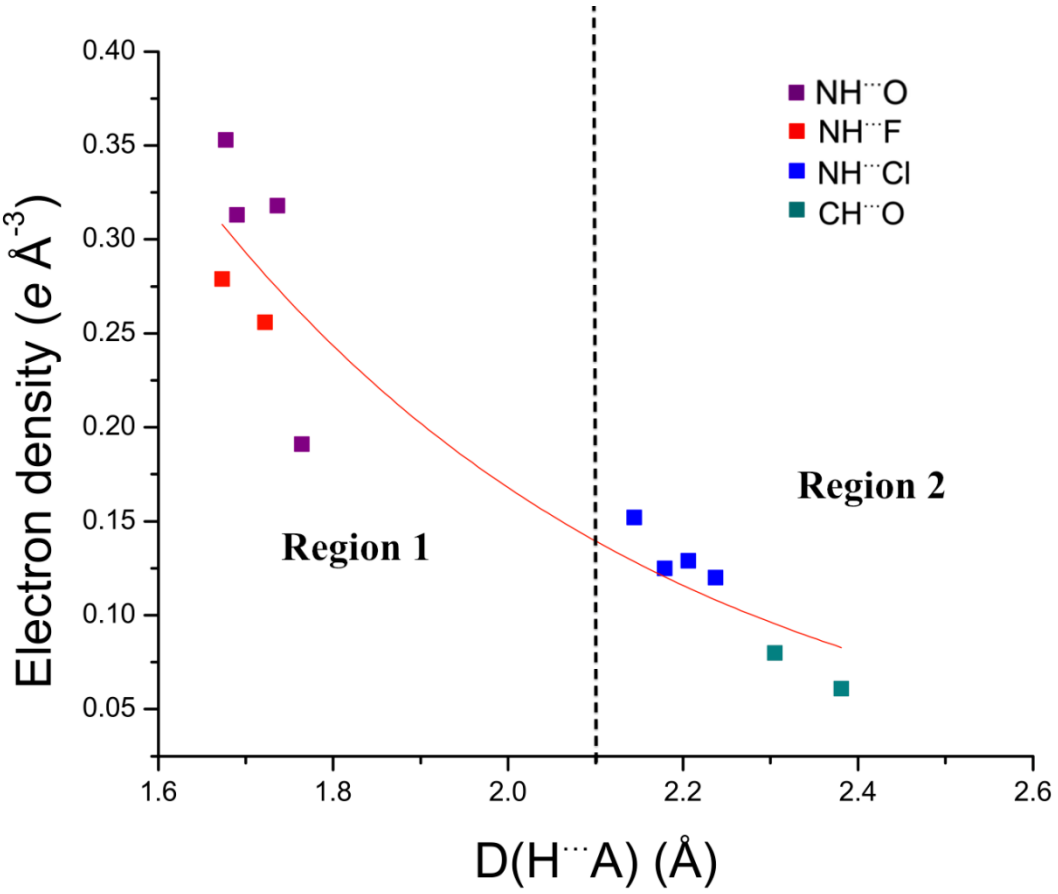

Figure 4.7: Exponential relationship between $\rho(\mathbf{r}_{BCP})$ and the H···A distance. The two regions of hydrogen bond interaction are shown.

As increases in $\rho(\mathbf{r}_{BCP})$ and $\nabla^2\rho(\mathbf{r}_{BCP})$ are both an indication of increasing hydrogen bond strength these exponential relationships suggest the suitability of estimating the relative hydrogen bond strengths from DHA distances (the combined hydrogen bond donor, hydrogen and hydrogen bond acceptor atom distance) a typical approach used to quantify hydrogen bonding in atomic resolution structural studies of anion-receptor complexes, in this series of structures.

In this series of anion-receptor complexes two distinct types of hydrogen bonding (Figure 4.7) are observed. Region 1 is an area of stronger hydrogen

bonding. It contains the N—H···anion hydrogen bonds of the fluoride and acetate complexes (**c.s.9**, **10**, and **11**) and is characterised by electron density values at the BCPs > 0.19 *e* Å^{-3} and H···A distances < 1.80 Å with the bond path between the D···A atoms shorter than the van der Waals radii of the individual atoms (tabulated in Table 1.2). Region 2 is a weaker hydrogen bonding area. The electron density at the BCPs < 0.15 *e* Å^{-3} and the H···A distance > 2.15 Å. This region contains both the N—H···Cl interactions of the chloride structures (**c.s.5** and **c.s.6**) and the C—H···O interactions in **c.s.9**. In each of these interactions the sum of the van der Waals radii of the interacting atoms is lower than the bond path between the D···A atoms.

4.4.3.2 Atomic Charges

Chapter 2 describes how atomic charges can be calculated for each atom in the crystal structure from the experimental electron density distribution. In this thesis the discussion is based on Bader's QTAIM partitioning which generates QTAIM charges.[66] The stockholder Hirshfeld charges have been included for completeness in A.7.2 and tend to agree (in terms of sign of the charges). By comparing the atomic charges, the charge transfer between individual units in the supramolecular systems could be probed. The effect of changes to individual components on the electron density distribution both in these groups and across the *entire* structure could be determined in this way. This is further correlated to changes in the electrostatic potential distributions. Figure 4.8 shows the QTAIM charges of key atoms in the *para* substituted series of complexes **c.s.6** (chloride), **c.s.9** (acetate) and **c.s.11** (fluoride).

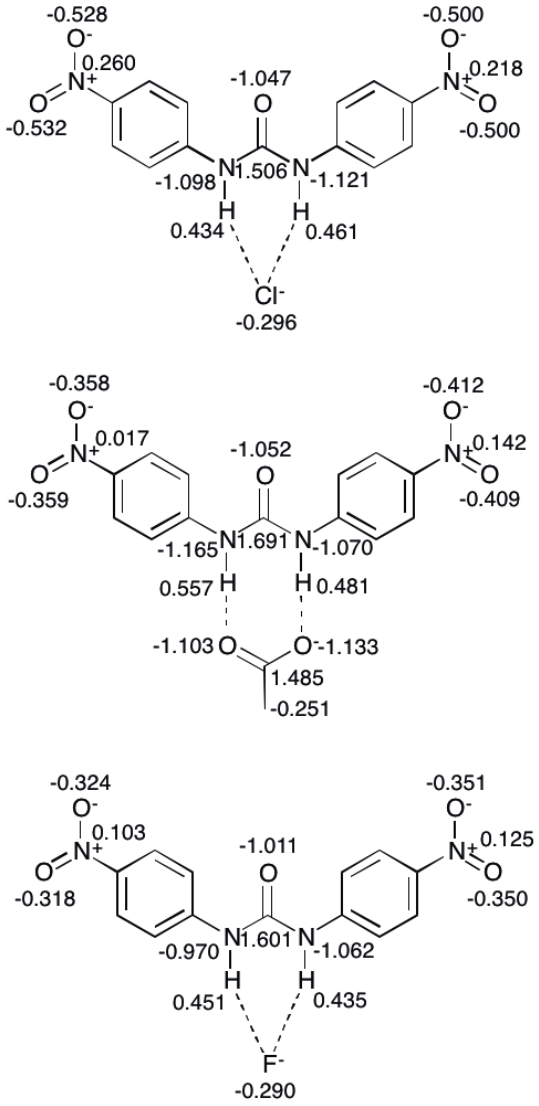

Figure 4.8: Integrated charges (units *e*) in key areas of the *para* substituted receptor structures top: **c.s.6** (chloride), middle: **c.s.9** (acetate) and bottom: **c.s.11** (fluoride).

As expected, electronegative atoms such as the oxygen atoms of the urea and nitro groups are negatively charged, while the electropositive urea hydrogen atoms are positively charged. The nitrogen atoms of the nitro groups are also positively charged. The difference in the charge of the urea oxygen atom across the structures, which is less negative in **c.s.11** (fluoride) than in **c.s.6** and **c.s.9** (chloride and acetate respectively) may reflect the dissimilarity in the

intermolecular interactions formed between the oxygen atoms; with **c.s.6** and **c.s.9** interacting with the TMA groups while in **c.s.11** the urea oxygen atom interacts with the phenyl ring of another receptor molecule.

The acetate oxygen atoms in **c.s.9** are highly negative, while the halide anions in **c.s.6** and **c.s.11** have less of a negative charge. The higher charges observed for the acetate anions (**c.s.9** and **c.s.10**) compared to the halide anions may be due to the different nature of the hydrogen bonding outlined above, where the acetate anions are involved in hydrogen bonding of a possibly partially covalent nature or boundary nature (as suggested by the $|V(\mathbf{r}_{BCP})/G(\mathbf{r}_{BCP})|$ ratio greater than 1 and the $H(\mathbf{r}_{BCP})$ less than zero)[82].

From **c.s.6** to **c.s.11**, as the basicity of the anion is increased, the charges of the urea nitrogen atoms become less negative. This perturbation of charge in the urea portion of the structures is shown to extend to the peripheral regions of the structure with the charge on the oxygen atoms of the nitro groups approaching closer to neutrality with increasing basicity. This is reflected in the changes in the electrostatic potential distribution of these regions displayed in Figure 4.9.

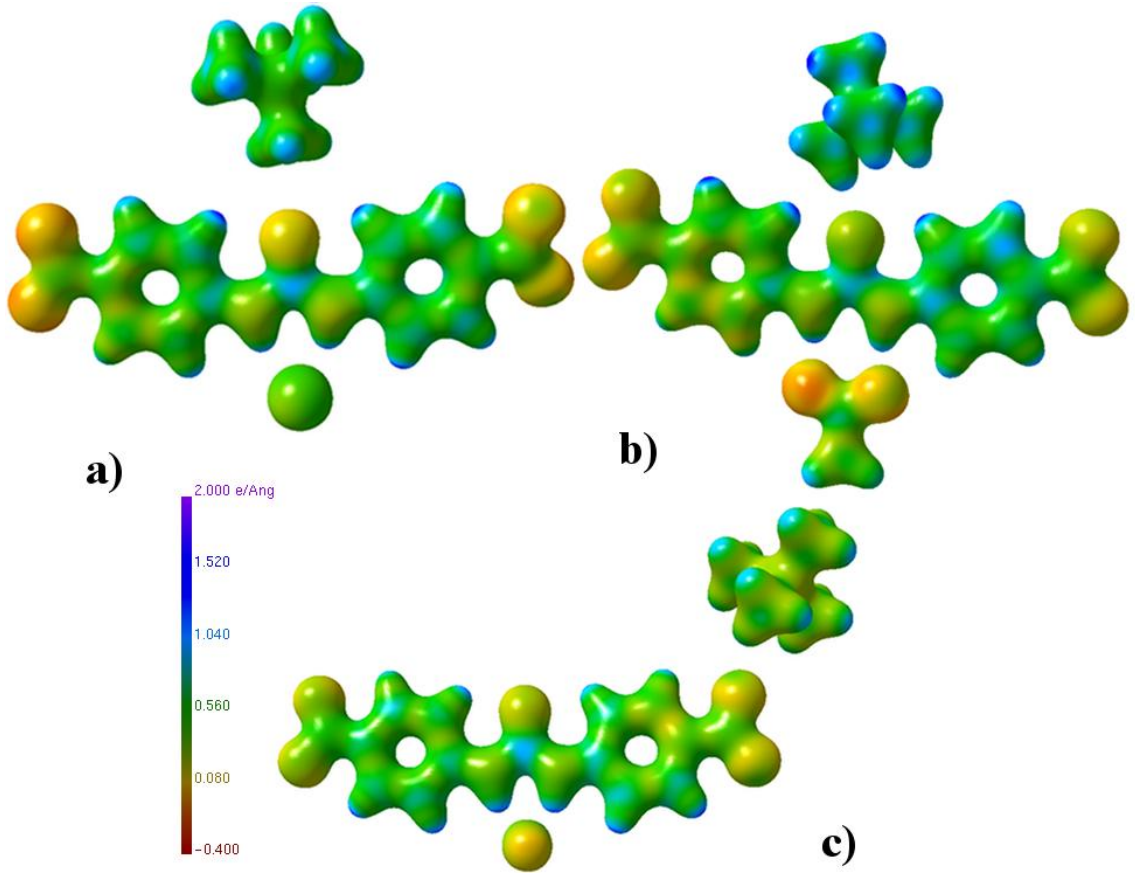

Figure 4.9: Electrostatic potential plots[180] (units e Å^{-1}) of **a) c.s.6**, **b) c.s.9** and **c) c.s.11**.

4.4.4 The substituent positional effect

Having looked at the effect of altering the anion across a series of anion-receptor complexes with a constant receptor present, the effect of the substituent position on the phenyl ring will now be discussed. This is analysed by comparing two sets of structures where a common anion is complexed to a different receptor scaffold. Altering the location of the nitro group in receptor **14** from the *para* to the *meta* position in receptor **13** allows an investigation into the effect of the different electron-withdrawing abilities of nitro groups in different positions. Between **c.s.5** and **c.s.6** (the chloride complexes of *meta* receptor **13** and *para* receptor **14** respectively) the only variation is the position of the nitro groups. The effect of further increasing the electron-withdrawing

nature of the substituent positioned on the phenyl rings of the receptor scaffold can be probed by comparison with the 1,3-bis(3,5-dinitrophenyl)urea receptor (**15**), which has two nitro groups on each phenyl ring and is therefore expected to cause a greater pull of electrons away from the urea and phenyl rings onto the nitro groups. Contrasting the two acetate complexes allows a comparison of the effect of *para* (**c.s.9**) and 3,5-dinitro (**c.s.10**) substitution of the receptor on the electron density distribution.

4.4.4.1 X—H···anion interactions and their strengths

The importance of verifying the existence of hydrogen bonding interactions has been discussed above. The electron density, Laplacian of the electron density and energy density values at the BCPs (see Table 4.2) were used to describe the N—H···anion interactions in **c.s.5** and **c.s.10** and characterised them as hydrogen bonds.

Figure 4.7 shows that in each set of comparison structures (**c.s.5** *vs.* **c.s.6** and **c.s.9** *vs.* **c.s.10**) the interactions of each class of hydrogen bond, N—H···Cl (found in **c.s.5** and **c.s.6**) and N—H···O (**c.s.9** and **c.s.10**) lie in the same region. The interactions of the chloride structures lie in region 2, that of weak hydrogen bonding, and those of the acetate structures in region 1, the strong hydrogen bond region.

In the chloride complexes **c.s.5** and **c.s.6** (with *meta* and *para* substituted receptors respectively), the values of $\rho(\mathbf{r}_{BCP})$, $\nabla^2\rho(\mathbf{r}_{BCP})$, $G(\mathbf{r}_{BCP})$, $V(\mathbf{r}_{BCP})$, and $H(\mathbf{r}_{BCP})$ at the observed N—H···Cl BCPs are consistent with classification of the hydrogen bonding as weak (as outlined by Rozas *et al.*, both $\nabla^2\rho(\mathbf{r}_{BCP})$ and $H(\mathbf{r}_{BCP}) > 0$).[80] Although as anticipated **c.s.5** and **c.s.6** (*meta vs. para* chloride) exhibit the same type of hydrogen bonding interaction, there is variation

between the values of the $\rho(\mathbf{r}_{BCP})$ and $\nabla^2\rho(\mathbf{r}_{BCP})$ of the N—H···Cl in **c.s.5** and **c.s.6**, which is higher than the estimated standard uncertainties on these values. The higher values observed in **c.s.5** suggest its hydrogen bonds are stronger.

In the acetate complexes (**c.s.9** and **c.s.10**, where the receptor is *para* and 3,5-dinitro substituted respectively) the distance between the atoms involved in the N—H···anion hydrogen bonding is shorter than the van der Waals radii of the atoms. Properties of the electron density at the BCPs of the hydrogen bonds, shown in Table 4.2 suggest that two differing types of hydrogen bonding interactions are present in these structures. The lower $\rho(\mathbf{r}_{BCP})$ and $\nabla^2\rho(\mathbf{r}_{BCP})$ values for the N—H···anion BCPs in **c.s.9** (*para* acetate) characterise weaker strength hydrogen bonding in this structure, compared to those interactions in **c.s.10** (3,5-dinitro acetate).[80]

Using the source function approach[71,72,181] (described in Chapter 2), it is possible to calculate how different regions of the structure contribute to the electron density at a BCP. The combined contribution of the DHA atoms to the electron density at the hydrogen bond BCPs support the weaker hydrogen bonding in **c.s.9** compared to **c.s.10**, with the contribution greater from the DHA atoms in **c.s.10** than **c.s.9**. (The full source function analysis is shown in Table 4.3 below.) The value of $H(\mathbf{r}_{BCP})$ and $|V(\mathbf{r}_{BCP})|/G(\mathbf{r}_{BCP})$ for the N—H(3A)···O(7) BCPs in **c.s.9** and N—H(3A)···O(10) and H(4A)···O(11) BCPs in **c.s.10** (shown in Table 4.3) suggest these are medium strength boundary type hydrogen bonds unlike the weaker purely electrostatic hydrogen bonding interactions found in the other structures. This may be due to the geometry of the anion in the acetate structures (**c.s.9** and **c.s.10**), where there is a more linear arrangement of the hydrogen bond, with each urea N—H hydrogen bond donor group forming a hydrogen bond atom with one of the oxygen atoms of the acetate,

while in the halide structures (**c.s.5**, **6** and **11**) the anion has bifurcated hydrogen bonds. In the acetate complexes (*para* **c.s.9** and 3,5-dinitro **c.s.10**) the shorter hydrogen bonds correspond to medium strength intermediate type interactions.

Table 4.3: Source function contributions to N–H···anion interactions.

Hydrogen bond	Donor (%)	Acceptor (%)	Hydrogen (%)	Sum of DHA (%)
c.s.6. *Para* receptor: chloride				
N(2)···Cl(1)	49.05	53.67	-51.58	51.14
N(3)···Cl(1)	50.73	55.93	-56.10	50.56
c.s.9. *Para* receptor: acetate				
N(2)···O(6)	38.64	13.06	-28.36	23.34
N(3)···O(7)	21.90	28.53	2.78	53.21
c.s.11. *Para* receptor: fluoride				
N(2)···F(1)	29.33	48.45	-9.27	68.51
N(3)···F(1)	28.50	44.50	-7.09	65.91
c.s.5. *Meta* receptor: chloride				
N(2)···Cl(1)	47.20	52.81	-48.46	51.55
N(3)···Cl(1)	40.99	52.66	-38.02	55.63
c.s.10. 3,5-dinitro receptor: acetate				
N(3)···O(10)	19.98	27.53	3.19	50.70
N(4)···O(11)	21.30	37.11	8.46	66.87

There is a disparity between the solid-state and solution phase observations (reported in Section 3.3.1), as topological analysis of the electron density at the BCPs of the N—H···Cl interactions in **c.s.5** and **c.s.6** (*meta* and *para* chloride complexes respectively) suggests **c.s.5** has marginally stronger hydrogen bonds, while in solution the *para* substituted receptor (**14**) was shown to have stronger affinity for chloride than the *meta* substituted receptor (**13**), 118 *vs.* 56 M^{-1} (see Section 3.3.1). This may be caused by additional non-covalent

interactions between other components of the structure, such as TMA···nitro contacts, in the solid-state, that promote stronger association between receptor **13** and chloride in the crystalline environment. In **c.s.10** there is no evidence to support the deprotonation of the receptor by acetate suggested in solution, so the interactions in solution and the solid-state cannot be directly compared in this case.

While the classification of the two chloride structures (**c.s.5** and **c.s.6**) confirms the same nature of interaction, more variation is observed between the two acetate complexes (**c.s.9** and **c.s.10**, *para* and 3,5-dinitro substituted respectively). In the hydrogen bonds in the halide complexes studied here (**c.s.5**, **6** and **11**), the contribution the hydrogen atoms make to the electron density at the BCP has been quantified using the source function approach[71,72,181] and found to be negative. Therefore they act as electron density '*sinks*', implying that they are electrostatic in nature. This behaviour is not observed in **c.s.9** and **c.s.10**, where the majority of the hydrogen atoms act as '*sources*' for the electron density at the N—H···O hydrogen bonds, providing a positive contribution, which suggests a stronger interaction. According to the classification of Gilli & Gilli these N—H···O hydrogen bonds are resonance assisted hydrogen bonds.[17] The halide N—H···anion hydrogen bonds in the series are, according to the same classification, polarised assisted hydrogen bonds. This is not just a result of the anion type, as in **c.s.9** only one of the hydrogen atoms of the N—H bonds is a '*source*' and the other a '*sink*' for the electron density. Contrastingly, in **c.s.10** both hydrogen atoms are '*sources*' for the electron density, suggesting this effect is related to the additional nitro groups enhancing the acidity of the N—H bond and strengthening the association between the host and the guest. This is an interesting example of how changes in the electron density distribution at particular areas of interest

in the structures are caused by periphery modifications and also of how a systematic approach best reveals these effects.

In the two acetate complexes (**c.s.9** and **10**, with *para* and 3,5-dinitro substituted receptors respectively) geometric analysis reveals the presence of C—H···O interactions between the phenyl ring hydrogen atoms and acetate oxygen atoms (with H···A distances and DHA angles in **c.s.9** of 2.381 Å 136.86° and 2.305 Å 134.58° and in **10** of 2.535 Å 130.69° and 2.355 Å 131.72°). These fulfil the geometric standards set out by Wood *et al.*[14], (building on previous work[15,16]) in their study on hydrogen bonding using the Cambridge Structural Database where D—H···A angles $< 120°$ were ruled out from being hydrogen bonding interactions. However, bond paths between the respective H···A atoms are present in **c.s.9** while in **c.s.10** they are not. This is a powerful example of how systematic charge density analysis provides key information, as it is necessary to determine if an interaction is 'real' or an erroneous assumption of geometry. Additionally, this work demonstrates how modification of the receptor scaffold in this case has brought about changes in the intermolecular interactions observed in the crystal structure, as altering the receptor substitution pattern from *para* (**c.s.9**) to 3,5-dinitro (**c.s.10**) is accompanied by a change of the acetate anion from co-planarity with the receptor in **c.s.9** to non co-planarity of the acetate and receptor in **c.s.10**.

4.4.4.2 Electron density distribution across receptor

The differences in the electrostatic potential distributions in the complexes, caused by altering the position and number of electron-withdrawing substituents on the phenyl ring are shown in Figure 4.10 and Figure 4.11. Figure 4.10 compares chloride complexes **c.s.5** and **c.s.6** (*meta* substituted receptor *vs. para* substituted receptor respectively) while Figure 4.11 compares

acetate complexes **c.s.9** and **c.s.10** (*para* substituted receptor *vs.* 3,5-dinitro receptor). The variations appear to be mediated by the functionalisation of the receptor, as with a constant receptor but altered anion in the case of **c.s.6** *vs.* **c.s.9** (where the nitro group remains unchanged in the *para* position of the ring), there is minimal variation in the electrostatic potential distribution. When altering the receptor substituent pattern as in **c.s.5** *vs.* **c.s.6** and **c.s.9** and **c.s.10** the electrostatic potential distributions vary significantly across the entire structures. In Figure 4.10 the urea and phenyl ring areas of **c.s.5** display a greater positive electrostatic potential as compared to structure **c.s.6**. The nitro groups in **c.s.6**, which are *para* substituted, have a more negative electrostatic potential than those in **c.s.5**, where they are in the *meta* position, as predicted due to the greater electron-withdrawing ability of nitro groups in the *para* position.

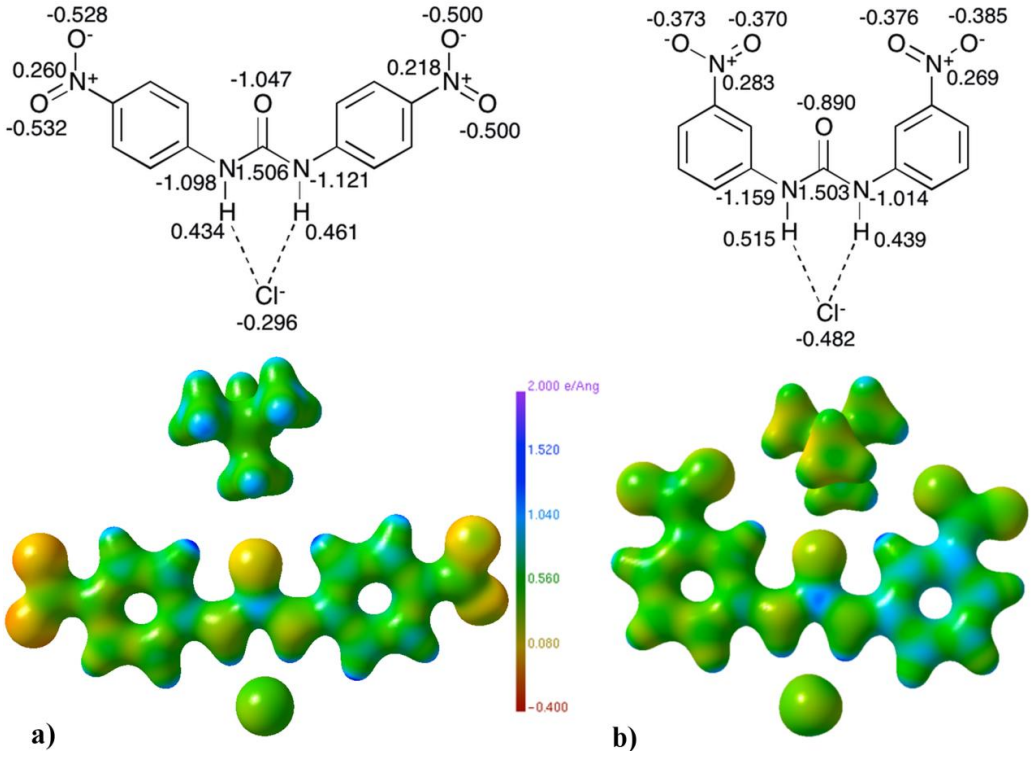

Figure 4.10: Electrostatic potential maps[180] (units of *e* Å^{-1}) and selected QTAIM charges (units of *e*) of **a) c.s.6** versus **b) c.s.5**.

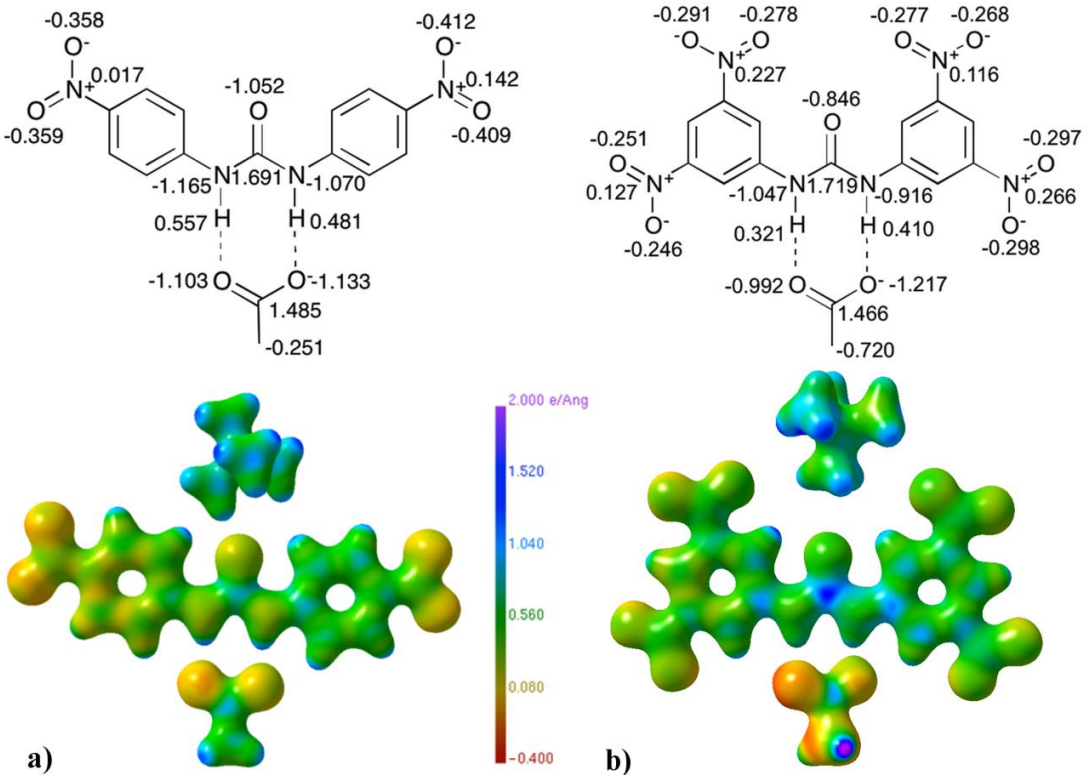

Figure 4.11: Electrostatic potential maps[180] (units of *e* Å^{-1}) and selected QTAIM charges (units of *e*) of **a) c.s.9** versus **b) c.s.10**.

When comparing the structure of the *para* substituted receptor with acetate, **c.s.9** and the acetate complex of the 3,5-dinitro substituted receptor **c.s.10** (Figure 4.11), major deviations in the electrostatic potential distribution of the acetate anion are detected. The acetate in structure **c.s.10** is carrying a greater negative electrostatic potential than the acetate in **c.s.9**. The electrostatic potential of the urea portion of the receptor in **c.s.10** is shown to have a larger variation than in **c.s.9**, with a higher positive electrostatic potential on the carbon atom of the urea. This matches the increase in hydrogen bond strength from **c.s.9** to **c.s.10**. The nitro groups of the *para* substituted complex (**c.s.9**) are shown to have a more negative electrostatic potential than those in **c.s.10**, where they are situated in both the 3 and 5 positions of the phenyl rings. The explanation for this could be that the electron-withdrawing effect exerted on

the urea group by the nitro groups (which is greater in **c.s.10**) is being spread over a larger number of nitro groups than in structure **c.s.9**. Thus there is less negative electrostatic potential distribution on the individual nitro groups but an overall greater contrast in the electrostatic potential distribution of the urea region in **c.s.10** when compared to **c.s.9**.

The differences observed in the electrostatic potential distribution can be correlated to the charges calculated using QTAIM theory (displayed graphically with the electrostatic potential plots in Figure 4.10 and Figure 4.11). In both comparison sets the partial charge of the anion is seen to differ. The charge associated with chloride in **c.s.6** (-0.296 *e*) is less negative than that of chloride in **c.s.5** (-0.482 *e*). In the acetate anion complexes the QTAIM charges for the oxygen atoms are, as expected, highly negative (~-1.00 *e*), however the difference is larger in **c.s.10** than **c.s.9**. The increase in the charge of the anion may be responsible for the observed difference between the hydrogen bonding between chloride structures (**c.s.5** and **c.s.6**) and acetate complexes (**c.s.9** and **c.s.10**).

Due to the differences in the receptor pattern (*para vs. meta* receptor both complexed to chloride in **c.s.6** and **c.s.5** and *para vs.* 3,5-dinitro with both complexed to acetate anion in **c.s.9** and **c.s.10**) the electronic distribution alters in the urea region of the receptor and this is observed in the variation of charges for these atoms (see Figure 4.10 and Figure 4.11). Variation in the electrostatic potential distribution of the nitro groups is also reflected in the difference in charges of the individual atoms present in the nitro groups.

Of further note is the difference in the properties of the C—N BCPs linking the nitro groups to the phenyl ring for a given anion. While the properties in **c.s.10** are similar to those observed in **c.s.9**, the values of the electron density and

Laplacian of the electron density at the BCPs in the *meta* complex, **c.s.5**, between C(6)—N(1) and C(12)—N(4) are lower than the values observed in **c.s.6**. These match those of **c.s.9** and **c.s.11**, suggesting this is a result of altering the location of the nitro group from the *para* to *meta* position. This is linked to the difference observed in the $\nabla^2\rho(\mathbf{r}_{BCP})$ and bond ellipticity profiles along the bond paths of the urea region of the structures (see Appendix A.5). In **c.s.5** and **c.s.10** the profiles of these bond paths contrast markedly to those in **c.s.6**, **9** and **11**, suggesting the changes are a result of the altering electron-withdrawing nature of the nitro groups in varying positions on the phenyl rings, affecting the electron density distribution in the urea region to a lesser or greater extent. These may also reflect a difference between the mesomeric electron-withdrawing effects possible in the *para* series of complexes (**c.s.6** – **c.s.9** – **c.s.11**) with the inductive electron-withdrawing effects (**c.s.5** and **c.s.10**).

Changes to particular regions of the receptor scaffold have been shown to have an observable effect on the electron density distribution across the entire structure, not just the immediate area of substitution. Variation in charge, the properties of the electron density at the BCPs, and the electrostatic potential distribution are evident across the series of structures reported in this chapter.

4.4.5 Additional non-covalent interactions

Electron density distribution is also able to detect the presence of other non-covalent interactions in the anion-receptor complexes in addition to the N—H···anion interactions and these are now discussed.

4.4.5.1 TMA···O=C interactions

Topological analysis shows the presence of intermolecular interactions between the C—H bonds of the TMA cation and urea oxygen atom in all five structures, excluding **c.s.11**, due to the different position of the TMA cation in **c.s.11**. These are weak closed-shell interactions, as evidenced both by the low $\rho(\mathbf{r}_{BCP})$ values and low positive $\nabla^2\rho(\mathbf{r}_{BCP})$ values (see Table 4.4). The nature of these interactions varies between the structures, with multiple carbon and hydrogen atoms of the TMA groups involved in the interactions in **c.s.5** and **c.s.6**, while in **c.s.9** and **c.s.10** only one carbon of the TMA cation is involved in these interactions.

Additionally, in structures **c.s.5**, **c.s.6** and **c.s.9** C—H···C interactions between the phenyl rings of the receptor molecule and carbon atoms of TMA are noted (see Table 4.5).

Table 4.4: Table of the BCPs for the TMA···O=C contacts present in the structures.

Critical Point	$\rho(\mathbf{r}_{BCP})$ (e Å^{-3})	$\nabla^2\rho(\mathbf{r}_{BCP})$ (e Å^{-5})	R_{ij} (Å)	d_1 (A—CP) (Å)	d_2 (CP—B) (Å)	ϵ
O(1)···C(15)	0.056(2)	0.912(1)	2.9490	1.4398	1.5092	2.32
O(1)···H(15A)	0.056(2)	0.912(1)	2.7784	1.4398	1.3386	2.32
O(1)···H(15C)	0.056(2)	0.912(1)	2.9622	1.4398	1.5224	2.32
O(1)···H(14C)	0.039(5)	0.654(2)	2.5792	1.5001	1.0791	0.29
O(1)···H(17C)	0.067(9)	1.166(2)	2.3469	1.4107	0.9361	0.08
O(1)···C(15)	0.050(3)	0.776(2)	3.2739	1.4364	1.8376	0.08
O(1)···C(17)	0.046(2)	0.714(2)	3.2809	1.4636	1.8173	0.13
O(1)···H(15C)	0.050(3)	0.776(2)	2.5618	1.4364	1.1254	0.08
O(1)···H(17C)	0.046(2)	0.714(2)	2.6562	1.4636	1.1926	0.13
O(1)···C(16)	0.057(2)	0.774(2)	3.0395	1.4455	1.5941	0.09
O(1)···H(16C)	0.057(2)	0.774(2)	2.8178	1.4455	1.3723	0.09

Table 4.5: Table of the CPs for the TMA···H=C contacts present in the structures.

Critical Point	$\rho(\mathbf{r}_{BCP})$ (e Å^{-3})	$\nabla^2\rho(\mathbf{r}_{BCP})$ (e Å^{-5})	R_{ij} (Å)	d_1 (A—CP) (Å)	d_2 (CP—B) (Å)	ϵ	Type
c.s.6. *Para* receptor: chloride							
C(15)···H(5)	0.001(3)	0.194(2)	3.4145	2.2495	1.1650	0.00	RCP
c.s.9. *Para* receptor: acetate							
C(17)···H(5)	0.037(3)	0.549(1)	2.9070	1.7910	1.1160	1.92	BCP
c.s.5. *Meta* receptor: chloride							
C(15)···H(13)	0.023(5)	0.440(3)	3.2298	2.0690	1.1608	0.57	BCP
C(17)···H(13)	0.005(4)	0.194(2)	3.4817	2.2654	1.2163	0.00	RCP

4.4.5.2 Phenyl C—H···O=C interactions

In each of the anion-receptor complexes intramolecular hydrogen bonds between the urea group oxygen atom and both the aromatic C—H bonds *ortho* to the urea are characterised by bond paths and BCPs between C(5)···O(1) and C(13)···O(1). These are accompanied by bond paths between the hydrogen atoms of these carbons and the oxygen atoms (H(5)···O(1) and H(13)···O(1)). The length of both the bond paths between the hydrogen atoms and oxygen atoms (< 2.90 Å) and the carbon atoms and oxygen atoms (< 3.22 Å) are less than the van der Waals radii of the atoms. In addition the values of the electron density and the Laplacian of the electron density at the BCPs suggest that there is a combination of weak C−H···O and *'carbon bonding'*, initially described in theoretical studies by Mani and Arunan[182] and observed experimentally in charge density studies by Thomas *et al.*[183] The presence of a ring critical point between both C(4) and O(1) and C(8) and O(1) in each of the structures also emphasizes the interaction between the urea and phenyl rings, and suggests the presence of a six-membered ring (see Table 4.6).

Table 4.6: C—H···O=C interactions in phenyl groups of structures.

Critical Point	$\rho(\mathbf{r}_{BCP})$ (e Å^{-3})	$\nabla^2\rho(\mathbf{r}_{BCP})$ (e Å^{-5})	R_{ij} (Å)	d_1 (A—CP) (Å)	d_2 (CP—B) (Å)	ϵ	Type
c.s.6. *Para* receptor: chloride							
O(1)···C(4)	0.085(2)	1.446(2)	3.0360	1.4545	1.5814	0.00	RCP
O(1)···C(8)	0.085(2)	1.430(2)	3.0469	1.4463	1.6006	0.00	RCP
O(1)···C(5)	0.106(2)	1.635(2)	2.9214	1.3294	1.5920	0.11	BCP
O(1)···C(13)	0.106(3)	1.670(2)	2.9299	1.3212	1.6088	0.08	BCP
c.s.9. *Para* receptor: acetate							
O(1)···C(4)	0.105(3)	1.620(2)	2.9868	1.4270	1.5598	0.00	RCP
O(1)···C(8)	0.102(3)	1.571(2)	3.0076	1.4197	1.5879	0.00	RCP
O(1)···C(5)	0.132(4)	1.970(3)	2.8631	1.2804	1.5827	0.09	BCP
O(1)···C(13)	0.124(4)	1.833(2)	2.8907	1.3125	1.5782	0.13	BCP
c.s.11. *Para* receptor: fluoride							
O(1)···C(4)	0.103(2)	1.500(2)	3.0795	1.4170	1.6625	0.00	RCP
O(1)···C(8)	0.097(2)	1.403(1)	3.1073	1.4252	1.6821	0.00	RCP
O(1)···C(5)	0.115(3)	1.710(2)	2.9339	1.3123	1.6216	0.35	BCP
O(1)···C(13)	0.102(2)	1.492(2)	2.9367	1.3443	1.5923	0.57	BCP
c.s.5. *Meta* receptor: chloride							
O(1)···C(4)	0.102(3)	1.584(2)	3.0287	1.4126	1.6161	0.00	RCP
O(1)···C(8)	0.102(3)	1.574(2)	3.0197	1.4135	1.6062	0.00	RCP
O(1)···C(5)	0.124(4)	1.834(2)	2.8991	1.3058	1.5933	0.24	BCP
O(1)···C(13)	0.120(4)	1.806(2)	2.8714	1.2995	1.5719	0.16	BCP
c.s.10. 3,5-dinitro receptor: acetate							
O(1)···C(4)	0.125(3)	1.783(3)	2.9855	1.3720	1.6135	0.00	RCP
O(1)···C(8)	0.125(3)	1.756(3)	2.9864	1.3966	1.5899	0.00	RCP
O(1)···C(5)	0.143(4)	2.005(3)	2.8321	1.2842	1.5479	0.48	BCP
O(1)···C(13)	0.142(3)	2.007(3)	2.8471	1.2868	1.5604	0.47	BCP

4.4.5.3 TMA···NO_2 interactions

Altering the position of the nitro groups to the *meta* position of the receptor scaffold, as in structures **c.s.5** and **c.s.10**, leads to the presence of additional intermolecular interactions in the crystal structures. The low $\rho(\mathbf{r}_{BCP})$ and $\nabla^2\rho(\mathbf{r}_{BCP})$ values at the BCPs suggests that these interactions are among the

weakest found in the structures and are formed due to the closer proximity of these atoms resulting from the *meta* position of the nitro group on the phenyl ring (see Table 4.7).

Table 4.7: TMA···NO_2 interactions in meta substituted crystal structures, **c.s.5** and **c.s.10**.

Critical Point	$\rho(\mathbf{r}_{BCP})$ (e Å^{-3})	$\nabla^2\rho(\mathbf{r}_{BCP})$ (e Å^{-5})	R_{ij} (Å)	d_1 (A—CP) (Å)	d_2 (CP—B) (Å)	ϵ	Type
c.s.5. *Meta* receptor: chloride							
O(2)···H(14A)	0.05(1)	0.809(3)	2.4670	1.4527	1.0143	0.02	BCP
O(5)···H(15A)	0.026(5)	0.487(3)	2.7173	1.5760	1.1413	0.45	BCP
O(5)···H(16C)	0.039(8)	0.675(3)	2.5659	1.4897	1.0762	0.06	BCP
O(5)···H(17B)	0.027(7)	0.502(3)	2.7089	1.5523	1.1566	0.30	BCP
c.s.10. 3,5-dinitro receptor: acetate							
O(2)···H(16B)	0.027(6)	0.429(4)	2.7789	1.5831	1.1957	0.11	BCP
O(7)···H(17A)	0.059(1)	0.788(1)	2.8762	1.4528	1.4234	0.54	BCP
O(7)···H(17B)	0.059(1)	0.788(1)	2.9060	1.4528	1.4532	0.54	BCP

4.4.6 Electron density distribution in free ligand 14 (c.s.3)

The previous sections of this chapter have compared the electron density distribution in related anion-receptor complexes and the effect of varying both the anion and receptor substitution pattern. There is also merit in studying the electron density distribution in a free ligand crystal structure and thus studying the effect of anion recognition on the electron density distribution.

The crystal structure (**c.s.3**) of 1,3-bis(4-nitrophenyl)urea (free ligand **14**) has been discussed in terms of standard resolution studies in Chapter 3. Now the electron density distribution in **c.s.3** will be described and some comparison with the crystal structures of the anion-receptor complexes (**c.s.6**, **9** and **11**) of this receptor (**14**) undertaken.

4.4.6.1 Aspherical atom refinement

The quality of the crystal used to obtain the X-ray diffraction data was far from ideal for the aspherical atom refinement, with split peaks observable in certain directions when collecting the X-ray diffraction data. This is reflected in the quality of the resulting multipole modelling (see Table 4.8) and in some areas of the structure the electron density distribution does not look perfect (see static deformation density and negative Laplacian maps in Appendix A.4). The resolution was cut-off at $(\sin\theta)/\lambda = 1.00$ Å^{-1} for this reason and also to reduce the residual density. The RDA plot in Appendix A.3 shows that the final residual density is the result of noise in the model as it has a Gaussian distribution across the unit cell and is not caused by a systematic error in the model used. The data was collected at Diamond Light Source[171] (with the aid of Claire Wilson) at 35K. Due to the lower quality of the data, any analysis and conclusions are made with caution and supported by theoretical studies discussed in Section 4.4.7.

Table 4.8: Refinement details for multipole modelling of **c.s.3**.

Structure	**c.s.3**
Formula	$C_{13}H_{10}N_4O_5$
Crystal system	Orthorhombic
Space group	*Pna*2_1
a (Å)	13.8899(18)
b (Å)	24.389(3)
c (Å)	3.6682(4)
α (°),β (°), γ (°)	90, 90, 90
V (Å^3)	1242.6(3)
Multipole Refinement	
R(F)	0.0295
R(F^2)	0.0600
GoF	1.7611
Nref/Nvar	16.8966
$\Delta\rho$(r) (*e* Å^{-3})	-0.294/ 0.398

4.4.6.2 Covalent bonding

After performing experimental modelling of the electron density distribution in **c.s.3**, topological analysis of the bonding was conducted. The electron density distribution in **c.s.3** is shown graphically in Appendix A.4 (see the static deformation density plots and negative Laplacian maps). These look similar to the electron density distribution plots of **c.s.5-6** and **c.s.9-11**. From the topological analysis all expected covalent bonds in the structure were found, indicated by the presence of a bond path linking the atoms that are chemically bonded and a BCP located at a point on each of the bond paths (see molecular

graph of **c.s.3** in Appendix A.4). The property of the electron density at the BCPs for each covalent bond are in agreement with those found in the anion-receptor complexes, for example the electron density and Laplacian of the electron density values at the BCPs of the C=O bonds are 3.2 e Å^{-3} and -44 e Å^{-5}, the conjugated phenyl ring C—C bonds 2.2 e Å^{-3} and -22 e Å^{-5}, the phenyl ring C—H bonds 1.9 e Å^{-3} and -20 e Å^{-5} and the N—H bonds 2.3 e Å^{-3} and -34 e Å^{-5} respectively. The binding of an anion by the receptor molecule should cause a significant change in the chemistry of the receptor, and could thus be expected to be accompanied by differences in the electron density distribution in the receptor molecule. The fact that this is not observed, with the properties of the electron density at the BCPs in the covalent bonds in the receptor molecule matching the range observed in the anion-receptor complexes, does however make sense, as the binding of an anion (through a non-covalent interaction) should not change the nature of the covalent bonds in the receptor. Further supporting this are the plots of the Laplacian of the electron density and the ellipticity along the bond path (see Appendix A.5), which in **c.s.3** are not significantly different to those found in **c.s.6**, **c.s.9** and **c.s.11**. The effect of anion binding on the electron density distribution in the receptor may be detected by looking at other properties such as the electrostatic potential distribution in the receptor and the atomic charges of the atoms in the receptor molecule and comparing these properties to those in the anion-receptor complexes.

4.4.6.3 Non-covalent interactions

Although the receptor in **c.s.3** is not bound to an anion, there are other non-covalent interactions that are suggested by geometry that the receptor

molecule could be involved in. As opposed to the commonly observed α-tape motif there are NO_2···H—N contacts. The topological analysis of the bonding in **c.s.3** indicates that these interactions are actually present in the crystal, not simply erroneously applied by geometry (see Table 4.9).

Table 4.9: N—H···NO_2 hydrogen bonding interactions in **c.s.3** and other non-covalent interactions.

Critical Point	$\rho(\mathbf{r}_{BCP})$ (e Å^{-3})	$\nabla^2\rho(\mathbf{r}_{BCP})$ (e Å^{-5})	R_{ij} (Å)	d_1 (A—CP) (Å)	d_2 (CP—B) (Å)	ϵ	Type
O(4)···H(2A)	0.04(1)	1.425(1)	2.2750	1.4177	0.8573	1.12	BCP
O(5)···H(3A)	0.072(3)	3.145(2)	1.9720	1.3010	0.6710	0.38	BCP
O(1)···H(5)	0.112(3)	1.581(3)	2.3302	1.3355	0.9946	0.33	BCP
O(1)···H(13)	0.124(4)	1.738(3)	2.2917	1.3257	0.9660	0.40	BCP
O(1)···C(4)	0.106(3)	1.476(3)	3.0764	1.4181	1.6583	0.00	RCP
O(1)···C(8)	0.155(4)	1.584(3)	3.0601	1.4258	1.6343	0.00	RCP

It is interesting to note the varying strengths of the two O···H hydrogen bonds of the NO_2···urea interactions implied by the differences in the values of the electron density and Laplacian of the electron density at the BCP. The O(5)···H(3A) appears to be significantly stronger than the O(4)···H(2A) as suggested by the higher $\rho(\mathbf{r}_{BCP})$ and $\nabla^2\rho(\mathbf{r}_{BCP})$ values. Both of the bond paths are shorter than the combined van der Waals radii of oxygen (1.52 Å[21]) and hydrogen (1.09 Å[22]) however that of O(5)···H(3A) is around 0.3 Å shorter. The increased bond strength of the urea···nitro O(5)···H(3A) hydrogen bond may be linked to the greater linearity of the hydrogen bond, with the ∠ DHA angle 169.9°, compared to 159.7° for the O(4)···H(2A) hydrogen bond. The more linear hydrogen bond could result in a better overlap of the orbitals involved in the hydrogen bonding.

As in the anion-receptor complexes there are bond paths and RCPs between the urea and phenyl ring (C(4)—O(1) and C(8)—O(1)) that indicate the presence of a *pseudo* six-membered ring, and bond paths and BCPs between O(1) and H(5) and H(13) that denote a non-covalent interaction between the O(1) oxygen atom of the urea and the hydrogen atom in the *ortho* position of the ring. This could suggest that the receptor is held in an arrangement that holds it ready to bind an anion.

4.4.6.4 Electrostatic potential distribution and QTAIM atomic charges

Using the experimental electron density distribution the QTAIM atomic charges (see Figure 4.12) and experimental electrostatic potential distribution (see Figure 4.13) for the receptor molecule in **c.s.3** were calculated. The main deviations from the anion-receptor complexes in terms of atomic charges are those of the nitro groups. In **c.s.3**, the oxygen atoms of the nitro groups carry a significantly smaller negative charge, (~ -0.167 *e* compared to an average of -0.365 *e* in the anion-receptor complexes). The hydrogen atoms of the urea N—H group have a large positive charge of 0.525 *e* and 0.561 *e.* These two observations may be due to the NO_2···urea hydrogen bonding in the receptor molecule. As in the crystal structures of the anion-receptor complexes, the carbon atoms in **c.s.3** where the nitro group and urea groups attach to the phenyl rings are highly positively charged. The electrostatic potential distribution across **c.s.3** displayed in Figure 4.13 (two views- one of the front and one of the back of the receptor molecule) shows that the electrostatic potential distribution in the receptor ligand (**14**) is very similar to the distribution across the receptor that is observed in the anion-receptor complexes (**c.s.6**, **c.s.9** and **c.s.11**). The main difference is the electrostatic

potential distribution in the nitro groups, which varies even across the anion-receptor complexes, and matches the difference already discussed in the QTAIM charges of the nitro group atoms. The electrostatic potential distribution across the receptor in **c.s.3** illustrates the electrophilic regions of the receptor molecule, particularly the region belonging to the hydrogen atoms of the urea group, which are attractive to electrons, and in this case are a suitable area for an anion to bind. More nucleophilic regions are also represented, such as the oxygen atoms of the urea and nitro groups, which provide regions for interacting with more electron deficient groups, for example the nitro groups hydrogen bonding to the urea N—H bonds. Due to the packing in **c.s.3** the urea oxygen atom is not involved in any intermolecular non-covalent interactions.

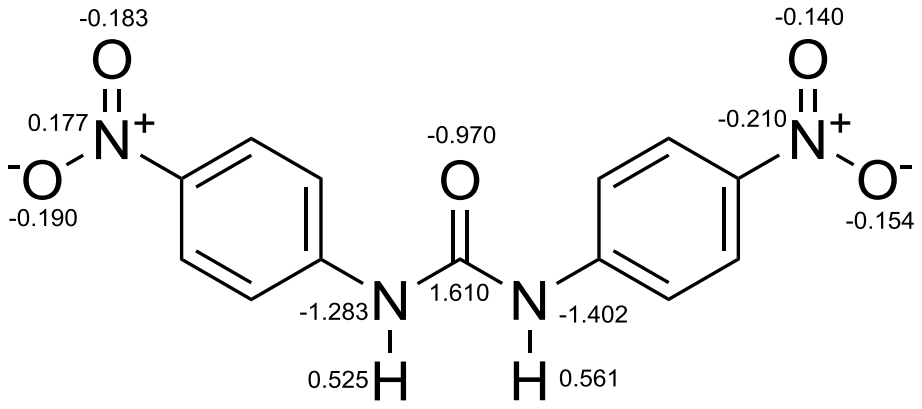

Figure 4.12: Atomic charges in **c.s.3** given in units of *e*.

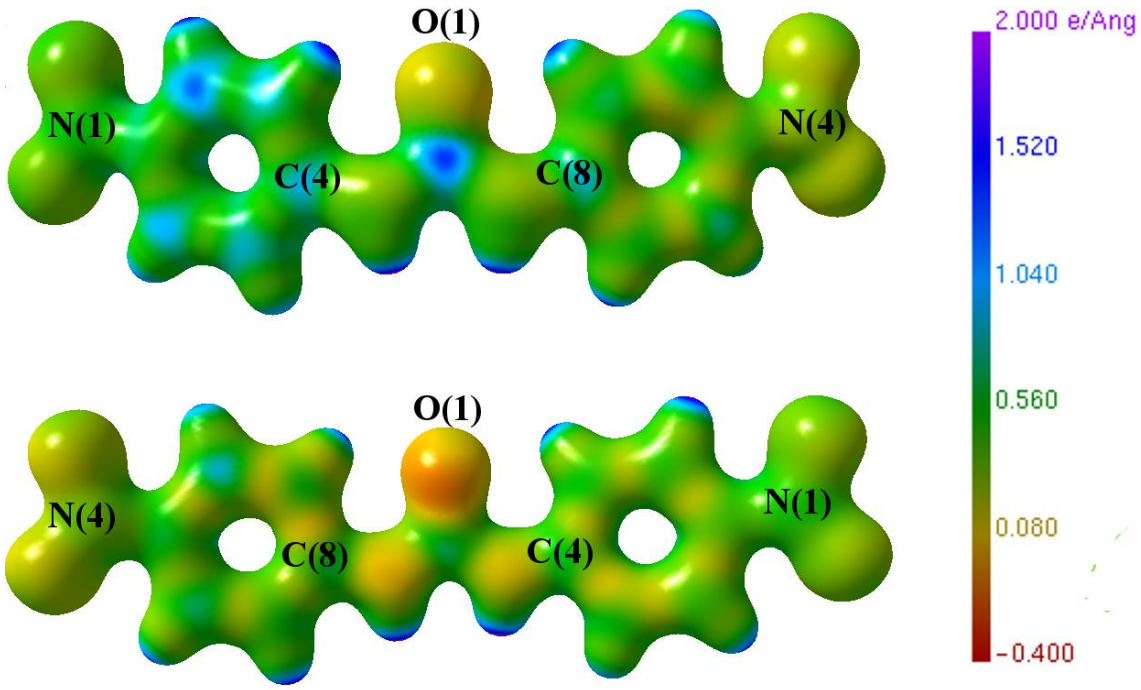

Figure 4.13: Plot of electrostatic potential distribution (units of *e* Å^{-1}) across **c.s.3**. Top: front view and bottom: back view. Plotted using the MolIso[180] program.

4.4.7 Theoretical studies

In order to provide a bench-mark standard for the accuracy of the multipole modelling described above, theoretical studies were performed on all the receptor structures reported in this chapter. The geometry from the multipole refinements of each structure were taken as a starting point for DFT-based computational studies. For **c.s.11** (the fluoride complex of the *para*-substituted receptor) the disorder model used in the experimental electron density distribution modelling was removed to ease computational demands. In the DFT modelling, performed in Gaussian98[184] the B3LYP[29,185]/6-311^{++}G**[30] functional/ basis sets were used. Subsequently, the theoretical electron density distribution was analysed using AIM2000[186]. Highlighted topological details of

the covalent bond BCPs and N—H···anion hydrogen bond BCPs are given in Appendix A.6.

The values of the electron density and Laplacian of the electron density at the BCPs for the covalent bonds in all the crystal structures (**c.s.3**, **c.s.5-6** and **c.s.9-11**) fall into a very small range, with little variation between the crystal structures. This may be due to the calculations being performed on isolated molecules in the gas phase, and as such effects of the crystalline environment and different intermolecular contacts are not taken into account. The values of the electron density and Laplacian of the electron density at the BCPs of the phenyl ring covalent bonds match well those found from the experimental charge density analysis. However, the properties of the nitro group (N—O) bonds and urea carbonyl C=O bonds are very different. For the experimental analysis the average N—O values of the electron density and Laplacian of the electron density at the BCP are 3.3 e Å^{-3} and -7.7 e Å^{-5} respectively while the theoretical values are 3.3 e Å^{-3} and -24.0 e Å^{-5}. For the C=O bonds the average experimental electron density and Laplacian of the electron density values are 3.0 e Å^{-3} and -41.0 e Å^{-5} while the theoretical values are 2.7 e Å^{-3} and -12.0 e Å^{-5}. This discrepancy has been noted previously by Birkedal *et al.*,[163] in the case of urea carbonyl bonds from DFT-calculations. The properties of the nitro group BCPs in experimental charge density investigations has been discussed in Section 7.5.4 and similar behaviour observed by Woźniak[81,169]. Non-ideal behaviour of nitro groups in experimental multipole modelling may be the cause of the lack of correlation between the experimental and theoretical values.

While the values of the electron density and Laplacian of the electron density at the BCPs of the N—H···anion hydrogen bonds do not match directly, they also

follow the trend that the electron density and Laplacian of the electron density at the BCP increase from chloride (**c.s.6**) < acetate (**c.s.9**) < fluoride (**c.s.11**). For each anion comparison set (chloride **c.s.5** and **c.s.6** and acetate **c.s.9** and **c.s.10**) the values of the electron density and Laplacian of the electron density at the BCP fall within a very similar range diagnostic for the N—H···anion hydrogen bond type.

For **c.s.3**, the experimental electron density distribution of which is discussed above in Section 4.4.6, the areas of the structure such as the phenyl ring and urea group (excluding the C=O carbonyl bond) good agreement is again observed between the two theoretically and experimentally derived properties of the electron density at the BCPs. This suggests that it is feasible to draw the limited conclusions made on the electron density distribution in **c.s.3** despite the low quality of the crystal used and less than ideal diffraction data obtained for this structure.

4.5 Conclusions

This chapter moved from an analysis of a series of anion-receptor complexes based on purely geometric arguments to one focusing on the electron density distribution across a family of related anion-receptor complexes. It showed that only high resolution studies allow genuine interactions to be distinguished from those only inferred by geometric arrangements derived from routine resolution studies. Geometric criteria have been shown to be of greater validity in the characterisation of strong interactions than weak interactions.

Hydrogen bonds have been quantified and classified as belonging to two distinct groupings classified as regions of strong and weak bonding

respectively by using charge density analysis instead of inferring strength from geometry.

This information about the strength of interactions in the solid-state is normally only available to supramolecular chemists by titration techniques in solution. This provides a new dimension to single crystal X-ray diffraction studies of particular supramolecular relevance when applied across a series of related complexes. Thus, as in solution, stronger interactions are observed between more anionic guests and receptors than less basic guests in the solid-state, as has been shown by the increased electron density and Laplacian of the electron density values at the BCPs for N—H···fluoride interactions compared to N—H···chloride hydrogen bonds.

It has been shown that the behaviour of an anion-receptor complex can be achieved by tuning its receptor through peripheral modification. This has been shown to change the character of the hydrogen bonding between the receptor and anion, introduce additional weak yet stabilising interactions and alter the charge distribution and electrostatic potential distribution across the anion.

Theoretical studies have shown the relative accuracy of the experimental electron density distribution modelling and has allowed the assessment of the electron density distribution in a less than ideal crystal sample (**c.s.3**). This allowed the comparison of the electron density distribution in a free ligand as opposed to an anion-receptor complex to be undertaken, with a certain level of confidence.

Chapter 5: Thiourea-based anion-receptors compared to analogous ureas

5.1 Extending the family of compounds

The structures discussed in Chapters 3 and 4 offered an opportunity to study the effect of changing the anion across a common receptor. The position of the nitro group on the phenyl ring was also varied between *ortho*, *meta* and *para* to probe the effect of the substituent position and the anion binding properties, crystal structures and electron density distribution in the system. This was expanded by studying the 1,3-bis(3,5-dinitrophenyl)urea receptor, with an increased number of electron-withdrawing substituents added to the receptor scaffold.

Additionally, this family of urea-based structures has the potential to be a subset of a larger group of receptors, where greater variety in the structure of the compounds allows for comparison of the crystal packing, anion binding properties and electronic distribution across a more diverse range. The effect of greater modifications, such as altering the substituent/ electron-withdrawing group on the phenyl ring of the receptor and changing the main anion binding functionality (urea *vs.* thiourea for example) can be determined. Moving from symmetrically substituted systems to unsymmetrical ones means internal comparisons of properties within the structures can be performed and further complexity can be introduced to the family.

5.1.1 Motivation for extending the series

As previously discussed ureas are a key group for anion binding (see Section 3.1). However, the thiourea moiety is often incorporated in place of an urea. This is due to the greater acidity of thiourea over corresponding urea compounds, which means stronger interactions are expected. Thioureas are particularly exploited in anion transporters, where the higher lipophilicity of this group in comparison to ureas, means that transport ability is enhanced.[187,188] With basic anions, the higher acidity of the thiourea group means that deprotonation by the anion is more likely than in urea-based systems.[189] The larger van der Waals radius of sulfur in comparison to oxygen (1.80 Å *vs.* 1.52 Å, respectively[21]) means that the thiourea moiety has a much lower preference for planarity in comparison to urea, due to steric clashes with other atoms present in thiourea compounds. The weaker hydrogen bond acceptor ability of sulfur means that the α-tape motif commonly observed in the crystal structures of urea compounds is not seen in the crystal structures of thioureas and other interactions form the basis for the crystal packing. These factors suggest that there can be large differences between the behaviour and properties of analogous ureas and thioureas and that it is worthwhile to expand the simple family of molecules reported in Chapters 3 and 4 to include thiourea-based receptors. Custelcean[190,191] has described how studies of thiourea co-crystal structures have been far less widely explored in comparison to their analogous ureas and gives further weight to the importance of the study reported in this chapter. Grabowsky *et al.*, have studied the difference in the electron density distribution in three protease inhibitor compounds, where the peripheral units of the structure are maintained but the central reactive region differs from aziridine to oxirane to olefin.[192]

Nitro groups are not the only electron-withdrawing substituent incorporated into anion-receptors. Cyano (-CN), halogen (-F, Cl, Br), and trifluormethyl ($-CF_3$) substituents on a phenyl ring have all been exploited in anion-receptor chemistry. As well as changing the strength of the electron-withdrawing effect, and hence the polarisation of the N—H bonds, different substituents can alter the solubility and the lipophilicity of the anion receptor. The $-CF_3$ substituent is particularly popular in anion transporters due to the combination of enhanced anion binding, due to the electron-withdrawing effect, and improved lipophilicity, which enables the molecules to cross membranes. It is therefore advantageous to look at what effects these changes have on the electron density distribution in the structures.

A final change that can be effected is to move from symmetrical systems to unsymmetrical systems, where the receptor has an asymmetrical substitution pattern. This can aid in the preparation for looking at more complex systems, where multiple anion binding groups and substitution patterns are used and describe and rationalise electron density distributions in these receptors and their complexes. It also allows for the study of the polarisation within a receptor where different substituents are used and could be a measure of the strength and range of their effects on the electron density distribution.

The additional crystal structures included will be discussed further below.

5.1.2 Compounds within the 'new' extended series

Using the rationale outlined above the family of compounds was extended to include *ortho*, *meta* and *para* thioureas (**16**-**18**). As only anion-receptor complexes of the *para* thiourea were obtained, just the synthesis, characterisation, solid-state and solution phase anion binding properties, and

high resolution X-ray diffraction studies on this compound (**18**) will be reported in this thesis.

The original 1,3-bis(4-nitrophenyl)urea **14** was replaced with cyano and trifluoromethyl substituted receptors (**19** and **20**, respectively) and their analogous thioureas also included (**21** and **22**). For a number of reasons (positional disorder, too complex an asymmetric unit, not strong or clean enough diffraction etc.) none of the crystal structures of the anion complexes of these receptors were suitable for high resolution charge density analysis, and hence they will not be further discussed in this thesis. (CIFs are found in the electronic Appendix that accompanies this thesis).

Finally, two unsymmetrical nitro substituted receptors (urea and thiourea respectively) were added to our structural family (**23** and **24**). These were successfully crystallised with chloride and allowed for a comparison with the chloride structure (**c.s.6**) of receptor **14** fully characterised in Chapters 3 and 4 and with the chloride structure of symmetrically *para* substituted thiourea **18**.

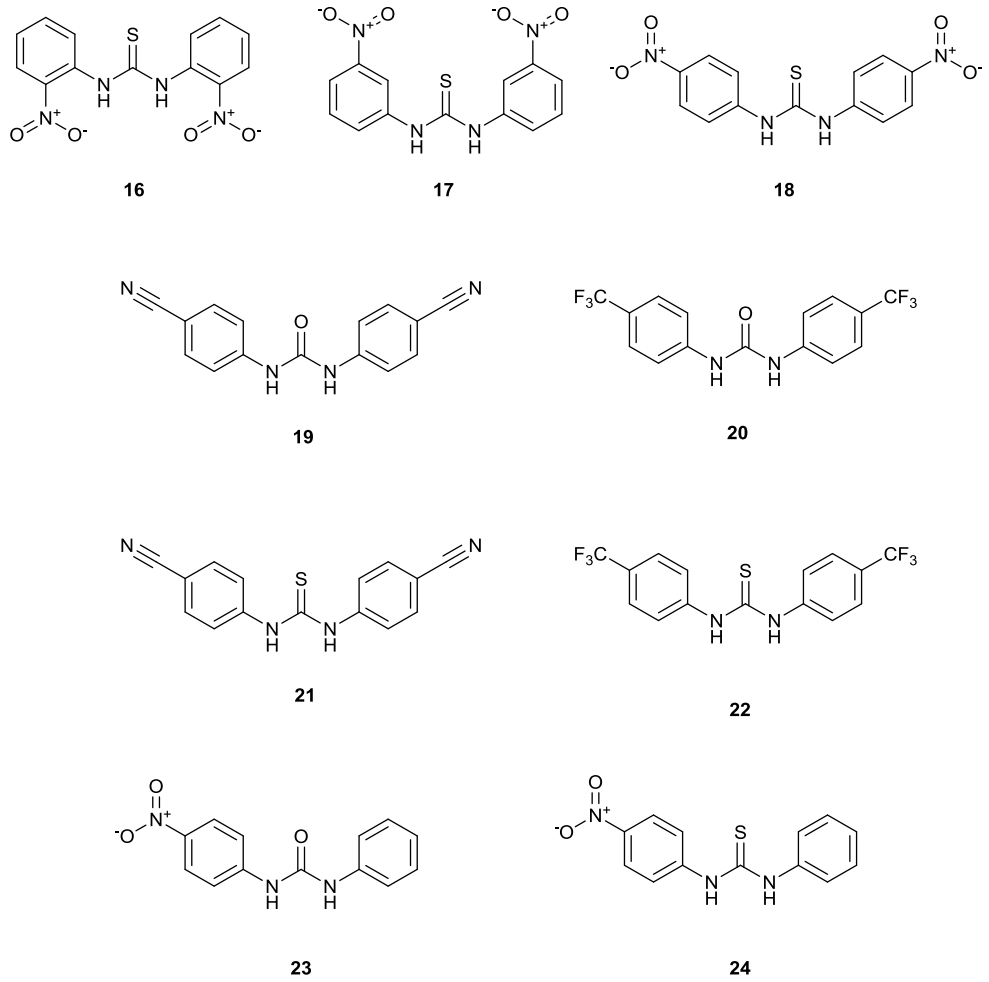

Figure 5.1: Subsets for extension of the original anion-receptor family.

It can be seen how ideally the family would be completed but crystallisation considerations prevented all the compounds shown in Figure 5.1 from being included in the following discussion. The series of compounds **18**, **23**, and **24** represents a compact, complete and suitable subset for further analysis, discussion and comparison to **14**, given below.

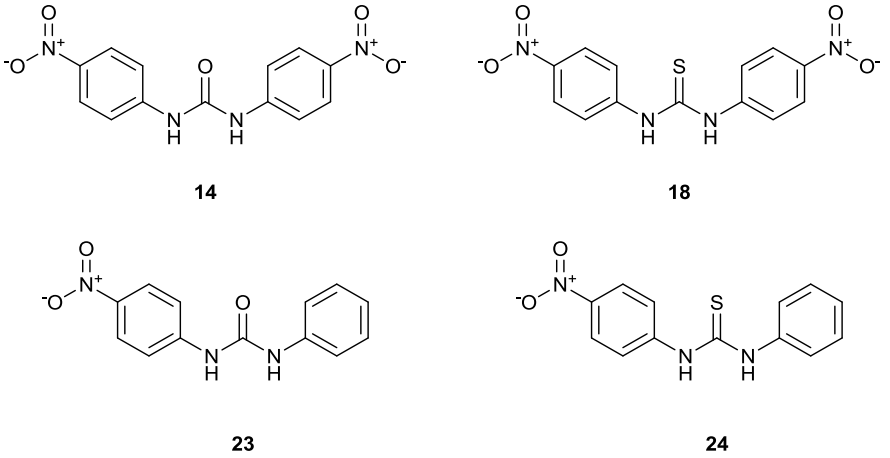

14 18 23 24

Figure 5.2: Receptors **18**, **23** and **24** for which chloride complexes were obtained and comparison was made with receptor **14** from Chapters 3 and 4 which has a comparable chloride complex crystal structure.

5.2 Structural analysis at standard resolution

5.2.1 Solution state studies

To assess the ability of the receptors to bind chloride (the anion with which crystal structures were obtained) in solution, ^{1}H NMR titrations were conducted in a 0.5% H_2O–d_6–DMSO solvent mix (see Section 7.3 for methodology). The results are shown in Table 5.1. The chloride was added as the TBA salt for consistency with the titrations performed in Chapter 3.

Table 5.1: Affinity constants K_{ass} (M^{-1}) from ^{1}H NMR titration studies.

Receptor	**18**	**23**	**24**
K_{ass} (M^{-1})	49.7 (1%)	57.5 (8%)	31.9 (3%)

The titrations could be fitted to a 1:1 binding model, however it was shown in the solid-state that the thiourea receptors form 2:1 receptor: anion complexes and no 1:1 crystal structures were obtained. It may be an effect of the loss of solvent and a solid-state consequence, however the Job plots conducted on these compounds (see Appendix A.1) suggest there is not necessarily a purely 1:1 interaction occurring for all these receptors (see Job plots for receptors **23** and **24**), despite the fact that the titration data can be modelled as such. The interpretation of these Job plots was made additionally difficult due to the severe peak broadening of the proton resonance of the N—H urea bond whose changing chemical shift was being followed during the Job plot. Modelling of these receptors with a 2:1 binding model in WINEQNMR was not successful.

Table 5.1 shows that all the affinity constants are relatively low, probably due to the low basicity of chloride. The urea has the strongest affinity of the receptors in this subset, when taking the error in the affinity constant into account, it has marginally better affinity than the symmetrically substituted thiourea, and has higher affinity than its analogous thiourea. The effect of the loss of an electron-withdrawing substituent on the receptor can be observed with the lowered affinity for chloride of **24** in comparison to **18** (unsymmetrical substitution *vs.* symmetrical nitro substitution).

5.2.2 Solid-state analysis

A series of crystallisations were undertaken for the three receptors, in a variety of solvents, both as single and mixed solvent systems. The aim was to crystallise both the free ligands and the anion-receptor complexes. Using TMA Cl resulted in a crystal structure of a chloride complex of **24** (unsymmetrical thiourea) but in the case of **23** and **18** (unsymmetrical urea and symmetrical thiourea) no crystals of complexes were obtained. This led to the use of TEA

Cl, which allowed the series of chloride complexes to be completed. Although crystallisations with the salts of fluoride and acetate were attempted these did not yield any suitable crystals. The full details of the crystallisation procedures can be found in the Experimental section of this thesis.

Table 5.2 details the crystal structures that were obtained across this series of receptors and the numbering of these crystal structures in this thesis.

Table 5.2: Crystal structures of the free ligands and complexes of receptors **14**, **18**, **23**-**24**.

Receptor	Free receptor	Chloride complex
14	✓**c.s.3**	✓ **c.s.6**
18	✓**c.s.13**	✓**c.s.16**
23	✓**c.s.14**	✓**c.s.17**
24	✓**c.s.15**	✓**c.s.18**

5.2.2.1 Single crystal X-ray diffraction

The crystal structures of the chloride complexes and free ligands are now discussed (excluding **c.s.3** and **c.s.6**, which have been discussed in Section 3.3.2.) The crystallographic data for the free ligands are tabulated below in Table 5.3, while those for the chloride complexes can be found in Section 5.3.2 in Table 5.5 (as they contain the details of the fitting statistics for the multipole refinements of these crystal structures).

Table 5.3: Crystallographic information for the free ligand crystal structures **13**, **14** and **15**.

Structure	**c.s.13**	**c.s.14**	**c.s.15**
Formula	$C_{13}H_{10}N_4O_4S$	$C_{13}H_{11}N_3O_3$	$C_{13}H_{11}N_3O_2S$
Crystal system	Monoclinic	Monoclinic	Monoclinic
Space group	$P2_1/c$	$P2_1$	$P2_1/n$
a (Å)	8.2109(5)	4.590(4)	5.6328(7)
b (Å)	25.4709(18)	8.336(7)	7.7579(9)
c (Å)	12.5244(9)	15.282(13)	28.178(4)
α (°)	90.00	90.00	90.00
β (°)	96.054(2)	96.929(17)	92.324(7)
γ (°)	90.00	90.00	90.00
V (Å^3)	2604.7(3)	580.5(9)	1230.3(3)
Final R indexes	R_1 = 0.0502	R_1 = 0.0448	R_1 = 0.0428
[I>=2σ (I)]	wR_2 = 0.1416	wR_2 = 0.1159	wR_2 = 0.1002
Final R indexes	R_1 = 0.0569	R_1 = 0.0492	R_1 = 0.0562
[all data]	wR_2 = 0.1463	wR_2 = 0.1185	wR_2 = 0.1066
GoF on F^2	1.059	1.071	1.024
$\Delta\rho$(r) (*e* Å^{-3})	0.77/-0.74	0.16/-0.29	0.26/-0.24

In **c.s.13** (the free ligand of receptor **18**, 1,3-bis(4-nitrophenyl)thiourea) there are two independent molecules in the asymmetric unit, with eight molecules making up the unit cell. The packing in the structure builds up through S···S contacts (interaction distance of 3.271 Å) and hydrogen bonding (D···A distances from 2.978 – 3.011 Å) between the nitro groups and the thiourea N—H hydrogen bond donor groups. The unit cell in **c.s.14** contains two molecules, with urea α-tape hydrogen bonding (N—H···O) replacing the nitro···H—N contacts observed in the symmetrical free ligands (**c.s.3** and **c.s.13**). The packing in **c.s.14** leads to columns of urea molecules with the nitro group of each urea molecule on the same side of the column linked by C—H···O contacts of nitro groups and unsubstituted phenyl rings extending the structure. In **c.s.15** the substitution of the urea in **c.s.14** for a thiourea molecule leads to the alteration of the hydrogen bonding from a linear tape to

a zig-zag non-planar (N—H···S) tape. Here the zig-zag layers are linked as in **c.s.14** through C—H···O short contacts, however the nitro group alternates position in the zig-zag layer. The receptors have varied geometries, with the two receptor **18** molecules in **c.s.13** relatively flat (the angles between the phenyl ring planes are 20° and 6.6° and the torsion angles between the thiourea and phenyl ring 12.4°, -2.2°, 5.1° and 15.9°). However, in the asymmetric structures, the urea (**c.s.14**) and thiourea (**c.s.15**) molecules are twisted significantly out of the plane of the phenyl rings (the angle between the phenyl rings is 27.6° in **c.s.14** and 42.39° in **c.s.15** and the torsion angles are -45.8° and 42.8° in **c.s.14** and -107.4° and 103.1° in **c.s.15**).

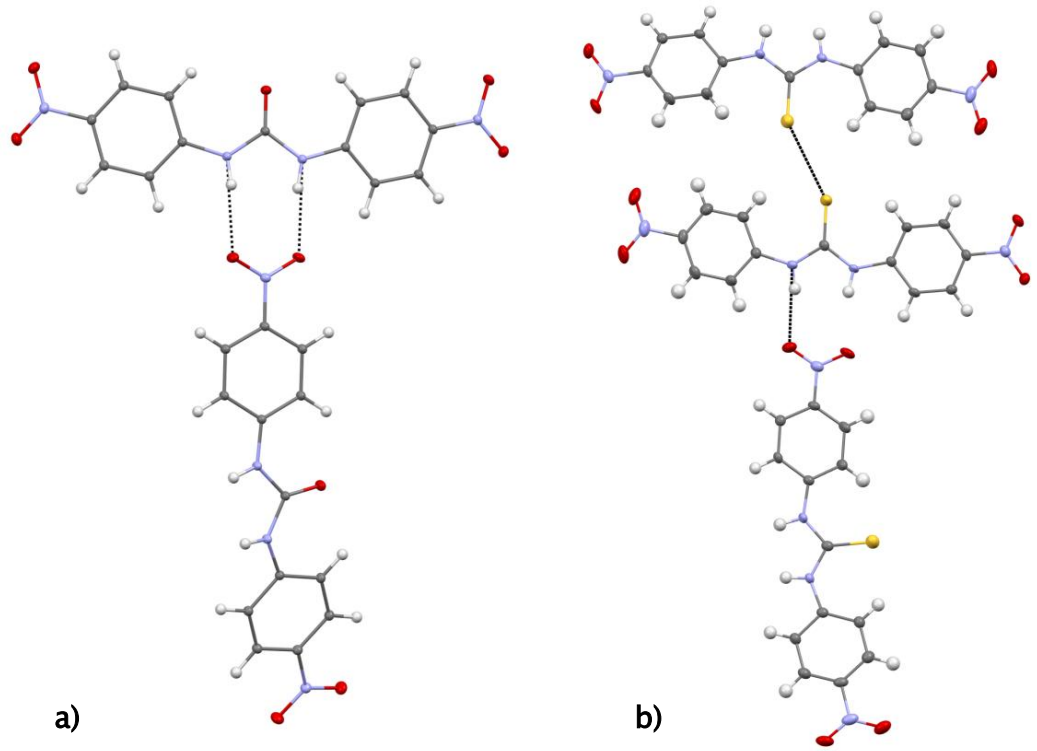

Figure 5.3: Hydrogen bonding interactions in **a) c.s.3** (receptor **14**) and **b) c.s.13** (receptor **18**). The S···S short contacts the thiourea sulfur atoms in **c.s.13** participate in are also displayed in **b)**.

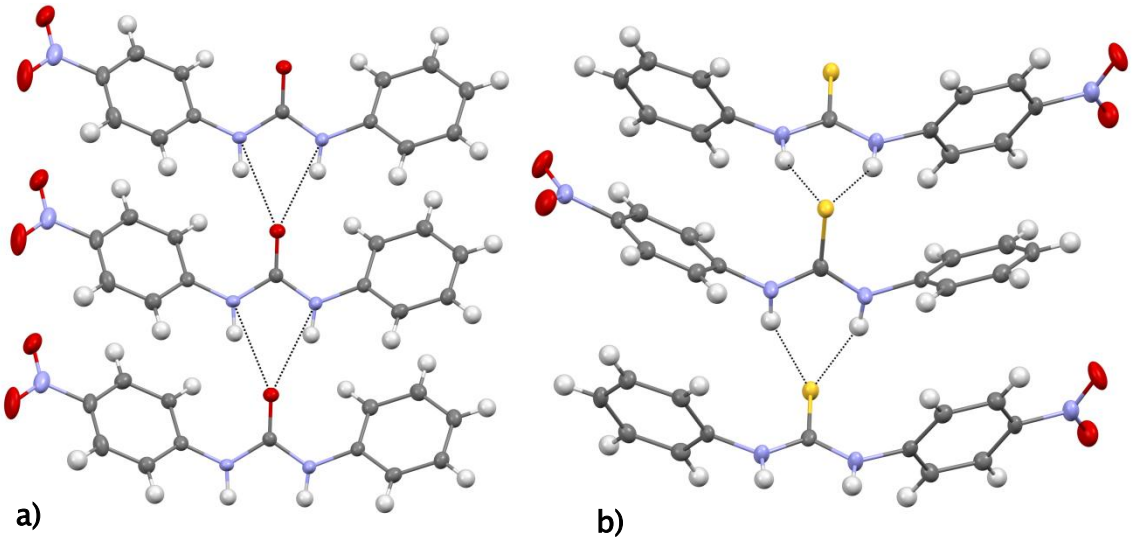

Figure 5.4: Hydrogen bonding in **a) c.s.14** (receptor **23**) and **b) c.s.15** (receptor **24**).

Upon anion binding the coplanarity of receptor **18** decreases (the angle between the phenyl ring planes are 10.2° and 10.0° and the torsion angles between the thiourea and the phenyl ring are -26.6°, -23.5°, -32.7° and 31.4° in **c.s.16**– the chloride complex), while in the unsymmetrically substituted structures the coplanarity increases, but the urea/thiourea receptors are still twisted (the angles between phenyl rings are 21.1° in **c.s.17**, 63.2° and 47.3° in **c.s.18** and the torsion angles are -24.8° and -4.8° in **c.s.17** and -23.9°, 14.3°, 40.3° and 23.4° in **c.s.18**).

The chloride complex of urea receptor **23** (**c.s.17**) is a 1:1 anion: receptor complex and crystallises in the monoclinic space group $P2_1/n$, with the unit cell comprised of four receptor molecules, four cations and four chloride anions. In contrast, both the thiourea chloride complexes crystallise in the triclinic space group $P\bar{1}$ with a 2:1 ratio of receptor to anion, with the unit cell in both cases (**c.s.16** and **c.s.18**) consisting of four receptor molecules, two anions and two counter-cations for charge balance. In **c.s.17** the packing appears to build up due to NO_2···TEA, TEA···C=O, Cl···TEA and NO_2···H—C(phenyl)

contacts. In the analogous thiourea **c.s.18** the packing is slightly different, with the chloride anion complexed by two ligands and therefore not involved in any other interactions. There are S···NO_2, S···TMA, TMA···NO_2 contacts and T-shaped π···π type interactions of the phenyl rings. In the symmetrical thiourea chloride complex (**c.s.16**) the situation is very similar, however the chloride appears to be interacting with TEA as well as the two receptor molecules. In this crystal structure however, the main contacts seem to be S···TEA, NO_2···H—C(phenyl) and TEA···NO_2 interactions. In both thiourea structures, the sulfur atoms of each receptor molecule are in a unique crystalline environment. As such, the electron density distribution in the two receptors in this region would be expected to be significantly different. As observed in Chapter 3 in each crystal structure of the three anion-receptor complexes, the counter-cation (whether TMA or TEA) is located in a different part of the unit cell, with its own unique set of interactions.

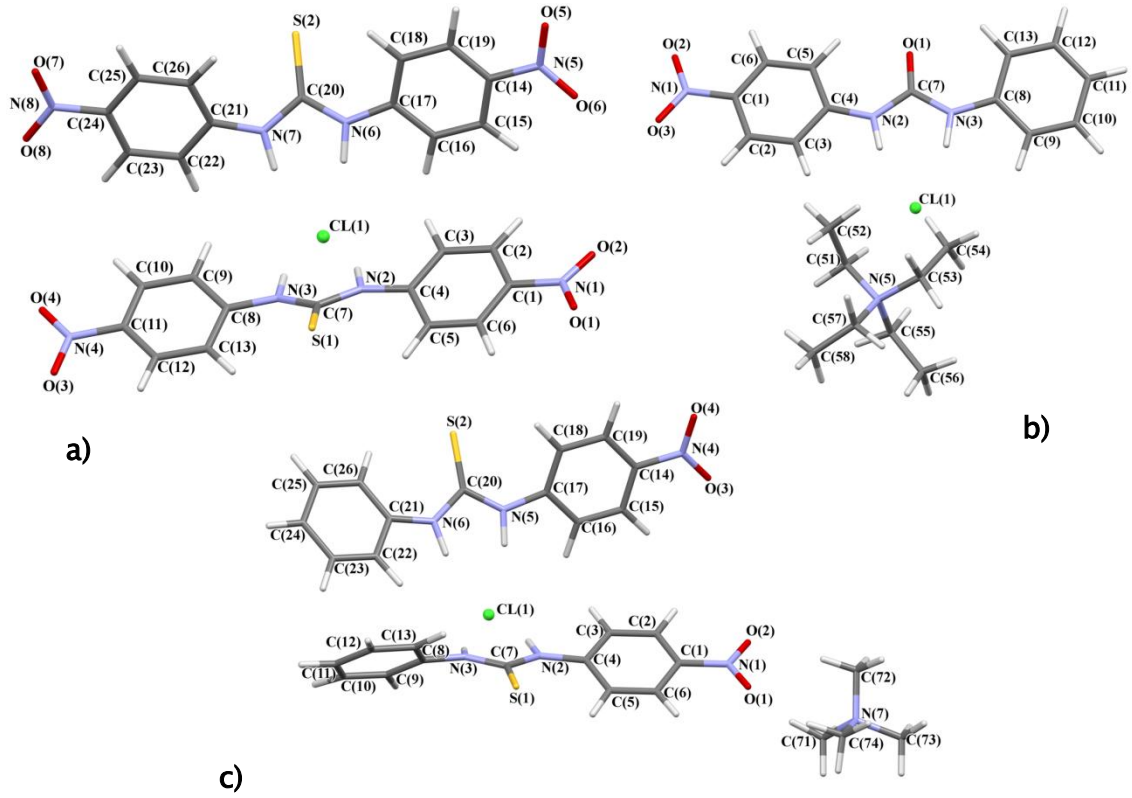

Figure 5.5: Figures of complexes discussed in this chapter displaying the atom labelling scheme: **a) c.s.16**, **b) c.s.17**, **c) c.s.18**. Atoms drawn as capped sticks, with the chloride anions drawn in ball and stick for clarity. Red = oxygen, blue = nitrogen, green = chloride and gold = sulfur.

5.2.2.1.1 Hydrogen bonding

The types of hydrogen bonding observed in each of the crystal structures has been touched upon briefly above. Table 5.4 gives a detailed geometric description of these hydrogen bonds. It can be seen from the table that the NO_2···H—N(urea) hydrogen bonds in the free ligand structure of the symmetrical thiourea (**c.s.13**) tend to be the most linear (DHA angle >160°). The least linear are the hydrogen bonds of the linear and zig-zag α-tape type found in **c.s.14** and **c.s.15**. The shortest distances, suggesting that these are the strongest hydrogen bonds are those of the N—H···O hydrogen bonds of the urea α-tape (**c.s.14**) with the distances of the N—H···S interactions in **c.s.15**

longer. In **c.s.14** the hydrogen bonds D···A distances are shorter than the combined van der Waals radii of the donor and acceptor atoms, however, in **c.s.15** the D···A distances are longer than the combined van der Waals radii, which may account for the zig-zag conformation observed in this structure.

The range of the D···A distances of the urea N—H···Cl hydrogen bonds in the chloride complex of **c.s.17** fall within the range of the thiourea N—H···Cl hydrogen bonds D···A distances (**c.s.16** and **c.s.18**). This means it is difficult to draw conclusions as to the relative strength of these hydrogen bonds based on geometric analysis. In both thiourea complexes (**c.s.16** and **c.s.18**) there is a greater range of variation in the hydrogen bond D···A distances than in the urea complex (**c.s.17**), this effect could be due to the 2:1 receptor: anion ratio in the thiourea complexes compared to the 1:1 ratio of the anion to the receptor in the urea chloride complex. In **c.s.18** the D···A distances are shorter for the urea N—H hydrogen bond donor attached to the phenyl ring, which is substituted with a nitro group in comparison to the hydrogen bond donor attached to an unsubstituted phenyl ring.

Table 5.4: Hydrogen bonding distances and angles for **c.s.13**-**c.s.18**.

Crystal structure	D—H (Å)	H···A (Å)	D···A (Å)	∠ DHA (°)
		Free ligand crystal structures		
c.s.13	0.88[$]	2.12	2.981 (3)	167.3
	0.88[$]	2.11	2.978 (3)	166.9
	0.88[†]	2.25	3.093 (3)	161.3
	0.88[†]	2.15	3.011 (3)	166.8
c.s.14	0.88	2.03	2.847 (4)	154.2
	0.88	2.10	2.883 (3)	148.1
c.s.15	0.88	2.70	3.514 (2)	154.1
	0.88	2.63	3.461 (2)	157.0
		Chloride complexes crystal structures		
c.s.16	0.88	2.28	3.145 (2)	167.8
	0.88	2.39	3.225 (2)	159.2
	0.88	2.50	3.349 (2)	162.3[δ]
	0.88	2.42	3.276 (2)	165.7[δ]
c.s.17	0.88	2.37	3.220 (2)	161.9
	0.88	2.41	3.240 (2)	158.2
c.s.18	0.88	2.31	3.178 (1)	169.6
	0.88	2.43	3.273 (1)	160.7
	0.88	2.33	3.168 (1)	158.9
	0.88	2.39	3.246 (1)	165.1

[$]Symmetry to generate equivalent atoms: x, -y+3/2, z-1/2. [†]Symmetry to generate equivalent atoms: x+1/2, -y+3/2, z-1/2. [δ]Symmetry to generate equivalent atoms: x+1, y, z

5.2.2.1.2 Hirshfeld surface Analysis

The nature of the packing and intermolecular interactions in each crystal structure were further analysed using Hirshfeld surface analysis.[109-112] The Hirshfeld surfaces and fingerprint plots of the free ligand crystal structures are shown in Figure 5.6. In each case, upon anion binding the packing efficiency in the crystal structure decreases, as the fingerprint plots of the chloride complexes (see Figure 5.7) are more diffuse at higher distances. The shape of the fingerprint plots for each set of thiourea free ligands and chloride complexes are relatively similar, while for the urea receptor the change in the fingerprint plot upon anion binding is fairly dramatic with the loss of the O···H tips, which correspond to the nitro···H—N(urea) contacts. From the plots of the relative contributions of each interaction that build up the Hirshfeld surface, it is also observed that the O···H interactions' contribution markedly decreases upon anion binding by all three receptors, in the urea (29.5% in **c.s.14** decreases to 15.8% in **c.s.17**) and both sets of thiourea receptor structures (18.8% in **c.s.15** in comparison to 11.8% in **c.s.18** and 41.1% in **c.s.13** in comparison to the 25.9% in **c.s.16**). This is accompanied by an increase in the contribution of the H···H contacts (19.8% in **c.s.13** increases to 25.2% in **c.s.16**, 28.8% in **c.s.14** increases to 51.9% in **c.s.17** and 30% in **c.s.15** to 36.9% in **c.s.18**). In the complexes the Hirshfeld surfaces are mainly comprised of H···H and C···H interactions, with smaller but valuable contributions from H···Cl and O···H contacts.

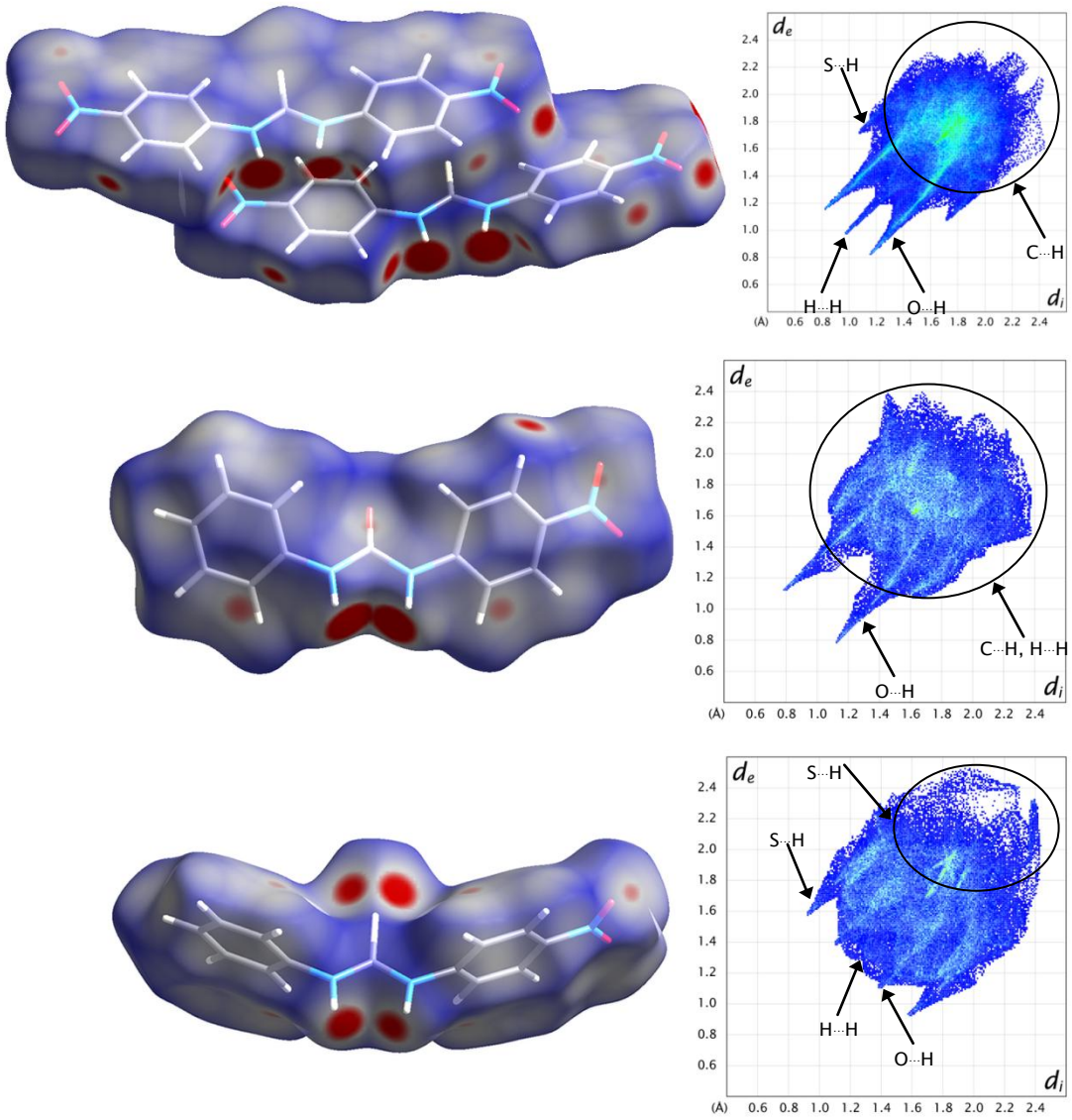

Figure 5.6: Hirshfeld surfaces *(left)* and fingerprint plots *(right)* of the free ligand structures: top **c.s.13**, middle **c.s.14** and bottom **c.s.15**. Relevant intermolecular interactions e.g. S···H, O···H, C···H and H···H short contacts are highlighted, as appropriate, on the fingerprint plots.

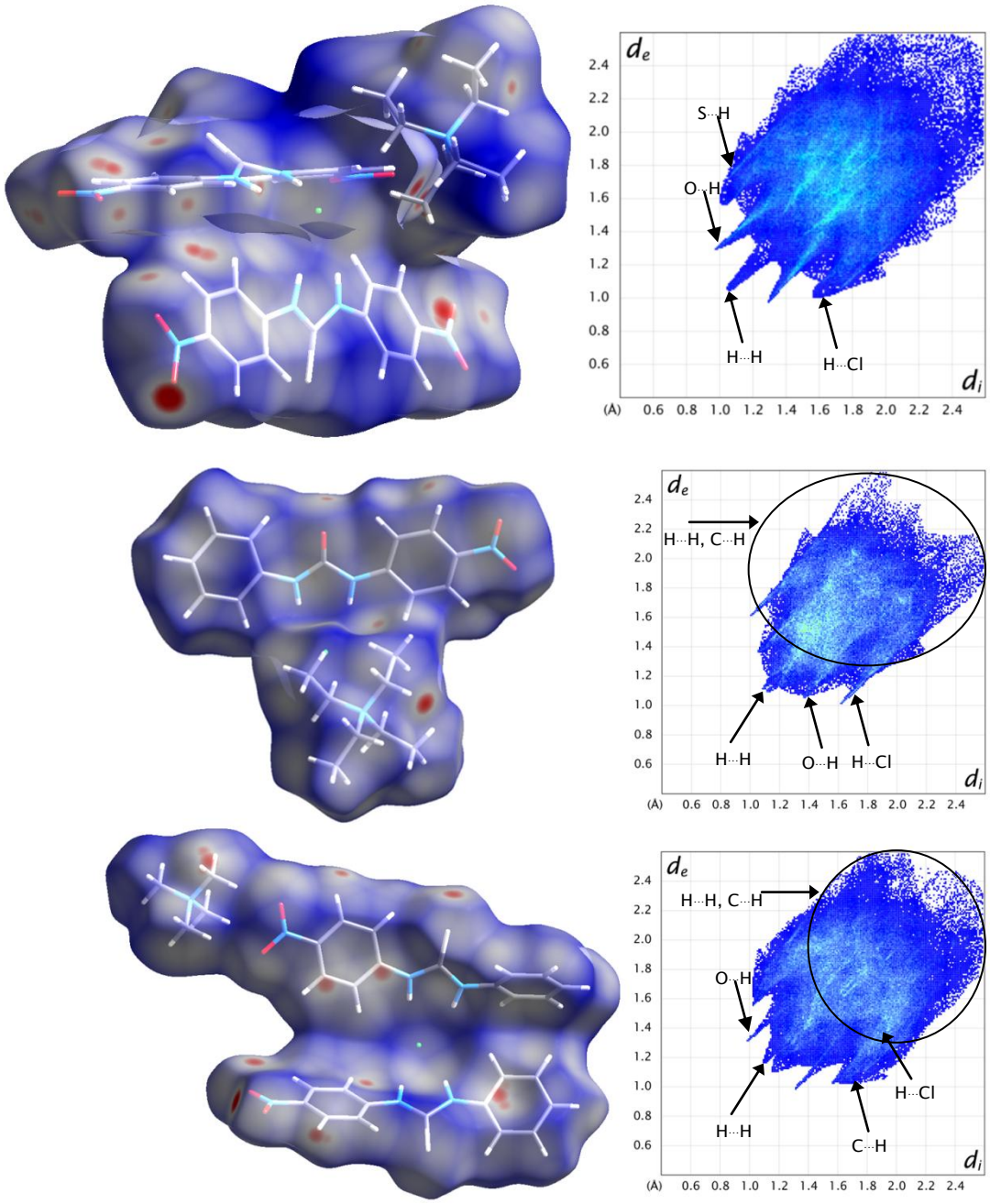

Figure 5.7: Hirshfeld surfaces (*left*) and fingerprint plots (*right*) of the anion-receptor complexes: top **c.s.16**, middle **c.s.17** and bottom **c.s.18**. The main intermolecular interactions that contribute to the Hirshfeld surfaces are indicated on the fingerprint plots.

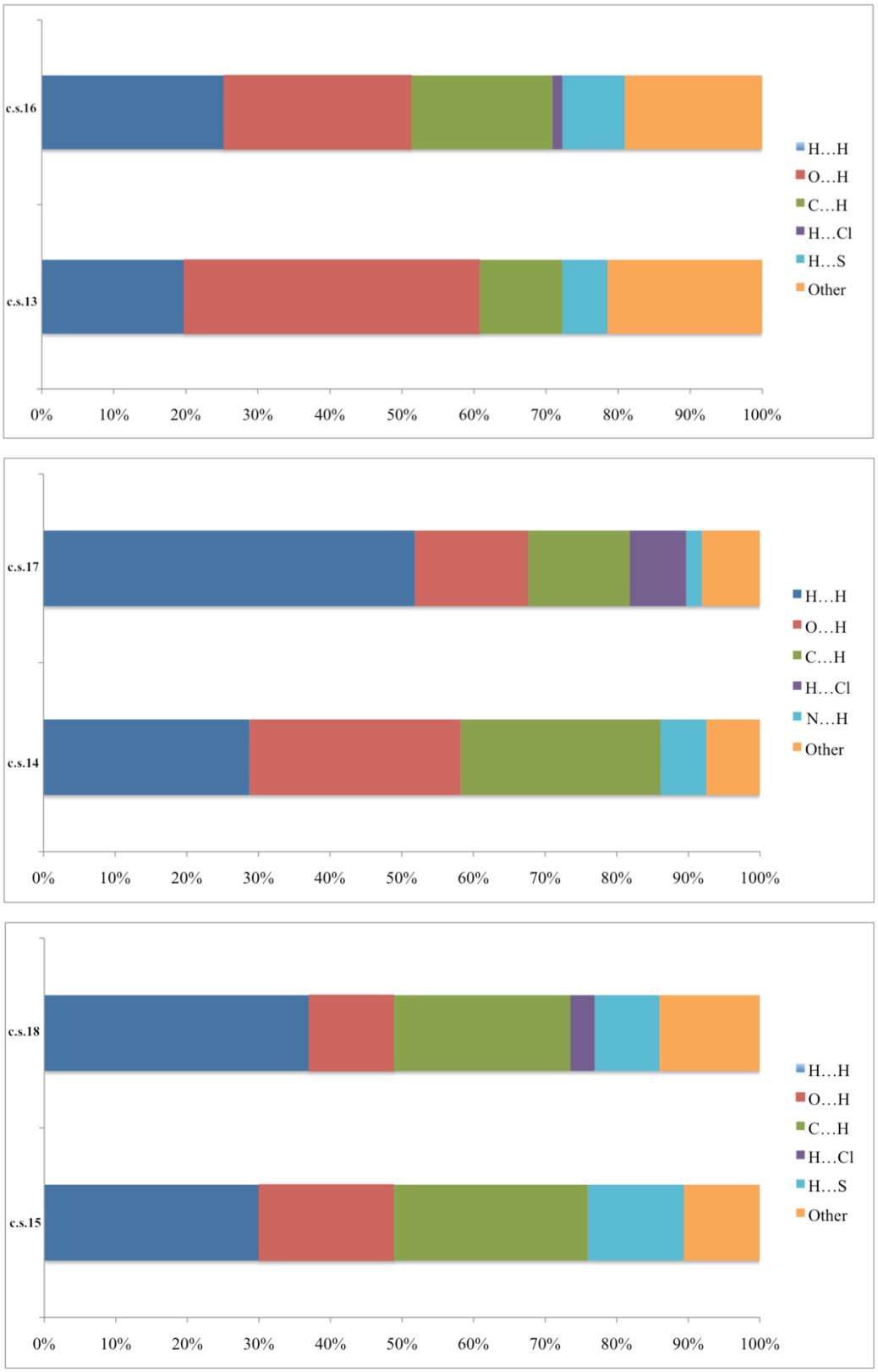

Figure 5.8: Contribution of non-covalent interactions to the Hirshfeld surface in the free ligand structures and the anion-receptor complexes. Top comparison set: **c.s.13** *vs.* **c.s.16**, middle: **c.s.14** *vs.* **c.s.17** and bottom: **c.s.15** *vs.* **c.s.18**.

5.3 High resolution studies

After the standard resolution crystallographic studies of the anion-receptor complexes discussed above, the electron density distribution was modelled in the structures (**c.s.16**, **c.s.17** and **c.s.18**).

5.3.1 Technical aspects of the charge density modelling

An aspherical refinement of the electron density distribution in **c.s.16** and **c.s.18** (the thiourea crystal structures) was performed in the same manner as those described in Chapter 4. Sulfur modelling can be non-trivial in charge density studies as the default radial function parameters implemented in XD2006[193] are generally inappropriate. It is often necessary to test a series of n(*l*) values for sulfur and see which set best fits the electron density at and around the sulfur atom. Others have advocated using a κ'-restricted multipole model (KRMM), with fixed κ and κ' values taken from theoretical multipole parameter databases.[194] Here, the approach of Espinosa[195] and Dominiak and Coppens[196] was followed, with several radial function parameters tested. However, in this case it was found that the default values of n(1,2,3,4) = 4 4 4 4, gave the best model for the electron density distribution at the sulfur atom. At the end of the refinements the residual density around the sulfur atom was fairly high (see Table 5.5) and distributed in a shashlik-like[197] pattern. For this reason, it was assumed that some anharmonic motion may be present and the introduction of Gram Charlier coefficients[198] to model this was attempted. However, this did not improve and in some cases worsened the residual density. Therefore, a κ' parameter for sulfur was introduced and significantly lessened the residual density and was therefore incorporated into the final model. The residual density was shown to be a feature of the resolution of the data, as revealed by truncation at different levels of $\sin\theta/\lambda$ (for example in

c.s.18 at 0.8 Å^{-1} the residual density is ~-0.3/0.3 *e* Å^{-3} and at 1.1 Å^{-1} is ~-0.6/0.6 *e* Å^{-3}). When refined freely, the κ' value was physically unreasonable, and was therefore constrained by linking to the κ value. In the final stage of the refinement of each crystal structure all variables were refined together, with the exception of κ and κ' values, to allow for convergence. The quality of the crystals used to collect data for **c.s.16** were slightly suspect, with the possibility of the crystal being twinned and a minor disorder component present at high resolution around the sulfur atom. It was not possible to collect a lower (< 100K) temperature dataset to lessen the likelihood of disorder. The disorder was not included in the final multipole model, as the final refinement was similar to the much higher quality **c.s.18**, and so analysis of **c.s.16** and its comparison to the other structures is made with caution.

The data for **c.s.17** was modelled using InvariomTool[117], as multiple attempts at data collection were unsuccessful at collecting a dataset of significant quality for a standard aspherical atom refinement. This was because of rapid decay of the diffraction intensity at high resolution. Crystal growth screening and optimisation could not improve this. Therefore, the approach of Dittrich and co-workers[120] was used and the initial multipole parameters were transferred from the invariom database. A block refinement was then conducted. The positional and anisotropic thermal displacements parameters of the non-hydrogen atoms were refined against all the reflections and then the position and ADPs of the hydrogen atoms were refined against the low angle data. Subsequently the scale factor was refined, followed by refinement of the previously transferred multipole parameters, while the κ and κ' values were kept fixed to those obtained from the invariom database. The results of the multipole refinement are given in Table 5.5. Due to the inability to separate the thermal vibrations and nuclear positions at this lower resolution the

hydrogen atoms in **c.s.17** were not modelled as anisotropic by use of the SHADE server (as is the case in both **c.s.16** and **c.s.18**) and so the hydrogen atoms remain isotropic in **c.s.17**.

5.3.2 Results and discussion

The resulting charge density model for each crystal structure was deemed to be of significant quality to allow for comparison of the electron density distribution across the three crystal structures. The results of the refinements can be seen in Table 5.5, which details the quality of the refinement, and in Appendix A.3, where the residual density in the (thio)urea plane of each structure is graphically displayed and the RDA[62] shows that the residual density is distributed in a Gaussian manner across the unit cell. The high data: parameter ratio indicates that overfitting of the model has been avoided. The electron density distribution in each of the three crystal structures is also displayed through static deformation density and negative Laplacian maps (see Appendix A.4), which show the electron density distribution is as would be expected in the (thio)urea and phenyl ring groups of the receptor molecules in each crystal structure.

Table 5.5: Multipole and invariom refinement of **c.s.16**, **c.s.17** and **c.s.18**.

Structure	**c.s.16**	**c.s.17**	**c.s.18**
Formula	$C_{34}H_{40}ClN_9O_8S_2$	$C_{21}H_{31}ClN_4O_3$	$C_{30}H_{34}ClN_7O_4S_2$
Crystal system	Triclinic	Monoclinic	Triclinic
Space group	$P\bar{1}$	$P2_1/n$	$P\bar{1}$
a (Å)	8.968 (2)	8.410 (6)	9.1587 (14)
b (Å)	15.649 (4)	24.362 (18)	10.2436 (16)
c (Å)	15.899 (4)	11.143 (8)	17.871 (3)
α (°)	113.0610 (10)	90	87.983 (6)
β (°)	103.685 (3)	106.286 (7)	79.043 (5)
γ (°)	101.701 (2)	90	72.220 (6)
V (Å^3)	1882.6 (8)	2191 (3)	15669 (4)
	Multipole Refinement		
R(F)	0.0396	0.0450	0.0348
R(F^2)	0.0544	0.0927	0.0378
GoF	2.5564	1.8307	1.7461
Nref/Nvar	24.43	46.22	27.8886
$\Delta\rho$(**r**) (*e* Å^{-3})	-0.729/ 0.674	-0.300/ 0.435	-0.557/ 0.650

5.3.3 Theoretical studies

As with the symmetrical urea anion-receptor complexes (reported in Chapter 4), theoretical studies using Gaussian98[184] and AIM2000[186] were conducted on **c.s.16**, **c.s.17** and **c.s.18**. In these theoretical studies the B3LYP functional[29,185] with the 6-311++G**[30] basis sets and diffuse functions were used to correctly model the hydrogen atoms and hydrogen bonding interactions in each structure. Again, this was necessary to evaluate the experimentally modelled electron density distribution in the three structures, particularly that in **c.s.17**, which was modelled using the non-standard invariom refinement.

The electron density distribution as modelled by theory, was studied primarily by looking at the properties of the electron density at the bond critical points (see Appendix A.6 for tables of the properties of the covalent bonds in each

structure). These were in good agreement with the theoretical studies on **c.s.5**, **c.s.6** and **c.s.9-11** reported in Section 4.4.7. The properties of similar bonds in each structure show little variation across the three structures (except the C=S and C=O bonds) and are tabulated below in Table 5.6.

Table 5.6:Theoretical properties of the electron density at the BCPs of the covalent bonds in **c.s.16-18**.

Bond	$\rho(\mathbf{r}_{BCP})$ (e Å^{-3})	$\nabla^2\rho(\mathbf{r}_{BCP})$ (e Å^{-5})
C=S	1.445	-1.542
C=O	2.749	-9.533
C=S	1.434	-2.498
N—O	3.338	-24.665
	3.345	-25.143
	3.310	-24.490
C—N nitro	1.782	-16.507
	1.780	-16.068
	1.755	-15.133
C—N phenyl urea	1.970	-19.365
	1.973	-19.483
	1.948	-19.053
C—N urea	2.216	-22.060
	2.097	-22.372
	2.133	-22.029
C—C phenyl	2.087	-20.833
	2.073	-20.532
	2.080	-20.695

C—H phenyl	1.918	-23.806
	1.913	-23.605
	1.913	-23.649
N—H	2.304	-42.785
	2.295	-43.566
	2.305	-43.562
C—N TMA/TEA	1.580	-12.658
	1.557	-12.402
	1.634	-13.459
C—C TEA$^{\delta}$	1.665	-13.819
	1.664	-13.817
	-	-
C—H TMA/TEA	1.957	-24.418
	1.958	-24.476
	2.034	-26.584

Top value in each bond is **c.s.16**, middle **c.s.17** and bottom **c.s.18** . $^{\delta}$In **c.s.18** the cation is TMA.

As will be shown below, these values match fairly well with those of the experimental electron density distribution, except for the C=S/ C=O bonds (see Birkedal *et al.*[163] for explanation) and the N—O bonds of the nitro groups. This suggests that the experimental modelling is of a suitable quality.

5.3.3.1 Common structural features

Common features of each anion-receptor complex were expected to be similar between **c.s.16**, **c.s.17** and **c.s.18**, and fit with the values described in the series of bis-substituted receptors (see Chapter 4). Full topological analysis of the electron density distribution determined the presence of all the expected

covalent BCPs, and Appendix A.6 includes tables of the properties of the electron density at the BCPs for all covalent bonds in the three crystal structures. The electronic properties of the bonds in key structural areas of the anion-receptor complexes, the phenyl rings and (thio)urea moieties were assessed. The average values of the electron density ($\rho(\mathbf{r}_{BCP})$) and the Laplacian of the electron density ($\nabla^2\rho(\mathbf{r}_{BCP})$) at the BCPs (bond critical points) of the bond paths for these covalent bonds are shown in Table 5.7 below. It can be seen from the values of the electron density and the Laplacian of the electron density at the BCPs that there is limited variation between the values in the non-substituted and nitro-substituted phenyl ring bonds, and between the urea and thiourea, and the symmetrical and non-symmetrical thiourea (as was seen in the theoretical studies). Also, when compared to the chloride complex of the symmetrical urea receptor (**c.s.6** reported in Chapter 4) **c.s.16** (the symmetrical thiourea chloride complex) had covalent bonds in the phenyl ring and (thio)urea group with remarkably similar properties in terms of electron density (with the exception of the C=S and C=O bonds, as would be predicted). This is illustrated through the bond ellipticity profile plots of the phenyl ring groups along the bond path for **c.s.16**, **c.s.17** and **c.s.18** (see Appendix A.5). Differences in the C=S and C=O bond ellipticity profiles and the Laplacian of the electron density along these bond paths for the thiourea (**c.s.16** and **c.s.18**) *vs.* the urea-based structure (**c.s.17**) are also observed (see Appendix A.5.13).

Table 5.7: Average properties at the BCPs for covalent bonds in **c.s.16**, **c.s.17** and **c.s.18**.

Bond	$\rho(\mathbf{r}_{BCP})$ (e Å^{-3})	$\nabla^2\rho(\mathbf{r}_{BCP})$ (e Å^{-5})	R_{ij} (Å)
C=S/ C=O	1.5	-3.2	1.6776
	3.0	-32.6	1.2216
	1.4	-3.4	1.6797
C—C nitro substituted phenyl ring	2.1	-16.8	1.3943
	2.2	-18.4	1.3957
	2.1	-16.1	1.3952
C—H nitro substituted phenyl ring	1.9	-17.9	1.0835
	1.8	-17.6	1.0831
	1.8	-16.4	1.0834
C—C non nitro substituted phenyl ring$^{\delta}$	-	-	-
	2.1	-16.9	1.3985
	2.2	-17.0	1.3963
C—H non nitro substituted phenyl ring$^{\delta}$	-	-	-
	1.8	-16.4	1.0830
	1.8	-15.1	1.0835
N—H	2.3	-33.1	1.0095
	2.2	-31.8	1.0092
	2.2	-28.8	1.0092

Top line in each row is **c.s.16**, middle **c.s.17** and bottom **c.s.18**. $^{\delta}$ In **c.s.16** there are no non-nitro substituted phenyl rings and so this entry is empty.

The QTAIM atomic charges for every atom in all three structures have been tabulated in Appendix A.7. As would be predicted by the chemistry in these systems the tetraalkylammonium cation in both **c.s.17** and **c.s.18** was positively charged (in **c.s.17** TEA has 0.268 e charge and in **c.s.18** TMA is

0.376 *e*), however in **c.s.16** the TEA cation has a slight negative charge -0.050 *e*. The chloride anion, as its nature would suggest, is negatively charged (-0.163 *e* in **c.s.16**, -0.455*e* in **c.s.17** and -0.066*e* in **c.s.18**) in all three structures.

As previously noted in the symmetrical urea series (see Chapter 4), the carbon atoms of the phenyl rings to which the (thio)ureas are bonded are highly positively charged in all three crystal structures (**c.s.16**-**c.s.18**). In the symmetrical thiourea chloride complex **c.s.16** all the carbon atoms which have a nitro group attached to them have a positive charge excluding C(1) (charge -0.068 *e*). In the unsymmetrical structures, where the nitro group is attached to the phenyl ring the carbon atom has a strong positive charge, while the analogous *para* position on the unsubstituted phenyl ring has a much lower (as in structure **c.s.17**) or negative (the case in structure **c.s.18**) charge. As would be expected for the nitro groups, the oxygen atoms are highly negative (more so in the thiourea complexes **c.s.16** and **c.s.18** than the urea complex **c.s.17**) and the nitrogen atoms are all positively charged (except N(4) in **c.s.16**).

The QTAIM charges observed for the sulfur atoms (positive values) were not anticipated. They were expected to be similar to the atomic charge of the oxygen atom of the urea groups in **c.s.17** and those reported in Chapter 4. The polarisation of the C=S bond means the carbon atom carries a partial positive charge and the sulfur atom a partial negative charge. The partial charge of the carbon atom calculated using the QTAIM method in the thiourea-based receptors (**c.s.16** and **c.s.18**) are significantly less positive (0.4 - 0.6 *e*) than that of the carbon atom of the thiourea structure (**c.s.17**) where the charge is 1.3 *e*. This may be linked to the observed sulfur atom partial charges calculated using QTAIM. Another reason may be the difference in the size of

the atomic radii and atomic basins between sulfur and oxgyen and the different electronegativities of these atoms.

Due to the observed QTAIM partial charges of the sulfur atoms, the stockholder charges were investigated. These are calculated using an alternative partitioning procedure to that of QTAIM charges (see Section 2.3.4.5 for an explanation of each method) and stockholder partitioning generally results in lower values for the atom charges but are expected to agree with the QTAIM partitioning results in terms of sign of charge (i.e. both giving positive or negative charges for a particular atom). This was generally the case, however the chloride charges did not match between the two methods in **c.s.16** and **c.s.18** and in **c.s.18** one sulfur has different signs for the charges from the two partitioning methods. For consistency with the results from Chapter 4 the discussion in this chapter will again be based on QTAIM calculated charges (see Figure 5.9).

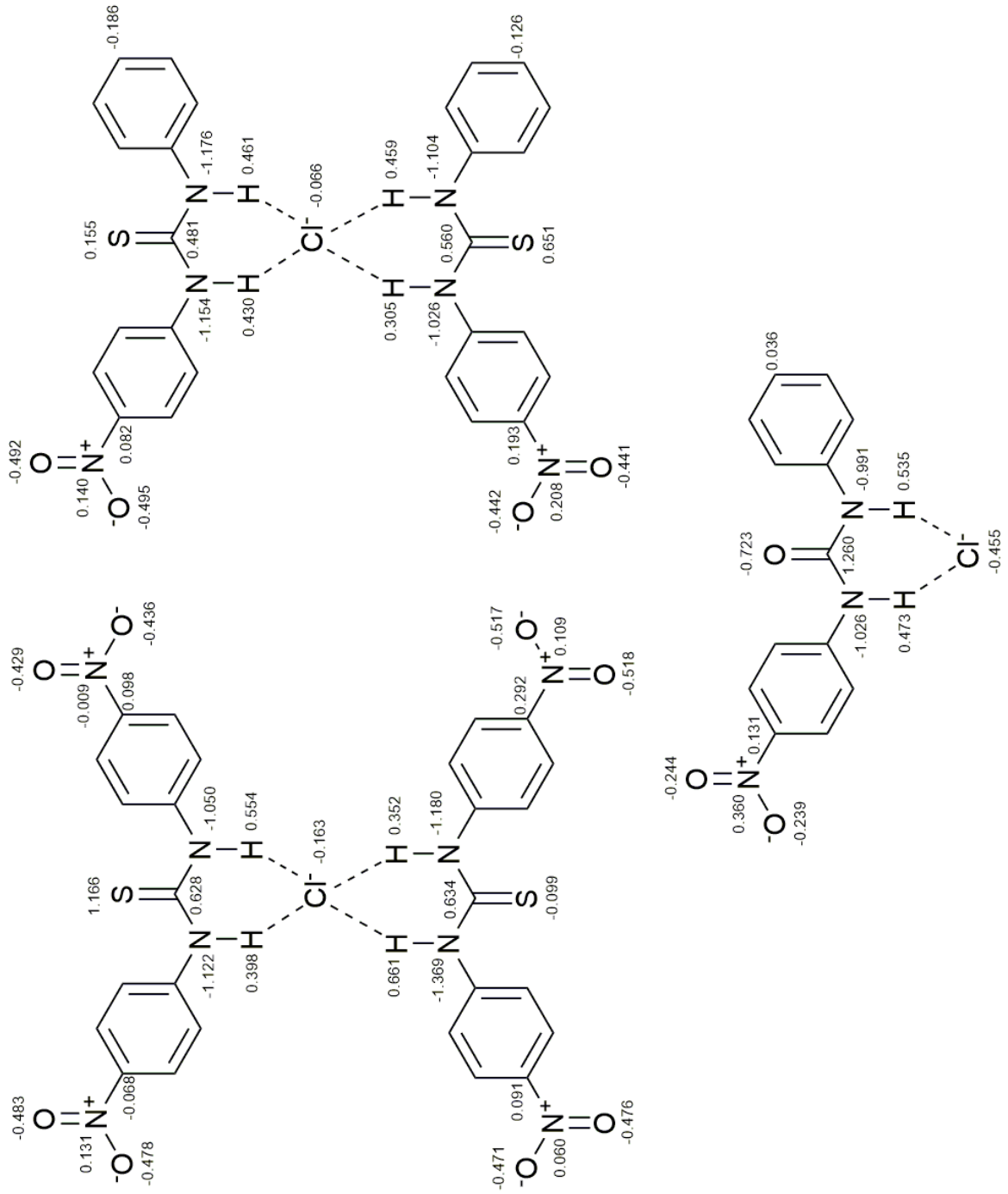

Figure 5.9: QTAIM atomic charges in **c.s.16**, **c.s.17** and **c.s.18**.

5.3.3.2 Hydrogen bonding

The presence of hydrogen bonding between the thio(urea) N—H bonds and the chloride anion in each structure (**c.s.16**–**18**) was determined by topological analysis and the presence of a bond path between each hydrogen atom of the (thio)urea group and the chloride anion and an associated BCP located on the bond path (molecular graph plots displaying both BPs and BCPs for the covalent bonds and hydrogen bonds are found in Appendix A.6). Figure 5.10 displays the hydrogen binding between the chloride anion and thiourea N—H bonds of one of the receptor molecules in **c.s.18**. The favourable arrangement of the hydrogen atoms with the valence shell depletion is shown.

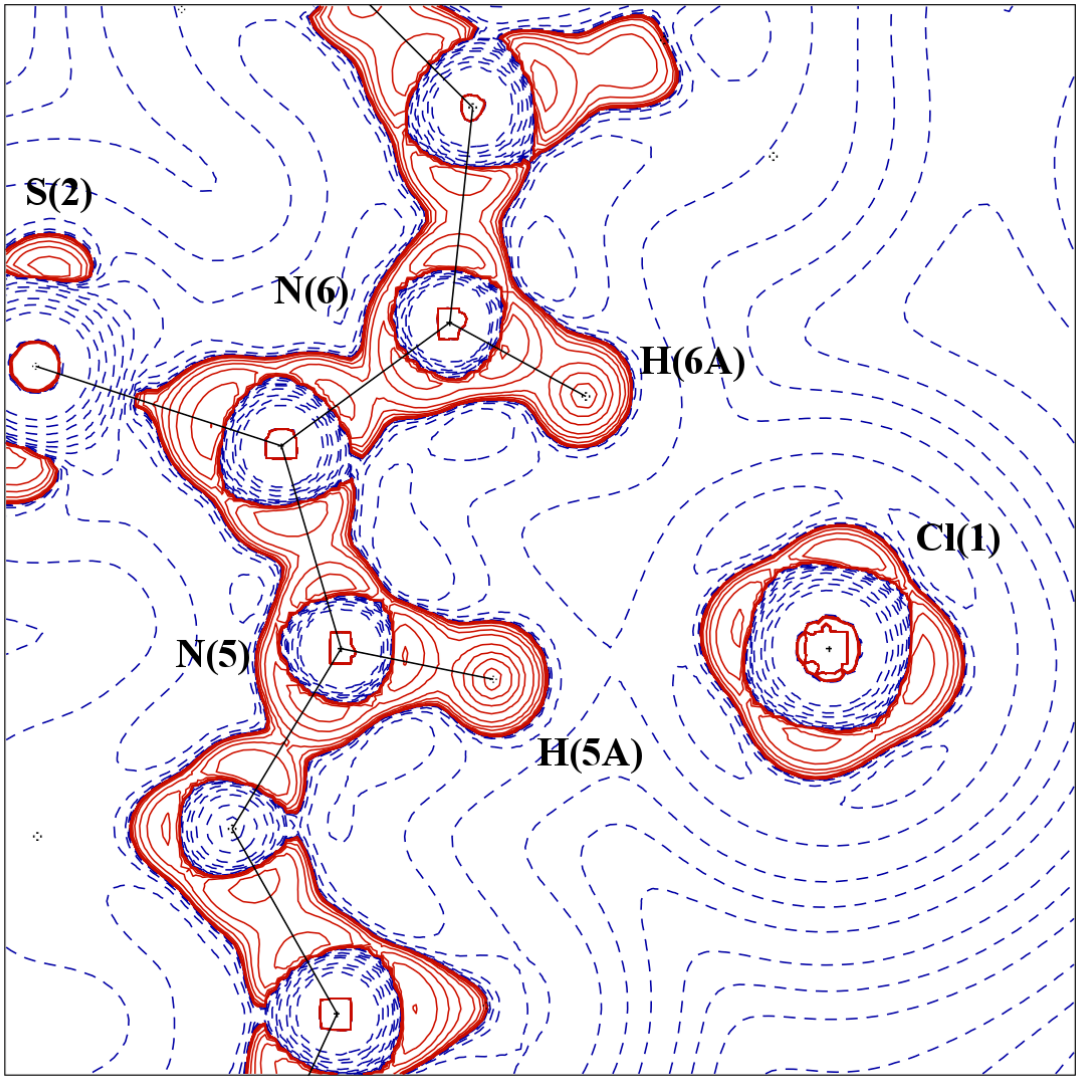

Figure 5.10: :$-\nabla^2\rho(\mathbf{r})$ charge density plot of the hydrogen bonding interactions between the thiourea N—H of the second receptor molecule and the chloride anion in **c.s.18**. Map drawn in the plane of the N(5) Cl(1) N(6) atoms. Positive electron density shown in red, negative electron density in blue. Contours are in a logarithmic scale (e Å^{-5}).

The properties of the electron density at the BCPs of each hydrogen bond (see Table 5.8) show these are weak, closed-shell interactions. This is demonstrated by the value of the Laplacian of the electron density at the BCP (> 0), the $|V(\mathbf{r}_{BCP})|/ G(\mathbf{r}_{BCP})$, which is <1, and the $H(\mathbf{r}_{BCP})$, in each case > 0.[80]

These interactions fall into the weak Region 2 type hydrogen bonding described in Section 4.4.3.1.

Table 5.8: Properties of the electron density at the BCPs of the hydrogen bonding interactions in **c.s.16**, **c.s.17** and **c.s.18**.

H···A	$\rho(\mathbf{r}_{BCP})$ (e Å^{-3})	$\nabla^2\rho(\mathbf{r}_{BCP})$ (e Å^{-5})	R_{ij} H···A (Å)	$G(\mathbf{r}_{BCP})$ (a.u)	$V(\mathbf{r}_{BCP})$ (a.u)	$\lvert V(\mathbf{r}_{BCP})\rvert$ / $G(\mathbf{r}_{BCP})$	E_{HB} (kJ mol^{-1})	$H(\mathbf{r}_{BCP})$ (kJ mol^{-1})
c.s.16: Symmetrical thiourea complex								
H(2A)···Cl	0.06(3)	1.585(5)	2.4302	0.012	−0.007	0.623	−9.759	11.825
H(3A)···Cl	0.06(2)	1.589(5)	2.4048	0.012	−0.008	0.629	−9.932	11.707
H(6A)···Cl	0.09(4)	2.36(2)	2.2070	0.019	−0.013	0.684	−16.685	15.453
H(7A)···Cl	0.10(3)	2.25(1)	2.2741	0.018	−0.013	0.725	−17.413	13.240
c.s.17: Unsymmetrical urea complex								
H(2A)···Cl	0.09(2)	1.974(9)	2.2804	0.016	−0.011	0.698	−14.407	12.474
H(3A)···Cl	0.07(2)	1.487(3)	2.4149	0.012	−0.008	0.663	−10.037	10.212
c.s.18: Unsymmetrical thiourea complex								
H(2A)···Cl	0.12(2)	2.107(2)	2.1947	0.018	−0.014	0.779	−18.320	10.373
H(3A)···Cl	0.09(1)	1.425(2)	2.3555	0.012	−0.009	0.753	−11.710	7.695
H(5A)···Cl	0.16(2)	2.042(5)	2.1941	0.020	−0.018	0.914	−23.412	4.396
H(6A)···Cl	0.10(2)	1.718(4)	2.2849	0.015	−0.011	0.774	−14.765	8.631

An interesting observation is that in both **c.s.17** and **c.s.18** the strength of the hydrogen bond is dependent on the substitution of the phenyl ring to which the N—H hydrogen bond donor group is attached. Where there is a nitro group present the value of the electron density and the Laplacian of the electron density at the bond critical point are increased, when compared to those values for the hydrogen bonds of the (thio)urea groups attached to an unsubstituted phenyl ring. The bond path length (R_{ij}) is also lengthened where the hydrogen

bond donor group is on the non-substituted side of the receptor. This is a direct observation of the hydrogen bond donor strengthening caused by the electron-withdrawing substituents. The effect is more noticeable when viewing the values of $\nabla^2\rho(\mathbf{r}_{BCP})$ for each structure.

The fact that the chloride anion is bound by two thiourea receptor molecules in **c.s.16** and **c.s.18** means that the total strength of the hydrogen bonding is greater in the thiourea structures, than in the urea structures, as would be expected by the increased hydrogen bond donor strength of the thiourea N—H bonds.

It is of interest that the hydrogen bond strength in the symmetrical thiourea (**c.s.16**) varies, not between the N—H hydrogen bond donor groups in the same receptor, but between the two receptors. The first receptor (with atoms N(2) N(3) S(1) H(2A) and H(3A)) has weaker hydrogen bonds (see the values of $\rho(\mathbf{r}_{BCP})$ and $\nabla^2\rho(\mathbf{r}_{BCP})$ in Table 5.8) than the second receptor molecule receptor (which contains atoms N(6) N(7) S(2) H(6A) and H(7A)).

5.3.3.3 Electrostatic Potential

The differences in the electron density distribution across the entire molecular ensemble between the urea- (**c.s.17**) and thiourea-based (**c.s.16** and **c.s.18**) structures was probed by studying the atomic charges (calculated using QTAIM theory) and the electrostatic potential distributions in the crystal structures (visualised using the MolIso program[180] and shown in Figure 5.11-**c.s.16**, Figure 5.12-**c.s.17** and in Figure 5.13-**c.s.18**).

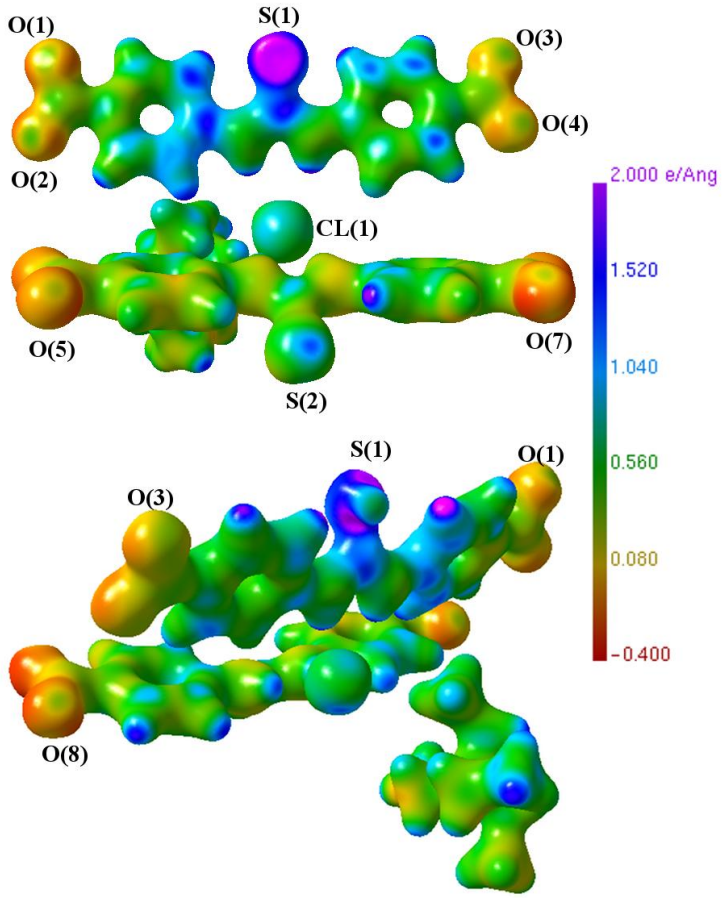

Figure 5.11: Two views of the electrostatic potential distribution plot (units of e Å^{-1}) of **c.s.16**.

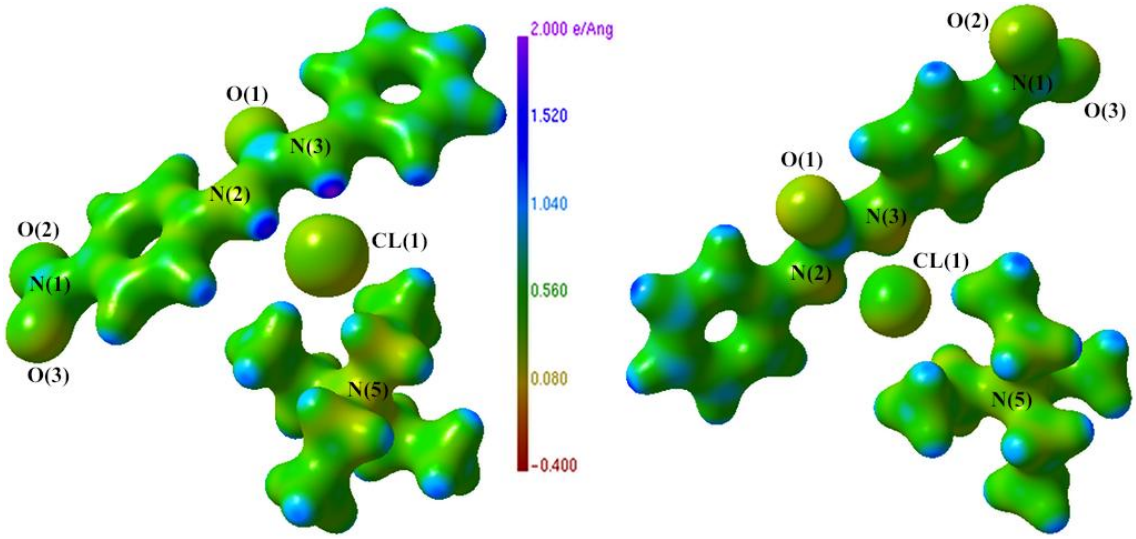

Figure 5.12: Two views of the electrostatic potential distribution plot (units of e Å^{-1}) of **c.s.17**.

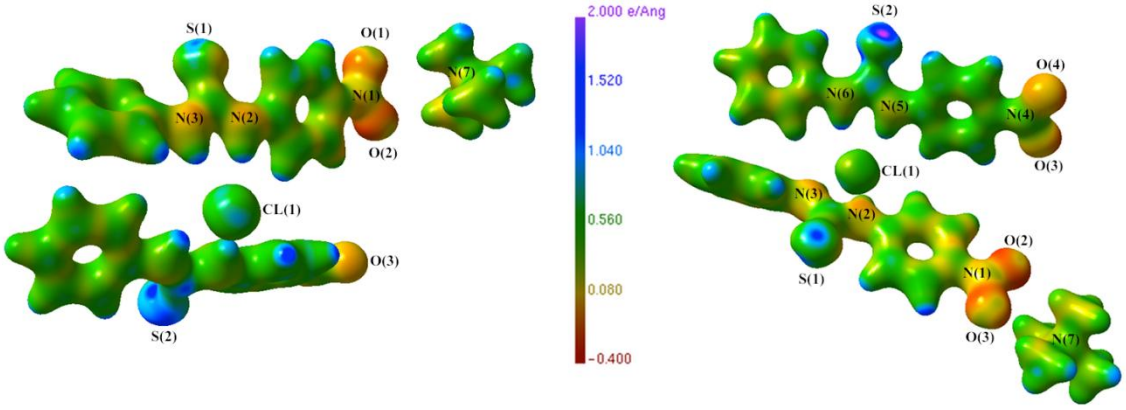

Figure 5.13: Two views of the electrostatic potential distribution plot (units of e Å^{-1}) of **c.s.18**.

Across the three crystal structures there is a large variation in the electrostatic potential distributions. The electrostatic potential distribution of both the TEA/TMA groups and chloride anions in all three structures are similar, as would be excepted as they are constant units in the series of structures. The electrostatic potential distribution of the nitro groups varies significantly between **c.s.17** (less negative electrostatic potential) and **c.s.16** and **c.s.18** (higher negative electrostatic potential), and matches the trends in the atomic charges of the nitrogen (higher positive charge in **c.s.17**) and oxygen atoms (higher negative charge in **c.s.16** and **c.s.18**) in these groups. The most striking difference is the electrostatic potential distributions around the urea and thiourea. In **c.s.17** the oxygen has a slightly negative electrostatic potential (matching the charge of this atom (-0.723e)) while the sulfur atoms in **c.s.16** and **c.s.18** have a positive electrostatic potential (again this matches their charges of 1.166 e (S(1)) and -0.099 e (S(2)) in **c.s.16** and 0.155 e (S(1)) and 0.651e (S(2)) in **c.s.18**).

Differences between the electrostatic potential of the two receptor molecules in the thiourea structures **c.s.16** and **c.s.18** are clearly visible. The contrast is most marked between the two sulfur atoms, which have considerably variable

charges (see above) and electrostatic potential distributions. This may be linked to the differences in the close contacts in which the different sulfur atoms are involved, see those mentioned in Table 5.9. For instance in **c.s.18** S(1) participates in interactions with the nitro groups of another thiourea group while S(2) has interactions with the hydrogen atoms of a TMA group.

Table 5.9: Sulfur atom non-covalent interactions in **c.s.16** and **c.s.18**.

Critical Point	$\rho(r_{BCP})$ (e Å^{-3})	$\nabla^2\rho(r_{BCP})$ (e Å^{-5})	R_{ij} (Å)	d_1 A—BCP (Å)	d_2 BCP—B (Å)	ϵ
c.s.16						
S(1)···N(7)§	0.035(2)	0.495(3)	3.2624	1.6820	1.5804	0.25
S(2) ···H(96B)δ	0.05(2)	0.654(5)	2.8488	1.7969	1.0519	0.04
S(2) ···H(93B)ξ	0.03(2)	0.537(4)	2.8110	1.8312	0.9798	0.09
c.s.18						
S(1) ···N(4)†	0.049(1)	0.714(2)	3.4984	1.6849	1.8135	0.62
S(1) ···O(3)†	0.049(1)	0.714(2)	3.1779	1.6849	1.4930	0.62
S(2) ···H(72A)‡	0.020(7)	0.407(3)	2.9296	1.8328	1.0968	0.09
S(2) ···H(73A)‡	0.018(7)	0.341(3)	2.9148	1.7884	1.1264	0.03

§Symmetry used to generate interaction 1-x, 1-y, 1-z, δsymmetry used to generate interaction -1+x, y, z, ξsymmetry used to generate interaction 2-x, 1-y, 2-z, †symmetry used to generate interaction 1-x, -y, -z ‡ symmetry used to generate interaction 1-x, 1-y, -z.

In all three crystal structures bond paths between the oxygen or sulfur atoms of the (thio)urea moiety and hydrogen atoms in the *ortho* position of the ring indicate that an interaction is taking place resulting in the formation of a

pseudo six-membered ring (in **c.s.16** this is only found for one receptor molecule). These are slightly weaker in the thiourea-based (**c.s.16** and **c.s.18**) than in the urea-based anion-receptor complex **c.s.17**, possibly due to the thiourea receptor molecules being twisted further out of the plane of the phenyl rings than the urea group in **c.s.17** and the associated bond path length is longer for the contacts involving the thioureas (see Table 5.10).

Table 5.10: Weaker non-covalent interactions in **c.s.16**, **c.s.17** and **c.s.18**.

Critical Point	$\rho(\mathbf{r}_{BCP})$ (e Å^{-3})	$\nabla^2\rho(\mathbf{r}_{BCP})$ (e Å^{-5})	R_{ij} (Å)	d_1 A—BCP (Å)	d_2 BCP—B (Å)	ϵ
Intramolecular interactions						
c.s.16						
S(2)···H(18)	0.097(5)	1.079(4)	2.6218	1.5935	1.0283	0.08
S(2)···H(26)	0.090(3)	1.067(3)	2.7025	1.6521	1.0504	0.80
c.s.17						
O(1)···H(5)	0.155(2)	1.928(5)	2.1722	1.2861	0.8861	0.53
O(1)···H(13)	0.101(2)	1.473(4)	2.3485	1.3276	1.0208	0.33
c.s.18						
S(1)···H(5)	0.094(3)	1.221(3)	2.6491	1.6010	1.0481	0.25
S(1)···H(13)	0.076(2)	0.972(2)	2.7812	1.6262	1.1549	0.60
S(2)···H(18)	0.084(3)	1.182(3)	2.6042	1.5732	1.0310	0.09
S(2)···H(26)	0.071(2)	0.947(3)	2.6512	1.5679	1.0833	0.35

5.3.4 Comparison of the electron density distribution with that in the Chapter 4 crystal structures

The series of receptors reported in this chapter allow comparison with the 1,3-bis(4-nitrophenyl)urea chloride complex (**c.s.6**) discussed in Chapter 4. The electronic properties at the BCPs of the covalent bonds in the crystal structures matched well to those analysed in Chapter 4. The TMA and TEA were consistent with the behaviour observed in the TMA cation in the 1,3-bis(4-nitrophenyl)urea complex. Comparing the urea portion of **c.s.6** with **c.s.17**, the difference between the atoms was less extreme, with the oxygen atom carrying a charge of -0.723 *e* in **c.s.17** compared to the charge of -1.047 *e* for the 1,3-bis(4-nitrophenyl)urea and the two carbon atoms were 1.260 *e* in **c.s.17** (the unsymmetrical urea complex) and 1.506 *e* in **c.s.6** (1,3-bis(4-nitrophenyl)urea). The nitrogen atoms of the urea were -1.260 *e* and -0.991 *e* in **c.s.17** and -1.098 *e* and -1.121 *e* in **c.s.6**.

In the thiourea-based complexes, while the nitrogen atoms carry similar charges to those atoms in the urea structures (**c.s.6** and **c.s.17**), the sulfur atom charges and carbon atom charges vary from those in the urea structures significantly. This is reflected in the properties of the bond critical points of the bonds in the (thio)urea group, where for **c.s.17** they agree well with those in the 1,3-bis(4-nitrophenyl)urea complex. However, deviation in behaviour is observed in **c.s.16** and **c.s.18**, where the electron density and Laplacian of the electron density at the C=S BCP is substantially different (1.45 *e* $Å^{-3}$ and -3.3 *e* $Å^{-5}$). This suggests this is a property of the change from urea to thiourea rather than that of symmetrical nitro substitution *vs.* unsymmetrical nitro substitution.

Table 5.11: Atom charges in **c.s.6**, **c.s.16**, **c.s.17** and **c.s.18**.

Atom	Charge (*e*)	Atom	Charge (*e*)
c.s.6			
O(1)	-1.047	N(2)	-1.098
C(7)	1.506	N(3)	-1.121
c.s.16			
S(1)	1.166	N(2)	-1.122
S(2)	-0.099	N(3)	-1.050
C(7)	0.628	N(6)	-1.369
C(20)	0.634	N(7)	-1.180
c.s.17			
O(1)	-0.723	N(2)	-1.026
C(7)	1.260	N(3)	-0.991
c.s.18			
S(1)	0.155	N(2)	-1.154
S(2)	0.651	N(3)	-1.176
C(7)	0.481	N(5)	-1.026
C(20)	0.560	N(6)	-1.104

5.4 Conclusions

The unsymmetrical substitution of the receptor molecules in this series is shown to alter the packing and intermolecular contacts in both the receptor free ligand crystal structures and the anion-receptor complexes. The variation from urea to thiourea substantially changes the packing and anion binding properties (2: 1 receptor: anion in the thiourea complex *versus* 1:1 receptor: anion in the urea complex). Anion binding appears to effect dramatic changes in the crystal structures as illustrated by Hirshfeld surface analysis. Charge density analysis is able to more thoroughly describe and illustrate these alterations by mapping the electron density distribution across the anion-receptor complexes. Hydrogen bond strength was determined and shown to be weak in nature and also dependent on the position of the hydrogen bond donor group on the asymmetrically substituted receptor. Differences in the electron density distribution, atomic charges and electrostatic potential distribution across two of the 'same' receptor molecules in the thiourea 2:1 complexes illustrate how properties of molecules can vary greatly depending on the crystalline environment.

The difference between the properties of the thiourea and urea receptors is illustrated in this series of complexes, for instance in the properties of the electron density distribution at the BCPs for the C=O and C=S bonds and the atomic charges of the atoms in these functional groups. This suggests that a very simple change often employed in anion-receptor chemistry has dramatic consequences on the electron density distribution across the crystal structures, alters the behaviour of the receptor and drives the changes in the overall anion-receptor complexes observed.

Chapter 6: Conclusions and further work

6.1 Conclusions

The in-depth standard structural analysis undertaken on the crystal structures reported in this thesis using a variety of techniques, single crystal X-ray and neutron diffraction experiments, Hirshfeld surface mapping, and complemented by ^{1}H NMR titration studies (to study the anion binding properties of the receptor molecules in solution) provided detailed information and understanding of the chemistry, solid-state arrangement and properties of the anion-receptors and their resulting anion-receptor complexes. The determination of the accurate positions of the protons of the urea N—H group in the receptor molecules offered a valuable insight into the chemistry of these systems, establishing that they are salts and that no proton migration or transfer occurs. This is one of the most comprehensive crystallographic studies on anion-receptor complexes to date.

Despite this, however detailed the analysis, the conclusions reached at standard resolution in the solid-state are limited to deductions based on geometric arguments and assumptions (in the case of hydrogen bonding analysis) and/or qualitative discussion of the crystal structure assembly (Hirshfeld surface analysis).

Analysis of the electron density distribution in the crystal structures provides a more fundamental understanding of the underlying chemistry of the complexes. In each anion-receptor complex the nature and strength of the hydrogen bond was determined using well-established charge density criteria. Introducing three variations to the set of crystal structures- change of anion, of substituent position and of anion binding group (from urea to thiourea),

allowed a systematic approach to be taken and direct comparisons to be made across a series of crystal structures.

Looking across a series of anions from chloride to acetate to fluoride the increase in hydrogen bond strength that accompanies increasing basicity of anion was observed in the solid-state, matching the behaviour noted in solution. This is the first time this has been achieved in anion-receptor chemistry.

Changing the position of the electron-withdrawing substituent at the periphery of the anion-receptor (from *para* to *meta* to 3,5-dinitro) and modifying the anion binding unit (from urea to thiourea) alters the electron density distribution in the anion-receptor complexes, and their resultant properties, including atomic charges and the electrostatic potential distribution. This effect is not isolated to the site of modification but can be observed across the receptor molecule.

The effect of anion binding on electron density distributions was also investigated, by comparing the electron density distribution in an uncomplexed receptor molecule to that in the anion complexes of that receptor. This is work that can be built upon, as the lower quality of the X-ray diffraction data of the free ligand structure only allows conservative analysis and the conclusions made should be viewed with a certain level of caution.

The initial family of receptors was expanded to include molecules that were asymmetrically substituted. That asymmetrical substitution of an anion-receptor can also significantly alter both the hydrogen bond pattern and strength and the electron density distribution in the anion-receptor complexes was demonstrated. The strength of a hydrogen bond from a urea N—H

attached to an electron-withdrawing group appears to be stronger than that from a N—H without an electron-withdrawing group.

The crystal structures in this thesis were designed to be fairly simple, as were the anion-receptor molecules, so that modifications to a common receptor scaffold could be easily introduced. Thus the electron density distribution in an extensive range of anion-receptor complexes could be examined. Systematic studies, such as this, are powerful as they allow multiple effects to be analysed, while limiting the amount of labour intensive data collection and refinement that must be performed. Another benefit is that the presence of one badly behaving but interesting chemical sample is not debilitating. Multipole refinements of less than ideal samples in this thesis could be treated with greater confidence as they were viewed in a series, with other better behaved samples acting as internal standards. Theoretical studies also supplemented the analysis in such cases.

One result of this research is that the electron density distribution in an anion-receptor complex has been derived when low quality crystals and diffraction data prohibit full multipole modelling using the invariom approach. This may provide a route for the charge density analysis of far more complex anion-receptor complexes and thus the understanding of the function and behaviour of a wider range of systems.

To conclude, charge density analysis presents a picture of both the electron density distribution across each molecular entity and the crystal structure as a whole. In this thesis it has substantially added to the knowledge gained from standard resolution X-ray diffraction structural studies and complementary techniques (including proton NMR titrations) on anion-receptor complexes. These give information about how anion-receptor molecules and anions

interact as units, but only focus on particular parts of the molecular ensemble. Charge density analysis provides otherwise unobtainable detailed insight into the strength and nature of intermolecular interactions (via approaches such as the source function) and links the properties of the chemical groups in one part of a molecular structure to the electron density distribution in other areas of that same structure.

6.2 Future work

This systematic study across a series of anion-receptor complexes has allowed a deeper understanding of how changing both the host and the guest effects the overall properties of the supramolecular assemblies. Moving on from this, and following the example of others who look at drug interactions using charge density analysis, the electron density distribution of an anion-receptor complex could be studied as it performs its function or in its working environment. One example of this would be the study of an anion transporter, which binds an anion in the exterior hydrophilic part of a lipid membrane and transports it across the hydrophobic part of the membrane. To begin this challenging task the crystallisation of a potent, known anion transporter could be performed with lipid molecules to gain understanding of the interactions between the lipid bilayer and anion transporter. As anion transporters often contain flexible chains (mimicking the lipid molecules), to improve lipophilicity and solubility, the likelihood of some form of disorder being present is high. This means that quantum mechanical calculations, particularly periodic studies, could be particularly valuable and the use of the invariom or other similar databases helpful. One could also look at studying the function of molecular machines, including rotaxanes and catanenes in a similar manner, both their final assembled structure and their individual building blocks to

better understand the processes by which they form and the interactions that hold them together.

This thesis has focused on relatively simple anion-receptor molecules, which bind anions through hydrogen bonding. Many anion-receptors exploit multiple interactions to strengthen the association of the anion and receptor. Examining the electron density distribution in some of these systems, for example those which combine hydrogen and halogen bonding, would allow the contribution of each type of anion binding interaction to the overall anion recognition process to be calculated. Determining a scale for the different interaction types would be beneficial for supramolecular chemists when designing molecules for a specific task. To generate such a scale would be quite an undertaking, it would require a large number of examples and detailed statistical analysis of the derived interaction energies. To begin this, databases which allow a model of the electron density distribution to be generated (using transferable multipole populations) for datasets collected at standard resolution could be tested and may provide insight into the practicability of this proposal.

Chapter 7: Experimental

7.1 Synthesis

7.1.1 Chemicals and reagents

Unless otherwise stated, reagents were used as supplied from commercial sources without further purification. Solvents used were not dried unless stated in the following procedures.

7.1.2 Instrumental methods

NMR data was recorded using a Bruker AVII300/400 FT-NMR spectrometer in the indicated solvent at 298 K. All data are referenced to the residual protio-solvent peak in the case of proton NMR, or the solvent peak set in the case of ^{13}C NMR. Chemical shift values are reported in ppm. Abbreviations are used for spin multiplicity: br = broad signal s = singlet, d = doublet, t = triplet, q= quartet, dd = double doublet, m = multiplet.

7.1.3 Synthesis of compounds reported in Chapters 3 and 4

The syntheses below refer to compounds referred to in Chapters 3 and 4. The syntheses were adapted from literature procedures of Perveen *et al.*,[199] Miyahara,[200] and all compounds have been previously reported in the literature.

1,3-Bis(2-nitrophenyl)urea (12)

2-Nitrophenylisocyanate (0.36 g, 2.22×10^{-3} moles, 1.5 eq) was dissolved in DCM (15 mL). 2-Nitroaniline (0.20 g, 1.45×10^{-3} moles, 1.0 eq) was added followed by triethylamine (0.5 mL, 3.59×10^{-3} moles, 2.5 eq) and the solution stirred overnight. The resulting solid was filtered and washed with DCM, and

the solid was recrystallised from chloroform and hexane. This resulted in a yellow solid (0.08 g, 2.65×10^{-4} moles, 18%). MP = 232-235°C. ^{1}H NMR (300 MHz, d_6–DMSO, δ = ppm): 7.19 (t, 7.7 Hz, 2H, CH), 7.68 (t, 7.3 Hz, 2H, CH), 8.26 (dd, 8.4 Hz, 1.5 Hz, 2H, CH), 8.58 (d, 8.8 Hz, 2H, CH), 10.17 (br.s., 2H, NH).

1,3-Bis(3-nitrophenyl)urea (13)

3-Nitrophenylisocyanate (0.36 g, 2.22×10^{-3} moles, 1.5 eq) was dissolved in DCM (50 mL). 3-Nitroaniline (0.20 g, 1.45×10^{-3} moles, 1.0 eq) was added followed by triethylamine (0.5 mL, 3.59×10^{-3} moles, 2.5 eq) and the solution stirred overnight. The resulting solid was isolated by filtration and washed with DCM, and the solid was recrystallised from a mixture of chloroform and hexane. This resulted in a yellow solid (0.37 g, 1.22×10^{-3} moles, 84 %). MP = 250-252°C. ^{1}H NMR (300 MHz, d_6–DMSO, δ = ppm): 7.59 (t, 8.3 Hz, 2H, CH), 7.77 (d, 6.8 Hz, 2H, CH), 7.85 (d, 6.8 Hz, 2H, CH), 8.55 (t, 2.0 Hz, 2H, CH), 9.75 (br. s., 2H, NH).

1,3-Bis(4-nitrophenyl)urea (14)

4-Nitrophenylisocyanate (0.38 g, 2.32×10^{-3} moles, 1.6 eq) was dissolved in DCM (50 mL). 4-Nitroaniline (0.20 g, 1.45×10^{-3} moles, 1.0 eq) was added followed by triethylamine (0.50 mL, 3.59×10^{-3} moles, 2.5 eq) and the solution stirred overnight. The resulting solid was isolated by filtration and washed with DCM, and the solid was recrystallised from acetonitrile. This resulted in a yellow powder (0.078 g, 2.58×10^{-4} moles, 18 %). MP > 300°C. ^{1}H NMR (300 MHz, d_6–DMSO, δ = ppm): 7.73 (d, 9.4 Hz, 4H, CH), 8.22 (d, 9.0 Hz, 4H, CH), 9.66 (br. s., 2H, NH).

1,3-Bis(3,5-dinitrophenyl)urea (15)

3,5-Dinitrophenylisocyanate (0.12 g, 5.74×10^{-4} moles, 1.0 eq) was dissolved in toluene (50 mL). 3,5-Dinitroaniline (0.10 g, 5.46×10^{-4} moles, 1.0 eq) was added followed by triethylamine (2.00 mL, 1.43×10^{-2} moles, 26.3 eq). The reaction was heated at reflux overnight under a nitrogen atmosphere. A precipitate formed and this was isolated by filtration to yield a pale yellow solid (0.098 g, 2.50×10^{-4} moles, 46%). MP >270°C (decomposition). ^{1}H NMR (300 MHz, d_6–DMSO, δ = ppm): 8.46 (t, 1.8 Hz, 2H, CH), 8.80 (d, 1.8 Hz, 4H, CH), 10.13 (s, 2H, NH).

7.1.4 Synthesis of compounds reported in Chapter 5

The syntheses below refer to compounds referred to in Chapter 5. The syntheses were adapted from literature procedures of Perveen *et al.,*[199] and Miyahara[200] and all compounds have been previously reported in the literature.

1,3-Bis(2-nitrophenyl)thiourea (16)

2-Nitrophenylisothiocyanate (0.18 g, 1.00 x10^{-3} moles, 1.0 eq) was dissolved in pyridine (5 mL) and 2-nitroaniline (0.20 g, 1.50 x10^{-3} moles, 1.5 eq) dissolved in pyridine (5 mL) was added. The clear orange solution was stirred overnight under a nitrogen atmosphere. The solvent was removed and the resulting solid purified by recrystallisation from ethyl acetate and hexane. This resulted in a yellow solid (0.09 g, 2.70 x10^{-4} moles, 27%). MP = 155-157°C. ^{1}H NMR: (400 MHz, $CDCl_3$, δ = ppm): 7.30-7.42 (m, 2H, CH), 7.65-7.79 (m, 2H, CH), 8.19 (dd, 8.4 Hz, 1.5 Hz, 2H, CH), 8.44 (d, 8.1 Hz, 2H, CH), 10.14 (br. s, 2H, NH).

1,3-Bis(3-nitrophenyl)thiourea (17)

3-Nitrophenylisothiocyanate (0.18 g, 1.00 x10^{-3} moles, 1.0 eq) was dissolved in pyridine (7 mL) and 3-nitroaniline (0.20 g, 1.50 x10^{-3} moles, 1.5 eq) dissolved in pyridine (8 mL) was added. The clear orange solution was stirred overnight under a nitrogen atmosphere. The solvent was removed and the resulting solid dissolved in ethyl acetate (50 mL) and washed with HCl (1M, 50mL) and the organic and aqueous layers separated. The organic layer was washed with saturated sodium bicarbonate (50 mL) followed by brine (50 mL). The organic layer was dried over $MgSO_4$ and then filtered. The solvent was removed *in vacuo* and the solid purified by recrystallisation from ethyl acetate and hexane. This resulted in a yellow solid (0.13 g, 4.10 x10^{-4} moles, 40%). MP = 170-172°C. ^{1}H NMR: (300 MHz, d_6-DMSO, δ = ppm): 7.60-7.69 (m, 2H, CH), 7.92 (m, 2H, CH), 8.01 (dd, 8.2 Hz, 2 Hz, 2H, CH), 8.52 (t, 2.2 Hz, 2H, CH), 10.45 (br. s, 2H, NH).

1,3-Bis(4-nitrophenyl)thiourea (18)

4-Nitrophenylisothiocyanate (0.18 g, 1.00 x10^{-3} moles, 1.0 eq) was dissolved in pyridine (5 mL) and 4-nitroaniline (0.20 g, 1.45 x10^{-3} moles, 1.5 eq) in pyridine (5 mL) was added. The clear orange solution was stirred overnight under a nitrogen atmosphere. The solvent was removed *in vacuo* and the resulting solid dissolved in ethyl acetate and washed with 1M HCl and the organic and aqueous layers separated. The organic layer was washed with saturated sodium bicarbonate followed by brine. The organic layer was then dried over $MgSO_4$. After filtration the solvent was removed *in vacuo* and the solid purified by recrystallisation from ethyl acetate/hexane. This resulted in a yellow solid (0.096 g, 3.02 x10^{-4} moles, 30%). MP = 193-196°C. ^{1}H NMR (300

MHz, d_6–DMSO, δ = ppm): 7.85 (d, J=8.8 Hz, 4H, CH), 8.24 (d, J=8.8 Hz, 4H, CH), 10.77 (br. s, 2H, NH).

1,3-Bis(4-cyanophenyl)urea (19)

4-Cyanophenylisocyanate (0.61 g, 4.23 x10^{-3} moles, 1.0 eq) was dissolved in toluene (30 mL). 4-Aminobenzonitrile (0.50 g, 4.23 x10^{-3} moles, 1.0 eq) was dissolved in toluene (30 mL) and added, followed by triethylamine (2.00 mL, 1.43 x10^{-2} moles, 3.4 eq). The reaction was stirred overnight under a nitrogen atmosphere. A precipitate formed and was isolated by filtration to yield a white solid. This was then dissolved in isopropanol (150 mL) and washed with HCl (1M, 150 mL) followed by saturated sodium bicarbonate (150 mL), which led to the precipitation of the product, which was isolated by filtration to yield a white solid (0.56 g, 2.13 x10^{-3} moles, 50%). MP > 250°C. ^{1}H NMR (300 MHz, d_6–DMSO, δ = ppm): 7.63 (d, 8.8 Hz, 4H, CH), 7.75 (d, 8.8 Hz, 4H, CH), 9.42 (br. s, 2H, NH).

1,3-Bis[4-(trifluoromethyl)phenyl]urea (20)

4-(Trifluoromethyl)phenylisocyanate (0.29 mL, 2.00 x10^{-3} moles, 1.0 eq) was dissolved in toluene (10 mL). 4-(Trifluoromethyl)aniline (0.25 mL, 2.00 x10^{-3} moles, 1.0 eq) dissolved in toluene (10 mL) was added dropwise and the reaction stirred overnight under a nitrogen atmosphere. The solvent was removed *in vacuo* to yield a white solid (0.588 g, 1.69 x10^{-3} moles, 84%). MP = 228-230°C. ^{1}H NMR (300 MHz, d_6–DMSO, δ = ppm): 7.57-7.75 (m, 8H, CH), 9.23 (s, 2H, NH).

1,3-Bis(4-cyanophenyl)thiourea (21)

4-Cyanophenylisothiocyanate (0.50 g, 4.23 x10^{-3} moles, 1.0 eq) was dissolved in pyridine (25 mL) and 4-aminobenzonitrile (0.50 g, 4.23 x10^{-3} moles, 1.5 eq)

dissolved in pyridine (15 mL) was added. The clear orange solution was stirred for 3 days under a nitrogen atmosphere. The solvent was removed and the resulting solid dissolved in ethyl acetate (50 mL) and washed with HCl (1M, 50 mL) and the organic and aqueous layers separated. The organic layer was washed with saturated sodium bicarbonate (50 mL) followed by brine (50 mL). The organic layer was then dried over $MgSO_4$ and filtered. The solvent was removed *in vacuo* and the solid purified by recrystallisation from ethyl acetate and hexane. This resulted in an off-yellow solid (0.40 g, 1.44 $x10^{-3}$ moles, 34%). MP = 179-181°C. ^1H NMR (300 MHz, d_6-DMSO, δ = ppm): 7.69-7.85 (m, 8H, CH), 10.51 (s, 2H).

1,3-Bis[4-(trifluoromethyl)phenyl]thiourea (22)

4-(Trifluoromethyl)phenylisothiocyanate (0.40 g, 2.00 $x10^{-3}$ moles, 1.0 eq) was dissolved in still dried diethylether (10 mL). 4-(Trifluoromethyl)aniline (0.25 mL, 2.00 $x10^{-3}$ moles, 1.0 eq) dissolved in still dried diethylether (5 mL) was added dropwise and the reaction stirred overnight under a nitrogen atmosphere. The resulting precipitate was isolated by filtration to yield a white solid (0.583 g, 1.60 $x10^{-3}$ moles, 80%). MP = 161-163°C. ^1H NMR (300 MHz, d_6-DMSO, δ = ppm): 7.73 (q, 8.8 Hz, 8H, CH), 10.35 (s, 2H, NH).

1-(4-Nitrophenyl)-3-phenylurea (23)

4-Nitrophenylisocyanate (0.5 g, 3.05 $x10^{-3}$ moles, 1.0 eq) was dissolved in toluene (70 mL). To this was added aniline (0.25 mL, 3.05 $x10^{-3}$ moles, 1.0 eq). A white precipitate formed. This was stirred overnight at room temperature under a nitrogen atmosphere. The solid was filtered and dried under vacuum (white solid, 0.73 g, 2.86 $x10^{-3}$ moles, 94 %). MP: 212-214°C. ^1H NMR (300 MHz, d_6-DMSO, δ = ppm): 7.02 (t, 0.75 Hz, 1H, CH), 7.31 (t, 7.91

Hz, 2H, CH), 7.47 (d, 7.54 Hz, 2H, CH), 7.69 (d, 9.42 Hz, 2H, CH), 8.19 (d, 9.04 Hz, 2H, CH), 8.90 (s, 1H, NH), 9.42 (s, 1H, NH).

1-(4-Nitrophenyl)-3-phenylthiourea (24)

Aniline (0.23 mL, 2.78 x 10^{-3} moles, 1.0 eq) was dissolved in DCM (35 mL). 4-Nitrophenylisothiocyanate (0.5 g, 2.78 x 10^{-3} moles, 1.0 eq) dissolved in DCM (35 mL) was added. The yellow solution was left to stir overnight at room temperature under a nitrogen atmosphere. The solvent was removed *in vacuo*, and a yellow solid formed. This was recrystallised from ethanol. The solid was filtered and washed with hexane to yielded a yellow solid (0.36 g, 1.32 x10^{-3} moles, 47 %). MP: 150-152°C. ^{1}H NMR (300 MHz, d_6-DMSO, δ = ppm): 7.17 (t, 7.54 Hz, 1H, CH), 7.37 (t, 7.54 Hz, 2H, CH), 7.49 (d, 7.54 Hz, 2H, CH), 7.84 (d, 9.2 Hz, 2H, CH), 8.20 (d, 9.04 Hz, 2H, CH), 10.26 (br. s., 1H, NH), 10.36 (br. s., 1H, NH).

7.2 Crystallisations

A range of crystallisation conditions were trialled and tested during the course of this thesis. This included altering the ratio of salt and receptor (usually between 1-10 equivalents of salt to receptor) and the solvent compositions used (varied until dissolution of the solid material was achieved). The method of crystallisation, vapour diffusion or slow diffusion was also varied. The crystallisation procedures reported in this thesis are those which resulted in the formation of crystals suitable for the X-ray diffraction studies.

7.2.1 Crystallisations of structures reported in Chapters 3 and 4

The methods for the crystallisation of single crystals included in Chapters 3 and 4.

7.2.1.1 Free ligand crystallisations

1,3-Bis(2-nitrophenyl)urea (12) - c.s.1

The compound was dissolved in a mixture of dichloromethane, isopropanol and acetonitrile, in a roughly 1:1:1 ratio. Crystals grew upon slow evaporation of the mixed solvent system.

1,3-Bis(3-nitrophenyl)urea (13) - c.s.2

The compound was dissolved in a mixture of methanol, diethylether and hexane, in a roughly 1:1:1 ratio. Crystals grew upon slow evaporation of the mixed solvent system. Matched unit cell of Etter *et al.*.[131]

1,3-Bis(4-nitrophenyl)urea (14) - c.s.3

The compound was dissolved in acetonitrile and methanol (50/50 solvent mixture). Crystals grew upon slow evaporation of the mixed solvent system.

7.2.1.2 Solvates

1,3-Bis(3,5-dinitrophenyl)urea (15) - c.s.4

The compound was dissolved in dimethyl sulfoxide. Crystals grew upon slow evaporation of the solvent with heat provided by placing on top of an oven.

7.2.1.3 Anion-receptor complexes

1,3-Bis(3-nitrophenyl)urea with TMA chloride - c.s.5

Crystals were grown by vapour diffusion of diethyl ether into an isopropanol solution of TMA chloride (3 eq) and 1,3-bis(3-nitrophenyl)urea (1 eq).

1,3-Bis(4-nitrophenyl)urea with TMA chloride - c.s.6

Crystals were grown by vapour diffusion of diethyl ether into a solution of TMA chloride (2 eq) and 1,3-bis(4-nitrophenyl)urea (1 eq) in acetonitrile.

1,3-Bis(3,5-dinitrophenyl)urea with TMA chloride - c.s.7

Crystals were grown by vapour diffusion of diethyl ether into a mixed acetonitrile (5/8th of the solvent mixture) and methanol (3/8th of the solvent mixture) solution of TMA chloride (4 eq) and 1,3-bis(3,5-dinitrophenyl)urea (1 eq).

1,3-Bis(3-nitrophenyl)urea with TMA acetate - c.s.8

Crystals were grown by vapour diffusion of diethyl ether into a solution of TMA acetate (3 eq) and 1,3-bis(3-nitrophenyl)urea (1 eq) in acetonitrile.

1,3-Bis(4-nitrophenyl)urea with TMA acetate - c.s.9

Crystals were grown by vapour diffusion of diethyl ether into a solution of TMA acetate (2 eq) and 1,3-bis(4-nitrophenyl)urea (1 eq) in acetonitrile.

1,3-Bis(3,5-dinitrophenyl)urea with TMA acetate - c.s.10

Crystals were grown by vapour diffusion of diethyl ether into a mixed acetonitrile and methanol solution of TMA acetate (10 eq.) and 1,3-bis(3,5-dinitrophenyl)urea (1 eq). The solvent mixture was roughly 60: 40 acetonitrile: methanol.

1,3-Bis(4-nitrophenyl)urea with TMA fluoride - c.s.11

Crystals were grown by slow evaporation of an acetonitrile solution of TMA fluoride (3 eq) and 1,3-bis(4-nitrophenyl)urea (1 eq).

1,3-Bis(4-nitrophenyl)urea with TMA sulfate - c.s.12

Crystals were grown by slow evaporation of a mixed acetonitrile (50%) and methanol (50%) solution of TMA sulfate (3 eq) and 1,3-bis(4-nitrophenyl)urea (1 eq).

7.2.2 Crystallisations of structures in Chapter 5

The methods for the crystallisation of single crystals included in Chapter 5.

7.2.2.1 Free ligands

1,3-Bis(4-nitrophenyl)thiourea (18) - c.s.13

The compound was dissolved in acetonitrile (50%) and acetone (50%) with gently heating. Undissolved solid was filtered and the filtrate was left for the solvent to slowly evaporate yielding single crystals.

1-(4-Nitrophenyl)-3-phenylurea (23) - c.s.14

The compound was suspended in methanol. TMACl was added in methanol and lead to full dissolution of the solution. Crystals of the free ligand grew upon slow evaporation of the solution.

1-(4-Nitrophenyl)-3-phenylthiourea (24) - c.s.15

The compound was dissolved in methanol. Vapour diffusion of diethyl ether into the solution resulted in crystals.

7.2.2.2 Anion-receptor complexes

1,3-Bis(4-nitrophenyl)thiourea with TEA chloride - c.s.16

Crystals were grown by slow evaporation of an acetonitrile solution of TEA chloride (5 eq) and 1,3-bis(4-nitrophenyl)thiourea (1 eq).

1-(4-Nitrophenyl)-3-phenylurea with TEA chloride - c.s.17

Crystals were grown by the vapour diffusion of diethyl ether in an acetonitrile solution of TEA chloride (5 eq) and 1-(4-nitrophenyl)-3-phenylurea (1 eq).

1-(4-Nitrophenyl)-3-phenylthiourea with TMA chloride - c.s.18

Crystals were grown by vapour diffusion of diethyl ether into a mixed 1:1 methanol and ethanol solvent solution of TMA chloride (2 eq) and 1-(4-nitrophenyl)-3-phenylthiourea (1 eq).

7.3 Proton NMR titration studies

7.3.1 Methodology

1.5 mL of a 0.01 M solution of the appropriate receptor was prepared. Of this solution, 0.5 mL was added to a NMR tube, which was then sealed with an air tight suber seal. The remaining 1 mL of the receptor solution was used to make a 0.15 M solution of the desired guest. The anion/receptor solution was titrated into the NMR tube in small aliquots and a ^{1}H NMR spectrum was recorded after each addition. This resulted in an increasing concentration of guest throughout the experiment while the receptor concentration was kept constant. Chemical shifts for each peak were calibrated to the solvent peak. The data was fitted to a relevant binding model using WinEQNMR2[151] in order to generate values for the binding constant(s).

7.4 Proton NMR Job plots

7.4.1.1 Methodology

Two solutions were prepared; the first was a 3 mL 0.01 M solution of the receptor and the second was a 3 mL 0.01 M of the guest. 0.5 mL of the receptor was added to an NMR tube. The volume of receptor solution was then decreased by 0.05 mL and the amount of guest solution was increased by 0.05 mL for each successive NMR tube until a 9:1 anion: receptor ratio was reached. A ^{1}H NMR spectrum was recorded for each of the ten samples, and calibrated to the solvent peak. This data was used to produce a Job plot in accordance with the methods described by Job.[201] The molar fraction of the receptor (χ_r) was plotted against the values given by the formula given in Equation 7.1.

(Eq. 7.1) $$y = \frac{\delta_{obs} - \delta_{int}}{\delta_{fin} - \delta_{int}} \chi_r$$

where δ_{obs} is the observed chemical shift, δ_{int} is the initial chemical shift and δ_{fin} is the final chemical shift.

7.5 Single crystal X-ray diffraction

X-ray diffraction datasets were collected at low temperatures using an Oxford Cryosystems 700 Series CryoStream (100, 120 K), or a N-Helix dual flow nitrogen and helium cooler (30 - 100K).

7.5.1 Details of X-ray diffractometers

7.5.1.1 Laboratory based equipment

Three laboratory based diffractometers, equipped with molybdenum targets, were used to collect the X-ray diffraction data in this thesis.

Datasets for **c.s.1**, **c.s.6**, **c.s.7**, and **c.s.8** were collected on a Bruker-Nonius FR591 rotating anode CCD diffractometer. This diffractometer was equipped with confocal focussing mirrors, and a graphite monochromator.

Datasets for **c.s.9**, **c.s.15**, **c.s.16**, and **c.s.18** were collected on a Rigaku FR-E+ SuperBright Very High Flux rotating anode equipped with VariMax high flux (HF) optics, to achieve a beam of 100 μm, and a Saturn 724+ 18bit CCD detector.[202]

Datasets for **c.s.4**, **c.s.12**, **c.s.13** and **c.s.14** were collected on a Rigaku FR-E+ SuperBright Very High Flux rotating anode equipped with VariMax very high flux (VHF), to achieve a focused beam of 70μm, and a Saturn 724+ 18bit CCD detector.[202]

7.5.1.2 Synchrotron equipment

Datasets for **c.s.3**, **c.s.5**, **c.s.10**, **c.s.11**, and **c.s.17** were collected at the Diamond Light Source on the I19 beamline. A Crystal Logic 4-kappa diffractometer equipped with a Rigaku Saturn 724+ CCD detector.[171]

7.5.2 High resolution data collection

In this thesis four datasets (**c.s.6**, **c.s.9**, **c.s.16** and **c.s.18**) were collected on the laboratory sources described above. The remaining five datasets (**c.s.3**, **c.s.5**, **c.s.10**, **c.s.11** and **c.s.17**) were collected on the small molecule single crystal diffraction beamline I19 at Diamond Light Source (also described above). For **c.s.3**, **c.s.10**, **c.s.11** and **c.s.17** datasets were collected at a wavelength of 0.6889 Å and using the bimorph mirrors set to provide a slightly defocused beam at the sample positions. The dataset for **c.s.5** was collected at 0.4859 Å and without the mirror focussing. Diffractometer control and data processing were carried out using CrystalClear-SM Expert 2.0[203]

In the synchrotron studies described in Chapter 4 the datasets were collected according to a calculated strategy to satisfy the criteria of 100% completeness with a 10-fold redundancy to a given resolution limit. These resolution limits were 0.45 Å for **c.s.10** and **c.s.11** and 0.35 Å in the case of **c.s.5,** where the shorter wavelength made higher resolution data accessible. Two detector swing angle settings were used for these calculated strategies – 30° and 70° for **c.s.11** and **c.s.10** and 30 and 60 degrees for **c.s.5**. Additional data were collected with a detector swing angle of 0° for **c.s.5** and **c.s.10** to ensure that a complete set of low angle reflections were collected and none were lost through peak saturation. This was planned for **c.s.11** as well but unfortunately the crystal was lost part way through the data collection and not all planned data were collected. A second dataset for this system was collected on a different and considerably smaller crystal however, due to its higher quality, the first, less complete than intended data set was used. Different exposure times (ranging between 0.5 seconds to 6 seconds exposure per degree), image widths (0.5 and 1°) and levels of attenuation were used for each of the detector settings and for each of the samples. The total data collection times were approximately 3 hours (cut short through crystal loss), 7 hours and 9 hours for **c.s.11**, **c.s.5** and **c.s.10** respectively.

For **c.s.3** and **c.s.17** (discussed in Chapter 5) a similar approach to that outlined above was employed. The maximum resolution was 0.46 Å and two swing angle detector settings of 30 and 60° used for the data collection.

A similar approach was again used when collecting data using laboratory sources (**c.s.6**, **c.s.9**, **c.s.16** and **c.s.18** in Chapters 4 and 5). Due to the resolution of the molybdenum radiation (0.71073 Å) the aim in each data collection was to achieve a maximum data resolution between 0.42 and 0.40 Å,

with a redundancy of around 6 and 100 % completeness. Each data collection took up to 72 hours to complete.

7.5.3 High resolution data processing

In each case data for the individual detector swing angle settings were integrated separately using EVALCCD[204] (**c.s.6**) or in CrystalClear 2.0/2.1 or 3.0 with d*trek[203] (remaining crystal structures).

The subsets were then scaled and merged together using SORTAV.[205]

7.5.4 Aspherical atom model refinement strategy

The multipole refinements were performed using the XD2006 software suite[193] with the core and valence scattering factors of all atoms derived from the Clementi-Roetti wave functions[55]. The refinement was performed on F for all reflections with $I > 3\sigma(I)$.

Initially, only the scale factor was refined against the whole resolution range of diffraction data. The positional and anisotropic displacement parameters of the non-hydrogen atoms were refined against the reflections with $\sin(\theta)/\lambda > 0.7$ Å^{-1}. The treatment of the hydrogen atoms in each crystal structure is discussed in the main body of this thesis, see Sections 4.3.1 and Sections 5.3.1.

Next, multipole populations were then refined with the level of multipole gradually increased from monopole up to the final level: hexadecapole for heteroatoms while those of carbon atoms were truncated at the octopole level. For the hydrogen atoms a single bond directed (z-directed) dipole population was refined. For non hydrogen atoms an expansion (κ) parameter was refined while κ' was fixed as 1.00. Chemically equivalent atoms were constrained to

share the same expansion/contraction (κ/κ') parameters while throughout the multipole refinement the κ/κ' parameters were fixed to values of $\kappa = \kappa' = 1.20$.

A consistent local coordinate axis system was used for all the structures. An overall charge neutrality constraint was applied to all of the structures in this study. The κ parameters were refined during the sequential multipole refinement and then fixed at the final stage of the refinement to allow for convergence of the other variables.

The X-ray data used in the refinement were truncated to an appropriate $\sin(\theta)/\lambda$ limit as outlined by Herbst-Irmer *et al.*[206] For all the crystal structures the Hirshfeld rigid bond test[59] was applied in the final stages of the refinement and the values of the difference of mean square displacement amplitudes (DMSDAs) used as a test of refinement quality.

Initially, unconstrained refinement of the nitro groups produced a chemically unreasonable range of $\nabla^2\rho(\mathbf{r}_{BCP})$ values. Woźniak and co-authors have previously observed similar behaviour in nitro groups.[81,169] Consequently *mm*2 symmetry constraints for the nitrogen atoms of these groups were imposed and the two oxygen atoms in each nitro group were constrained to be chemically identical.

Information about the way the disorder of the TMA cation in **c.s.11** can be found in Section 4.3.2, the modelling of sulfur in **c.s.16** and **c.s.18** in Section 5.3.1, and the Invariom refinement of **c.s.11** and **c.s.17** in Sections 4.3.2 and 5.3.1 respectively in the main body of this thesis.

7.6 Single crystal neutron diffraction

7.6.1 Details of SXD instrument at ISIS Neutron and Spallation Source

The neutron diffraction experiments were conducted on the time-of-flight (TOF) single crystal Laue diffractometer (SXD) (at the ISIS neutron spallation source (Chilton, UK)).[153] The CIFs for the structures refined using the neutron diffraction studies are found in the electronic Appendix (**c.s.5_neutron** and **c.s.9_neutron**).

7.6.2 Details of sample preparation, data collection, processing and refinement

The data were collected at 100K for consistency with the X-ray diffraction data. For **c.s.9** two crystals (2.0 x 1.0 x 0.8 mm and 1.5 x 1.0 x 1.0 mm) were mounted onto a sample pip using aluminium tape while for **c.s.5** one crystal (7.0 x 1.0 x 0.8 mm) was again mounted onto a sample pip using aluminium tape. The pips were attached to a centre stick, the respective centre sticks were inserted into a pre-cooled closed-cycle refrigerator (CCR) already mounted on the SXD beamline. These crystals were grown analogously to those used in the X-ray diffraction studies, however crystal growth was conducted in a fridge to slow-down the process of crystallisation. The crystals of **c.s.9** were mounted in differing orientations and the data for the two separate crystal lattices deconvoluted and subsequently integrated using the SXD2001[207] program and the structures refined using SHELXL[208] with the single batch of wavelength and extinction-correction reflections. A numerical absorption correction was applied, with the wavelength dependent linear absorption coefficient (μ) calculated as $4.546 + 0.020\ \lambda\ cm^{-1}$ for **c.s.9** and $4.1083 + 0.058\ \lambda\ cm^{-1}$ for **c.s.5**.

Appendices

A.1 NMR titration and Job plots for receptors in Chapter 3 and Chapter 5

A.1.1 Titration of 1,3-bis(2-nitrophenyl)urea (12) with TMA acetate

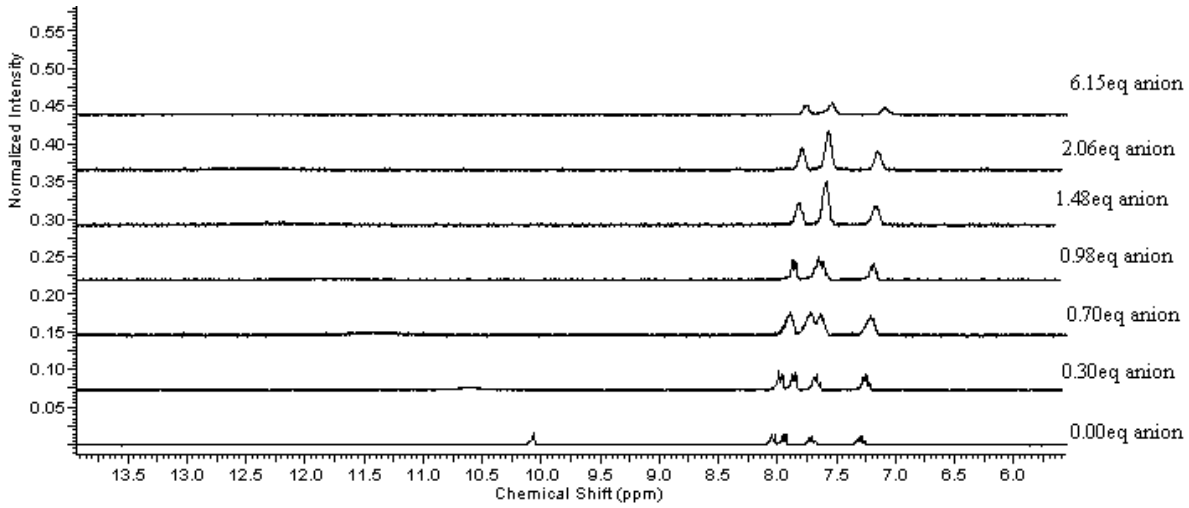

A.1.1: Stack plot of titration of receptor **12** with TMA acetate.

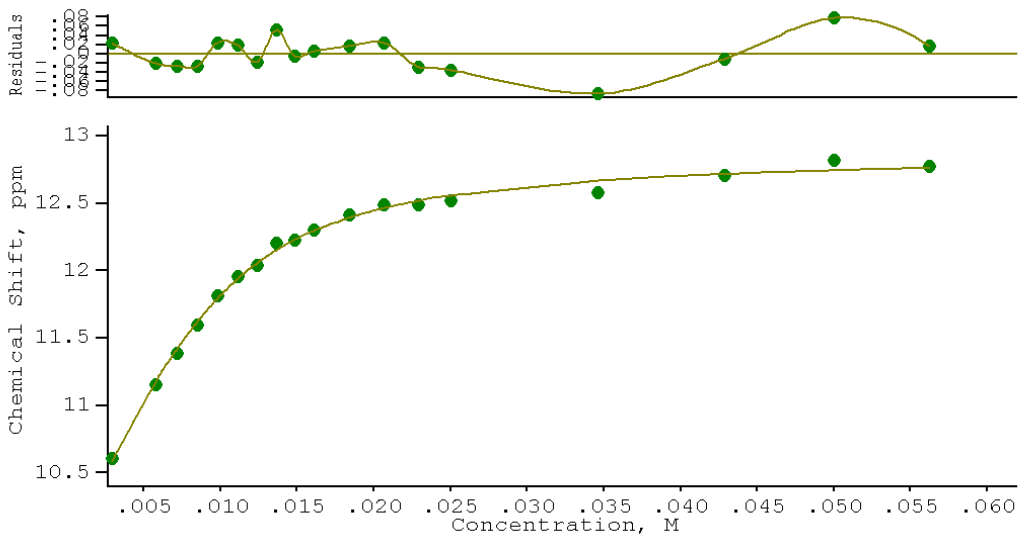

K_{ass} = 514 M^{-1} Error = 9%

A.1.2: Fit plot of titration of receptor **12** with TMA acetate.

A.1.2 Titration of 1,3-bis(2-nitrophenyl)urea (12) with TBA chloride

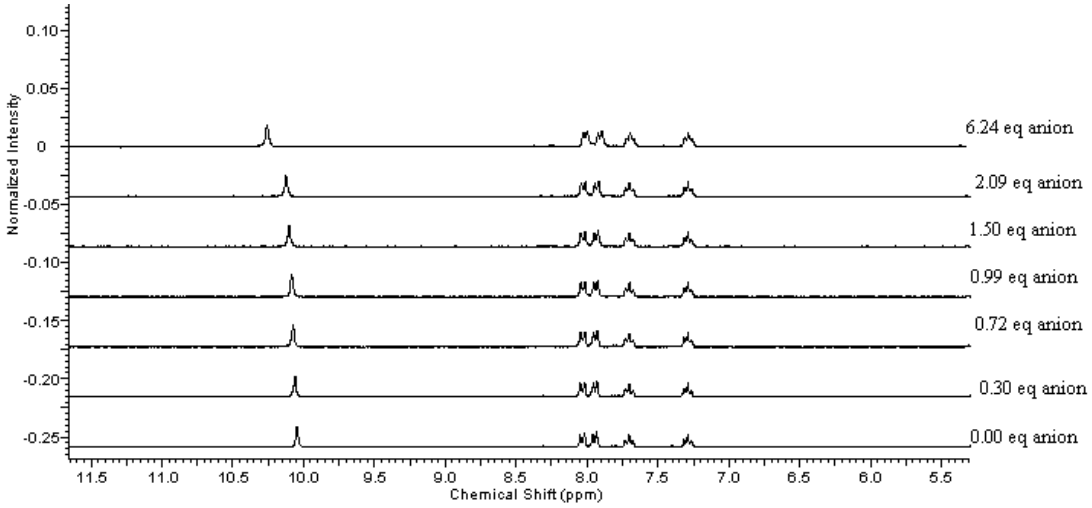

A.1.3: Stack plot of titration of receptor **12** with TBA chloride.

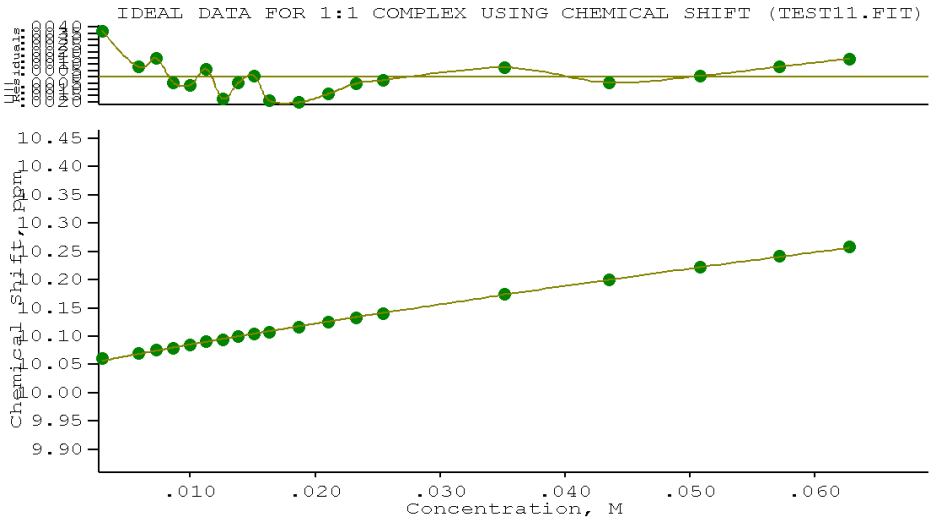

K_{ass} < 10 M^{-1} Error N. A.

A.1.4: Fit plot of titration of receptor **12** with TBA chloride.

A.1.3 Titration of 1,3-bis(2-nitrophenyl)urea (12) with TBA fluoride

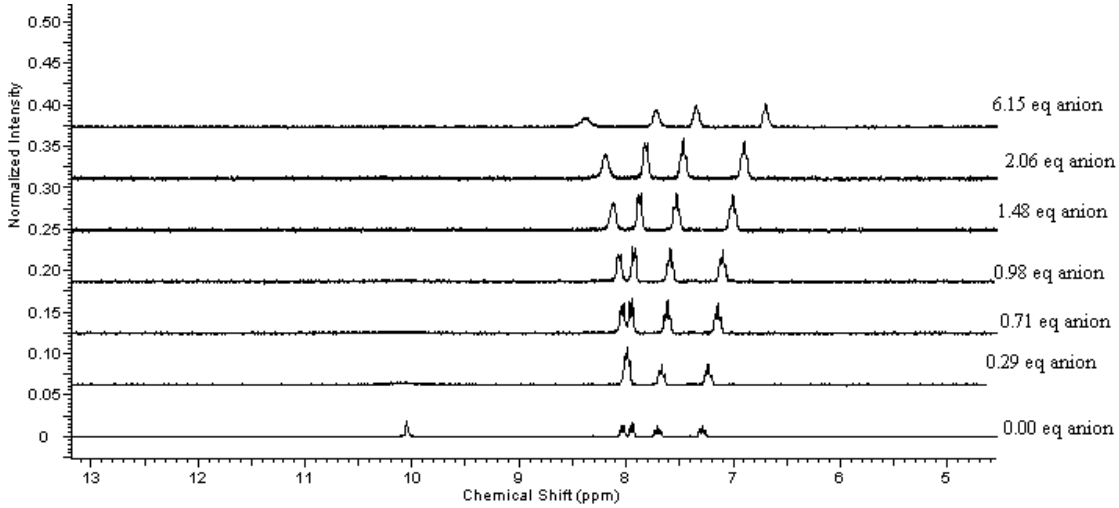

A.1.5: Stack plot of titration of receptor **12** with TBA fluoride.

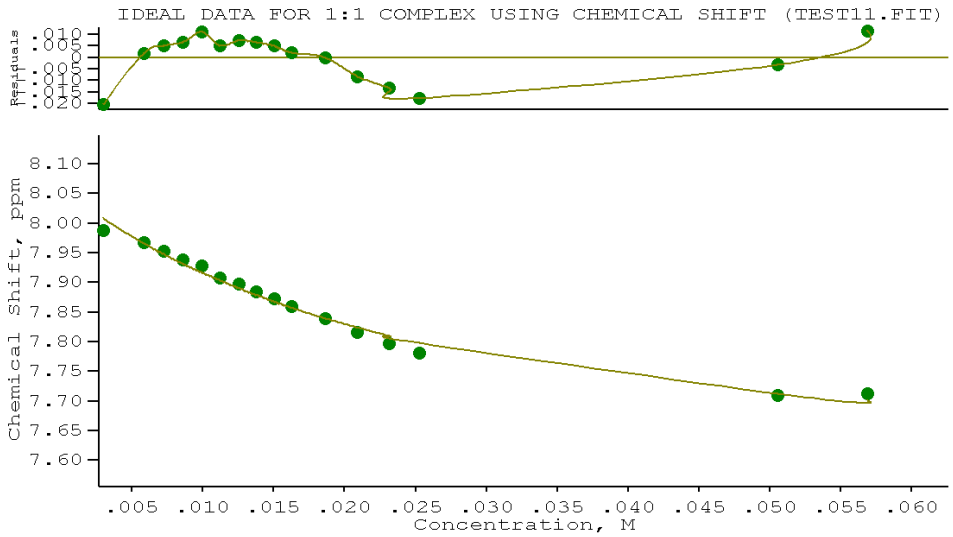

K_{ass} < 61 M^{-1} Error = 15%

A.1.6: Fit plot of titration of receptor **12** with TBA fluoride.

A.1.4 Titration of 1,3-bis(3-nitrophenyl)urea (13) with TMA acetate

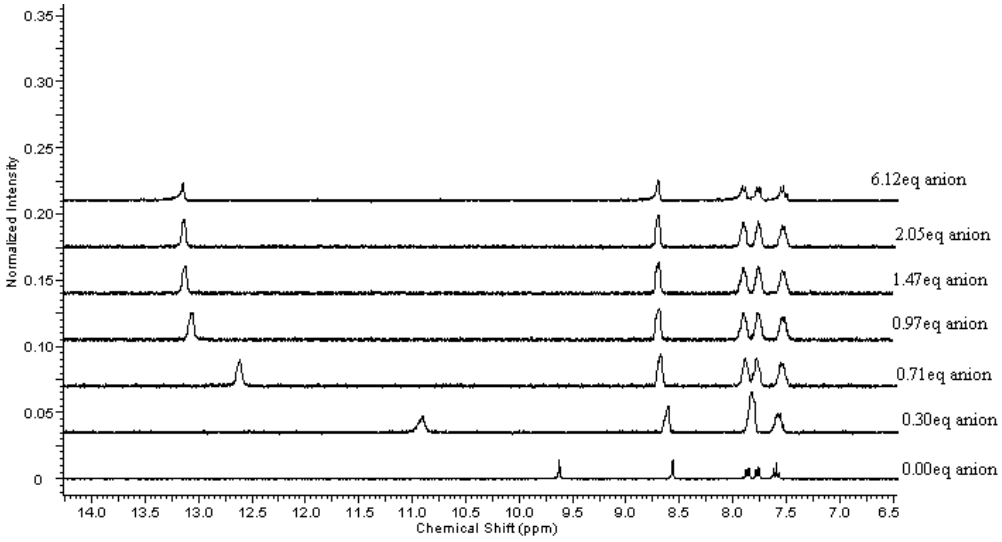

A.1.7: Stack plot of titration of receptor **13** with TMA acetate.

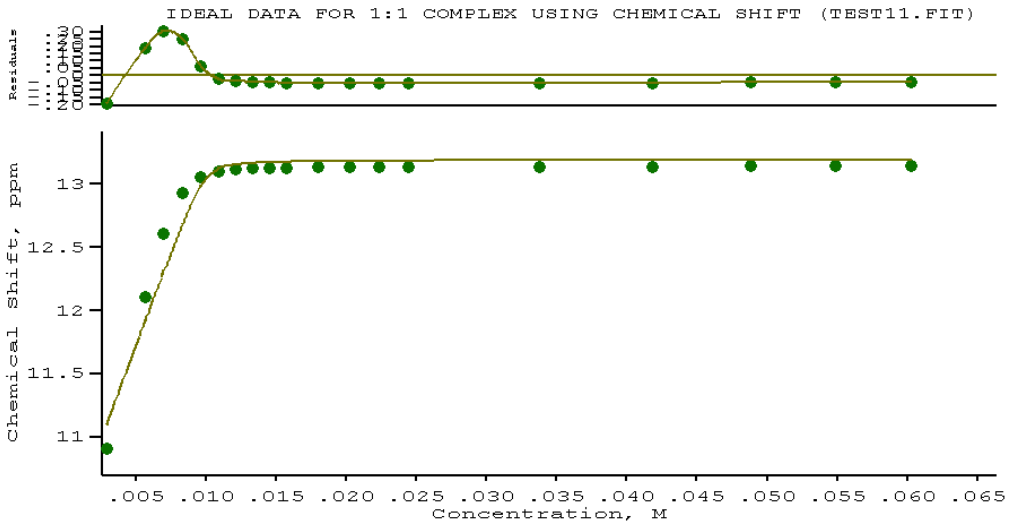

$K_{ass} > 10^4\ M^{-1}$ Error N. A.

A.1.8: Fit plot of titration of receptor **13** with TMA acetate.

A.1.5 Titration of 1,3-bis(3-nitrophenyl)urea (13) with TBA chloride

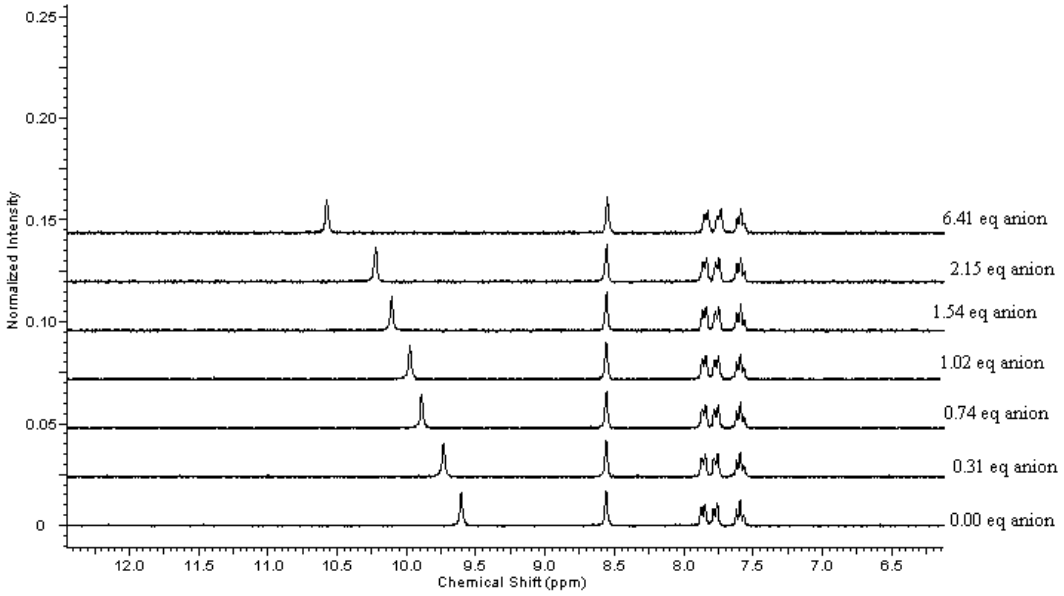

A.1.9: Stack plot of titration of receptor **13** with TBA chloride.

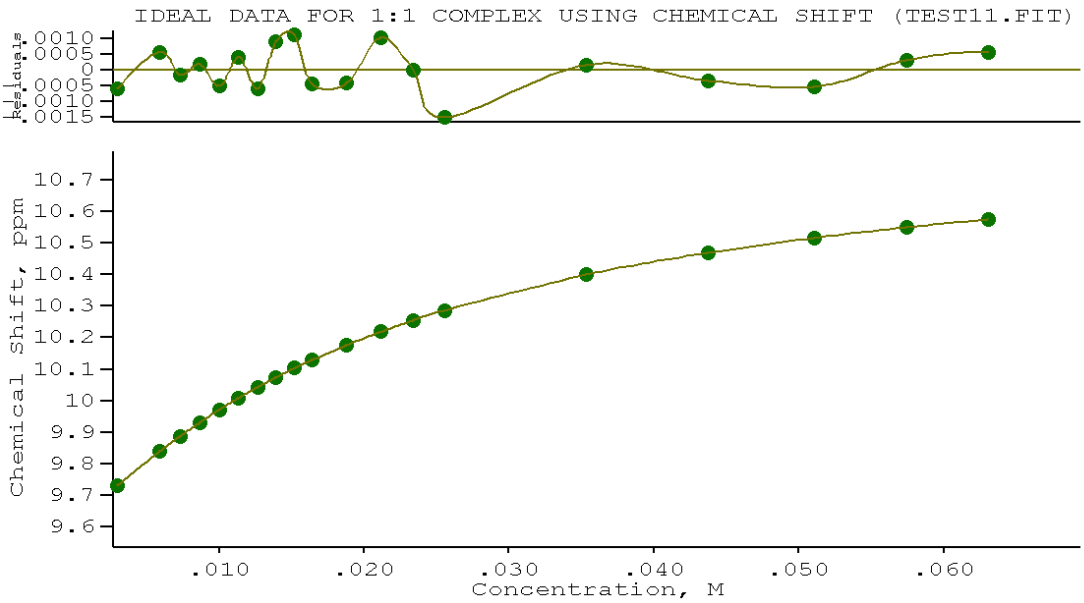

K_{ass} = 56 M^{-1} Error = 0.4%

A.1.10: Fit plot of titration of receptor **13** with TBA chloride.

A.1.6 Titration of 1,3-bis(3-nitrophenyl)urea (13) with TBA fluoride

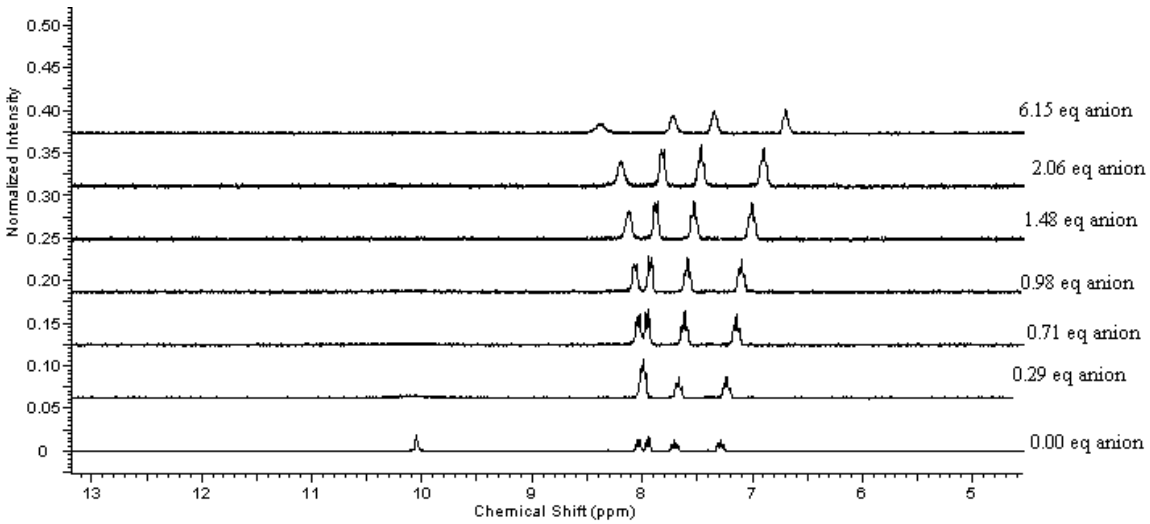

A.1.11: Stack plot of titration of receptor **13** with TBA fluoride.

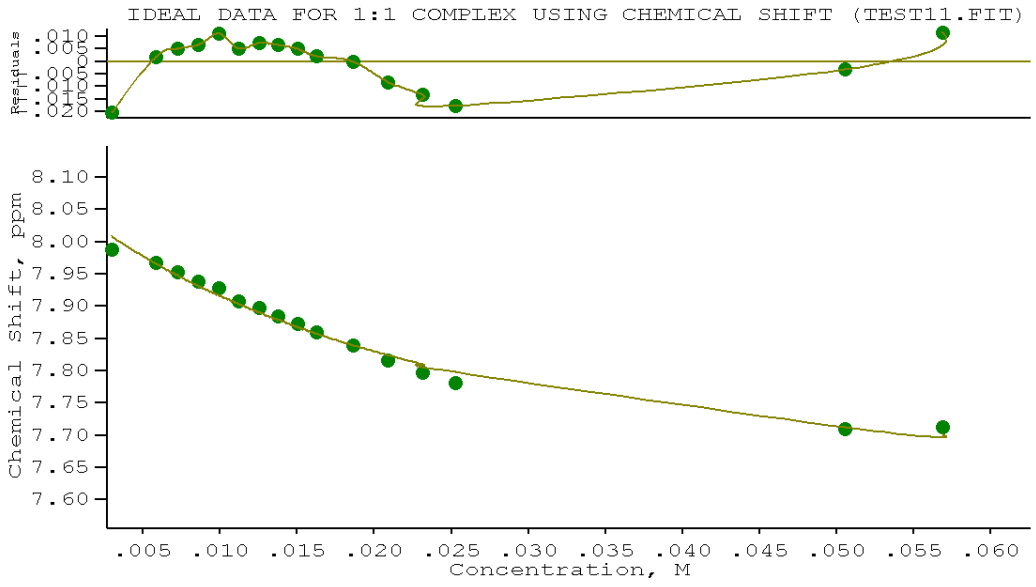

K_{ass} = 182 M^{-1} Error = 8%

A.1.12: Fit plot of titration of receptor **13** with TBA fluoride.

A.1.7 Titration of 1,3-bis(4-nitrophenyl)urea (14) with TMA acetate

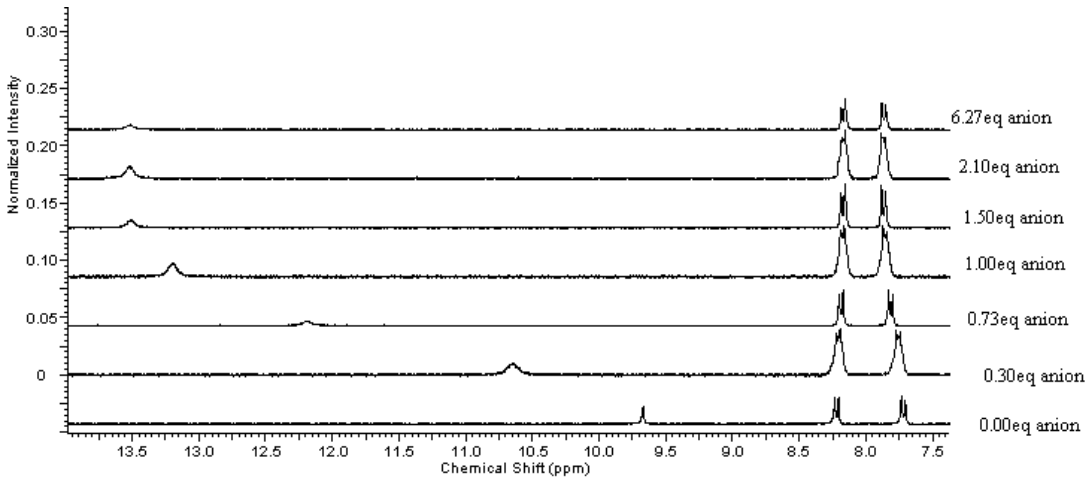

A.1.13: Stack Plot of titration of receptor **14** with TMA acetate.

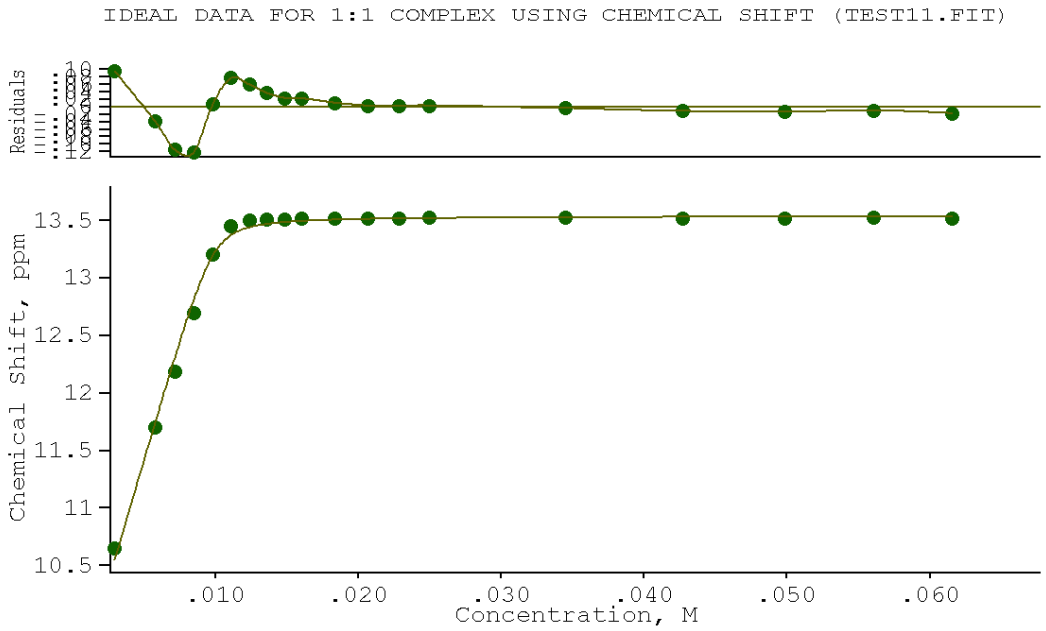

$K_{ass} > 10^4\ M^{-1}$ Error N. A.

A.1.14: Fit Plot for titration of receptor **14** with TMA acetate.

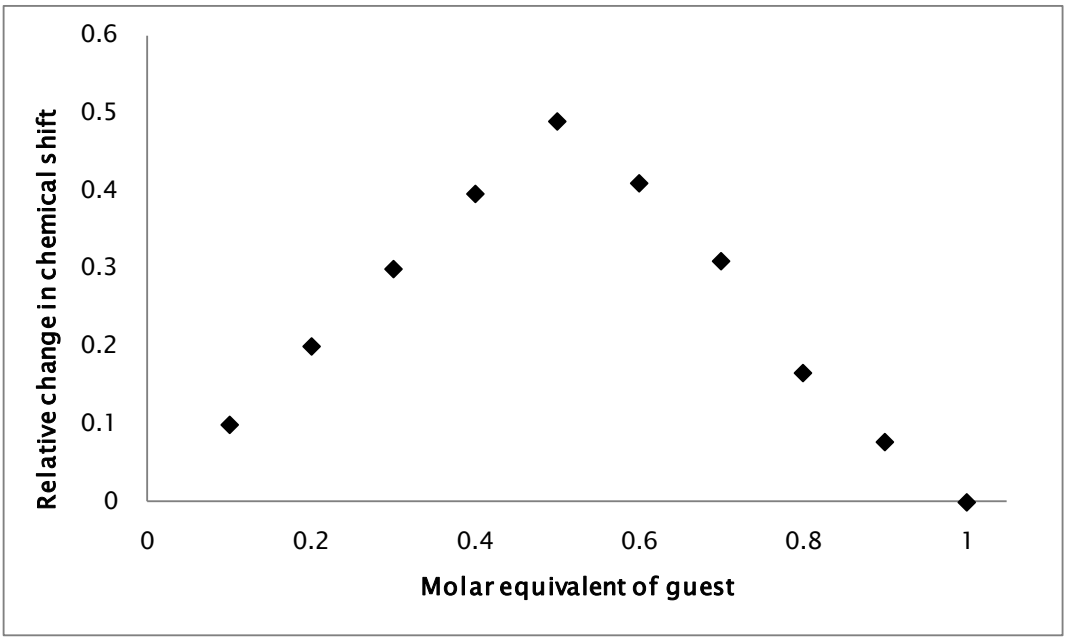

A.1.15: Job plot of receptor **14** with TMA acetate showing 1:1 stoichiometry.

A.1.8 Titration of 1,3-bis(4-nitrophenyl)urea (14) with TBA chloride

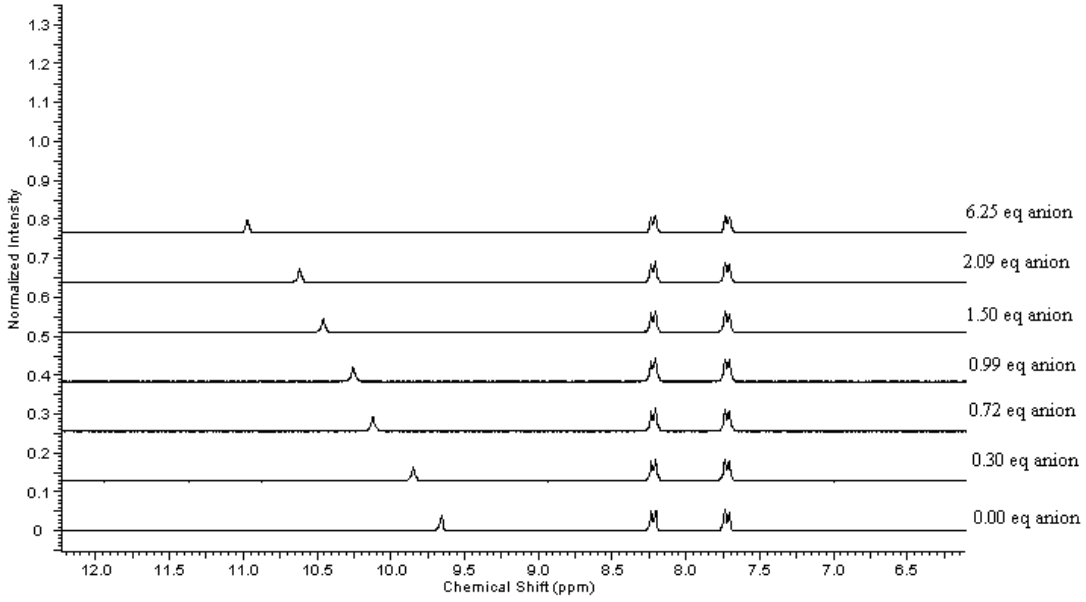

A.1.16: Stack plot of titration of receptor **14** with TBA chloride.

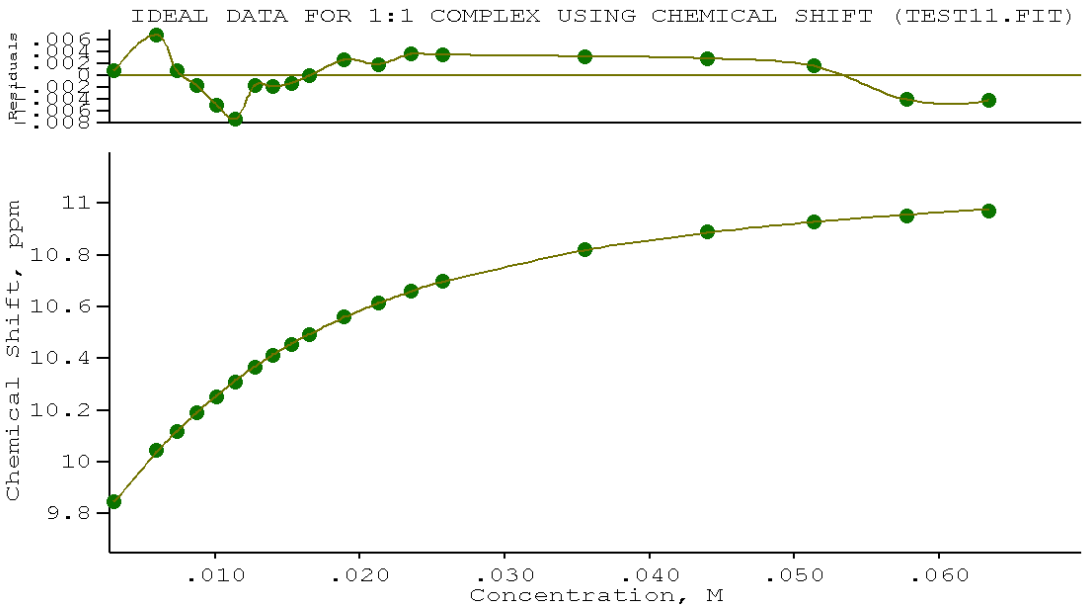

K_{ass} = 118 M^{-1} Error = 1.5%

A.1.17: Fit plot of titration of receptor **14** with TBA chloride.

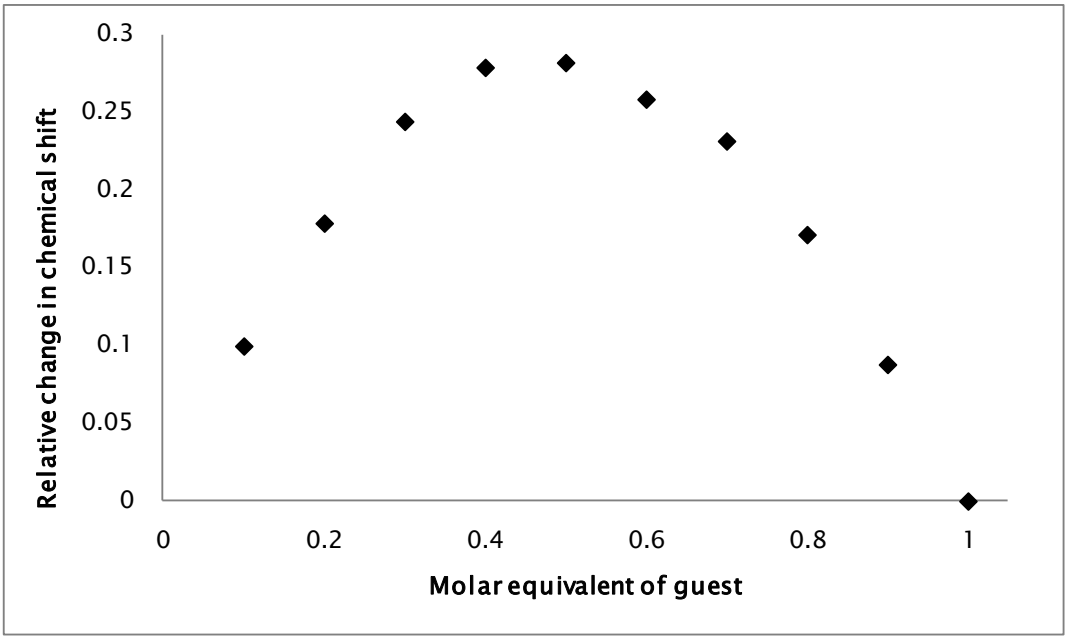

A.1.18: Job plot of receptor **14** with TBA chloride showing 1:1 stoichiometry.

A.1.9 Titration of 1,3-bis(4-nitrophenyl)urea (14) with TBA fluoride

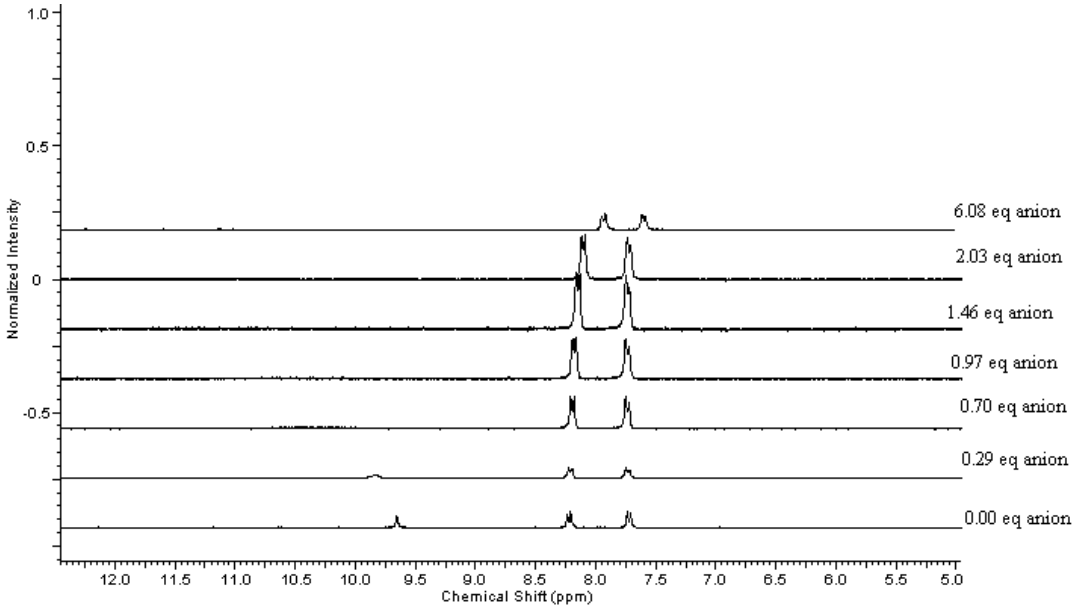

A.1.19: Stack plot of titration of receptor **14** with TBA fluoride.

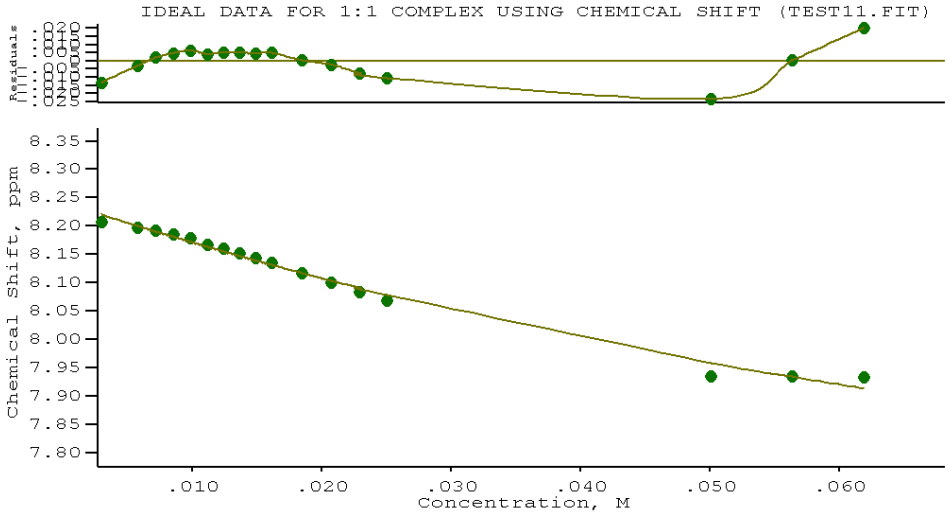

K_{ass} < 10 M^{-1} Error N. A.

A.1.20: Fit plot of titration of receptor **14** with TBA fluoride.

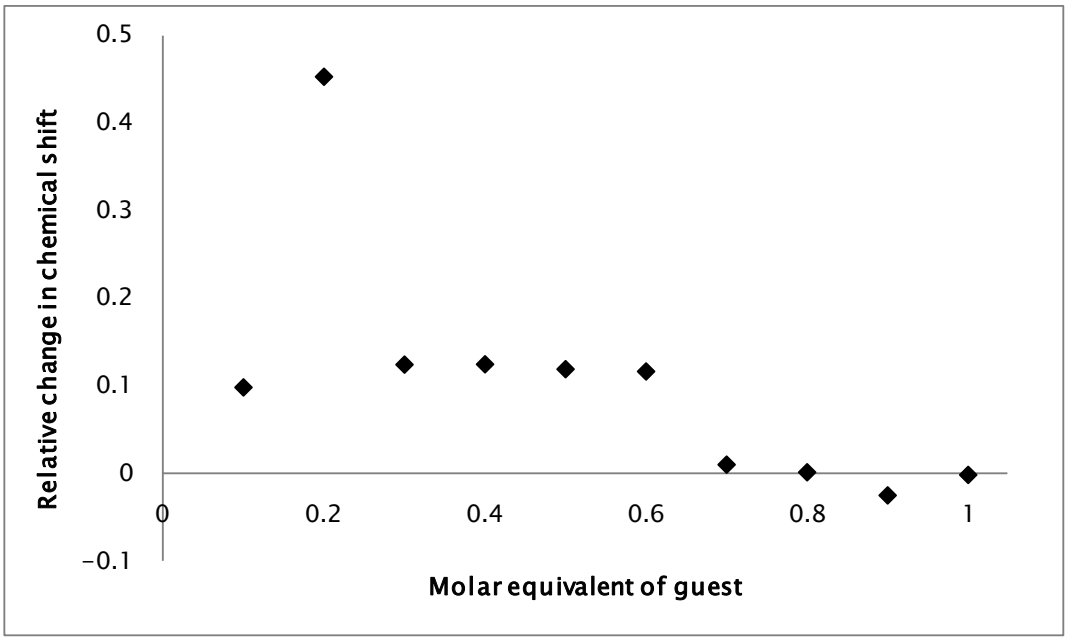

A.1.21: Job plot of receptor **14** with TBA fluoride suggesting deprotonation.

A.1.10 Titration of 1,3-bis(4-nitrophenyl)urea (14) with TBA hydroxide

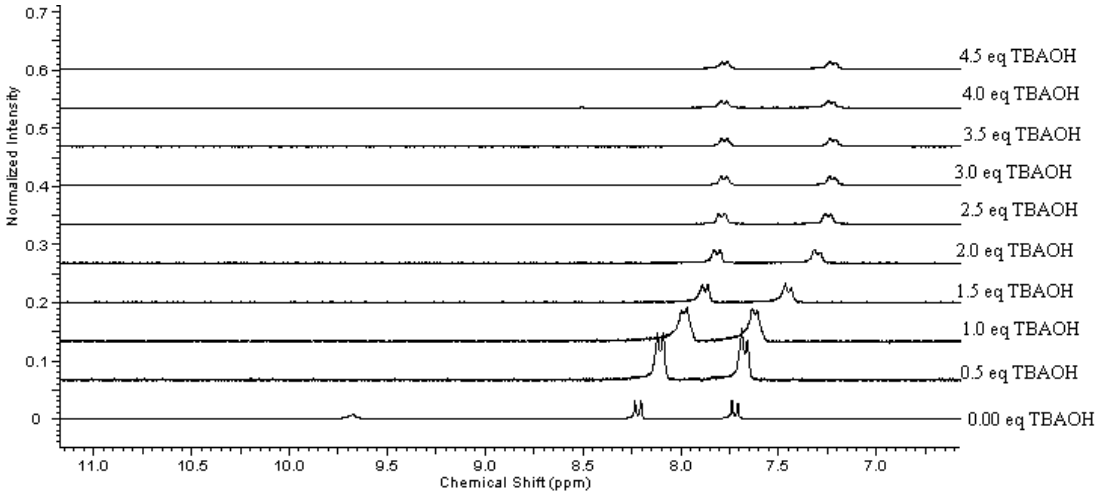

A.1.22: Stack plot of titration of receptor **14** with TBA hydroxide.

A.1.11 Titration of 1,3-bis(3,5-dinitrophenyl)urea (15) with TMA acetate

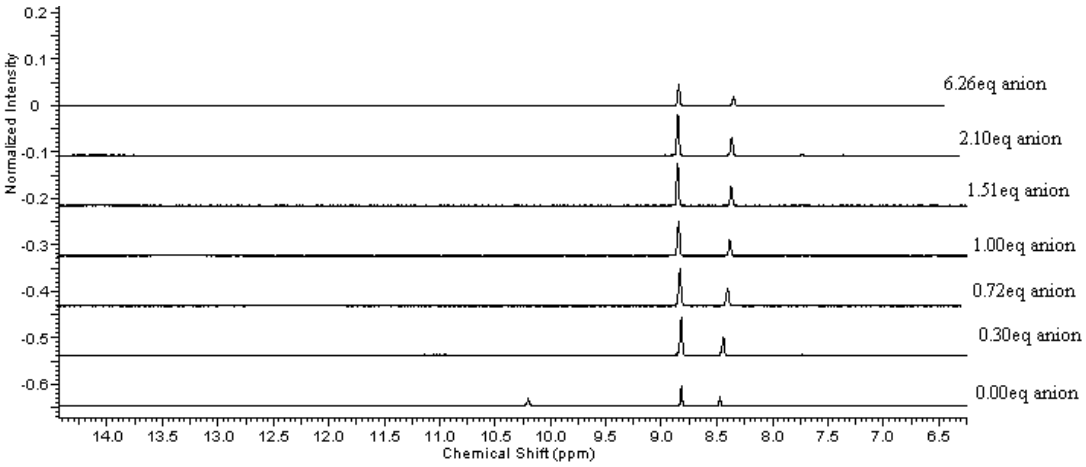

A.1.23: Stack plot of titration of receptor **15** with TMA acetate.

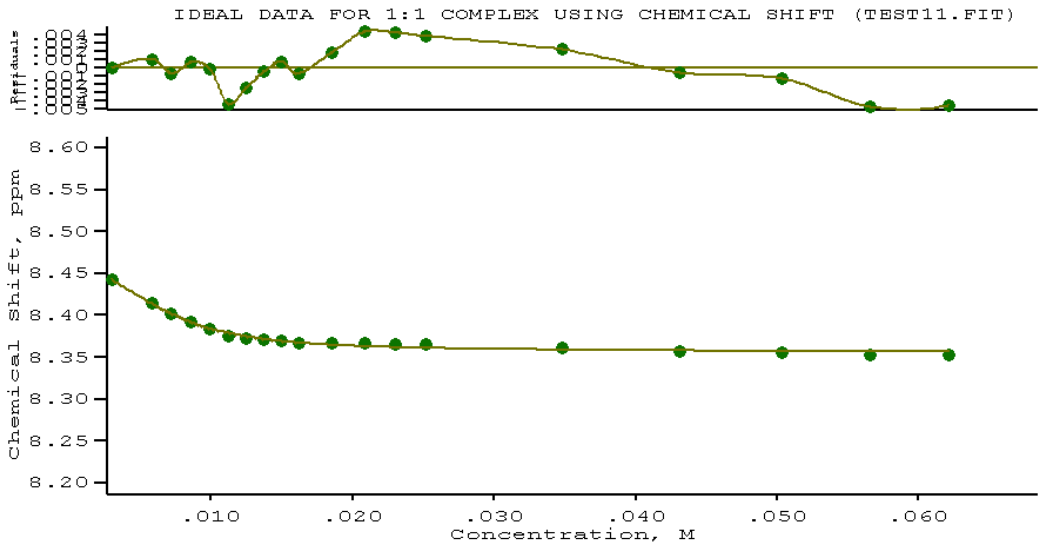

K_{ass} = 1239 M^{-1} Error = 2%

A.1.24: Fit plot of titration of receptor **15** with TMA acetate.

A.1.12 Titration of 1,3-bis(3,5-dinitrophenyl)urea (15) with TBA hydroxide

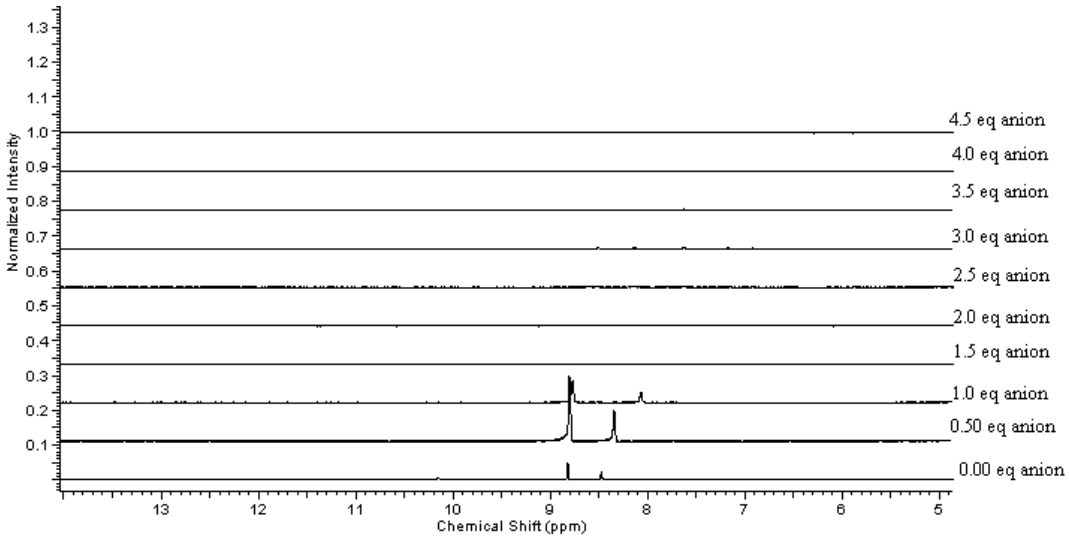

A.1.25: Stack plot of titration of receptor **15** with TBA hydroxide.

A.1.13 Titration of 1,3-bis(4-nitrophenyl)thiourea (18) with TBA chloride

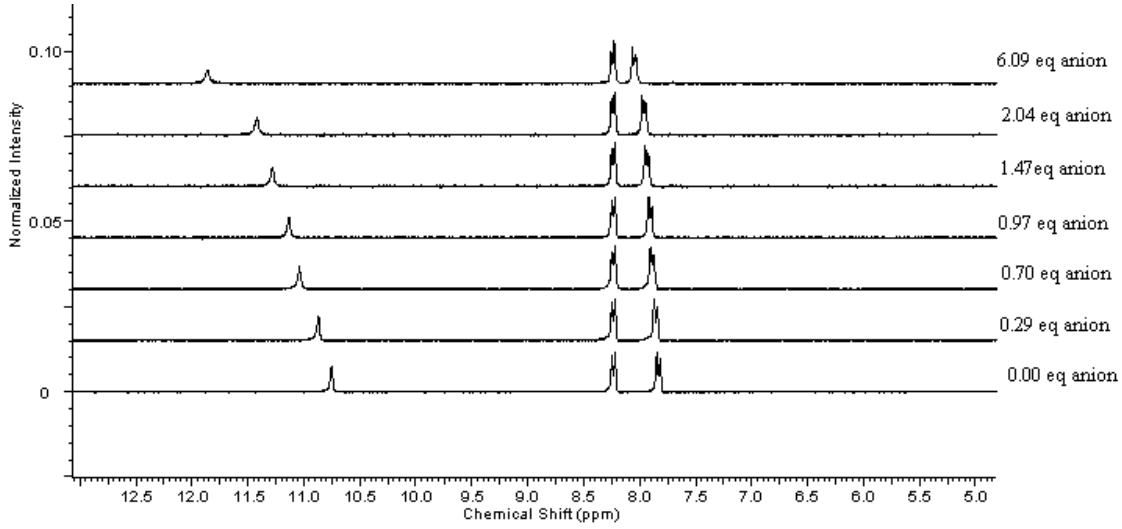

A.1.26: Stack plot of titration of receptor **18** with TBA chloride.

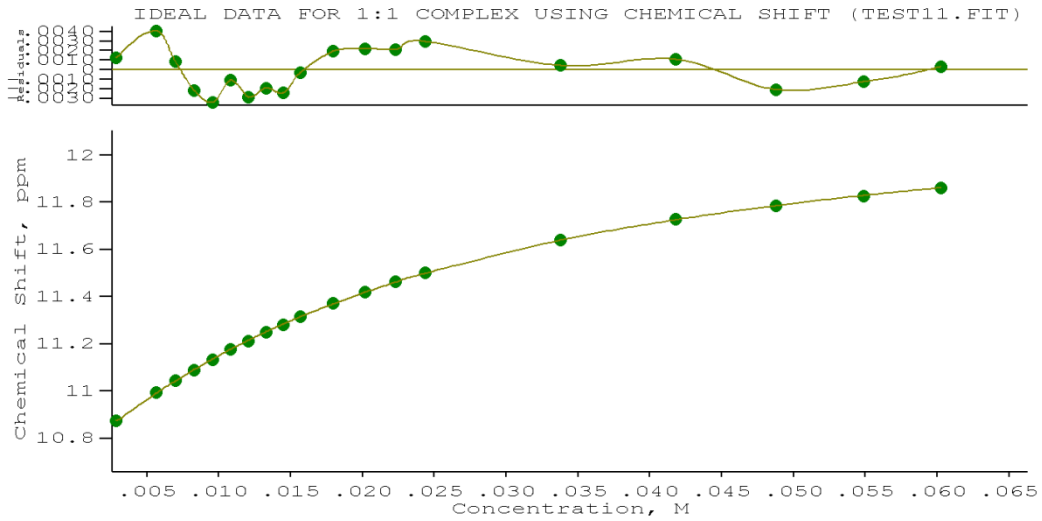

K_{ass} = 50 M^{-1} Error = 1%

A.1.27: Fit plot of titration of receptor **18** with TBA chloride.

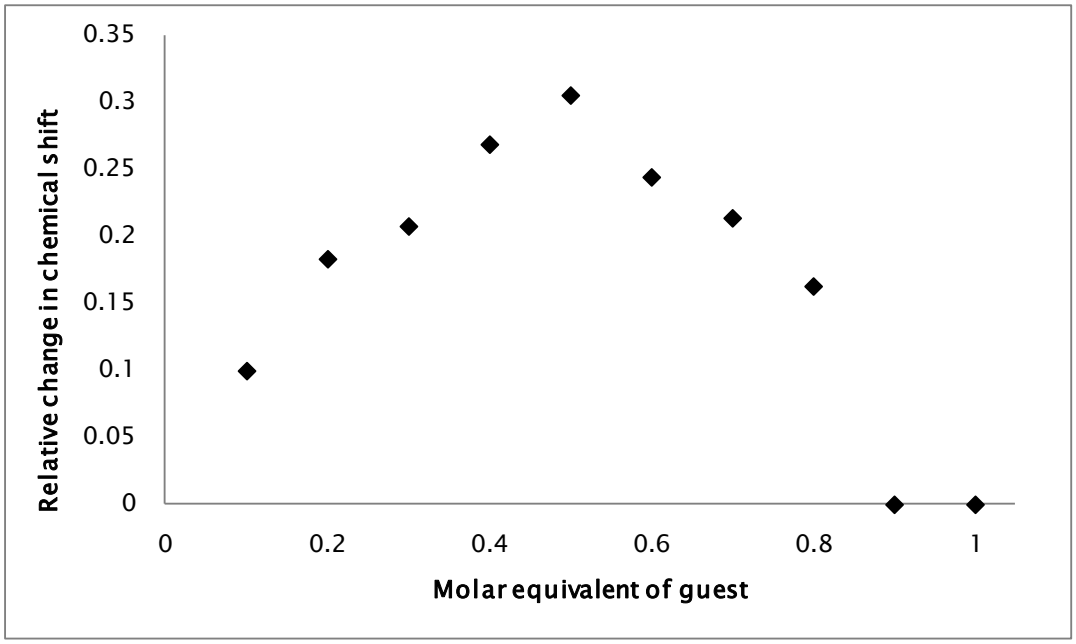

A.1.28: Job plot of receptor **18** with TBA chloride.

A.1.14 Titration of 1-(4-nitrophenyl)-3-phenylurea (23) with TBA chloride

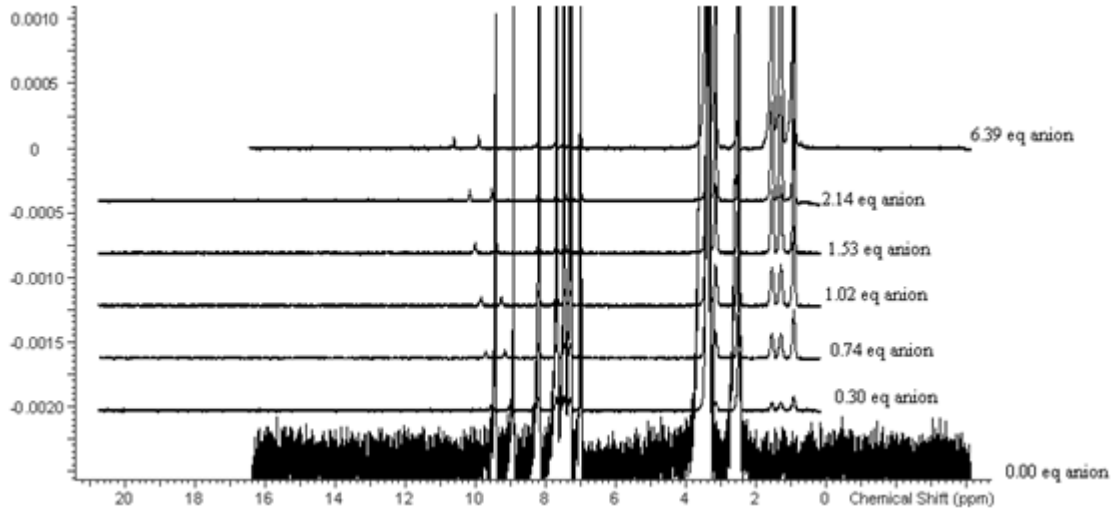

A.1.29: Stack plot of titration of receptor **23** with TBA chloride.

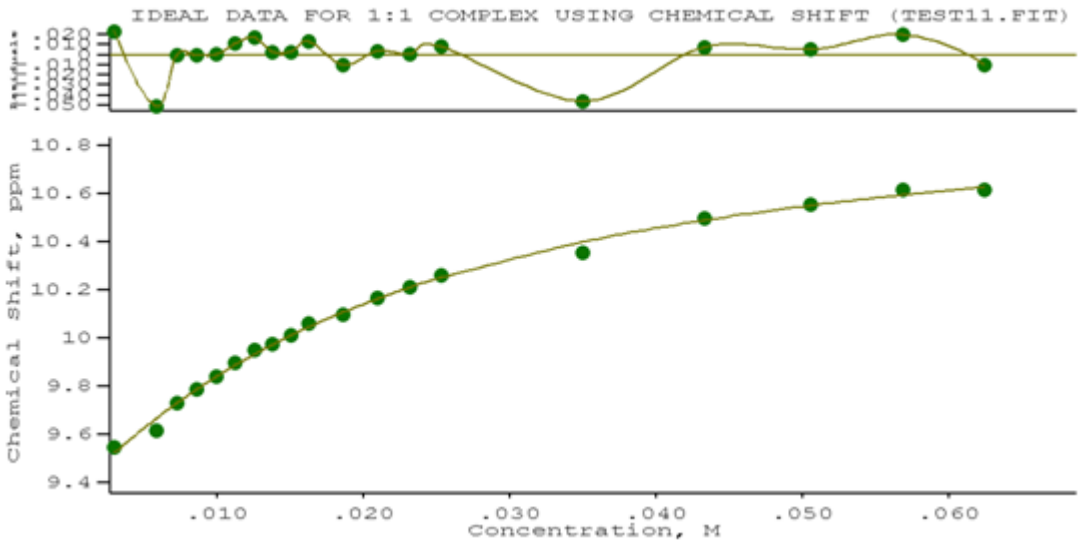

K_{ass} = 58.0 M^{-1} Error = 9%

A.1.30: Fit plot of titration of receptor **23** with TBA chloride.

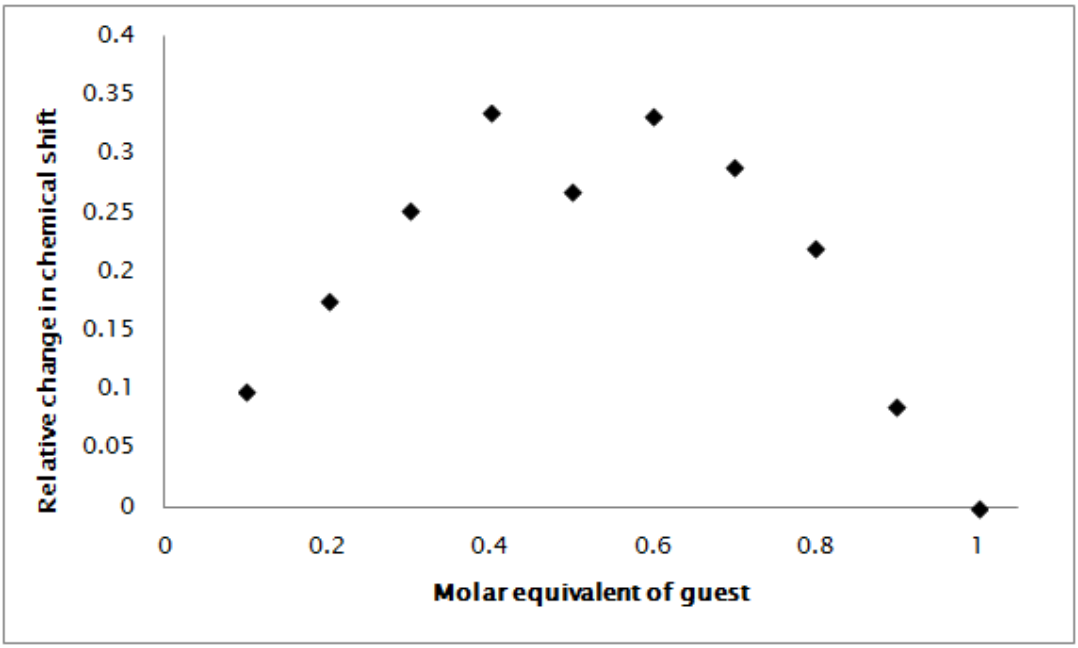

A.1.31: Job plot of receptor **23** with TBA chloride.

A.1.15 Titration of 1-(4-nitrophenyl)-3-phenylthiourea (24) with TBA chloride

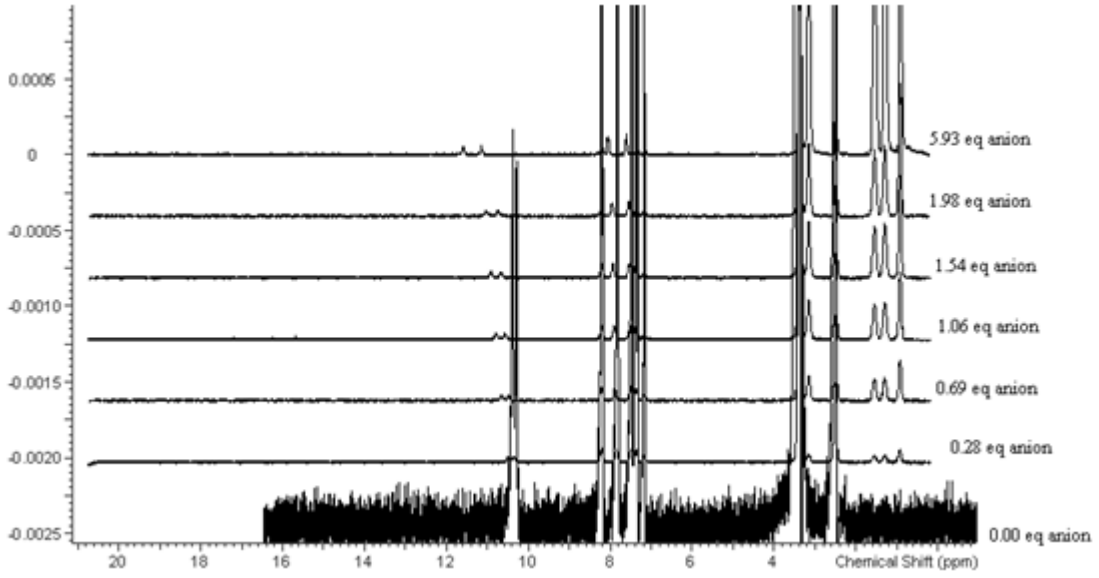

A.1.32: Stack plot of titration of receptor **24** with TBA chloride.

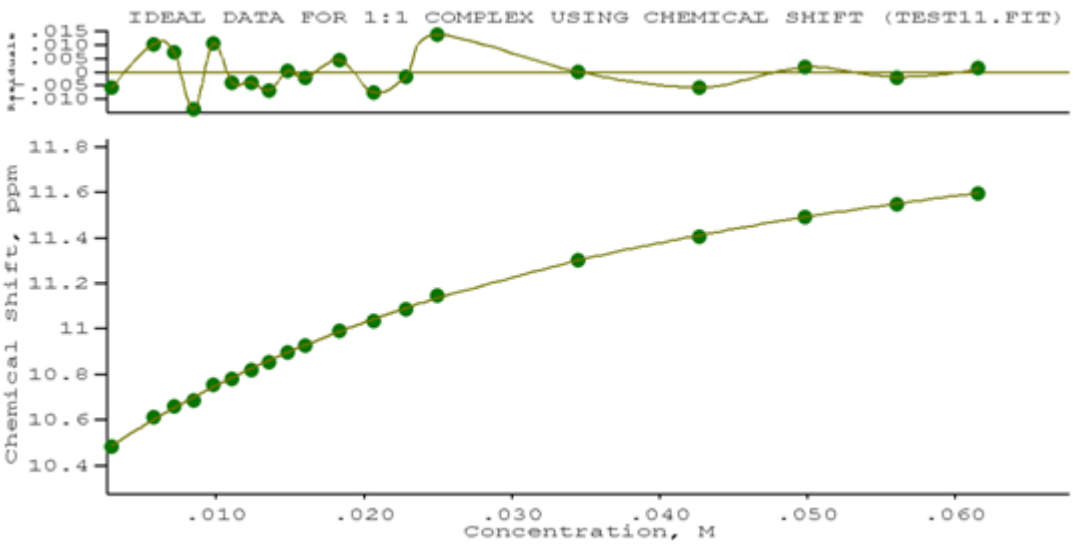

K_{ass} > 32 M^{-1}, Error 4%

A.1.33: Fit plot of titration of receptor **24** with TBA chloride.

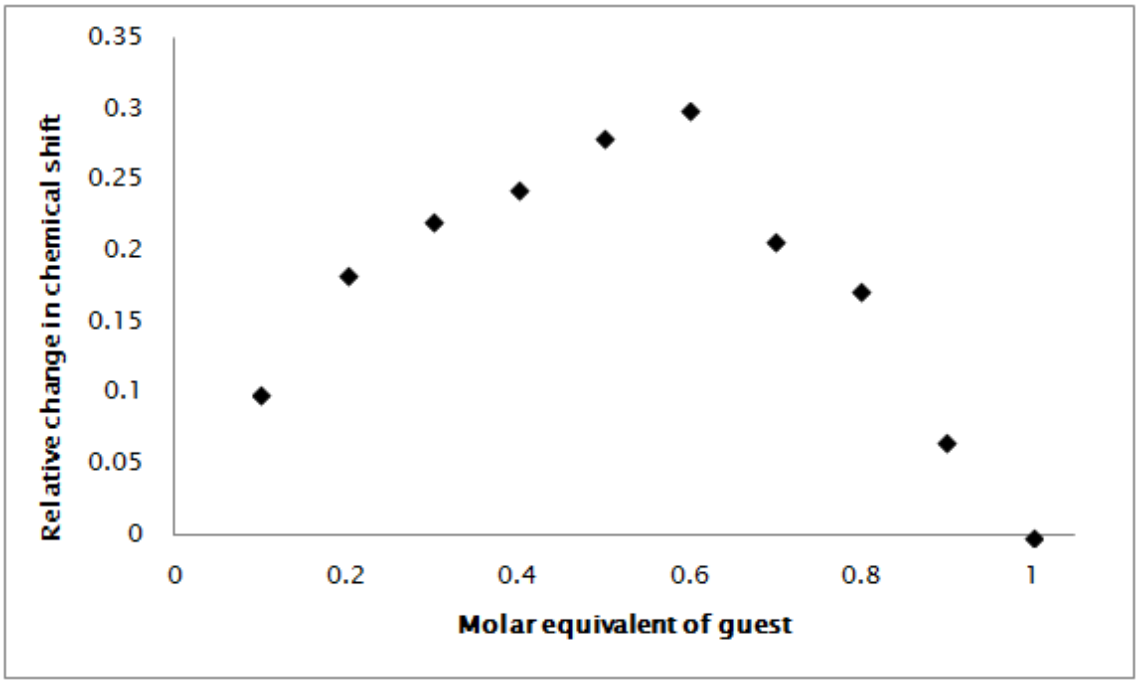

A.1.34 Job plot of receptor **24** with TBA chloride.

A.2 Hirshfeld surface plots of anion–receptor complexes in Chapter 3

A.2.1 Hirshfeld surface and fingerprint plot of receptor in c.s.5

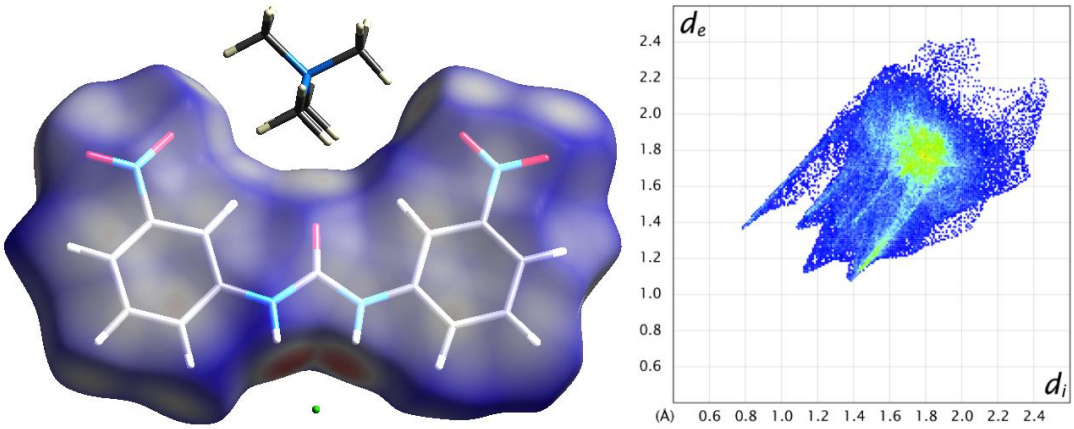

A.2.1: Hirshfeld surface plot and fingerprint for receptor molecule of **c.s.5**.

A.2.2 Hirshfeld surface and fingerprint plot of receptor in c.s.6

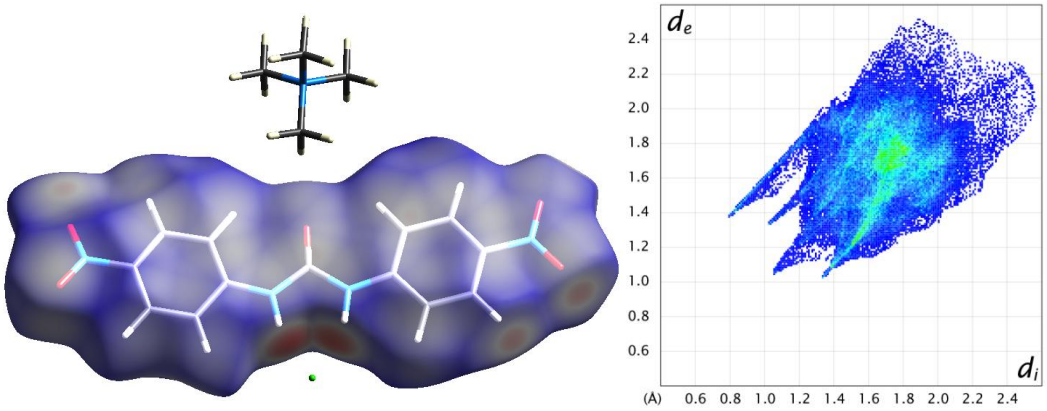

A.2.2: Hirshfeld surface plot and fingerprint for receptor molecule of **c.s.6**.

A.2.3 Hirshfeld surface and fingerprint plot of receptor in c.s.8

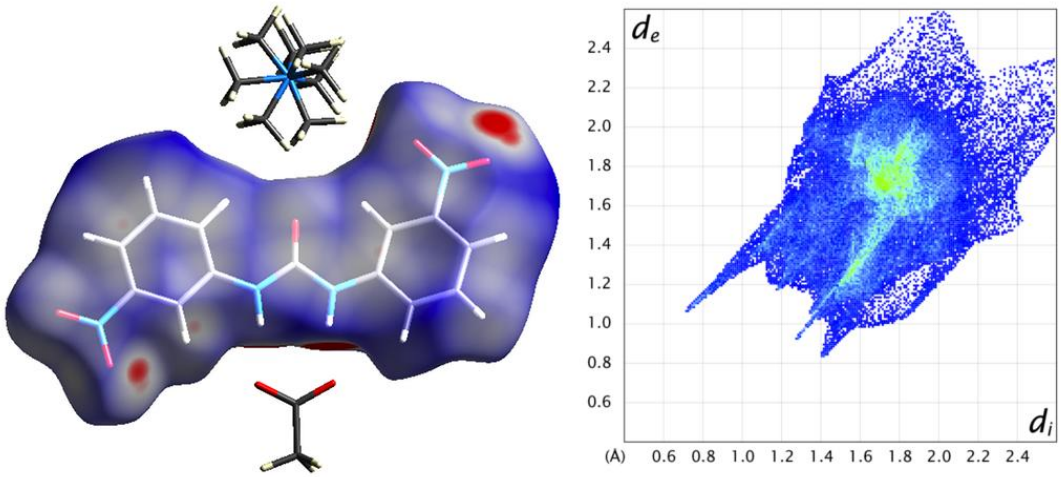

A.2.3: Hirshfeld surface plot and fingerprint for receptor molecule of **c.s.8**.

A.2.4 Hirshfeld surface and fingerprint plot of receptor in c.s.9

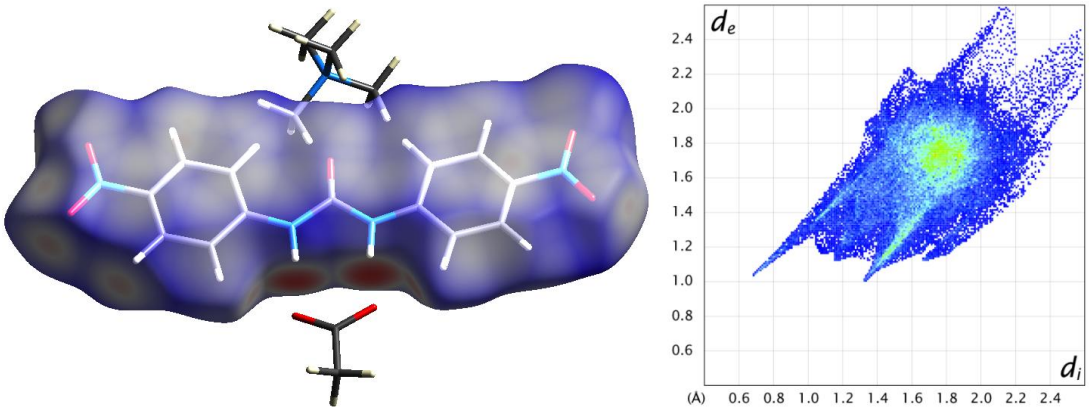

A.2.4: Hirshfeld surface plot and fingerprint for receptor molecule of **c.s.9**.

A.2.5 Hirshfeld surface and fingerprint plot of receptor in c.s.10

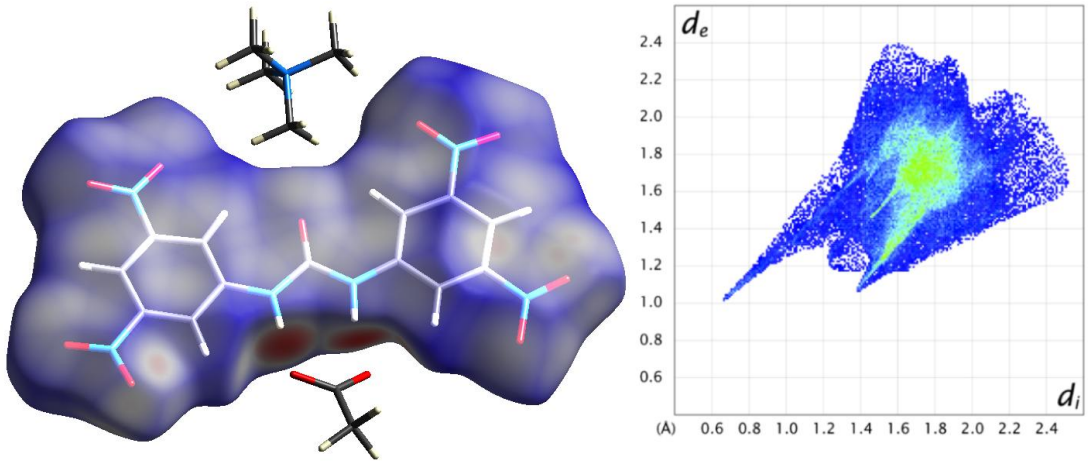

A.2.5: Hirshfeld surface plot and fingerprint for receptor molecule of **c.s.10**.

A.2.6 Hirshfeld surface and fingerprint plot of receptor in c.s.11

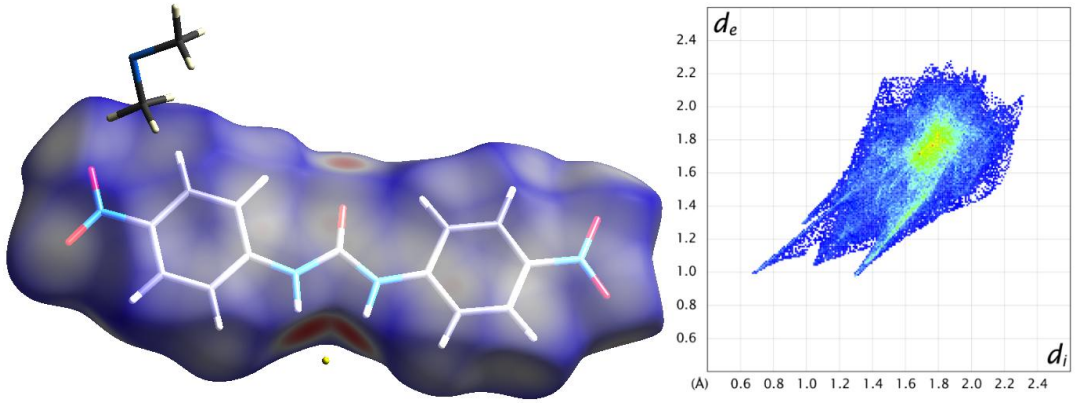

A.2.6: Hirshfeld surface plot and fingerprint for receptor molecule of **c.s.11**.

A.3 Residual density plots and RDA analysis of Chapter 4 and Chapter 5 crystal structures multipole modelling

Residual electron density plots are drawn in the plane of the receptor molecule (except Figure A.3.12 which is the plane of the TMA group) after full multipole refinement. Positive electron density is shown in red and negative electron density in blue. Zero-level contours are dashed. Contours are at 0.1 *e* Å^{-3} with cut-off at 0.9 *e* Å^{-3}.

Fractal dimension distribution plots show the residual density distribution across the unit cell. The Gaussian nature of the distribution suggests that the refined multipole model is adequate.

A.3.1 Residual density analysis of c.s.3

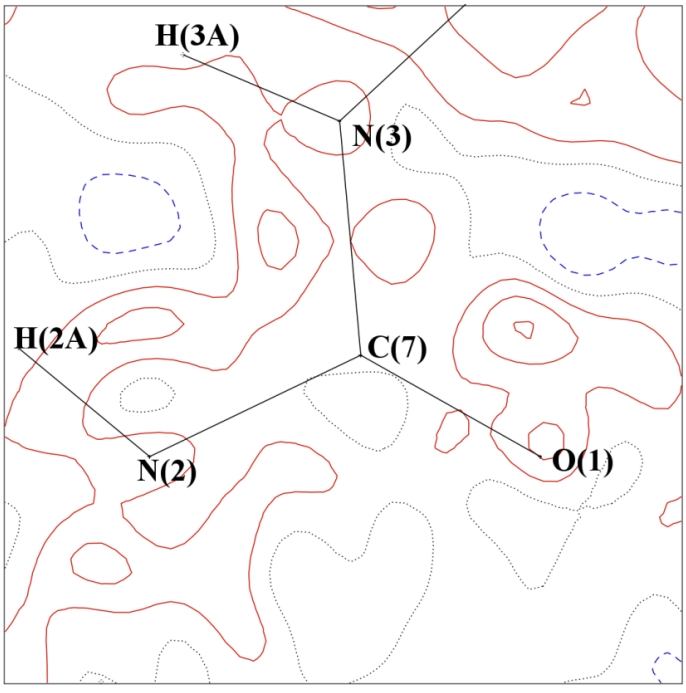

A.3.1: Residual electron density plot of **c.s.3**.

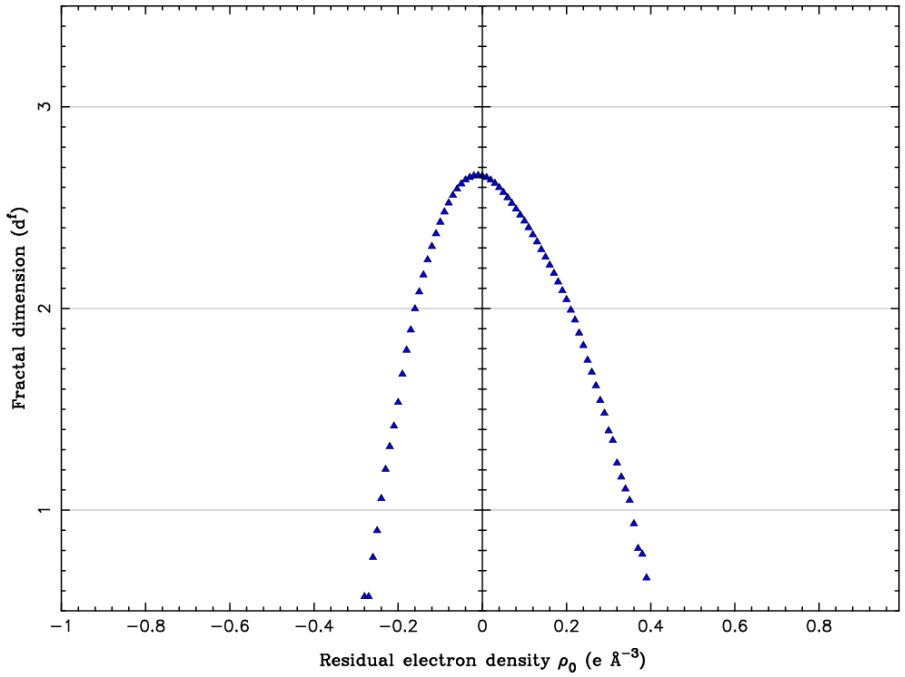

A.3.2: Fractal dimension distribution of residual density plot of **c.s.3**.

A.3.2 Residual density analysis of c.s.5

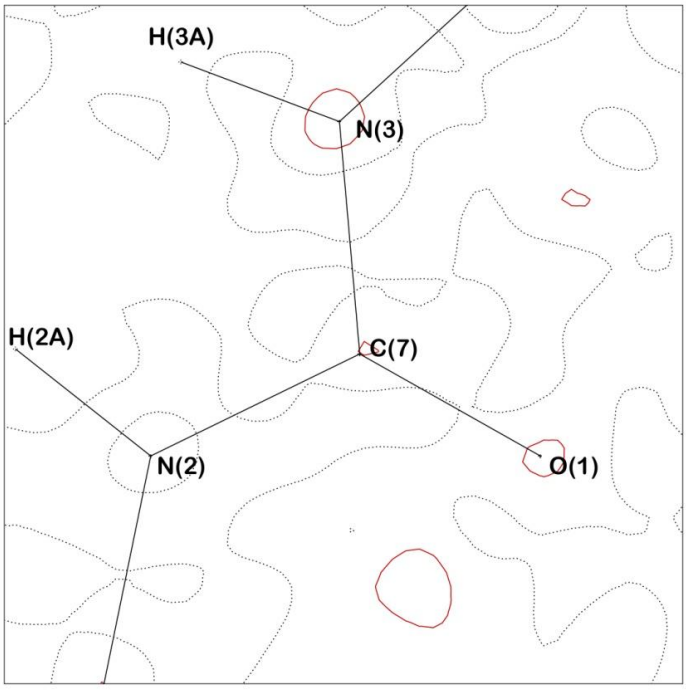

A.3.3: Residual electron density plot of **c.s.5**.

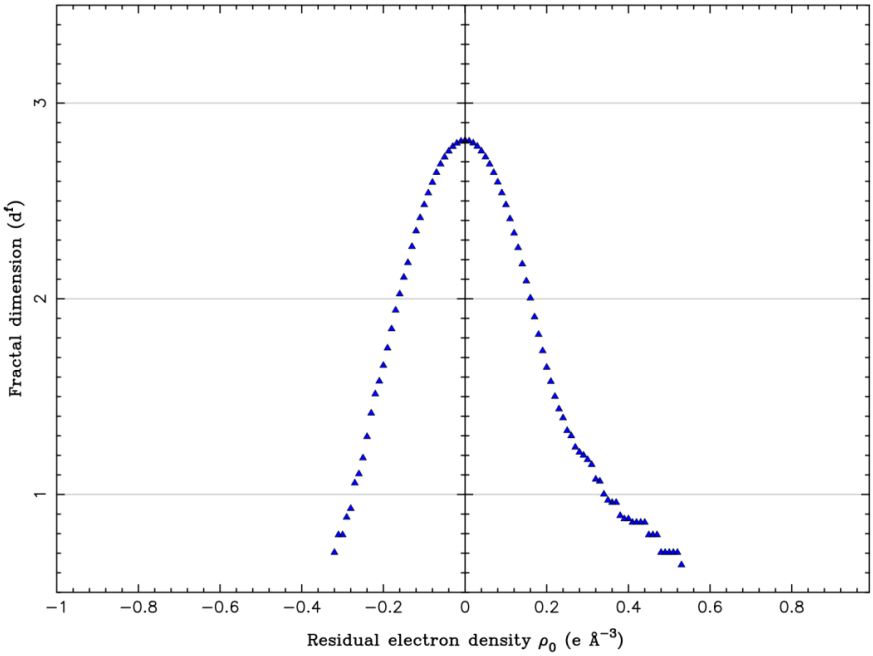

A.3.4: Fractal dimension distribution of residual density plot of **c.s.5**.

A.3.3 Residual density analysis of c.s.6

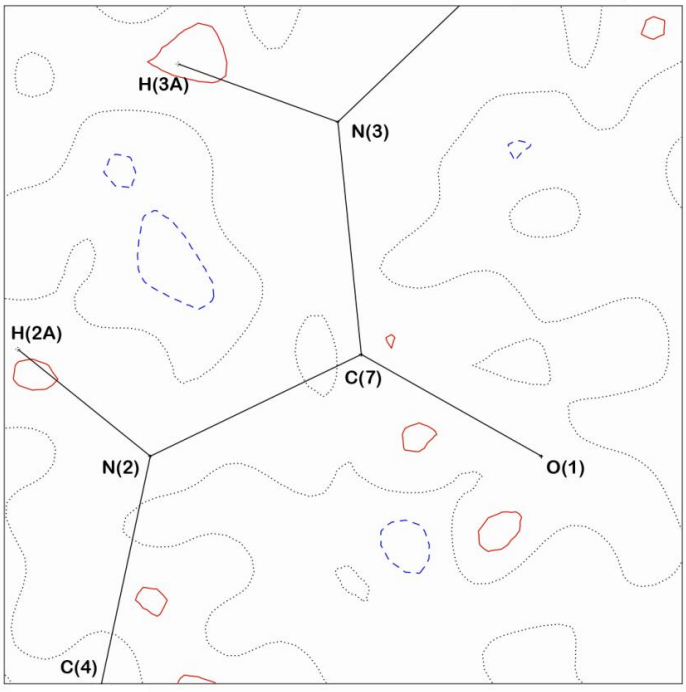

A.3.5: Residual electron density plot of **c.s.6**.

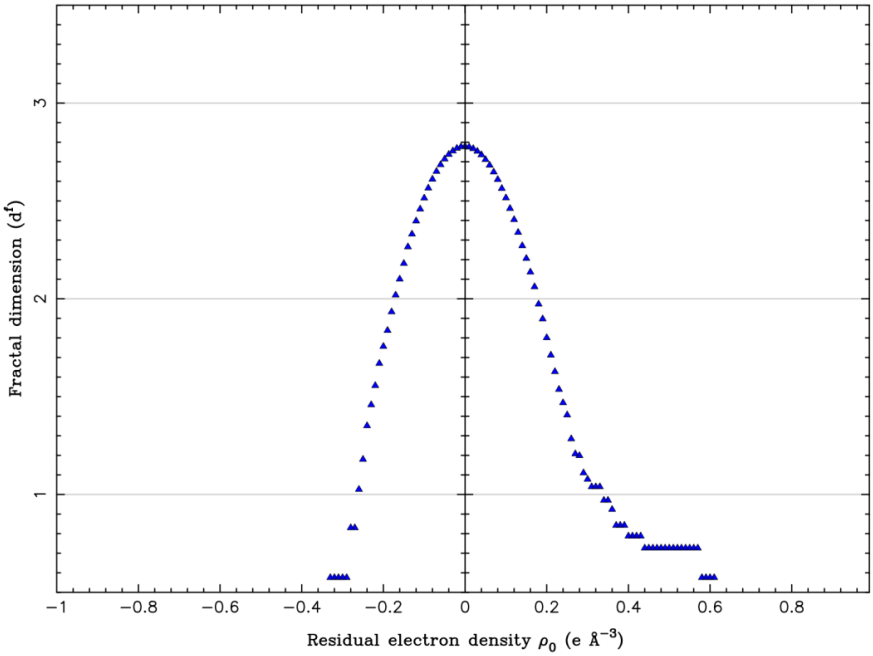

A.3.6: Fractal dimension distribution of residual density plot of **c.s.6**.

A.3.4 Residual density analysis of c.s.9

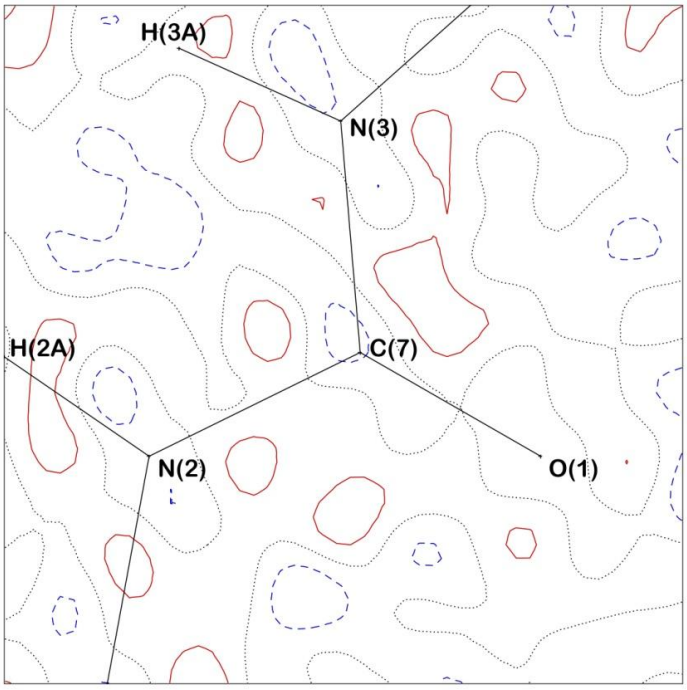

A.3.7: Residual electron density plot of **c.s.9**.

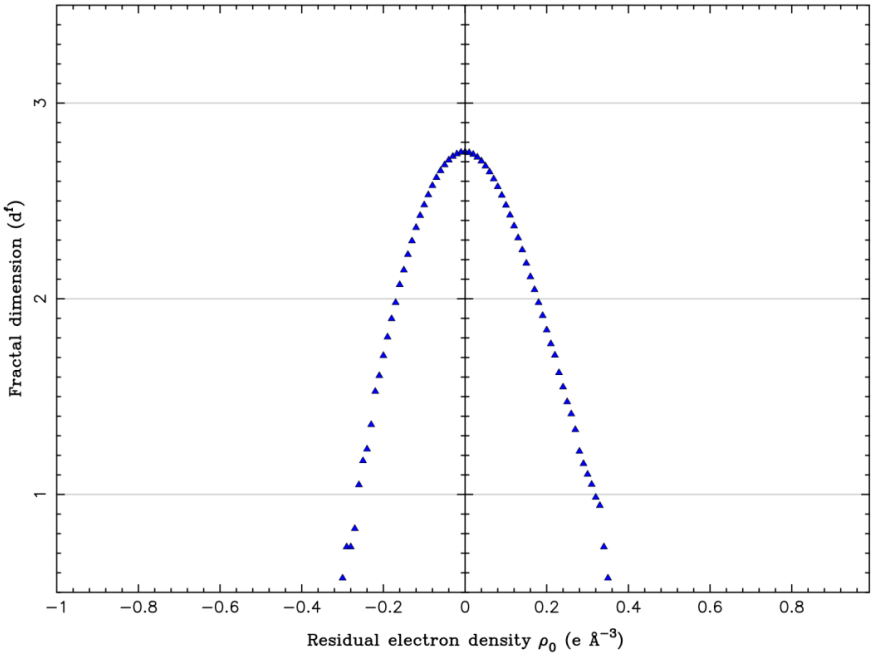

A.3.8: Fractal dimension distribution of residual density plot of **c.s.9**.

A.3.5 Residual density analysis of c.s.10

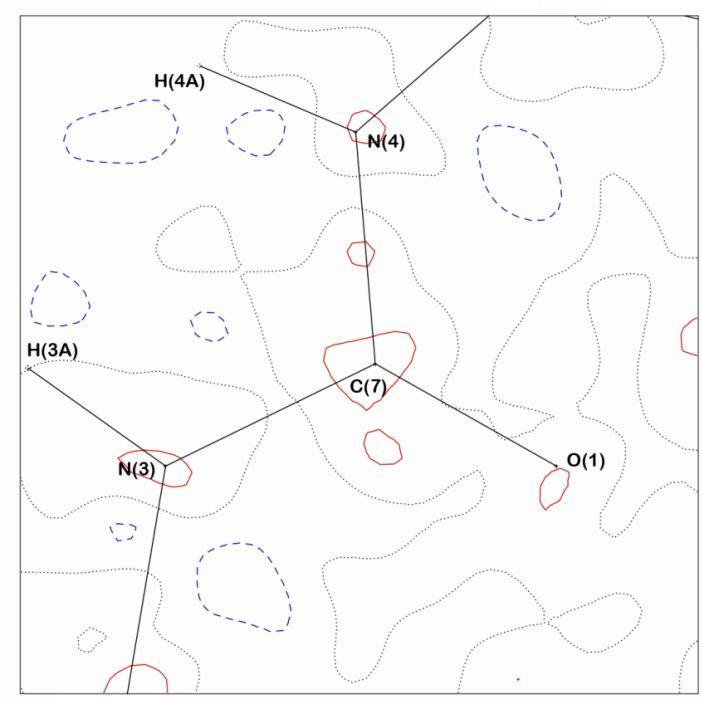

A.3.9: Residual electron density plot of **c.s.10**.

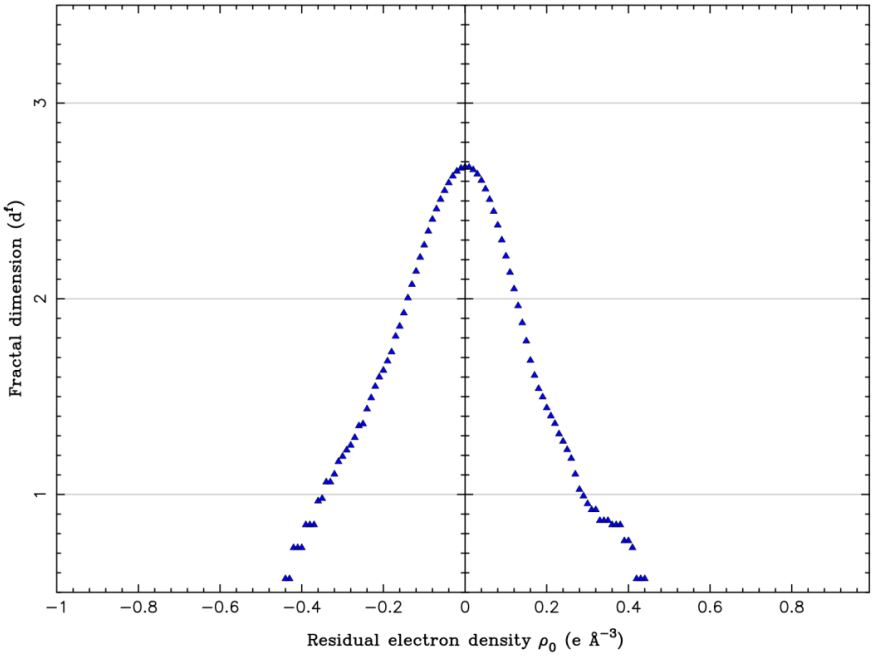

A.3.10: Fractal dimension distribution of residual density plot of **c.s.10**.

A.3.6 Residual density analysis of c.s.11

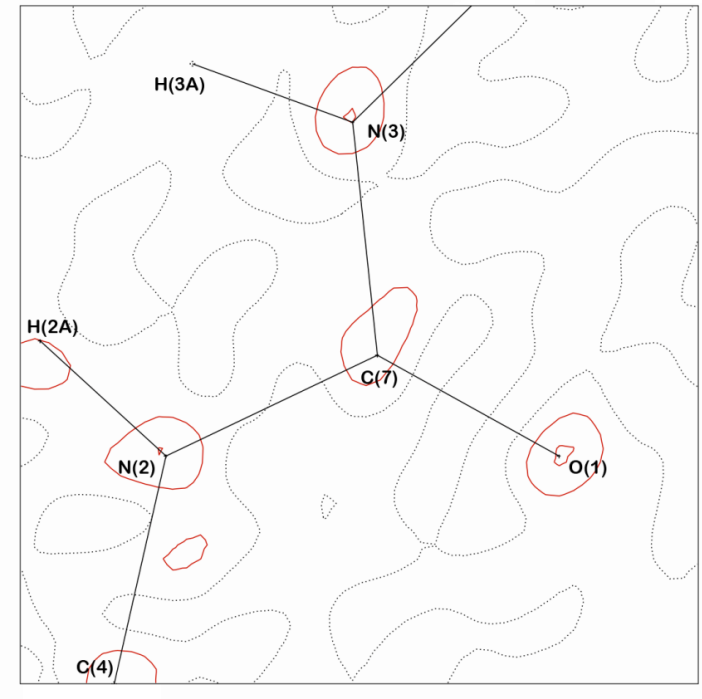

A.3.11: Residual electron density plot of **c.s.11**.

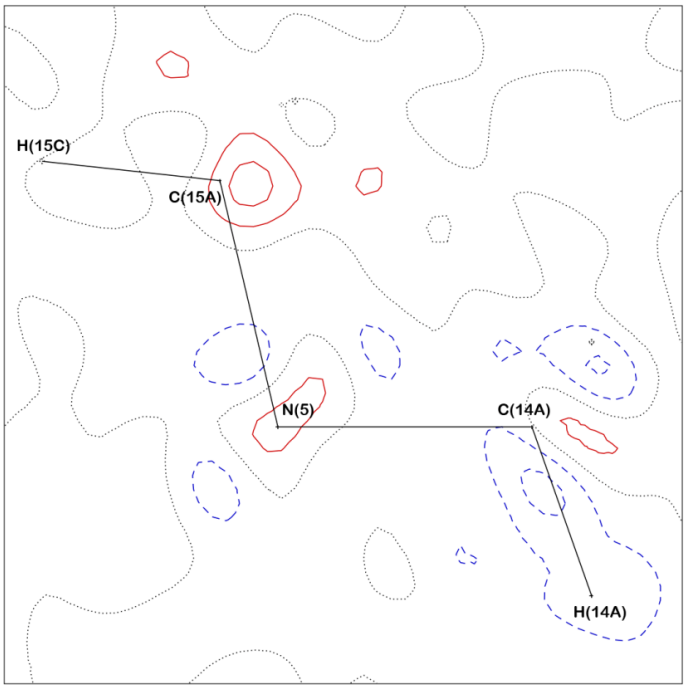

A.3.12: Residual density plot after multipole refinement (with multipole parameters for the TMA cation taken from the invariom database[117]) in the plane of the TMA cation.

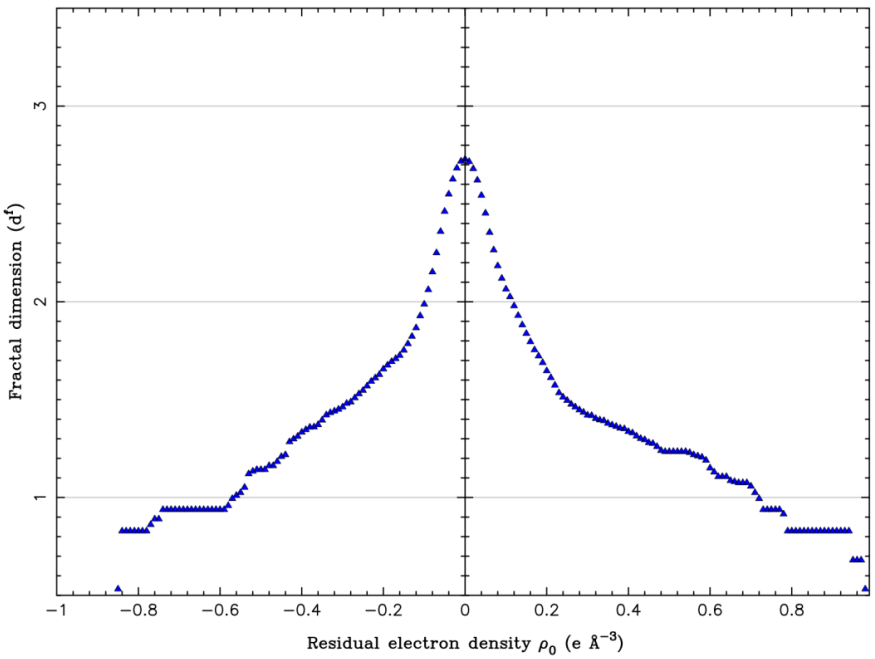

A.3.13: Fractal dimension distribution of residual density plot of **c.s.11** modelled ignoring the disorder of TMA group. The large residual electron density seen is located around the TMA cation. The methyl carbons of this group have large thermal displacements parameters.

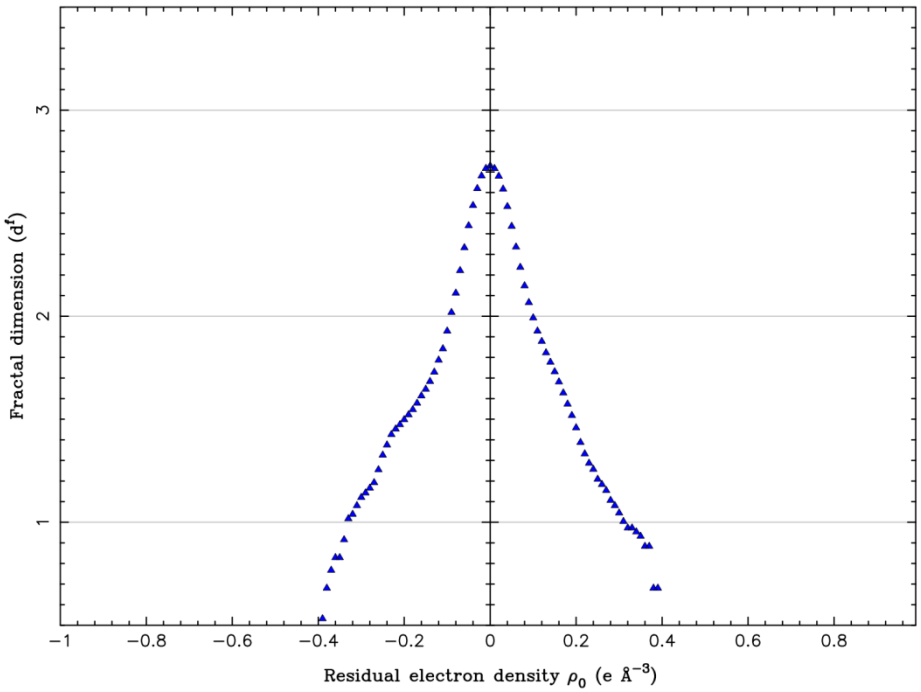

A.3.14: Fractal dimension distribution of residual density plot of **c.s.11** after disorder refinement of TMA cation and invariom multipole population transfer for TMA group, and refinement of the final model. The plot shows that the residual density has been markedly reduced following this strategy and that it is now distributed in a Gaussian-like manner, suggesting that it is noise and all the density has been incorporated into the model. This illustrates the improvement in the final model.

A.3.7 Residual density analysis of c.s.16

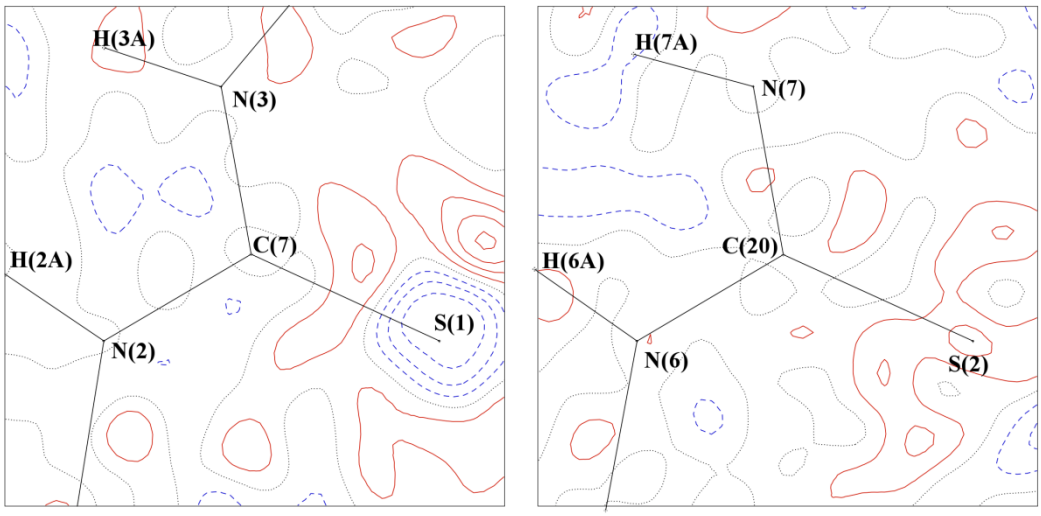

A.3.15: Residual electron density plot of **c.s.16** in the plane of the two receptor molecules in the crystal structure (*left* receptor N(2) S(1) N(3) and *right* N(6) S(2) N(7)).

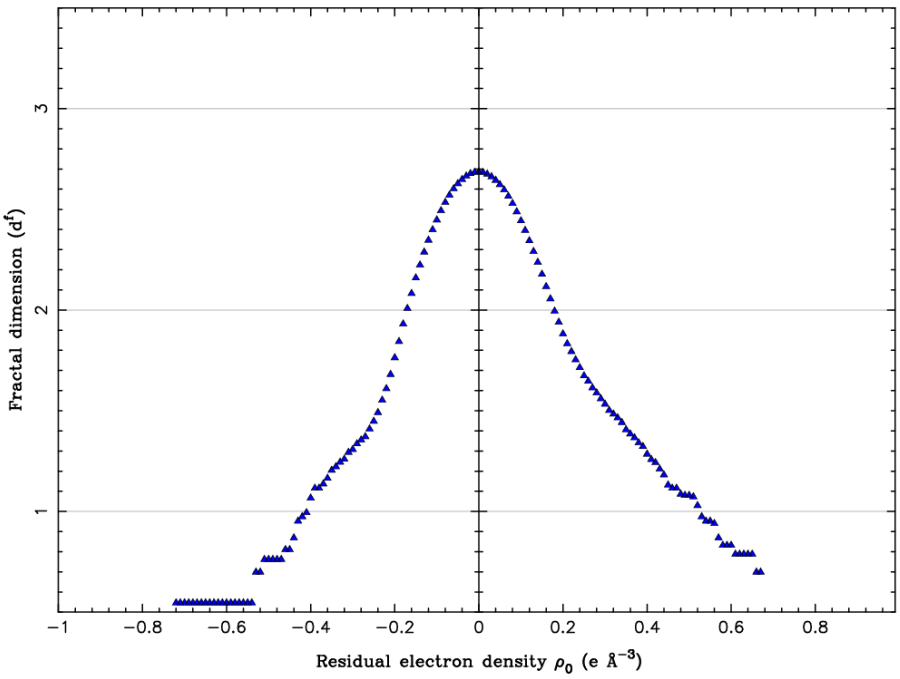

A.3.16: Fractal dimension distribution of residual density plot of **c.s.16**.

A.3.8 Residual density analysis of c.s.17

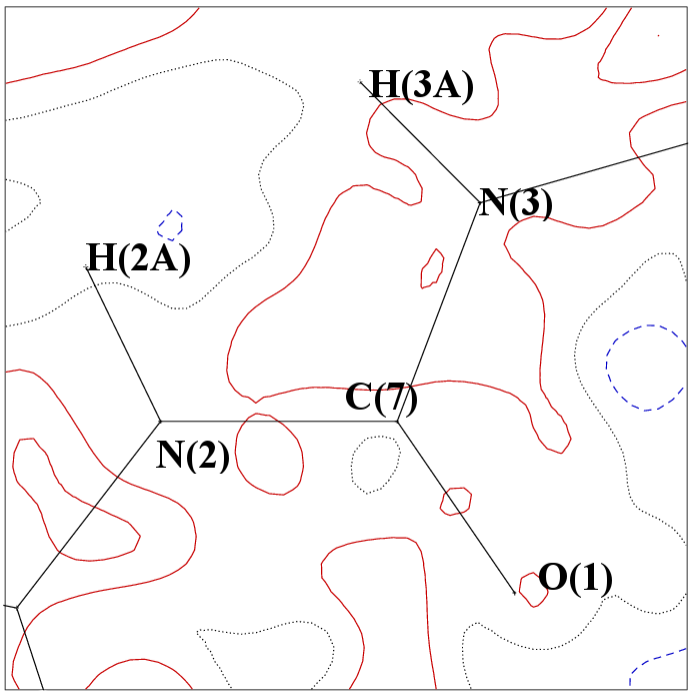

A.3.17: Residual electron density plot of **c.s.17** (no cut off).

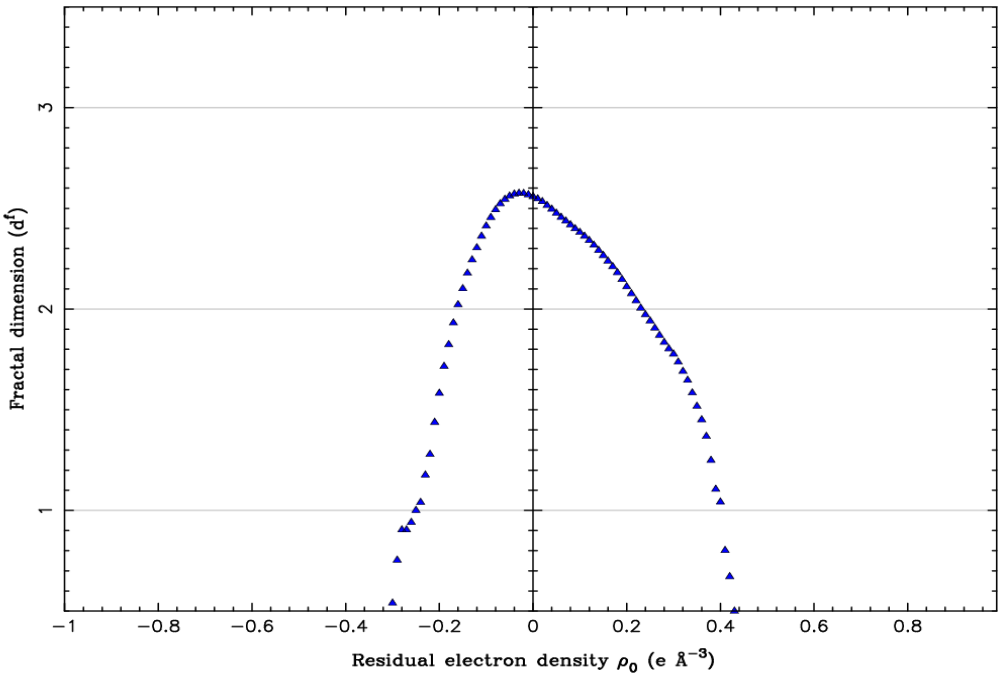

A.3.18: Fractal dimension distribution of residual density plot of **c.s.17:** The non-ideal Gaussian distribution is due to the Invariom refinement as opposed to the full multipole refinement of the X-ray diffraction data.

A.3.9 Residual density analysis of c.s.18

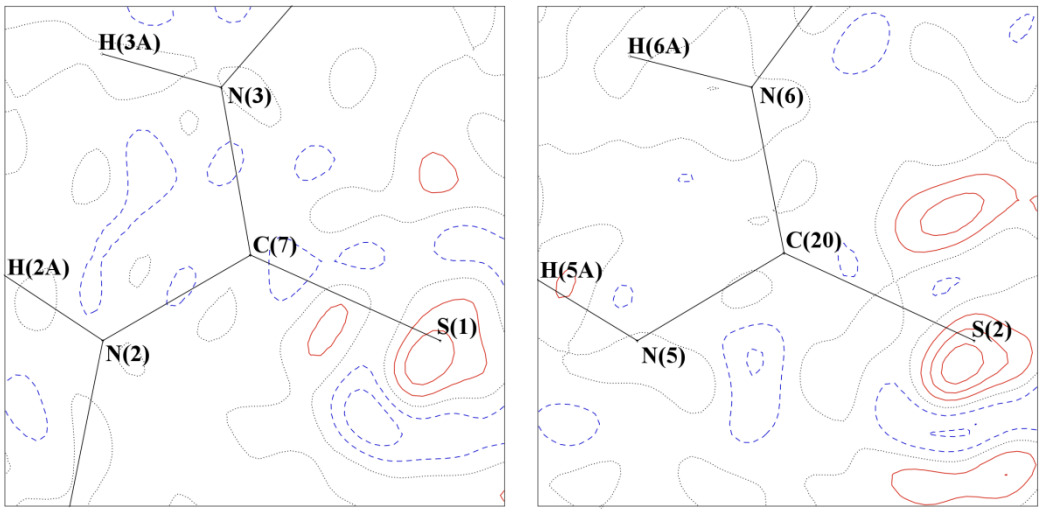

A.3.19: Residual electron density plot of **c.s.18** in the plane of the two receptor molecules in the crystal structure (*left* receptor N(2) S(1) N(3) and *right* N(5) S(2) N(6)).

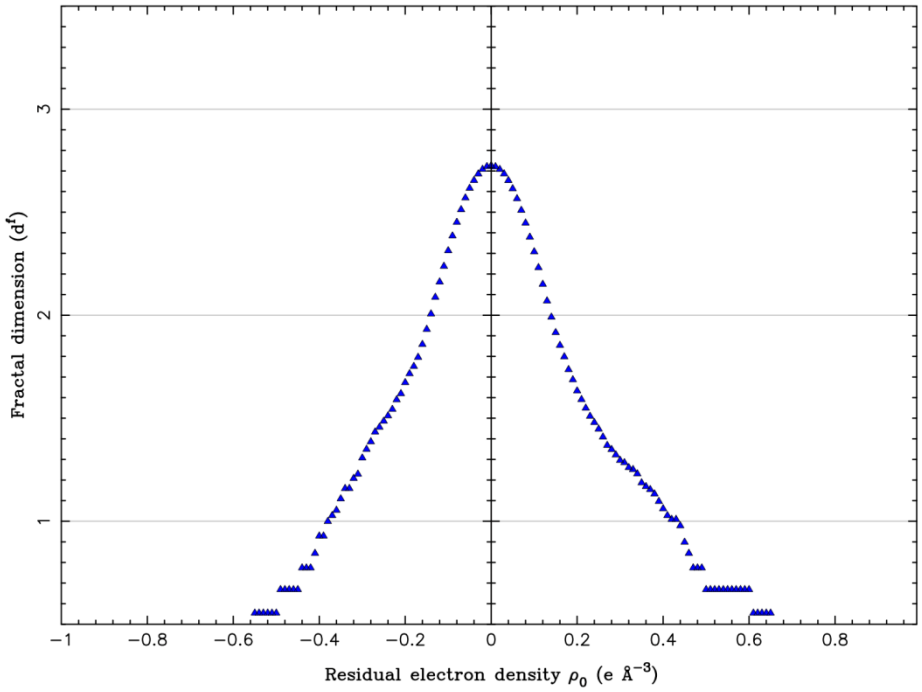

A.3.20: Fractal dimension distribution of residual density plot of **c.s.18**.

A.4 Electron density distribution as illustrated by static deformation density and negative Laplacian maps and molecular graph plots.

Static deformation charge density distribution maps show the whole receptor molecule (*left*) and the anion binding region (*right*) of the structure. Positive electron density is shown in red, negative electron density in blue. Zero contours are dashed. Contours are at 0.1 e Å^{-3}.

Negative Laplacian ($-\nabla^2\rho(\mathbf{r})$) charge density distribution maps are also drawn in the plane of urea group of the receptor molecule. Positive electron density is shown in red, negative electron density in blue. Contours are in a logarithmic scale, e Å^{-5}.

Bond path plots display the nuclear positions of the atoms in each structure, the bond paths (paths of maximum electron density linking these nuclear positions), and the position of the bond critical points (saddle points along the bond paths where electron density is at a minimum along the nuclear axis and at a maximum in the direction perpendicular to the molecular axis.).

A.4.1 Electron density distribution in c.s.3

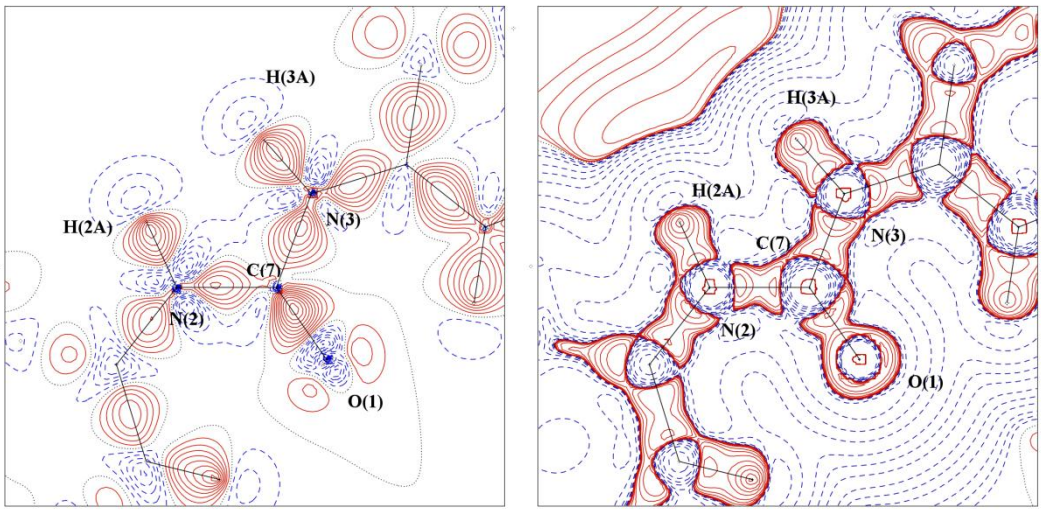

A.4.1: Electron density distribution in the urea portion of **c.s.3**. Static deformation charge density distribution map *(left)*, $-\nabla^2\rho(\mathbf{r})$ charge density distribution map *(right)*.

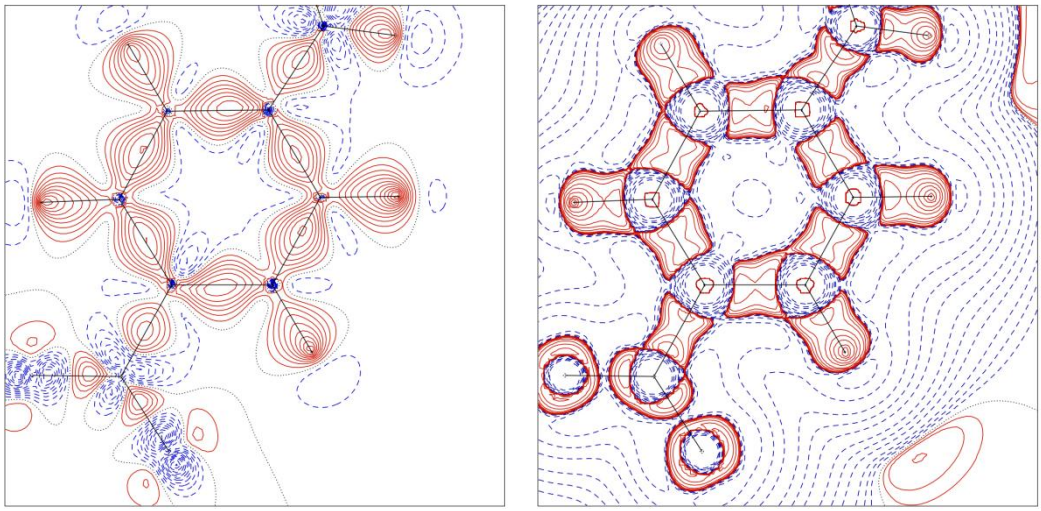

A.4.2: Electron density distribution in the phenyl ring portion of **c.s.3**. Static deformation charge density distribution map *(left)*, $-\nabla^2\rho(\mathbf{r})$ charge density distribution map *(right)*.

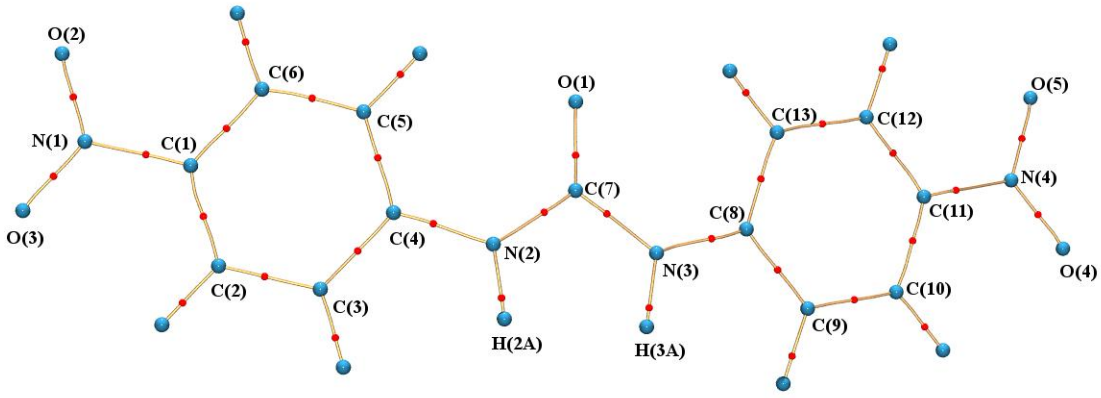

A.4.3: Bond path plot of **c.s.3** displaying the nuclear positions of the atoms in the structure, the bond paths and the position of the bond critical points.

A.4.2 Electron density distribution in c.s.5

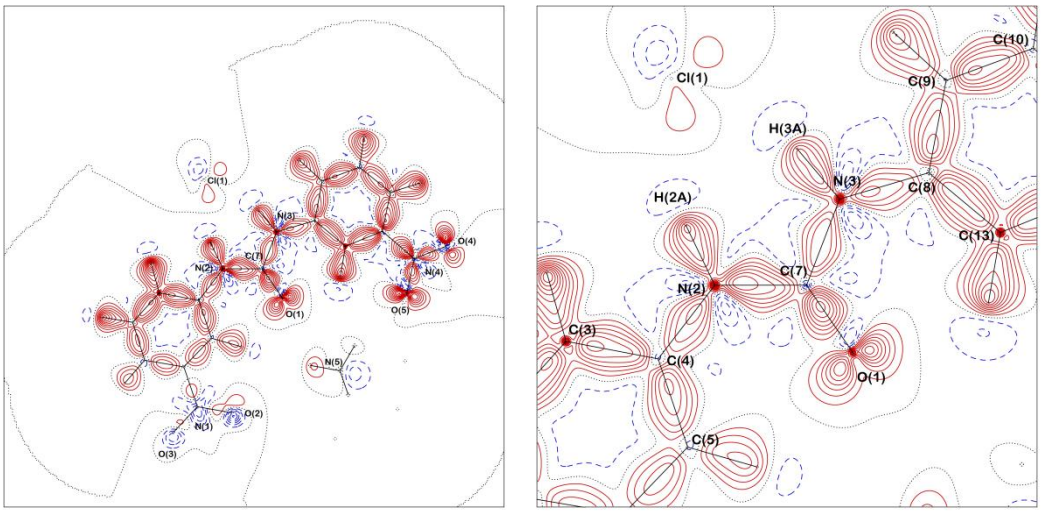

A.4.4: Static deformation charge density distribution maps of whole receptor molecule (*left*) and anion binding region (*right*) of **c.s.5**. The chloride anion, nitro groups and TMA groups displayed do not lie in the plane of the urea in which the map was drawn.

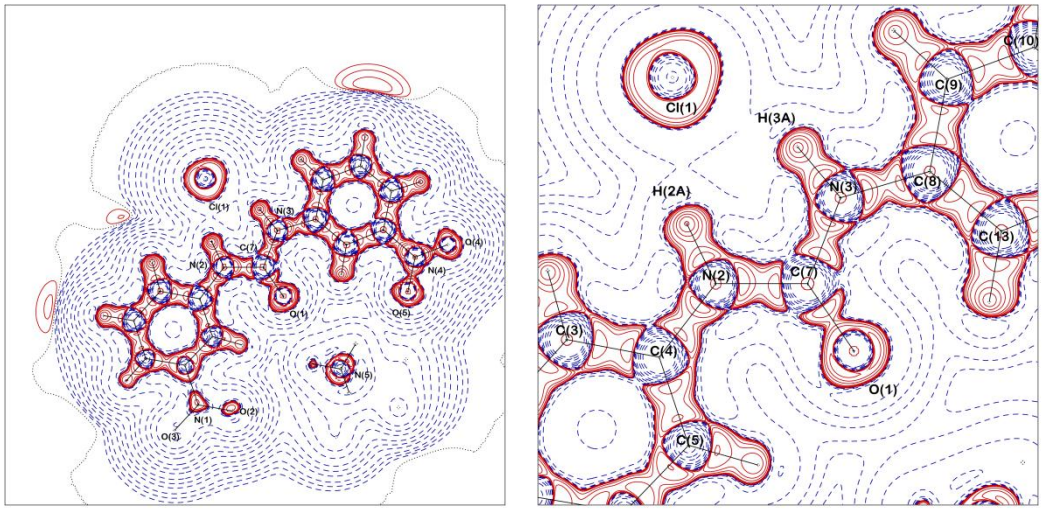

A.4.5: $-\nabla^2\rho(\mathbf{r})$ charge density distribution maps of whole receptor molecule (*left*) and anion binding region (*right*) of **c.s.5**. Map drawn in the plane of the urea group.

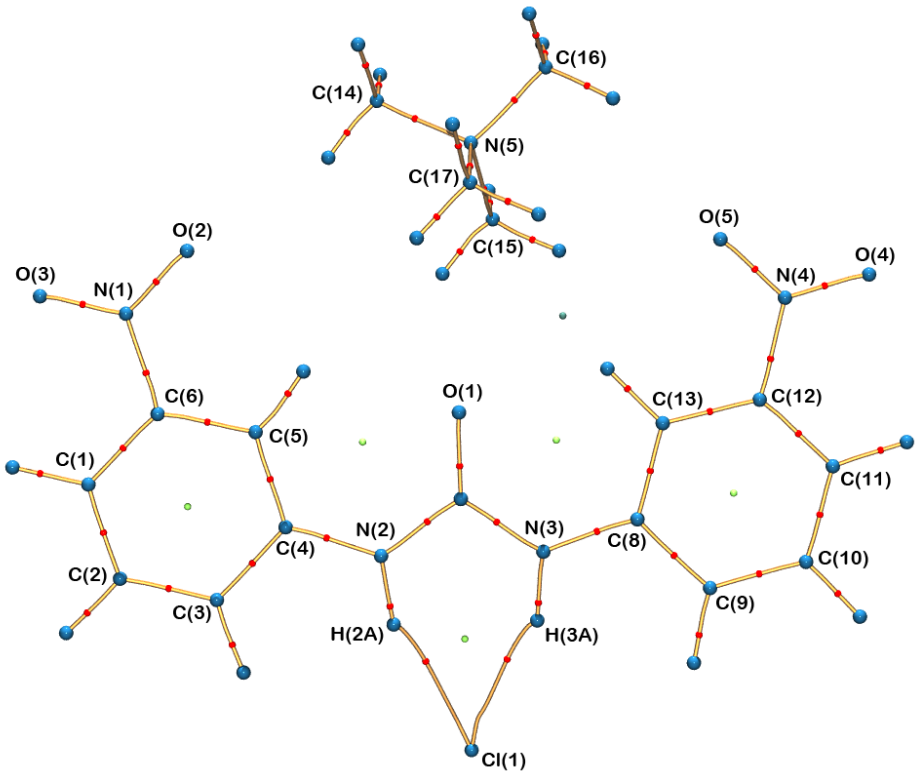

A.4.6: Bond path plot of **c.s.5** displaying the nuclear positions of the atoms in the structure, the bond paths and the position of the bond critical points.

A.4.3 Electron density distribution in c.s.6

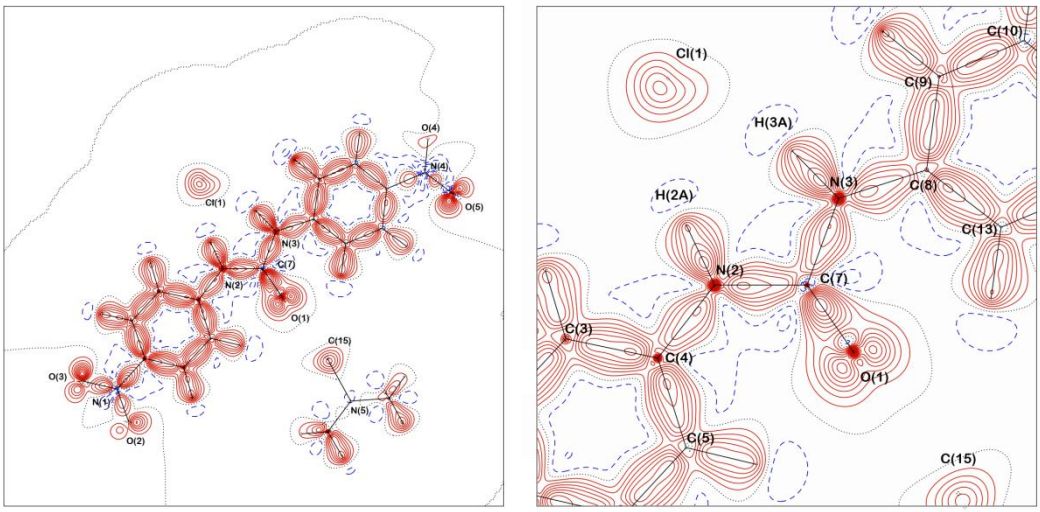

A.4.7: Static deformation charge density distribution maps of whole receptor molecule (*left*) and anion binding region (*right*) of **c.s.6**. The chloride anion, nitro groups and TMA groups displayed do not lie in the plane of the urea in which the map was drawn.

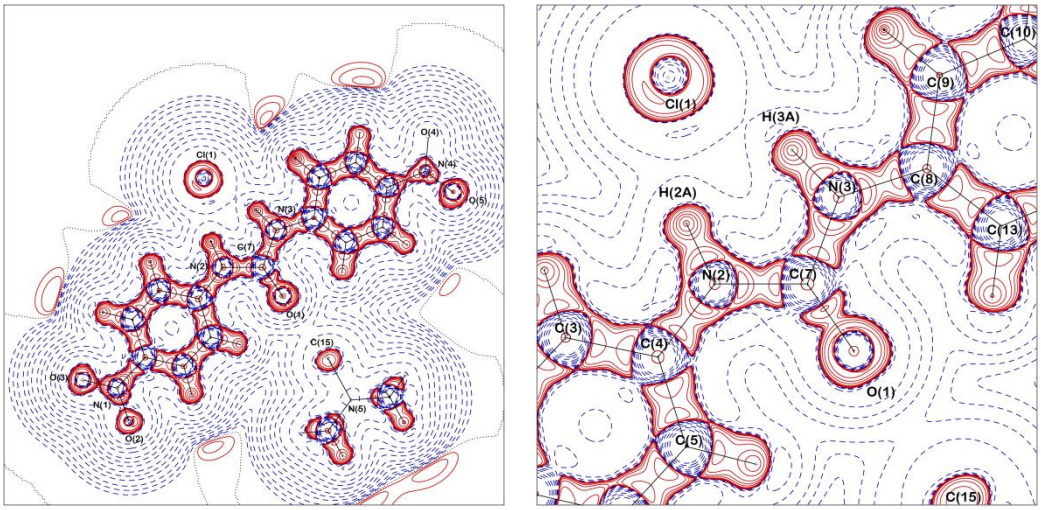

A.4.8: $-\nabla^2\rho(\mathbf{r})$ charge density distribution maps of whole receptor molecule (*left*) and anion binding region (*right*) of **c.s.6**. Map drawn in the plane of the urea group.

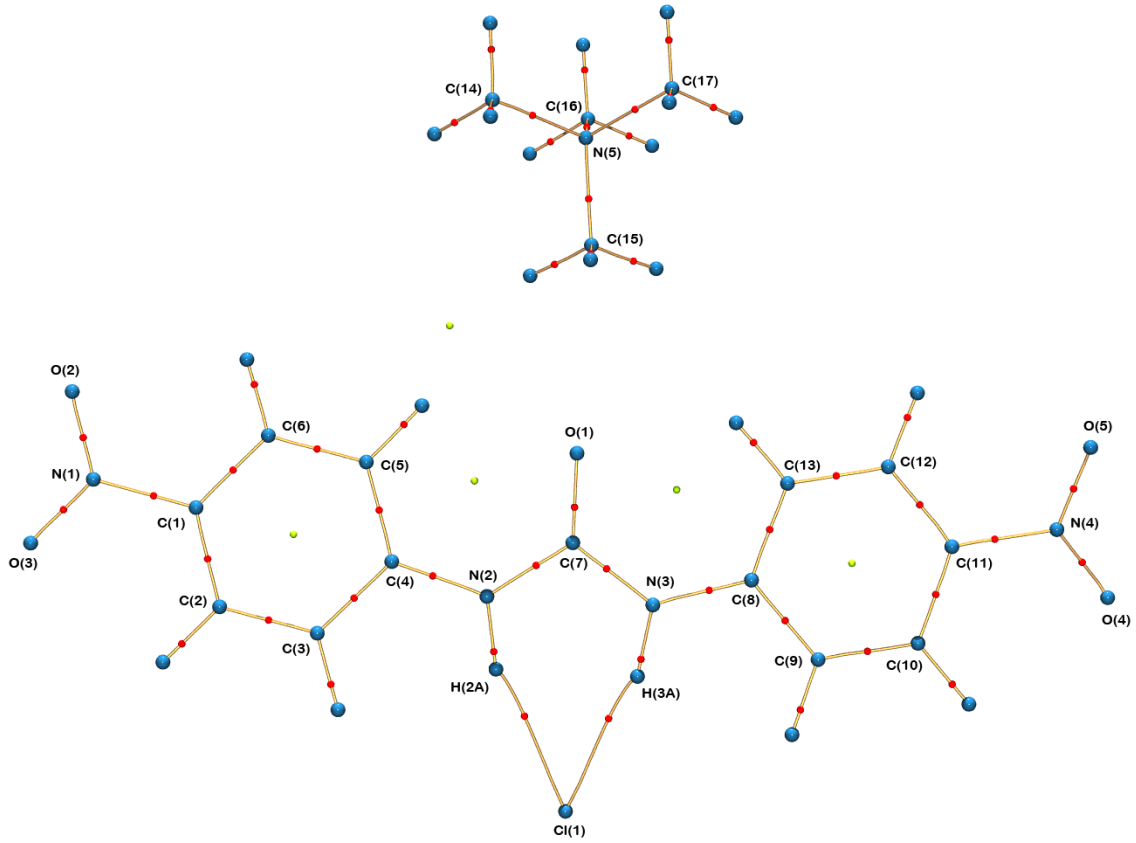

A.4.9: Bond path plot of **c.s.6** displaying the nuclear positions of the atoms in the structure, the bond paths and the position of the bond critical points.

A.4.4 Electron density distribution in c.s.9

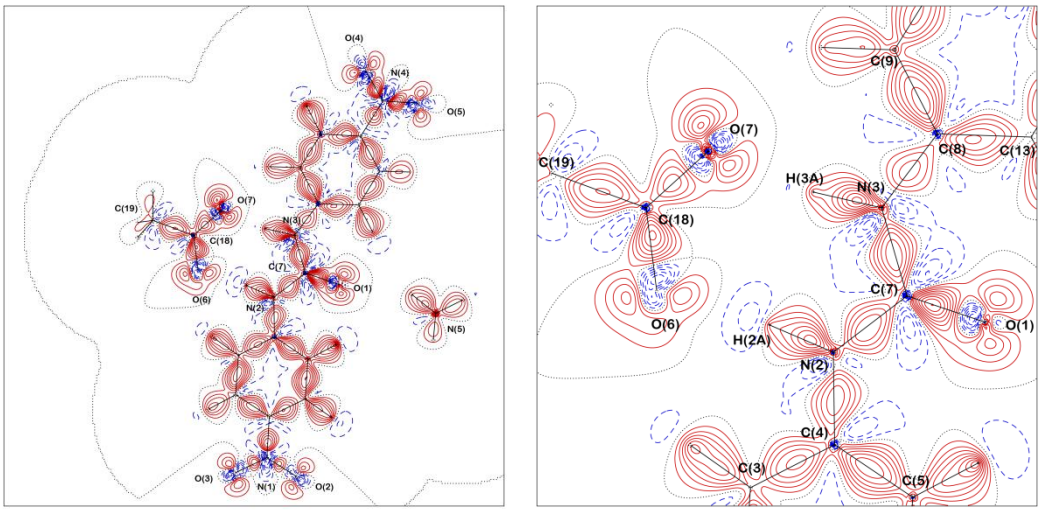

A.4.10: Static deformation charge density distribution maps of whole receptor molecule (*left*) and anion binding region (*right*) of **c.s.9**. The TMA group and nitro groups displayed do not lie in the plane of the urea in which the map was drawn.

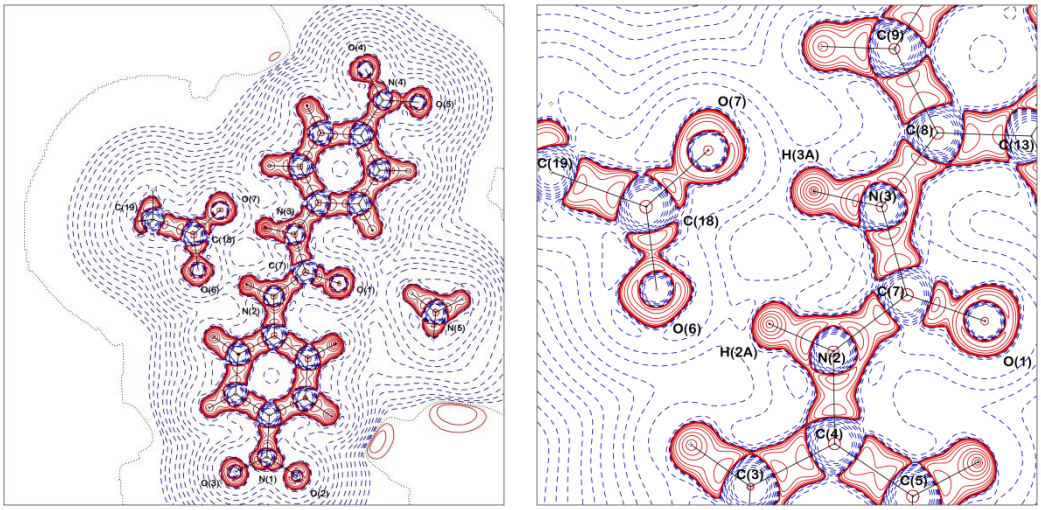

A.4.11: $-\nabla^2\rho(\mathbf{r})$ charge density distribution maps of whole receptor molecule (*left*) and anion binding region (*right*) of **c.s.9**. Map drawn in the plane of the urea group.

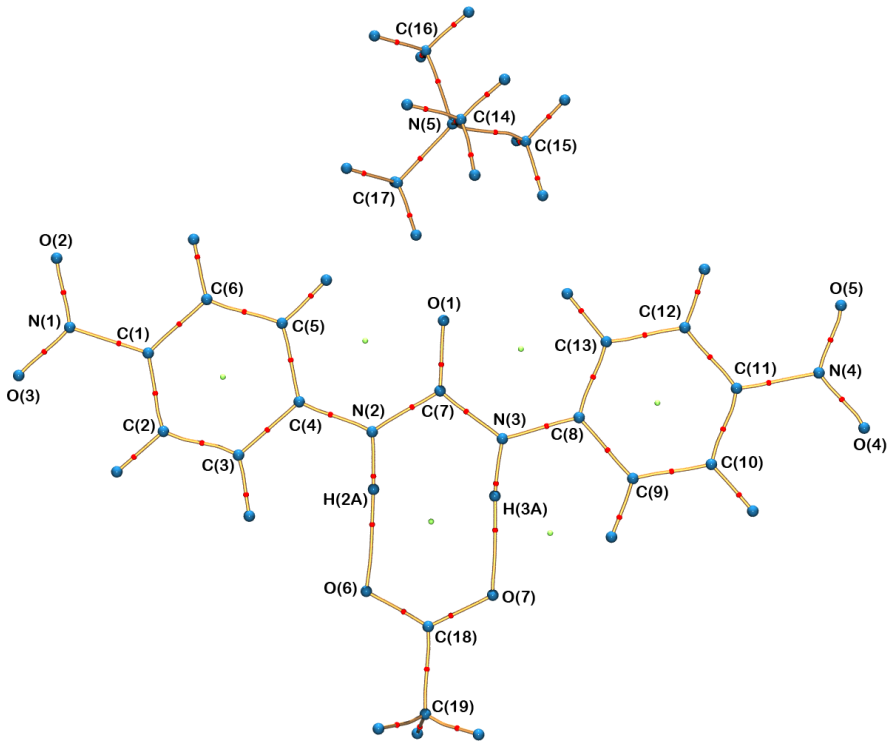

A.4.12: Bond path plot of **c.s.9** displaying the nuclear positions of the atoms in the structure, the bond paths and the position of the bond critical points.

A.4.5 Electron density distribution in c.s.10

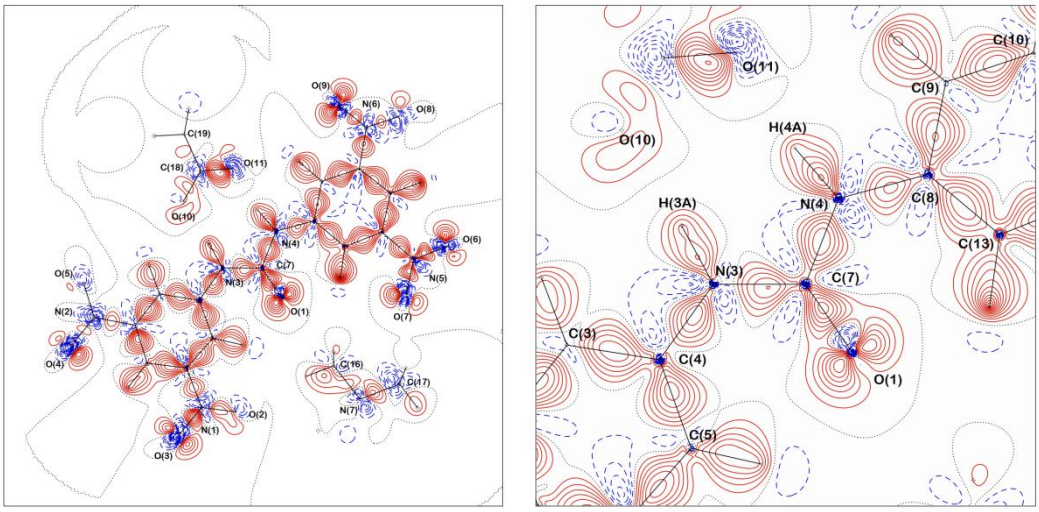

A.4.13: Static deformation charge density distribution maps of whole receptor molecule (*left*) and anion binding region (*right*) of **c.s.10**. The acetate anion, nitro groups and TMA groups displayed do not lie in the plane of the urea in which the map was drawn.

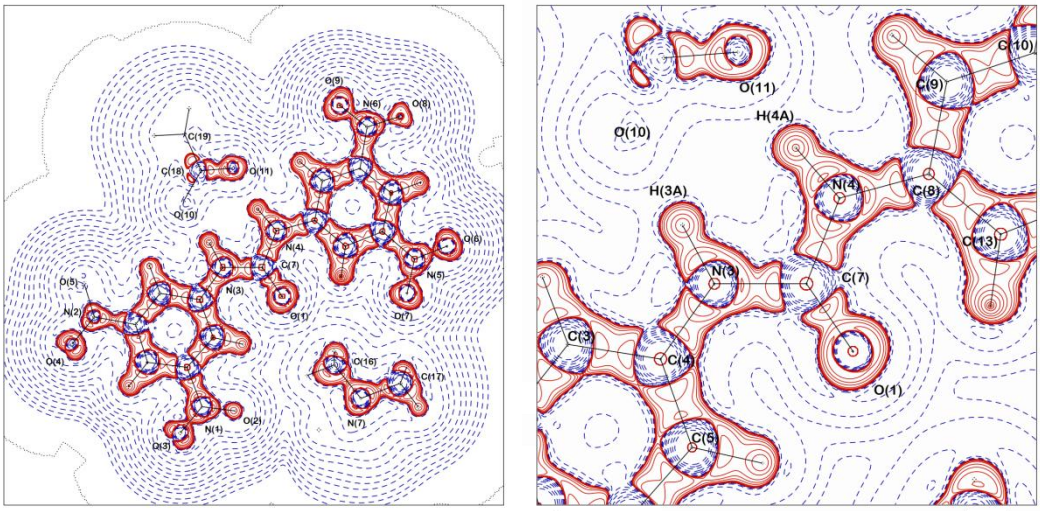

A.4.14: $-\nabla^2\rho(\mathbf{r})$ charge density distribution maps of whole receptor molecule (*left*) and anion binding region (*right*) of **c.s.10**. Map drawn in the plane of the urea group.

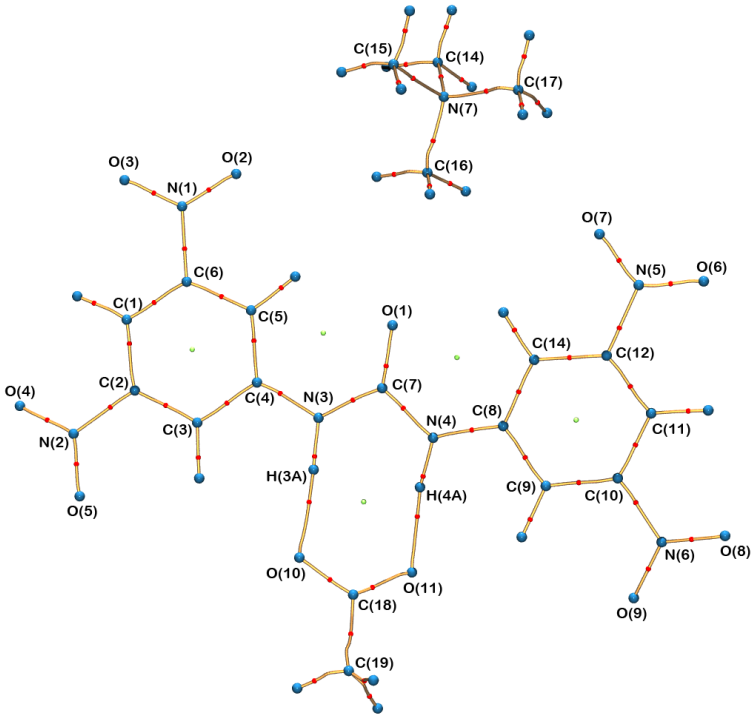

A.4.15: Bond path plot of **c.s.10** displaying the nuclear positions of the atoms in the structure, the bond paths and the position of the bond critical points.

A.4.6 Electron density distribution in c.s.11

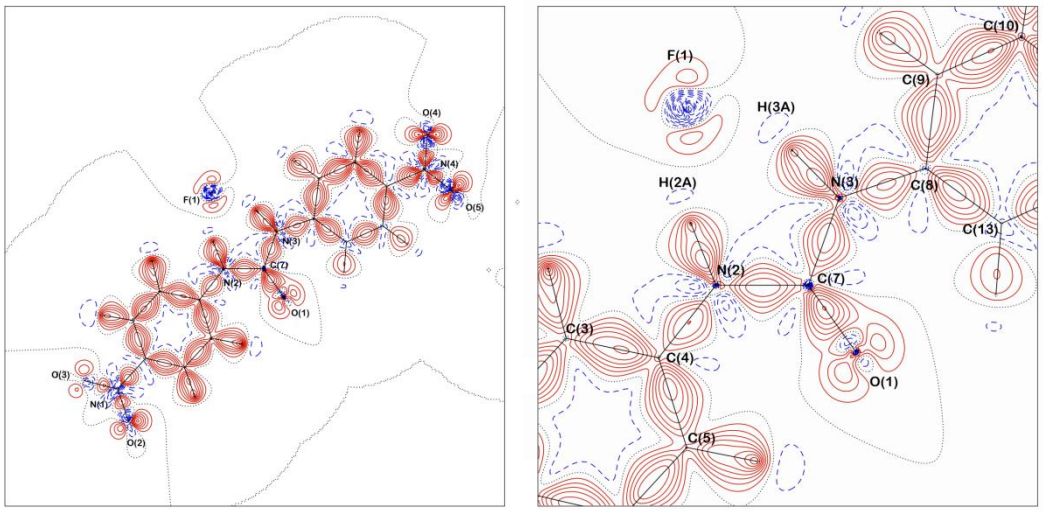

A.4.16: Static deformation charge density distribution maps of whole receptor molecule (*left*) and anion binding region (*right*) of **c.s.11**. The nitro groups and TMA group displayed do not lie in the plane of the urea in which the map was drawn.

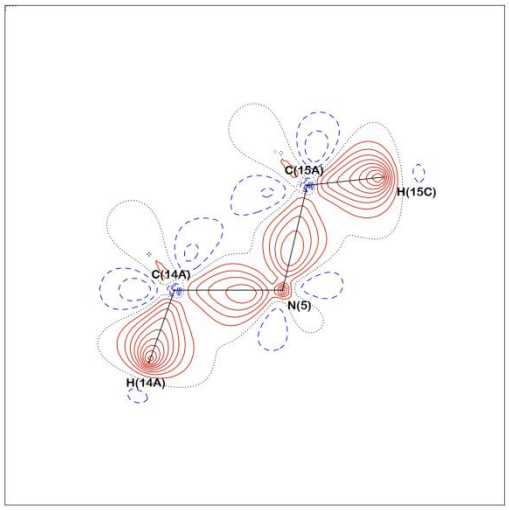

A.4.17: Static deformation charge density distribution map of part of the TMA group of **c.s.11** after Invariom based multipole refinement of the crystal structure.

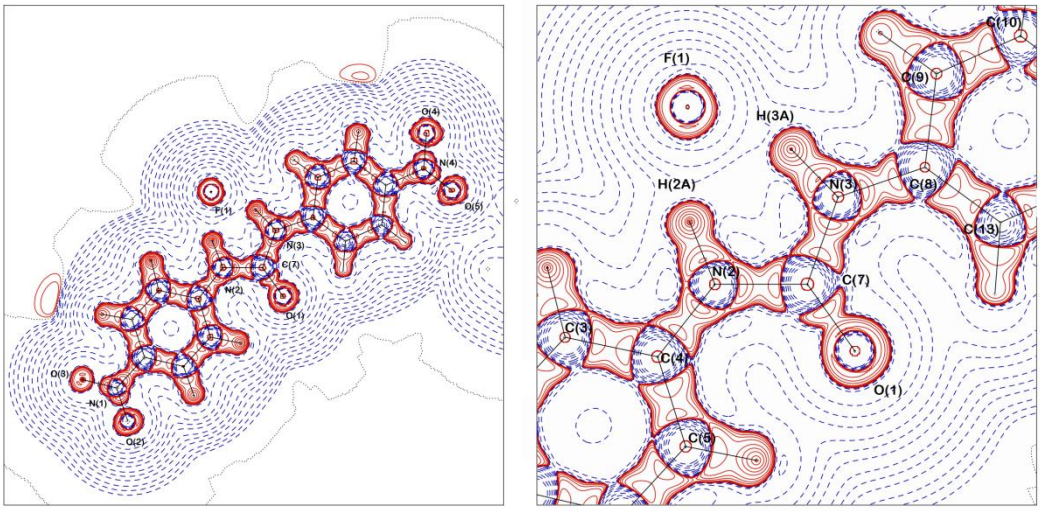

A.4.18: $-\nabla^2\rho(\mathbf{r})$ charge density distribution maps of whole receptor molecule (*left*) and anion binding region (*right*) of **c.s.11**. Map drawn in the plane of the urea group.

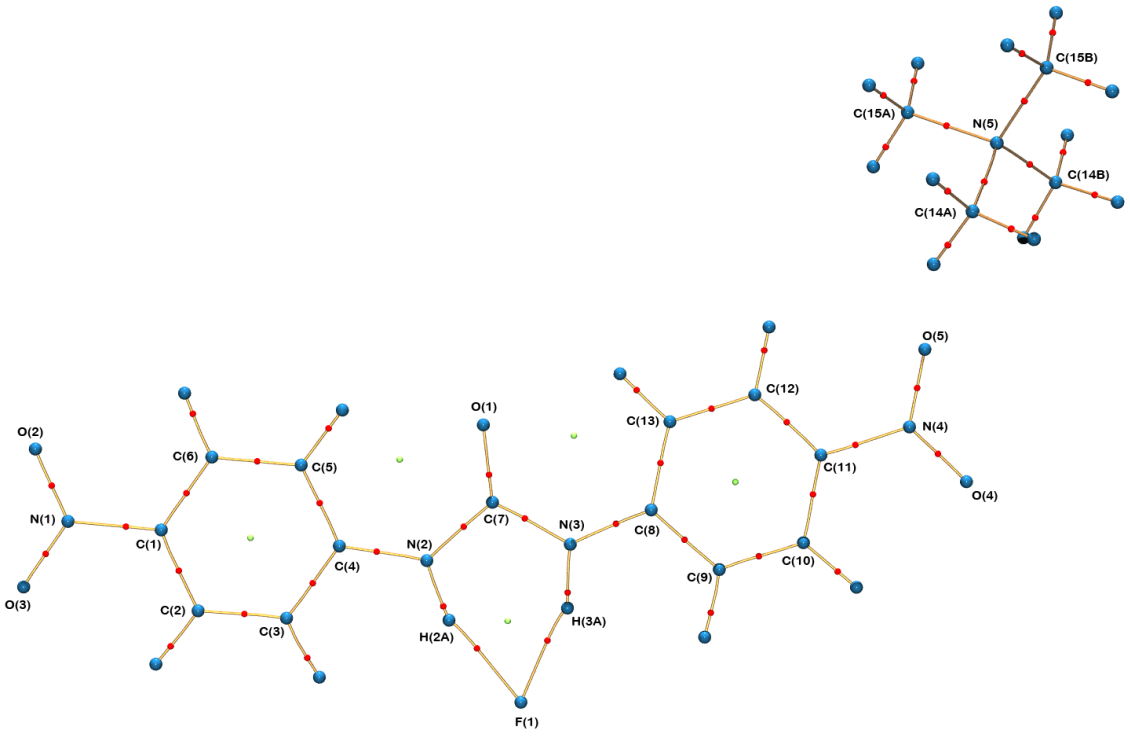

A.4.19: Bond path plot of **c.s.11** displaying the nuclear positions of the atoms in the structure, the bond paths and the position of the bond critical points.

A.4.7 Electron density distribution in c.s.16

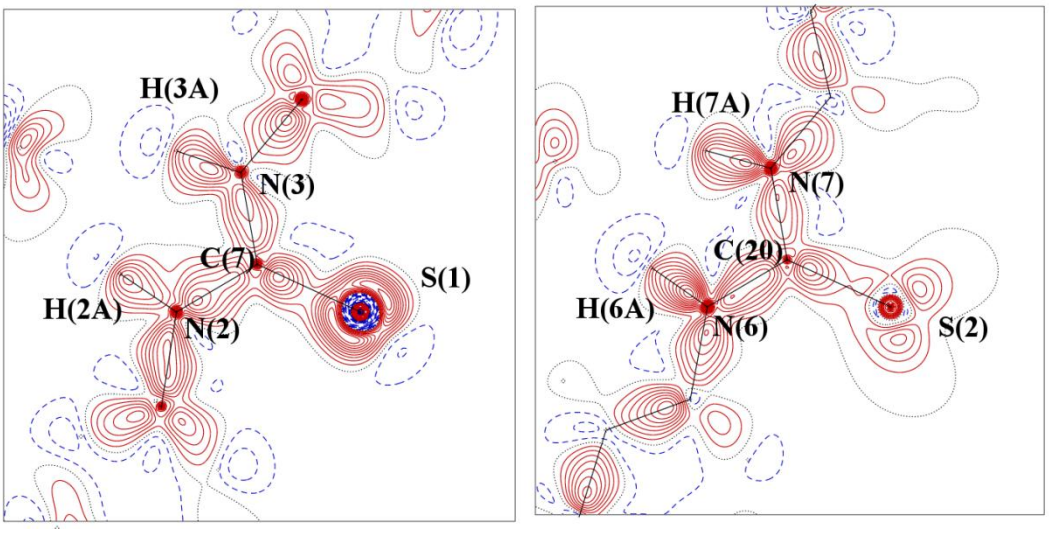

A.4.20: Static deformation charge density distribution maps of receptor molecules in **c.s.16** in plane of N(2) S(1) N(3) (*left*) and plane of N(6) S(2) N(7) (*right*).

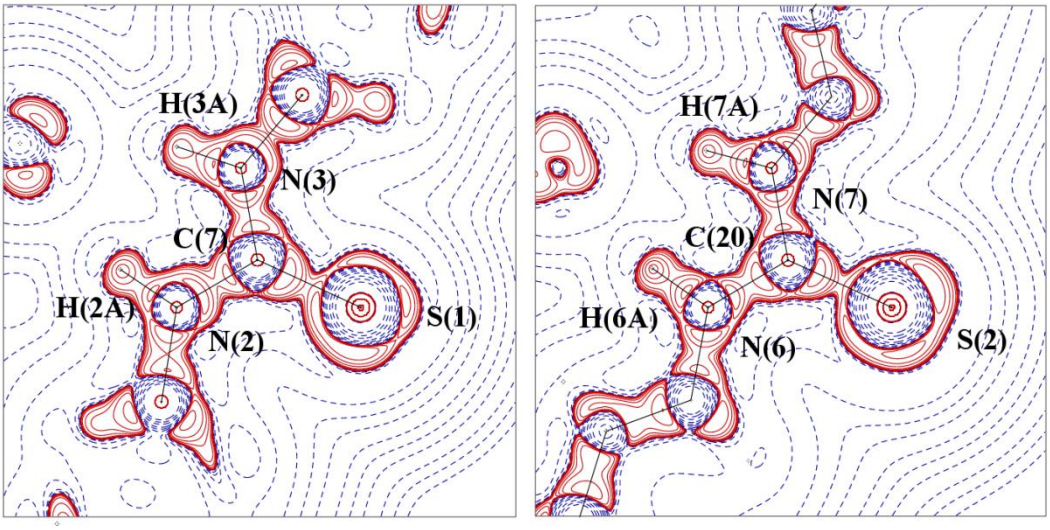

A.4.21: $-\nabla^2\rho(\mathbf{r})$ charge density distribution maps of receptor molecules in **c.s.16** in plane of N(2) S(1) N(3) (*left*) and plane of N(6) S(2) N(7) (*right*).

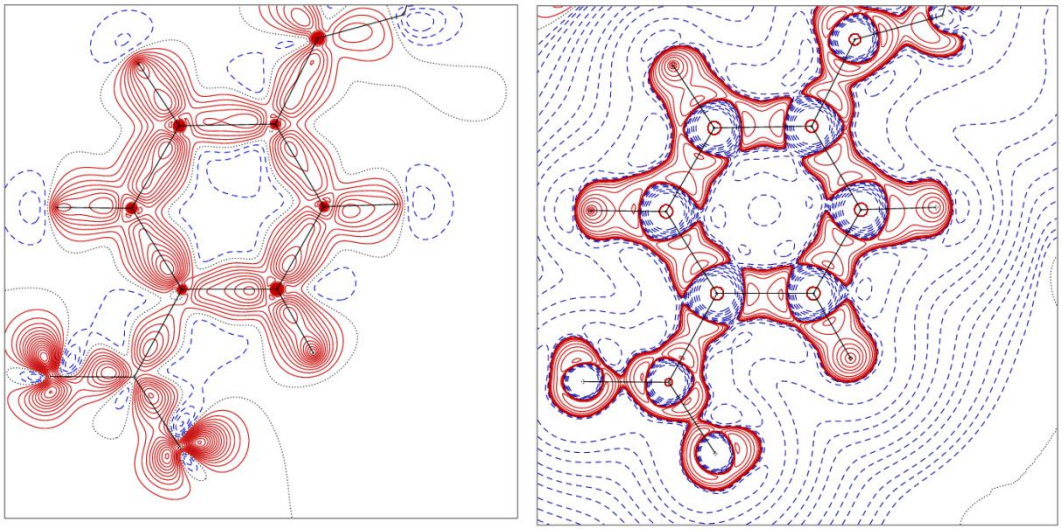

A.4.22: Electron density distribution across a representative phenyl ring (drawn in the plane of the C(24) C(25) and C(26) atoms) in **c.s.16**. Static deformation charge density map (*left*) and $:-\nabla^2\rho(\mathbf{r})$ charge density plot (*right*).

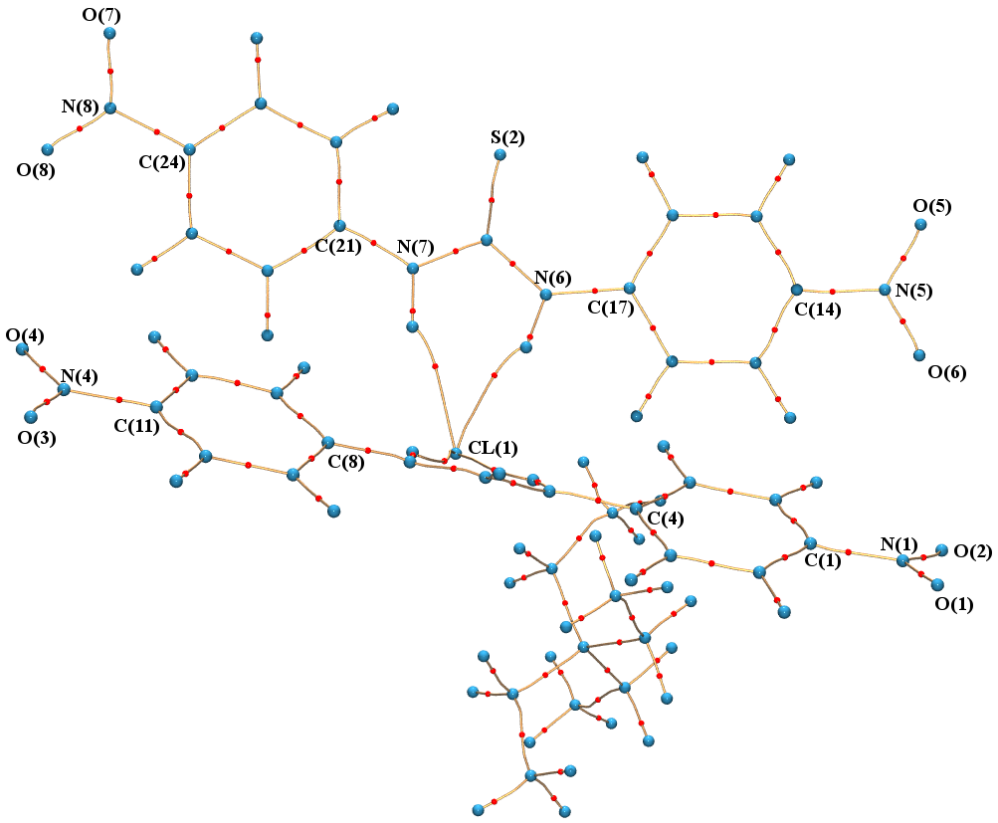

A.4.23: Bond path plot of **c.s.16** displaying the nuclear positions of the atoms in the structure, the bond paths and the position of the bond critical points.

A.4.8 Electron density distribution in c.s.17

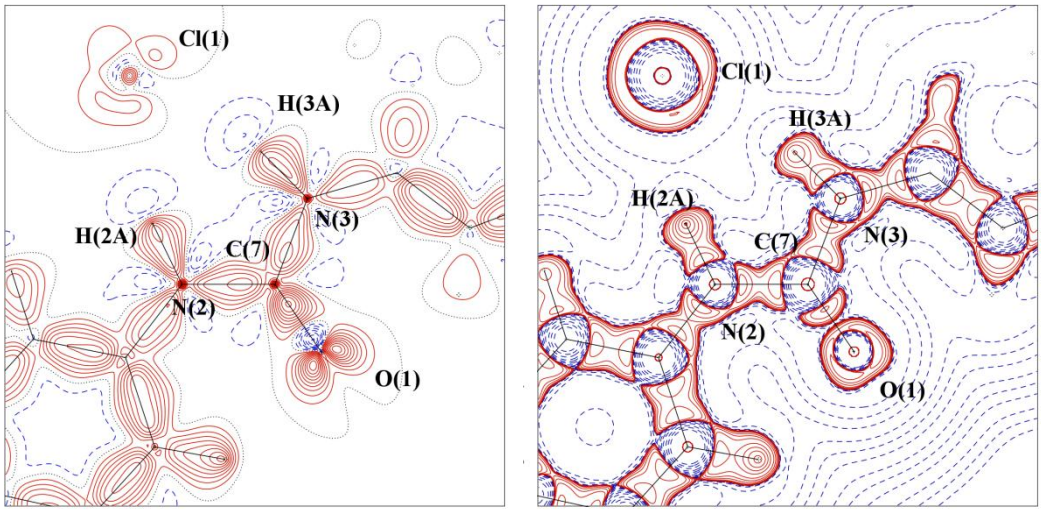

A.4.24: Electron density distribution across the urea portion of **c.s.17**. Static deformation charge density map (*left*) and :$-\nabla^2\rho(\mathbf{r})$ charge density plot (*right*).

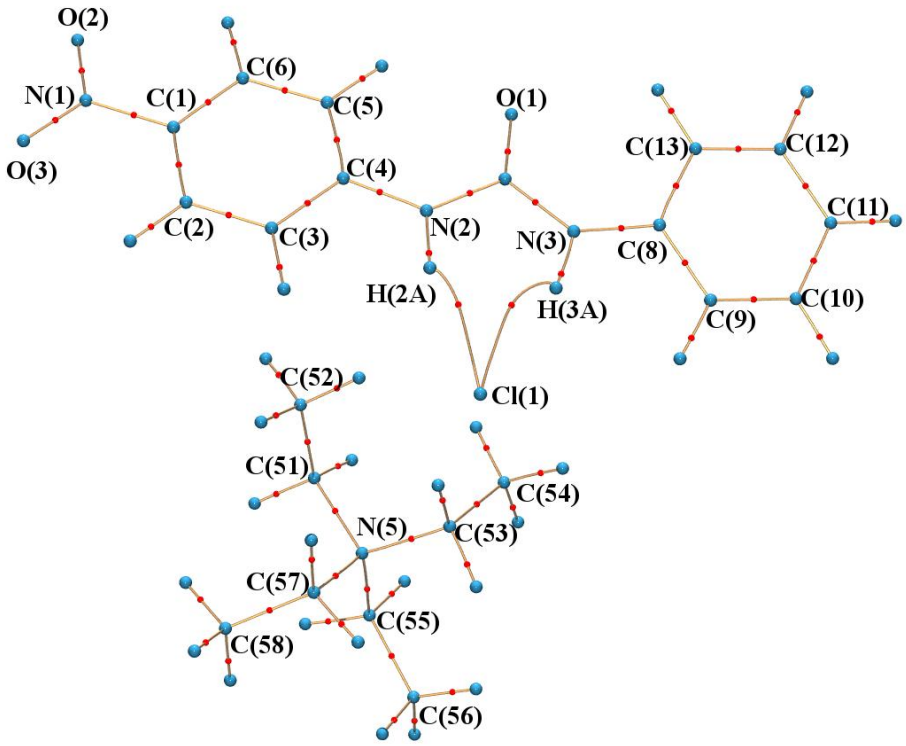

A.4.25: Bond path plot of **c.s.17** displaying the nuclear positions of the atoms in the structure, the bond paths and the position of the bond critical points.

A.4.9 Electron density distribution in c.s.18

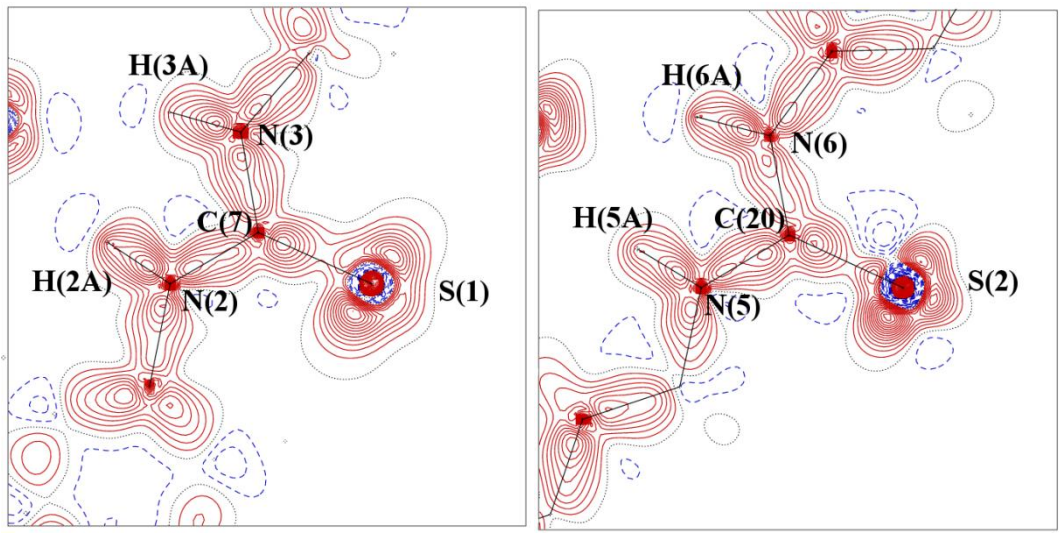

A.4.26: Static deformation charge density distribution maps of receptor molecules in **c.s.18** in plane of N(2) C(7) S(1) (*left*) and plane of N(5) C(20) S(2) (*right*).

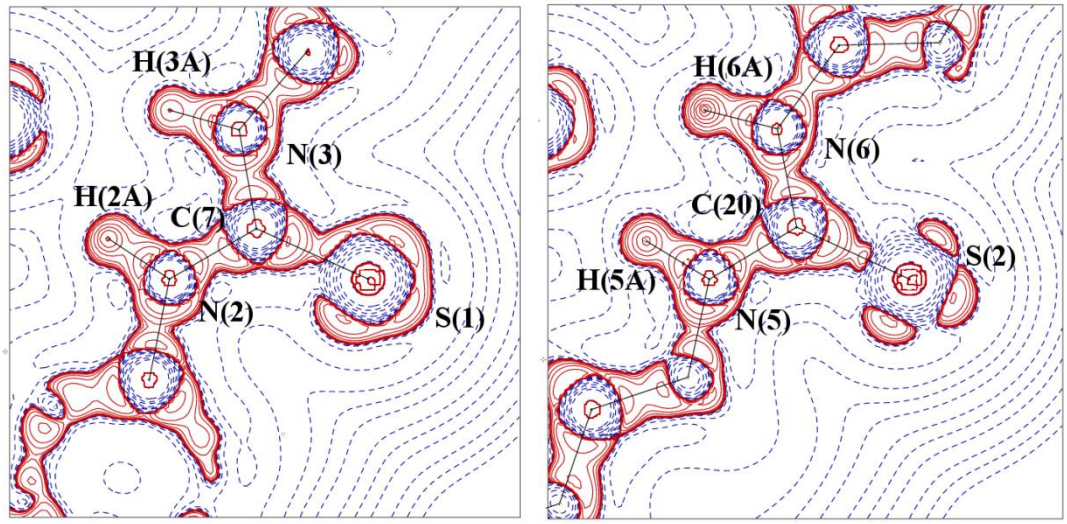

A.4.27: $-\nabla^2\rho(\mathbf{r})$ charge density distribution maps of receptor molecules in **c.s.18** in plane of N(2) C(7) S(1) (*left*) and plane of N(5) C(20) S(2) (*right*).

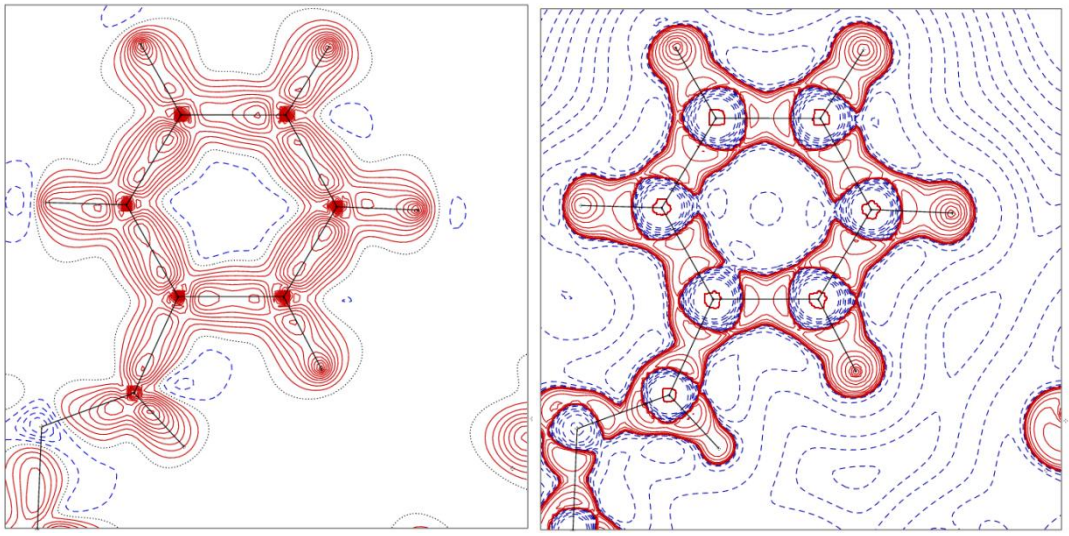

A.4.28: Electron density distribution across a representative phenyl ring (drawn in the plane of the C(21) C(22) and C(23) atoms) in **c.s.18**. Static deformation charge density map (*left*) and :$-\nabla^2\rho(\mathbf{r})$ charge density plot (*right*).

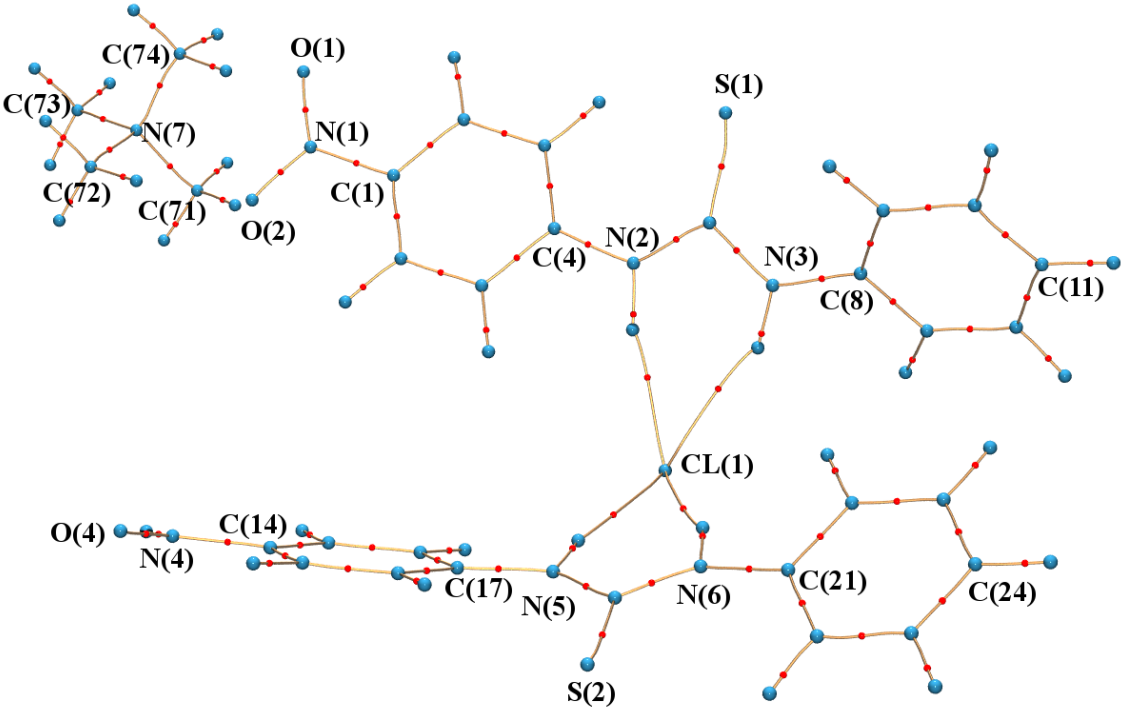

A.4.29: Bond path plot of **c.s.18** displaying the nuclear positions of the atoms in the structure, the bond paths and the position of the bond critical points.

A.5 Bond path plots of areas of interest in high resolution crystal structures

A.5.1 Phenyl ring bond path plots in c.s.3

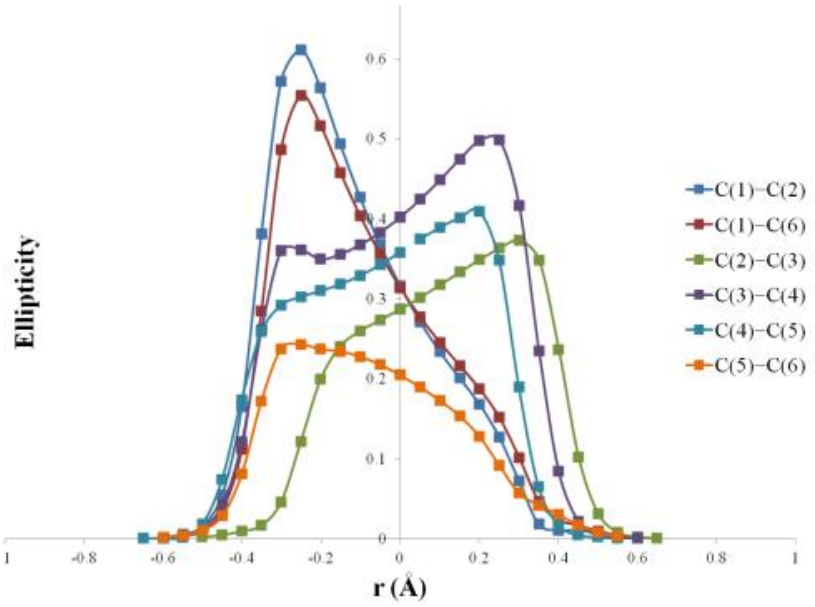

A.5.1: Graph of bond ellipticity along the bond paths for phenyl ring C(1) – C(6) in **c.s.3**.

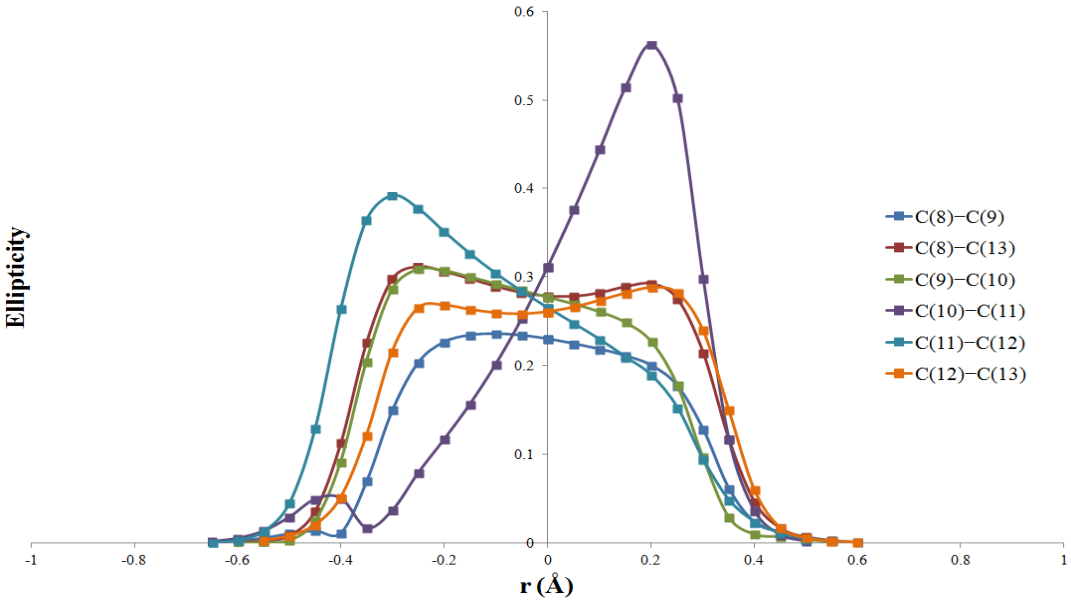

A.5.2: Graph of bond ellipticity along the bond paths for phenyl ring C(8) – C(13) in **c.s.3**.

A.5.2 Phenyl ring bond path plots in c.s.5

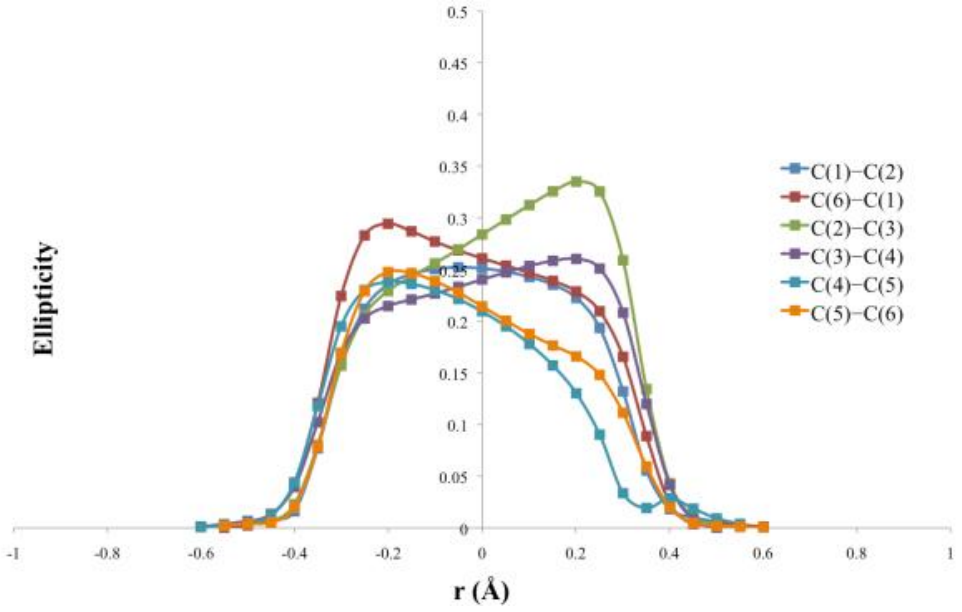

A.5.3: Graph of bond ellipticity along the bond paths for phenyl ring C(1) – C(6) in **c.s.5**.

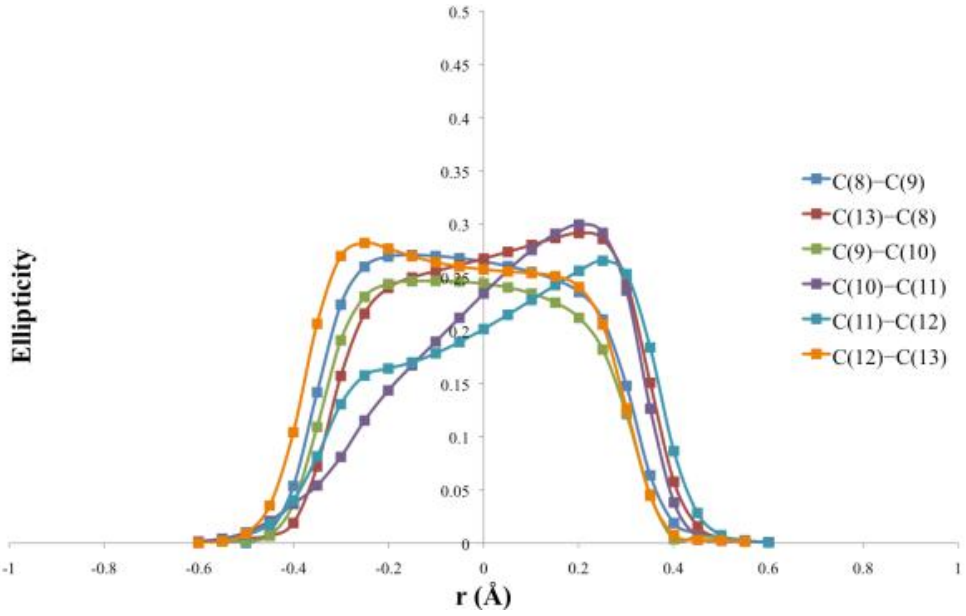

A.5.4: Graph of bond ellipticity along the bond paths for phenyl ring C(8) – C(13) in **c.s.5**.

A.5.3 Phenyl ring bond path plots in c.s.6

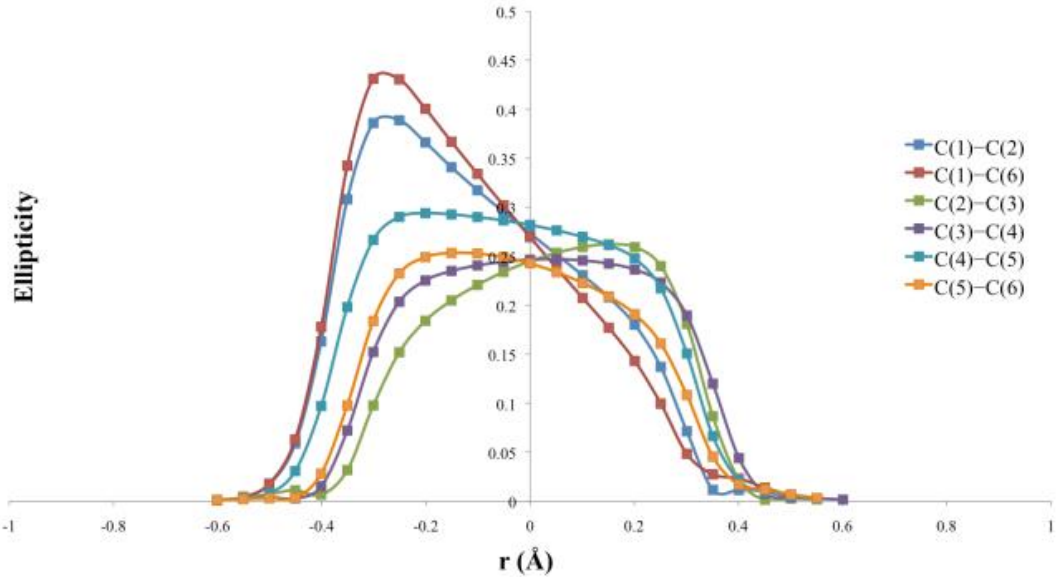

A.5.5: Graph of bond ellipticity along the bond paths for phenyl ring C(1) – C(6) in **c.s.6**.

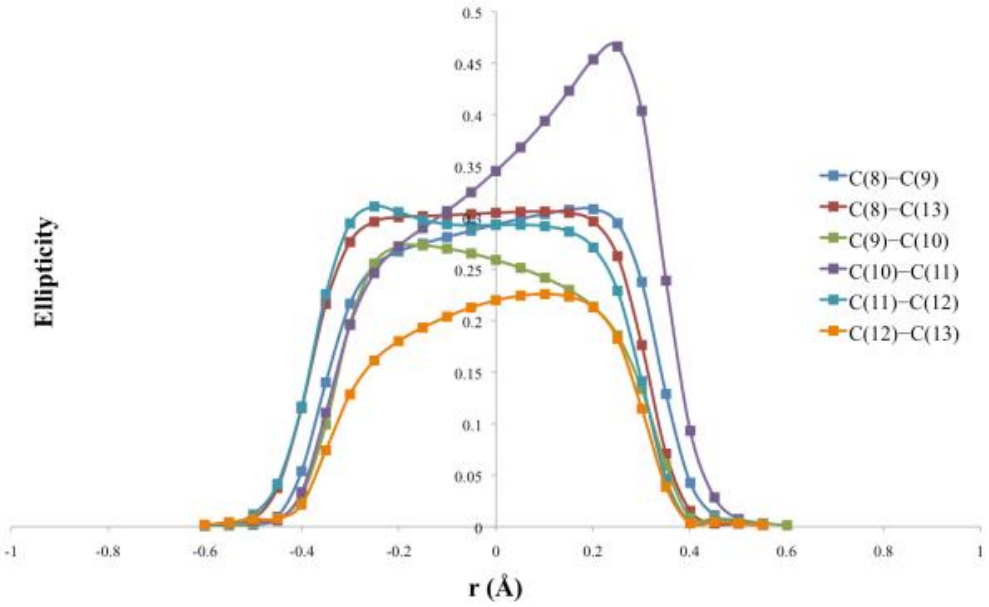

A.5.6: Graph of bond ellipticity along the bond paths for phenyl ring C(8) – C(13) in **c.s.6**.

A.5.4 Phenyl ring bond path plots in c.s.9

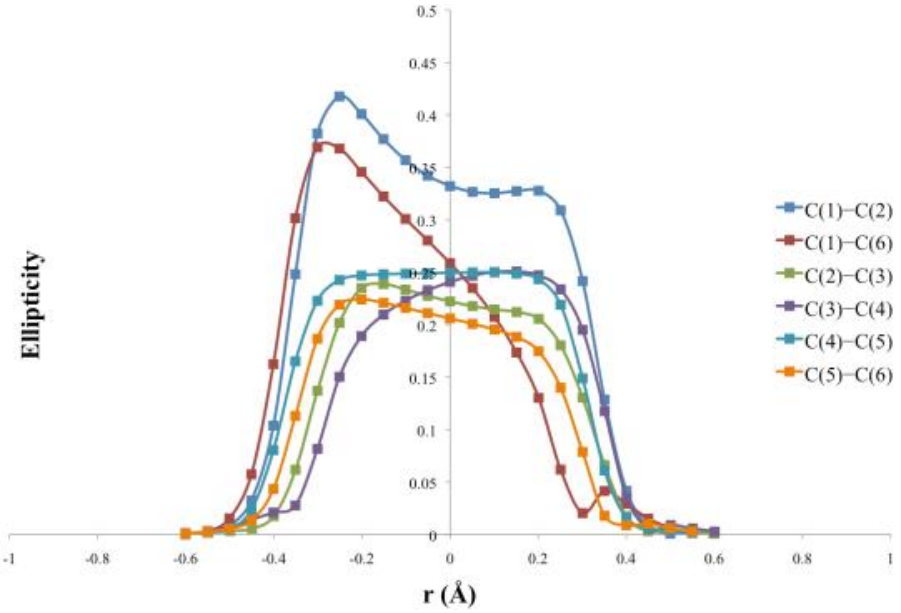

A.5.7: Graph of bond ellipticity along the bond paths for phenyl ring C(1) – C(6) in **c.s.9**.

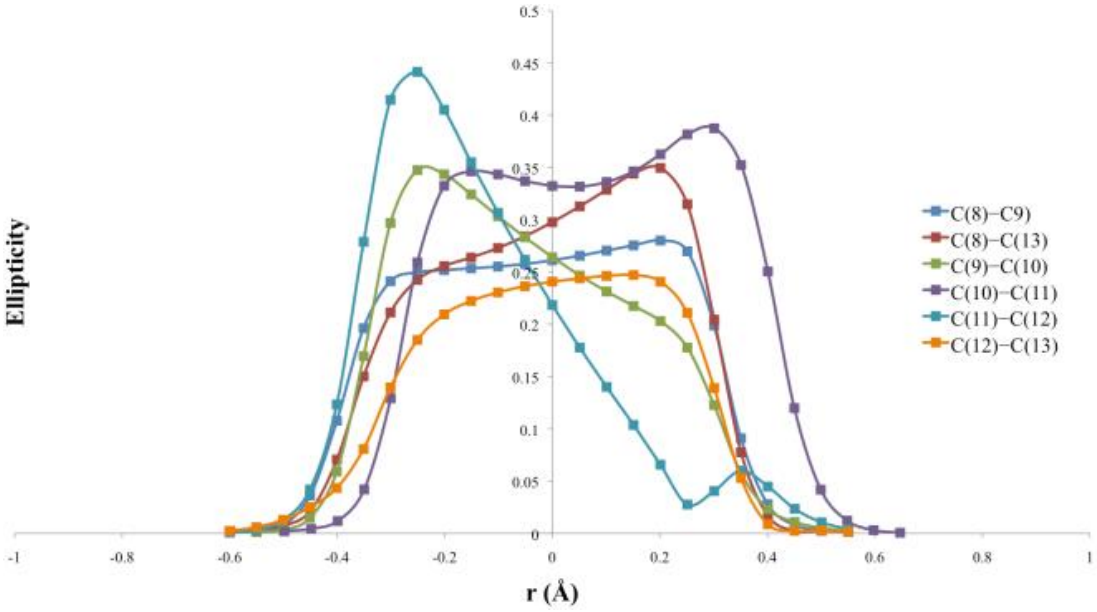

A.5.8: Graph of bond ellipticity along the bond paths for phenyl ring C(8) – C(13) in **c.s.9**.

A.5.5 Phenyl ring bond path plots in c.s.10

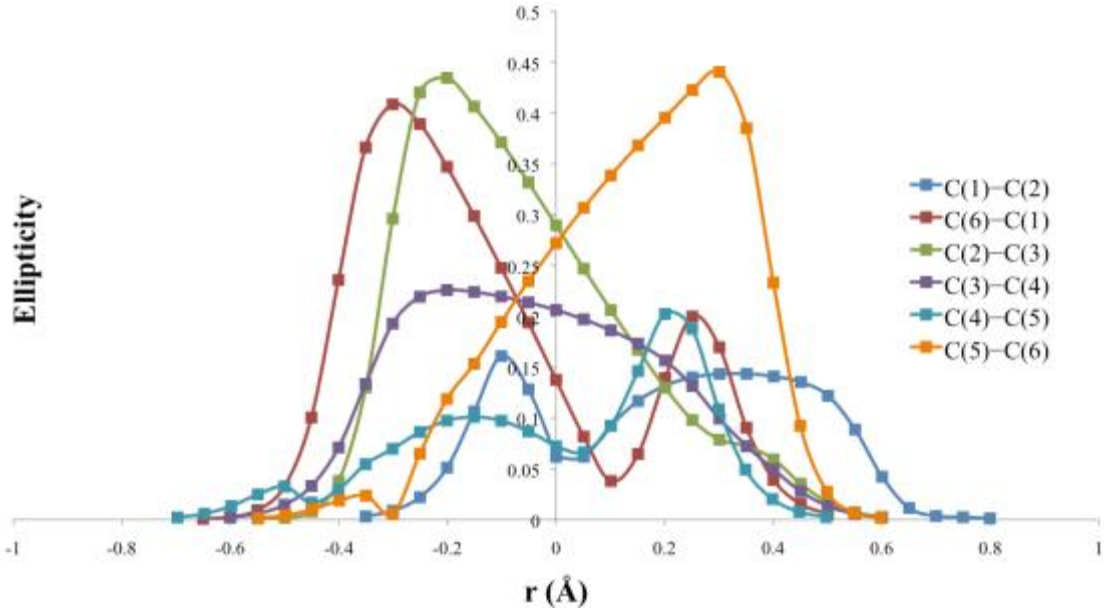

A.5.9: Graph of bond ellipticity along the bond paths for phenyl ring C(1) – C(6) in **c.s.10**.

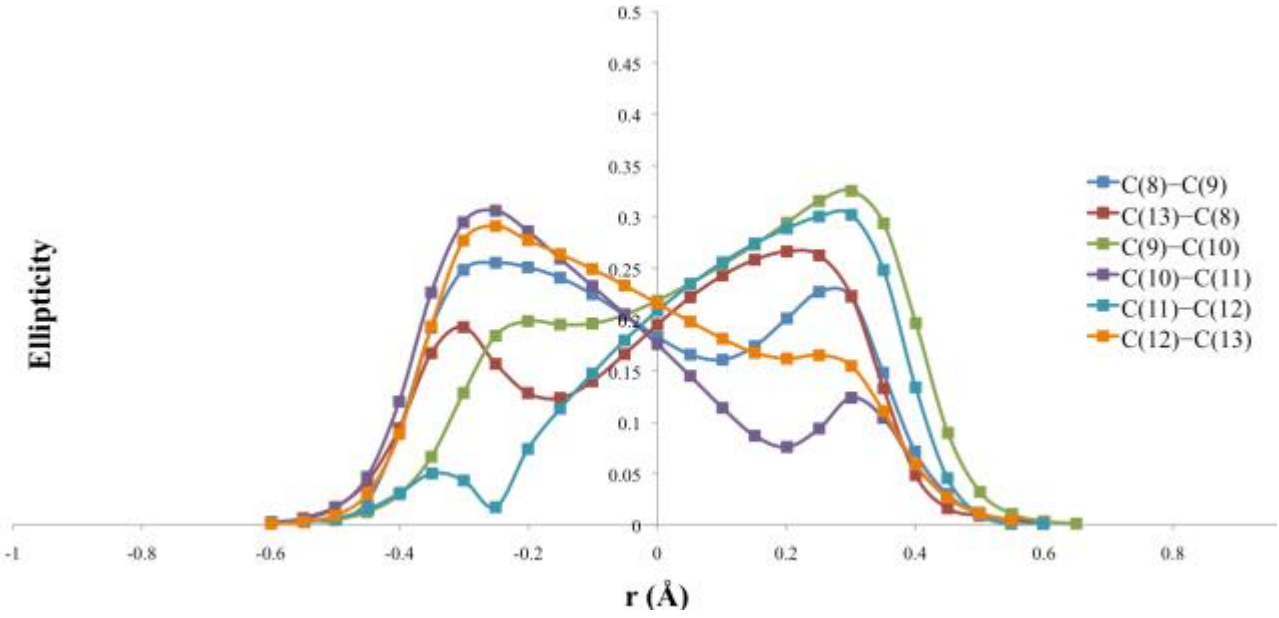

A.5.10: Graph of bond ellipticity along the bond paths for phenyl ring C(8) – C(13) in **c.s.10**.

A.5.6 Phenyl ring bond path plots in c.s.11

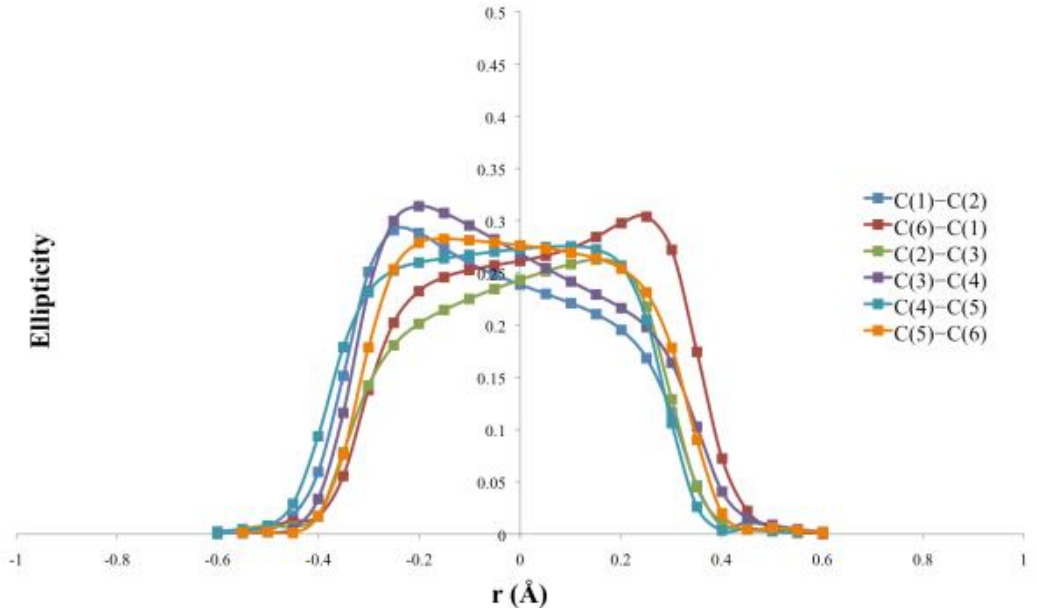

A.5.11: Graph of bond ellipticity along the bond paths for phenyl ring C(1) – C(6) in **c.s.11**.

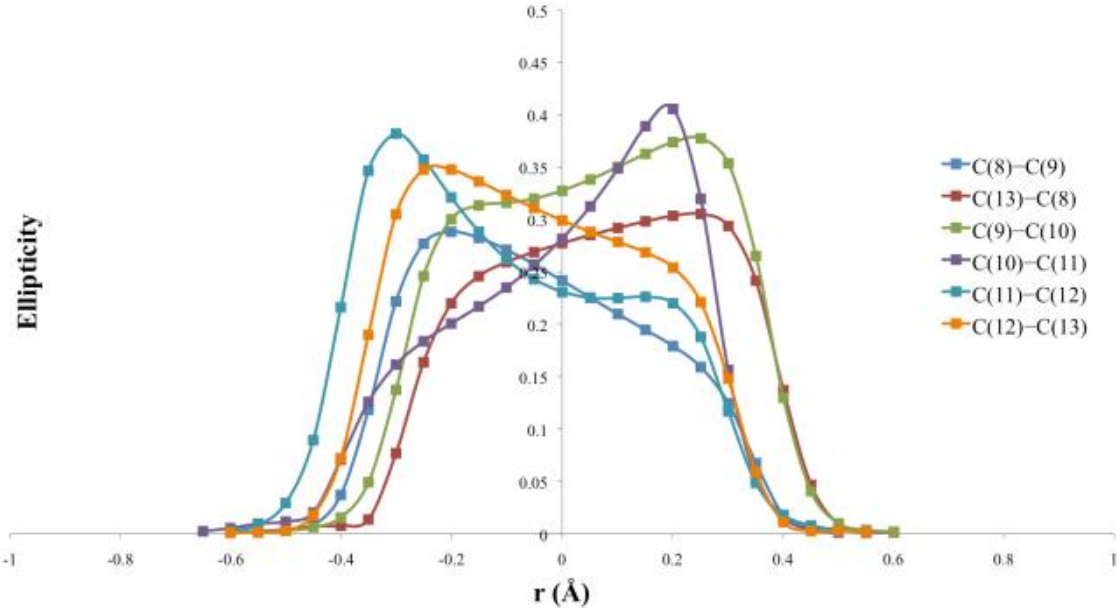

A.5.12: Graph of bond ellipticity along the bond paths for phenyl ring C(8) – C(13) in **c.s.11**.

A.5.7 Phenyl ring bond path plots in c.s.16

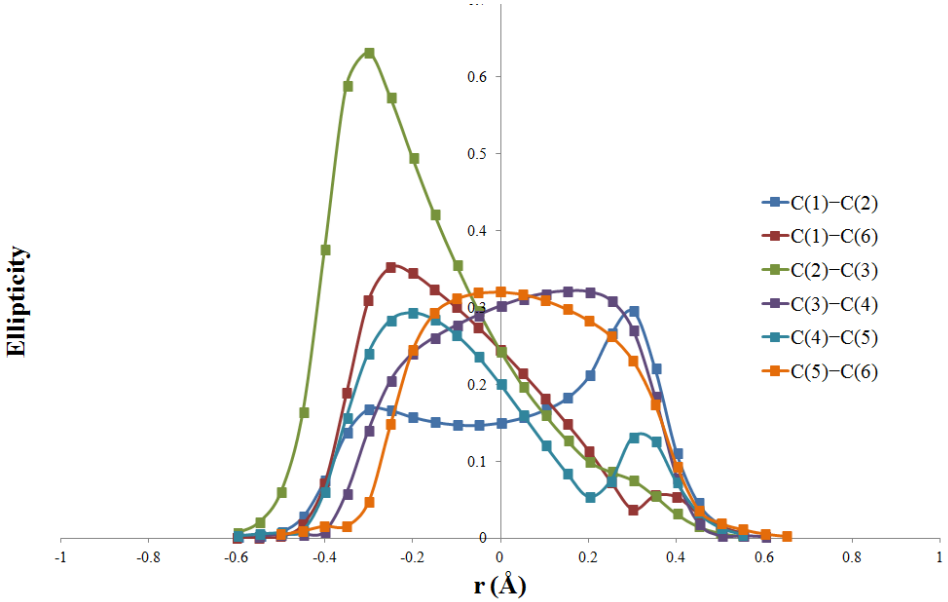

A.5.13: Graph of bond ellipticity along the bond paths for phenyl ring C(1) – C(6) in **c.s.16**.

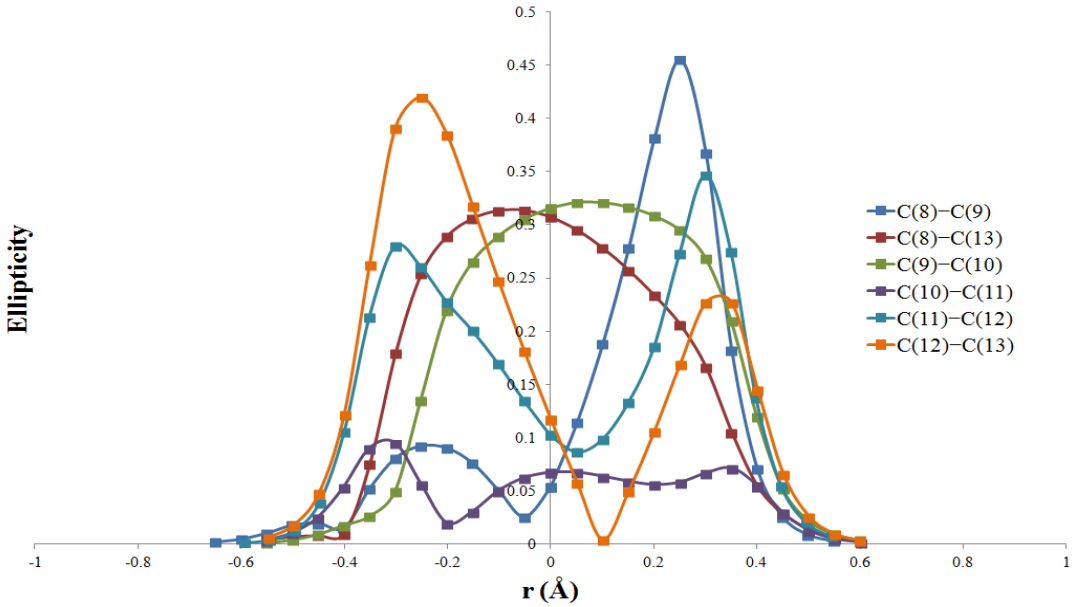

A.5.14: Graph of bond ellipticity along the bond paths for phenyl ring C(8) – C(13) in **c.s.16**.

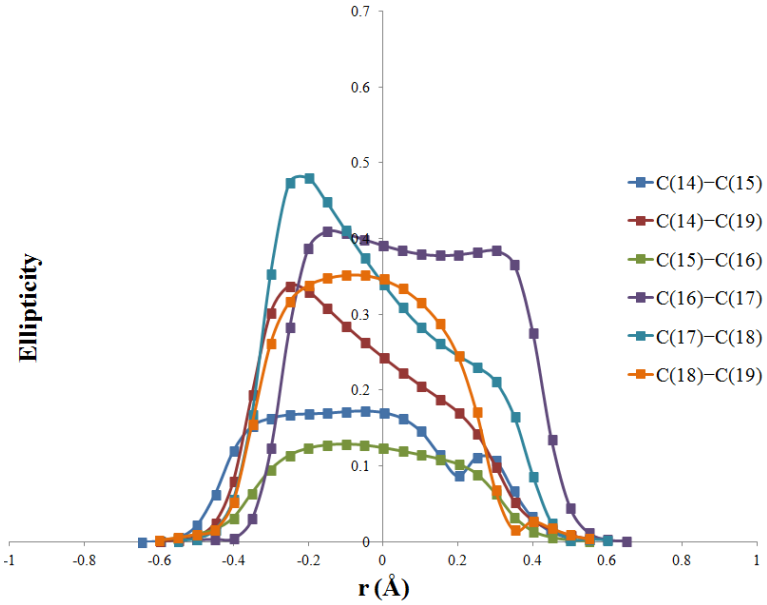

A.5.15: Graph of bond ellipticity along the bond paths for phenyl ring C(14) – C(19) in **c.s.16**.

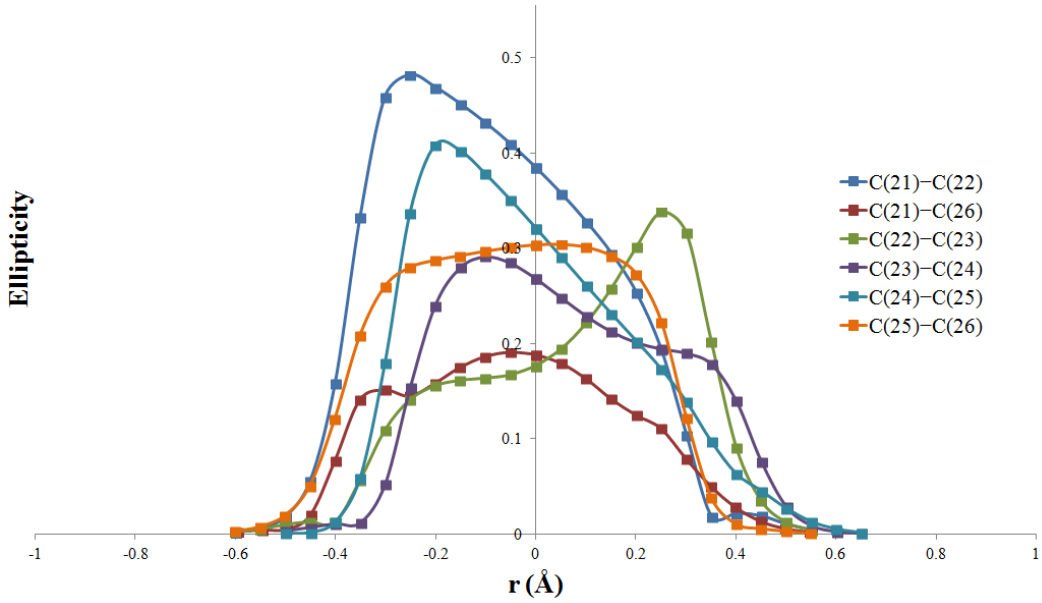

A.5.16: Graph of bond ellipticity along the bond paths for phenyl ring C(21) – C(26) in **c.s.16**.

A.5.8 Phenyl ring bond path plots in c.s.17

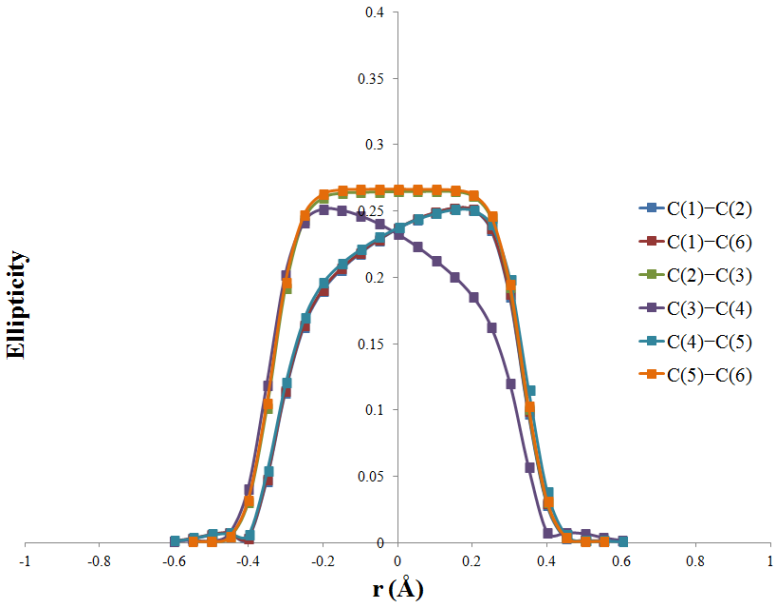

A.5.17: Graph of bond ellipticity along the bond paths for phenyl ring C(1) – C(6) in **c.s.17**.

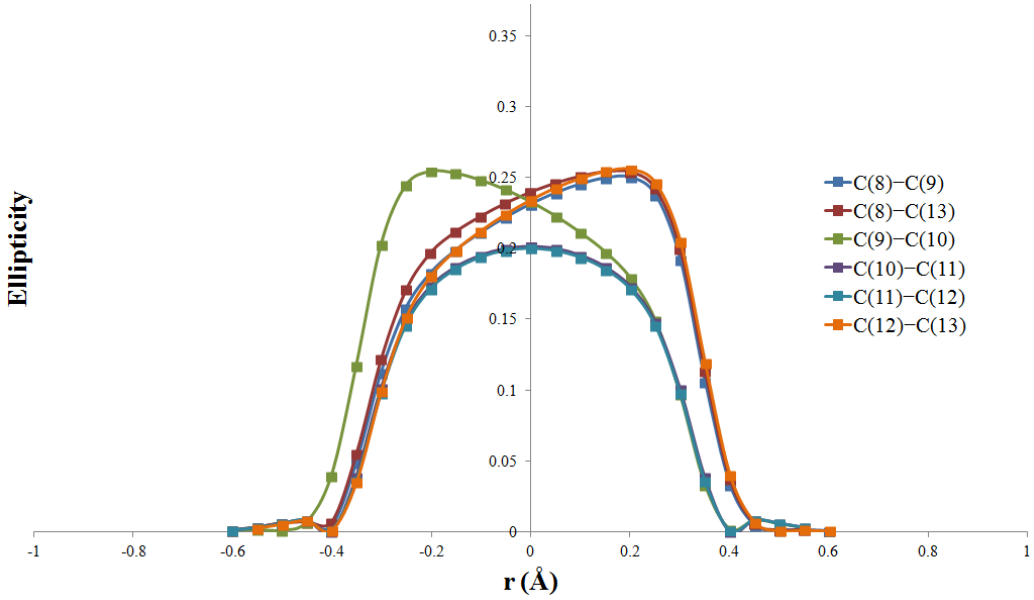

A.5.18: Graph of bond ellipticity along the bond paths for phenyl ring C(8) – C(13) in **c.s.17**.

A.5.9 Phenyl ring bond path plots in c.s.18

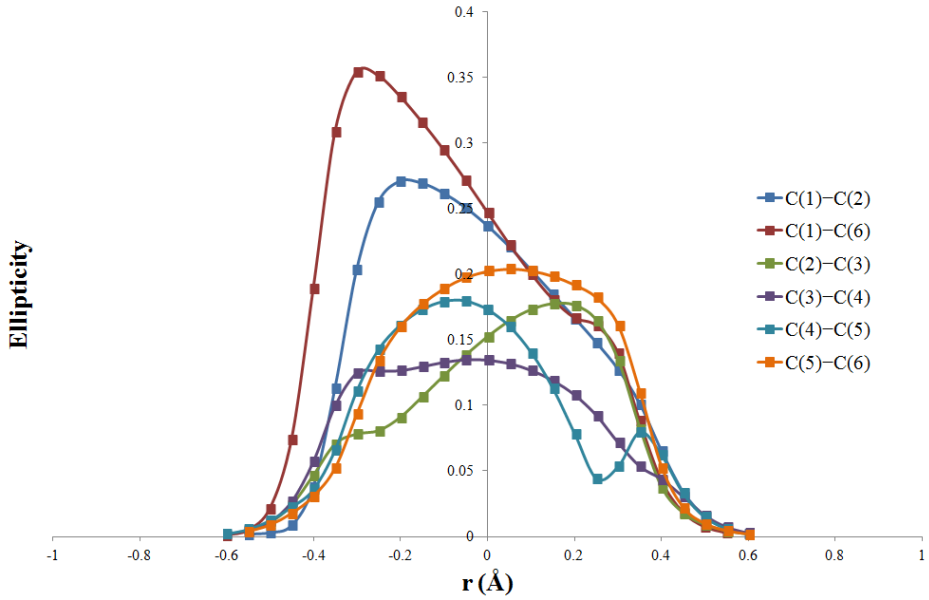

A.5.19: Graph of bond ellipticity along the bond paths for phenyl ring C(1) – C(6) in **c.s.18**.

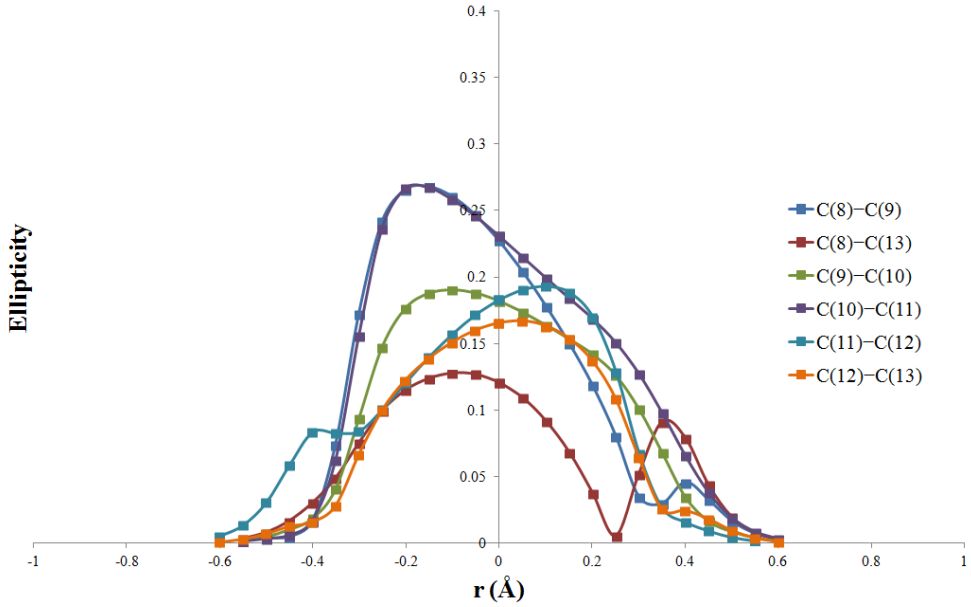

A.5.20: Graph of bond ellipticity along the bond paths for phenyl ring C(8) – C(13) in **c.s.18**.

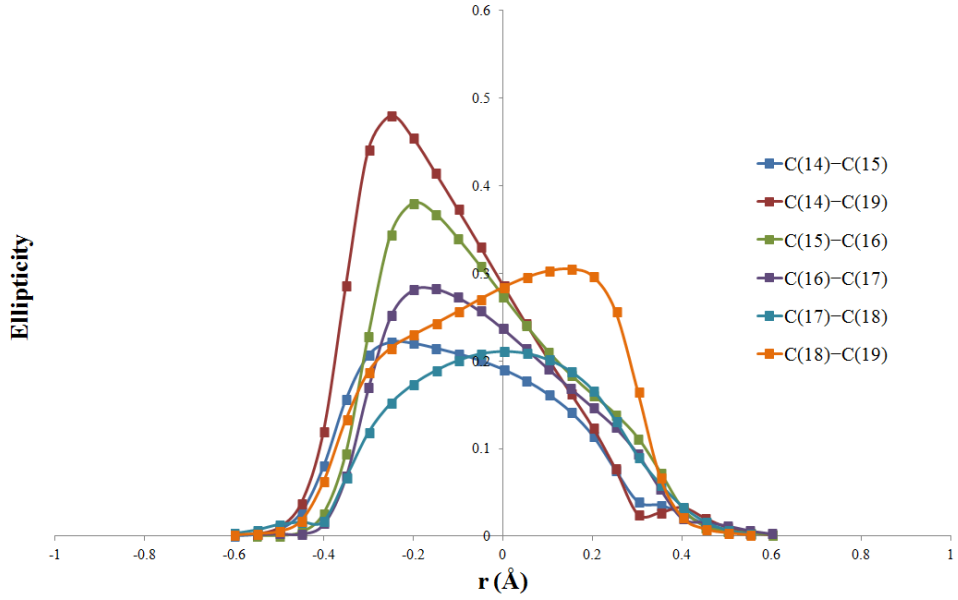

A.5.21: Graph of bond ellipticity along the bond paths for phenyl ring C(14) – C(19) in **c.s.18**.

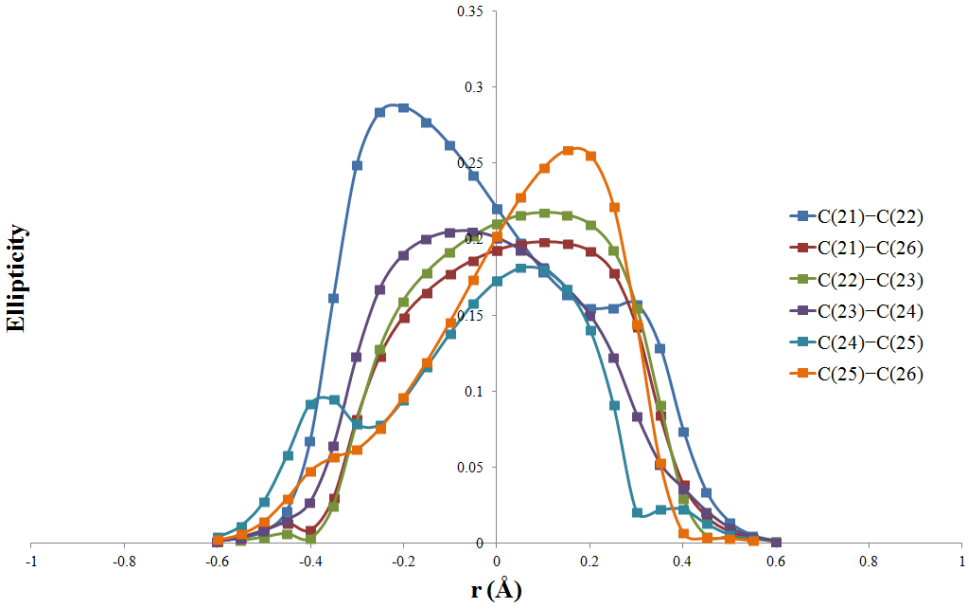

A.5.22: Graph of bond ellipticity along the bond paths for phenyl ring C(21) – C(26) in **c.s.18**.

A.5.10 Urea bond path plots in c.s.3

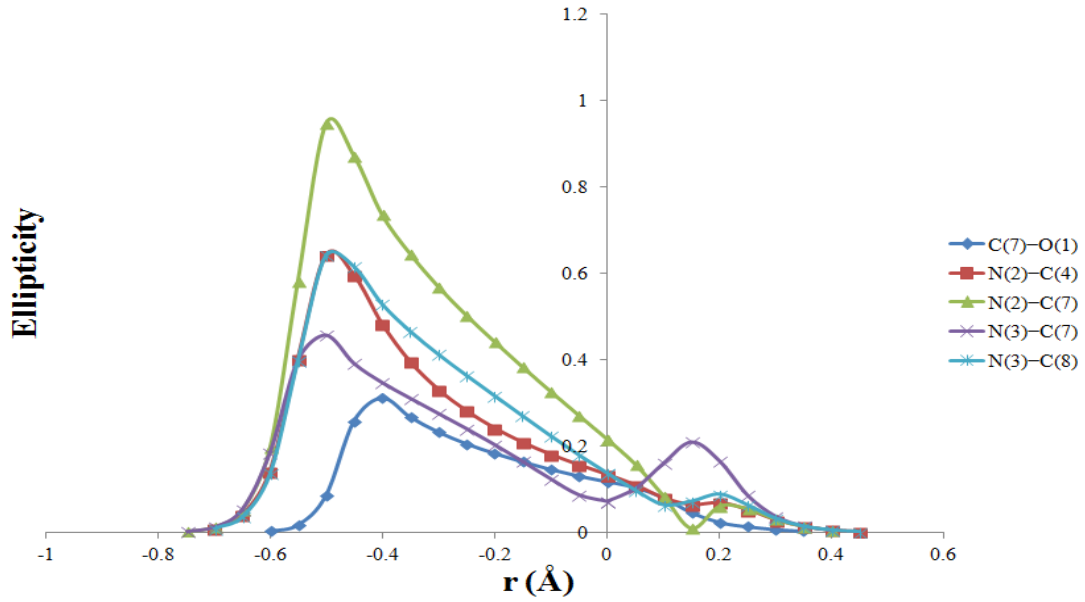

A.5.23 Bond ellipticity along the urea bond paths.

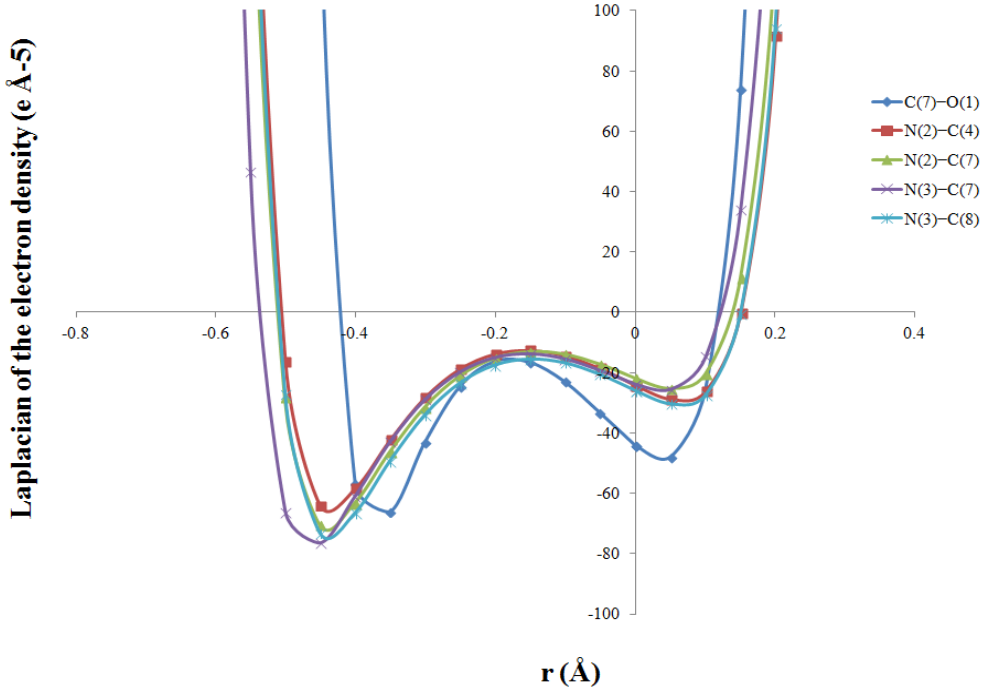

A.5.24: $\nabla^2\rho(\mathbf{r})$ along the urea bond paths.

A.5.11 Urea bond path plots in c.s.6, 9 and 11

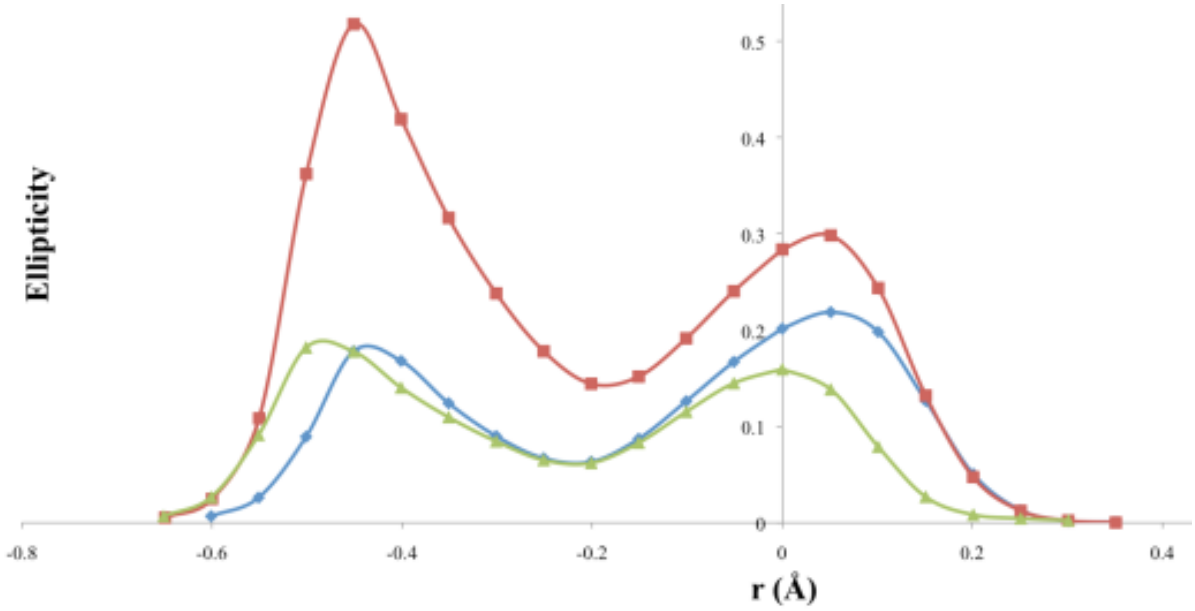

A.5.25: Bond ellipticity along the C(7)−O(1) bond path of the urea group. Blue = **c.s.6**, Red = **c.s.9**, Green = **c.s.11**.

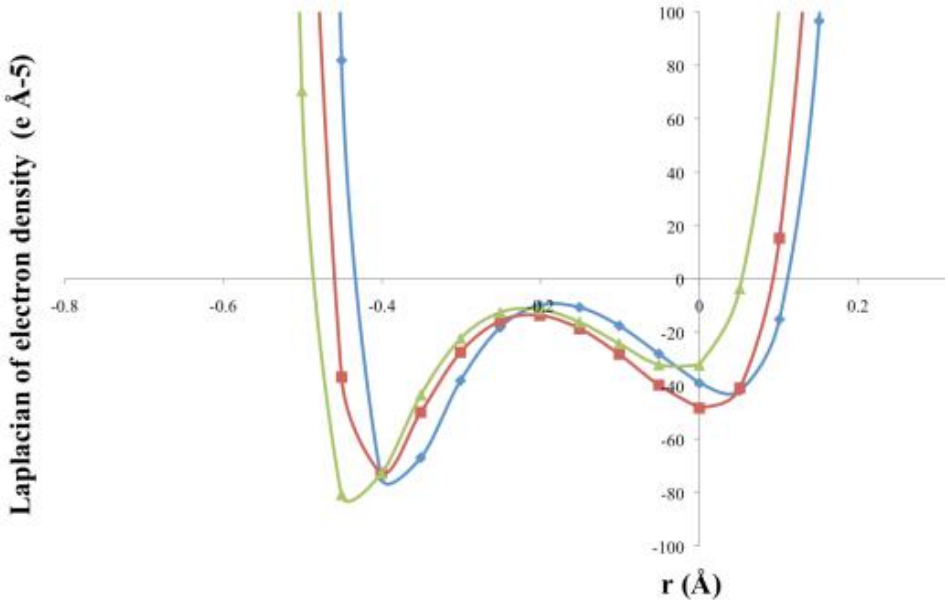

A.5.26: $\nabla^2\rho(\mathbf{r})$ along the C(7)−O(1) bond path of the urea group. Blue = **c.s.6**, Red = **c.s.9**, Green = **c.s.11**.

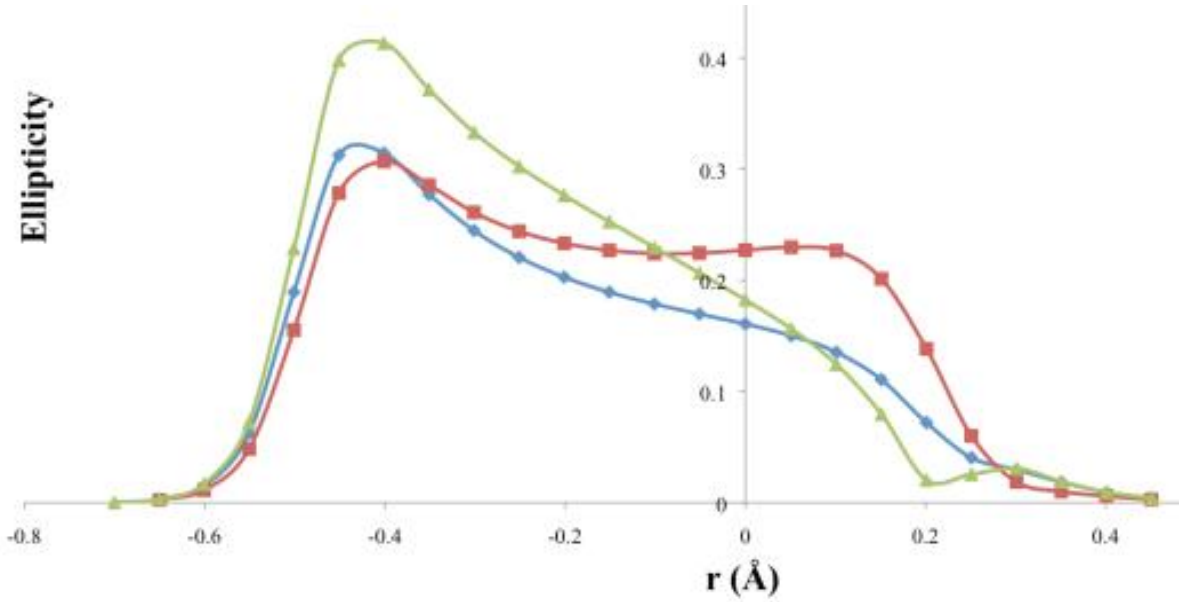

A.5.27: Bond ellipticity along the N(2)−C(4) bond path of the urea group. Blue = **c.s.6**, Red = **c.s.9**, Green = **c.s.11**.

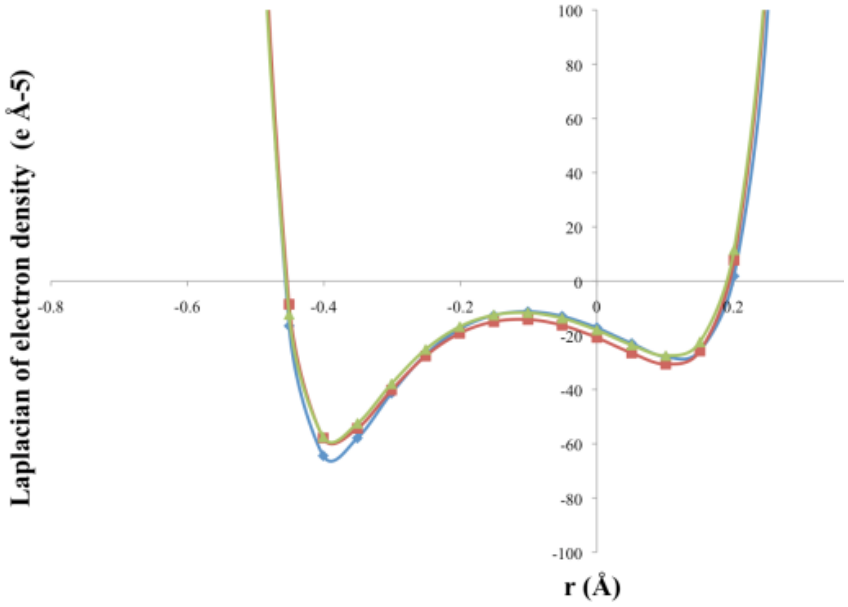

A.5.28: $\nabla^2\rho(\mathbf{r})$ along the N(2)−C(4) bond path of the urea group. Blue = **c.s.6**, Red = **c.s.9**, Green = **c.s.11**.

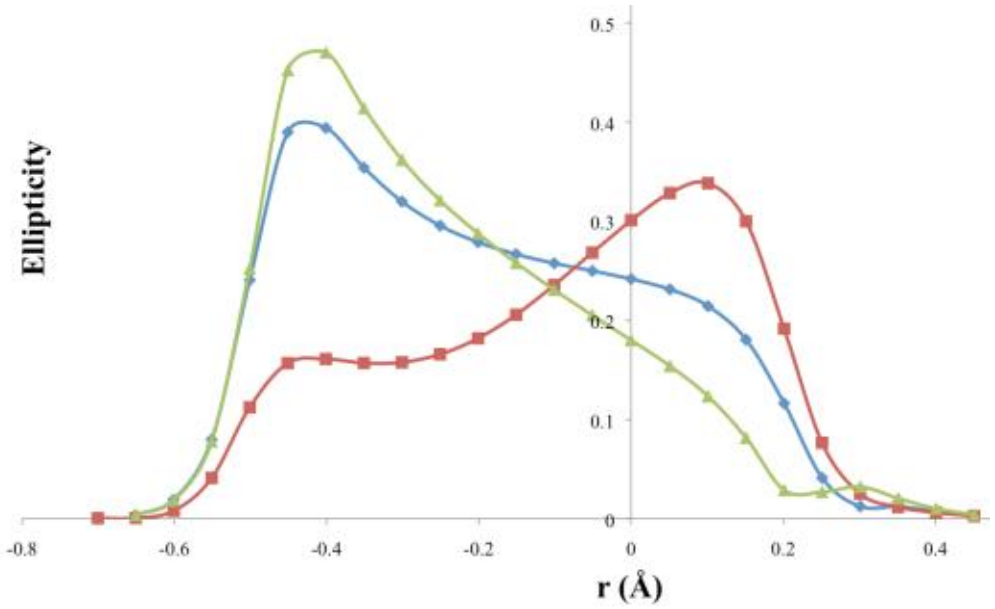

A.5.29: Bond ellipticity along the N(2)−C(7) bond path of the urea group. Blue = **c.s.6**, Red = **c.s.9**, Green = **c.s.11**.

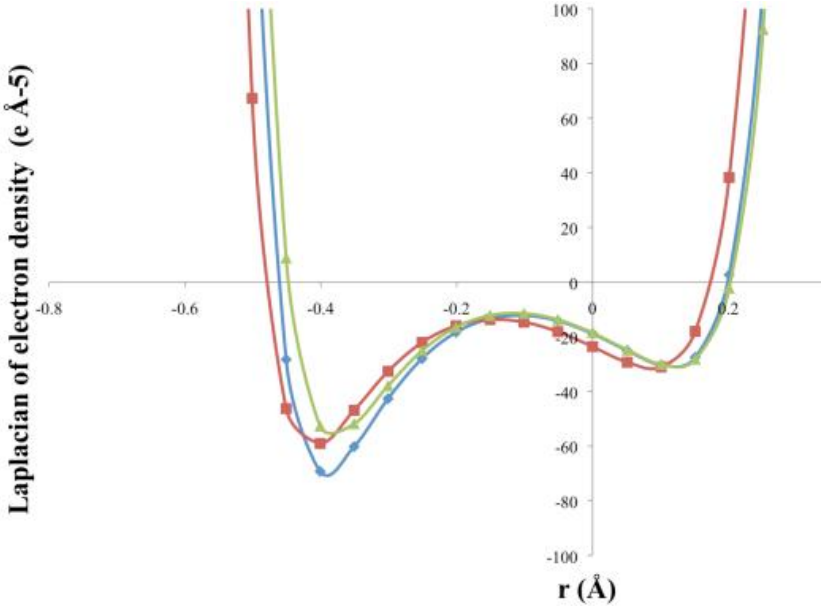

A.5.30: $\nabla^2\rho(\mathbf{r})$ along the N(2)−C(7) bond path of the urea group. Blue = **c.s.6**, Red = **c.s.9**, Green = **c.s.11**.

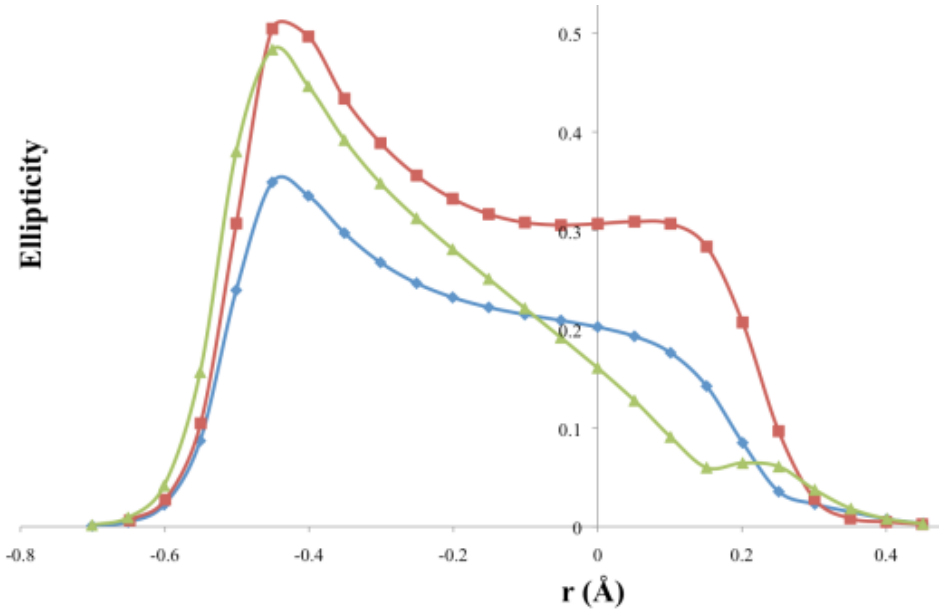

A.5.31: Bond ellipticity along the N(3)−C(7) bond path of the urea group. Blue = **c.s.6**, Red = **c.s.9**, Green = **c.s.11**.

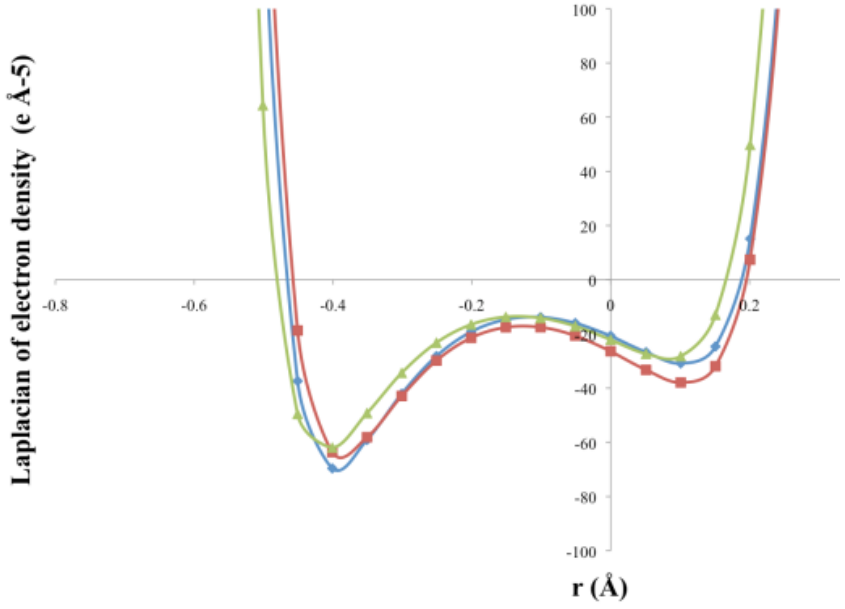

A.5.32: $\nabla^2\rho(\mathbf{r})$ along the N(3)−C(7) bond path of the urea group. Blue = **c.s.6**, Red = **c.s.9**, Green = **c.s.11**.

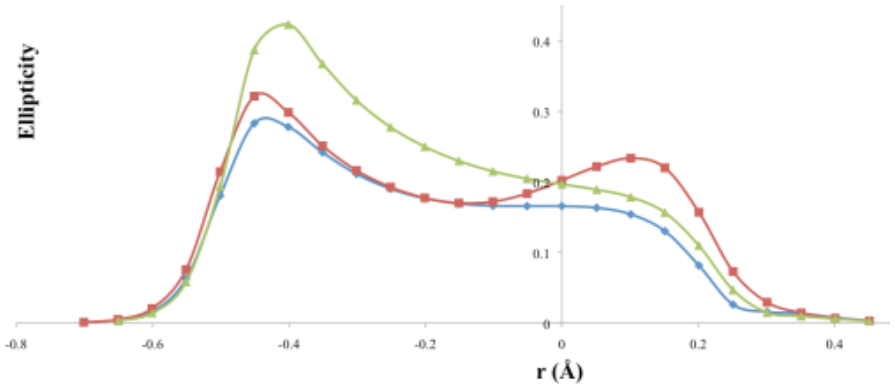

A.5.33: Bond ellipticity along the N(3)−C(8) bond path of the urea group. Blue = **c.s.6**, Red = **c.s.9**, Green = **c.s.11**.

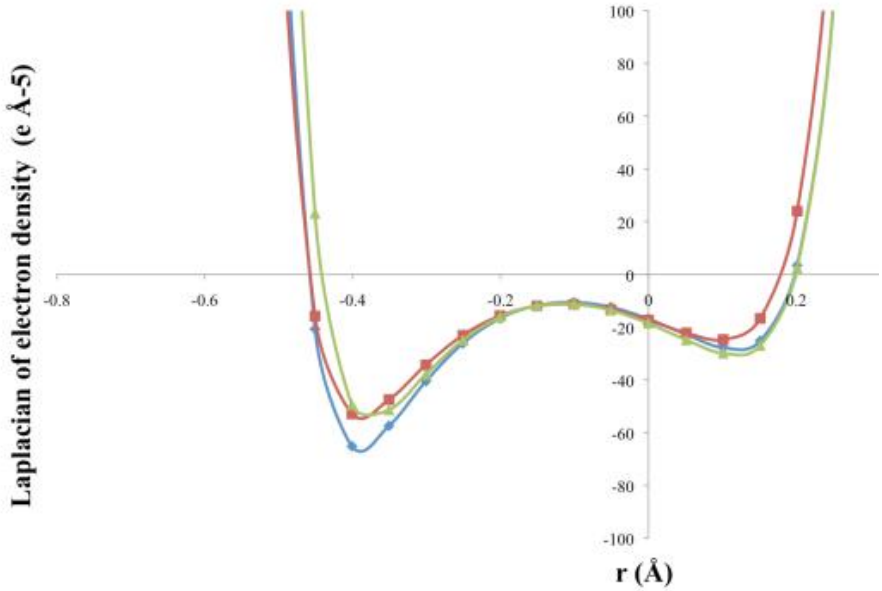

A.5.34: $\nabla^2\rho(\mathbf{r})$ along the N(3)−C(8) bond path of the urea group. Blue = **c.s.6**, Red = **c.s.9**, Green = **c.s.11**.

A.5.12 Urea bond path plots in c.s.5 and c.s.10

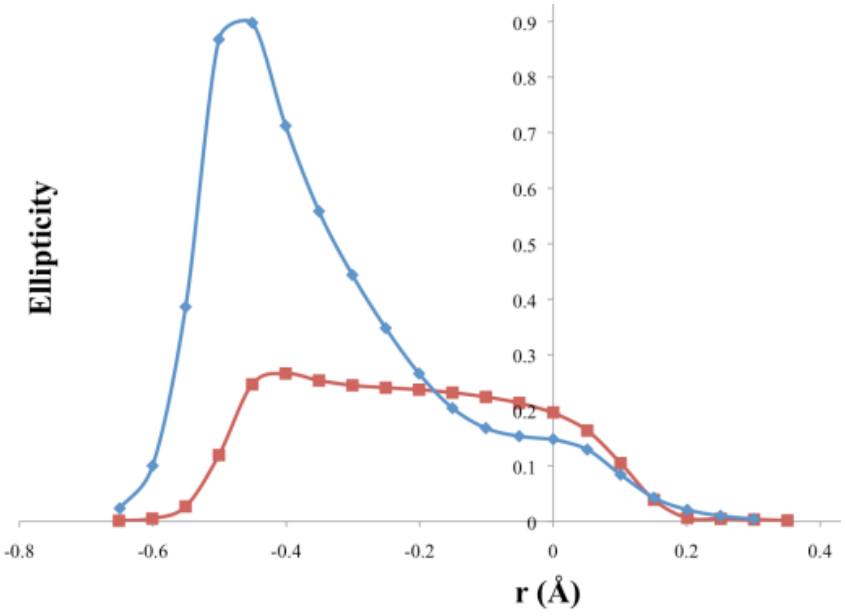

A.5.35: Bond ellipticity along the C(7)−O(1) bond path of the urea group. Red = **c.s.5**, Blue = **c.s.10**.

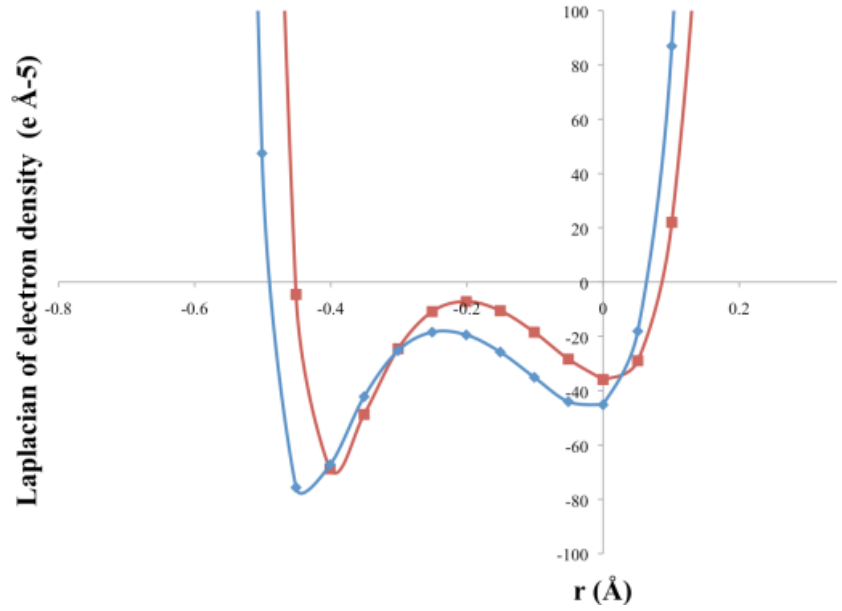

A.5.36:$\nabla^2\rho(\mathbf{r})$ along the C(7)−O(1) bond path of the urea group. Red = **c.s.5**, Blue = **c.s.10**.

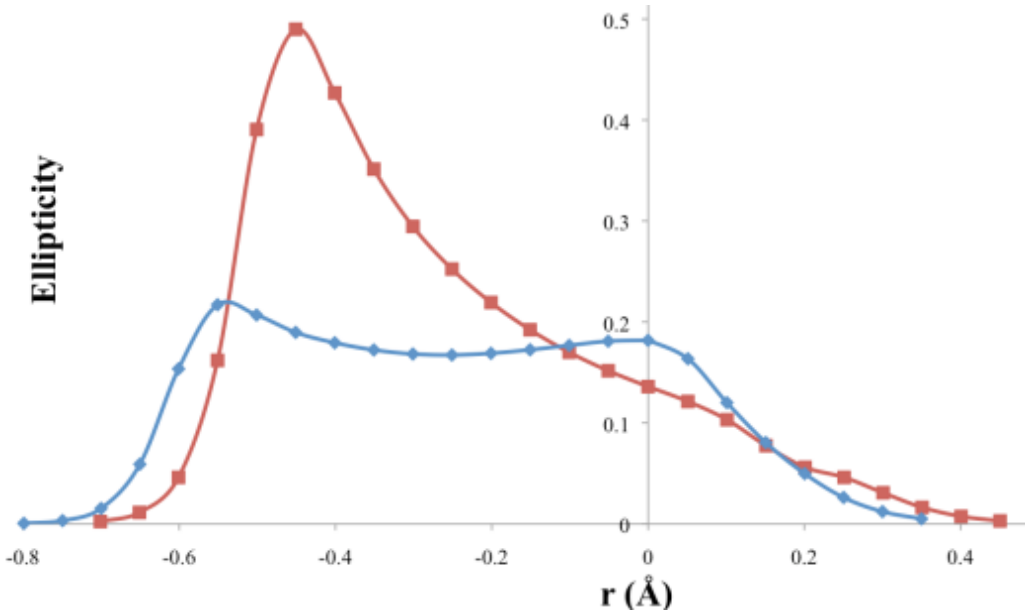

A.5.37: Bond ellipticity along the N(2)−C(4)/ N(3)−C(4) bond path of the urea group. Red = **c.s.5**, Blue = **c.s.10**.

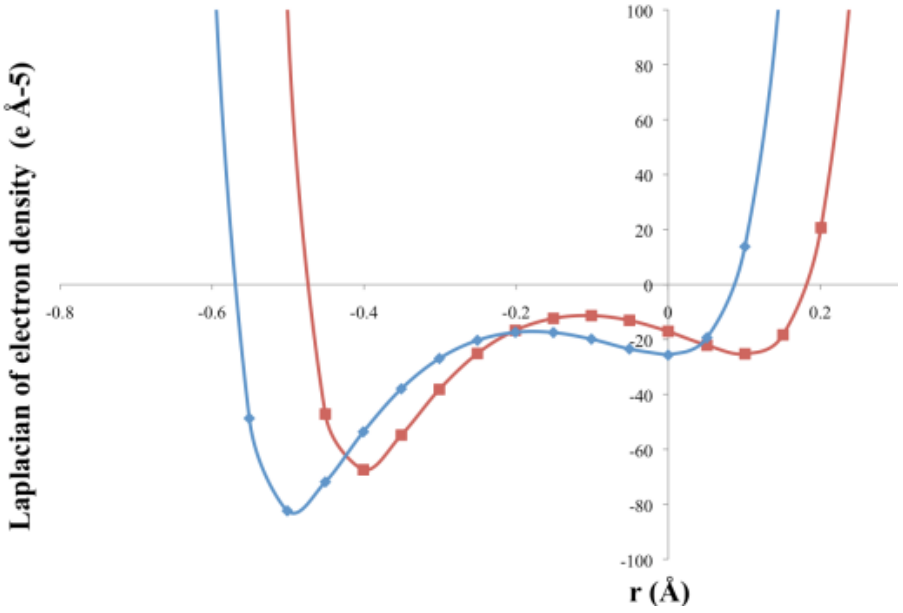

A.5.38: $\nabla^2\rho(\mathbf{r})$ along the N(2)−C(4)/ N(3)−C(4) bond path of the urea group. Red = **c.s.5**, Blue = **c.s.10**.

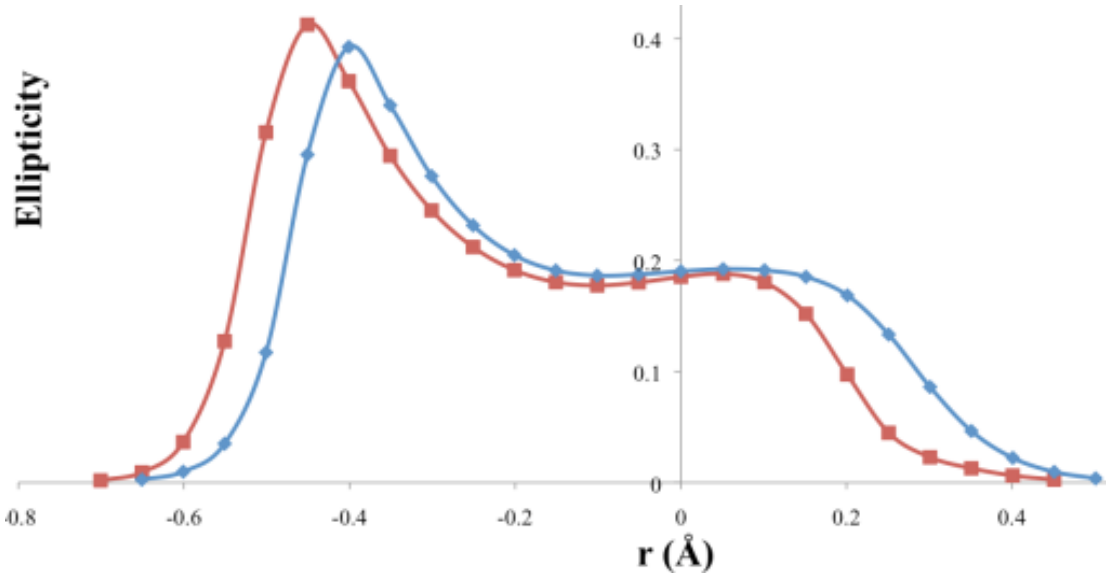

A.5.39: Graph of the bond ellipticity along the N(2)−C(7)/ N(3)−C(7) bond path of the urea group. Red = **c.s.5**, Blue = **c.s.10**.

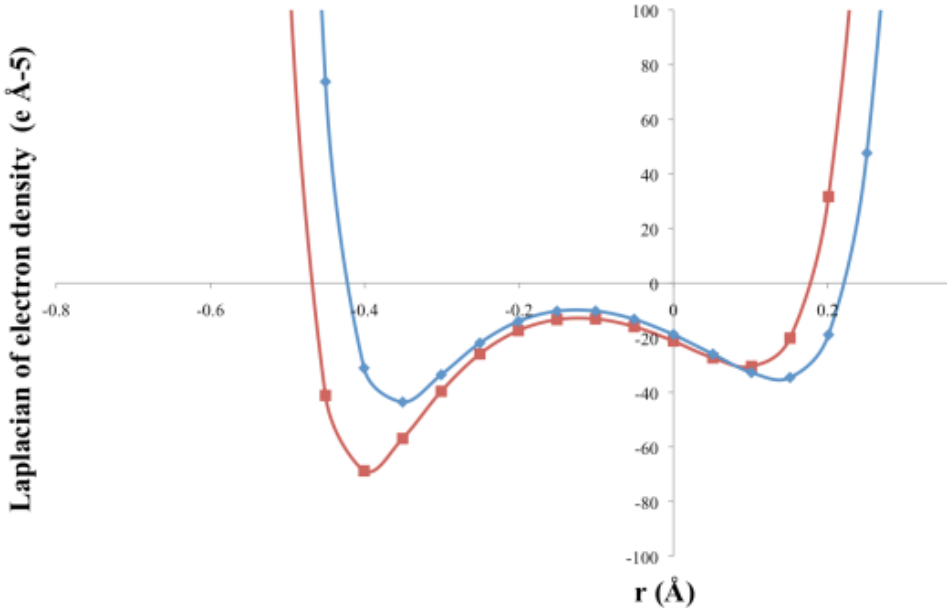

A.5.40: $\nabla^2\rho(\mathbf{r})$ along the N(2)−C(7)/ N(3)−C(7) bond path of the urea group. Red = **c.s.5**, Blue = **c.s.10**.

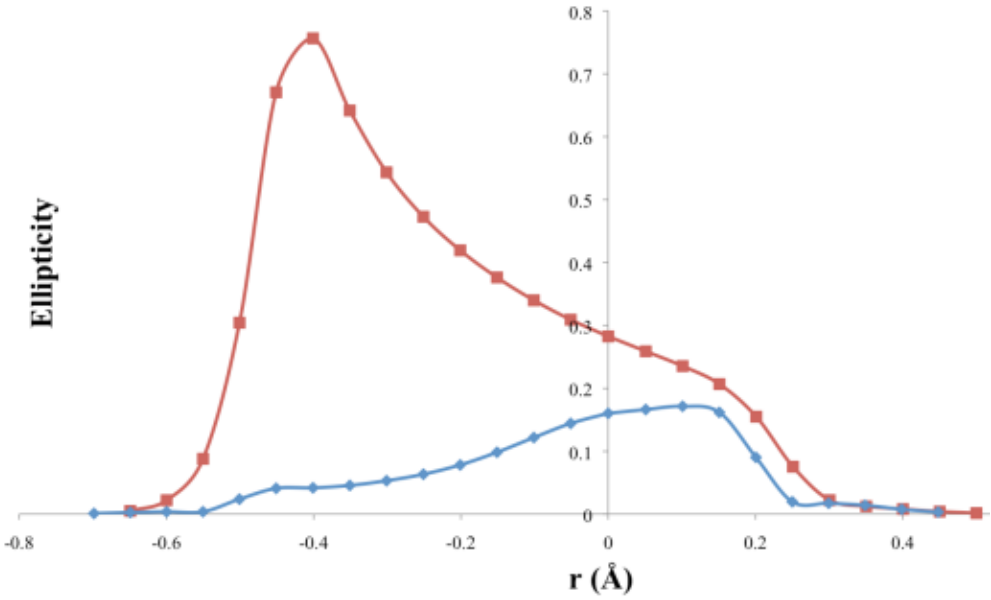

A.5.41:Bond ellipticity along the N(3)−C(7)/ N(4)−C(7) bond path of the urea group (*left*). Red = **c.s.5**, Blue = **c.s.10**.

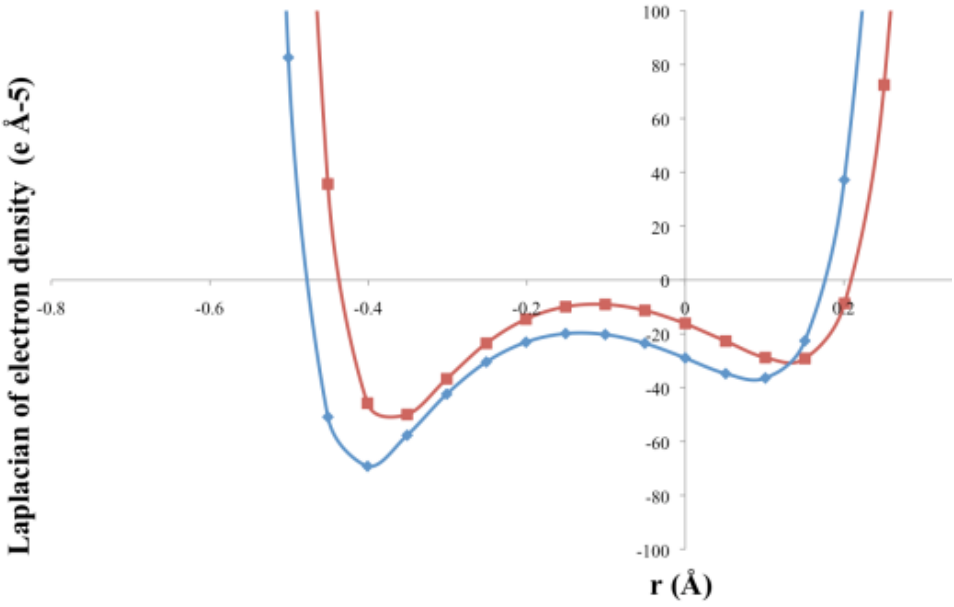

A.5.42:$\nabla^2\rho(\mathbf{r})$ along the N(3)−C(7)/ N(4)−C(7) bond path of the urea group. Red = **c.s.5**, Blue = **c.s.10**.

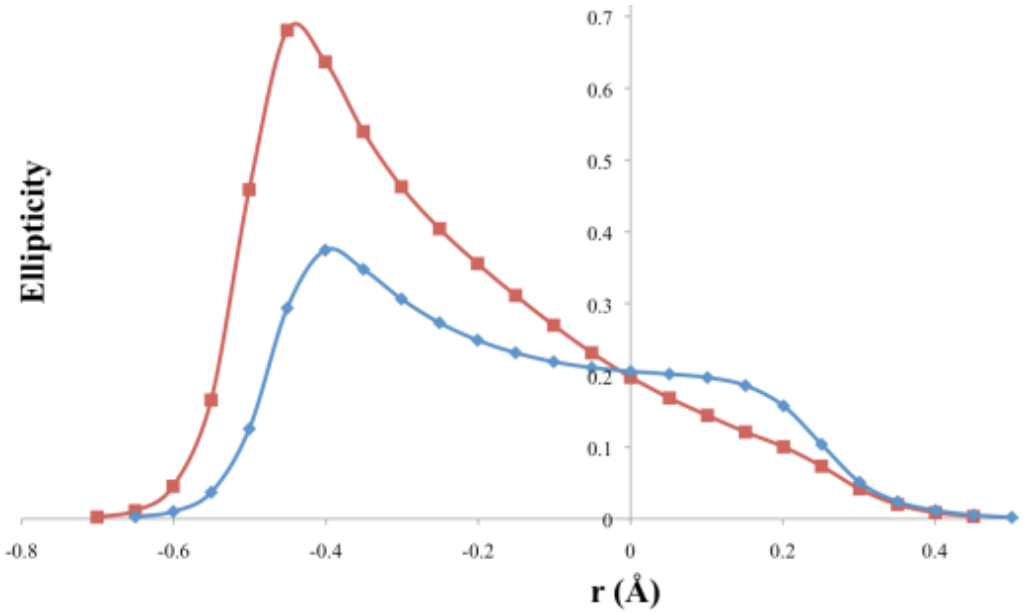

A.5.43: Bond ellipticity along the N(3)−C(8)/ N(4)−C(8) bond path of the urea group**.** Red = **c.s.5**, Blue = **c.s.10**.

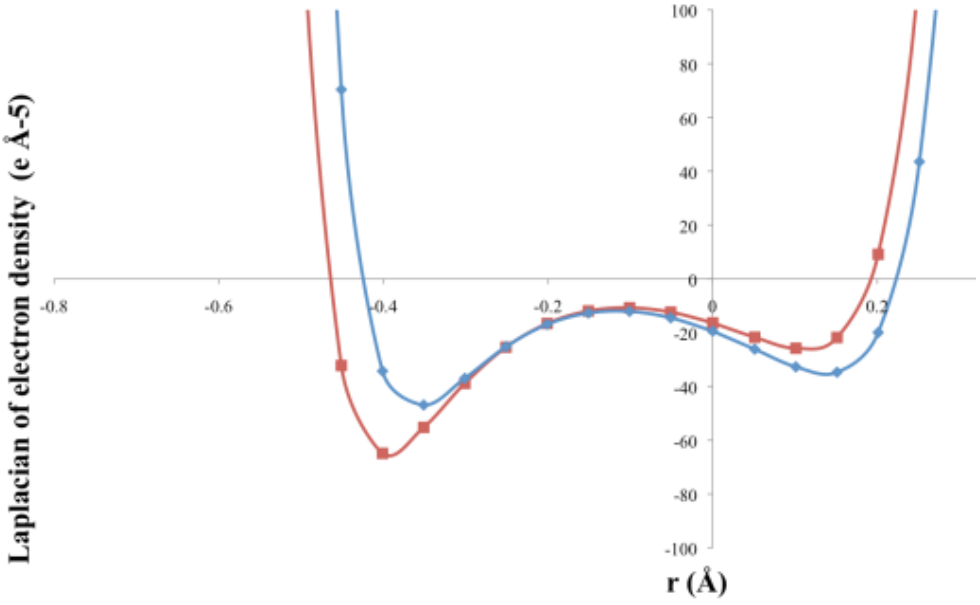

A.5.44: $\nabla^2\rho(\mathbf{r})$ along the N(3)−C(8)/ N(4)−C(8) bond path of the urea group (*right*). Red = **c.s.5**, Blue = **c.s.10**.

A.5.13 (Thio)urea bond path plots in c.s.16, c.s.17 and c.s.18

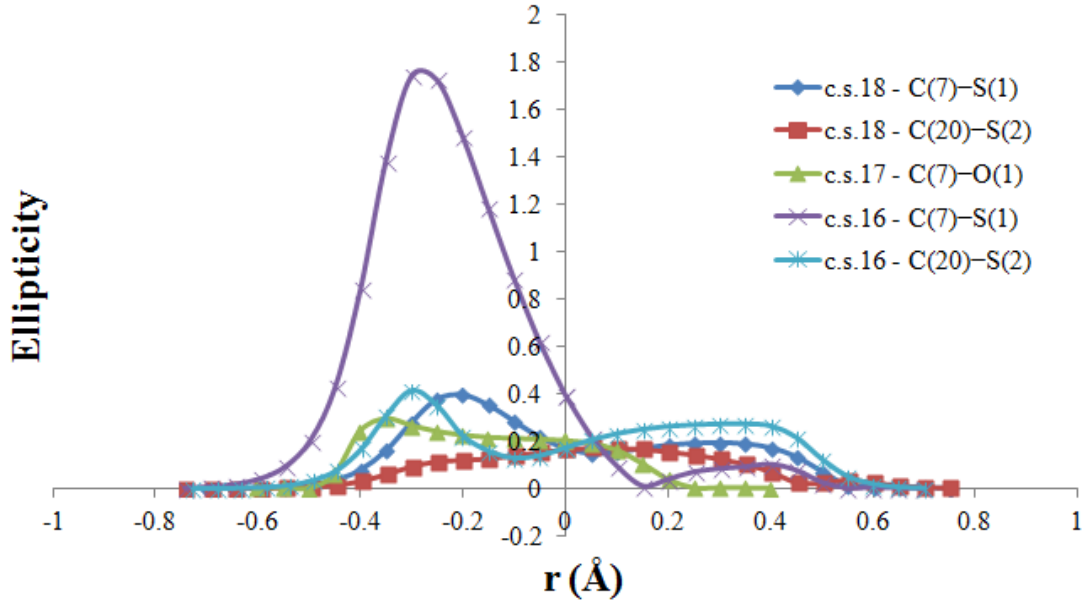

A.5.45: Bond ellipticity along the C–S/ C–O bond path of the (thio)urea groups in **c.s.16**, **c.s.17** and **c.s.18**.

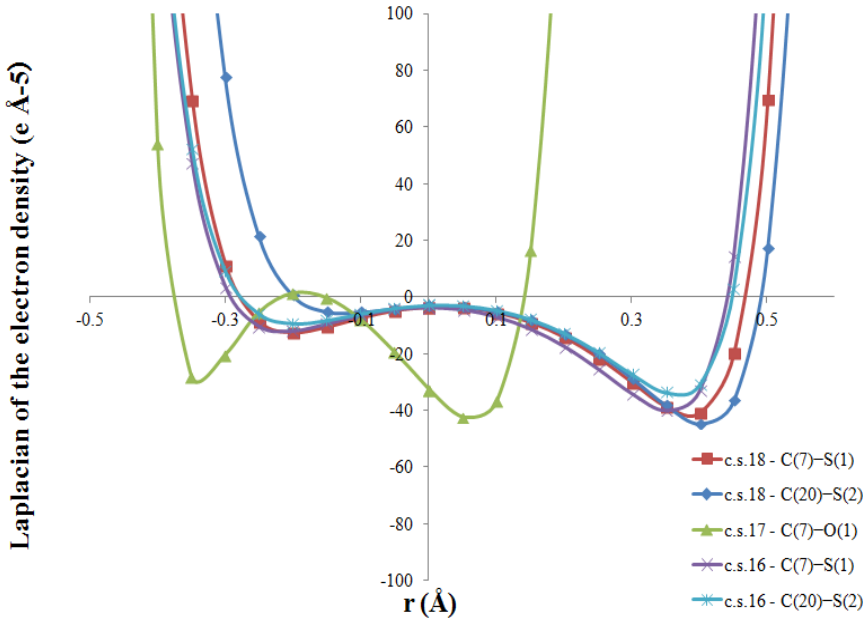

A.5.46: $\nabla^2\rho(\mathbf{r})$ along the urea/thiourea C–S/ C–O bond path in **c.s.16**, **c.s.17** and **c.s.18**.

A.6 Topological properties of BCPs

Electronic properties of the covalent bonds at the BCPs in all the structures discussed in Chapters 4 and 5 are now given.

A.6.1 Experimental topological analysis

T.A.6.1: BCPs in structure **c.s.3** (experimental data).

Bond	$\rho(\mathbf{r})$ (e A^{-3})	$\nabla^2\rho(\mathbf{r})$ (e A^{-5})	R_{ij} (Å)	d_1 (Å)	d_2 (Å)	λ_1	λ_2	λ_3	ε
O(1)−C(7)	3.20(7)	-44.1(3)	1.2215	0.7310	0.4904	-30.64	-27.42	13.95	0.12
O(2)−N(1)	3.13(5)	-1.0(2)	1.2363	0.6116	0.6247	-26.20	-22.66	47.82	0.16
O(3)−N(1)	3.14(5)	-1.2(2)	1.2359	0.6116	0.6243	-26.27	-22.71	47.81	0.16
O(4)−N(4)	3.20(4)	-4.6(2)	1.2395	0.6112	0.6282	-26.80	-25.03	47.19	0.07
O(5)−N(4)	3.19(5)	-4.8(2)	1.2404	0.6117	0.6287	-26.86	-25.02	47.14	0.07
N(1)−C(1)	1.89(5)	-17.2(2)	1.4560	0.8383	0.6177	-15.49	-12.16	10.47	0.27
N(2)−C(4)	2.08(6)	-24.1(2)	1.3940	0.8439	0.5501	-17.01	-15.00	7.87	0.13
N(2)−C(7)	2.04(6)	-21.8(2)	1.3856	0.8433	0.5423	-16.91	-13.90	9.07	0.22
N(2)−H(2A)	2.26(9)	-31.8(2)	1.0100	0.7278	0.2821	-29.85	-26.35	24.42	0.13
N(3)−C(7)	2.08(6)	-23.8(2)	1.3902	0.8645	0.5257	-16.33	-15.22	7.79	0.07
N(3)−C(8)	2.16(6)	-25.9(2)	1.3869	0.8401	0.5468	-18.29	-16.07	8.50	0.14
N(3)−H(3A)	2.31(9)	-35.9(5)	1.0093	0.7512	0.2581	-31.37	-30.38	25.85	0.03
N(4)−C(11)	1.89(6)	-22.0(3)	1.4382	0.9350	0.5032	-15.06	-12.26	5.35	0.23
C(1)−C(2)	2.14(5)	-20.7(1)	1.3974	0.7025	0.6950	-17.20	-13.07	9.61	0.32
C(1)−C(6)	2.19(5)	-22.1(1)	1.3931	0.6882	0.7049	-17.91	-13.63	9.47	0.31
C(2)−C(3)	2.15(5)	-21.9(1)	1.3864	0.6282	0.7583	-16.94	-13.17	8.21	0.29
C(2)−H(2)	1.80(7)	-17.5(2)	1.0832	0.6848	0.3984	-16.63	-15.15	14.28	0.10
C(3)−C(4)	2.08(5)	-20.3(1)	1.4114	0.7143	0.6971	-17.37	-12.39	9.47	0.40
C(3)−H(3)	1.89(8)	-19.5(2)	1.0833	0.6772	0.4062	-17.84	-16.14	14.47	0.10
C(4)−C(5)	2.15(5)	-22.0(1)	1.4084	0.7635	0.6450	-17.85	-13.15	8.97	0.36
C(5)−C(6)	2.19(5)	-22.6(1)	1.3943	0.7139	0.6804	-17.42	-14.47	9.31	0.20
C(5)−H(5)	1.91(7)	-21.3(2)	1.0832	0.7023	0.3809	-18.59	-17.02	14.30	0.09
C(6)−H(6)	1.89(8)	-20.0(2)	1.0836	0.6780	0.4056	-17.40	-16.08	13.46	0.08
C(8)−C(9)	2.10(5)	-20.0(1)	1.4142	0.7177	0.6965	-16.38	-13.32	9.70	0.23
C(8)−C(13)	2.18(5)	-21.4(1)	1.4099	0.7275	0.6825	-17.75	-13.89	10.25	0.28
C(9)−C(10)	2.26(5)	-23.2(1)	1.3833	0.7228	0.6605	-18.33	-14.35	9.44	0.28
C(9)−H(9)	1.90(8)	-20.2(2)	1.0837	0.6879	0.3958	-18.08	-16.14	14.02	0.12
C(10)−C(11)	2.23(5)	-24.0(1)	1.3979	0.7556	0.6423	-18.73	-14.27	9.01	0.31

C(10)−H(10)	1.90(7)	-19.5(2)	1.0831	0.6517	0.4313	-16.88	-15.47	12.89	0.09
C(11)−C(12)	2.16(5)	-21.4(1)	1.4005	0.7587	0.6418	-17.09	-13.51	9.23	0.27
C(12)−C(13)	2.21(5)	-20.9(1)	1.3898	0.6803	0.7095	-17.29	-13.71	10.14	0.26
C(12)−H(12)	1.85(8)	-18.8(2)	1.0830	0.7172	0.3658	-17.75	-17.26	16.21	0.03
C(13)−H(13)	1.86(8)	-19.5(2)	1.0836	0.7037	0.3799	-17.42	-16.81	14.76	0.04

T.A.6.2: BCPs in structure **c.s.5** (experimental data).

Bond	$\rho(\mathbf{r})$ (e A^{-3})	$\nabla^2\rho(\mathbf{r})$ (e A^{-5})	R_{ij} (Å)	d_1 (Å)	d_2 (Å)	λ_1	λ_2	λ_3	ε
O(1)−C(7)	2.86(5)	-35.9(2)	1.2257	0.7570	0.4687	-28.05	-23.45	15.64	0.20
O(2)−N(1)	3.25(4)	-4.7(2)	1.2300	0.6126	0.6174	-31.14	-26.81	53.28	0.16
O(3)−N(1)	3.27(4)	-5.0(2)	1.2268	0.6115	0.6153	-31.40	-26.96	53.40	0.16
O(4)−N(4)	3.35(4)	-14.2(2)	1.2223	0.6418	0.5805	-34.64	-29.04	49.49	0.19
O(5)−N(4)	3.31(4)	-13.3(2)	1.2279	0.6437	0.5841	-34.13	-28.62	49.43	0.19
N(1)−C(6)	1.65(4)	-9.1(1)	1.4705	0.8797	0.5909	-11.62	-10.86	13.35	0.07
N(2)−C(4)	2.03(4)	-17.0(1)	1.3934	0.8104	0.5830	-16.56	-14.57	14.11	0.14
N(2)−C(7)	2.20(4)	-21.2(1)	1.3746	0.8035	0.5712	-18.92	-15.96	13.65	0.19
N(2)−H(2A)	2.02(6)	-27.0(4)	1.0244	0.7806	0.2438	-28.30	-26.84	28.17	0.05
N(3)−C(7)	2.08(4)	-16.1(1)	1.3788	0.7768	0.6020	-17.81	-13.89	15.57	0.28
N(3)−C(8)	2.03(4)	-16.4(1)	1.3930	0.8018	0.5912	-16.83	-14.06	14.54	0.20
N(3)−H(3A)	2.13(6)	-25.7(3)	1.0117	0.7616	0.2500	-29.12	-27.47	30.93	0.06
N(4)−C(12)	1.71(4)	-10.7(1)	1.4666	0.8730	0.5936	-12.61	-11.39	13.32	0.11
N(5)−C(14)	1.55(5)	-8.2(2)	1.4892	0.8985	0.5908	-9.70	-9.30	10.81	0.04
N(5)−C(15)	1.54(4)	-6.7(1)	1.4947	0.8734	0.6213	-10.57	-8.99	12.81	0.17
N(5)−C(16)	1.59(4)	-6.1(1)	1.4986	0.8661	0.6324	-10.49	-9.43	13.79	0.11
N(5)−C(17)	1.59(4)	-7.3(1)	1.4955	0.8681	0.6274	-1124	-9.38	13.34	0.20
C(1)−C(2)	2.04(4)	-16.4(1)	1.3937	0.7051	0.6886	-16.02	-12.80	12.42	0.25
C(1)−C(6)	2.13(4)	-16.6(1)	1.3892	0.7058	0.6833	-16.75	-13.28	13.39	0.26
C(1)−H(1)	1.81(6)	-15.2(2)	1.0863	0.7372	0.3491	-18.06	-17.14	19.99	0.05
C(2)−C(3)	2.14(4)	-16.86(9)	1.3884	0.7001	0.6883	-16.89	-13.16	13.19	0.28
C(2)−H(2)	1.87(6)	-15.5(2)	1.0643	0.6991	0.3652	-18.29	-17.04	19.86	0.07
C(3)−C(4)	2.07(3)	-16.53(8)	1.4059	0.7071	0.6988	-16.34	-13.18	12.99	0.24
C(3)−H(3)	1.78(6)	-15.6(2)	1.0771	0.7179	0.3593	-17.30	-16.65	18.33	0.04
C(4)−C(5)	2.04(3)	-16.60(9)	1.3977	0.7064	0.6913	-15.86	-13.11	12.37	0.21
C(5)−C(6)	2.06(4)	-15.50(9)	1.3918	0.6910	0.7008	-15.73	-12.95	13.19	0.21
C(5)−H(5)	1.83(6)	-17.1(2)	1.0911	0.7463	0.3448	-18.58	-17.63	19.11	0.05
C(8)−C(9)	1.95(3)	-14.22(8)	1.4064	0.7146	0.6918	-14.93	-11.81	12.52	0.26

C(8)−C(13)	2.05(3)	-16.11(9)	1.3972	0.7050	0.6922	-16.04	-12.65	12.57	0.27
C(9)−C(10)	2.10(4)	-16.79(9)	1.3901	0.7022	0.6880	-16.49	-13.26	12.96	0.24
C(9)−H(9)	1.75(6)	-14.5(2)	1.0664	0.7081	0.3583	-16.88	-16.39	18.74	0.03
C(10)−C(11)	2.04(4)	-16.26(9)	1.3939	0.6971	0.6968	-15.90	-12.88	12.52	0.23
C(10)−H(10)	1.83(6)	-16.3(2)	1.0784	0.7029	0.3754	-17.57	-16.78	18.04	0.05
C(11)−C(12)	2.14(4)	-18.3(1)	1.3884	0.6760	0.7124	-16.83	-14.02	12.53	0.20
C(11)−H(11)	1.77(5)	-14.0(2)	1.0780	0.7366	0.3414	-17.75	-16.78	20.56	0.06
C(12)−C(13)	2.10(4)	-17.96(9)	1.3891	0.7220	0.6670	-16.87	-13.42	12.34	0.26
C(13)−H(13)	1.85(6)	-17.8(2)	1.0877	0.7282	0.3595	-18.34	-17.26	17.81	0.06
C(14)−H(14A)	1.74(7)	-12.9(2)	1.0782	0.7154	0.3628	-16.51	-15.17	18.76	0.09
C(14)−H(14B)	1.78(7)	-15.4(2)	1.1013	0.7395	0.3618	-17.01	-16.14	17.80	0.05
C(14)−H(14C)	1.73(7)	-12.5(2)	1.1043	0.7507	0.3536	-16.58	-15.51	19.58	0.07
C(15)−H(15A)	1.72(7)	-13.4(2)	1.0868	0.7223	0.3645	-15.95	-15.70	18.28	0.02
C(15)−H(15B)	1.83(6)	-14.5(2)	1.0892	0.7127	0.3765	-17.17	-16.09	18.72	0.07
C(15)−H(15C)	1.76(7)	-12.9(2)	1.0778	0.7220	0.3558	-16.71	-15.65	19.44	0.07
C(16)−H(16A)	1.78(7)	-13.6(2)	1.0750	0.6930	0.3820	-16.80	-14.70	17.88	0.14
C(16)−H(16B)	1.81(6)	-15.4(2)	1.1089	0.7063	0.4026	-16.98	-14.84	16.42	0.14
C(16)−H(16C)	1.66(7)	-10.2(2)	1.0694	0.6902	0.3792	-14.66	-13.66	18.11	0.07
C(17)−H(17A)	1.76(6)	-13.1(2)	1.1172	0.7557	0.3616	-17.07	-15.41	19.38	0.11
C(17)−H(17B)	1.68(8)	-12.0(2)	1.0434	0.6063	0.4371	-13.40	-12.57	13.66	0.09
C(17)−H(17C)	1.84(7)	-14.6(2)	1.0867	0.7274	0.3593	-17.85	-16.03	19.30	0.11

T.A.6.3: BCPs in structure **c.s.6** (experimental data).

Bond	$\rho(\mathbf{r})$ (e A^{-3})	$\nabla^2\rho(\mathbf{r})$ (e A^{-5})	R_{ij} (Å)	d_1 (Å)	d_2 (Å)	λ_1	λ_2	λ_3	ε
O(1)−C(7)	3.07(4)	- 39.1(2)	1.2237	0.7379	0.4859	-31.23	-25.99	18.09	0.20
O(2)−N(1)	3.36(3)	-10.1(1)	1.2377	0.6472	0.5905	-33.29	-29.95	53.11	0.11
O(3)−N(1)	3.40(4)	-11.0(2)	1.2314	0.6449	0.5865	-33.81	-30.44	53.27	0.11
O(5)−N(4)	3.29(4)	-3.2(2)	1.2411	0.6297	0.6114	-32.40	-26.36	55.54	0.23
O(4)−N(4)	3.29(3)	-3.3(1)	1.2404	0.6294	0.6110	-32.46	-26.39	55.56	0.23
N(1)−C(1)	1.83(3)	-13.43(9)	1.4505	0.8512	0.5993	-15.70	-12.20	14.48	0.29
N(2)−C(4)	2.10(3)	-17.13(9)	1.3867	0.7923	0.5944	-17.64	-15.20	15.72	0.16
N(2)−C(7)	2.17(3)	-19.0(1)	1.3851	0.7956	0.5896	-19.38	-15.61	15.95	0.24
N(2)−H(2A)	2.16(5)	-25.2(3)	1.0090	0.7647	0.2443	-29.46	-28.54	32.84	0.03
N(3)−C(7)	2.16(3)	-20.7(1)	1.3817	0.8010	0.5807	-19.43	-16.16	14.91	0.20
N(3)−C(8)	2.11(3)	-16.80(9)	1.3867	0.7936	0.5931	-17.57	-15.07	15.84	0.17
N(3)−H(3A)	2.22(5)	-29.7(3)	1.0090	0.7669	0.2421	-31.10	-30.08	31.47	0.03

N(5)−C(14)	1.62(3)	-6.61(8)	1.4984	0.8642	0.6343	-11.37	-10.91	15.67	0.04
N(5)−C(15)	1.66(3)	-5.89(8)	1.4956	0.8512	0.6443	-11.66	-10.98	16.75	0.06
N(5)−C(16)	1.70(3)	-7.09(8)	1.5012	0.8600	0.6412	-12.01	-11.94	16.86	0.01
N(5)−C(17)	1.63(3)	-6.99(8)	1.4969	0.8646	0.6323	-11.45	-11.16	15.61	0.03
N(4)−C(11)	1.85(3)	-13.07(9)	1.4532	0.8573	0.5959	-14.77	-13.02	14.71	0.13
C(1)−C(2)	2.18(2)	-18.48(6)	1.3969	0.7205	0.6764	-17.98	-14.12	13.61	0.27
C(1)−C(6)	2.15(2)	-18.02(6)	1.3957	0.7208	0.6749	-17.59	-13.86	13.43	0.27
C(2)−C(3)	2.16(2)	-17.46(6)	1.3840	0.6954	0.6886	-17.22	-13.83	13.59	0.24
C(2)−H(2)	1.88(4)	-17.1(1)	1.0830	0.7227	0.3604	-18.52	-17.82	19.27	0.04
C(3)−C(4)	2.10(2)	-16.97(6)	1.4119	0.6960	0.7159	-16.98	-13.62	13.63	0.25
C(3)−H(3)	1.83(4)	-16.6(1)	1.0830	0.7235	0.3595	-18.10	-17.20	18.67	0.05
C(4)−C(5)	2.07(2)	-17.35(6)	1.4083	0.7258	0.6825	-17.17	-13.39	13.21	0.28
C(5)−C(6)	2.14(2)	-17.50(6)	1.3898	0.6969	0.6929	-17.20	-13.84	13.53	0.24
C(5)−H(5)	1.86(4)	-18.5(1)	1.0831	0.7273	0.3558	-18.83	-17.74	18.09	0.06
C(6)−H(6)	1.83(4)	-16.2(1)	1.0831	0.7263	0.3567	-18.03	-17.29	19.10	0.04
C(8)−C(9)	2.08(2)	-16.70(6)	1.4130	0.7173	0.6957	-17.05	-13.18	13.52	0.29
C(8)−C(13)	2.08(2)	-17.12(6)	1.4093	0.7341	0.6751	-17.25	-13.22	13.35	0.30
C(9)−C(10)	2.19(3)	-19.11(7)	1.3838	0.6851	0.6987	-18.04	-14.33	13.25	0.26
C(9)−H(9)	1.86(4)	-18.9(1)	1.0830	0.7256	0.3574	-18.80	-17.81	17.74	0.06
C(10)−C(11)	2.15(3)	-17.19(7)	1.3983	0.7090	0.6893	-17.86	-13.28	13.94	0.35
C(10)−H(10)	1.83(4)	-17.5(1)	1.0830	0.7293	0.3537	-18.45	-17.64	1856	0.05
C(11)−C(12)	2.10(3)	-17.22(7)	1.3955	0.7211	0.6744	-17.19	-13.29	13.26	0.29
C(12)−C(13)	2.18(3)	-18.78(6)	1.3920	0.7194	0.6726	-17.62	-14.44	13.28	0.22
C(12)−H(12)	1.84(4)	-17.1(1)	1.0831	0.7223	0.3609	-18.39	-17.39	18.70	0.06
C(13)−H(13)	1.89(4)	-18.6(1)	1.0831	0.7256	0.3575	-19.06	-18.06	18.52	0.06
C(14)−H(14A)	1.92(4)	-16.7(1)	1.0592	0.6781	0.3811	-18.43	-17.39	19.08	0.06
C(14)−H(14B)	1.86(4)	-14.8(1)	1.0590	0.6921	0.3669	-18.03	-16.96	20.22	0.06
C(14)−H(14C)	1.91(4)	-16.7(1)	1.0591	0.6949	0.3642	-18.53	-17.84	19.66	0.04
C(15)−H(15A)	1.88(4)	-14.6(1)	1.0592	0.6842	0.3749	-17.92	-16.69	20.04	0.07
C(15)−H(15B)	1.84(5)	-13.9(1)	1.0592	0.6871	0.3721	-17.60	-16.34	20.02	0.08
C(15)−H(15C)	1.81(4)	-13.9(1)	1.0592	0.6405	0.4187	-16.02	-14.85	17.01	0.08
C(16)−H(16A)	1.89(4)	-15.7(1)	1.0591	0.6771	0.3821	-17.74	-17.20	19.29	0.03
C(16)−H(16B)	1.92(4)	-16.6(1)	1.0590	0.6991	0.3600	-18.89	-18.15	20.45	0.04
C(16)−H(16C)	1.88(4)	-16.0(1)	1.0591	0.6839	0.3751	-17.76	-17.22	19.02	0.03
C(17)−H(17A)	1.94(4)	-17.1(1)	1.0590	0.7061	0.3529	-19.22	-18.78	20.87	0.02
C(17)−H(17B)	1.88(4)	-16.0(1)	1.0592	0.6708	0.3884	-17.75	-16.87	18.61	0.05
C(17)−H(17C)	1.90(4)	-16.5(1)	1.0590	0.6863	0.3727	-18.35	-17.53	19.34	0.05

T.A.6.4: BCPs in structure **c.s.9** (experimental data).

Bond	$\rho(\mathbf{r})$ (e A^{-3})	$\nabla^2\rho(\mathbf{r})$ (e A^{-5})	R_{ij} (Å)	d_1 (Å)	d_2 (Å)	λ_1	λ_2	λ_3	ε
O(1)−C(7)	3.02(5)	-48.5(3)	1.2299	0.7659	0.4640	-33.99	-26.47	11.96	0.28
O(4)−N(4)	3.51(5)	-16.1(2)	1.2348	0.628	0.6111	-35.73	-31.35	51.01	0.14
O(5)−N(4)	3.52(5)	-16.3(2)	1.2333	0.6232	0.6101	-35.83	-31.46	51.02	0.14
O(3)−N(1)	3.23(4)	-4.8(2)	1.2376	0.6113	0.6263	-29.52	-25.65	50.40	0.15
O(2)−N(1)	3.24(4)	-4.9(2)	1.2361	0.6107	0.6253	-29.60	-25.72	50.45	0.15
O(6)−C(18)	2.74(5)	-37.6(2)	1.2642	0.7786	0.4856	-26.86	-22.01	11.28	0.22
O(7)−C(18)	2.48(5)	-20.2(3)	1.2575	0.8251	0.4324	-23.02	-19.86	22.72	0.16
N(1)−C(1)	1.86(4)	-18.6(2)	1.4487	0.9012	0.5475	-15.07	-11.71	8.14	0.29
N(2)−C(4)	2.12(4)	-20.8(1)	1.3828	0.7930	0.5898	-18.09	-14.74	12.08	0.23
N(2)−C(7)	2.09(4)	-23.7(1)	1.3898	0.8200	0.5698	-18.83	-14.47	9.64	0.30
N(2)−H(2A)	1.90(6)	-22.7(3)	1.0443	0.7986	0.2457	-25.61	-24.60	27.52	0.04
N(3)−C(7)	2.28(4)	-26.3(1)	1.3726	0.7907	0.5818	-21.44	-16.41	11.56	0.31
N(3)−C(8)	1.99(4)	-17.3(1)	1.3871	0.8030	0.5841	-15.86	-13.19	11.72	0.20
N(3)−H(3A)	1.82(6)	-18.3(3)	1.0483	0.8108	0.2375	-24.90	-23.78	30.40	0.05
N(4)−C(11)	1.69(4)	-13.6(2)	1.4515	0.8932	0.5583	-12.30	-10.09	8.75	0.22
N(5)−C(14)	1.62(4)	-9.2(1)	1.5049	0.8764	0.6285	-11.05	-10.34	12.17	0.07
N(5)−C(15)	1.62(4)	-9.8(1)	1.4963	0.8602	0.6361	-12.37	-10.00	12.58	0.24
N(5)−C(16)	1.66(4)	-8.8(1)	1.4992	0.8650	0.6342	-12.01	-9.73	12.89	0.23
N(5)−C(17)	1.64(4)	-10.2(1)	1.4966	0.8779	0.6189	-11.29	-10.22	11.35	0.10
C(1)−C(2)	2.09(3)	-18.46(9)	1.4009	0.7041	0.6968	-16.55	-12.43	10.52	0.33
C(1)−C(6)	1.97(3)	-17.38(9)	1.3960	0.7384	0.6576	-14.80	-11.75	9.17	0.26
C(2)−C(3)	2.21(3)	-21.15(9)	1.3839	0.6828	0.7011	-17.31	-14.16	10.32	0.22
C(2)−H(2)	1.74(5)	-15.2(2)	1.0833	0.7092	0.3741	-15.89	-15.40	16.13	0.03
C(3)−C(4)	1.97(3)	-17.48(9)	1.4154	0.6840	0.7314	-14.95	-12.05	9.52	0.24
C(3)−H(3)	1.77(5)	-15.1(2)	1.1006	0.7396	0.3610	-17.28	-15.54	17.74	0.11
C(4)−C(5)	2.11(3)	-20.57(9)	1.4112	0.7319	0.6793	-16.99	-13.59	10.02	0.25
C(5)−C(6)	2.21(3)	-21.47(9)	1.3887	0.7036	0.6851	-17.29	-14.34	10.17	0.21
C(5)−H(5)	1.77(5)	-16.4(1)	1.1019	0.7215	0.3804	-16.90	-15.25	15.79	0.11
C(6)−H(6)	1.80(5)	-18.3(2)	1.1042	0.7630	0.3412	-18.17	-17.29	17.18	0.05
C(8)−C(9)	2.06(3)	-18.30(9)	1.4152	0.7378	0.6774	-16.35	-12.96	11.02	0.26
C(8)−C(13)	1.92(3)	-16.91(9)	1.4097	0.7347	0.6751	-15.25	-11.75	10.10	0.30
C(9)−C(10)	2.04(3)	-17.57(9)	1.3828	0.7006	0.6822	-15.55	-12.30	10.28	0.26
C(9)−H(9)	1.69(5)	-14.2(2)	1.1008	0.7517	0.3491	-16.59	-15.53	17.94	0.07

C(10)−C(11)	1.96(4)	-17.3(1)	1.3968	0.6391	0.7576	-15.59	-11.71	9.96	0.33
C(10)−H(10)	1.81(5)	-16.7(2)	1.0857	0.7161	0.3696	-17.55	-16.21	17.08	0.08
C(11)−C(12)	2.16(3)	-19.8(1)	1.3906	0.7006	0.6900	-16.97	-13.93	11.12	0.22
C(12)−C(13)	2.04(3)	-17.08(9)	1.3903	0.7112	0.6792	-15.36	-12.38	10.66	0.24
C(12)−H(12)	1.73(5)	-15.0(2)	1.0742	0.7225	0.3517	-16.59	-16.14	17.76	0.03
C(13)−H(13)	1.88(5)	-18.7(2)	1.0904	0.7272	0.3631	-18.56	-17.27	17.16	0.07
C(14)−H(14A)	1.86(5)	-18.3(2)	1.0702	0.7300	0.3402	-18.37	-17.78	17.84	0.03
C(14)−H(14B)	1.67(5)	-14.1(2)	1.1031	0.7343	0.3689	-15.20	-15.06	16.20	0.01
C(14)−H(14C)	1.68(6)	-13.4(2)	1.1125	0.7667	0.3458	-16.05	-15.88	18.48	0.01
C(15)−H(15A)	1.74(6)	-14.2(3)	1.0948	0.7903	0.3045	-18.21	-17.47	21.45	0.04
C(15)−H(15B)	1.78(5)	-16.5(1)	1.0817	0.6869	0.3949	-16.16	-15.54	15.20	0.04
C(15)−H(15C)	1.86(6)	-17.5(1)	1.1194	0.7134	0.4060	-16.85	-16.53	15.90	0.02
C(16)−H(16A)	1.83(5)	-15.9(2)	1.0969	0.7308	0.3661	-17.35	-17.05	18.54	0.02
C(16)−H(16B)	1.72(6)	-14.6(2)	1.0851	0.7564	0.3287	-17.16	-16.43	19.01	0.04
C(16)−H(16C)	1.80(5)	-17.8(1)	1.0885	0.6731	0.4154	-16.46	-15.03	13.67	0.09
C(17)−H(17A)	1.76(5)	-14.4(2)	1.0786	0.7065	0.3721	-16.34	-15.68	17.59	0.04
C(17)−H(17B)	1.75(5)	-14.9(2)	1.0725	0.7186	0.3539	-16.75	-16.17	18.00	0.04
C(17)−H(17C)	1.80(5)	-15.4(2)	1.0991	0.7480	0.3511	-17.23	-16.88	18.66	0.02
C(18)−C(19)	1.74(3)	-12.70(7)	1.5220	0.7579	0.7642	-12.98	-10.88	11.17	0.19
C(19)−H(19A)	1.77(5)	-15.1(1)	1.0934	0.7050	0.3884	-15.76	-15.46	16.09	0.02
C(19)−H(19B)	1.80(5)	-16.3(2)	1.0853	0.7470	0.3383	-17.71	-17.05	18.47	0.04
C(19)−H(19C)	1.64(5)	-12.8(2)	1.0748	0.7227	0.3521	-15.58	-14.72	17.48	0.06

T.A.6.5: BCPs in structure **c.s.10** (experimental data).

Bond	$\rho(\mathbf{r})$ (e A^{-3})	$\nabla^2\rho(\mathbf{r})$ (e A^{-5})	R_{ij} (Å)	d_1 (Å)	d_2 (Å)	λ_1	λ_2	λ_3	ε
O(1)-C(7)	2.89(6)	-45.2(3)	1.2323	0.7912	0.4411	-32.03	-27.90	14.75	0.15
O(2)−N(1)	3.41(5)	-12.3(2)	1.2343	0.6209	0.6134	-32.33	-29.29	49.34	0.10
O(3)−N(1)	3.48(5)	-13.8(2)	1.2247	0.6176	0.6070	-33.17	-30.09	49.42	0.10
O(4)−N(2)	3.35(4)	-10.9(2)	1.2299	0.6308	0.5992	-30.46	-28.74	48.27	0.06
O(5)−N(2)	3.31(5)	-10.1(2)	1.2354	0.6326	0.6028	-30.03	-28.31	48.24	0.06
O(6)−N(5)	3.32(4)	-10.6(2)	1.2279	0.6252	0.6027	-30.78	-28.06	48.28	0.10
O(7)−N(5)	3.35(4)	-11.1(2)	1.2232	0.6235	0.5997	-31.07	-28.32	48.33	0.10
O(8)−N(6)	3.29(4)	-13.6(2)	1.2313	0.6481	0.5832	-30.81	-27.99	45.22	0.10
O(9)−N(6)	3.30(5)	-13.9(2)	1.2295	0.6475	0.5820	-30.95	-28.16	45.20	0.10
O(10)−C(18)	3.16(5)	-44.4(2)	1.2562	0.7257	0.5305	-31.10	-26.92	13.60	0.16
O(11)−C(18)	2.64(6)	-27.8(3)	1.2676	0.8486	0.4190	-29.40	-28.27	29.85	0.04
N(3)−C(4)	2.02(5)	-25.7(2)	1.3903	0.8980	0.4923	-17.28	-14.62	6.21	0.18

N(3)−C(7)	2.16(4)	-19.6(1)	1.3807	0.7640	0.6167	-17.75	-14.91	13.09	0.19
N(3)−H(3A)	2.02(8)	-19.0(4)	1.0092	0.7561	0.2531	-26.40	-25.81	33.18	0.02
N(1)−C(6)	1.79(4)	-14.4(1)	1.4738	0.8250	0.6488	-13.65	-12.44	11.69	0.10
N(2)−C(2)	1.72(4)	-16.3(1)	1.4714	0.8884	0.5829	-12.89	-11.13	7.74	0.16
N(4)−C(7)	2.26(4)	-29.0(1)	1.3752	0.8108	0.5644	-20.27	-17.47	8.74	0.16
N(4)−C(8)	2.08(4)	-19.5(1)	1.3878	0.7730	0.6148	-17.46	-14.49	12.50	0.21
N(4)−H(4A)	1.98(8)	-19.6(5)	1.0095	0.7757	0.2338	-26.91	-26.59	33.87	0.01
N(5)−C(12)	1.78(4)	-16.5(1)	1.4739	0.8908	0.5832	-13.70	-11.31	8.49	0.21
N(6)−C(10)	1.78(4)	-17.0(1)	1.4719	0.8951	0.5768	-13.28	-12.07	8.37	0.10
N(7)−C(14)	1.46(4)	-9.5(1)	1.5002	0.8883	0.6120	-8.99	-7.60	7.07	0.18
N(7)−C(15)	1.55(5)	-12.2(2)	1.4881	0.9110	0.5772	-10.12	-8.23	6.13	0.23
N(7)−C(16)	1.60(5)	-8.7(1)	1.5013	0.8862	0.6151	-11.21	-7.15	9.64	0.57
N(7)−C(17)	1.55(5)	-8.1(1)	1.5027	0.8888	0.6139	-10.37	-8.55	10.85	0.21
C(1)−C(6)	2.14(4)	-20.0(1)	1.3924	0.6449	0.7475	-15.28	-13.43	8.66	0.14
C(1)−C(2)	1.98(6)	-14.6(3)	1.3946	0.4685	0.9262	-11.73	-11.04	8.18	0.06
C(1)−H(1)	1.81(6)	-15.2(2)	1.0836	0.7287	0.3550	-17.05	-16.27	18.13	0.05
C(6)−C(5)	2.13(4)	-21.0(1)	1.3893	0.7425	0.6468	-16.54	-13.01	8.56	0.27
C(5)−C(4)	1.96(4)	-19.3(1)	1.4088	0.6010	0.8078	-13.52	-12.61	6.88	0.07
C(5)−H(5)	1.86(7)	-18.1(2)	1.0832	0.7377	0.3455	-17.81	-17.54	17.29	0.02
C(4)−C(3)	2.05(4)	-18.95(9)	1.4078	0.7059	0.7019	-15.41	-12.77	9.24	0.21
C(3)−C(2)	2.22(4)	-23.12(9)	1.3853	0.7170	0.6683	-17.87	-13.86	8.61	0.29
C(3)−H(3)	1.79(6)	-17.3(2)	1.0835	0.7051	0.3784	-16.47	-16.05	15.18	0.03
C(8)−C(13)	2.06(4)	-19.40(9)	1.4056	0.7136	0.6920	-15.49	-12.96	9.04	0.20
C(8)−C(9)	2.04(4)	-19.45(8)	1.4099	0.7384	0.6714	-15.43	-13.05	9.03	0.18
C(13)−C(12)	2.17(4)	-20.86(9)	1.3919	0.6833	0.7085	-16.69	-13.73	9.56	0.22
C(13)−H(13)	1.86(6)	-17.1(2)	1.0835	0.6862	0.3973	-16.44	-16.09	15.48	0.02
C(12)−C(11)	2.14(4)	-21.8(1)	1.3861	0.7359	0.6501	-16.60	-13.73	8.53	0.21
C(11)−C(10)	2.16(4)	-21.6(1)	1.3937	0.6701	0.7236	-16.47	-14.00	8.83	0.18
C(11)−H(11)	1.91(6)	-18.3(2)	1.0830	0.7155	0.3675	-18.31	-17.40	17.42	0.05
C(10)−C(9)	2.18(4)	-22.2(1)	1.3833	0.7481	0.6351	-16.79	-13.79	8.38	0.22
C(9)−H(9)	1.87(6)	-17.5(2)	1.0830	0.7084	0.3746	-17.11	-16.92	16.53	0.01
C(14)−H(14A)	1.76(7)	-15.4(3)	1.0592	0.7332	0.3260	-17.28	-16.57	18.43	0.04
C(14)−H(14B)	1.79(7)	-17.0(2)	1.0599	0.7061	0.3538	-16.95	-15.89	15.82	0.07
C(14)−H(14C)	1.82(7)	-17.1(2)	1.0598	0.6850	0.3748	-16.30	-15.93	15.12	0.02
C(15)−H(15A)	2.05(9)	-22.0(4)	1.0630	0.7444	0.3186	-22.02	-20.11	20.12	0.09
C(15)−H(15B)	1.82(9)	-21.9(4)	1.0591	0.7652	0.2939	-20.67	-18.38	17.15	0.12
C(15)−H(15C)	1.90(8)	-26.0(2)	1.0666	0.6490	0.4177	-20.43	-15.30	9.77	0.34
C(16)−H(16A)	1.73(6)	-15.6(2)	1.0610	0.6588	0.4021	-14.78	-13.89	13.03	0.06
C(16)−H(16B)	1.72(8)	-13.52(3)	1.0619	0.7190	0.3428	-16.74	-14.74	17.96	0.14

C(16)−H(16C)	1.73(7)	-15.8(2)	1.0594	0.6657	0.3937	-15.09	-13.64	12.89	0.11
C(17)−H(17A)	1.53(7)	-11.8(2)	1.0606	0.6200	0.4406	-11.71	-10.45	10.39	0.12
C(17)−H(17B)	1.75(7)	-15.0(2)	1.0591	0.6475	0.4116	-15.43	-11.99	12.41	0.29
C(17)−H(17C)	1.66(8)	-11.1(3)	1.0599	0.6976	0.3623	-15.34	-12.74	17.02	0.20
C(18)−C(19)	1.64(4)	-13.07(9)	1.5096	0.7918	0.7178	-10.34	-8.09	5.35	0.28
C(19)−H(19A)	1.57(8)	-17.9(4)	1.0606	0.7955	0.2651	-16.40	-15.07	13.54	0.09
C(19)−H(19B)	1.60(8)	-12.4(4)	1.0610	0.7658	0.2952	-14.60	-13.72	15.88	0.06
C(19)−H(19C)	1.34(8)	-10.3(2)	1.0718	0.6607	0.4111	-9.34	-7.20	6.26	0.30

T.A.6.6: BCPs in structure **c.s.11** (experimental data).

Bond	$\rho(\mathbf{r})$ (e A^{-3})	$\nabla^2\rho(\mathbf{r})$ (e A^{-5})	R_{ij} (Å)	d_1 (Å)	d_2 (Å)	λ_1	λ_2	λ_3	ε
O(1)−C(7)	2.84(4)	-32.3(2)	1.2287	0.7886	0.4401	-27.89	-24.06	19.62	0.16
O(2)−N(1)	3.27(3)	-7.0(1)	1.2350	0.6226	0.6124	-30.16	-27.71	50.86	0.09
O(3)−N(1)	3.26(3)	-6.7(1)	1.2372	0.6234	0.6138	-29.97	-27.54	50.81	0.09
O(4)−N(4)	3.16(5)	-2.1(2)	1.2417	0.6227	0.6190	-29.29	-24.51	51.75	0.19
O(5)−N(4)	3.158(0)	-2.2(1)	1.2423	0.6231	0.6192	-29.29	-24.62	51.71	0.19
N(2)−C(4)	2.06(3)	-18.01(9)	1.3850	0.7954	0.5896	-16.68	-14.10	12.78	0.18
N(2)−C(7)	2.13(3)	-19.67(9)	1.3852	0.7938	0.5914	-17.54	-14.86	12.72	0.18
N(2)−H(2A)	2.05(5)	-23.3(3)	1.0092	0.7698	0.2394	-27.92	-27.52	32.15	0.01
N(3)−C(8)	2.11(3)	-18.5(9)	1.3765	0.7830	0.5935	-17.33	-14.48	13.32	0.20
N(3)−C(7)	2.09(3)	-22.2(1)	1.3858	0.8200	0.5659	-17.35	-14.95	10.18	0.16
N(3)−H(3A)	2.13(5)	-25.0(3)	1.0091	0.7632	0.2459	-28.83	-28.06	31.85	0.03
N(1)−C(1)	1.72(3)	-12.8(1)	1.4508	0.9020	0.5488	-12.15	-10.12	9.42	0.20
N(4)−C(11)	1.80(3)	-14.0(1)	1.4486	0.8859	0.5627	-13.71	-10.61	10.29	0.29
N(5)−C(15A)	1.782(0)	-10.466(0)	1.4958	0.8390	0.6568	-12.70	-12.68	14.91	0.00
N(5)−C(14A)	1.748(0)	-9.477(0)	1.5027	0.8392	0.6635	-12.35	-12.25	15.12	0.01
N(5)−C(15B)	1.778(0)	-10.331(0)	1.4968	0.8392	0.6576	-12.65	-12.61	14.93	0.00
N(5)−C(14B)	1.762(0)	-9.947(0)	1.4977	0.8378	0.6599	-12.59	-12.41	15.06	0.01
C(5)−C(4)	2.03(2)	-16.72(6)	1.4086	0.6632	0.7452	-15.52	-12.19	10.99	0.27
C(5)−C(6)	2.09(2)	-18.35(6)	1.3915	0.6841	0.7074	-16.39	-12.84	10.89	0.28
C(5)−H(5)	1.84(4)	-17.3(1)	1.0831	0.7215	0.3617	-17.64	-17.14	17.51	0.03
C(4)−C(3)	2.04(2)	-17.07(5)	1.4167	0.7240	0.6928	-15.88	-12.52	11.34	0.27
C(1)−C(6)	2.06(2)	-17.91(6)	1.3971	0.7037	0.6934	-16.07	-12.74	10.91	0.26
C(1)−C(2)	2.08(2)	-17.85(6)	1.4000	0.6971	0.7029	-16.05	-12.96	11.16	0.24
C(3)−C(2)	2.13(2)	-19.86(6)	1.3847	0.6611	0.7236	-16.75	-13.47	10.36	0.24
C(3)−H(3)	1.77(3)	-16.3(1)	1.0840	0.7151	0.3688	-16.98	-16.22	16.93	0.05
C(6)−H(6)	1.85(4)	-17.0(1)	1.0832	0.7386	0.3446	-18.55	-17.69	19.22	0.05

C(2)−H(2)	1.86(3)	-18.8(1)	1.0832	0.7142	0.3690	-18.11	-17.06	16.34	0.06
C(8)−C(9)	2.02(2)	-17.11(6)	1.4169	0.6986	0.7183	-15.60	-12.56	11.05	0.24
C(8)−C(13)	2.00(2)	-17.56(6)	1.4120	0.7482	0.6638	-15.69	-12.28	10.42	0.28
C(11)−C(12)	2.15(3)	-18.97(7)	1.3991	0.7395	0.6597	-16.50	-13.41	10.95	0.23
C(11)−C(10)	2.09(3)	-20.26(8)	1.4000	0.6293	0.7707	-16.65	-13.00	9.39	0.28
C(9)−C(10)	2.17(3)	-19.67(7)	1.3826	0.6538	0.7288	-17.21	-12.97	10.52	0.33
C(9)−H(9)	1.74(4)	-15.1(1)	1.0837	0.6898	0.3939	-15.93	-14.97	15.80	0.06
C(13)−C(12)	2.11(2)	-18.10(6)	1.3906	0.6814	0.7092	-16.47	-12.68	11.06	0.30
C(13)−H(13)	1.78(4)	-16.6(1)	1.0831	0.7188	0.3643	-16.99	-16.42	16.83	0.03
C(12)−H(12)	1.85(4)	-17.6(1)	1.0832	0.7105	0.3728	-17.70	-16.64	16.78	0.06
C(10)−H(10)	1.87(4)	-19.8(1)	1.0832	0.7016	0.3816	-18.57	-16.79	15.51	0.11
C(15)−H(15A)	1.876(0)	-18.277(0)	1.0590	0.6711	0.3879	-16.93	-16.26	14.91	0.04
C(15)−H(15B)	1.875(0)	-18.280(0)	1.0590	0.6711	0.3879	-16.93	-16.26	14.92	0.04
C(15)−H(15C)	1.875(0)	-18.284(0)	1.0590	0.6711	0.3879	-16.94	-16.26	14.92	0.04
C(14)−H(14A)	1.876(0)	-18.276(0)	1.0590	0.6711	0.3879	-16.92	-16.26	14.91	0.04
C(14)−H(14B)	1.875(0)	-18.278(0)	1.0590	0.6711	0.3879	-16.93	-16.26	14.91	0.04
C(14)−H(14C)	1.874(0)	-18.291(0)	1.0590	0.6708	0.3882	-16.94	-16.24	14.89	0.04
C(15B)−H(15D)	1.875 (0)	-18.282(0)	1.0590	0.6711	0.3879	-16.93	-16.26	14.91	0.04
C(15B)−H(15E)	1.876(0)	-18.275(0)	1.0590	0.6711	0.3879	-16.93	-16.26	14.91	0.04
C(15B)−H(15F)	1.875(0)	-18.283(0)	1.0590	0.6711	0.3879	-16.93	-16.26	14.92	0.04
C(14B)−H(14D)	1.874 (0)	-18.292(0)	1.0590	0.6709	0.3881	-16.94	-16.25	14.90	0.04
C(14B)−H(14E)	1.876(0)	-18.275(0)	1.0590	0.6712	0.3878	-16.92	-16.27	14.92	0.04
C(14B)−H(14F)	1.875(0)	-18.289(0)	1.0590	0.6710	0.3880	-16.94	-16.25	14.90	0.04

T.A.6.7: BCPs in structure **c.s.16** (experimental data).

Bond	$\rho(\mathbf{r})$ (e A^{-3})	$\nabla^2\rho(\mathbf{r})$ (e A^{-5})	R_{ij} (Å)	d_1 (Å)	d_2 (Å)	λ_1	λ_2	λ_3	ε
S(2)−C(20)	1.48(6)	-2.7(1)	1.6837	0.8508	0.8330	-8.10	-6.90	12.30	0.17
S(1)−C(7)	1.49(7)	-3.6(1)	1.6714	0.8564	0.8149	-11.98	-8.58	16.95	0.40
O(5)−N(5)	3.53(7)	-15.2(3)	1.2355	0.6284	0.6051	-36.89	-32.52	54.23	0.13
O(6)−N(5)	3.52(7)	-14.8(3)	1.2355	0.6289	0.6066	-36.70	-32.31	54.21	0.14
O(7)−N(8)	3.41(7)	-8.7(3)	1.2320	0.6271	0.6048	-33.56	-29.56	54.44	0.14
O(8)−N(8)	3.43(7)	-9.0(3)	1.2290	0.629	0.6031	-33.82	-29.69	54.52	0.14
O(1)−N(1)	3.53(8)	-16.0(3)	1.2309	0.6250	0.6059	-36.26	-33.29	53.55	0.09
O(2)−N(1)	3.54(8)	-16.1(3)	1.2281	0.6241	0.6041	-36.32	-33.43	53.66	0.09
O(3)−N(4)	3.52(8)	-7.4(4)	1.2287	0.6270	0.6017	-33.99	-30.86	57.47	0.10
O(4)−N(4)	3.53(8)	-7.4(3)	1.2283	0.6268	0.6016	-34.03	-30.89	57.48	0.10

N(9)−C(91)	1.36(7)	-5.7(2)	1.5186	0.8954	0.6232	-9.81	-6.49	10.62	0.51
N(9)−C(93)	1.50(7)	-7.1(2)	1.5147	0.8604	0.6543	-10.76	-9.32	12.95	0.16
N(9)−C(95)	1.48(7)	-6.1(2)	1.5120	0.8976	0.6144	-10.29	-7.79	11.98	0.32
N(9)−C(97)	1.63(7)	-6.4(2)	1.5198	0.8430	0.6767	-12.00	-10.00	15.64	0.20
N(5)−C(14)	1.71(7)	-8.5(2)	1.4580	0.8666	0.5914	-13.68	-9.55	14.68	0.43
N(6)−C(17)	2.09(7)	-19.1(2)	1.3935	0.8171	0.5764	-18.93	-14.25	14.10	0.33
N(6)−C(20)	2.37(7)	-21.1(2)	1.3640	0.7729	0.5911	-19.59	-18.48	16.97	0.06
N(6)−H(6A)	2.2(1)	-42.6(8)	1.0095	0.8046	0.2049	-3586	-34.40	27.66	0.04
N(7)−C(20)	2.12(7)	-16.7(2)	1.3711	0.7937	0.5774	-17.28	-14.59	15.13	0.18
N(7)−C(21)	2.15(7)	-14.6(2)	1.4002	0.7755	0.6246	-17.65	-15.49	18.52	0.14
N(7)−H(7A)	2.4(1)	-27.6(6)	1.0090	0.7378	0.2713	-32.45	-29.20	34.01	0.11
N(8)−C(24)	1.79(7)	-12.3(2)	1.4594	0.8520	0.6073	-15.18	-11.68	14.55	0.30
N(1)−C(1)	1.76(7)	-11.2(2)	1.4607	0.8581	0.6026	-13.50	-12.56	14.84	0.07
N(2)−C(4)	2.34(7)	-24.7(2)	1.3973	0.7847	0.6126	-21.20	-20.22	16.68	0.05
N(2)−C(7)	2.23(7)	-14.9(2)	1.3717	0.7821	0.5896	-17.39	-15.24	17.76	0.14
N(2)−H(2A)	2.3(1)	-25.3(5)	1.0095	0.7236	0.2859	-28.79	-26.91	30.42	0.07
N(3)−C(7)	2.20(7)	-21.2(2)	1.3673	0.7917	0.5755	-19.34	-16.69	14.79	0.16
N(3)−C(8)	2.14(7)	-8.5(2)	1.3966	0.7274	0.6692	-15.88	-14.57	21.96	0.09
N(3)−H(3A)	2.3(1)	-36.7(7)	1.0098	0.7623	0.2475	-32.38	-31.56	27.24	0.03
N(4)−C(11)	1.63(7)	-7.0(2)	1.4594	0.8765	0.5828	-11.48	-10.05	14.51	0.14
C(91)−C(92)	1.54(7)	-7.5(2)	1.5126	0.8251	0.6875	-9.90	-8.98	11.37	0.10
C(91)−H(91A)	1.6(1)	-9.4(4)	1.0922	0.7502	0.3421	-15.86	-14.83	21.25	0.07
C(91)−H(91B)	1.8(1)	-16.7(4)	1.0922	0.7332	0.3590	-18.65	-16.66	18.63	0.12
C(92)−H(92A)	1.8(1)	-12.7(3)	1.0610	0.6690	0.3921	-1518	-14.70	17.17	0.03
C(92)−H(92B)	1.7(1)	-13.1(4)	1.0618	0.6866	0.3752	-15.64	-14.92	17.49	0.05
C(92)−H(92C)	1.8(1)	-12.0(5)	1.0591	0.7161	0.3430	-17.23	-16.45	21.64	0.05
C(93)−C(94)	1.67(8)	-8.2(2)	1.5289	0.7501	0.7788	-12.13	-9.64	13.56	0.26
C(93)−H(93A)	1.8(1)	-14.6(5)	1.0933	0.7739	0.3195	-18.88	-17.41	21.70	0.08
C(93)−H(93B)	1.7(1)	-12.7(4)	1.0922	0.7176	0.3745	-15.96	-14.41	17.71	0.11
C(94)−H(94A)	1.7(1)	-7.7(4)	1.0637	0.5834	0.4803	-13.83	-6.91	13.07	1.00
C(94)−H(94B)	1.9(2)	-17.0(5)	1.0594	0.7259	0.3335	-19.52	-17.37	19.92	0.12
C(95)−C(96)	1.46(6)	-4.8(1)	1.5134	0.7194	0.7940	-9.46	-7.07	11.70	0.34
C(95)−H(95A)	1.8(1)	-14.9(3)	1.0925	0.6908	0.4017	-16.37	-14.54	16.00	0.13
C(95)−H(95B)	1.6(1)	-11.7(3)	1.0923	0.6922	0.4001	-14.22	-13.13	15.70	0.08
C(96)−H(96A)	1.7(1)	-13.2(4)	1.0597	0.6922	0.3675	-15.90	-15.34	18.07	0.04
C(96)−H(96B)	1.9(1)	-17.5(5)	1.0592	0.7413	0.3179	-20.10	-19.22	21.80	0.05
C(96)−H(96C)	1.7(1)	-11.2(4)	1.0641	0.6862	0.3779	-15.49	-14.77	19.01	0.05
C(97)−C(98)	1.71(8)	-9.7(2)	1.5141	0.7591	0.7550	-11.57	-11.05	12.96	0.05
C(97)−H(97A)	1.7(1)	-14.0(3)	1.0933	0.6947	0.3986	-15.73	-14.51	16.29	0.08

C(97)−H(97B)	1.9(1)	-15.2(3)	1.0930	0.6843	0.4087	-16.30	-15.59	16.70	0.05
C(98)−H(98A)	1.5(2)	-13.1(7)	1.0639	0.7597	0.3042	-15.70	-15.08	17.72	0.04
C(98)−H(98B)	1.6(2)	-14.4(9)	1.0593	0.7870	0.2723	-18.45	-16.89	20.95	0.09
C(98)−H(98C)	1.9(2)	-14.3(5)	1.0610	0.6988	0.3622	-17.83	-15.90	19.45	0.12
C(14)−C(15)	2.01(7)	-15.2(2)	1.3934	0.7599	0.6335	-15.42	-13.17	13.35	0.17
C(14)−C(19)	2.12(7)	-15.7(2)	1.3883	0.6948	0.6935	-16.63	-13.38	14.35	0.24
C(15)−C(16)	2.25(7)	-21.1(2)	1.3840	0.7248	0.6591	-18.29	-16.27	13.41	0.12
C(15)−H(15)	1.8(1)	-15.8(3)	1.0831	0.7116	0.3714	-17.86	-17.12	19.15	0.04
C(16)−C(17)	1.98(7)	-14.4(2)	1.4062	0.6400	0.7662	-15.78	-11.35	12.72	0.39
C(16)−H(16)	1.8(1)	-14.8(3)	1.0834	0.7016	0.3818	-17.20	-15.92	18.36	0.08
C(17)−C(18)	2.24(6)	-20.8(2)	1.4019	0.6653	0.7366	-19.61	-14.63	13.40	0.34
C(18)−C(19)	2.07(7)	-14.0(2)	1.3929	0.7144	0.6785	-16.11	-11.96	14.07	0.35
C(18)−H(18)	1.8(1)	-15.4(4)	1.0836	0.7622	0.3214	-19.16	-17.46	21.26	0.10
C(19)−H(19)	1.8(1)	-15.2(3)	1.0831	0.7170	0.3661	-18.55	-16.99	20.32	0.09
C(21)−C(22)	1.97(6)	-15.1(2)	1.4049	0.7136	0.6913	-16.51	-11.92	13.34	0.38
C(21)−C(26)	2.01(7)	-15.5(2)	1.3997	0.7370	0.6627	-15.86	-13.34	13.66	0.19
C(22)−C(23)	2.32(7)	-19.5(2)	1.3896	0.7156	0.6740	-18.49	-15.72	14.72	0.18
C(22)−H(22)	2.0(1)	-21.9(4)	1.0837	0.7404	0.3433	-20.75	-20.29	19.17	0.02
C(23)−C(24)	2.24(7)	-18.5(2)	1.3920	0.6292	0.7629	-18.08	-14.26	13.80	0.27
C(23)−H(23)	1.9(1)	-20.6(4)	1.0833	0.7437	0.3396	-20.10	-18.70	18.15	0.08
C(24)−C(25)	2.13(7)	-18.6(2)	1.3886	0.6427	0.7460	-17.87	-13.52	12.74	0.32
C(25)−C(26)	2.19(7)	-17.4(2)	1.3882	0.7334	0.6548	-17.79	-13.64	13.99	0.30
C(25)−H(25)	2.0(1)	-17.6(4)	1.0835	0.7236	0.3599	-20.40	-18.79	21.61	0.09
C(26)−H(26)	1.7(1)	-18.1(4)	1.0838	0.7501	0.3337	-18.05	-17.39	17.36	0.04
C(1)−C(2)	2.34(7)	-21.0(2)	1.3902	0.7147	0.6755	-19.30	-16.79	15.05	0.15
C(1)−C(6)	2.20(7)	-16.5(2)	1.3912	0.7010	0.6902	-17.48	-14.04	15.05	0.25
C(2)−C(3)	2.22(7)	-21.0(2)	1.3885	0.7281	0.6604	-19.12	-15.39	13.46	0.24
C(2)−H(2)	2.1(1)	-24.6(4)	1.0832	0.7418	0.3414	-22.20	-21.17	18.79	0.05
C(3)−C(4)	2.14(7)	-19.7(2)	1.4044	0.6863	0.7181	-18.76	-14.41	13.43	0.30
C(3)−H(3)	1.7(1)	-14.6(4)	1.0833	0.7526	0.3308	-17.57	-16.18	19.13	0.09
C(4)−C(5)	2.08(7)	-16.8(2)	1.4038	0.7238	0.6800	-16.71	-13.92	13.82	0.20
C(5)−C(6)	2.21(7)	-16.1(2)	1.3911	0.6433	0.7478	-17.53	-13.28	14.71	0.32
C(5)−H(5)	1.9(1)	-22.4(4)	1.0836	0.7385	0.3451	-19.93	-19.76	17.27	0.01
C(6)−H(6)	1.9(1)	-19.7(4)	1.0838	0.7460	0.3378	-20.27	-19.66	20.21	0.03
C(8)−C(9)	2.07(7)	-14.5(2)	1.4030	0.7493	0.6537	-14.81	-14.06	14.37	0.05
C(8)−C(13)	2.09(7)	-13.2(2)	1.4048	06932	0.7116	-16.27	-12.45	15.55	0.31
C(9)−C(10)	1.98(7)	-10.6(2)	1.3872	0.6522	0.7349	-14.44	-10.98	14.84	0.32
C(9)−H(9)	1.7(1)	-10.5(3)	1.0838	0.7300	0.3538	-16.51	-15.94	21.93	0.04
C(10)−C(11)	2.20(7)	-19.0(2)	1.3906	0.6689	0.7216	-16.99	-15.91	13.88	0.07

C(10)−H(10)	1.8(1)	-17.9(4)	1.0837	0.7345	0.3491	-18.87	-18.02	18.99	0.05
C(11)−C(12)	2.00(7)	-13.0(2)	1.3878	0.7060	0.6818	-14.62	-13.27	14.88	0.10
C(12)−C(13)	2.13(7)	-15.4(2)	1.3913	0.6817	0.7096	-16.03	-14.35	14.95	0.12
C(12)−H(12)	1.9(1)	-21.3(4)	1.0830	0.7514	0.3316	-20.60	-19.88	19.17	0.04
C(13)−H(13)	1.8(1)	-16.6(3)	1.0835	0.6849	0.3987	-17.06	-16.17	16.65	0.05

T.A.6.8: BCPs in structure **c.s.17** (experimental data).

Bond	$\rho(\mathbf{r})$ (e A^{-3})	$\nabla^2\rho(\mathbf{r})$ (e A^{-5})	Rij (Å)	d_1 (Å)	d_2 (Å)	λ_1	λ_2	λ_3	ε
O(1)−C(7)	2.98(8)	-32.6(3)	1.2216	0.7064	0.5152	-27.31	-22.70	17.42	0.20
O(2)−N(1)	3.14(9)	4.7(4)	1.2247	0.6245	0.6001	-26.06	-21.34	52.09	0.22
O(3)−N(1)	3.09(4)	5.4(2)	1.2314	0.6268	0.6046	-25.58	-20.92	51.88	0.22
N(1)−C(1)	2.00(3)	-13.42(9)	1.4551	0.7990	0.6561	-16.34	-13.91	16.83	0.18
N(2)−C(4)	2.09(4)	-13.6(1)	1.3865	0.7796	0.6069	-16.44	-14.20	17.01	0.16
N(2)−C(7)	2.17(5)	-16.6(2)	1.3909	0.7677	0.6232	-18.62	-15.19	17.25	0.23
N(2)−H(2A)	2.19(9)	-29.6(4)	1.0090	0.7293	0.2597	-29.67	-26.93	27.05	0.10
N(3)−C(7)	2.21 (5)	-18.0(2)	1.3731	0.7613	0.6618	-18.93	-15.86	16.78	0.19
N(3)−C(8)	2.03(4)	-12.6(1)	1.4054	0.7783	0.6272	-15.85	-14.12	17.38	0.12
N(3)−H(3A)	2.25(9)	-34.0(5)	1.0094	0.7541	0.2553	-31.04	-28.61	25.62	0.09
N(5)−C(51)	1.63(3)	-6.84(7)	1.5175	0.8501	0.6674	-10.88	-10.88	14.92	0.00
N(5)−C(53)	1.67(1)	-8.49(4)	1.5210	0.8585	0.625	-11.53	-11.44	14.48	0.01
N(5)−C(55)	1.67(1)	-8.36(4)	1.5193	0.8571	0.6621	-11.54	-11.32	14.50	0.02
N(5)−C(57)	1.68(2)	-8.57(4)	1.5190	0.8578	0.6611	-11.56	-11.48	14.47	0.01
C(1)−C(2)	2.18(2)	-18.68(5)	1.3913	0.6986	0.6927	-17.53	-14.17	13.02	0.24
C(1)−C(6)	2.18(2)	-18.64(5)	1.3925	0.6991	0.6934	-17.51	-14.15	13.02	0.24
C(2)−C(3)	2.18(1)	-19.39(4)	1.3840	0.6925	0.6915	-17.89	-14.15	12.65	0.26
C(2)−H(2)	1.86(6)	-17.4(1)	1.0830	0.6836	0.3994	-17.27	-15.97	15.88	0.08
C(3)−C(4)	2.111(0)	-16.939(1)	1.4135	0.7041	0.7093	-16.73	-13.57	13.37	0.23
C(3)−H(3)	1.795(0)	-16.791(0)	1.0830	0.6967	0.3864	-16.95	-15.70	15.86	0.08
C(4)−C(5)	2.131(0)	-17.404(1)	1.4064	0.7036	0.7028	-16.97	-13.71	13.27	0.24
C(5)−C(6)	2.176(0)	-19.201(0)	1.3865	0.6938	0.6928	-17.84	-14.08	12.72	0.27
C(5)−H(5)	1.848(0)	-19.439(0)	1.0831	0.6991	0.3840	-17.96	-16.76	15.29	0.07
C(6)−H(6)	1.794(0)	-16.721(0)	1.0831	0.6969	0.3862	-16.92	-15.70	15.89	0.08

C(8)−C(9)	2.153(0)	-17.943(1)	1.4005	0.7032	0.6973	-17.15	-13.93	13.14	0.23
C(8)−C(13)	2.131(0)	-17.541(1)	1.4049	0.7040	0.7009	-17.02	-13.73	13.21	0.24
C(9)−C(10)	2.11(2)	-17.21(4)	1.3947	0.7013	0.6935	-16.67	-13.52	12.98	0.23
C(9)−H(9)	1.793(0)	-16.721(0)	1.0831	0.6967	0.3865	-16.90	-15.68	15.86	0.08
C(10)−C(11)	2.06(2)	-15.58(4)	1.3993	0.6997	0.6995	-15.71	-13.07	13.21	0.20
C(10)−H(10)	1.76(2)	-16.17(5)	1.0830	0.6917	0.3913	-16.01	-15.72	15.56	0.02
C(11)−C(12)	2.077(0)	-15.877(0)	1.3953	0.6975	0.6977	-15.83	-13.19	13.14	0.20
C(11)−H(11)	1.762(0)	-16.201(0)	1.0830	0.6915	0.3915	-16.02	-15.72	15.54	0.02
C(12)−C(13)	2.106(0)	-17.095(0)	1.3964	0.6944	0.7020	-16.63	-13.47	13.01	0.23
C(12)−H(12)	1.764(0)	-16.194(0)	1.0830	0.6918	0.3912	-16.02	-15.73	15.56	0.02
C(13)−H(13)	1.795(0)	-16.767(0)	1.0830	0.6966	0.3865	-16.92	-15.69	15.85	0.08
C(51)−C(52)	1.66(2)	-9.49(5)	1.5193	0.7604	0.7589	-11.35	-10.80	12.66	0.05
C(51)−H(51A)	1.82(6)	-16.5(1)	1.0920	0.6915	0.4005	-15.88	-15.39	14.81	0.03
C(51)−H(51B)	1.78(1)	-15.15(4)	1.0921	0.6937	0.3984	-15.45	-15.09	15.38	0.02
C(52)−H(52A)	1.77(6)	-15.7(2)	1.0594	0.6692	0.3902	-15.69	-14.68	14.71	0.07
C(52)−H(52B)	1.79(1)	-15.83(4)	1.0591	0.6616	0.3975	-16.00	-14.58	14.75	0.10
C(52)−H(53C)	1.79(1)	-15.88(4)	1.0590	0.6619	0.3971	-16.02	-14.62	14.76	0.10
C(53)−C(54)	1.663(0)	-9.628(0)	1.5165	0.7587	0.7578	-11.43	-10.86	12.66	0.05
C(53)−H(53A)	1.782(0)	-15.205(0)	1.0920	0.6937	0.3983	-15.55	-15.04	15.38	0.03
C(53)−H(53B)	1.779(0)	-15.015(0)	1.0922	0.6940	0.3982	-15.36	-15.09	15.43	0.02
C(54)−H(54A)	1.785(0)	-15.546(0)	1.0595	0.6624	0.3971	-15.69	-14.69	14.84	0.07
C(54)−H(54B)	1.790(0)	-15.867(0)	1.0590	0.6617	0.3973	-16.03	-14.59	14.75	0.10
C(54)−H(54C)	1.793(0)	-15.878(0)	1.0590	0.6621	0.3969	-16.03	-14.62	14.77	0.10
C(55)−C(56)	1.674(1)	-9.809(1)	1.5127	0.7575	0.7552	-11.52	-10.93	12.65	0.05
C(55)−H(55A)	1.75(6)	-15.1 (1)	1.0921	0.7023	0.3899	-15.35	-15.00	15.23	0.02
C(55)−H(55B)	1.780(1)	-15.203(1)	1.0921	0.6936	0.3985	-15.52	-15.06	15.37	0.03
C(56)−H(56A)	1.792(0)	-15.827(0)	1.0591	0.6622	0.3969	-15.93	-14.68	14.79	0.09
C(56)−H(56B)	1.795(0)	-15.864(0)	1.0591	0.6623	0.3967	-16.04	-14.61	14.78	0.10
C(56)−H(56C)	1.793(0)	-15.874(0)	1.0590	0.6620	0.3970	-16.05	-14.60	14.77	0.10
C(57)−C(58)	1.673(0)	-9.805(0)	1.5126	0.7570	0.7556	-11.53	-10.92	12.65	0.06
C(57)−H(57A)	1.782(0)	-15.153(0)	1.0921	0.6940	0.3981	-15.48	-15.08	15.41	0.03
C(57)−H(57B)	1.780(0)	-15.166(0)	1.0921	0.6937	0.3984	-15.50	-15.06	15.39	0.03
C(58)−H(58A)	1.790(0)	-15.794(0)	1.0591	0.6622	0.3970	-15.88	-14.70	14.79	0.08

C(58)−H(58B)	1.794(0)	-15.861(0)	1.0590	0.6622	0.3968	-15.99	-14.65	14.78	0.09
C(58)−H(58C)	1.793(0)	-15.881(0)	1.0590	0.6620	0.3970	-16.04	-14.61	14.77	0.10

T.A.6.9: BCPs in structure **c.s.18** (experimental data).

Bond	$\rho(\mathbf{r})$ (e A^{-3})	$\nabla^2\rho(\mathbf{r})$ (e A^{-5})	Rij (Å)	d_1 (Å)	d_2 (Å)	λ_1	λ_2	λ_3	ε
S(1)−C(7)	1.47(5)	-3.1(1)	1.6736	0.8074	0.8663	-9.08	-7.77	13.75	0.17
S(2)−C(20)	1.41(5)	-3.6(1)	1.6858	0.8414	0.8444	-10.60	-9.08	16.06	0.17
O(1)−N(1)	3.33(7)	-0.9(3)	1.2354	0.6256	0.6098	-31.82	-26.85	57.79	0.18
O(2)−N(1)	3.34(7)	-1.0(3)	1.2346	0.6254	0.6093	-31.89	-26.92	57.82	0.18
O(3)−N(4)	3.41(5)	-10.0(2)	1.2284	0.6121	0.6163	-34.18	-31.18	55.36	0.10
O(4)−N(4)	3.38(5)	-9.4(2)	1.2323	0.6135	0.6188	-33.80	-30.82	55.22	0.10
N(1)−C(1)	1.90(5)	-8.9(1)	1.4586	0.8086	0.655	-14.90	-13.49	19.46	0.10
N(2)−C(4)	2.09(5)	-11.9(2)	1.3970	0.7892	0.6077	-16.36	-14.77	19.26	0.11
N(2)−C(7)	2.32(5)	-19.8(2)	1.3688	0.7787	0.5901	-20.40	-16.91	17.47	0.21
N(2)−H(2A)	2.32(7)	-34.4(4)	1.0094	0.7752	0.2342	-33.68	-33.46	32.76	0.01
N(3)−C(7)	2.36(5)	-18.6(2)	1.3660	0.7657	0.6003	-19.37	-17.93	18.70	0.08
N(3)−C(8)	2.17(5)	-15.2(2)	1.4086	0.7879	0.6207	-17.45	-16.75	18.96	0.04
N(3)−H(3A)	2.19(7)	-29.9(4)	1.0091	0.7779	0.2312	-31.65	-31.00	32.78	0.02
N(4)−C(14)	1.84(4)	-8.4(1)	1.4561	0.8190	0.6371	-14.59	-12.86	19.04	0.13
N(5)−C(17)	2.06(4)	-12.8(1)	1.3970	0.7971	0.5998	-16.83	-14.79	18.86	0.14
N(5)−C(20)	2.34(5)	-16.9(2)	1.3721	0.7517	0.6204	-20.13	-16.99	20.20	0.18
N(5)−H(5A)	2.20(8)	-23.4(4)	1.0092	0.7595	0.2497	-29.85	-28.98	35.40	0.03
N(6)−C(20)	2.18(5)	-16.2(2)	1.3559	0.7737	0.5822	-17.13	-15.95	16.85	0.07
N(6)−C(21)	2.15(4)	-15.0(1)	1.4049	0.7855	0.6194	-17.98	-15.98	18.93	0.12
N(6)−H(6A)	2.14(8)	-27.8(5)	1.0092	0.7751	0.2341	-31.08	-29.31	32.55	0.06
N(7)−C(71)	1.58(5)	-3.2(1)	1.4966	0.8532	0.6433	-10.65	-9.92	17.33	0.07
N(7)−C(72)	1.56(5)	-4.3(1)	1.4927	0.8582	0.6345	-11.52	-9.12	16.33	0.26
N(7)−C(73)	1.69(5)	-2.9(1)	1.4918	0.8283	0.6635	-12.00	-10.37	19.42	0.16
N(7)−C(74)	1.66(5)	-8.1(1)	1.4937	0.8610	0.6327	-12.70	-11.38	16.03	0.12
C(1)−C(2)	2.20(4)	-17.6(1)	1.3912	0.6922	0.6990	-17.89	-14.47	14.77	0.24
C(1)−C(6)	2.16(5)	-17.1(1)	1.3918	0.7375	0.6542	-17.55	-14.07	14.54	0.25

C(2)−C(3)	2.26(4)	-18.5(1)	1.3858	0.6851	0.7007	-18.03	-15.64	15.13	0.15
C(2)−H(2)	1.93(6)	-17.2(2)	1.0839	0.7260	0.3579	-19.60	-18.15	20.57	0.08
C(3)−C(4)	2.10(4)	-15.8(1)	1.4100	0.6838	0.7262	-16.27	-14.34	14.82	0.13
C(3)−H(3)	1.84(6)	-16.4(2)	1.0831	0.7328	0.3503	-18.34	-17.94	19.93	0.02
C(4)−C(5)	2.08(4)	-15.3(1)	1.4033	0.7128	0.6905	-16.19	-13.80	14.68	0.17
C(5)−C(6)	2.23(4)	-18.0(1)	1.3907	0.6864	0.7043	-18.16	-15.10	15.23	0.20
C(5)−H(5)	1.77(6)	-15.1(2)	1.0843	0.7558	0.3285	-18.36	-17.89	21.19	0.03
C(6)−H(6)	1.77(7)	-16.7(2)	1.0833	0.7432	0.3401	-17.80	-17.70	18.79	0.01
C(8)−C(9)	2.09(4)	-14.5(1)	1.4002	0.6826	0.7176	-16.10	-13.11	14.68	0.23
C(8)−C(13)	2.16(4)	-17.7(1)	1.3996	0.6927	0.7069	-16.87	-15.05	14.26	0.12
C(9)−C(10)	2.25(4)	-18.0(1)	1.3948	0.6696	0.7252	-17.92	-15.16	15.06	0.18
C(9)−H(9)	1.82(6)	-15.6(2)	1.0838	0.7235	0.3603	-17.76	-17.22	19.34	0.03
C(10)−C(11)	2.21(4)	-18.9(1)	1.3925	0.6658	0.7267	-18.26	-14.83	14.23	0.23
C(10)−H(10)	1.79(6)	-14.7(2)	1.0834	0.7037	0.3797	-17.11	-15.92	18.36	0.07
C(11)−C(12)	2.08(5)	-16.2(1)	1.3967	0.7376	0.6591	-16.26	-13.74	13.75	0.18
C(11)−H(11)	1.84(7)	-14.5(2)	1.0831	0.7326	0.3505	-18.84	17.38	21.68	0.08
C(12)−C(13)	2.20(4)	-17.5(1)	1.3964	0.7001	0.6963	-17.42	-14.94	14.81	0.17
C(12)−H(12)	1.77(6)	-13.6(2)	1.0848	0.7199	0.3649	-17.09	-16.40	19.92	0.04
C(13)−H(13)	1.84(6)	-15.6(2)	1.0831	0.7403	0.3428	-18.46	-17.81	20.72	0.04
C(14)−C(15)	2.04(4)	-15.5(1)	1.3918	0.7239	0.6678	-16.16	-13.57	14.20	0.19
C(14)–C(19)	2.16(4)	-15.7(1)	1.3907	0.6953	0.6954	-17.75	-13.80	15.82	0.29
C(15)−C(16)	2.19(4)	-16.9(1)	1.3860	0.6606	0.7254	-18.10	-14.21	15.42	0.27
C(15)−H(15)	1.85(7)	-17.9(2)	1.0833	0.7402	0.3431	-19.15	-18.51	19.71	0.03
C(16)−C(17)	2.13(4)	-15.1(1)	1.4089	0.6725	0.7364	-17.18	-13.89	15.93	0.24
C(16)−H(16)	1.81(6)	-15.8(2)	1.0830	0.6993	0.3837	-17.27	-16.66	18.15	0.04
C(17)−C(18)	1.97(4)	-13.2(1)	1.4014	0.7363	0.6651	-15.27	-12.60	14.65	0.21
C(18)−C(19)	2.14(4)	-14.8(1)	1.3906	0.7270	0.6636	-17.29	-13.46	15.94	0.28
C(18)−H(18)	1.90(7)	-17.0(2)	1.0833	0.7352	0.3481	-19.32	-18.55	20.85	0.04
C(19)−H(19)	1.80(6)	-14.7(2)	1.0830	0.7310	0.3520	-17.84	-17.39	20.58	0.03
C(21)−C(22)	2.12(4)	-15.0(1)	1.4034	0.7078	0.6955	-16.59	-13.60	15.16	0.22
C(21)−C(26)	2.18(4)	-17.1(1)	1.3998	0.7091	0.6907	-17.45	-14.63	14.99	0.19
C(22)−C(23)	2.30(4)	-18.8(1)	1.3885	0.6792	0.7093	-18.79	-15.52	15.46	0.21
C(22)−H(22)	1.77(6)	-13.2(2)	1.0831	0.7310	0.3521	-17.60	-16.60	20.96	0.06

C(23)−C(24)	2.22(4)	-17.9(1)	1.3940	0.6988	0.6952	-18.00	-14.98	15.04	0.20
C(23)−H(23)	1.80(6)	-15.3(2)	1.0835	0.7191	0.3644	-17.46	-17.13	19.26	0.02
C(24)−C(25)	2.09(4)	-15.0(1)	1.3928	0.7324	0.6604	-15.93	-13.58	14.51	0.17
C(24)−H(24)	1.82(6)	-13.5(2)	1.0832	0.7194	0.3638	-18.20	-16.65	21.30	0.09
C(25)−C(26)	2.20(4)	-16.9(1)	1.3965	0.7259	0.6706	-17.60	-14.64	15.35	0.20
C(25)−H(25)	1.81(6)	-14.9(2)	1.0831	0.7127	0.3703	-17.42	-16.75	19.27	0.04
C(26)−H(26)	1.88(6)	-19.6(2)	1.0837	0.7467	0.3370	-19.42	-18.89	18.68	0.03
C(71)−H(71A)	1.88(7)	-16.0(2)	1.0592	0.7043	0.3550	-18.37	-17.92	20.32	0.02
C(71)−H(71B)	1.84(8)	-13.8(3)	1.0593	0.7039	0.3554	-17.95	-17.10	21.27	0.05
C(71)−H(71C)	1.91(7)	-16.3(2)	1.0595	0.6921	0.3674	-18.81	-17.55	20.05	0.07
C(72)−H(72A)	1.91(7)	-16.5(2)	1.0591	0.6913	0.3678	-19.02	-17.58	20.10	0.08
C(72)−H(72B)	1.76(7)	-11.8(2)	1.0616	0.6734	0.3882	-16.26	-15.27	19.72	0.06
C(72)−H(72C)	1.86(8)	-12.4(3)	1.0598	0.7326	0.3272	-18.80	-18.02	24.44	0.04
C(73)−H(73A)	1.77(7)	-13.0(2)	1.0591	0.6613	0.3978	-16.89	-14.72	18.56	0.15
C(73)−H(73B)	1.75(8)	-12.0(3)	1.0591	0.7031	0.3560	-17.05	-15.77	2082	0.08
C(73)−H(73C)	1.84(7)	-15.1(3)	1.0598	0.7135	0.3463	-18.42	-17.23	20.58	0.07
C(74)−H(74A)	1.86(7)	-16.7(2)	1.0599	0.6993	0.3606	-18.65	-17.20	19.17	0.08
C(74)−H(74B)	2.02(9)	-19.2(4)	1.0591	0.7646	0.2945	-22.47	-21.45	24.76	0.05
C(74)−H(74C)	1.73(7)	-13.6(2)	1.0604	0.6540	0.4064	-15.82	-14.76	17.03	0.07

A.6.2 Theoretical topological analysis

T.A.6.10: BCPs in structure **c.s.3** (theoretical data).

Bond	$\rho(\mathbf{r})$ (e A^{-3})	$\nabla^2\rho(\mathbf{r})$ (e A^{-5})
O(1)−C(7)	2.777	-9.299
O−N nitro	3.298	-23.678
O−N nitro	3.309	-23.977
O−N nitro	3.276	-23.246
O−N nitro	3.273	-23.192
C−N nitro	1.787	-16.624
C−N nitro	1.848	-17.015
C−N urea−phenyl	1.960	-18.338

C−N urea−phenyl	1.989	-18.579
C−N urea	2.079	-22.041
C−N urea	2.053	-21.417
C−C	2.075	-20.609
C−C	2.102	-20.942
C−C	2.034	-19.775
C−C	2.027	-19.721
C−C	2.081	-20.599
C−C	2.095	-21.000
C−C	2.020	-19.471
C−C	2.117	-21.250
C−C	2.077	-20.649
C−C	2.070	-20.493
C−C	2.095	-20.868
C−C	2.023	-19.665
C−H	1.923	-24.055
C−H	1.896	-23.141
C−H	1.926	-24.140
C−H	1.929	-24.128
C−H	1.894	-23.101
C−H	1.923	-24.074
C−H	1.927	-24.183
C−H	1.931	-24.178
N−H	2.313	-39.021
N−H	2.309	-39.018

T.A.6.11: BCPs in structure **c.s.5** (theoretical data).

Bond	$\rho(\mathbf{r})$ (e A^{-3})	$\nabla^2\rho(\mathbf{r})$ (e A^{-5})
O(1)−C(7)	2.706	-8.965

O(2)−N(1)	3.327	-24.966
O(3)−N(1)	3.354	-25.063
O(4)−N(4)	3.401	-26.123
O(5)−N(4)	3.340	-25.545
N(1)−C(6)	1.721	-15.230
N(2)−C(4)	1.998	-20.147
N(2)−C(7)	2.132	-23.038
N(2)−H(2A)	2.281	-45.209
N(3)−C(7)	2.112	-22.653
N(3)−C(8)	2.004	-20.436
N(3)−H(3A)	2.274	-45.595
N(4)−C(12)	1.728	-15.230
N(5)−C(14)	1.613	-13.206
N(5)−C(15)	1.620	-13.688
N(5)−C(16)	1.626	-13.688
N(5)−C(17)	1.647	-14.074
C(1)−C(2)	2.085	-20.725
C(1)−C(6)	2.105	-21.207
C(2)−C(3)	2.099	-21.014
C(1)−H(1)	1.917	-23.713
C(3)−C(4)	2.058	-20.436
C(2)−H(2)	1.910	-23.713
C(4)−C(5)	2.072	-20.436
C(5)−C(6)	2.092	-20.918
C(5)−H(5)	1.923	-23.906
C(3)−H(3)	1.923	-24.002
C(8)−C(9)	2.058	-20.436
C(8)−C(13)	2.072	-20.532
C(9)−C(10)	2.105	-21.110
C(9)−H(9)	1.923	-24.002
C(10)−C(11)	2.078	-20.629

C(10)−H(10)	1.917	-23.713
C(11)−C(12)	2.105	-21.207
C(12)−C(13)	2.099	-21.014
C(11)−H(11)	1.917	-23.713
C(13)−H(13)	1.923	-23.906
C(14)−H(14A)	2.024	-26.123
C(14)−H(14B)	2.031	-26.605
C(14)−H(14C)	2.038	-26.701
C(15)−H(15A)	2.045	-26.991
C(15)−H(15B)	2.031	-26.412
C(15)−H(15C)	2.031	-26.412
C(16)−H(16A)	2.024	-26.316
C(16)−H(16B)	2.024	-26.316
C(16)−H(16C)	2.051	-26.991
C(17)−H(17A)	2.024	-26.316
C(17)-H(17B)	2.045	-26.894
C(17)−H(17C)	2.038	-26.701
H(2A)···CL(1)	0.175	1.533
H(3A)···CL(1)	0.199	1.677

T.A.6.12: BCPs in structure **c.s.6** (theoretical data).

Bond	$\rho(\mathbf{r})$ (e A^{-3})	$\nabla^2\rho(\mathbf{r})$ (e A^{-5})
O(1)−C(7)	2.740	-9.832
O(2)−N(1)	3.266	-23.038
O(3)−N(1)	3.320	-24.484
O(4)−N(4)	3.259	-23.038
O(5)−N(4)	3.259	-22.942
N(1)−C(1)	1.795	-16.291
N(2)−C(4)	2.018	-20.339
N(2)−C(7)	2.072	-21.978

N(2)−H(2A)	2.294	-43.763
N(3)−C(7)	2.105	-22.460
N(3)−C(8)	2.004	-19.665
N(3)−H(3A)	2.294	-44.052
N(4)−C(11)	2.004	-19.665
N(5)−C(14)	1.620	-13.592
N(5)−C(15)	1.640	-14.170
N(5)−C(16)	1.593	-12.531
N(5)−C(17)	1.593	-12.917
C(1)−C(2)	2.072	-20.436
C(1)−C(6)	2.078	-20.725
C(2)−C(3)	2.112	-21.110
C(2)−H(2)	1.910	-20.821
C(3)−C(4)	2.031	-19.857
C(3)−H(3)	1.896	-23.135
C(4)−C(5)	2.031	-19.857
C(5)−C(6)	2.092	-20.821
C(5)−H(5)	1.930	-24.195
C(6)−H(6)	1.923	-24.099
C(8)−C(9)	2.031	-19.761
C(8)−C(13)	2.024	-19.761
C(9)−C(10)	2.112	-21.207
C(9)−H(9)	1.910	-23.520
C(10)−C(11)	2.072	-20.532
C(10)−H(10)	1.917	-23.906
C(11)−C(12)	2.078	-20.725
C(12)−C(13)	2.085	-20.629
C(12)−H(12)	1.923	-24.002
C(13)−H(13)	1.930	-24.099
C(14)−H(14A)	2.031	-26.509

C(14)−H(14B)	2.024	-26.316
C(14)−H(14C)	2.045	-26.991
C(15)−H(15A)	2.031	-26.412
C(15)−H(15B)	2.031	-26.412
C(15)−H(15C)	2.031	-26.412
C(16)−H(16A)	2.564	-40.775
C(16)−H(16B)	2.578	-41.064
C(16)−H(16C)	2.126	-29.015
C(17)−H(17A)	2.024	-26.219
C(17)-H(17B)	2.058	-27.473
C(17)−H(17C)	2.024	-26.219
H(2A)···CL(1)	0.165	1.562
H(3A)···CL(1)	0.182	1.735

T.A.6.13: BCPs in structure **c.s.9** (theoretical data).

Bond	$\rho(\mathbf{r})$ (e A^{-3})	$\nabla^2\rho(\mathbf{r})$ (e A^{-5})
O(1)−C(7)	2.672	-9.158
O(2)−N(1)	3.273	-23.424
O(3)−N(1)	3.273	-23.231
O(4)−N(4)	3.286	-23.713
O(5)−N(4)	3.300	-23.906
O(6)−C(18)	2.483	-10.603
O(7)−C(18)	2.504	-9.254
N(1)−C(1)	1.802	-16.194
N(2)−C(4)	2.045	-20.725
N(2)−H(2A)	2.261	-47.041
N(2)−C(7)	2.078	-22.074
N(3)−C(7)	2.146	-23.231
N(3)−C(8)	2.024	-20.532
N(3)−H(3A)	2.261	-47.426

N(4)−C(11)	1.795	-16.194
N(5)−C(14)	1.586	-13.110
N(5)−C(15)	1.626	-13.784
N(5)−C(16)	1.626	-13.784
N(5)−C(17)	1.606	-13.013
C(1)−C(2)	2.058	-20.339
C(1)−C(6)	2.078	-20.629
C(2)−C(3)	2.119	-21.207
C(2)−H(2)	1.923	-24.099
C(3)−C(4)	2.024	-19.665
C(3)−H(3)	1.930	-24.099
C(4)−C(5)	2.024	-19.665
C(5)−C(6)	2.099	-20.821
C(5)−H(5)	1.917	-23.520
C(6)−H(6)	1.917	-23.713
C(8)−C(9)	2.024	-19.761
C(8)−C(13)	2.031	-19.857
C(9)−C(10)	2.119	-21.303
C(9)−H(9)	1.930	-24.292
C(10)−C(11)	2.078	-20.821
C(10)−H(10)	1.923	-24.002
C(11)−C(12)	2.099	-21.014
C(12)−C(13)	2.085	-20.629
C(12)−H(12)	1.917	-23.713
C(13)−H(13)	1.910	-23.424
C(14)−H(14A)	2.024	-26.316
C(14)−H(14B)	2.024	-26.316
C(14)−H(14C)	2.045	-26.991
C(15)−H(15A)	2.038	-26.701
C(15)−H(15B)	2.031	-26.412

C(15)−H(15C)	2.031	-26.412
C(16)−H(16A)	2.031	-26.509
C(16)−H(16B)	2.031	-26.509
C(16)−H(16C)	2.031	-26.509
C(17)−H(17A)	2.058	-27.376
C(17)-H(17B)	2.031	-26.412
C(17)−H(17C)	2.031	-26.509
C(18)−C(19)	1.687	-14.266
C(19)−H(19A)	1.984	-25.063
C(19)−H(19B)	1.957	-24.581
C(19)−H(19C)	1.971	-24.773
H(2A)···O(6)	0.256	2.699
H(3A)···O(7)	0.304	3.085

T.A.6.14: BCPs in structure **c.s.10** (theoretical data).

Bond	$\rho(\mathbf{r})$ (e A^{-3})	$\nabla^2\rho(\mathbf{r})$ (e A^{-5})
O(1)−C(7)	2.686	-9.543
O(2)−N(1)	3.259	-23.231
O(3)−N(1)	3.388	-25.737
O(5)−N(2)	3.239	-22.171
O(4)−N(2)	3.374	-25.448
O(6)−N(5)	3.313	-24.002
O(7)−N(5)	3.347	-24.484
O(8)−N(6)	3.354	-24.870
O(9)−N(6)	3.374	-26.123
O(10)−C(18)	2.517	-9.350
O(11)−C(18)	2.463	-11.085
N(1)−C(6)	1.721	-15.520
N(2)−C(2)	1.748	-16.387
N(3)−C(4)	2.038	-21.207

N(3)−H(3A)	2.254	-47.234
N(3)−C(7)	2.112	-22.749
N(4)−C(7)	2.139	-23.231
N(4)−H(4A)	2.247	-47.330
N(4)−C(8)	2.038	-21.110
N(5)−C(12)	1.721	-15.423
N(6)−C(10)	1.755	-16.484
N(7)−C(14)	1.593	-12.628
N(7)−C(15)	1.620	-13.495
N(7)−C(16)	1.626	-13.784
N(7)−C(17)	1.660	-14.363
C(1)−C(2)	2.085	-20.725
C(1)−C(6)	2.085	-20.725
C(2)−C(3)	2.126	-21.496
C(1)−H(1)	1.917	-24.099
C(3)−C(4)	2.051	-20.243
C(3)−H(3)	1.937	-24.581
C(4)−C(5)	2.031	-19.761
C(5)−C(6)	2.105	-21.110
C(5)−H(5)	1.930	-24.195
C(8)−C(9)	2.045	-20.147
C(8)−C(13)	2.045	-19.954
C(9)−C(10)	2.132	-21.592
C(9)−H(9)	1.937	-24.773
C(10)−C(11)	2.092	-20.918
C(11)−H(11)	1.923	-24.099
C(11)−C(12)	2.112	-21.303
C(12)−C(13)	2.092	-20.821
C(13)−H(13)	1.930	-24.195
C(14)−H(14A)	2.045	-26.798

C(14)−H(14B)	2.038	-26.701
C(14)−H(14C)	2.045	-26.798
C(15)−H(15A)	2.038	-26.701
C(15)−H(15B)	2.045	-26.798
C(15)−H(15C)	2.024	-26.316
C(16)−H(16A)	2.031	-26.509
C(16)−H(16B)	2.031	-26.412
C(16)−H(16C)	2.038	-26.701
C(17)−H(17A)	2.024	-26.316
C(17)-H(17B)	2.038	-26.701
C(17)−H(17C)	2.031	-26.412
C(18)−C(19)	1.728	-15.038
C(19)−H(19A)	1.957	-24.002
C(19)−H(19B)	1.944	-24.099
C(19)−H(19C)	1.485	-24.484
H(3A)···O(10)	0.297	2.988
H(4A)···O(11)	0.344	3.277

T.A.6.15: BCPs in structure **c.s.11** (theoretical data).

Bond	$\rho(\mathbf{r})$ (e A^{-3})	$\nabla^2\rho(\mathbf{r})$ (e A^{-5})
O(1)−C(7)	2.706	-10.314
O(2)−N(1)	3.307	-24.195
O(3)−N(1)	3.212	-22.074
O(4)−N(4)	3.280	-23.424
O(5)−N(4)	3.266	-24.002
N(1)−C(1)	1.802	-16.098
N(2)−C(4)	2.058	-20.629
N(2)−H(2A)	2.261	-47.715
N(2)−C(7)	2.092	-22.364
N(3)−C(7)	2.085	-22.267

N(3)−C(8)	2038	-20.821
N(3)−H(3A)	2.267	-47.523
N(4)−C(11)	1.775	-15.038
N(5)−C(14)	1.660	-14.170
N(5)−C(15)	1.640	-13.399
C(1)−C(2)	2.065	-20.436
C(1)−C(6)	2.072	-20.629
C(2)−C(3)	2.119	-21.207
C(2)−H(2)	1.923	-23.906
C(3)−C(4)	2.018	-19.665
C(3)−H(3)	1.910	-23.617
C(4)−C(5)	2.018	-19.665
C(5)−C(6)	2.072	-20.532
C(5)−H(5)	1.923	-23.906
C(6)−H(6)	1.923	-23.906
C(8)−C(9)	2.024	-19.857
C(8)−C(13)	2.045	-20.339
C(9)−C(10)	2.099	-20.821
C(9)−H(9)	1.910	-23.617
C(10)−C(11)	2.065	-20.436
C(10)−H(10)	1.903	-23.424
C(11)−C(12)	2.072	-20.629
C(12)−C(13)	2.078	-20.436
C(12)−H(12)	1.923	-24.002
C(13)−H(13)	1.930	-24.195
C(14)−H(14A)	2.024	-26.412
C(14)−H(14B)	2.031	-26.412
C(14)−H(14C)	2.024	-26.123
C(15)−H(15A)	2.031	-26.412
C(15)−H(15B)	2.051	-27.183

C(15)−H(15C)	2.031	-26.509
H(2A)···F(1)	0.317	3.663
H(3A)···F(1)	0.276	3.133

T.A.6.16: BCPs in structure **c.s.16** (theoretical data).

Bond	$\rho(\mathbf{r})$ (e A^{-3})	$\nabla^2\rho(\mathbf{r})$ (e A^{-5})
N(1)−O(1)	3.320	-24.224
N(1)−O(2)	3.341	-24.740
N(1)−C(1)	1.779	-16.494
C(1)−C(2)	2.098	-21.073
C(2)−C(3)	2.096	-20.841
C(3)−C(4)	2.063	-20.404
C(4)−C(5)	2.076	-20.753
C(5)−C(6)	2.099	-20.940
C(6)−C(1)	2.113	-21.424
C(2)−H(2)	1.919	-23.934
C(3)−H(3)	1.902	-23.318
C(6)−H(6)	1.924	-24.068
C(5)−H(5)	1.926	-23.980
C(4)−N(2)	1.956	-19.064
N(2)−H(2A)	2.300	-42.762
N(2)−C(7)	2.122	-22.246
C(7)−S(1)	1.437	-2.128
C(7)−N(3)	2.142	-22.132
N(3)−H(3A)	2.302	-43.289
N(3)−C(8)	1.983	-19.602
C(8)−C(9)	2.058	-20.341
C(9)−C(10)	2.105	-20.981
C(10)−C(11)	2.092	-20.946

C(11)−C(12)	2.118	-21.520
C(12)−C(13)	2.084	-20.635
C(13)−C(8)	2.060	-20.439
C(9)−H(9)	1.898	-23.087
C(10)−H(10)	1.913	-23.719
C(12)−H(12)	1.925	-24.104
C(13)−H(13)	1.931	-24.151
C(11)−N(4)	1.789	-16.566
N(4)−O(3)	3.328	-24.348
N(4)−O(4)	3.312	-24.141
N(5)−O(5)	3.346	-24.887
N(5)−O(6)	3.350	-24.917
N(5)−C(14)	1.780	-16.459
C(14)−C(15)	2.104	-21.220
C(15)−C(16)	2.106	-21.070
C(16)−C(17)	2.068	-20.501
C(17)−C(18)	2.049	-20.180
C(18)−C(19)	20.89	-20.736
C(19)−C(14)	2.114	-21.440
C(15)−H(15)	1.921	-23.966
C(16)−H(16)	1.904	-23.349
C(18)−H(18)	1.928	-24.026
C(19)−H(19)	1.922	-24.003
C(17)−N(6)	1.972	-19.318
N(6)−C(20)	2.133	-22.064
N(6)−H(6A)	2.307	-42.780
N(7)−C(20)	2.105	-21.799
C(20)−S(2)	1.454	-0.956
N(7)−C(21)	1.970	-19.475
N(7)−H(7A)	2.307	-42.308

C(21)−C(22)	2.065	-20.444
C(22)−C(23)	2.093	-20.753
C(23)−C(24)	2.106	-21.228
C(24)−C(25)	2.097	-21.065
C(25)−C(26)	2.092	-20.793
C(21)−C(26)	2.051	-20.274
C(22)−H(22)	1.904	-23.281
C(23)−H(23)	1.917	-23.858
C(25)−H(25)	1.922	-23.978
C(26)−H(26)	1.929	-24.070
C(24)−N(8)	1.780	-16.509
N(8)−O(7)	3.344	-24.772
N(8)−O(8)	3.363	-25.291
N(9)−C(93)	1.575	-12.750
C(93)−C(94)	1.669	-13.878
C(93)−H(alkyl)	1.914	-23.416
C(93)−H(alkyl)	1.912	-23.393
C(94)−H(alkyl)	1.989	-25.205
C(94)−H(alkyl)	1.985	-25.093
C(94)−H(alkyl)	1.995	-25.174
N(9)−C(95)	1.566	-12.523
C(95)−C(96)	1.640	-13.368
C(95)−H(alkyl)	1.912	-23.361
C(95)−H(alkyl)	1.927	-23.795
C(96)−H(alkyl)	1.986	-24.967
C(96)−H(alkyl)	1.989	-25.366
C(96)−H(alkyl)	1.986	-25.070
N(9)−C(97)	1.615	-12.715
C(97)−C(98)	1.685	-14.170
C(97)−H(alkyl)	1.914	-23.441

C(97)−H(alkyl)	1.916	-23.467
C(98)−H(alkyl)	1.989	-25.206
C(98)−H(alkyl)	1.980	-24.973
C(98)−H(alkyl)	1.981	-24.846
N(9)−C(91)	1.566	-12.644
C(91)−C(92)	1.665	-13.860
C(91)−H(alkyl)	1.908	-23.237
C(91)−H(alkyl)	1.920	-23.540
C(92)−H(alkyl)	1.977	-24.637
C(92)−H(alkyl)	1.980	-25.079
C(92)−H(alkyl)	1.989	-25.097
H(2A)···Cl(1)	0.158	1.588
H(3A)···Cl(1)	0.194	1.804
H(5A)···Cl(1)	0.140	1.445
H(6A)···Cl(1)	0.124	1.279

T.A.6.17: BCPs in structure **c.s.17** (theoretical data).

Bond	$\rho(\mathbf{r})$ (e A^{-3})	$\nabla^2\rho(\mathbf{r})$ (e A^{-5})
O(1)−C(7)	2.749	-9.533
O(2)−N(1)	3.372	-25.599
O(3)−N(1)	3.317	-24.687
N(1)−C(1)	1.780	-16.068
N(2)−C(4)	2.019	-20.203
N(2)−H(2A)	2.294	-43.809
N(2)−C(7)	2.051	-21.618
N(3)−C(7)	2.144	-23.125
N(3)−C(8)	1.927	-18.764
N(3)−H(3A)	2.296	-43.324
N(5)−C(51)	1.565	-12.610

N(5)−C(53)	1.525	-11.635
N(5)−C(55)	1.577	-12.792
N(5)−C(57)	1.562	-12.572
C(1)−C(2)	2.099	-21.141
C(1)−C(6)	2.096	-21.055
C(2)−C(3)	2.109	-21.004
C(2)−H(2)	1.916	-23.798
C(3)−C(4)	2.027	-19.763
C(3)−H(3)	1.922	-23.380
C(4)−C(5)	2.048	-20.276
C(5)−C(6)	2.099	-20.907
C(5)−H(5)	1.931	-24.186
C(6)−H(6)	1.923	-24.002
C(8)−C(9)	2.075	-20.607
C(8)−C(13)	2.047	-20.061
C(9)−C(10)	2.071	-20.370
C(9)−H(9)	1.900	-23.237
C(10)−C(11)	2.056	-20.183
C(10)−H(10)	1.901	-23.341
C(11)−C(12)	2.079	-20.661
C(11)−H(11)	1.896	-23.195
C(12)−C(13)	2.068	-20.356
C(12)−H(12)	1.905	-23.443
C(13)−H(13)	1.922	-23.867
C(51)−C(52)	1.651	-13.574
C(53)−C(54)	1.658	-13.671
C(55)−C(56)	1.674	-14.018
C(57)−C(58)	1.675	-14.006
C(51)−H(alkyl)	1.913	-23.388
C(51)−H(alkyl)	1.909	-23.276

C(53)−H(alkyl)	1.940	-24.315
C(53)−H(alkyl)	1.906	-23.194
C(55)−H(alkyl)	1.911	-23.370
C(55)−H(alkyl)	1.914	-23.433
C(57)−H(alkyl)	1.924	-23.704
C(57)−H(alkyl)	1.911	-23.344
C(52)−H(alkyl)	1.987	-25.108
C(52)−H(alkyl)	1.985	-25.143
C(52)−H(alkyl)	2.003	-25.597
C(54)−H(alkyl)	1.986	-25.150
C(54)−H(alkyl)	1.989	-25.289
C(54)−H(alkyl)	1.979	-24.873
C(56)−H(alkyl)	1.985	-24.985
C(56)−H(alkyl)	1.980	-25.034
C(56)−H(alkyl)	1.988	-25.116
C(58)−H(alkyl)	1.984	-25.027
C(58)−H(alkyl)	1.984	-25.159
C(58)−H(alkyl)	1.985	-25.015
H(2A)···Cl(1)	0.166	1.549
H(3A)···Cl(1)	0.157	1.514

T.A.6.18: BCPs in structure **c.s.18** (theoretical data).

Bond	$\rho(\mathbf{r})$ (e A^{-3})	$\nabla^2\rho(\mathbf{r})$ (e A^{-5})
S(1)−C(7)	1.444	-1.940
S(2)−C(20)	1.424	-3.056
O(1)−N(1)	3.291	-24.237
O(2)−N(1)	3.294	-24.427
O(3)−N(4)	3.342	-25.077
O(4)−N(4)	3.313	-24.221

N(1)−C(1)	1.737	-14.398
N(2)−C(4)	1.987	-20.112
N(2)−C(7)	2.109	-21.581
N(2)−H(2A)	2.299	-44.540
N(3)−C(7)	2.146	-22.518
N(3)−C(8)	1.907	-18.123
N(3)−H(3A)	2.302	-42.892
N(7)−C(71)	1.624	-13.276
N(7)−C(72)	1.630	-13.671
N(7)−C(73)	1.659	-14.359
N(7)−C(74)	1.625	-12.531
C(1)−C(2)	2.097	-21.211
C(1)−C(6)	2.101	-21.243
C(2)−C(3)	2.107	-20.956
C(2)−H(2)	1.918	-23.877
C(3)−C(4)	2.047	-20.272
C(3)−H(3)	1.918	-23.773
C(4)−C(5)	2.058	-20.543
C(5)−C(6)	2.085	-20.557
C(5)−H(5)	1.931	-24.168
C(6)−H(6)	1.919	-23.859
C(8)−C(9)	2.077	-20.554
C(8)−C(13)	2.076	-20.655
C(9)−C(10)	2.069	-20.395
C(9)−H(9)	1.902	-23.300
C(10)−C(11)	2.090	-20.881
C(10)−H(10)	1.903	-23.408
C(11)−C(12)	2.072	-20.527
C(11)−H(11)	1.900	-23.311
C(12)−C(13)	2.070	-20.398
C(12)−H(12)	1.905	-23.449

C(13)−H(13)	1.921	-23.825
N(4)−C(14)	1.774	-15.869
N(5)−C(17)	1.980	-19.881
N(5)−C(20)	2.098	-21.608
N(6)−C(20)	2.178	-22.411
N(6)−C(21)	1.917	-18.097
N(5)−H(5A)	2.305	-43.612
N(6)−H(6A)	2.313	-43.203
C(14)−C(15)	2.096	-21.090
C(15)−C(16)	2.101	-20.872
C(16)−C(17)	2.049	-20.222
C(17)−C(18)	2.063	-20.567
C(18)−C(19)	2.089	-20.699
C(19)−C(14)	2.105	-21.254
C(15)−H(15)	1.914	-23.736
C(16)−H(16)	1.909	-23.481
C(18)−H(18)	1.930	-24.109
C(19)−H(19)	1.922	-23.983
C(21)−C(22)	2.069	-20.461
C(22)−C(23)	2.099	-20.990
C(23)−C(24)	2.083	-20.793
C(24)−C(25)	2.087	-20.815
C(25)−C(26)	2.069	-20.392
C(21)−C(26)	2.059	-20.320
C(22)−H(22)	1.904	-23.309
C(23)−H(23)	1.910	-23.548
C(24)−H(24)	1.896	-23.199
C(25)−H(25)	1.904	-23.417
C(26)−H(26)	1.926	-23.922
C(71)−H(alkyl)	2.031	-26.449

C(71)−H(alkyl)	2.027	-26.367
C(71)−H(alkyl)	2.055	-27.343
C(72)−H(alkyl)	2.032	-26.495
C(72)−H(alkyl)	2.042	-26.848
C(72)−H(alkyl)	2.031	-26.481
C(73)−H(alkyl)	2.033	-26.491
C(73)−H(alkyl)	2.032	-26.515
C(73)−H(alkyl)	2.031	-26.482
C(74)−H(alkyl)	2.027	-26.446
C(74)−H(alkyl)	2.022	-26.085
C(74)−H(alkyl)	2.049	-27.007
H(2A)···Cl(1)	0.182	1.663
H(3A)···Cl(1)	0.134	1.385
H(5A)···Cl(1)	0.180	1.718
H(6A)···Cl(1)	0.150	1.518

A.7 Atomic charges

A.7.1 QTAIM charges calculated from the electron density distribution in each of the crystal structures discussed in Chapters 4 and 5.

T.A.7.1: Atomic integrated QTAIM properties (/*e*) of **c.s.3**.

Atom	Atomic Population (*e*)	Net charge (*e*)	Atomic Lagrangian (a.u)
O(1)	8.970	-0.970	3.3320×10^{-4}
O(2)	8.183	-0.183	-7.0447×10^{-4}
O(3)	8.190	-0.190	1.5052×10^{-4}
O(4)	8.154	-0.154	-2.5781×10^{-4}
O(5)	8.140	-0.140	2.3133×10^{-5}
N(1)	6.883	0.117	2.3343×10^{-3}
N(2)	8.283	-1.283	8.9141×10^{-3}
N(3)	8.402	-1.402	5.0789×10^{-3}
N(4)	7.210	-0.210	5.0201×10^{-4}
C(1)	5.885	0.115	-2.1816×10^{-3}
C(2)	5.864	0.136	5.0998×10^{-3}
C(3)	6.199	-0.199	2.8425×10^{-3}
C(4)	5.669	0.331	-3.5640×10^{-3}
C(5)	6.003	-0.003	1.0053×10^{-3}
C(6)	5.969	0.031	7.4227×10^{-3}
C(7)	4.390	1.610	-8.1874×10^{-3}
C(8)	5.652	0.348	-5.5497×10^{-3}
C(9)	6.256	-0.256	-3.0685×10^{-3}
C(10)	5.999	0.001	-2.9056×10^{-3}
C(11)	5.599	0.401	-8.5961×10^{-3}
C(12)	5.950	0.050	-1.7658×10^{-3}
C(13)	6.134	-0.134	-1.8257×10^{-3}
H(2)	0.873	0.127	5.6541×10^{-5}
H(3)	1.023	-0.023	3.3848×10^{-3}
H(5)	0.814	0.186	-1.9255×10^{-4}
H(6)	0.840	0.162	7.6332×10^{-6}
H(9)	0.824	0.176	3.7840×10^{-4}

H(10)	0.995	0.005	6.2011×10^{-5}
H(12)	0.842	0.158	1.7625×10^{-5}
H(13)	0.823	0.177	3.6005×10^{-4}
H(2A)	0.475	0.525	2.1947×10^{-5}
H(3A)	0.439	0.561	-8.6416×10^{-5}

T.A.7.2: Atomic integrated QTAIM properties (/*e*) of **c.s.5**.

Atom	Atomic Population (*e*)	Net charge (*e*)	Atomic Lagrangian (a.u)
Cl(1)	17.482	-0.482	5.1171×10^{-3}
O(1)	8.890	-0.890	4.621×10^{-4}
O(2)	8.370	-0.370	-3.9625×10^{-5}
O(3)	8.373	-0.373	2.4369×10^{-5}
O(4)	8.385	-0.385	1.7030×10^{-5}
O(5)	8.376	-0.376	-1.9000×10^{-5}
N(1)	6.717	0.283	-5.3033×10^{-5}
N(2)	8.159	-1.159	4.2163×10^{-3}
N(3)	8.014	-1.014	-3.7288×10^{-4}
N(4)	6.731	0.269	-6.2319×10^{-3}
N(5)	7.812	-0.812	-5.3608×10^{-3}
C(1)	6.136	-0.136	1.6192×10^{-3}
C(2)	6.051	-0.051	2.3200×10^{-3}
C(3)	6.188	-0.188	-1.9964×10^{-3}
C(4)	5.564	0.436	4.4844×10^{-3}
C(5)	6.099	-0.099	1.5926×10^{-3}
C(6)	5.708	0.292	5.8421×10^{-4}
C(7)	4.497	1.503	-5.6654×10^{-4}
C(8)	5.627	0.373	-3.8448×10^{-3}
C(9)	6.050	-0.050	-1.2366×10^{-3}
C(10)	5.936	0.064	2.1686×10^{-3}
C(11)	6.069	-0.069	1.3039×10^{-4}
C(12)	5.771	0.229	1.2607×10^{-3}
C(13)	6.060	-0.060	2.5721×10^{-3}
C(14)	6.168	-0.168	5.3022×10^{-3}
C(15)	6.027	-0.027	5.1650×10^{-3}

C(16)	5.963	0.037	1.0397×10^{-2}
C(17)	6.025	-0.025	6.1925×10^{-3}
H(1)	0.874	0.126	2.1925×10^{-4}
H(2)	0.997	0.003	-5.4225×10^{-6}
H(3)	0.838	0.162	1.3715×10^{-5}
H(5)	0.769	0.231	7.1964×10^{-4}
H(9)	0.893	0.107	4.9589×10^{-5}
H(10)	0.908	0.092	-2.1992×10^{-5}
H(11)	0.881	0.119	-1.9698×10^{-5}
H(13)	0.766	0.234	4.6134×10^{-4}
H(14A)	0.899	0.101	3.3242×10^{-4}
H(14B)	0.756	0.244	4.3147×10^{-5}
H(14C)	0.839	0.161	2.6713×10^{-5}
H(15A)	0.847	0.153	3.3593×10^{-4}
H(15B)	0.965	0.035	6.9625×10^{-4}
H(15C)	0.884	0.116	-4.7933×10^{-4}
H(16A)	0.940	0.060	5.0646×10^{-5}
H(16B)	0.862	0.138	2.0053×10^{-5}
H(16C)	0.918	0.082	-3.7317×10^{-4}
H(17A)	0.836	0.164	-2.8347×10^{-5}
H(17B)	1.055	-0.055	-7.4447×10^{-5}
H(17C)	0.872	0.128	-2.8063×10^{-4}
H(2A)	0.485	0.515	2.3498×10^{-4}
H(3A)	0.561	0.439	-6.6159×10^{-4}

T.A.7.3: Atomic integrated QTAIM properties (/*e*) of **c.s.6**.

Atom	Atomic Population (*e*)	Net charge (*e*)	Atomic Lagrangian (a.u)
Cl(1)	17.296	-0.296	4.8178×10^{-3}
O(1)	9.047	-1.047	1.0811×10^{-4}
O(2)	8.528	-0.528	2.358×10^{-4}
O(3)	8.532	-0.532	6.5751×10^{-5}
O(4)	8.500	-0.500	1.0146×10^{-4}
O(5)	8.500	-0.500	-1.4803×10^{-4}
N(1)	6.740	0.260	-1.0396×10^{-3}

N(2)	8.098	-1.098	2.8992×10^{-3}
N(3)	8.121	-1.121	7.7730×10^{-5}
N(4)	6.782	0.218	-2.7230×10^{-3}
N(5)	7.930	-0.930	1.7449×10^{-2}
C(1)	5.823	0.177	1.3921×10^{-3}
C(2)	6.096	-0.096	6.2566×10^{-4}
C(3)	6.111	-0.111	-2.4336×10^{-3}
C(4)	5.652	0.348	2.3717×10^{-3}
C(5)	6.007	-0.007	2.8160×10^{-3}
C(6)	6.049	-0.049	-3.3163×10^{-3}
C(7)	4.494	1.506	-4.8031×10^{-3}
C(8)	5.660	0.340	5.3388×10^{-3}
C(9)	6.114	-0.114	-2.4080×10^{-3}
C(10)	6.071	-0.071	4.3161×10^{-3}
C(11)	5.787	0.213	5.5666×10^{-3}
C(12)	5.979	0.021	2.7422×10^{-3}
C(13)	6.008	-0.008	3.1211×10^{-3}
C(14)	5.826	0.174	-7.4033×10^{-3}
C(15)	5.782	0.218	-6.5715×10^{-3}
C(16)	5.851	0.149	-2.8639×10^{-3}
C(17)	5.806	0.194	-6.0781×10^{-3}
H(2)	0.846	0.154	1.3955×10^{-4}
H(3)	0.819	0.181	-9.6069×10^{-6}
H(5)	0.766	0.234	1.0429×10^{-4}
H(6)	0.817	0.183	8.8546×10^{-5}
H(9)	0.749	0.251	-2.9003×10^{-5}
H(10)	0.803	0.197	-8.5883×10^{-5}
H(12)	0.844	0.156	-3.7284×10^{-4}
H(13)	0.794	0.206	3.3874×10^{-4}
H(14A)	0.949	0.051	-1.0725×10^{-5}
H(14B)	0.952	0.048	1.4915×10^{-4}
H(14C)	0.881	0.119	-1.3456×10^{-5}
H(15A)	0.950	0.050	-2.5833×10^{-5}
H(15B)	0.940	0.060	-1.2954×10^{-4}
H(15C)	0.976	0.024	1.5374×10^{-4}

H(16A)	0.966	0.034	6.0685×10^{-5}
H(16B)	0.932	0.068	6.8646×10^{-5}
H(16C)	0.908	0.092	5.9650×10^{-5}
H(17A)	0.906	0.093	1.2846×10^{-4}
H(17B)	0.974	0.026	7.4247×10^{-5}
H(17C)	0.929	0.071	7.6634×10^{-5}
H(2A)	0.566	0.434	-4.7707×10^{-5}
H(3A)	0.539	0.461	4.3218×10^{-4}

T.A.7.4: Atomic integrated QTAIM properties (/*e*) of **c.s.9**.

Atom	Atomic Population (*e*)	Net charge (*e*)	Atomic Lagrangian (a.u)
O(1)	9.052	-1.052	2.9712×10^{-4}
O(2)	8.358	-0.358	5.0352×10^{-4}
O(3)	8.359	-0.359	6.2221×10^{-5}
O(4)	8.409	-0.409	-7.9510×10^{-6}
O(5)	8.418	-0.412	-7.4437×10^{-6}
O(6)	9.103	-1.103	2.5813×10^{-4}
O(7)	9.113	-1.133	7.8101×10^{-4}
N(1)	6.983	0.017	2.1194×10^{-4}
N(2)	8.165	-1.165	3.9730×10^{-4}
N(3)	8.070	-1.070	2.9803×10^{-3}
N(4)	6.858	0.142	-2.5592×10^{-4}
N(5)	7.905	-0.905	-2.4760×10^{-3}
C(1)	5.738	0.262	3.7768×10^{-4}
C(2)	6.175	-0.175	9.1148×10^{-4}
C(3)	6.194	-0.194	3.8941×10^{-3}
C(4)	5.685	0.315	2.3618×10^{-3}
C(5)	6.145	-0.145	2.1528×10^{-3}
C(6)	6.094	-0.094	3.3924×10^{-3}
C(7)	4.309	1.691	-6.9819×10^{-3}
C(8)	5.673	0.327	-1.2197×10^{-2}
C(9)	6.200	-0.200	2.1128×10^{-4}
C(10)	5.852	0.148	2.4140×10^{-3}
C(11)	5.804	0.196	-4.4653×10^{-3}

C(12)	6.097	-0.096	1.1573×10^{-3}
C(13)	6.006	-0.006	5.6591×10^{-4}
C(14)	6.074	-0.074	1.2094×10^{-2}
C(15)	5.878	0.122	9.4041×10^{-3}
C(16)	5.923	0.077	8.7482×10^{-3}
C(17)	5.939	0.061	1.0953×10^{-2}
C(18)	4.515	1.485	8.6268×10^{-6}
C(19)	6.251	-0.251	8.2879×10^{-3}
H(2)	0.862	0.138	-79712×10^{-6}
H(3)	0.826	0.174	3.2353×10^{-4}
H(5)	0.820	0.180	5.6993×10^{-5}
H(6)	0.688	0.312	1.1316×10^{-4}
H(9)	0.789	0.211	1.6491×10^{-4}
H(10)	0.836	0.164	-7.8876×10^{-5}
H(12)	0.831	0.169	2.6326×10^{-5}
H(13)	0.796	0.204	1.3524×10^{-4}
H(14A)	0.803	0.197	4.6932×10^{-5}
H(14B)	0.792	0.208	-1.0501×10^{-5}
H(14C)	0.812	0.188	4.0416×10^{-6}
H(15A)	0.809	0.191	-9.2525×10^{-5}
H(15B)	0.961	0.039	-6.0710×10^{-5}
H(15C)	0.939	0.061	4.3633×10^{-5}
H(16A)	0.983	0.017	2.1774×10^{-4}
H(16B)	0.775	0.225	1.9768×10^{-5}
H(16C)	0.930	0.070	1.1156×10^{-5}
H(17A)	0.994	0.006	2.9108×10^{-4}
H(17B)	0.882	0.118	2.8101×10^{-4}
H(17C)	0.847	0.153	7.0459×10^{-4}
H(19A)	0.926	0.074	2.8138×10^{-5}
H(19B)	0.829	0.171	1.0211×10^{-5}
H(19C)	0.918	0.082	-2.1897×10^{-5}
H(2A)	0.443	0.557	-7.2685×10^{-4}
H(3A)	0.519	0.481	2.5838×10^{-4}

T.A.7.5: Atomic integrated QTAIM properties (/*e*) of **c.s.10**.

Atom	Atomic Population (*e*)	Net charge (*e*)	Atomic Lagrangian (a.u)
O(1)	8.846	-0.846	-7.0875×10^{-4}
O(2)	8.278	-0.278	1.5247×10^{-4}
O(3)	8.291	-0.291	-4.9568×10^{-6}
O(4)	8.251	-0.251	2.3551×10^{-5}
O(5)	8.246	-0.246	-8.5715×10^{-6}
O(6)	8.268	-0.268	5.0366×10^{-5}
O(7)	8.277	-0.277	4.6423×10^{-4}
O(8)	8.297	-0.297	1.3943×10^{-5}
O(9)	8.298	-0.298	4.6710×10^{-5}
O(10)	8.992	-0.992	2.0531×10^{-4}
O(11)	9.217	-1.217	-3.5004×10^{-4}
N(1)	6.773	0.227	-1.2743×10^{-2}
N(2)	6.873	0.127	6.1789×10^{-3}
N(3)	8.047	-1.047	-1.3347×10^{-3}
N(4)	7.916	-0.916	3.4216×10^{-4}
N(5)	6.884	0.116	7.3208×10^{-3}
N(6)	6.734	0.266	-8.6235×10^{-5}
N(7)	8.006	-1.006	6.5106×10^{-4}
C(1)	5.683	0.317	-1.2325×10^{-3}
C(2)	6.093	-0.093	1.5860×10^{-4}
C(3)	6.234	-0.234	4.8258×10^{-3}
C(4)	5.610	0.390	4.8528×10^{-3}
C(5)	5.872	0.128	2.8971×10^{-3}
C(6)	5.920	0.080	1.3555×10^{-3}
C(7)	4.281	1.719	2.9280×10^{-3}
C(8)	5.642	0.358	-8.9396×10^{-3}
C(9)	5.890	0.110	-1.5112×10^{-3}
C(10)	5.893	0.107	-1.1379×10^{-3}
C(11)	5.871	0.129	-1.7484×10^{-3}
C(12)	5.832	0.168	-3.3819×10^{-4}
C(13)	6.073	-0.073	3.6108×10^{-3}
C(14)	5.825	0.175	6.9427×10^{-3}

C(15)	5.702	0.298	-8.6048×10^{-3}
C(16)	5.872	0.128	9.7070×10^{-3}
C(17)	5.648	0.352	2.1165×10^{-3}
C(18)	4.534	1.466	3.1791×10^{-2}
C(19)	6.720	-0.720	-3.0814×10^{-3}
H(1)	0.848	0.152	7.3486×10^{-5}
H(3)	0.870	0.130	1.1534×10^{-5}
H(5)	0.768	0.232	2.0058×10^{-4}
H(9)	0.902	0.098	2.3216×10^{-4}
H(11)	0.929	0.071	-8.2577×10^{-5}
H(13)	0.985	0.015	-8.1822×10^{-4}
H(14A)	0.916	0.084	2.7576×10^{-5}
H(14B)	0.921	0.079	1.9301×10^{-5}
H(14C)	0.989	0.011	1.3764×10^{-5}
H(15A)	0.944	0.056	-2.1637×10^{-5}
H(15B)	0.746	0.254	-2.1455×10^{-5}
H(15C)	0.954	0.046	-8.1557×10^{-4}
H(16A)	0.937	0.063	4.9775×10^{-5}
H(16B)	0.899	0.101	2.4337×10^{-4}
H(16C)	0.978	0.022	-6.9631×10^{-5}
H(17A)	0.941	0.059	7.2743×10^{-5}
H(17B)	1.003	-0.003	-2.7784×10^{-4}
H(17C)	0.975	0.025	-5.3444×10^{-7}
H(19A)	0.489	0.511	-1.9586×10^{-7}
H(19B)	0.720	0.280	-3.1018×10^{-6}
H(19C)	0.625	0.375	-6.5990×10^{-5}
H(3A)	0.679	0.321	-1.0152×10^{-3}
H(4A)	0.590	0.410	5.9298×10^{-5}

T.A.7.6: Atomic integrated QTAIM properties (/*e*) of **c.s.11**.

Atom	Atomic Population (*e*)	Net charge (*e*)	Atomic Lagrangian (a.u)
F(1)	9.290	-0.290	-5.7809×10^{-4}
O(1)	9.011	-1.011	-1.2643×10^{-4}
O(2)	8.324	-0.324	-2.6075×10^{-5}

O(3)	8.318	-0.318	4.6422×10^{-4}
O(4)	8.351	-0.351	2.6827×10^{-4}
O(5)	8.350	-0.350	-2.2867×10^{-5}
N(1)	6.897	0.103	6.4623×10^{-3}
N(2)	7.970	-0.970	7.7008×10^{-4}
N(3)	8.062	-1.062	-3.2674×10^{-3}
N(4)	6.875	0.125	-2.5049×10^{-3}
N(5)	7.917	-0.917	-4.5423×10^{-3}
C(1)	5.701	0.299	-1.5430×10^{-3}
C(2)	6.147	-0.147	1.0896×10^{-3}
C(3)	5.967	0.033	3.6940×10^{-3}
C(4)	5.756	0.244	3.0926×10^{-3}
C(5)	6.081	-0.081	2.3509×10^{-3}
C(6)	6.079	-0.079	1.9248×10^{-3}
C(7)	4.399	1.601	-1.3263×10^{-2}
C(8)	5.633	0.367	-1.1486×10^{-2}
C(9)	6.105	-0.105	-7.7499×10^{-4}
C(10)	6.107	-0.107	-7.4777×10^{-3}
C(11)	5.788	0.212	-7.9231×10^{-3}
C(12)	6.109	-0.109	7.1514×10^{-4}
C(13)	5.920	0.080	-4.5570×10^{-3}
C(14A)	5.716	0.284	8.2182×10^{-3}
C(15A)	5.724	0.276	1.6918×10^{-3}
C(14B)	5.726	0.274	-2.0186×10^{-3}
C(15B)	5.708	0.292	1.5590×10^{-2}
H(2)	0.796	0.204	-9.3670×10^{-5}
H(3)	0.846	0.154	7.1222×10^{-6}
H(5)	0.838	0.162	1.3013×10^{-4}
H(6)	0.869	0.131	3.2640×10^{-5}
H(9)	0.902	0.098	-2.5723×10^{-6}
H(10)	0.877	0.123	9.7757×10^{-5}
H(12)	0.863	0.137	-7.1401×10^{-5}
H(13)	0.825	0.175	-1.6582×10^{-3}
H(14A)	1.015	-0.015	-2.2952×10^{-5}
H(14B)	1.016	-0.016	-6.9204×10^{-5}

H(14C)	1.016	-0.016	-1.1389×10^{-4}
H(15A)	1.015	-0.015	-5.4371×10^{-5}
H(15B)	1.015	-0.015	-6.3879×10^{-6}
H(15C)	1.015	-0.015	2.2826×10^{-5}
H(14D)	1.016	-0.016	-5.9992×10^{-5}
H(14E)	1.015	-0.015	2.3673×10^{-5}
H(14F)	1.018	-0.018	-5.2172×10^{-4}
H(15D)	1.016	-0.016	-2.0492×10^{-5}
H(15E)	1.015	-0.015	8.1611×10^{-5}
H(15F)	1.015	-0.015	-8.1807×10^{-5}
H(2A)	0.549	0.451	7.8159×10^{-4}
H(3A)	0.565	0.435	1.8583×10^{-3}

T.A.7.7: Atomic integrated QTAIM properties (/*e*) of **c.s.16**.

Atom	Atomic Population (*e*)	Net charge (*e*)	Atomic Lagrangian (a.u)
CL(1)	17.163	-0.163	-1.3670×10^{-4}
S(2)	16.099	-0.099	1.9872×10^{-3}
S(1)	14.834	1.166	-5.1875×10^{-3}
O(5)	8.476	-0.476	-2.1651×10^{-4}
O(6)	8.471	-0.471	-7.8857×10^{-4}
O(7)	8.518	-0.518	-1.8368×10^{-4}
O(8)	8.517	-0.517	9.9540×10^{-4}
O(1)	8.483	-0.483	-1.5416×10^{-4}
O(2)	8.478	-0.478	-8.9338×10^{-4}
O(3)	8.429	-0.429	-1.9486×10^{-5}
O(4)	8.436	-0.436	1.4695×10^{-4}
N(9)	7.998	-0.998	-1.7926×10^{-2}
N(5)	6.940	0.060	4.9791×10^{-3}
N(6)	8.369	-1.369	5.6059×10^{-3}
N(7)	8.180	-1.180	8.0997×10^{-4}
N(8)	6.891	0.109	1.2905×10^{-2}
N(1)	6.869	0.131	2.0621×10^{-3}
N(2)	8.122	-1.122	5.6545×10^{-3}
N(3)	8.050	-1.050	2.0733×10^{-4}

N(4)	7.009	-0.009	-9.5107×10^{-3}
C(91)	5.801	0.199	-4.6434×10^{-3}
C(92)	6.243	-0.243	1.3602×10^{-3}
C(93)	6.163	-0.163	-4.3021×10^{-3}
C(94)	6.059	-0.059	-1.6923×10^{-3}
C(95)	5.687	0.313	4.6441×10^{-3}
C(96)	6.451	-0.451	4.9070×10^{-3}
C(97)	6.075	-0.075	-4.6154×10^{-3}
C(98)	6.469	-0.469	1.4031×10^{-3}
C(14)	5.909	0.091	4.0715×10^{-3}
C(15)	5.875	0.125	6.9612×10^{-3}
C(16)	5.751	0.249	4.1558×10^{-3}
C(17)	5.679	0.321	5.0052×10^{-3}
C(18)	6.285	-0.285	2.2258×10^{-3}
C(19)	6.030	-0.030	4.0248×10^{-3}
C(20)	5.366	0.634	3.7315×10^{-3}
C(21)	5.693	0.307	6.0971×10^{-3}
C(22)	6.186	-0.186	2.3537×10^{-3}
C(23)	6.021	-0.021	4.9192×10^{-3}
C(24)	5.708	0.292	1.0539×10^{-2}
C(25)	6.227	-0.227	2.4606×10^{-3}
C(26)	5.993	0.007	4.7077×10^{-3}
C(1)	6.068	-0.068	-3.4557×10^{-4}
C(2)	6.180	-0.180	1.6268×10^{-3}
C(3)	5.760	0.240	3.0662×10^{-3}
C(4)	5.599	0.401	3.9262×10^{-3}
C(5)	5.950	0.050	-1.9109×10^{-4}
C(6)	6.260	-0.260	5.3956×10^{-3}
C(7)	5.372	0.628	7.3313×10^{-5}
C(8)	5.940	0.060	-3.0168×10^{-2}
C(9)	6.123	-0.123	-8.4004×10^{-3}
C(10)	5.796	0.204	-1.0460×10^{-2}
C(11)	5.902	0.098	-6.8950×10^{-3}
C(12)	6.103	-0.103	-6.2890×10^{-3}
C(13)	6.148	-0.148	-1.0448×10^{-3}

H(91A)	0.964	0.036	2.7153×10^{-4}
H(91B)	0.909	0.091	-5.3411×10^{-4}
H(92A)	0.949	0.051	2.2923×10^{-5}
H(92B)	0.926	0.074	-3.5095×10^{-4}
H(92C)	0.983	0.017	-5.9359×10^{-4}
H(93A)	0.820	0.180	3.2059×10^{-4}
H(93B)	0.825	0.175	-1.7879×10^{-4}
H(94A)	0.924	0.076	1.5616×10^{-4}
H(94B)	0.878	0.122	1.2667×10^{-4}
H(94C)	1.107	-0.107	3.4531×10^{-4}
H(95A)	0.859	0.141	-1.6295×10^{-4}
H(95B)	0.815	0.185	3.2919×10^{-4}
H(96A)	0.992	0.008	6.4572×10^{-4}
H(96B)	0.862	0.138	4.1537×10^{-4}
H(96C)	1.011	-0.011	-1.7034×10^{-4}
H(97A)	0.970	0.030	-2.2839×10^{-4}
H(97B)	0.956	0.044	-8.1533×10^{-4}
H(98A)	0.615	0.385	6.8477×10^{-6}
H(98B)	0.630	0.370	2.2196×10^{-4}
H(98C)	1.013	-0.013	-7.2442×10^{-6}
H(15)	0.912	0.088	3.5507×10^{-4}
H(16)	0.906	0.094	1.7707×10^{-4}
H(18)	0.805	0.195	3.7795×10^{-4}
H(19)	0.991	0.009	-2.3435×10^{-4}
H(22)	0.758	0.242	-9.3760×10^{-6}
H(23)	0.683	0.316	-3.6946×10^{-5}
H(25)	1.012	-0.012	-7.0310×10^{-4}
H(26)	0.623	0.377	3.8575×10^{-4}
H(6A)	0.339	0.661	1.2913×10^{-4}
H(7A)	0.648	0.352	-5.2983×10^{-4}
H(2)	0.728	0.272	-5.7177×10^{-5}
H(3)	0.726	0.274	1.7195×10^{-5}
H(5)	0.638	0.362	7.2990×10^{-5}
H(6)	0.796	0.204	5.2521×10^{-5}
H(9)	0.909	0.091	-2.2350×10^{-4}

H(10)	0.807	0.193	-1.0460×10^{-4}
H(12)	0.669	0.331	-8.5111×10^{-5}
H(13)	0.803	0.197	3.4751×10^{-4}
H(2A)	0.602	0.398	-2.1886×10^{-4}
H(3A)	0.446	0.554	6.0440×10^{-4}

T.A.7.8: Atomic integrated QTAIM properties (/*e*) of **c.s.17**.

Atom	Atomic Population (*e*)	Net charge (*e*)	Atomic Lagrangian (a.u.)
CL(1)	17.455	-0.455	2.6778×10^{-3}
O(1)	8.723	-0.723	2.3375×10^{-4}
O(2)	8.244	-0.244	4.1304×10^{-4}
O(3)	8.239	-0.239	2.3057×10^{-4}
N(1)	6.640	0.360	3.7114×10^{-3}
N(2)	8.026	-1.026	-7.4668×10^{-4}
N(3)	7.991	-0.991	3.2880×10^{-3}
N(5)	7.872	-0.872	-2.7915×10^{-3}
C(1)	5.869	0.131	2.1109×10^{-3}
C(2)	6.002	-0.002	1.5442×10^{-3}
C(3)	6.010	-0.010	3.0996×10^{-3}
C(4)	5.769	0.231	-1.9438×10^{-3}
C(5)	6.057	-0.057	2.0125×10^{-3}
C(6)	6.011	-0.011	-5.2732×10^{-4}
C(7)	4.740	1.260	3.7362×10^{-3}
C(8)	5.807	0.193	-3.3356×10^{-3}
C(9)	6.013	-0.013	-1.4044×10^{-3}
C(10)	5.969	0.031	-2.0516×10^{-3}
C(11)	5.964	0.036	-1.1921×10^{-3}
C(12)	5.968	0.032	-6.2819×10^{-5}
C(13)	6.007	-0.007	2.0005×10^{-3}
C(51)	5.851	0.149	3.8923×10^{-3}

C(52)	5.925	0.075	-5.1691×10^{-3}
C(53)	5.839	0.161	-2.6094×10^{-4}
C(54)	5.897	0.103	7.3622×10^{-3}
C(55)	5.831	0.169	1.1645×10^{-2}
C(56)	5.902	0.098	-1.0808×10^{-3}
C(57)	5.837	0.163	9.5652×10^{-4}
C(58)	5.903	0.097	5.8561×10^{-4}
H(2)	1.011	-0.011	-6.8489×10^{-5}
H(3)	0.939	0.061	3.3147×10^{-5}
H(5)	0.897	0.103	-3.7812×10^{-4}
H(6)	0.933	0.067	-6.2537×10^{-5}
H(9)	0.936	0.064	1.9563×10^{-4}
H(10)	0.941	0.059	-1.2854×10^{-5}
H(11)	0.942	0.058	-2.1582×10^{-5}
H(12)	0.941	0.059	2.5240×10^{-6}
H(13)	0.937	0.063	5.8164×10^{-4}
H(51A)	0.958	0.042	5.9680×10^{-4}
H(51B)	1.013	-0.013	-1.9407×10^{-4}
H(52A)	0.935	0.065	-1.8360×10^{-5}
H(52B)	0.999	0.001	7.2376×10^{-4}
H(52C)	0.996	0.004	4.9287×10^{-4}
H(53A)	1.021	-0.021	-1.9219×10^{-3}
H(53B)	1.008	-0.008	-2.1643×10^{-5}
H(54A)	0.992	0.008	5.1548×10^{-5}
H(54B)	0.998	0.002	-4.2848×10^{-4}
H(54C)	0.997	0.003	-1.2467×10^{-4}
H(55A)	0.945	0.055	-1.2059×10^{-4}
H(55B)	1.012	-0.012	2.4829×10^{-4}
H(56A)	0.996	0.004	-3.0408×10^{-6}
H(56B)	0.996	0.004	4.8734×10^{-4}
H(56C)	0.997	0.003	-3.7008×10^{-5}

H(57A)	1.010	-0.010	6.3642×10^{-4}
H(57B)	1.012	-0.012	5.4721×10^{-4}
H(58A)	0.996	0.004	5.1694×10^{-6}
H(58B)	0.998	0.002	-8.3301×10^{-4}
H(58C)	0.996	0.004	-2.1272×10^{-4}
H(2A)	0.527	0.473	8.3198×10^{-4}
H(3A)	0.465	0.535	-4.5073×10^{-4}

T.A.7.9: Atomic integrated QTAIM properties (/*e*) of **c.s.18**.

Atom	Atomic Population (*e*)	Net charge (*e*)	Atomic Lagrangian (a.u.)
CL(1)	17.066	-0.066	8.9024×10^{-4}
S(1)	15.845	0.155	1.4899×10^{-4}
S(2)	15.349	0.651	3.3757×10^{-4}
O(1)	8.492	-0.492	-9.8845×10^{-4}
O(2)	5.495	-0.495	6.3093×10^{-4}
O(3)	8.442	-0.442	3.0141×10^{-4}
O(4)	8.441	-0.441	-6.3917×10^{-5}
N(1)	6.860	0.140	-2.5521×10^{-3}
N(2)	8.154	-1.154	2.2538×10^{-3}
N(3)	8.176	-1.176	2.8037×10^{-3}
N(4)	6.792	0.208	1.3227×10^{-2}
N(5)	8.026	-1.026	3.1553×10^{-3}
N(6)	8.104	-1.104	3.8156×10^{-4}
N(7)	7.841	-0.841	1.3133×10^{-2}
C(1)	5.918	0.082	-4.1264×10^{-3}
C(2)	6.155	-0.155	-1.5715×10^{-4}
C(3)	6.145	-0.145	8.4241×10^{-4}
C(4)	5.747	0.253	-3.3121×10^{-4}
C(5)	6.035	-0.035	1.9198×10^{-3}

C(6)	6.040	-0.040	2.1305×10^{-3}
C(7)	5.519	0.481	-9.3525×10^{-3}
C(8)	5.699	0.301	5.7106×10^{-3}
C(9)	6.193	-0.193	-2.9944×10^{-3}
C(10)	6.105	-0.105	1.3673×10^{-3}
C(11)	6.186	-0.186	3.1607×10^{-3}
C(12)	6.025	-0.025	4.3938×10^{-3}
C(13)	6.160	-0.160	-1.1413×10^{-3}
C(14)	5.807	0.193	6.8894×10^{-3}
C(15)	5.933	0.067	4.3421×10^{-3}
C(16)	6.069	-0.069	8.8341×10^{-4}
C(17)	5.785	0.215	7.4541×10^{-3}
C(18)	6.160	-0.160	4.9312×10^{-3}
C(19)	6.033	0.033	2.5632×10^{-3}
C(20)	5.440	0.560	5.4929×10^{-3}
C(21)	5.782	0.218	1.3686×10^{-3}
C(22)	6.129	-0.129	9.6846×10^{-4}
C(23)	6.204	-0.204	9.9124×10^{-4}
C(24)	6.126	-0.126	5.2539×10^{-3}
C(25)	6.108	-0.108	3.0719×10^{-3}
C(26)	6.170	-0.170	-5.3078×10^{-3}
C(71)	5.979	0.021	-3.8269×10^{-3}
C(72)	5.927	0.073	8.9041×10^{-3}
C(73)	5.934	0.066	-1.2340×10^{-3}
C(74)	5.888	0.112	-1.8631×10^{-4}
H(2)	0.855	0.145	4.2892×10^{-5}
H(3)	0.813	0.187	-4.7243×10^{-5}
H(5)	0.793	0.207	7.2176×10^{-4}
H(6)	0.701	0.299	6.8204×10^{-5}
H(9)	0.817	0.183	2.8342×10^{-6}
H(10)	0.876	0.124	2.0878×10^{-5}

H(11)	0.950	0.050	-3.5827 x10^{-6}
H(12)	0.877	0.123	-1.5333 x10^{-5}
H(13)	0.834	0.166	1.8868 x10^{-6}
H(15)	0.752	0.248	9.2766 x10^{-6}
H(16)	0.836	0.164	-1.2174 x10^{-4}
H(18)	0.821	0.179	1.1655 x10^{-4}
H(19)	0.852	0.148	1.5474 x10^{-4}
H(22)	0.889	0.111	-1.0688 x10^{-4}
H(23)	0.872	0.128	1.5323 x10^{-4}
H(24)	0.976	0.024	8.6745 x10^{-6}
H(25)	0.860	0.140	2.3856 x10^{-6}
H(26)	0.679	0.321	-1.3997 x10^{-4}
H(71A)	0.898	0.102	-6.0493 x10^{-5}
H(71B)	0.924	0.076	-1.3698 x10^{-5}
H(71C)	0.921	0.079	5.2644 x10^{-5}
H(72A)	0.949	0.051	4.2802 x10^{-5}
H(72B)	1.026	-0.026	-1.2603 x10^{-5}
H(72C)	0.930	0.070	-5.9085 x10^{-5}
H(73A)	0.983	0.017	9.9322 x10^{-6}
H(73B)	0.940	0.060	2.1117 x10^{-5}
H(73C)	0.851	0.149	-2.2433 x10^{-6}
H(74A)	0.842	0.158	-6.7710 x10^{-5}
H(74B)	0.808	0.192	3.7203 x10^{-4}
H(74C)	0.983	0.017	-1.1498 x10^{-4}
H(2A)	0.570	0.430	-8.2355 x10^{-5}
H(3A)	0.539	0.461	1.3115 x10^{-4}
H(5A)	0.695	0.305	-4.0549 x10^{-5}
H(6A)	0.541	0.459	1.9354 x10^{-4}

A.7.2 Stockholder charges calculated from the electron density distribution in each of the crystal structures discussed in Chapter 4 and 5.

T.A.7.10: Stockholder charges (/*e*) of atoms in **c.s.3**.

Atom	Multipole (*e*)	Net charge (*e*)
O(1)	8.233	-0.233
O(2)	8.034	-0.034
O(3)	8.035	-0.035
O(4)	7.957	0.043
O(5)	7.919	0.081
N(1)	6.881	0.119
N(2)	7.104	-0.104
N(3)	7.137	-0.137
N(4)	6.966	0.034
C(1)	6.124	-0.124
C(2)	6.067	-0.067
C(3)	6.087	-0.087
C(4)	6.018	-0.018
C(5)	6.065	-0.065
C(6)	6.036	-0.036
C(7)	5.942	0.058
C(8)	6.028	-0.028
C(9)	6.136	-0.136
C(10)	6.082	-0.082
C(11)	6.069	-0.069
C(12)	6.080	-0.080
C(13)	6.113	-0.113
H(2)	0.891	0.109
H(3)	0.956	0.044
H(5)	0.879	0.121
H(6)	0.845	0.155
H(9)	0.841	0.159
H(10)	0.912	0.088

H(12)	0.911	0.089
H(13)	0.901	0.099
H(2A)	0.748	0.252
H(3A)	0.762	0.238

T.A.7.11: Stockholder charges (/*e*) of atoms in **c.s.5**.

Atom	Multipole (*e*)	Net charge (*e*)
Cl(1)	17.347	-0.347
O(1)	8.156	-0.156
O(2)	8.129	-0.129
O(3)	8.152	-0.152
O(4)	8.160	-0.160
O(5)	8.116	-0.116
N(1)	6.803	0.197
N(2)	7.141	-0.141
N(3)	7.081	-0.081
N(4)	6.820	0.180
N(5)	6.926	0.074
C(1)	6.066	-0.066
C(2)	6.073	-0.073
C(3)	6.089	-0.089
C(4)	5.928	0.072
C(5)	6.048	-0.048
C(6)	5.980	0.020
C(7)	5.839	0.161
C(8)	5.931	0.069
C(9)	5.991	0.009
C(10)	5.970	0.030
C(11)	6.043	-0.043
C(12)	5.964	0.036
C(13)	6.059	-0.059
C(14)	6.150	-0.150
C(15)	6.096	-0.096
C(16)	6.093	-0.093

C(17)	6.143	-0.143
H(1)	0.958	0.042
H(2)	0.990	0.010
H(3)	0.899	0.101
H(5)	0.919	0.081
H(9)	0.930	0.070
H(10)	0.912	0.088
H(11)	0.972	0.028
H(13)	0.902	0.098
H(14A)	0.982	0.018
H(14B)	0.874	0.126
H(14C)	0.952	0.048
H(15A)	0.929	0.071
H(15B)	0.982	0.018
H(15C)	0.974	0.026
H(16A)	0.951	0.049
H(16B)	0.877	0.123
H(16C)	0.968	0.032
H(17A)	0.946	0.054
H(17B)	0.956	0.044
H(17C)	0.975	0.025
H(2A)	0.865	0.135
H(3A)	0.910	0.090

T.A.7.12: Stockholder charges (/*e*) of atoms in **c.s.6**.

Atom	Multipole (*e*)	Net charge (*e*)
Cl(1)	17.214	-0.214
O(1)	8.318	-0.318
O(2)	8.294	-0.294
O(3)	8.294	-0.294
O(4)	8.274	-0.274
O(5)	8.275	-0.275
N(1)	6.861	0.139
N(2)	7.137	-0.137

N(3)	7.135	-0.135
N(4)	6.895	0.105
N(5)	7.018	-0.018
C(1)	6.019	-0.019
C(2)	6.092	-0.092
C(3)	6.061	-0.061
C(4)	5.931	0.069
C(5)	5.995	0.005
C(6)	6.038	-0.038
C(7)	5.813	0.187
C(8)	5.948	0.052
C(9)	6.034	-0.034
C(10)	6.015	-0.015
C(11)	6.017	-0.017
C(12)	5.983	0.017
C(13)	6.032	-0.032
C(14)	6.050	-0.050
C(15)	6.074	-0.074
C(16)	6.091	-0.091
C(17)	6.049	-0.049
H(2)	0.915	0.085
H(3)	0.884	0.116
H(5)	0.871	0.129
H(6)	0.899	0.101
H(9)	0.831	0.169
H(10)	0.878	0.122
H(12)	0.897	0.103
H(13)	0.894	0.106
H(14A)	0.925	0.075
H(14B)	0.952	0.048
H(14C)	0.907	0.093
H(15A)	0.954	0.046
H(15B)	0.948	0.052
H(15C)	0.903	0.097
H(16A)	0.940	0.060

H(16B)	0.950	0.050
H(16C)	0.912	0.088
H(17A)	0.940	0.060
H(17B)	0.929	0.071
H(17C)	0.924	0.076
H(2A)	0.901	0.099
H(3A)	0.888	0.112

T.A.7.13: Stockholder charges (/*e*) of atoms in **c.s.9**.

Atom	Multipole (*e*)	Net charge (*e*)
O(1)	8.181	-0.181
O(2)	8.166	-0.166
O(3)	8.168	-0.168
O(4)	8.201	-0.201
O(5)	8.205	-0.205
O(6)	8.297	-0.297
O(7)	8.214	-0.214
N(1)	6.914	0.086
N(2)	7.088	-0.088
N(3)	7.066	-0.066
N(4)	6.865	0.135
N(5)	6.949	0.051
C(1)	6.047	-0.047
C(2)	6.138	-0.138
C(3)	6.128	-0.128
C(4)	5.951	0.049
C(5)	6.096	-0.096
C(6)	6.063	-0.063
C(7)	5.824	0.176
C(8)	5.908	0.092
C(9)	6.081	-0.081
C(10)	5.992	0.008
C(11)	5.981	0.019
C(12)	6.001	-0.001

C(13)	6.029	-0.029
C(14)	6.031	-0.031
C(15)	6.022	-0.022
C(16)	6.041	-0.041
C(17)	6.037	-0.037
C(18)	5.964	0.036
C(19)	6.089	-0.089
H(2)	0.934	0.066
H(3)	0.954	0.046
H(5)	0.922	0.078
H(6)	0.867	0.133
H(9)	0.930	0.070
H(10)	0.909	0.091
H(12)	0.920	0.080
H(13)	0.916	0.084
H(14A)	0.909	0.091
H(14B)	0.880	0.120
H(14C)	0.939	0.061
H(15A)	0.971	0.029
H(15B)	0.933	0.067
H(15C)	0.915	0.085
H(16A)	0.998	0.002
H(16B)	0.921	0.079
H(16C)	0.878	0.122
H(17A)	0.992	0.008
H(17B)	0.938	0.062
H(17C)	0.968	0.032
H(19A)	0.941	0.059
H(19B)	0.944	0.056
H(19C)	0.968	0.032
H(2A)	0.889	0.111
H(3A)	0.928	0.072

T.A.7.14: Stockholder charges (/*e*) of atoms in **c.s.10**.

Atom	Multipole (*e*)	Net charge (*e*)
O(1)	7.990	0.010
O(2)	8.069	-0.069
O(3)	8.092	-0.092
O(4)	8.039	-0.039
O(5)	8.032	-0.032
O(6)	8.056	-0.056
O(7)	8.033	-0.033
O(8)	8.061	-0.061
O(9)	8.060	-0.060
O(10)	8.301	-0.301
O(11)	8.168	-0.168
N(1)	6.841	0.159
N(2)	6.866	0.134
N(3)	6.974	0.026
N(4)	6.928	0.0722
N(5)	6.887	0.113
N(6)	6.808	0.192
N(7)	6.910	0.090
C(1)	6.164	-0.164
C(2)	6.050	-0.050
C(3)	6.080	-0.080
C(4)	5.934	0.066
C(5)	6.085	-0.085
C(6)	6.026	-0.026
C(7)	5.786	0.214
C(8)	5.914	0.086
C(9)	6.048	-0.048
C(10)	6.034	-0.034
C(11)	6.063	-0.063
C(12)	6.055	-0.055
C(13)	6.104	-0.104
C(14)	5.945	0.055
C(15)	5.875	0.125

C(16)	6.023	-0.023
C(17)	5.974	0.026
C(18)	6.080	-0.080
C(19)	6.319	-0.319
H(1)	0.989	0.011
H(3)	0.948	0.052
H(5)	0.960	0.040
H(9)	0.989	0.011
H(11)	0.999	0.001
H(13)	1.009	-0.009
H(14A)	0.997	0.003
H(14B)	0.978	0.022
H(14C)	0.989	0.011
H(15A)	1.041	-0.041
H(15B)	0.906	0.094
H(15C)	0.866	0.134
H(16A)	0.927	0.073
H(16B)	0.999	0.001
H(16C)	0.970	0.030
H(17A)	0.902	0.098
H(17B)	0.980	0.020
H(17C)	1.032	-0.032
H(19A)	0.948	0.052
H(19B)	1.068	-0.068
H(19C)	0.866	0.134
H(3A)	0.989	0.011
H(4A)	0.973	0.027

T.A.7.15: Stockholder charges (/*e*) of atoms in **c.s.11**.

Atom	Multipole (*e*)	Net charge (*e*)
F(1)	9.134	-0.134
O(1)	8.168	-0.168
O(2)	8.140	-0.140
O(3)	8.134	-0.134

O(4)	8.139	-0.139
O(5)	8.109	-0.109
N(1)	6.863	0.137
N(2)	7.016	-0.016
N(3)	7.052	-0.052
N(4)	6.896	0.104
N(5)	7.075	-0.075
C(1)	6.010	-0.010
C(2)	6.041	-0.041
C(3)	6.014	-0.014
C(4)	5.993	0.007
C(5)	6.093	-0.093
C(6)	6.045	-0.045
C(7)	5.870	0.130
C(8)	5.939	0.061
C(9)	6.074	-0.074
C(10)	5.985	0.015
C(11)	6.103	-0.103
C(12)	6.137	-0.137
C(13)	6.003	-0.003
C(14A)	6.082	-0.082
C(15A)	6.083	-0.083
C(14B)	6.085	-0.085
C(15B)	6.083	-0.083
H(2)	0.875	0.125
H(3)	0.899	0.101
H(5)	0.934	0.066
H(6)	0.962	0.038
H(9)	0.903	0.097
H(10)	0.889	0.111
H(12)	0.921	0.079
H(13)	0.909	0.091
H(14A)	0.968	0.032
H(14B)	0.974	0.026
H(14C)	0.965	0.035

H(15A)	0.967	0.033
H(15B)	0.969	0.031
H(15C)	0.967	0.033
H(14D)	0.966	0.034
H(14E)	0.968	0.032
H(14F)	0.991	0.009
H(15D)	0.966	0.034
H(15E)	0.967	0.033
H(15F)	0.967	0.033
H(2A)	0.921	0.079
H(3A)	0.931	0.069

T.A.7.16: Stockholder charges (/*e*) of atoms in **c.s.16**.

Atom	Multipole (*e*)	Net charge (*e*)
CL(1)	16.975	0.025
S(2)	16.126	-0.126
S(1)	15.056	0.944
O(5)	8.267	-0.267
O(6)	8.267	-0.267
O(7)	8.332	-0.332
O(8)	8.331	-0.331
O(1)	8.288	-0.288
O(2)	8.276	-0.276
O(3)	8.219	-0.219
O(4)	8.226	-0.226
N(9)	7.026	-0.026
N(5)	6.987	0.013
N(6)	7.226	-0.226
N(7)	7.272	-0.272
N(8)	6.949	0.051
N(1)	6.927	0.073
N(2)	7.239	-0.239
N(3)	7.152	-0.152
N(4)	7.023	-0.023

C(91)	5.936	0.064
C(92)	6.168	-0.168
C(93)	6.171	-0.171
C(94)	6.121	-0.121
C(95)	5.986	0.014
C(96)	6.213	-0.213
C(97)	6.181	-0.181
C(98)	6.067	-0.067
C(14)	6.058	-0.058
C(15)	5.929	0.071
C(16)	5.960	0.040
C(17)	5.995	0.005
C(18)	6.117	-0.117
C(19)	6.074	-0.074
C(20)	5.965	0.035
C(21)	5.928	0.072
C(22)	6.050	-0.050
C(23)	6.074	-0.074
C(24)	5.976	0.024
C(25)	6.102	-0.102
C(26)	5.958	0.042
C(1)	6.147	-0.147
C(2)	6.063	-0.063
C(3)	5.830	0.170
C(4)	5.840	0.160
C(5)	5.990	0.010
C(6)	6.142	-0.142
C(7)	5.856	0.144
C(8)	6.088	-0.088
C(9)	6.131	-0.131
C(10)	5.880	0.120
C(11)	6.021	-0.021
C(12)	6.041	-0.041
C(13)	6.070	-0.070
H(91A)	1.022	-0.022

H(91B)	0.966	0.034
H(92A)	0.959	0.041
H(92B)	0.940	0.060
H(92C)	1.050	-0.050
H(93A)	1.001	-0.000
H(93B)	0.925	0.075
H(94A)	0.849	0.151
H(94B)	0.980	0.020
H(94C)	0.969	0.031
H(95A)	0.896	0.104
H(95B)	0.871	0.129
H(96A)	0.996	0.004
H(96B)	0.989	0.011
H(96C)	1.018	-0.018
H(97A)	0.958	0.042
H(97B)	0.949	0.051
H(98A)	0.809	0.191
H(98B)	0.891	0.109
H(98C)	1.021	-0.021
H(15)	0.932	0.068
H(16)	0.920	0.080
H(18)	0.943	0.057
H(19)	0.995	0.005
H(22)	0.861	0.139
H(23)	0.822	0.178
H(25)	1.029	-0.029
H(26)	0.794	0.206
H(6A)	0.829	0.171
H(7A)	0.944	0.056
H(2)	0.852	0.148
H(3)	0.856	0.144
H(5)	0.759	0.241
H(6)	0.903	0.097
H(9)	0.982	0.018
H(10)	0.880	0.120

H(12)	0.832	0.168
H(13)	0.809	0.191
H(2A)	0.882	0.118
H(3A)	0.826	0.174

T.A.7.17: Stockholder charges (/*e*) of atoms in **c.s.17**.

Atom	Multipole (*e*)	Net charge (*e*)
CL(1)	17.325	-0.325
O(1)	8.107	-0.107
O(2)	8.032	-0.032
O(3)	8.035	-0.035
N(1)	6.819	0.181
N(2)	7.149	-0.149
N(3)	7.119	-0.119
N(5)	7.055	-0.055
C(1)	6.053	-0.053
C(2)	6.078	-0.078
C(3)	6.045	-0.045
C(4)	6.042	-0.042
C(5)	6.057	-0.057
C(6)	6.047	-0.047
C(7)	5.863	0.137
C(8)	6.033	-0.033
C(9)	6.045	-0.045
C(10)	5.998	0.002
C(11)	5.994	0.006
C(12)	5.996	0.004
C(13)	6.051	-0.051
C(51)	6.089	-0.089
C(52)	6.061	-0.061

C(53)	6.097	-0.097
C(54)	6.069	-0.069
C(55)	6.074	-0.074
C(56)	6.069	-0.069
C(57)	6.093	-0.093
C(58)	6.067	-0.067
H(2)	0.957	0.043
H(3)	0.922	0.078
H(5)	0.941	0.059
H(6)	0.926	0.074
H(9)	0.919	0.081
H(10)	0.907	0.093
H(11)	0.908	0.092
H(12)	0.907	0.093
H(13)	0.937	0.063
H(51A)	0.937	0.063
H(51B)	0.980	0.020
H(52A)	0.922	0.078
H(52B)	0.958	0.042
H(52C)	0.947	0.053
H(53A)	1.005	-0.005
H(53B)	0.979	0.021
H(54A)	0.948	0.052
H(54B)	0.948	0.052
H(54C)	0.946	0.054
H(55A)	0.944	0.056
H(55B)	0.976	0.024
H(56A)	0.946	0.054
H(56B)	0.948	0.052
H(56C)	0.947	0.053
H(57A)	0.978	0.022

H(57B)	0.980	0.020
H(58A)	0.946	0.054
H(58B)	0.948	0.052
H(58C)	0.944	0.056
H(2A)	0.874	0.126
H(3A)	0.845	0.155

T.A.7.18: Stockholder charges (/*e*) of atoms in **c.s.18**.

Atom	Multipole (*e*)	Net charge (*e*)
CL(1)	16.972	0.028
S(1)	16.025	-0.025
S(2)	15.558	0.442
O(1)	8.238	-0.238
O(2)	8.243	-0.243
O(3)	8.259	-0.259
O(4)	8.258	-0.258
N(1)	6.998	0.002
N(2)	7.218	-0.218
N(3)	7.247	-0.247
N(4)	6.860	0.140
N(5)	7.193	-0.193
N(6)	7.174	-0.174
N(7)	7.031	-0.031
C(1)	6.086	-0.086
C(2)	6.132	-0.132
C(3)	6.072	-0.072
C(4)	5.996	0.004
C(5)	6.000	0.000
C(6)	6.006	-0.006
C(7)	5.977	0.023

C(8)	6.028	-0.028
C(9)	6.123	-0.123
C(10)	6.078	-0.078
C(11)	6.029	-0.029
C(12)	6.039	-0.039
C(13)	6.070	-0.070
C(14)	6.010	-0.010
C(15)	5.980	0.020
C(16)	6.048	-0.048
C(17)	5.987	0.013
C(18)	6.082	-0.082
C(19)	6.062	-0.062
C(20)	5.867	0.133
C(21)	6.037	-0.037
C(22)	6.129	-0.129
C(23)	6.106	-0.106
C(24)	6.088	-0.088
C(25)	6.081	-0.081
C(26)	6.082	-0.082
C(71)	6.099	-0.099
C(72)	6.096	-0.096
C(73)	6.061	-0.061
C(74)	6.023	-0.023
H(2)	0.929	0.071
H(3)	0.896	0.104
H(5)	0.911	0.089
H(6)	0.834	0.166
H(9)	0.886	0.114
H(10)	0.892	0.108
H(11)	0.979	0.021
H(12)	0.921	0.079

H(13)	0.929	0.071
H(15)	0.855	0.145
H(16)	0.849	0.151
H(18)	0.906	0.094
H(19)	0.920	0.080
H(22)	0.957	0.043
H(23)	0.919	0.081
H(24)	0.986	0.014
H(25)	0.895	0.105
H(26)	0.824	0.176
H(71A)	0.933	0.067
H(71B)	0.967	0.033
H(71C)	0.931	0.069
H(72A)	0.942	0.058
H(72B)	0.980	0.020
H(72C)	1.034	-0.034
H(73A)	0.926	0.074
H(73B)	0.964	0.036
H(73C)	0.920	0.080
H(74A)	0.880	0.120
H(74B)	0.997	0.003
H(74C)	0.913	0.087
H(2A)	0.891	0.109
H(3A)	0.873	0.127
H(5A)	0.937	0.063
H(6A)	0.877	0.123

A.8 Copyright permissions

A.8.1 Copyright permission for re-use of published articles associated with this thesis:

- Kirby, I. L; Pitak, M. B; Wenzel, M; Wilson, C; Sparkes, H. A; Coles, S. J; Gale, P. A., *CrystEngComm*, 2013, **15**, 9003 - 9010
- Kirby, I. L; Brightwell, M; Pitak, M. B; Wilson, C; Coles, S. J; Gale, P. A., *Phys. Chem. Chem. Phys.*, 2014, **16**, 10943 - 10958

Thursday, September 04, 2014 12:50 PM

Dear Isabelle

The Royal Society of Chemistry (RSC) hereby grants permission for the use of your paper(s) specified below in the printed and microfilm version of your thesis. You may also make available the PDF version of your paper(s) that the RSC sent to the corresponding author(s) of your paper(s) upon publication of the paper(s) in the following ways: in your thesis via any website that your university may have for the deposition of theses, via your university's Intranet or via your own personal website. We are however unable to grant you permission to include the PDF version of the paper(s) on its own in your institutional repository. The Royal Society of Chemistry is a signatory to the STM Guidelines on Permissions (available on request).

Please note that if the material specified below or any part of it appears with credit or acknowledgement to a third party then you must also secure permission from that third party before reproducing that material.

Please ensure that the thesis states the following:
Reproduced by permission of The Royal Society of Chemistry
and include a link to the paper on the Royal Society of Chemistry's website.

Please ensure that your co-authors are aware that you are including the paper in your thesis.

Regards
Gill Cockhead
Publishing Contracts & Copyright Executive

Gill Cockhead
Publishing Contracts & Copyright Executive
Royal Society of Chemistry,
Thomas Graham House,
Science Park, Milton Road,
Cambridge, CB4 0WF, UK
Tel +44 (0) 1223 432134

A.8.2 Copyright permission for reproduction of Figure 2.7

Copyright permission for reproduction of Figure 2.7 in *Acta Crystallogr.Sect. B.*, 1999, **55**, 563-572 from the IUCr.

Reply Reply All Forward

Re: Copyright permission

Jill Bradshaw [jb@iucr.org]

To: Kirby I.L.

30 September 2014 14:21

Dear Isabelle

Thank you for your email.

Permission is hereby granted, on behalf of the IUCr, for you to reproduce the material specified below, subject to the following conditions:

1. Reproduction is intended in a primary journal, secondary journal, CD-ROM, book or thesis.

2. The original article in which the material appeared is cited.

3. IUCr's copyright permission is indicated next to the Figure/Table in print. In electronic form, this acknowledgement must be visible at the same time as the Figure, and must be hyperlinked to the article (http://dx.doi.org/10.1107/S0108768199002128).

Material specified:

Figures 3(c) and 4(c) of Espinosa, Souhassou, Lachekar & Lecomte (1999). Acta Cryst. B55, pp. 563-572.

Best wishes

Jill Bradshaw

A.8.3 Copyright permission for reproduction of Figure 2.9

Copyright permission for reproduction of Figure 2.9 in *CrystEngComm*, 2005, **7**, 608–611 from The Royal Society of Chemistry (RSC).

A.8.4 Copyright permission for reproduction of Figure 2.10

Copyright permission for reproduction of Figure 2.10 in *Cryst. Growth Des.*, 2011, **11**, 1855–1862 from the American Chemical Society (ACS).

List of References

1. J.-M. Lehn, *Science*, 1993, **260**, 1762–1763.

2. D. J. Cram, *Angew. Chemie Int. Ed.*, 1986, **25**, 1039–1057.

3. J. L. Sessler, P. A. Gale, and W.-S. Cho, *Anion Receptor Chemistry*, 2006, RSC, Cambridge, UK.

4. A. Bianchi, K. Bowman-James, and E. Garcia-Espana, *Supramolecular Chemistry of Anions*, 1997, John Wiley & Sons, Inc., New York, USA.

5. M. P. Anderson, D. P. Rich, R. J. Gregory, A. E. Smith, and M. J. Welsh, *Science*, 1991, **251**, 679–682.

6. P. A. Gale, *Acc. Chem. Res.*, 2006, **39**, 465–475.

7. R. D. Shannon and C. T. Prewitt, *Acta Crystallogr. Sect. B*, 1969, **25**, 925–946.

8. R. D. Shannon, *Acta Crystallogr. Sect. A*, 1976, **32**, 751–767.

9. F. Hofmeister, *Arch. Exp. Pathol. Pharmacol.*, 1888, **24**, 247–260.

10. P. Metrangolo, T. Pilati, and G. Resnati, *CrystEngComm*, 2006, **8**, 946–947.

11. G. R. Desiraju, P. S. Ho, L. Kloo, A. C. Legon, R. Marquardt, P. Metrangolo, P. Politzer, G. Resnati, and K. Rissanen, *Pure Appl. Chem.*, 2013, **85**, 1711–1713.

12. G. R. Desiraju, *Angew. Chemie Int. Ed.*, 1995, **34**, 2311–2327.

13. F. Allen, *Acta Crystallogr. Sect. B*, 2002, **58**, 380–388.

14. P. A. Wood, F. H. Allen, and E. Pidcock, *CrystEngComm*, 2009, **11**, 1563–1571.

15. G. R. Desiraju, *Chem. Commun.*, 2005, 2995–3001.

16. T. Steiner, *Angew. Chemie Int. Ed.*, 2002, **41**, 48–76.

17. G. Gilli and P. Gilli, *J. Mol. Struct.*, 2000, **552**, 1–15.

18. N. Busschaert, S. J. Bradberry, M. Wenzel, C. J. E. Haynes, J. R. Hiscock, I. L. Kirby, L. E. Karagiannidis, S. J. Moore, N. J. Wells, J. Herniman, G. J. Langley, P. N. Horton, M. E. Light, I. Marques, P. J. Costa, V. Felix, J. G. Frey, and P. A. Gale, *Chem. Sci.*, 2013, **4**, 3036–3045.

19. K. A. Connors, *Binding Constants*, 1987, John Wiley & Sons, Inc., New York, USA.

20. D. Braga, *Chem. Commun.*, 2003, 2751–2754.

21. A. Bondi, *J. Phys. Chem.*, 1964, **68**, 441–451.

22. R. S. Rowland and R. Taylor, *J. Phys. Chem.*, 1996, **100**, 7384–7391.

23. M. Schmidtmann, P. Coster, P. Henry, V. P. Ting, M. T. Weller, and C. C. Wilson, *CrystEngComm*, 2014, **16**, 1232–1236.

24. P. A. Gale, N. Busschaert, C. J. E. Haynes, L. E. Karagiannidis, and I. L. Kirby, *Chem. Soc. Rev.*, 2014, **43**, 205–241.

25. W. Koch and M. C. Holthausen, *A Chemist's Guide to Density Functional Theory*, 2000, WILEY-VCH Verlag GmbH, Weinheim, Germany.

26. S. Fux and M. Reiher, in *Electron Density and Chemical Bonding II*, ed. D. Stalke, *Struct. Bond.*, 2012, Springer-Verlag, Berlin Heidelberg, Germany, **147**, pp. 99–142.

27. P. Hohenberg and W. Kohn, *Phys. Rev. B*, 1964, **136**, 864–B871.

28. W. Kohn and L. J. Sham, *Phys. Rev. A*, 1965, **140**, 1133–A1138.

29. A. D. Becke, *J. Chem. Phys.*, 1993, **98**, 5648–5652.

30. P. C. Hariharan and J. A. Pople, *Theor. Chem. Acc.*, 1973, **28**, 213–222.

31. R. Dovesi, R. Orlando, A. Erba, C. M. Zicovich-Wilson, B. Civalleri, S. Casassa, L. Maschio, M. Ferrabone, M. De La Pierre, P. D'Arco, Y. Noël, M. Causà, M. Rérat, and B. Kirtman, *Int. J. Quantum Chem.*, 2014, **114**, 1287–1317.

32. W. Friedrich, P. Knipping, and M. Laue, *Sitzungsber. Math. Phys. Kl. K. Bayer. Akad. Wiss. München*, 1912, pp. 303–322.

33. W. H. Bragg and W. L. Bragg, *Proc. R. Soc. London A: Math. Phys. Eng. Sci.*, 1913, **88**, 428–438.

34. J. D. Watson and F. H. C. Crick, *Nature*, 1953, **171**, 737–738.

35. R. E. Franklin and R. G. Gosling, *Nature*, 1953, **171**, 740–741.

36. C. Brink, D. C. Hodgkin, J. Lindsey, J. Pickworth, J. H. Robertson, and J. G. White, *Nature*, 1954, **174**, 1169–1171.

37. K. Lonsdale, *Proc. R. Soc. London. Ser. A*, 1929, **123** , 494–515.

38. W. L. Bragg, *Proc. Camb. Philol. Soc.*, 1913, **17**, 43–57.

39. A. J. Blake, W. Clegg, J. M. Cole, J. S. O. Evans, P. Main, S. Parsons, and D. J. Watkin, *Crystal Structure Analysis, Principles and Practice 2nd Edition*, 2001, Oxford University Press, Oxford, UK.

40. W. Clegg, *Crystal Structure Determination*, 1998, Oxford University Press, Oxford, UK.

41. T. S. Koritsanszky and P. Coppens, *Chem. Rev.*, 2001, **101**, 1583–1628.

42. D. Stalke, *Electron Density and Chemical Bonding I: Experimental Charge Density Studies*, 2012, *Struct. Bond.*, **vol. 146**, Springer-Verlag, Berlin Heidelberg, Germany.

43. P. Coppens, *X-ray Charge Density and Chemical Bonding*, 1997, Oxford University Press, New York, USA.

44. L. Pauling, *J. Am. Chem. Soc.*, 1932, **54**, 988–1003.

45. M. Kaupp, B. Metz, and H. Stoll, *Angew. Chem.*, 2000, **112**, 4780–4782.

46. P. Macchi, *Crystallogr. Rev.*, 2013, **19**, 58–101.

47. B. Dawson, *Acta Crystallogr.*, 1961, **14**, 1271–1274.

48. R. F. Stewart, *Acta Crystallogr. Sect. A*, 1976, **32**, 565–574.

49. F. L. Hirshfeld, *Isr. J. Chem.*, 1977, **16**, 198–201.

50. N. K. Hansen and P. Coppens, *Acta Crystallogr. Sect. A*, 1978, **34**, 909–921.

51. S. C. Capelli, H.-B. Bürgi, B. Dittrich, S. Grabowsky, and D. Jayatilaka, *IUCrJ*, 2014, **1**, 361–379.

52. M. Woińska, D. Jayatilaka, M. A. Spackman, A. J. Edwards, P. M. Dominiak, K. Woźniak, E. Nishibori, K. Sugimoto, and S. Grabowsky, *Acta Crystallogr. Sect. A*, 2014, **70**, 483–498.

53. D. Jayatilaka and B. Dittrich, *Acta Crystallogr. Sect. A*, 2008, **64**, 383–393.

54. L. Checinska, W. Morgenroth, C. Paulmann, D. Jayatilaka, and B. Dittrich, *CrystEngComm*, 2013, **15**, 2084–2090.

55. E. Clementi and C. Roetti, *At. Data Nucl. Data Tables*, 1974, **14**, 177–478.

56. Z. Su and P. Coppens, *Acta Crystallogr. Sect. A*, 1998, **54**, 646–652.

57. E. Clementi and D. L. Raimondi, *J. Chem. Phys.*, 1963, **38**, 2686–2689.

58. M. R. V Jørgensen, V. R. Hathwar, N. Bindzus, N. Wahlberg, Y.-S. Chen, J. Overgaard, and B. B. Iversen, *IUCrJ*, 2014, **1**, 267–280.

59. F. Hirshfeld, *Acta Crystallogr. Sect. A*, 1976, **32**, 239–244.

60. L. J. Farrugia, *IUCrJ*, 2014, **1**, 265–266.

61. E. D. Stevens and P. Coppens, *Acta Crystallogr. Sect. A*, 1976, **32**, 915–917.

62. K. Meindl and J. Henn, *Acta Crystallogr. Sect. A*, 2008, **64**, 404–418.

63. U. Flierler and D. Stalke, in *Electron density and chemical bonding I: Experimental Charge Density Studies*, ed. D. Stalke, *Struct. Bond.*, 2012, Springer-Verlag, Berlin Heidelberg, Germany, **146**, pp. 1–20.

64. R. Kamiński, S. Domagała, K. N. Jarzembska, A. A. Hoser, W. F. Sanjuan-Szklarz, M. J. Gutmann, A. Makal, M. Malińska, J. M. Bak, and K. Woźniak, *Acta Crystallogr. Sect. A*, 2014, **70**, 72–91.

65. R. F. W. Bader, T. T. Nguyen-Dang and Y. Tal, *Reports Prog. Phys.*, 1981, **44**, 893.

66. R. F. W. Bader, *Atoms-in-Molecules: A Quantum Theory*, 1990, Oxford University Press, Oxford, UK.

67. R. J. Gillespie and P. L. A. Popelier, *Chemical bonding and Molecular Geometry from Lewis to Electron Densities*, 2001, Oxford University Press, Inc., New York, USA.

68. R. F. W. Bader, *J. Phys. Chem. A*, 2009, **113**, 10391-10396.

69. K. Collard and G. G. Hall, *Int. J. Quantum Chem.*, 1977, **12**, 623-637.

70. R. F. W. Bader, T. S. Slee, D. Cremer, and E. Kraka, *J. Am. Chem. Soc.*, 1983, **105**, 5061-5068.

71. R. F. W. Bader and C. Gatti, *Chem. Phys. Lett.*, 1998, **287**, 233-238.

72. C. Gatti, F. Cargnoni, and L. Bertini, *J. Comput. Chem.*, 2003, **24**, 422-436.

73. Y. Abramov, *Acta Crystallogr. Sect. A*, 1997, **53**, 264-272.

74. E. Espinosa, E. Molins, and C. Lecomte, *Chem. Phys. Lett.*, 1998, **285**, 170-173.

75. E. Espinosa, M. Souhassou, H. Lachekar, and C. Lecomte, *Acta Crystallogr. Sect. B*, 1999, **55**, 563-572.

76. E. Espinosa, C. Lecomte, and E. Molins, *Chem. Phys. Lett.*, 1999, **300**, 745-748.

77. E. Espinosa and E. Molins, *J. Chem. Phys.*, 2000, **113**, 5686-5694.

78. E. Espinosa, I. Alkorta, J. Elguero, and E. Molins, *J. Chem. Phys.*, 2002, **117**, 5529-5542.

79. I. Mata, I. Alkorta, E. Molins, and E. Espinosa, *Chem. Eur. J.*, 2010, **16**, 2442-2452.

80. I. Rozas, I. Alkorta, and J. Elguero, *J. Am. Chem. Soc.*, 2000, **122**, 11154-11161.

81. P. M. Dominiak, E. Grech, G. Barr, S. Teat, P. Mallinson, and K. Woźniak, *Chem. Eur. J.*, 2003, **9**, 963-970.

82. P. M. Dominiak, A. Makal, P. R. Mallinson, K. Trzcinska, J. Eilmes, E. Grech, M. Chruszcz, W. Minor, K. Woźniak, *Chem. Eur. J.*, 2006, **12**, 1941–1949.

83. A. Ranganathan, G. U. Kulkarni, and C. N. R. Rao, *J. Mol. Struct.*, 2003, **656**, 249–263.

84. P. Munshi and T. N. Guru Row, *CrystEngComm*, 2005, **7**, 608–611.

85. P. Munshi and T. N. Guru Row, *Crystallogr. Rev.*, 2005, **11**, 199–241.

86. P. Munshi and T. N. Guru Row, *J. Phys. Chem. A*, 2005, **109**, 659–672.

87. M.-D. Serb, R. Wang, M. Meven, and U. Englert, *Acta Crystallogr. Sect. B*, 2011, **67**, 552–559.

88. D. Chopra, T. S. Cameron, J. D. Ferrara, and T. N. Guru Row, *J. Phys. Chem. A*, 2006, **110**, 10465–10477.

89. A. Forni, *J. Phys. Chem. A*, 2009, **113**, 3403–3412.

90. T. T. T. Bui, S. Dahaoui, C. Lecomte, G. R. Desiraju, and E. Espinosa, *Angew. Chem.*, 2009, **121**, 3896–3899.

91. V. R. Hathwar, R. G. Gonnade, P. Munshi, M. M. Bhadbhade, and T. N. Guru Row, *Cryst. Growth Des.*, 2011, **11**, 1855–1862.

92. V. R. Hathwar and T. N. Guru Row, *Cryst. Growth Des.*, 2011, **11**, 1338–1346.

93. A. G. Dikundwar and T. N. Guru Row, *Cryst. Growth Des.*, 2012, **12**, 1713–1716.

94. M. E. Brezgunova, J. Lieffrig, E. Aubert, S. Dahaoui, P. Fertey, S. Lebègue, J. G. Ángyán, M. Fourmigué, and E. Espinosa, *Cryst. Growth Des.*, 2013, **13**, 3283–3289.

95. K. Kirschbaum, K. Poomani, D. A. Parrish, A. A. Pinkerton, and E. Zhurova, *J. Appl. Crystallogr.*, 2003, **36**, 1464–1466.

96. E. A. Zhurova, V. V Zhurov, D. Chopra, A. I. Stash, and A. A. Pinkerton, *J. Am. Chem. Soc.*, 2009, **131**, 17260–17269.

97. E. J. Yearley, E. A. Zhurova, V. V Zhurov, and A. A. Pinkerton, *J. Mol. Struct.*, 2008, **890**, 240–248.

98. E. J. Yearley, E. A. Zhurova, V. V Zhurov, and A. A. Pinkerton, *J. Am. Chem. Soc.*, 2007, **129**, 15013–15021.

99. D. Parrish, E. A. Zhurova, K. Kirschbaum, and A. A. Pinkerton, *J. Phys. Chem. B*, 2006, **110**, 26442–26447.

100. E. A. Zhurova, C. F. Matta, N. Wu, V. V Zhurov, and A. A. Pinkerton, *J. Am. Chem. Soc.*, 2006, **128**, 8849–8861.

101. P. R. Mallinson, K. Woźniak, G. T. Smith, and K. L. McCormack, *J. Am. Chem. Soc.*, 1997, **119**, 11502–11509.

102. P. R. Mallinson, G. T. Smith, C. C. Wilson, E. Grech, and K. Woźniak, *J. Am. Chem. Soc.*, 2003, **125**, 4259–4270.

103. K. Wozniak, P. R. Mallinson, G. T. Smith, C. C. Wilson, E. Grech, *J. Phys. Org. Chem.*, 2003, **16**, 764–771.

104. P. R. Mallinson, K. Woźniak, C. C. Wilson, K. L. McCormack, and D. S. Yufit, *J. Am. Chem. Soc.*, 1999, **121**, 4640–4646.

105. A. A. Hoser, Ł. Dobrzycki, M. J. Gutmann, and K. Woźniak, *Cryst. Growth Des.*, 2010, **10**, 5092–5104.

106. A. A. Hoser, K. N. Jarzembska, Ł. Dobrzycki, M. J. Gutmann and K. Woźniak, *Cryst. Growth Des.*, 2012, **12**, 3526–3539.

107. P. Munshi and T. N. Guru Row, *Cryst. Growth Des.*, 2006, **6**, 708–718.

108. P. Munshi, C. Jelsch, V. R. Hathwar, and T. N. Guru Row, *Cryst. Growth Des.*, 2010, **10**, 4670.

109. J. J. McKinnon, A. S. Mitchell, and M. A. Spackman, *Chem. Eur. J.*, 1998, **4**, 2136–2141.

110. J. J. McKinnon, M. A. Spackman, and A. S. Mitchell, *Acta Crystallogr. Sect. B*, 2004, **60**, 627–668.

111. M. A. Spackman and D. Jayatilaka, *CrystEngComm*, 2009, **11**, 19–32.

112. M. A. Spackman and J. J. McKinnon, *CrystEngComm*, 2002, **4**, 378–392.

113. J. J. McKinnon, D. Jayatilaka, and M. A. Spackman, *Chem. Commun.*, 2007, 3814–3816.

114. S. K. Wolff, D. J. Grimwood, J. J. McKinnon, M. J. Turner, D. Jayatilaka, and M. A. Spackman, University of Western Australia, 2012.

115. B. Dittrich, T. Koritsánszky, and P. Luger, *Angew. Chemie Int. Ed.*, 2004, **43**, 2718–2721.

116. B. Dittrich, C. B. Hubschle, K. Pröpper, F. Dietrich, T. Stolper, and J. J. Holstein, *Acta Crystallogr. Sect. B*, 2013, **69**, 91–104.

117. C. B. Hubschle, P. Luger, and B. Dittrich, *J. Appl. Crystallogr.*, 2007, **40**, 623–627.

118. K. Pröpper, J. J. Holstein, C. B. Hubschle, C. S. Bond, and B. Dittrich, *Acta Crystallogr. Sect. D*, 2013, **69**, 1530–1539.

119. B. Dittrich, C. B. Hubschle, P. Luger, and M. A. Spackman, *Acta Crystallogr. Sect. D*, 2006, **62**, 1325–1335.

120. B. Dittrich, C. B. Hubschle, J. J. Holstein, and F. P. A. Fabbiani, *J. Appl. Crystallogr.*, 2009, **42**, 1110–1121.

121. J. J. Holstein, C. B. Hubschle, and B. Dittrich, *CrystEngComm*, 2012, **14**, 2520–2531.

122. D. Kratzert, D. Leusser, J. J. Holstein, B. Dittrich, K. Abersfelder, D. Scheschkewitz, and D. Stalke, *Angew. Chemie Int. Ed.*, 2013, **52**, 4478–4482.

123. J. M. Bak, P. M. Dominiak, C. C. Wilson, and K. Wozniak, *Acta Crystallogr. Sect. A*, 2009, **65**, 490–500.

124. I. L. Kirby, M. B. Pitak, M. Wenzel, C. Wilson, H. A. Sparkes, S. J. Coles, and P. A. Gale, *CrystEngComm*, 2013, **15**, 9003–9010.

125. F. Wöhler, *Ann. Phys.*, 1828, **88**, 253–256.

126. J. W. Steed, *Chem. Soc. Rev.*, 2010, **39**, 3686–3699.

127. Z. Zhang and P. R. Schreiner, *Chem. Soc. Rev.*, 2009, **38**, 1187–1198.

128. A.-F. Li, J.-H. Wang, F. Wang, and Y.-B. Jiang, *Chem. Soc. Rev.*, 2010, **39**, 3729–3745.

129. S. J. Moore, C. J. E. Haynes, J. Gonzalez, J. L. Sutton, S. J. Brooks, M. E. Light, J. Herniman, G. J. Langley, V. Soto-Cerrato, R. Perez-Tomas, I. Marques, P. J. Costa, V. Felix, and P. A. Gale, *Chem. Sci.*, 2013, **4**, 103–117.

130. L. S. Reddy, S. K. Chandran, S. George, N. J. Babu, and A. Nangia, *Cryst. Growth Des.*, 2007, **7**, 2675–2690.

131. M. C. Etter, Z. Urbanczyk-Lipkowska, M. Zia-Ebrahimi, and T. W. Panunto, *J. Am. Chem. Soc.*, 1990, **112**, 8415–8426.

132. P. J. Smith, M. V Reddington, and C. S. Wilcox, *Tetrahedron Lett.*, 1992, **33**, 6085–6088.

133. E. Fan, S. A. Van Arman, S. Kincaid, and A. D. Hamilton, *J. Am. Chem. Soc.*, 1993, **115**, 369–370.

134. B. C. Hamann, N. R. Branda, and J. Rebek Jr., *Tetrahedron Lett.*, 1993, **34**, 6837–6840.

135. S. J. Brooks, P. R. Edwards, P. A. Gale, and M. E. Light, *New J. Chem.*, 2006, **30**, 65–70.

136. F. Werner and H.-J. Schneider, *Helv. Chim. Acta*, 2000, **83**, 465–478.

137. P. S. Lakshminarayanan, I. Ravikumar, E. Suresh, and P. Ghosh, *Chem. Commun.*, 2007, 5214–5216.

138. S. J. Brooks, P. A. Gale, and M. E. Light, *Chem. Commun.*, 2006, 4344–4346.

139. S. J. Brooks, S. E. García-Garrido, M. E. Light, P. A. Cole, and P. A. Gale, *Chem. Eur. J.*, 2007, **13**, 3320–3329.

140. M. G. Chudzinski, C. A. McClary, and M. S. Taylor, *J. Am. Chem. Soc.*, 2011, **133**, 10559–10567.

141. M. Chas and P. Ballester, *Chem. Sci.*, 2012, **3**, 186–191.

142. R. Custelcean, P. V. Bonnesen, N. C. Duncan, X. Zhang, L. A. Watson, G. Van Berkel, W. B. Parson, and B. P. Hay, *J. Am. Chem. Soc.*, 2012, **134**, 8525–8534.

143. M. J. Kim, H.-W. Lee, D. Moon, and K.-S. Jeong, *Org. Lett.*, 2012, **14**, 5042–5045.

144. J. M. Engle, C. N. Carroll, D. W. Johnson, and M. M. Haley, *Chem. Sci.*, 2012, **3**, 1105–1110.

145. Y.-P. Zhou, M. Zhang, Y.-H. Li, Q.-R. Guan, F. Wang, Z.-J. Lin, C.-K. Lam, X.-L. Feng, and H.-Y. Chao, *Inorg. Chem.*, 2012, **51**, 5099–5109.

146. C. Jia, B. Wu, S. Li, X. Huang, Q. Zhao, Q.-S. Li, and X.-J. Yang, *Angew. Chemie Int. Ed.*, 2011, **50**, 486–490.

147. S. Hussain, P. R. Brotherhood, L. W. Judd, and A. P. Davis, *J. Am. Chem. Soc.*, 2011, **133**, 1614–1617.

148. C. J. E. Haynes, S. J. Moore, J. R. Hiscock, I. Marques, P. J. Costa, V. Felix, and P. A. Gale, *Chem. Sci.*, 2012, **3**, 1436–1444.

149. C. Caltagirone, P. A. Gale, J. R. Hiscock, S. J. Brooks, M. B. Hursthouse, and M. E. Light, *Chem. Commun.*, 2008, 3007–3009.

150. M. Boiocchi, L. Del Boca, D. E. Gomez, L. Fabbrizzi, M. Licchelli, and E. Monzani, *J. Am. Chem. Soc.*, 2004, **126**, 16507–16514.

151. M. J. Hynes, *J. Chem. Soc. Dalt. Trans.*, 1993, 311–312.

152. A. O. F. Jones, M.-H. Lemee-Cailleau, D. M. S. Martins, G. J. McIntyre, I. D. H. Oswald, C. R. Pulham, C. K. Spanswick, L. H. Thomas, and C. C. Wilson, *Phys. Chem. Chem. Phys.*, 2012, **14**, 13273–13283.

153. D. A. Keen, M. J. Gutmann, and C. C. Wilson, *J. Appl. Crystallogr.*, 2006, **39**, 714–722.

154. F. H. Allen, O. Keenard, D. G. Watson, L. Brammer, A. G. Orpen, and R. Taylor, *International Tables for X-ray Crystallography*, 2006, vol. C.

155. F. H. Allen, O. Kennard, D. G. Watson, L. Brammer, A. G. Orpen, and R. Taylor, *J. Chem. Soc. Perkin Trans. 2*, 1987, S1–S19.

156. C. Janiak, *J. Chem. Soc. Dalt. Trans.*, 2000, 3885–3896.

157. C. A. Hunter and J. K. M. Sanders, *J. Am. Chem. Soc.*, 1990, **112**, 5525–5534.

158. I. L. Kirby, M. Brightwell, M. B. Pitak, C. Wilson, S. J. Coles, and P. A. Gale, *Phys. Chem. Chem. Phys.*, 2014, **16**, 10943–10958.

159. S. Grabowsky, T. Schirmeister, C. Paulmann, T. Pfeuffer, and P. Luger, *J. Org. Chem.*, 2011, **76**, 1305–1318.

160. F. Pan, R. Wang, and U. Englert, *CrystEngComm*, 2013, **15**, 1164–1172.

161. V. R. Hathwar, R. Pal, and T. N. Guru Row, *Cryst. Growth Des.*, 2010, **10**, 3306–3310.

162. R. Y. de Vries, D. Feil, and V. G. Tsirelson, *Acta Crystallogr. Sect. B*, 2000, **56**, 118–123.

163. H. Birkedal, D. Madsen, R. H. Mathiesen, K. Knudsen, H.-P. Weber, P. Pattison, and D. Schwarzenbach, *Acta Crystallogr. Sect. A*, 2004, **60**, 371–381.

164. K. Y. Suponitsky, V. G. Tsirelson, and D. Feil, *Acta Crystallogr. Sect. A*, 1999, **55**, 821–827.

165. V. Zavodnik, A. Stash, V. Tsirelson, R. de Vries, and D. Feil, *Acta Crystallogr. Sect. B*, 1999, **55**, 45–54.

166. M. Gryl, A. Krawczuk-Pantula, and K. Stadnicka, *Acta Crystallogr. Sect. B*, 2011, **67**, 144–154.

167. T. H. Nguyen, P. W. Groundwater, J. A. Platts, and D. E. Hibbs, *J. Phys. Chem. A*, 2012, **116**, 3420–3427.

168. K. Wozniak, H. He, J. Klinowski, W. Jones, and E. Grech, *J. Phys. Chem.*, 1994, **98**, 13755–13765.

169. K. Woźniak, P. R. Mallinson, C. C. Wilson, E. Hovestreydt, and E. Grech, *J. Phys. Chem. A*, 2002, **106**, 6897–6903.

170. I. V Fedyanin and K. A. Lyssenko, *CrystEngComm*, 2013, **15**, 10086–10093.

171. H. Nowell, S. A. Barnett, K. E. Christensen, S. J. Teat, and D. R. Allan, *J. Synchrotron Radiat.*, 2012, **19**, 435–441.

172. A. A. Hoser, P. M. Dominiak, and K. Wozniak, *Acta Crystallogr. Sect. A*, 2009, **65**, 300–311.

173. D. Stalke, *Electron Density and Chemical Bonding II: Theoretical Charge Density Studies*, 2012, *Struct. Bond.*, **vol. 147**, Springer-Verlag, Berlin Heidelberg, Germany.

174. A. Madsen, *J. Appl. Crystallogr.*, 2006, **39**, 757–758.

175. P. Munshi, C. Jelsch, V. R. Hathwar, and T. N. Guru Row, *Cryst. Growth Des.*, 2010, **10**, 1516–1526.

176. P. Munshi, E. Cameron, T. N. G. Row, J. D. Ferrara, and T. S. Cameron, *J. Phys. Chem. A*, 2007, **111**, 7888–7897.

177. U. Koch and P. L. A. Popelier, *J. Phys. Chem.*, 1995, **99**, 9747–9754.

178. F. G. Bordwell, *Acc. Chem. Res.*, 1988, **21**, 456–463.

179. F. G. Bordwell and D. Algrim, *J. Org. Chem.*, 1976, **41**, 2507–2508.

180. C. B. Hubschle and P. Luger, *J. Appl. Crystallogr.*, 2006, **39**, 901–904.

181. C. Gatti and L. Bertini, *Acta Crystallogr. Sect. A*, 2004, **60**, 438–449.

182. D. Mani and E. Arunan, *Phys. Chem. Chem. Phys.*, 2013, **15**, 14377–14383.

183. S. P. Thomas, M. S. Pavan, and T. N. Guru Row, *Chem. Commun.*, 2014, **50**, 49–51.

184. Gaussian 98. M. J. Frisch, G. W. Trucks, H. B. Schlegel, G. E. Scuseria, M. A. Robb, J. R. Cheeseman, V. G. Zakrzewski, J. A. Montgomery, R. E. Stratmann, J. C. Burant, S. Dapprich, J. M. Millam, A. D. Daniels, K. N. Kudin, M. C. Strain, O. Farkas, J. Tomasi, V. Barone, M. Cossi, R. Cammi, B. Mennucci, C. Pomelli, C. Adamo, S. Clifford, J. Ochterski, G. A. Petersson, P. Y. Ayala, Q. Cui, K. Morokuma, D. K. Malick, R. A. D, K. Raghavachari, J. B. Foresman, J. Cioslowski, J. V Ortiz, B. B. Stefanov, G. Liu, A. Liashenko, P. Piskorz, I. Komaromi, R. Gomperts, L. Martin, D. J. Fox, T. Keith, M. A. Al-Laham, C. Y. Peng, A. Nanayakkara, C. Gonzalez,

M. Challacombe, P. M. W. Gill, B. G. Johnson, W. Chen, M. W. Wong, J. L. Andres, M. Head-Gordon, E. S. Replogle, and J. A. Pople, 1998.

185. C. Lee, W. Yang, and R. G. Parr, *Phys. Rev. B*, 1988, **37**, 785-789.

186. *J. Comput. Chem.*, 2001, **22**, 545-559.

187. N. Busschaert, M. Wenzel, M. E. Light, P. Iglesias-Hernández, R. Pérez-Tomás, and P. A. Gale, *J. Am. Chem. Soc.*, 2011, **133**, 14136-14148.

188. N. J. Andrews, C. J. E. Haynes, M. E. Light, S. J. Moore, C. C. Tong, J. T. Davis, W. A. Harrell Jr., and P. A. Gale, *Chem. Sci.*, 2011, **2**, 256-260.

189. D. E. Gomez, L. Fabbrizzi, M. Licchelli, and E. Monzani, *Org. Biomol. Chem.*, 2005, **3**, 1495-1500.

190. R. Custelcean, *Chem. Commun.*, 2008, 295-307.

191. R. Custelcean, M. G. Gorbunova, and P. V. Bonnesen, *Chem. Eur. J.*, 2005, **11**, 1459-1466.

192. S. Grabowsky, T. Pfeuffer, W. Morgenroth, C. Paulmann, T. Schirmeister, and P. Luger, *Org. Biomol. Chem.*, 2008, **6**, 2295-2307.

193. A. Volkov, P. Macchi, L. J. Farrugia, C. Gatti, P. R. Mallinson, T. Richter, and T. Koritsanszky, 2006.

194. Y. A. Abramov, A. V. Volkov, and P. Coppens, *Chem. Phys. Lett.*, 1999, **311**, 81-86.

195. E. Espinosa, E. Molins, and C. Lecomte, *Phys. Rev. B*, 1997, **56**, 1820.

196. P. M. Dominiak and P. Coppens, *Acta Crystallogr. Sect. A*, 2006, **62**, 224-227.

197. R. Herbst-Irmer, J. Henn, J. J. Holstein, C. B. Hübschle, B. Dittrich, D. Stern, D. Kratzert, and D. Stalke, *J. Phys. Chem. A*, **117**, 633-641.

198. C. K. Johnson and H. A. Levy, *International Tables for X-ray Crystallography*, 1974.

199. S. Perveen, S. M. Abdul Hai, R. A. Khan, K. M. Khan, N. Afza, and T. B. Sarfaraz, *Synth. Commun.*, 2005, **35**, 1663-1674.

200. M. Miyahara, *Chem. Pharm. Bull.*, 1986, **34**, 1950–1960.

201. P. Job, *Ann. di Chim. Appl.*, 1928, **9**, 113–203.

202. S. J. Coles and P. A. Gale, *Chem. Sci.*, 2012, **3**, 683–689.

203. CrystalClear, 2011.

204. A. J. M. Duisenberg, L. M. J. Kroon-Batenburg, and A. M. M. Schreurs, *J. Appl. Crystallogr.*, 2003, **36**, 220–229.

205. R. Blessing, *J. Appl. Crystallogr.*, 1997, **30**, 421–426.

206. R. Herbst-Irmer, A. L. Spek, T. Schneider, M. Sawaya, and P. Muller, *Crystal Structure Refinement: A crystallographer's guide to Shelxl*, 2006, Oxford University Press, Oxford, UK.

207. M. J. Gutmann, 2005.

208. G. Sheldrick, *Acta Crystallogr. Sect. A*, 2008, **64**, 112–122.